

WRRRI Report No. 408

Environmental Conditions of the Animas and San Juan Watersheds Conference, Vol.II

Compendium Proceedings

2019 - 2020 - 2022- 2023 - 2024
Conferences



**Environmental Conditions
of the Animas and San Juan Watersheds Conference
Volume II**

NM WRI Report No. 408

**Conference Compendium Proceedings
2019, 2020, 2022, 2023, 2024**

Funding for this publication was provided through a Cooperative Agreement between the U.S. Environmental Protection Agency and the New Mexico Environment Department under MOA No. 17-667-1210-0002
(Long Term Monitoring Plan for the Gold King Mine Wastewater Spill)



Contents

Statements from 2019–2024 Conference Planning Committee Members.....	i
Papers Disclaimer - Creative Commons Licenses and Attributions.....	iii
Submitted Conference Proceedings Papers.....	1
Synoptic Analysis and WRF-Chem Model Simulation of Dust Events in the Southwestern United States.....	1
Planting Date and Plant Density Effects on Maize Growth, Yield and Water Use Efficiency.....	25
Database of Water Quality and Groundwater Elevation Within and Surrounding the Lee Acres Landfill, New Mexico, 1985–2020.....	43
Water Quality at Chaco Culture National Historical Park and the Potential Effects of Hydrocarbon Extraction.....	125
Studies of Animas River Watershed Bacterial Communities as Water Quality Indicators and their Relationship to the Aquatic Food Web.....	149
Deep Resistivity Geophysics of the San Juan–Silverton Caldera Complex, San Juan County, Colorado (USA).....	159
Groundwater Flow Model Investigation of the Vulnerability of Water Resources at Chaco Culture National Historical Park Related to Unconventional Oil and Gas Development.....	195
The Need for Constructing Endangered Fish Habitats that Conform to Climate-Driven Flow Changes in a Western U.S. River.....	239
Water-quality Change Following Remediation Using Structural Bulkheads in Abandoned Draining Mines, Upper Arkansas River and Upper Animas River, Colorado USA.....	257
Additional Resources.....	277
2019 Annual Animas and San Juan Watersheds Conference: Successes and Challenges from Headwaters to Lake Powell.....	279
Conference Photos.....	280
2019 Program.....	282
Oral & Poster Abstracts.....	285
Participant List.....	311
2020 Annual Animas and San Juan Watersheds Conference: Managing and Improving Water Quality in a Multijurisdictional Watershed.....	313
Conference Photos.....	314
2020 Program.....	316
Oral & Poster Abstracts.....	319
Participant List.....	339

**2022 Annual Animas and San Juan Watersheds Conference:
Collaborations, Perspectives, and Science Across the Watersheds.....347**

 Conference Photos.....348

 2022 Program..... 350

 Oral & Poster Abstracts.....355

 Participant List.....373

**2023 Annual Animas and San Juan Watersheds Conference:
Less Water: Planning, Adapting, and Resiliency.....379**

 Conference Photos.....380

 2023 Program..... 382

 Oral & Poster Abstracts.....389

 Participant List.....409

**2024 Annual Animas and San Juan Watersheds Conference:
Water Without Borders - Four Corners, Three Rivers.....413**

 Conference Photos.....414

 2024 Program..... 416

 Oral & Poster Abstracts.....421

 Participant List.....437

Statements from 2019–2024 Conference Planning Committee Members

Mark Sheely, NM WRRI

It has been a privilege to help coordinate the conferences from 2019 through 2024, first assisting longtime NM WRRI Senior Program Manager Cathy Ortega Klett for the 2019 conference, and then leading the coordination process myself after her retirement later that year. There was some appropriate timing in being introduced to the conference and the watersheds surrounding it when I was. I was only vaguely aware of the Gold King Mine Spill when I first started at NM WRRI in January 2019, having been a recent New Mexico transplant. My introduction to the watershed through planning meetings, background research, and then at the conference itself had me quickly learning about the wide array of watershed issues across this multi-jurisdictional watershed, including, but certainly not limited to, the Gold King Mine Spill. While the spill and subsequent response, monitoring, and remediation efforts had been the dominating topics of the first years of the conference, the leadership of an engaged planning committee highlighted the benefits of a conference program looking at the whole picture of the watershed across different disciplines and communities; different water uses and users.

Overall, the mission of these conferences was to provide a forum for scientists, agencies, local representatives, and community members to gather in order to both learn and educate each other with the conference presentations and field trips. The highlight of each conference is seeing presenters share information among their fellow colleagues and community members. Equally rewarding are the thoughtful questions and comments from community members. The 2020–2024 conferences have been offered free of charge and with a virtual attendance option in order to encourage more community attendance.

Like myself, there have been a number of new members to the planning committee who have stepped forward, along with those who have been involved with the conference planning since the first conference in 2016. I am incredibly grateful to every person who has served on the conference planning committee throughout my time at NM WRRI. I want to especially acknowledge the passion and driving force of Dennis McQuillan, who served on the planning committee from the very beginning of the conference until his retirement shortly after the 2019 conference. As Chief Scientist at New Mexico Environment Department (NMED), Dennis was closely involved with the response and monitoring efforts after the spill, recruiting top experts among state agencies and universities to develop and implement a long-term program to monitor the effects of the spill. Throughout his long career at NMED, “McQuillan developed new regulatory frameworks and programs aimed at advancing the health and safety of all New Mexicans through citizen engagement and education,” read a statement from the New Mexico Bureau of Geology and Mineral Resources, honoring him with their Earth Science Achievement Award. I was saddened to learn of his passing shortly before the 2023 conference. In honor of Dennis’ dedication to sharing accurate science-backed information with the public, I’m proud to have helped publish this compendium proceedings, which include nine papers, and a compilation of the program, photos, abstracts, and participant lists from each of the conferences.

I also wish to acknowledge the leadership of NM WRRI Director Sam Fernald and Senior Program Manager Carolina Mijares. Special thanks are given to staff members Jeanette Torres and Kylie Arrieta for their many hours of work to publish these proceedings. The conferences themselves would not have been possible without the efforts of NM WRRI staff and students, particularly NM WRRI Administrative Assistant MaryBeth Ewing.

Johanna Blake, U.S. Geological Survey

The Animas River and San Juan River Watersheds Conference has provided an excellent opportunity over the years for scientists, students, regulators, and community members to share knowledge about scientific and community efforts in these watersheds. The scientific foci in the watersheds have included biogeochemical water quality and sediment quality, sediment concentrations in water, microbial studies, and the effects contaminated water has on plants. Efforts at monitoring and scientific investigations since the Gold King Mine release in 2015 have identified further questions in the Animas and San Juan Rivers that go beyond the release of metals from a single spill. For example, the Navajo Nation EPA has identified areas of elevated metal concentrations along the San Juan River not associated with the Animas River. In addition, the conference has helped to build new collaborations that continue to move forward in understanding issues in these watersheds. The Animas and San Juan Watersheds Conference has been an important contributor to furthering ongoing collaboration and understanding these two important watersheds.

Kevin A. Lombard, New Mexico State University

Northwest New Mexico has 150,000 irrigated acres held within three watersheds: the Animas, La Plata, and San Juan. These river systems irrigate a diverse array of crops and nurture livestock, supporting the diverse livelihoods and cultures of gardeners, farmers and ranchers of all scale, from backyard to the largest contiguous farm in North America, the Navajo Agricultural Products Industry (NAPI), at over 70,000 acres. The Gold King Mine Spill of 2015 was a turning point in interagency cooperation in northwest New Mexico. The unprecedented collaboration between multiple agencies, colleges and universities, state and tribal entities, citizen scientists and the body of research held herein examining the Animas River, post spill, is helping to broaden our understanding of the greater San Juan River watershed and the interconnectivity of upstream and downstream users.

Elizabeth Stuffings, New Mexico Environment Department

The Animas and San Juan Watersheds Conference has facilitated the exchange of data and perspectives among four states, three EPA regions, three Tribes, numerous local and municipal agencies, and the public. The conference is a unique opportunity for interested parties to gather locally and discuss successes and challenges within the San Juan Basin. Important discussions have centered around water security, planning for an uncertain future, leveraging resources, native food sovereignty, and industrial and mining impact management. This discourse has fostered partnerships and collaborations that continue to tackle issues within the watershed. The conference provides a wonderful avenue for understanding the complex dynamics of the Animas and San Juan Rivers and strengthening the connections that exist throughout the watersheds.

Papers Disclaimer

Creative Commons Licenses and Attributions

The New Mexico Water Resources Research Institute has minimally edited the formatting of all submitted papers (e.g., figure positions, headers, font colors, styling, etc.) to conform to the design elements of this publication.

1

Synoptic Analysis and WRF-Chem Model Simulation of Dust Events in the Southwestern United States

© 2024 by Saroj Dhital, Nicholas P. Webb, Adrian Chappell, Michael L. Kaplan, Travis W. Nauman, Gayle Tyree, Michael C. Duniway, Brandon Edwards, Sandra L. LeGrand, Theodore W. Letcher, S. McKenzie Skiles, Patrick Naple, Nathaniel W. Chaney, and Jiaxuan Cai
<https://doi.org/10.1029/2023JD040650>

This work was published in the *Journal of Geophysical Research: Atmospheres* (Volume 129, Issue 13, ISSN 2169-897X) in July 2024, and is licensed under [CC BY 4.0](#)
Provisions of this license allow for this work to be:
Shared, copied and redistributed in any medium or format for any purpose, even commercially.
Adapted, remixed, transformed, and built upon for any purpose, even commercially.

2

Planting Date and Plant Density Effects on Maize Growth, Yield and Water Use Efficiency

© 2022 by Koffi Djaman, Samuel Allen, Dorlote S. Djaman, Komlan Koudahe, Suat Irmak, Naveen Puppala, Murali K. Darapuneni, and Sangamesh V. Angadi
<https://doi.org/10.1016/j.envc.2021.100417>

This work was published in *Environmental Challenges* (Volume 6, 100417, ISSN 2667-0100) in January 2022, and is licensed under [CC BY-NC-ND 4.0](#)
Provisions of this license allow for this work to be:
Shared, copied and redistributed in any medium or format with required adherence to attribution, non-commercial, and no derivatives restrictions.

3

Database of Water Quality and Groundwater Elevation Within and Surrounding the Lee Acres Landfill, New Mexico, 1985–2020

© 2022 by Erin L. Gray and Christina L. Ferguson
<https://doi.org/10.3133/dr1154>

This work was published in the *United States Geological Survey Numbered Series, U.S. Geological Survey Data Report 1154* (80 p. ISSN: 2771-9448 (online)) in 2022, and is in the public domain.

4

Water Quality at Chaco Culture National Historical Park and the Potential Effects of Hydrocarbon Extraction

© 2023 by Benjamin S. Linhoff, Kimberly R. Beisner, Andrew G. Hunt, and Zachary M. Shephard
<https://doi.org/10.1016/j.ejrh.2023.101430>

This work was published in the *Journal of Hydrology: Regional Studies*

(Volume 47, 101430, ISSN 2214-5818) in June 2023, and is licensed under [CC BY-NC-ND 4.0](https://creativecommons.org/licenses/by-nc-nd/4.0/)

Provisions of this license allow for this work to be:

Shared, copied and redistributed in any medium or format with required adherence to attribution, non-commercial, and no derivatives restrictions.

5

Studies of Animas River Watershed Bacterial Communities as Water Quality Indicators and Their Relationship to the Aquatic Food Web

© 2024 by Jennifer L. Lowell, Holly D. Vandever, and April Sandman

6

Deep Resistivity Geophysics of the San Juan–Silverton Caldera Complex, San Juan County, Colorado (USA)

© 2024 by Brian D. Rodriguez, Douglas B. Yager, Eric D. Anderson, Bennett E. Hoogenboom, Robert L. Runkel, Bruce D. Smith, and Maria Deszcz-Pan
<https://doi.org/10.1130/GES02550.1>

This work was published in the journal *Geosphere*, a publication of the Geological Society of America (Volume 20, Number 3) in April 2024, and is licensed under [CC BY-NC-4.0](https://creativecommons.org/licenses/by-nc/4.0/)

Provisions of this license allow for this work to be:

Shared, copied and redistributed in any medium or format, adapted, remixed, transformed, and built upon.

7

Groundwater Flow Model Investigation of the Vulnerability of Water Resources at Chaco Culture National Historical Park Related to Unconventional Oil and Gas Development

© 2023 by Zachary M. Shephard, Andre B. Ritchie, Benjamin S. Linhoff, and John J. Lunzer
<https://doi.org/10.3133/sir20235097>

This work was published in the *United States Geological Survey Numbered Series, U.S. Geological Survey Data Report 2023-5097* (39 p. ISSN 2328-0328 (online)) in 2023, and is in the public domain.

8

The Need for Constructing Endangered Fish Habitats that Conform to Climate-Driven Flow Changes in a Western U.S. River

© 2023 by Richard. A Valdez, Colleen Cunningham, Ali Effati, and Deborah L. Freeman
<https://doi.org/10.1111/1752-1688.13114>

This work was published in the *Journal of the American Water Resources Association (JAWRA)* (Volume 59, Issue 5, No. JAWR-22-0052-P) in February 2023, and is licensed under [CC BY-4.0](#)
Provisions of this license allow for this work to be:
Shared, copied and redistributed in any medium or format for any purpose, even commercially.
Adapted, remixed, transformed, and built upon for any purpose, even commercially.

9

Water-quality Change Following Remediation Using Structural Bulkheads in Abandoned Draining Mines, Upper Arkansas River and Upper Animas River, Colorado USA

© 2021 by Katherine Walton-Day, M. Alisa Mast, and Robert L. Runkel
<https://doi.org/10.1016/j.apgeochem.2021.104872>

This work was published in the *Journal Applied Geochemistry*, a journal of the International Association of Geochemistry (Volume 127,104872, ISSN 0883-2927) in April 2021, and is licensed under [CC BY-4.0](#)
Provisions of this license allow for this work to be:
Shared, copied and redistributed in any medium or format for any purpose, even commercially.
Adapted, remixed, transformed, and built upon for any purpose, even commercially.

Synoptic Analysis and WRF-Chem Model Simulation of Dust Events in the Southwestern United States

Saroj Dhital¹, Nicholas P. Webb¹, Brandon Edwards¹

¹USDA-ARS Jornada Experimental Range, Las Cruces, NM, USA

Adrian Chappell²

²School of Earth and Environmental Sciences, Cardiff University, Cardiff, UK

Michael L. Kaplan³

³Division of Atmospheric Sciences, Desert Research Institute, Reno, NV, USA

Travis W. Nauman⁴

⁴USDA-NRCS National Soil Survey Center, Lincoln, NE, USA

Gayle Tyree⁵, Michael C. Duniway⁵

⁵U.S. Geological Survey, Southwest Biological Science Center, Moab,
UT, USA

Sandra L. LeGrand⁶

⁶U.S. Army Engineer Research and Development Center,
Geospatial Research Laboratory, Alexandria, VA, USA

Theodore W. Letcher⁷

⁷U.S. Army Engineer Research and Development Center, Cold Regions Research
and Engineering Laboratory, Hanover, NH, USA

S. McKenzie Skiles⁸, Patrick Naple⁸

⁸Department of Geography, University of Utah, Salt Lake City, UT, USA

Nathaniel W. Chaney⁹, Jiaxuan Cai⁹

⁹Department of Civil and Environmental Engineering, Duke University,
Durham, NC, USA

ABSTRACT

Dust transported from rangelands of the Southwestern United States (US) to mountain snowpack in the Upper Colorado River Basin during spring (March–May) forces earlier and faster snowmelt, which creates problems for water resources and agriculture. To better understand the drivers of dust events, we investigated large-scale meteorology responsible for organizing two Southwest US dust events from two different dominant geographic locations: (a) the Colorado Plateau and (b) the northern Chihuahuan Desert. High-resolution Weather Research and Forecasting coupled with Chemistry model (WRF-Chem) simulations with the Air Force Weather Agency dust emission scheme incorporating a MODIS albedo-based drag-partition was used to explore land surface-atmosphere interactions driving two dust events. We identified commonalities in their meteorological setups. The meteorological analyses revealed that Polar and Sub-tropical jet stream interaction was a common upper-level meteorological feature before each of the two dust events. When the two jet streams merged, a strong northeast-directed pressure gradient upstream and over the source areas resulted in strong near-surface winds, which lifted available dust into the atmosphere. Concurrently, a strong mid-tropospheric flow developed over the dust source areas, which transported dust to the San Juan Mountains and southern Colorado snowpack. The WRF-Chem simulations reproduced both dust events, indicating that the simulations represented the dust sources that contributed to dust-on-snow events reasonably well. The representativeness of the simulated dust emission and transport in different geographic and meteorological conditions with our use of albedo-based drag partition provides a basis for additional dust-on-snow simulations to assess the hydrologic impact in the Southwest US.

PLAIN LANGUAGE SUMMARY

Dust transported from rangelands of the Southwestern United States (US) to the mountain snowpack in the Upper Colorado River Basin during spring (March–May) is a growing problem for water resources and agriculture. Understanding the drivers of dust events is essential to better forecast the possible impact of dust on water resources. We investigated the weather conditions that led to two dust events originating from the Colorado Plateau and northern Chihuahuan Desert. We also performed computer simulations with an improved dust emission model to explore the influence of vegetation on the susceptibility of landscapes to wind erosion during dust events. Our meteorological analysis revealed commonalities in the upper-level meteorology before dust event formation and provided valuable insights into where and when high-impact dust events may occur. However, further investigation is needed to generalize the impact of jet stream interaction on dust events' intensity. Our simulations represented the dust sources reasonably well by using an improved dust emission model. The improved dust emission and transport simulation under different meteorological and geographical conditions provided a basis for future dust-on-snow simulations to assess the hydrological impact in the Southwestern US.

1. INTRODUCTION

In spring (March–May), dust events across the Southwestern United States (hereafter Southwest) bring deleterious impacts on human health by degrading air quality (Achakulwisut et al., 2017; Hand et al., 2017, 2019); regional transportation by reducing visibility (Tong et al., 2023); ecosystem services and agricultural production by losing topsoil and associated nutrients and soil carbon (Duniway et al., 2019; Webb et al., 2017); and water resources by impacting dust radiative forcing of snow melt (Rahimi et al., 2020; Skiles & Painter, 2017). Dust transported from regionally active source areas affects mountain snowpack in the Upper Colorado River Basin (Skiles et al., 2015). Deposited dust changes snow properties (e.g., Skiles & Painter, 2018), accelerates snow melt (e.g., Skiles et al., 2015), and alters the hydrological cycle in the greater Colorado River Basin (CRB) (e.g., Painter et al., 2010) and Rio Grande Basin (RGB), the main water resources for more than 40 million people across the Southwest. Agriculture in the CRB generates US\$60 billion each year that is dependent on 90% of water resources in the basin (Thiel, 2013), and the RGB supports a US \$1 billion agricultural sector dependent on 85% of the basin's water resources annually (Kort, 2013), with both basins being important international sources of irrigation water. Therefore, accurately predicting dust events

is essential for forecasting the impacts of dust on the hydrological cycle for land and water management, agriculture, and livelihoods.

The Weather Research and Forecasting model (WRF; Skamarock et al., 2019) and WRF with Chemistry (WRF-Chem; Grell et al., 2005) are numerical models that simulate meteorological processes and atmospheric chemistry. WRF-Chem has a long history of being used as a tool to support studies of dust emission and atmospheric transport (e.g., Dhital et al., 2021; Parajuli et al., 2019; Solomos et al., 2018; Zhao et al., 2010). Convection-permitting WRF-Chem model simulations have been increasingly used to investigate the role of meteorology in organizing strong dust events and to assess impacts of transported dust (e.g., Adhikari & Mejia, 2022; Dhital et al., 2020, 2021; Evan et al., 2022; LeGrand et al., 2023; Rahimi et al., 2020; Solomos et al., 2018). These higher-resolution simulations are useful because they can resolve the mesoscale weather features and complex terrain that control near-surface winds over dust sources (e.g., Evan et al., 2022; LeGrand et al., 2023; Solomos et al., 2018). WRF-Chem has also been used as a tool to study the effect of dust on snow in the CRB (Oaida et al., 2015).

Currently, three dust emission schemes can be employed in the WRF-Chem model to simulate dust emission: the Goddard Global Ozone Chemistry Aerosol Radiation and Transport (GOCART); the Air Force Weather Agency (AFWA); and the University of Cologne scheme (UoC; see LeGrand et al., 2019) for a full description and baseline comparisons). A requirement for these dust emission schemes to accurately predict dust events impacting the CRB and RGB is to represent surface roughness, especially vegetation, and its spatiotemporal change. All three dust emission schemes, as implemented in WRF-Chem, incorporate a static mask designed to block dust emission from vegetated areas derived from a relatively coarse, 1-degree resolution land cover data set (LeGrand et al., 2019). The AFWA dust emission scheme further restricts dust emission from areas where the aerodynamic roughness length is > 20 cm. This setting effectively limits dust emission in the AFWA scheme to barren, cropland, savanna, grassland, or shrubland areas. The UoC scheme is the only dust emission scheme in WRF-Chem that includes some form of dynamic roughness effects on dust emission by using a form of the drag partition scheme developed by Raupach (1992). However, the UoC module estimates roughness conditions from monthly greenness fraction climatology data sets, which can lead to poor simulation outcomes under variable climate regimes (e.g., LeGrand et al., 2019).

Recently, LeGrand et al. (2023) incorporated the albedo-based drag partition (Chappell & Webb, 2016; hereafter CW16) into the AFWA dust emission scheme to represent the effects of vegetation and other non-erodible roughness elements on the wind shear velocity that drives dust emission. The albedo-based approach, which partitions drag of different scales of roughness (e.g., vegetation, rocks), may be implemented using Moderate Resolution Imaging Spectroradiometer (MODIS) land surface albedo data and either a bidirectional reflectance distribution function (BRDF) parameter or nadir BRDF adjusted reflectance (Chappell et al., 2018). LeGrand et al. (2023) demonstrated significant improvements in a simulation with the CW16 model over the original AFWA scheme for a Southwestern summertime convective dust event.

Synoptically-forced spring dust events are a common type of dust event in the Southwest and are thought to be the main driver of dust-on-snow events (Lei & Wang, 2014). We investigated large-scale meteorological conditions of two spring-season Southwest dust events originating in the two dominant, and geographically different, dust source areas of the Southwest. We then simulated the dust events using the WRF-Chem model following a similar approach to LeGrand et al. (2023) with the objective being to resolve the land surface-atmosphere interactions producing dust and how dust source area dynamics may be influencing dust emissions across the Southwest. Although the primary focus of this study is the numerical simulation of dust events, we purposefully added large-scale meteorological analyses to investigate upper-level meteorological precursors that drive dust events.

2. BRIEF DESCRIPTION OF DUST EVENTS

We simulated two spring dust events: (a) April 16–17, 2013 (A13) over the Colorado Plateau (CP) and (b) March 23–24, 2017 (M17) over the northern Chihuahuan Desert (Figure 1). During the A13 event, dust from the southwest CP was transported to the San Juan Mountains in Colorado, which resulted in the second strongest dust loading of 4.58 gm^{-2} in the 2013 water year (October–September) measured at the Senator Beck

Basin monitoring site (Skiles et al., 2015). A southwest-northeast oriented dust plume was present over the southwest CP on April 16th (Figure 1a). Around 1800 UTC on the 16th, the Meteorological Terminal Aviation Routine Weather Report (METAR) station at Cortez, Colorado (METAR, 2022), reported a visibility less than 10 km with a southwesterly wind speed of greater than 15 ms^{-1} (Figure S1 in Supporting Information S1). For two more hours, the southwesterly wind continued with a wind speed of $>10 \text{ ms}^{-1}$. Around 2000 UTC, visibility was reduced to $<2 \text{ km}$. Another METAR station at Durango, Colorado (METAR, 2022) also reported a reduction in visibility ($<10 \text{ km}$) with a southwesterly wind speed of $>10 \text{ ms}^{-1}$ around 1800 UTC.

In the M17 case, dust was primarily emitted from the northern Chihuahuan Desert, near the United States-Mexico border. A southwest-northeast-oriented, thick dust plume formed over El Paso, Texas (Figure 1b). The El Paso airport METAR station (METAR, 2022) reported visibility of $<10 \text{ km}$ $\sim 1800 \text{ UTC}$ on March 23 with a wind speed of 10 ms^{-1} (Figure S1 in Supporting Information S1). During 2000–2100 UTC, the visibility was reduced to $<2 \text{ km}$ with a west-southwesterly wind speed of $>15 \text{ ms}^{-1}$. Later, the dust plume widened and was advected poleward (<https://www.weather.gov/lub/events-2017-20170323-wind>).

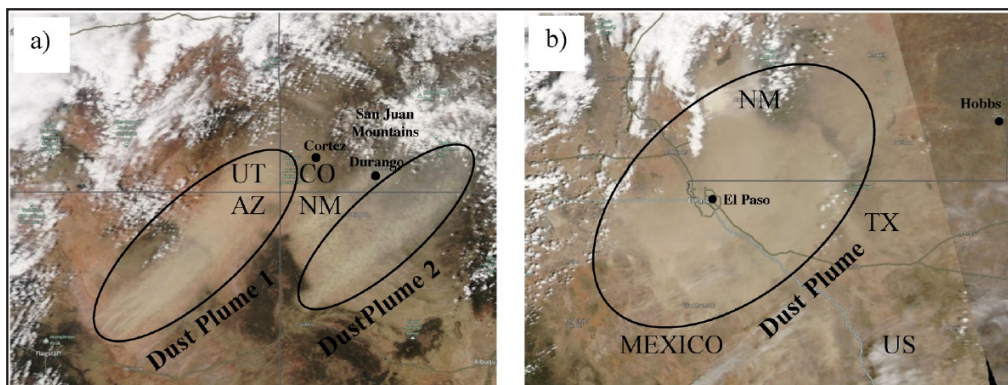


Figure 1. True-color image from MODIS-Aqua (a) 2013-04-16 and (b) 2017-03-23. Dust clouds appear brownish gray. Images were obtained from the National Aeronautics and Space Administration (NASA) Worldview platform (NASA Worldview, 2022).

3. DATA AND METHODOLOGY

3.1. Reanalysis Data Set

The fifth-generation European Center for Medium-Range Weather Forecasting, hourly, (0.25° horizontal pixel resolution) reanalysis data set ERA5 (Hersbach et al., 2020a, 2020b) was used to describe the large-scale meteorological features responsible for organization of the two dust events. ERA5 provides an hourly data set starting from 1979. We used charts of horizontal wind, and geopotential height at the 250 hPa and 600 hPa levels, to describe the upper- and mid-level dynamics. For near-surface meteorological interpretations, we used charts of mean sea level pressure (MSLP) and 10 m wind made from ERA5.

3.2. Model Description and Experimental Design

The WRF-Chem (version 4.2) (Grell et al., 2005) simulations were performed using a one-way nesting of three domains. The coarsest and outer domain has a horizontal of 18 km and subsequent additional nested domains have 6 and 2 km. The 18 km parent domain covered most of the Southwestern states (Figure 2). The atmosphere was divided into 41 vertical levels with the top of the atmosphere set at 50 hPa. The nested configuration used one-way forcing such that the inner domains did not feedback into their respective parent domains. The model was initialized using the ERA5 reanalysis data set, and the lateral boundaries of the parent domain were updated hourly. Both simulations were run for 42 hr. The A13 simulation started at 1200 UTC on 15 April 2013, and ended at 0600 UTC on 17 April 2013, while the M17 simulation started at 1200 UTC on 22 March 2017, and ended at 0600 UTC on 24 March 2017. The 2 km nested variables were saved every 30 min and used for all analyses presented here.

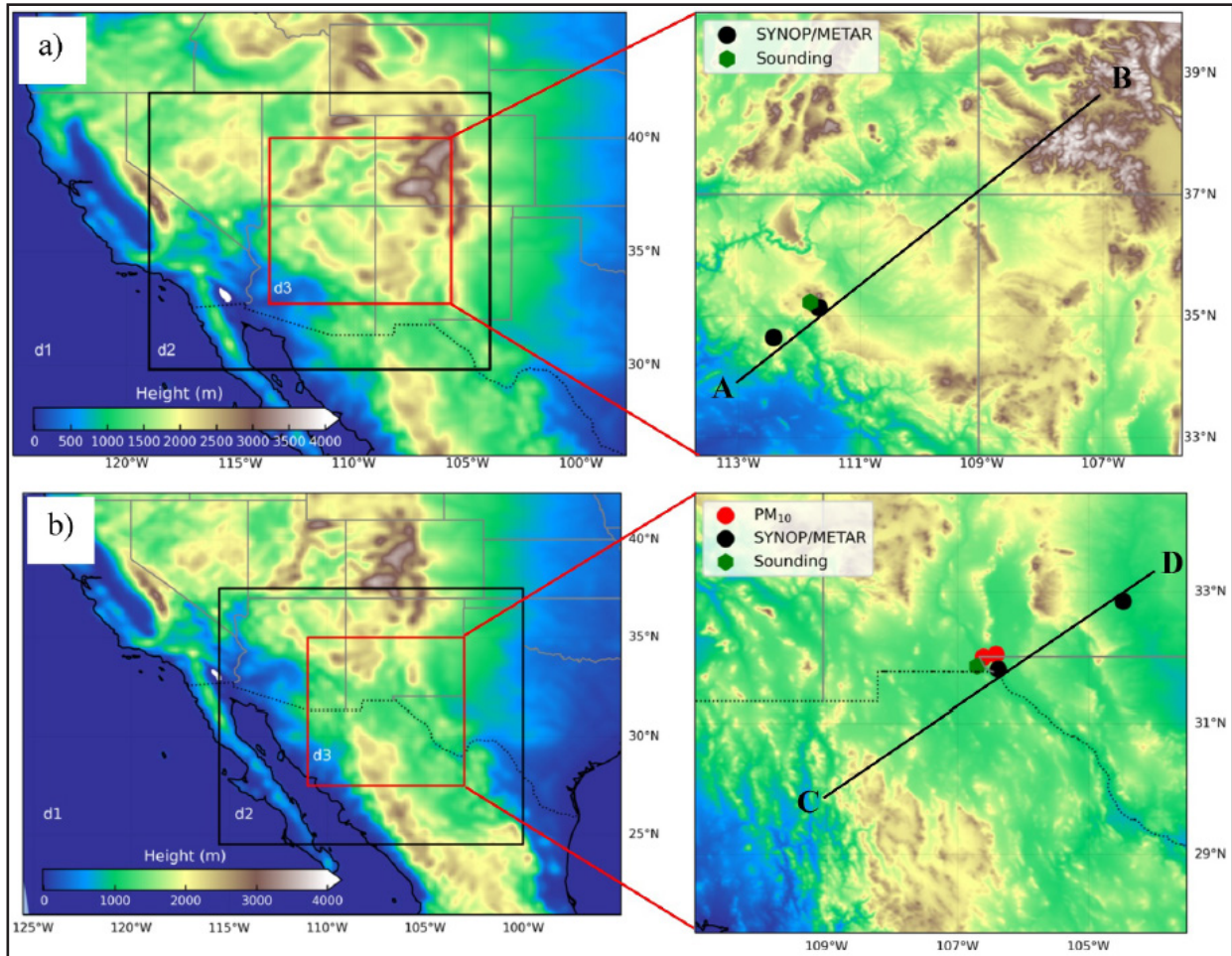


Figure 2. WRF-Chem simulation domains with available observational network for (a) A13 and (b) M17 dust events. The line AB (-113°W, 34°N to -107°W, 38.5°N) in Figure 1a and CD (-109°W, 30°N to -104.5°W, 33.5°N) in Figure 1b are for vertical cross-section analysis for the A13 and M17 cases, respectively.

3.2.1. Model Physics and Chemistry Parameterizations

The physics and chemistry parameterizations used in our simulations are summarized in Table 1. The cumulus parameterization was used only on the 18 km domain and follows the new Grell scheme (Grell & Dévényi, 2002). The inner nested domains (6 and 2 km) allowed convection to develop explicitly. All other physics and chemistry schemes used are identical across each domain. More details on the physical parameterizations can be found at https://www2.mmm.ucar.edu/wrf/users/physics/phys_references.html.

The chemistry option included was the GOCART aerosol module without ozone chemistry (Ginoux et al., 2001). The dust emission scheme followed the AFWA dust emission scheme (LeGrand et al., 2019) with the CW16 MODIS albedo-based drag partition which describes the aerodynamic roughness changing over space (500 m pixels) and over time (daily). A summary of the implementation of the CW16 drag partition in the AFWA dust emission scheme is presented in Section 3.2.2.

To compare the simulated dust evolution with the observation, we used simulated aerosol optical depth (AOD) at 550 nm and PM_{10} . We calculated AOD by vertically integrating extinction coefficients for the whole atmospheric column (see appendix C in Ukhov et al., 2021). PM_{10} is calculated using the following equation:

$$PM_{10} = \rho \cdot (\text{Dust}_1 + \text{Dust}_2 + \text{Dust}_3 + \text{Dust}_4.d_{10} + \text{SEAS}_1 + \text{SEAS}_2 + \text{SEAS}_3) \quad (1)$$

Where p is dry air density (kgm^{-3}), d_{10} ($=0.373$) is the mapping coefficient, and DUST_{1-4} and SEAS_{1-3} are mixing ratios (μgkg^{-1}) of the dust in the first four bins and sea-salt in the first three bins, respectively.

Table 1. Physics and chemistry schemes used in the WRF-chem model.

WRF-Chem		v4.2 (Grell et al., 2005)	
Simulation domains		3	
Horizontal resolutions		18 km, 6 km, and 2 km	
Vertical levels		41	
Initial and boundary conditions		ERA5 (Hersbach et al., 2020a, 2020b)	
Parameterizations	Scheme	Namelist variable	Option
Physics			
Microphysics	Thompson (Thompson et al., 2008)	mp_physics	8
Radiation (long and shortwave)	RRTMG (Iacono et al., 2008)	ra_lw(sw)_physics	4
Surface model	Noah (Ek et al., 2003)	sf_surface_physics	2
Surface layer	MYNN (Nakanishi & Niino, 2004a, 2004b)	sf_sfclay_physics	5
Planetary boundary layer	MYNN2.5 level (Nakanishi & Niino, 2004a, 2004b)	bl_pbl_physics	5
CumulusGrell 3D (Grell & Dévényi, 2002) cu_physics 5 parameterization (D01 only)			
Chemistry			
Chemistry	GOCART simple/no ozone chemistry	chem_opt	300
Dust emission	AFWA (LeGrand et al., 2019)	dust_opt	3
Aerosol Radiative feedbacks	Off	aer_ra_feedback	0
Aerosol optics	Maxwell approximation (Bohren & Huffman, 2007)	aer_op_opt	2

3.2.2. Implementation of Drag Partition in AFWA

The AFWA dust emission module, as implemented in WRF-Chem, does not represent dynamic roughness effects on dust emission. Instead, the default AFWA scheme incorporates a static mask designed to block dust emission from vegetated areas derived from a relatively coarse, 1-degree resolution land cover data set and further restricts dust emission from areas where the aerodynamic roughness length is >20 cm (LeGrand et al., 2019). This setting essentially limits dust emission in the AFWA scheme to areas classified by the model as barren, cropland, savanna, grassland, or shrubland.

For this study, we used a version of AFWA dust emission module configured with the CW16 drag partition described by LeGrand et al. (2023). Specifically, we used the ALT3 configuration of LeGrand et al. (2023), which removes all forms of vegetation masking built into the dust emission code. The ALT3 configuration also eliminates the influence of a dust source strength parameter that functions as a spatially varying available sediment supply tuning factor. Removing this source strength parameter effectively causes the emission scheme to assume that all areas are equally erodible.

In the base version of the AFWA dust scheme, saltation flux $Q(D_{s,p})$ ($\text{gcm}^{-1}\text{s}^{-1}$) is calculated following:

$$Q(D_{s,p}) = \begin{cases} C \frac{\rho_a}{g} u_*^3 \left(1 - \frac{u_{*ts}(D_{s,p}, \theta)^2}{u_*^2}\right) \left(1 + \frac{u_{*ts}(D_{s,p}, \theta)}{u_*}\right), & u_* > u_{*ts}(D_{s,p}, \theta) \\ 0, & u_* \leq u_{*ts}(D_{s,p}, \theta), \end{cases} \quad (2)$$

where $C = 1$ is a proportionality constant, ρ_a is air density at the lowest model level (g cm^{-3}), g is the acceleration due to gravity (cm s^{-2}), u_* is total wind friction velocity (or shear velocity) (cm s^{-1}), $u_{*ts}(D_{s,p}, \theta) = u_{*ts}(D_{s,p}) * f(\theta)$ is moisture-corrected entrainment threshold friction velocity (cms^{-1}), $D_{s,p}$ is effective diameter (μm) and $f(\theta)$ is the soil moisture correction function (Fécan et al., 1999). The entrainment threshold is fixed

over space to soil classes and varies over time only as a function of soil moisture. The approach is momentum limited that is, when there is sufficient momentum to exceed the threshold there is transport of sediment. Like other dust models, this approach assumes that there is an infinite supply of dry, loose erodible material available for transport given sufficient momentum. Following drag partition theory, the total wind shear velocity (u_*) is divided into wind shear velocity acting on roughness elements such as vegetation and rocks (u_{r*}) and the exposed soil surface (u_{s*}) following:

$$u_* = u_{r*} + u_{s*} \quad (3)$$

Since dust mobilization at the soil surface depends on u_{s*} rather than u_* (Chappell & Webb, 2016; Webb et al., 2020), the saltation flux $Q(D_{s,p})$ depends on u_{s*} and its corresponding entrainment threshold (u_{*ts}) value:

$$Q(D_{s,p}) = \begin{cases} C \frac{\rho_a}{g} u_{s*}^3 \left(1 - \frac{u_{*ts}(D_{s,p}, \theta)^2}{u_{s*}^2}\right) \left(1 + \frac{u_{*ts}(D_{s,p}, \theta)}{u_{s*}}\right), & u_{s*} > u_{*ts}(D_{s,p}, \theta) \\ 0, & u_{s*} \leq u_{*ts}(D_{s,p}, \theta) \end{cases} \quad (4)$$

The CW16 provides a method to directly parameterize u_{s*} based on the MODIS daily albedo product (Collection 6, MCD43A1; Schaaf & Wang, 2021). With this product, we calculated u_{s*}/U_h following:

$$\frac{u_{s*}}{U_h} = 0.0311 \left(e^{\frac{-w_{ns}^{1.131}}{0.016}} \right) + 0.007, \quad (5)$$

where w_{ns} was obtained from MODIS based on sheltering being equivalent to shadow (Raupach & Lu, 2004) cast by roughness following Chappell and Webb (2016), Chappell et al. (2018) and LeGrand et al. (2023), and U_h is the wind velocity at a given height (h) (ms^{-1})—used here at 10 m height above ground level (U_{10}). Finally, the friction velocity at the soil surface (u_{s*}) was obtained by multiplying u_{s*}/U_h by 10 m wind speed as in Equation 5 (above).

$$u_{s*} = U_{10m} * \left(\frac{u_{s*}}{U_h} \right) \quad (6)$$

Where U_{10m} is the 10 m wind speed. Detailed descriptions of the MODIS albedo-based drag partition approach (Chappell et al., 2018; Chappell & Webb, 2016) and its implementation in the AFWA dust emission scheme are provided in Michaels et al. (2022).

3.3. Observational Data Sets

To describe the evolution of the dust events and evaluate the WRF-Chem simulations, we used wind and visibility data sets from different METAR stations (METAR, 2022) distributed across the study area (Figure 2). Additionally, we used radiosonde data (Sounding, 2022) collected at 12-hr intervals from the weather balloons released at Flagstaff, Arizona, and Santa Teresa, New Mexico stations to evaluate model performance throughout the atmospheric column. To describe the dust evolution and model-dependent variable accuracy, we also used PM_{10} concentration and AOD data from surface observations and satellite retrievals at 10 km spatial resolution. The AOD data were obtained from MODIS at 550 nm (combined Dark Target and Deep Blue algorithm) (MODIS, 2022). The PM_{10} hourly data were obtained from the US Environmental Protection Agency (EPA) (PM_{10} , 2022). To describe the dust source areas within the WRF-Chem model, we assessed the vegetation conditions using plant functional group annual fractional cover estimated by the Rangeland Analysis Platform (RAP) including cover of annual forbs and grasses (AFG), perennial forbs and grasses (PFG), and shrubs (SHR) (Jones et al., 2018). As the RAP plant functional group cover estimates are modeled using historical Landsat satellite, gridded meteorological data and field data collected across the western US throughout the summer growing season, we used estimates from the years preceding the case study dust events (which occurred in spring 2013 and 2017) as those data would provide

better indicators of ground cover than estimates produced from field measurements collected in the same year but following the dust events.

4. RESULTS

4.1. Large-Scale Meteorological Conditions for Organization of the Dust Events

The large-scale meteorological description of these dust events is focused on the evolution of the Polar jet stream (PJ) and Sub-tropical jet stream (STJ), mid-tropospheric and low-level flow as both dust events were linked baroclinic mid-latitude cyclones. Figures 3 and 4 show the evolution of the 250 hPa (hereafter upper-level) and 600 hPa (hereafter mid-level) horizontal winds and geopotential height, MSLP, and 10 m wind for the A13 and M17 dust events, respectively.

In the A13 dust events, at 1800 UTC on the 15th, the PJ streak core was located over the Sierra Nevada Mountains and the STJ streak core was located over the subtropical Eastern Pacific (Figure 3a). The mid-level flow over the CP was weak (Figure 3b). As time progressed, the PJ and STJ streaks started to merge (Figure S2 in Supporting Information S1) and completed their merger at 1800 UTC on the 16th (Figure 3d). While merging, the PJ propagated toward the equator and the upper-level trough was located over southern California, while the STJ streak core propagated northeastward and was located over Baja California. When the PJ and STJ merged, strong mid-level southwesterly winds developed over the southwestern CP (northeastern Arizona), where dust was emitted (Figure 3e). For the next 12 hr, the unified PJ and STJ resulted in a strong jet streak over Mexico, southern California, and southern Arizona (Figure 3g). The intensification of the unified jet streak represents the culmination of an acceleration process evident earlier in the STJ streak. The mid-level southwesterly wind over the lower CP also intensified just below the left exit region of the unified jet streak core (Figure 3h). Additionally, a uniform, strong, southwesterly, mid-level sub-synoptic jet or “jetlet” extends from southwest Arizona to the CP.

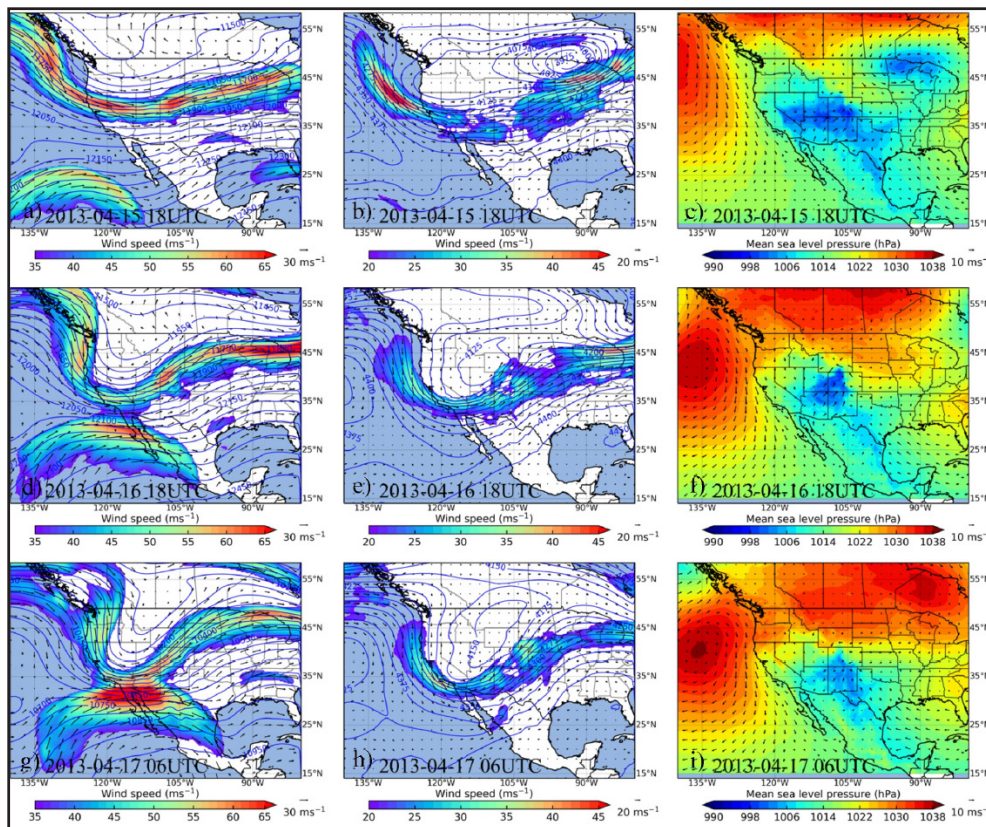


Figure 3. 36-hr evolution of (left column) 250 hPa horizontal wind isotachs (ms^{-1}) and geopotential height (m), (middle column) 600 hPa horizontal wind isotachs (ms^{-1}) and geopotential height (m), and (right column) 10 m wind barbs (ms^{-1}), and mean sea level pressure (hPa) for the A13 dust events. Meteorological fields are from ERA5.

At the surface, at 1800 UTC on the 15th, a surface cyclone was located over the CP and Great Basin with relatively strong southwesterly 10 m winds over Arizona and New Mexico compared to their surrounding (Figure 3c). Twenty-four hours later, at 1800 UTC on the 16th, when the PJ and STJ streaks unified, the cyclone center was located over the CP (Figure 3f). At this time, jet streak merging, surface minimum pressure over the CP, and mid-level wind maxima just over the CP occurred concurrently (Figures 3d–3f). The strong southwesterly near-surface wind caused by the strong pressure gradient between the intensifying surface cyclone over the CP and its upstream region lifted dust from the southwestern CP (Figures 3c and 3f and Figure S3 in Supporting Information S1). As the low-pressure system weakened and moved east, the near-surface southwesterly flow weakened, and dust emission ceased. However, strong mid-level flow persisted over the CP, enabling lofted dust to be transported to the San Juan Mountains.

In the M17 case, at 1800 UTC on the 22nd the PJ and STJ streaks started to merge over Baja California (Figure 4a). This merger is similar to the merger seen in the A13 case. However, in contrast to the A13 event, the mid-level wind over the CP was relatively weak at the time of the jet merger (Figure 4b). Twelve hours later, at 0600 UTC on the 23rd, as the PJ and STJ streaks continued to merge, a strong jet core developed over Baja California and the United States-Mexico border (Figure 4d). With this merger, southwesterly mid-level flow intensified over the CP and upstream over southwestern Arizona (Figure 4e). After 12 hr, at 1800 UTC on the 23rd, the unified jet core intensified further and was located over the northern Chihuahuan Desert (Figure 4g). The mid-level wind intensified in a similar manner and was located just below the exit region on the poleward side of the unified jet core (Figure 4h). A southwesterly-northeasterly oriented elongated band of mid-level winds formed over the northern Chihuahuan Desert.

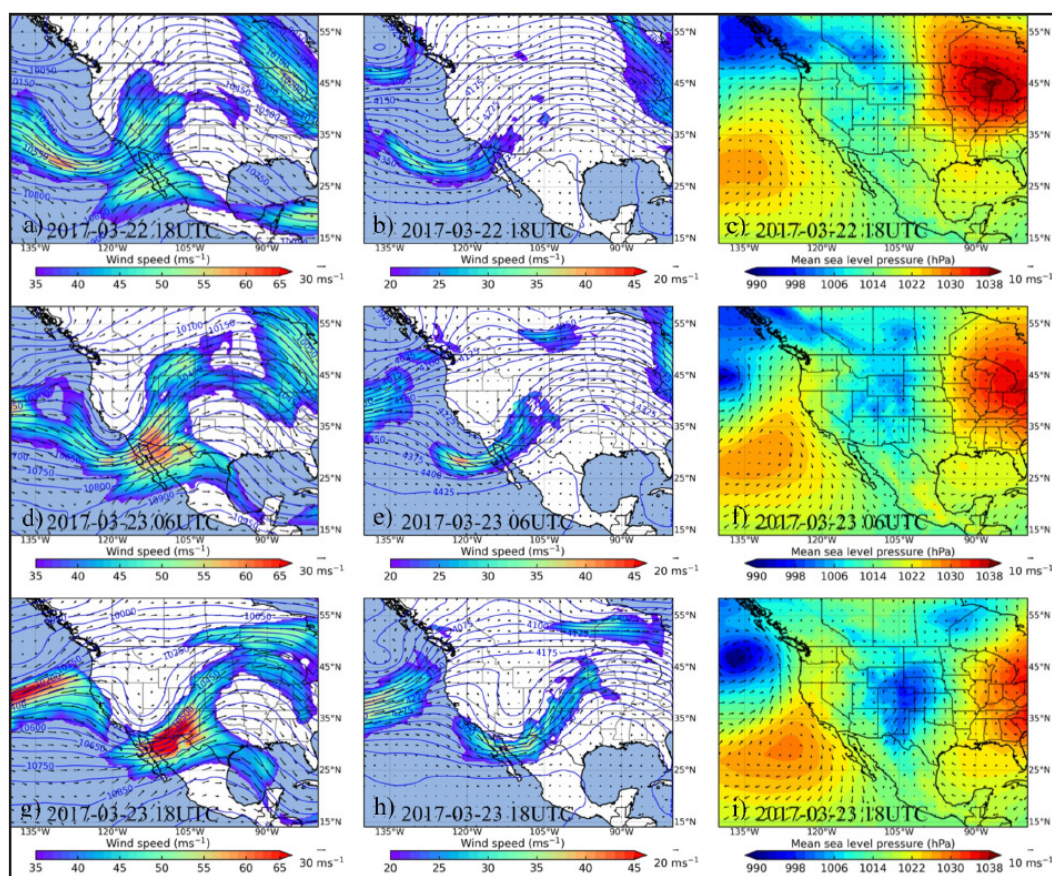


Figure 4. 24-hr evolution of (left column) 250 hPa horizontal wind isotachs (ms^{-1}) and geopotential height (m), (middle column) 600 hPa horizontal wind isotachs (ms^{-1}) and geopotential height (m), and (right column) 10 m wind barbs (ms^{-1}) and mean sea level pressure (hPa) for the M17 dust events. Meteorological fields are from ERA5.

At the surface, at 1800 UTC on the 22nd, that is, when the PJ and STJ streaks started to merge, relatively high pressure was resided over the New Mexico and its surrounding (Figure 4c). Over the northern Chihuahuan Desert, the near-surface wind was weak (Figure 4c). Twelve hours later, at 0600 UTC on the 23rd, when the PJ and STJ streaks merged and a unified jet streak formed, the low-pressure system started to move further equatorward over Colorado and northern New Mexico (Figure 4f). After 12 hr, at 1800 UTC on the 23rd, that is, when the unified jet intensified over the northern Chihuahuan Desert, the surface pressure deepened over Colorado and New Mexico (Figure 4i). Strong southwesterly-southerly near-surface flow developed due to the strong northeastward pressure gradient between Colorado and New Mexico and its upstream region over the Chihuahuan Desert (Figure 4i), which lifted dust from the northern Chihuahuan Desert. The mid-level wind maxima over the northern Chihuahuan Desert resulted in the transport of entrained dust toward the Colorado Rocky Mountains under the influence of lower-to-mid level cyclonic flow (Figures 4h and 4i).

4.2. WRF-Chem Simulations and Evaluation

4.2.1. Model Evaluation for Dust Emission and Transport

To evaluate the model performance, we compare observed and simulated wind patterns that drive dust emission and subsequent transport. The comparison between simulated and observed 10 m wind at the Flagstaff METAR station, for the A13 episode, showed that the model underestimated the wind speed between 0100 and 1300 UTC on the 16th (Figure 5a). Simulated winds ranged between 7 and 9 ms^{-1} , while observed winds ranged between 9 and 13 ms^{-1} . These discrepancies in wind patterns are probably because Flagstaff METAR station is situated in the valley region and the model did not capture the small-scale flow interaction in a complex terrain. Additionally, inaccurate representation of land use classification could be another factor for large discrepancy in high-elevation mountains in the Southwest (Gallagher et al., 2022). However, starting at 1400 UTC, observed and simulated wind speeds show a close correspondence. Between 1500 and 2300 UTC, observed wind speed ranged between 10 and 15 ms^{-1} , while simulated wind speed ranged between 11 and 12 ms^{-1} . A closer correspondence between observed and simulated wind speed is seen at the Sedona METAR station, where wind speed decreased during 0000–1200 UTC on the 16th (Figure 5b). Starting at 1300 UTC, when southwesterly winds arrived at this location, both simulated and observed wind speed started to increase.

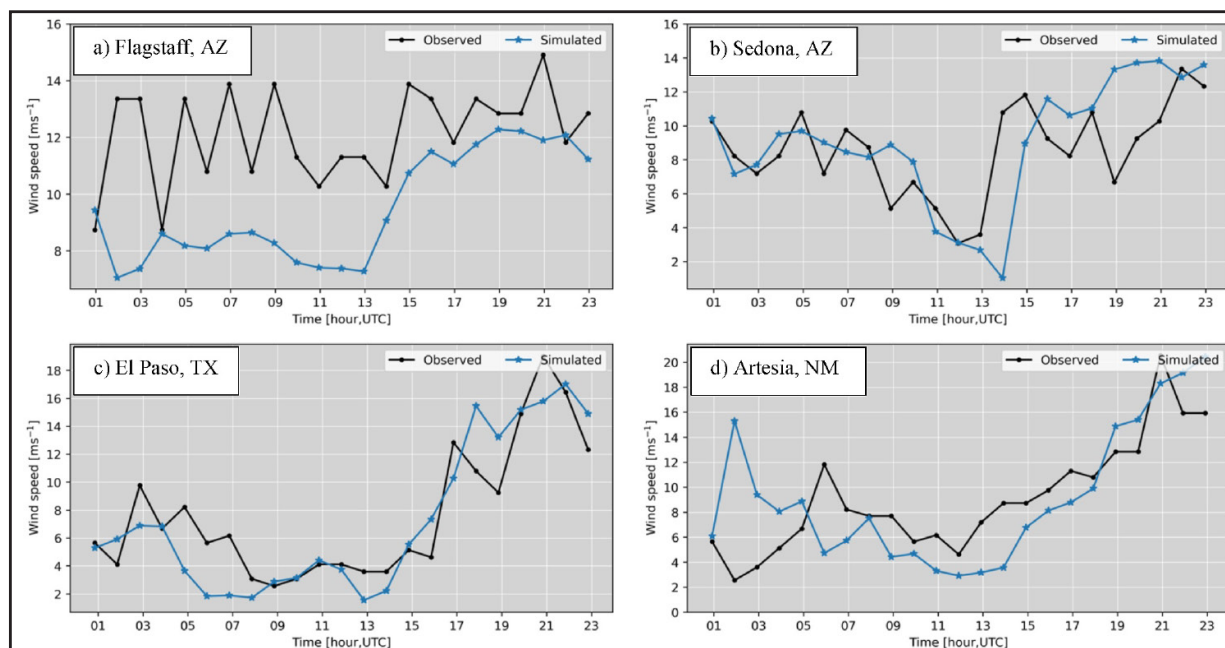


Figure 5. Observed and WRF-Chem simulated 10 m height wind speed at (a) Flagstaff and (b) Sedona in Arizona for 16 April 2013, and at the (c) El Paso Airport in Texas and (d) Artesia in New Mexico for 23 March 2017.

Wind comparison at the El Paso Airport METAR station for the M17 episode, shows that the observed 10 m wind on the 23rd decreased from 10 ms^{-1} at 0300 UTC to 3 ms^{-1} at 0900 UTC (Figure 5c). Beginning at 1000 UTC, wind speed started to increase and reached its peak value of $>18 \text{ ms}^{-1}$ at 2200 UTC. The simulated wind speed also followed a similar pattern. At the Artesia, METAR station, before 1200 UTC on the 23rd, wind speed remained mostly below 8 ms^{-1} except at 0600 UTC (12 ms^{-1}) (Figure 5d). Beginning at 1300 UTC, wind speed started to increase and reached its peak value of 20 ms^{-1} at 2100 UTC. The simulation also produced a similar pattern of 10 m wind at this location with very close correspondence during 1500–2300 UTC.

A sounding comparison at Flagstaff (KFGZ), for the A13 episode, shows intensified lower-mid tropospheric southwesterly winds at 1200 UTC compared to 0000 UTC on the 16th, suggesting strong southwesterly winds were responsible for dust lofting (Figures 6a and 6b). There was a strong increase in observed wind speed below 700 hPa. Compared to observation, the model underestimated the vertical profiles of wind at this station.

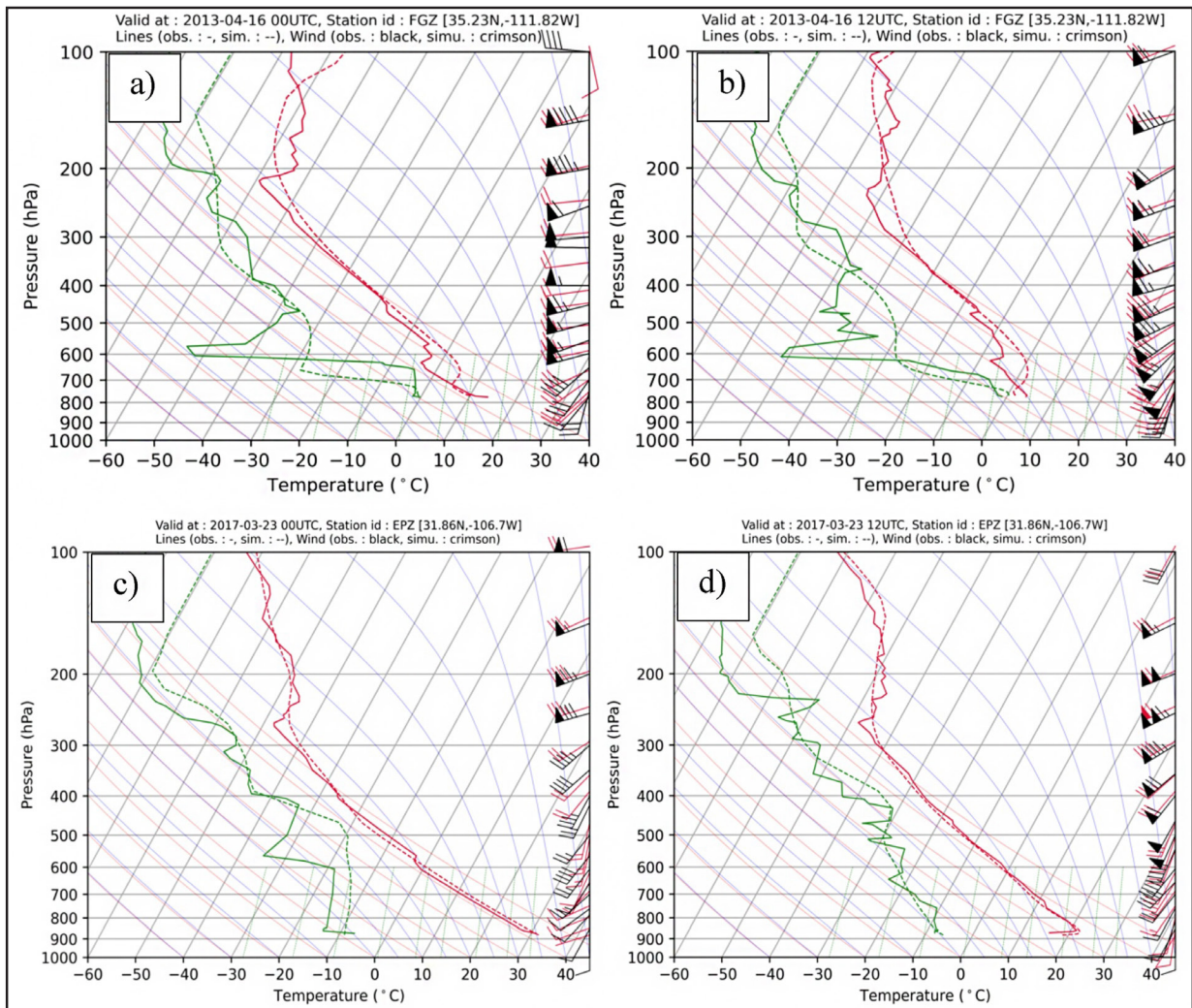


Figure 6. SkewT-LogP diagram at Flagstaff, Arizona (KFGZ) for (a) 0000 UTC and (b) 1200 UTC 16 April 2013, and at Santa Teresa, New Mexico (KEPZ) valid for (c) 0000 UTC and (d) 1200 UTC 23 March 2017.

Nevertheless, both observed and simulated winds show an increase in the southwesterly component at 1200 UTC compared to 0000 UTC. Additionally, temperatures below 700 hPa are in close agreement during these 12-hr. However, the model overestimated air temperature near the 600–700 hPa layer. Above 600 hPa, again both temperatures are in close agreement.

The Santa Teresa (KEPZ) simulated sounding, for the M17 dust events, shows close correspondence with the observed sounding (Figures 6c and 6d). Two notable features can be seen at 1200 UTC when compared to 0000 UTC: (a) intensification of the low-level southwesterly winds and development of the mid-level strong winds between 700 and 500 hPa, and (b) a deep dry adiabatic layer, suggesting a deep mixed layer. This deep mixed layer favors the mixing of lifted dust, and the strong mid-level southwesterly wind helps with the northeastward transport of dust. The above comparison with available observational data sets shows that the WRF-Chem model reproduced the general pattern of the observed meteorology in these two cases. Next, we evaluate dust evolution for the two events.

4.2.2. Dust Source Regions and Dust Loading Over the Colorado Plateau

In the A13 dust event, the southwest CP (mostly northeast Arizona) and northwest New Mexico were the major dust source regions (Figure 7). The simulations show dust emitting from different source regions across the southwestern CP. At 1200 UTC on the 16th, dust emission started with the arrival of southwesterly strong nearsurface flow (Figure 7a). At that time, a band of dust emission flux was present northeast of Flagstaff, Arizona and contributed to the evolution of the first dust plume as revealed in the simulated dust

load (Figure 7b). Two hours later at 1400 UTC, the dust emitting region expanded, dust emission flux intensified, and dust loading increased (Figures 7c and 7d). This resulted in a strong simulated northeast-traveling dust plume consistent with northeast-traveling observed dust plume (Figures 1d and 7c and 7d).

At 1400 UTC on the 16th, dust emission flux started to increase in Farmington, New Mexico resulting in a second dust plume (Figures 7a–7d). After 1400 UTC, dust emission flux further increased in the northeastern corner of Arizona and northwestern corner of the New Mexico, which resulted in two strong dust plumes consistent with observed dust plumes seen in the satellite imagery (Figures 1a and 1b and 7e and 7f). Both the dust plumes ultimately advected in a northeast direction toward the San Juan Mountains.

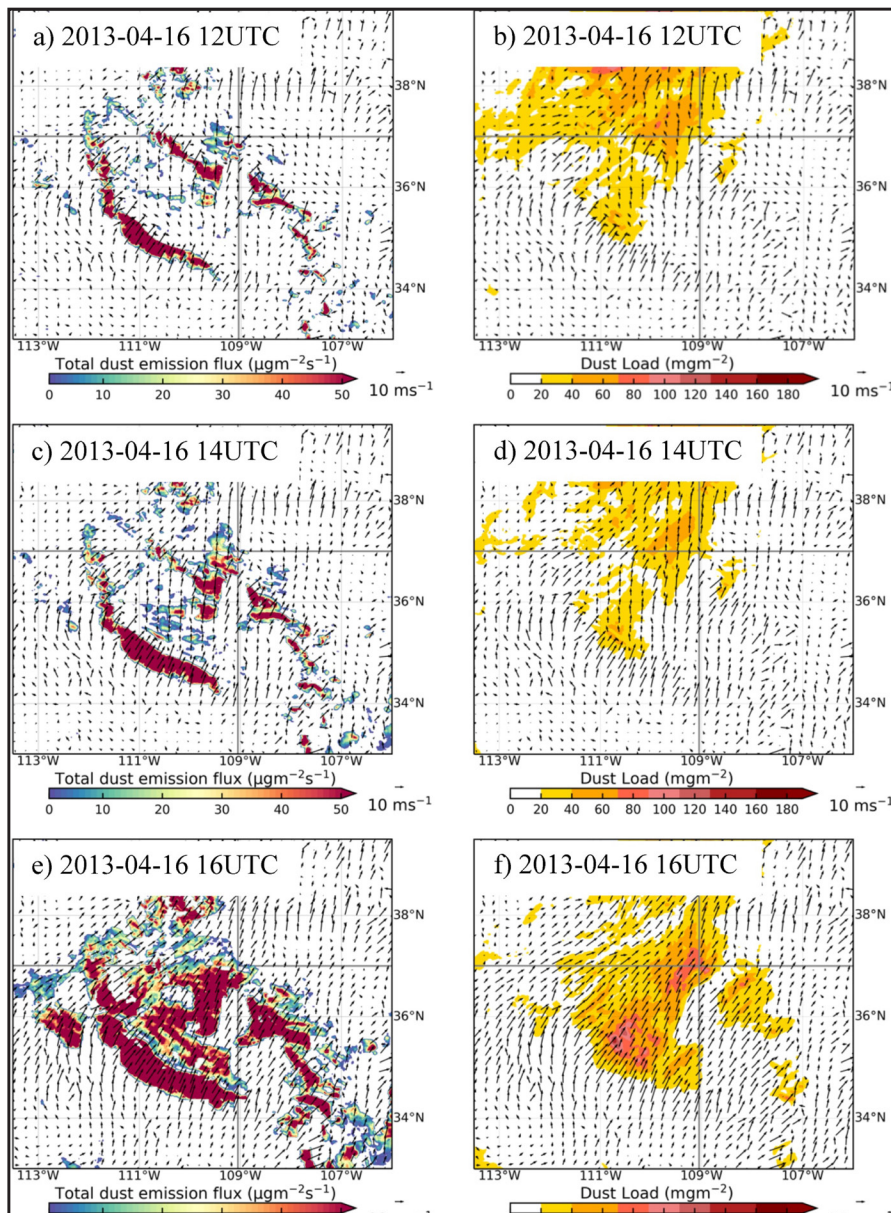


Figure 7. WRF-Chem simulated (a, c, e) 10 m wind and dust emission flux and (b, d, f) 10 m wind and dust load at (a, b) 1200, (c, d) 1400, and (e, f) 1600 UTC 16 April 2013 over the Colorado Plateau.

4.2.3. Spatiotemporal and Vertical Evolution of Dust Over the Colorado Plateau

Figure 8 shows AOD simulated at 2 km resolution and observed at 10 km resolution to compare the spatial evolution of dust plumes. Simulated AOD mostly comes from dust and observed AOD was attributed to dust in the absence of wildfire. At 1800 UTC on the 16th, the simulated dust plumes were present over the Four Corners region (AZ, UT, CO, and NM) (Figure 8a). Dust Plume 1 was present over the northeast corner of Arizona and extended to the Four Corners region and Dust Plume 2 was present over northwestern New Mexico in San Juan County. The closest MODIS-Terra overpass at 1810 UTC shows the coherent patterns of the dust plumes (Figure 8b). The peak AOD value of the observed and simulated Dust Plume 1 was ~ 0.9 . For Dust Plume 2, the peak observed AOD value was ~ 0.9 , while the simulated AOD was ~ 0.6 , which suggests that the model underestimated AOD in Dust Plume 2. Nevertheless, the spatial distribution of the simulated dust plumes closely matches the observed dust plumes (Figure 8, and Figure S4 in Supporting Information S1).

Figure 9 shows the vertical cross-sections of hourly simulated dust concentration and potential temperature along the lineAB(see Figure 2) for 1200–1900UTC on the 16th. We focused on the vertical distribution of dust since this is critical to long-range transport from the desert southwest into the San Juan Mountains. At 1200 UTC (local time 6 a.m.), the small dust emission flux just northeast of Flagstaff resulted in low magnitude near-surface dust concentration (Figure 9a). The stable PBL, as revealed by the low-level vertically compressed isentropes, did not allow the mixing of lifted dust to greater heights. Between 1300 and 1400 UTC, lofted dust remained near the surface in the stable PBL (Figures 9b and 9c). At 1500 UTC (local time 9 a.m.), the near-surface dust concentration started to increase due to intensifying southwesterly winds (Figure 9d). After sunrise, the PBL grew in response to diurnal heating at the surface which resulted in strong vertical mixing within the PBL and dust expansion to greater heights. Between 1600 and 1700 UTC, the dust

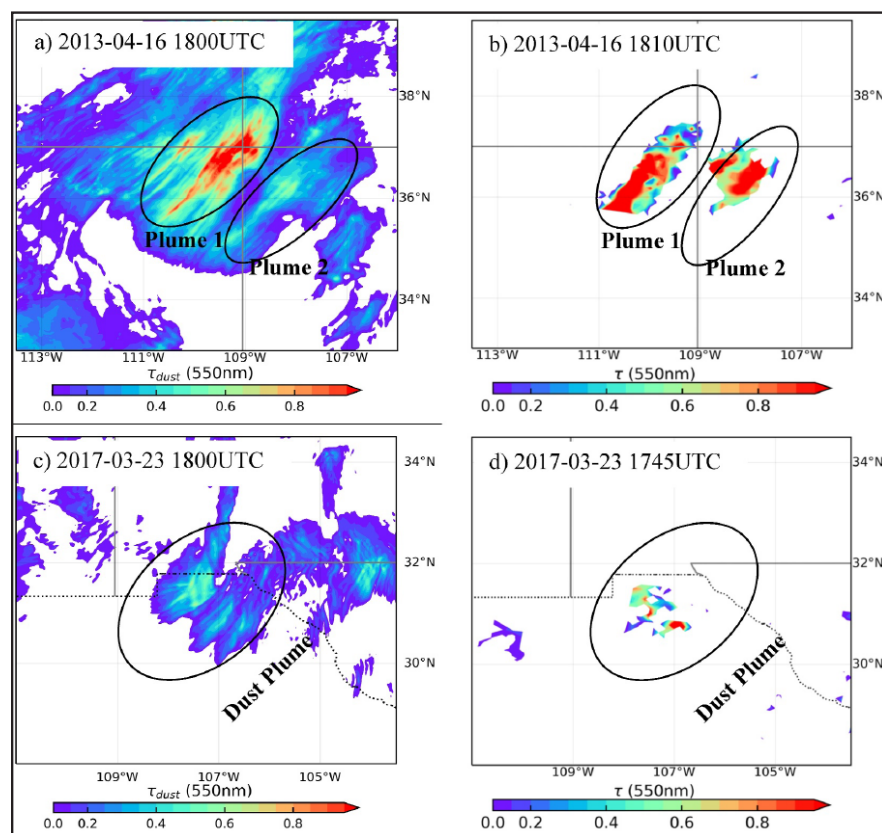


Figure 8. Comparison of aerosol optical depth, (left) WRF-Chem simulated at 2 km grid resolution and (right) MODIS-Terra at 10 km spatial resolution for (top panel) A13 and (bottom panel) M17 dust events.

layer advected northeastward and extended above 2 km in height between 35.5 and 38°N with a dust concentration of $\sim 1500 \mu\text{g kg}^{-1}$ (Figures 9e and 9f). The vertical expansion of the dust plume further increased between 1800 and 1900 UTC due to increasing dust emission flux and strong mixing in the deep PBL (Figures 7g and 9g and 9h). Around 1900 UTC, the dust layer was further advected poleward and made first contact with the San Juan Mountains, which is supported by the decrease in visibility at Cortez and Durango METAR stations with strong southwesterly winds (Figure 9h and Figure S1 in Supporting Information S1). The northeastward advection of the dust plumes to the San Juan Mountains was due to the strong mid-level southwesterly flow that developed over the CP region (discussed earlier in Section 4.1).

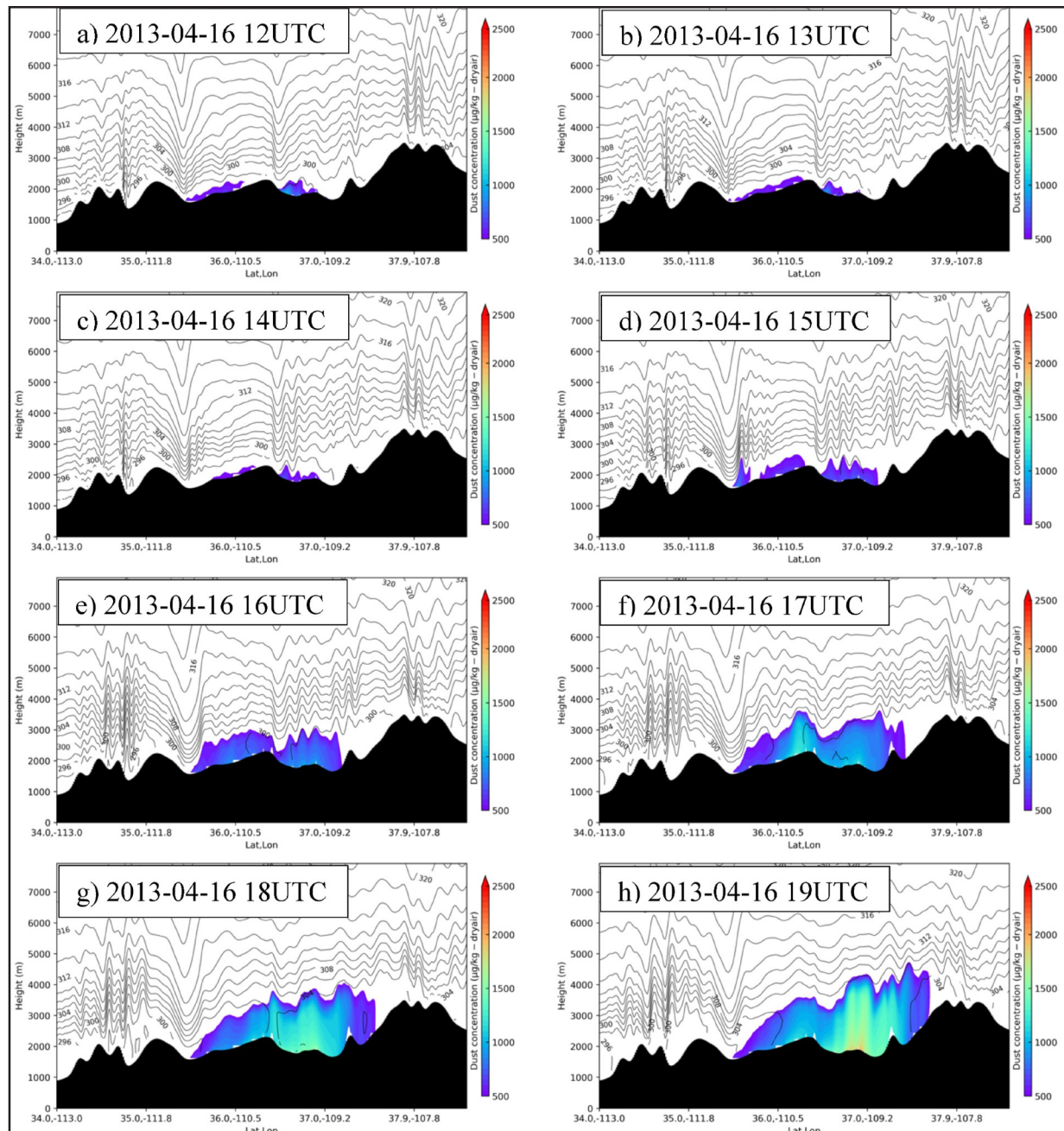


Figure 9. WRF-Chem simulated vertical cross-sections of potential temperature (K) and dust concentration along AB (see Figure 1) at (a) 1200, (b) 1300, (c) 1400, (d) 1500, (e) 1600, (f) 1700, (g) 1800, and (h) 1900 UTC 16 April 2013.

4.2.4. Dust Source Regions and Dust Loading Over the Chihuahuan Desert

The northern Chihuahuan Desert was the major dust source in the M17 dust event. Around 1400 UTC on the 23rd, the southwesterly flow over the northern Chihuahuan Desert was weak with little dust emission and no significant dust loading in the atmosphere (Figures 10a and 10b). Two hours later at 1600 UTC, the southwesterly flow intensified, which resulted in increased dust emission flux and dust loading across many parts of the northern Chihuahuan Desert near the United States-Mexico border (Figure 10c). Between 1600 and 1800 UTC, the southwesterly flow further intensified and resulted in more dust emissions from the northern Chihuahuan Desert (near northern Mexico, southern New Mexico, and western Texas). The intensified dust emission flux subsequently increased dust loading resulting in a northeastward-traveling strong dust plume consistent with the observed dust plume (Figures 1b and 10e–10h).

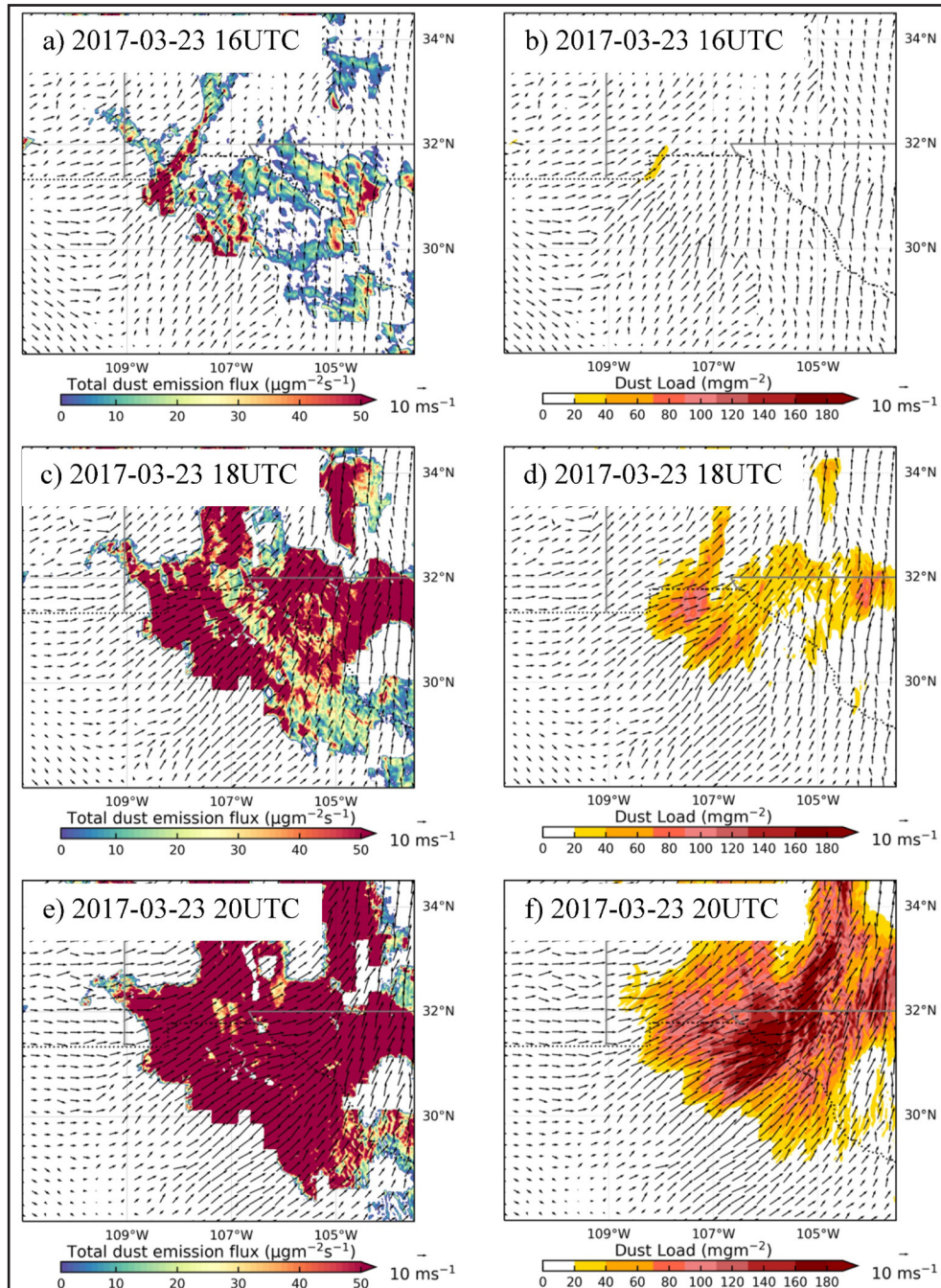


Figure 10. WRF-Chem simulated (a, c, e) 10 m wind and dust emission flux and (b, d, f) 10 m wind and dust load at (a, b) 1400, (c, d) 1600, and (e, f) 1800 UTC 23 March 2017.

4.2.5. Spatiotemporal and Vertical Evolution of Dust Over the Chihuahuan Desert

We used the simulated and observed AOD to describe the spatial evolution of the dust. At 1800 UTC on the 23rd, the simulation showed a thick dust plume over the northern Chihuahuan Desert (Figure 8c), near the United States-Mexico border. The closest MODIS-Terra overpass at 1745 UTC on the 23rd showed a similar pattern of the dust plume (Figure 8d). The peak value of the observed AOD was $\sim 0.6\text{--}0.8$, while the simulated peak value was ~ 0.6 , suggesting an underestimation of simulated AOD. Nonetheless, the spatial pattern of the observed dust plume was captured by the simulation (Figure 8d and Figure S4 in Supporting Information S1).

To describe the vertical evolution of the dust, we used the vertical cross-section of simulated dust and potential temperature along the line CD (see Figure 2). At 1700 UTC on the 23rd, dust emission flux over the northern Chihuahuan Desert was small, and a significant amount of dust was not present in a well-mixed layer (Figure 1a). One hour later at 1800 UTC, dust emission flux increased and resulted in a thick dust plume with a dust concentration of $\sim 700 \mu\text{g kg}^{-1}$ over the northern Chihuahuan Desert (Figure 11b). At 1900 UTC, the dust plume expanded horizontally and vertically in a growing daytime PBL and reached the El Paso, Texas region (Figure 11c). At 2000 UTC, while propagating northeastward, the dust plume expanded vertically reaching above 2.5 km due to strong vertical mixing (Figure 11d). Between 2000 and 2200 UTC, a strong dust plume impacted the El Paso region, which is supported by the decrease in visibility at the El Paso METAR station (Figures 11d–11f and Figure S1 in Supporting Information S1). Ultimately, the available dust plume was transported northeastward under the influence of strong mid-level southwesterly wind present over the northern Chihuahuan Desert/El Paso region (Figures 6c and 6d and Figure S5 in Supporting Information S1).

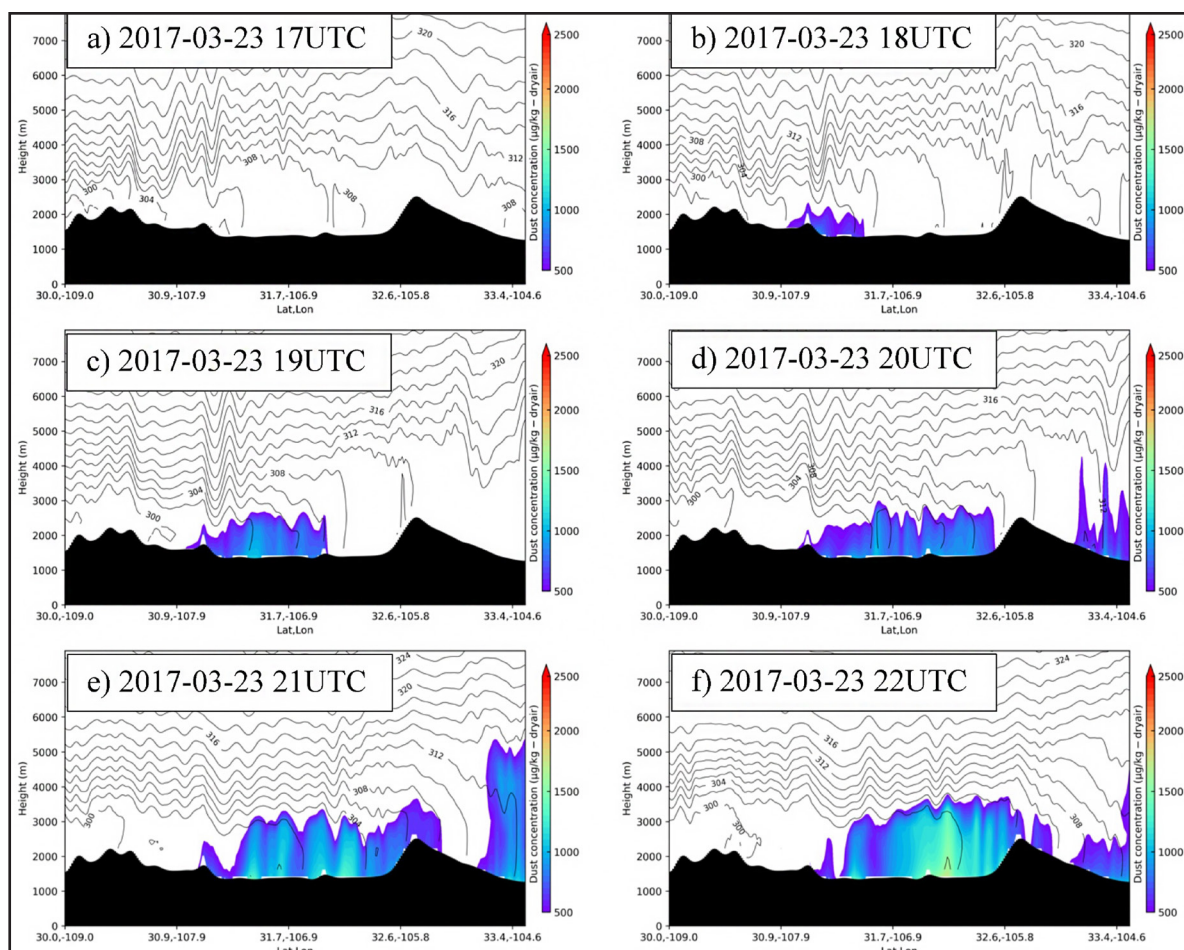


Figure 11. WRF-Chem simulated vertical cross-section of potential temperature (K) and dust concentration along CD (see Figure 1) at (a) 1700, (b) 1800, (c) 1900, (d) 2000, (e) 2100, and (f) 2200 UTC 23 March 2017.

4.2.6. PM_{10} Evolution Over the Chihuahuan Desert

We further evaluated simulated dust evolution by comparing hourly PM_{10} at two air quality stations in southern New Mexico (Figure 2b). At the West Mesa station, before the arrival of the dust event, PM_{10} concentration remained very low during 0000–1800 UTC on the 23rd (Figure 12a). At 1900 UTC, PM_{10} concentration jumped to $>200 \mu\text{g m}^{-3}$, reached its maximum value of $\sim 1300 \mu\text{g m}^{-3}$ at 2100 UTC, and started to decrease but the concentration remained between 300 and $600 \mu\text{g m}^{-3}$ between 2200 and 2300. During 1900–2300 UTC, the simulated PM_{10} remained between 450 and $850 \mu\text{g m}^{-3}$. The model showed some discrepancies with observed PM_{10} at different times during the dust event but followed a similar pattern to the observed PM_{10} .

A similar PM_{10} pattern was observed at the Anthony station, where observed PM_{10} started to increase at 1800 UTC on the 23rd, reached its maximum value of $>2,400 \mu\text{g m}^{-3}$ at 2100 UTC, and then decreased to $600 \mu\text{g m}^{-3}$ at 2300 UTC (Figure 12b). The simulated PM_{10} started to increase at 1700 UTC, reached its maximum value of $\sim 1,600 \mu\text{g m}^{-3}$ at 2200 UTC, and then decreased to $\sim 1,100 \mu\text{g m}^{-3}$ at 2300 UTC. Again, we found some differences in observed and simulated PM_{10} during this dust event; however, both simulated and observed trends follow a similar pattern.

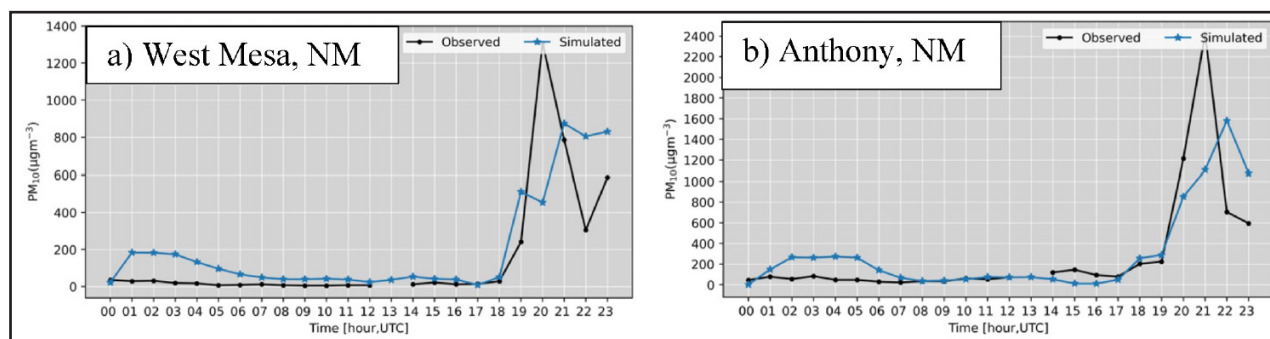


Figure 12. Hourly PM_{10} evolution at (a) West Mesa and (b) Anthony in New Mexico for 23 March 2017.

4.3. Analysis of Ground Cover Indicators in Modeled Dust Source Areas

Finally, we investigated and evaluated the dust sources in our WRF-Chem simulations. In the A13 case, the southwestern CP (northeastern Arizona) and Farmington, New Mexico, were the major sources that contributed to the two dust plumes. Large values of simulated dust emission fluxes were collocated with small annual fractional cover of annual forbs and grasses (AFG), PFG, and shrubs (SHR) in the preceding year (i.e., 2012). This outcome is supportive of the drag partition correction enabling dust emission from areas with overall less vegetation (Figures 13a–13c). The high dust-emitting regions in the southwest CP near the Little CRB seen in the simulation are recognized as having elevated susceptibility to dust emission on the CP (Li et al., 2013; Nauman et al., 2023).

In the M17 case, the primary modeled dust source region was the northern Chihuahuan Desert where vegetation cover was also very small (Figures 13c and 13d). Large dust emission fluxes were collocated with 2016 small annual fractional cover of AFG, PFG, and SHR. Although vegetation fractional cover data sets from the RAP are not available for the Mexican parts of the Chihuahuan Desert to compare dust emission fluxes and dust sources, these regions are recognized major sources of dust where wind can easily pick up dust due to sparse vegetation (Baddock et al., 2011; Kandakji et al., 2020). The strong southwesterly near-surface wind in both cases was able to entrain dust from likely dust source regions that were sparsely vegetated and made it available for long-range transport.

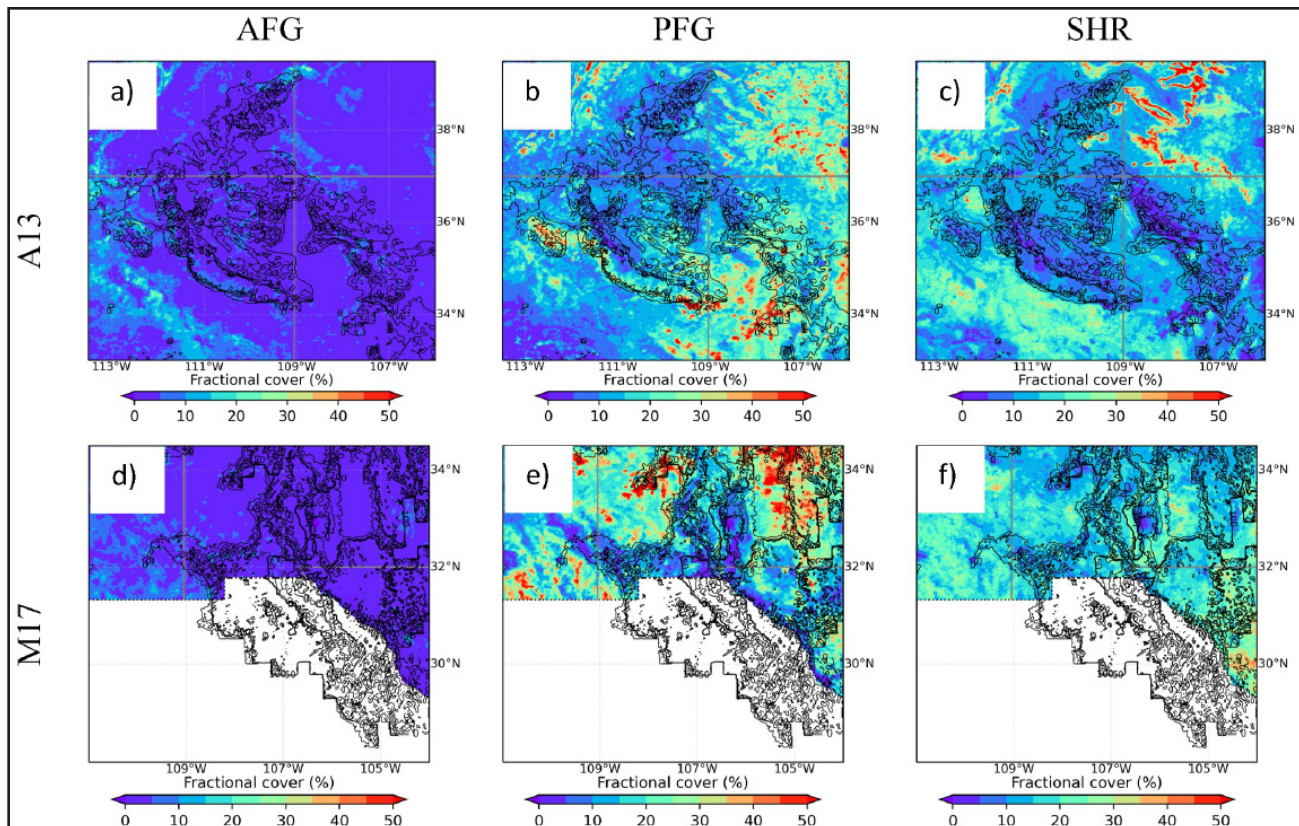


Figure 13. (a, b, c) Plant functional group annual fractional cover for 2012 and dust emission flux at 1800 UTC 16 April 2013 (black line contours). (d, e, f) Similar to Figures a, b, and c but for 2016 fractional cover and dust emission flux at 2000 UTC 23 March 2017.

5. DISCUSSION

Understanding the drivers of spring season (March–May) dust events in the southwestern US is important for monitoring and mitigating the effects of dust on water resources, agriculture, and air quality. We studied two dust events originating from geographically different dominant source areas of the Colorado Plateau and northern Chihuahuan Desert. The value of analyzing two case studies was to reveal how similar large-scale meteorology organizes dust events at two different dominant geographic source locations and evaluate the ability of the WRFChem model to represent these dust sources. Our large-scale meteorological analysis of the dust events indicates PJ and STJ interaction was a common upper-level meteorological feature before organization of the events. As our case studies encompassed dust emissions from across the Colorado Plateau and northern Chihuahuan Desert, this finding suggests the possible presence of upper-level jet interaction before dust events at different geographic locations in the Southwest. A previous study found similar jet interaction prior to a dust storm in the Southern High Plains (Kaplan et al., 2013) suggesting that upper-level jet interaction could be a meteorological precursor to dust events in the Southwest. A knowledge of such signals could be beneficial in dust storm operational forecasting and early warning systems to reduce the adverse operational impacts of blowing dust on landscapes, visibility for road traffic, air quality, and human health. For example, large-scale upper-level precursors were recently found to provide early warning of long-lived dust events in North Africa (Dhital et al., 2020; Orza et al., 2020). However, further investigation is needed with additional cases to assess the probability of and detailed dynamics of jet interaction before dust events are organized in the Southwest, to describe the nature of any mechanistic interactions, and to determine the implications for dust transport to snowpack in the CRB.

There remains a dearth of observational data sets in the Southwest US needed to rigorously test dust emission models (Webb et al., 2017). The Four Corners and northern Chihuahuan Desert (in Mexico) dust source regions are both sparsely monitored. Despite a large amount of dust being transported annually from the Colorado Plateau to the San Juan Mountains, there are no publicly accessible PM_{10} stations within the dust transport pathway. The only nearby PM_{10} observations are collected nearly 1° poleward of the San Juan Mountains. Nonetheless, assessment of our simulation results showed that WRF-Chem, with drag partition correction in the AFWA dust emission scheme, can simulate a general pattern of the spatiotemporal evolution of dust emission in geographically different source areas that contribute to dust-on-snow in the Southwest. Through comparison with satellite imagery of the dust plumes and plant functional group cover data sets, we assessed that the dust sources in the two geographic regions were well captured in our simulations. The pattern of simulated large dust emission flux in the southwestern Colorado Plateau, including the Little CRB, corresponds to a strong dust source region. Complementary research using similar and independent approaches has identified that the region between Flagstaff, Arizona and the Four Corners, including the Little CRB, are major dust sources on the Colorado Plateau (Hennen et al., 2022; Nauman et al., 2023). In the northern Chihuahuan Desert, our simulated pattern of large dust emission fluxes from unvegetated and poorly vegetated regions including dry playas is also consistent with previous studies (Baddock et al., 2011; Hennen et al., 2022). The large dust emitting regions in the simulations covering the southwestern Colorado Plateau and northern Chihuahuan Desert also correspond to regions of measured large spring season sediment flux (Bergametti & Gillette, 2010), dust emission hotspots that contribute to blowing dust on highways (Tong et al., 2023) and large PM concentration (Hand et al., 2017). In the southwestern Colorado Plateau and northern Chihuahuan Desert, fine dust ($PM_{2.5}$) concentration peaks ($1.7\text{--}2.22 \mu\text{gm}^{-3}$) are observed during the spring season (Hand et al., 2017).

Comparison of the simulated dust sources with plant functional group cover data enabled a novel assessment of the simulated dust sources and insights into the dust source area characteristics of our case study events. Not surprisingly, we found that the dust sources contributing to the largest dust emission fluxes in our simulations occurred on sparsely vegetated lands. Sparse vegetation is less effective at attenuating wind momentum and increases the probability of dust emission (Nauman et al., 2023; Webb et al., 2014). The patterns of large, simulated dust emission fluxes were collocated with a small fractional cover of annual and PFG, and shrubs. The variable annual precipitation regime across the Colorado Plateau and the Chihuahuan Desert impacts vegetation dynamics, which in turn modifies land surface roughness and changes the dynamics of dust emission and transport. Hence, future research could explore how regional drought impacts plant functional groups and land surface roughness and changes the dynamics of dust emission and transport.

Comparisons of the 2 km simulated meteorological and dust fields with point observational data sets for the two case studies also suggested reasonable model performance. We found some discrepancies in observed and simulated fields that warrant further attention. For example, the model underestimated the 10 m wind at the Flagstaff METAR station and underestimated the vertical wind profile at two sounding locations. At the Santa Teresa station, vertical profiles of simulated and observed wind were in close agreement up to 600 hPa but simulated winds were weaker above that. At the Flagstaff station, the near-surface winds were close to observations, but above 700 hPa, the simulated winds were weaker than observations. These discrepancies could be due to model performance or sub-grid scale heterogeneity and scale mismatches between the pointsource station data and 2 km model grid (Mues et al., 2018; Yver et al., 2013; Zhang, Pu, & Zhang, 2013; Zhang, Sartelet, et al., 2013). They could also reflect inadequacies in the model initial conditions. Additionally, the model overestimated AOD at some locations. The simulation estimated dust emission and AOD occurred across a much larger portion of the study area than observations in both cases. The simulated AOD in the A13 was much more extensive than that of the M17 and coincided with much greater wind friction velocity. As the surface roughness (u_{s*}/U_{10}) was unchanged over the 2-day simulations, and modeled wind speed during the dust events corresponded with measurements, we interpret the cause of the overestimation in dust emission being due to the model assuming that sediment availability for emission is unlimited over time. This issue is a common problem among dust models (e.g., Parajuli et al., 2019; Shao et al., 2007) and an effective solution to parameterizing dynamic soil erodibility at the regional scale is very limited. In the 2017 case, we observed that the simulated PM_{10} peaked 1 hr after the observed PM_{10} peak. One plausible explanation for this lag is

that the simulated wind was slightly weaker than the observed maximum wind approximately 2 hr prior to the observed PM_{10} peak. This may have resulted in less dust emission in the simulation and diminished PM_{10} .

Future research to evaluate and enhance the model performance, including better constraining dust-on-snow simulations and forecasting, would greatly benefit from improved monitoring of dust concentrations and dust emission fluxes within North American dust source regions. Additionally, there is a need to resolve large scale differences between numerical dust models (here 2 km resolution) and available observational data sets (point scale), which has been a challenging task (Haustein et al., 2015). As the already dry Southwest US is predicted to become even drier over the coming decades (Edwards et al., 2019), access to reliable dust monitoring data sets will be of critical importance for assessing the impacts and feedbacks among climate change, land uses, and land management on ecosystems and dust activity, dust-on-snow processes, and the implications of these interactions for agriculture water resources and dust mitigation (Webb et al., 2017). To effectively link these processes and evaluate the systems-levels interactions and impacts of dust-on-snow, it will be important to establish the accuracy of simulated dust emission fluxes and model representations of dust source area dynamics. Such efforts will necessarily shift the focus of dust model validation from almost exclusively testing advected dust concentrations and AOD to novel approaches that incorporate surface measurements and models of soil and vegetation, saltation mass fluxes, and dust emission.

The results from our two-spring season dust events simulations, and the improved simulation of a convective dust event in Arizona with the same drag-partition approach (LeGrand et al., 2023), give us confidence in the applicability of the Chappell and Webb (2016) albedo-based drag partition for simulating Southwest dust events under different meteorological and surface roughness conditions.

6. CONCLUSIONS

In this study, we investigated large-scale meteorological conditions leading to two spring-season Southwest US dust events. We found commonalities in upper-level meteorological circulations in these two cases. Our analyses revealed a common PJ and STJ interacting feature before the formation of dust events. When PJ and STJ merged resulting in a single unified jet, a strong mid-tropospheric flow developed. Within the near-surface boundary layer, a strong northeastward-directed pressure gradient developed just below and directly upstream of the exit region of the unified jet resulting in strong low-level winds capable of emitting dust from the source regions. The analyses suggest that PJ and STJ interaction could be a common upper-level meteorological precursor to Southwest dust events organized at different geographic locations. Such upper-level signals could be beneficial in operational dust storm forecasting and early warning systems to reduce the immediate adverse impact of dust events on human health and other environmental resources. Future work will extend and assess the probability of jet interaction before dust event formation in the Southwest with multiple cases and describe the nature of jet interaction and its role in dust emission and transport processes, most notably how these unified jets deepen the PBL mixed layers and accelerate the airflow.

We also simulated these two dust events using the WRF-Chem model with dynamic albedo-based drag partitioning within the AFWA dust emission scheme. We found that drag partition correction in the AFWA dust emission scheme can reasonably reproduce the spatiotemporal evolution of the dust plumes, which suggests its applicability in forecasting spring season dust events across different geographic and meteorological conditions in the Southwest. As the accurate simulation of dust events remains one of the major challenges in dust emission and transport modeling, the ability of albedo-model to simulate dust emission and transport in different geographic and meteorological conditions is beneficial for various applications, including operational dust forecasting, regional climate modeling, dust cycles analyses, etc. Future work could use a similar model configuration to simulate other dust events for its potential wider use in operational forecasting and research.

DATA AVAILABILITY STATEMENT

The observation and reanalysis data sets are freely available. ERA5 reanalysis data are available from Copernicus Climate Data Store (Hersbach et al., 2020a, 2020b) [Dataset]. METAR data are available from

the IOWA State University website (METAR) [Dataset]. MODIS-Aqua images are available from the NASA Worldview platform (NASA Worldview) [Dataset]. MODIS AOD data are available from the NASA Earth Data website (MODIS) [Dataset], while PM_{10} data are available from the US EPA website (PM_{10}) [Dataset]. The soundings are available from the University of Wyoming website (Sounding) [Dataset] and the WRF-Chem simulations results are reproducible. A detailed description of getting MODIS albedo data to modify the AFWA code is provided in LeGrand et al. (2023). Plant functional group data are available from the Google Earth Engine and detailed description of getting these data is available in RAP website (RAP, 2023) [Dataset]. Python software package was used to make figures (PYTHON, 2022) [Software].

ACKNOWLEDGMENTS

We thank three anonymous reviewers for their constructive comments, which helped to improve the manuscript. The funding for this work is supported by the National Aeronautics and Space Administration Grant 80NSSC20K1673. This research used resources provided by the SCINet project of the United States Department of Agriculture Agricultural Research Service (ARS), ARS project number 0500-00093-001-00-D to perform WRF-Chem simulations. Any use of trade, firm or product names is for descriptive purposes only and does not imply endorsement by the U.S. Government. During the development of the manuscript NPW and AC were in receipt of funding from the National Science Foundation (EAR-1853853) and Natural Environmental Research Council (NE/T002263/1,NERCDMP-2634).

REFERENCES

- Achakulwisut, P., Shen, L., & Mickley, L. J. (2017). What controls springtime fine dust variability in the western United States? Investigating the 2002–2015 increase in fine dust in the US Southwest. *Journal of Geophysical Research: Atmospheres*, 122(22), 12449–12467. <https://doi.org/10.1002/2017JD027208>
- Adhikari, P., & Mejia, J. F. (2022). Impact of transported dust aerosols on precipitation over the Nepal Himalayas using convection-permitting WRF-Chem simulation. *Atmospheric Environment: X*, 15, 15. <https://doi.org/10.1016/J.AEAOA.2022.100179>
- Baddock, M. C., Gill, T. E., Bullard, J. E., Acosta, M. D., & Rivera, N. I. R. (2011). Geomorphology of the Chihuahuan Desert based on potential dust emissions. *Journal of Maps*, 7(1), 249–259. <https://doi.org/10.4113/jom.2011.1178>
- Bergametti, G., & Gillette, D. A. (2010). Aeolian sediment fluxes measured over various plant/soil complexes in the Chihuahuan desert. *Journal of Geophysical Research*, 115(F3), F03044. <https://doi.org/10.1029/2009JF001543>
- Bohren, C. F., & Huffman, D. R. (2007). Absorption and scattering of light by small particles (p. 530). John Wiley & Sons, Ltd. <https://doi.org/10.1002/9783527618156>
- Chappell, A., & Webb, N. P. (2016). Using albedo to reform wind erosion modelling, mapping and monitoring. *Aeolian Research*, 23, 63–78. <https://doi.org/10.1016/j.aeolia.2016.09.006>
- Chappell, A., Webb, N. P., Guerschman, J. P., Thomas, D. T., Mata, G., Handcock, R. N., et al. (2018). Improving ground cover monitoring for wind erosion assessment using MODIS BRDF parameters. *Remote Sensing of Environment*, 204, 756–768. <https://doi.org/10.1016/j.rse.2017.09.026>
- Dhital, S., Kaplan, M. L., Orza, J. A. G., & Fiedler, S. (2020). Atmospheric dynamics of a Saharan dust outbreak over Mindelo, Cape Verde Islands, preceded by Rossby wave breaking: Multiscale observational analyses and simulations. *Journal of Geophysical Research: Atmospheres*, 125(18), 1–22. <https://doi.org/10.1029/2020JD032975>
- Dhital, S., Kaplan, M. L., Orza, J. A. G., & Fiedler, S. (2021). Poleward transport of African dust to the Iberian Peninsula organized by a barrier jet and hydraulic jumps: Observations and high-resolution simulation analyses. *Atmospheric Environment*, 261, 118574. <https://doi.org/10.1016/j.atmosenv.2021.118574>
- Duniway, M. C., Pfennigwerth, A. A., Fick, S. E., Nauman, T. W., Belnap, J., & Barger, N. N. (2019). Wind erosion and dust from US drylands: A review of causes, consequences, and solutions in a changing world. *Ecosphere*, 10(3). <https://doi.org/10.1002/ecs2.2650>
- Edwards, B. L., Webb, N. P., Brown, D. P., Elias, E., Peck, D. E., Pierson, F. B., et al. (2019). Climate change impacts on wind and water erosion on US rangelands. *Journal of Soil and Water Conservation*, 74(4), 405–418. <https://doi.org/10.2489/jswc.74.4.405>
- Ek, M. B., Mitchell, K. E., Lin, Y., Rogers, E., Grunmann, P., Koren, V., et al. (2003). Implementation of Noah land surface model advances in the National Centers for Environmental Prediction operational mesoscale Eta model. *Journal of Geophysical Research*, 108(D22), 2002JD003296. <https://doi.org/10.1029/2002JD003296>
- Evan, A. T., Porter, W., Clemesha, R., Kuwano, A., & Frouin, R. (2022). Measurements of a dusty density current in the western Sonoran desert. *Journal of Geophysical Research: Atmospheres*, 127(8), 1–22. <https://doi.org/10.1029/2021JD035830>
- Fécan, F., Marticorena, B., & Bergametti, G. (1999). Parametrization of the increase of the Aeolian erosion threshold wind friction velocity due to soil moisture for arid and semi-arid areas. *Annales Geophysicae*, 17(1), 149–157. <https://doi.org/10.1007/s00585-999-0149-7>

- Gallagher, A. R., LeGrand, S. L., Hodgdon, T. S., & Letcher, T. W. (2022). Simulating environmental conditions for southwest United States convective dust storms using the Weather Research and Forecasting model v4.1. ERDC TR-22-11. U.S. Army Engineer Research and Development Center. <https://doi.org/10.21079/11681/44963>
- Ginoux, P., Chin, M., Tegen, I., Prospero, J. M., Holben, B., Dubovik, O., & Lin, S.-J. (2001). Sources and distributions of dust aerosols simulated with the GOCART model. *Journal of Geophysical Research*, 106(D17), 20255–20273. <https://doi.org/10.1029/2000JD000053>
- Grell, G. A., & Dévényi, D. (2002). A generalized approach to parameterizing convection combining ensemble and data assimilation techniques. *Geophysical Research Letters*, 29(14), 10–13. <https://doi.org/10.1029/2002GL015311>
- Grell, G. A., Peckham, S. E., Schmitz, R., McKeen, S. A., Frost, G., Skamarock, W. C., & Eder, B. (2005). Fully coupled “online” chemistry within the WRF model. *Atmospheric Environment*, 39(37), 6957–6975. <https://doi.org/10.1016/j.atmosenv.2005.04.027>
- Hand, J. L., Gill, T. E., & Schichtel, B. A. (2017). Spatial and seasonal variability in fine mineral dust and coarse aerosol mass at remote sites across the United States. *Journal of Geophysical Research*, 122(5), 3080–3097. <https://doi.org/10.1002/2016JD026290>
- Hand, J. L., Gill, T. E., & Schichtel, B. A. (2019). Urban and rural coarse aerosol mass across the United States: Spatial and seasonal variability and long-term trends. *Atmospheric Environment*, 218(July), 117025. <https://doi.org/10.1016/j.atmosenv.2019.117025>
- Haustein, K., Washington, R., King, J., Wiggs, G., Thomas, D. S. G., Eckardt, F. D., et al. (2015). Testing the performance of state-of-the-art dust emission schemes using DO4Models field data. *Geoscientific Model Development*, 8(2), 341–362. <https://doi.org/10.5194/gmd-8-341-2015>
- Hennen, M., Chappell, A., Edwards, B. L., Faist, A. M., Kandakji, T., Baddock, M. C., et al. (2022). A North American dust emission climatology (2001–2020) calibrated to dust point sources from satellite observations. *Aeolian Research*, 54, 100766. <https://doi.org/10.1016/j.aeolia.2021.100766>
- Hersbach, H., Bell, B., Berrisford, P., Hirahara, S., Horányi, A., Muñoz-Sabater, J., et al. (2020a). The ERA5 global reanalysis. *Quarterly Journal of the Royal Meteorological Society*, 146(730), 1999–2049. <https://doi.org/10.1002/qj.3803>
- Hersbach, H., Bell, B., Berrisford, P., Hirahara, S., Horányi, A., Muñoz-Sabater, J., et al. (2020b). ERA-5 reanalysis data [Dataset]. <https://www.ecmwf.int/en/forecasts/datasets/reanalysis-datasets/era5>
- Iacono, M. J., Delamere, J. S., Mlawer, E. J., Shephard, M. W., Clough, S. A., & Collins, W. D. (2008). Radiative forcing by long-lived greenhouse gases: Calculations with the AER radiative transfer models. *Journal of Geophysical Research*, 113(13), 1–8. <https://doi.org/10.1029/2008JD009944>
- Jones, M. O., Allred, B. W., Naugle, D. E., Maestas, J. D., Donnelly, P., Metz, L. J., et al. (2018). Innovation in rangeland monitoring: Annual, 30 m, plant functional type percent cover maps for US Rangelands, 1984–2017. *Ecosphere*, 9(9), e02430. <https://doi.org/10.1002/ecs2.2430>
- Kandakji, T., Gill, T. E., & Lee, J. A. (2020). Identifying and characterizing dust point sources in the southwestern United States using remote sensing and GIS. *Geomorphology*, 353, 107019. <https://doi.org/10.1016/j.geomorph.2019.107019>
- Kaplan, M. L., Vellore, R. K., Lewis, J. M., Underwood, S. J., Pauley, P. M., Martin, J. E., et al. (2013). Subtropical-polar jet interactions in Southern Plains dust storms. *Journal of Geophysical Research: Atmospheres*, 118(23), 12893–12914. <https://doi.org/10.1002/2013JD020345>
- Kort, W. (2013). Climate change impacts on agriculture in the Rio Grande River Basin. School of Freshwater Sciences: Center for Water Policy at University of Wisconsin. Retrieved from http://uwm.edu/centerforwaterpolicy/wp-content/uploads/sites/170/2013/10/Rio-Grande_Agriculture_Final.pdf
- LeGrand, S. L., Letcher, T. W., Okin, G. S., Webb, N. P., Gallagher, A. R., Dhital, S., et al. (2023). Application of a satellite-retrieved sheltering parameterization (v1.0) for dust event simulation with WRF-Chem v4.1. *Geoscientific Model Development*, 16(3), 1009–1038. <https://doi.org/10.5194/gmd-16-1009-2023>
- LeGrand, S. L., Polashenski, C., Letcher, T. W., Creighton, G. A., Peckham, S. E., & Cetola, J. D. (2019). The AFWA dust emission scheme for the GOCART aerosol model in WRF-Chem v3.8.1. *Geoscientific Model Development*, 12(1), 131–166. <https://doi.org/10.5194/gmd-12-131-2019>
- Lei, H., & Wang, J. X. L. (2014). Observed characteristics of dust storm events over the western United States using meteorological, satellite, and air quality measurements. *Atmospheric Chemistry and Physics*, 14(15), 7847–7857. <https://doi.org/10.5194/acp-14-7847-2014>
- Li, J., Okin, G. S., McKenzie Skiles, S., & Painter, T. H. (2013). Relating variation of dust on snow to bare soil dynamics in the western United States. *Environmental Research Letters*, 8(4), 044054. <https://doi.org/10.1088/1748-9326/8/4/044054>
- METAR. (2022). METAR data [Dataset]. <https://mesonet.agron.iastate.edu/request/download.phtml>
- Michaels, M. L., Letcher, T. W., Legrand, S. L., Webb, N. P., & Putnam, J. B. (2022). Implementation of an albedo-based drag partition into the WRF-Chem v4.1 AFWA dust emission module. Cold Regions Research and Engineering Laboratory. <https://hdl.handle.net/11681/42782>
- MODIS. (2022). MODIS AOD data [Dataset]. <https://ladsweb.modaps.eosdis.nasa.gov>
- Mues, A., Lauer, A., Lupascu, A., Rupakheti, M., Kuik, F., & Lawrence, M. G. (2018). WRF and WRF-Chem v3.5.1 simulations of meteorology and black carbon concentrations in the Kathmandu Valley. *Geoscientific Model Development*, 11(6), 2067–2091. <https://doi.org/10.5194/gmd-11-2067-2018>
- Nakanishi, M., & Niino, H. (2004a). Development of an improved turbulence closure model for the atmospheric boundary layer. *Journal of the Meteorological Society of Japan*, 87(5), 895–912. <https://doi.org/10.2151/jmsj.87.895>
- Nakanishi, M., & Niino, H. (2004b). An improved Mellor–Yamada Level-3 Model with condensation physics: Its design and verification. *Boundary-Layer Meteorology*, 112, 1–31. <https://doi.org/10.1023/B:BOUN.0000020164.04146.98>

- NASA Worldview. (2022). MODIS-Aqua images [Dataset]. <https://www.earthdata.nasa.gov/worldview>
- Nauman, T. W., Munson, S. M., Dhital, S., Webb, N. P., & Duniway, M. C. (2023). Synergistic soil, land use, and climate influences on wind erosion on the Colorado Plateau: Implications for management. *Science of the Total Environment*, 893(December 2022), 164605. <https://doi.org/10.1016/j.scitotenv.2023.164605>
- Oaida, C. M., Xue, Y., Flanner, M. G., Skiles, S. M. K., De Sales, F., & Painter, T. H. (2015). Improving snow albedo processes in WRF/SSiB regional climate model to assess impact of dust and black carbon in snow on surface energy balance and hydrology over western US. *Journal of Geophysical Research*, 120(8), 3228–3248. <https://doi.org/10.1002/2014JD022444>
- Orza, J. A. G., Dhital, S., Fiedler, S., & Kaplan, M. L. (2020). Large scale upper-level precursors for dust storm formation over North Africa and poleward transport to the Iberian Peninsula. Part I: An observational analysis. *Atmospheric Environment*, 237, 117688. <https://doi.org/10.1016/j.atmosenv.2020.117688>
- Painter, T. H., Deems, J. S., Belnap, J., Hamlet, A. F., Landry, C. C., & Udall, B. (2010). Response of Colorado River runoff to dust radiative forcing in snow. *Proceedings of the National Academy of Sciences of the United States of America*, 107(40), 17125–17130. <https://doi.org/10.1073/PNAS.0913139107>
- Parajuli, S. P., Stenchikov, G. L., Ukhov, A., & Kim, H. (2019). Dust emission modeling using a new high-resolution dust source function in WRF-Chem with implications for air quality. *Journal of Geophysical Research: Atmospheres*, 124(17–18), 10109–10133. <https://doi.org/10.1029/2019JD030248>
- PM₁₀. (2022). PM₁₀ data [Dataset]. https://aq5.epa.gov/aqsweb/airdata/download_files.html
- PYTHON. (2022). Python matplotlib software package [Software]. <https://matplotlib.org/>
- Rahimi, S., Liu, X., Zhao, C., Lu, Z., & Lebo, Z. J. (2020). Examining the atmospheric radiative and snow-darkening effects of black carbon and dust across the Rocky Mountains of the United States using WRF-Chem. *Atmospheric Chemistry and Physics*, 20(18), 10911–10935. <https://doi.org/10.5194/acp-20-10911-2020>
- RAP. (2023). Plant functional groups data [Dataset]. <https://rangelands.app/products/>
- Raupach, M. R. (1992). Drag and drag partition on rough surfaces. *Boundary-Layer Meteorology*, 60(4), 374–396. <https://doi.org/10.1007/bf00155203>
- Raupach, M. R., & Lu, H. (2004). Representation of land-surface processes in aeolian transport models. *Environmental Modelling & Software*, 19(2), 93–112. [https://doi.org/10.1016/S1364-8152\(03\)00113-0](https://doi.org/10.1016/S1364-8152(03)00113-0)
- Schaaf, C., & Wang, Z. (2021). MODIS/Terra+Aqua BRDF/albedo model parameters daily L3 Global - 500m V061. NASA EOSDIS Land Processes Distributed Active Archive Center. <https://doi.org/10.5067/MODIS/MCD43A1.061>
- Shao, Y., Leys, J. F., McTainsh, G. H., & Tews, K. (2007). Numerical simulation of the October 2002 dust event in Australia. *Journal of Geophysical Research*, 112(D8), D08207. <https://doi.org/10.1029/2006JD007767>
- Skamarock, W. C., Klemp, J. B., Dudhia, J., Gill, D. O., Liu, Z., Berner, J., et al. (2019). A Description of the advanced research WRF model version 4.1. <https://doi.org/10.5065/1dfh-6p97>
- Skiles, S. M., Painter, T. H., Belnap, J., Holland, L., Reynolds, R. L., Goldstein, H. L., & Lin, J. (2015). Regional variability in dust-on-snow processes and impacts in the Upper Colorado River Basin. *Hydrological Processes*, 29(26), 5397–5413. <https://doi.org/10.1002/hyp.10569>
- Skiles, S. M. K., & Painter, T. (2017). Daily evolution in dust and black carbon content, snow grain size, and snow albedo during snowmelt, Rocky Mountains, Colorado. *Journal of Glaciology*, 63(237), 118–132. <https://doi.org/10.1017/jog.2016.125>
- Skiles, S. M. K., & Painter, T. H. (2018). Assessment of radiative forcing by light-absorbing particles in snow from in situ observations with radiative transfer modeling. *Journal of Hydrometeorology*, 19(8), 1397–1409. <https://doi.org/10.1175/JHM-D-18-0072.1>
- Solomos, S., Kalivitis, N., Mihalopoulos, N., Amiridis, V., Kouvarakis, G., Gkikas, A., et al. (2018). From tropospheric folding to Khamsin and Foehn winds: How atmospheric dynamics advanced a record-breaking dust episode in Crete. *Atmosphere*, 9(7), 240. <https://doi.org/10.3390/atmos9070240>
- Sounding. (2022). Upper air sounding data [Dataset]. <https://weather.uwyo.edu/upperair/sounding.html>
- Thiel, A. (2013). Climate change impacts on agriculture in the Colorado River Basin. School of Freshwater Sciences: Center for Water Policy at University of Wisconsin. Retrieved from https://uwm.edu/centerforwaterpolicy/wp-content/uploads/sites/170/2013/10/Colorado_Agriculture_Final.pdf
- Thompson, G., Field, P. R., Rasmussen, R. M., & Hall, W. D. (2008). Explicit forecasts of winter precipitation using an improved bulk microphysics scheme. Part II: Implementation of a new snow parameterization. *Monthly Weather Review*, 136(12), 5095–5115. <https://doi.org/10.1175/2008MWR2387.1>
- Tong, D. Q., Gill, T. E., Sprigg, W. A., Van Pelt, R. S., Baklanov, A. A., Barker, B. M., et al. (2023). Health and safety effects of airborne soil dust in the Americas and beyond. *Reviews of Geophysics*, 61(2), e2021RG000763. <https://doi.org/10.1029/2021RG000763>
- Ukhov, A., Ahmadov, R., Grell, G., & Stenchikov, G. (2021). Improving dust simulations in WRF-Chem v4.1.3 coupled with the GOCART aerosol module. *Geoscientific Model Development*, 14(1), 473–493. <https://doi.org/10.5194/gmd-14-473-2021>
- Webb, N. P., Chappell, A., LeGrand, S. L., Ziegler, N. P., & Edwards, B. L. (2020). A note on the use of drag partition in aeolian transport models. *Aeolian Research*, 42, 100560. <https://doi.org/10.1016/J.AEOLIA.2019.100560>
- Webb, N. P., Okin, G. S., & Brown, S. (2014). The effect of roughness elements on wind erosion: The importance of surface shear stress distribution. *Journal of Geophysical Research: Atmospheres*, 119(10), 6066–6084. <https://doi.org/10.1002/2014JD021491>

- Webb, N. P., Van Zee, J. W., Karl, J. W., Herrick, J. E., Courtright, E. M., Billings, B. J., et al. (2017). Enhancing wind erosion monitoring and assessment for US rangelands. *Rangelands*, 39(3–4), 85–96. <https://doi.org/10.1016/j.rala.2017.04.001>
- Yver, C. E., Graven, H. D., Lucas, D. D., Cameron-Smith, P. J., Keeling, R. F., & Weiss, R. F. (2013). Evaluating transport in the WRF model along the California coast. *Atmospheric Chemistry and Physics*, 13(4), 1837–1852. <https://doi.org/10.5194/acp-13-1837-2013>
- Zhang, H., Pu, Z., & Zhang, X. (2013). Examination of errors in near-surface temperature and wind from WRF numerical simulations in regions of complex terrain. *Weather and Forecasting*, 28(3), 893–914. <https://doi.org/10.1175/WAF-D-12-00109.1>
- Zhang, Y., Sartelet, K., Wu, S.-Y., & Seigneur, C. (2013). Application of WRF/Chem-MADRID and WRF/Polyphemus in Europe – Part 1: Model description, evaluation of meteorological predictions, and aerosol–meteorology interactions. *Atmospheric Chemistry and Physics*, 13(14), 6807–6843. <https://doi.org/10.5194/acp-13-6807-2013>
- Zhao, C., Liu, X., Leung, L. R., Johnson, B., McFarlane, S. A., Gustafson, W. I., Jr., et al. (2010). The spatial distribution of mineral dust and its shortwave radiative forcing over North Africa: Modeling sensitivities to dust emissions and aerosol size treatments. *Atmospheric Chemistry and Physics*, 10(18), 8821–8838. <https://doi.org/10.5194/acp-10-8821-2010>

Planting Date and Plant Density Effects on Maize Growth, Yield and Water Use Efficiency

Koffi Djaman¹, Samuel Allen¹

¹Department of Plant and Environmental Sciences,
Agricultural Science Center at Farmington, New Mexico State University

Dorlote S. Djaman², Komlan Koudahe²

²Biological and Agricultural Engineering Department, Kansas State University

Suat Irmak³

³Agricultural and Biological Engineering Department,
The Pennsylvania State University

Naveen Puppala⁴, Sangamesh V. Angadi⁴

⁴Department of Plant and Environmental Sciences,
Agricultural Science Center at Clovis, New Mexico State University

Murali K. Darapuneni⁵

⁵Department of Plant and Environmental Sciences,
Agricultural Science Center at Tucumcari, New Mexico State University

ABSTRACT

Weather conditions in the southwestern United States are variable and influence crop growing periods with late spring and early fall frosts which significantly impact cropping seasons. With the development of new maize hybrids, grain yield, evapotranspiration, and water use efficiency can be substantially impacted by planting density and planting date. Thus, the optimum plant density and planting date for maximum grain yield must be determined for local conditions. Field experiments were conducted at NMSU Agricultural Science Center in Farmington to evaluate six plant densities (54,700; 64,600; 74,600, 88,000; 101,700; and 120,100 pph) under seven planting dates (from April 23 to June 5 in 2019 and from April 21 to June 10 in 2020) to determine the planting window and the optimum density. Plots were sprinkler irrigated and crop management was similar across all planting dates during the two growing seasons. The results showed that crop height and leaf area index varied with plant density and planting date. Grain yield also varied with plant density and planting date. The highest grain yield (16.8 Mg ha⁻¹) was observed under the density 101,700 pph which showed statistically similar yield as the density 88,000 pph and the first planting trended to provide the best grain yield in 2019. In 2020, the highest grain yield (17Mg ha⁻¹) was obtained under the density 88,000 pph on May 18 planting date. Plant density 88,000 pph was revealed as the optimum density that maximized grain yield and WUE and maize planting after May 25 is not recommended.

Abbreviations: ANOVA, analysis of variance; CWUE, crop water use efficiency; DOY, day of the year; ET_a, actual evapotranspiration; ET_o, reference evapotranspiration; LAI, leaf area index; LSD, least significant difference; NMSU, New Mexico state university; pph, plant per hectare; RH_{min}, minimum relative humidity; RH_{max}, maximum relative humidity; RH_{mean}, average relative humidity; T_{min}, minimum temperature; T_{max}, maximum temperature; T_{mean}, average temperature, TU, thermal unit; US, United States; WUE, water use efficiency; u₂, wind speed; R_s, solar radiation.

1. INTRODUCTION

Maize (*Zea mays L.*) is one of the major crops across the United States and its production in 2019 was 346 million tons (United State Department of Agriculture- National Agricultural Statistics Service USDA-NASS, 2020). Maize grain yield is strongly impacted by plant density, planting patterns, tillage types, water management, soil types, soil hydrological and chemical properties, and other management practices (Ciampitti and Vyn, 2012 ; Haegele Jason et al., 2014; Assefa et al., 2016). Optimization of plant density is the main strategy for increasing yield. High plant density exposes the plant to shading which prevents the plant from fully capturing light resulting in reductions in leaf development, leaf area index, leaf photosynthesis, and untimely total biomass production and grain yield (Yang et al., al.2017; Raza et al., al.2019; Feng et al., al.2019). Similarly, Ciampitti and Vyn (2012) and Timlin et al. (2014) stated that high plant density adversely affects plant growth due to insufficient sunlight and carbohydrate assimilation.

However, high plant density might yield greater if the germplasm or hybrid is tolerant to high competition among plants to light, nutrients, and water (Brekke et al., 2011 ; Berzsenyi and Tokatlidis, 2012). Dias et al. (2019) reported an optimum plant density of 78,500 pph for hybrid DKB390 and 71,000 pph for hybrid BG7049YH from different plant densities ranging from 60,000 to 90,000 pph in Brazil. Gou et al. (2017) found that maize leaf length and width decreased as plant density increased, while Haarhoff and Swanepoel (2019) reported that maize yield response to plant density is season dependent with more impact during the driest season while grain yield is not affected by plant density during a season with the highest early season rainfall. Ren et al. (2016) investigated six maize plant densities (37,500; 52,500; 67,500; 82,500; 97,500 and 112,500 pph) under rainfed conditions in Shouyang (China) and found an important maize grain yield variation related to the seasonal rainfall amounts. According to Ren et al. (2016) , grain yield decreased with increasing plant density in the extremely dry year while it had a parabolic relationship with plant density in dry, wet, and extreme wet years.

Liu et al. (2010) suggested that the optimum plant densities for maize cultivars Nongda 108 and Zhengdan 958 are 57,000 pph and 97,000 pph, respectively to achieve maximum grain yield and water use efficiency. Nevertheless, Shi et al. (2008) study indicated that maize response to plant density is cultivar dependent. The maize cultivars Yedan19 and Jidan159 showed a 7.1% decrease in grain yield from plant density 55,000 to 85,000 pph and 20.7% from 45,000 to 75,000 pph. Many other field studies have reported the effects of planting dates and plant densities on maize yield. In Maryland, an increase in maize grain yield with plant density from 56,000 to 128,000 pph was reported by Teasdale (1998) . In Brazil, a plant density of 80,000 pph is considered the optimum plant population (Beruski et al., 2020). In addition, maize crop yield is also significantly affected by planting dates.

Across the US, maize planting dates vary with climatic conditions and geographic situations. These conditions are determinants for the choice of maize cultivar or hybrid relative maturity by maize producers. The late spring frosts and/ or early fall frosts could be detrimental to maize production in terms of yield quantity and quality (Djaman et al., 2020). Overall, early plantings improve maize grain yield and quality as plants reach their physiological maturity before the occurrence of fall low air temperatures, and/ or early fall frost (Irmak and Djaman, 2016; Long et al., 2017; Djaman et al., 2020). Maize optimum planting window is location and maize hybrid relative maturity date dependent and the optimum planting window is narrower in northern sites and wider in southern sites, except the North Central US (Baum et al., 2019). However, early planting is usually jeopardized by a low soil temperature as well as high soil moisture conditions for machinery operation and seed germination under humid and sub-humid climatic conditions (Cassman, 2016). Nielsen et al. (2002) and Parker et al. (2016) pointed out that too early maize planting was associated with potentially under-optimal soil and weather planting conditions while too late planting exposes plants to a reduced growing season length, low temperatures, and low-income solar radiation. Crop dry biomass and kernel weight decreases with delaying planting date due to low and decreasing temperature and radiation during the grain filling stage (Andrade et al., 1993). Yield reduction is observed when maize is planted before or later the optimum planting window (Zhou et al., 2016). Different optimum planting windows for maize are recommended across the US depending on the location even within the same State (Abendroth et al., 2017; Long et al., 2017; Baum et al., 2019). Early planting before mid-April is most likely to be affected by freezing soils, cooler soil temperatures for adequate plant emergence, and early establishment (Kucharik, 2008;

Long et al., 2017).). A significant correlation between maize planting date and latitude with maximal maize grain yield when planting window was 89–106 day of the year (DOY) for the 30–35°N, 107–118 DOY for the 35–40 °N, <119 DOY for 40–45°N, and < 129 DOY for 45–50 °N (Long et al., 2017). Nafziger (1994) revealed the last week of April as the optimum planting window for maize in the US Corn Belt while Baum et al. (2019) reported the period of April 22 - May 10 to be the optimum maize planting window across the central Corn Belt. Tollenaar and Bruulsema (1998) and Shrestha et al. (2018) found that under late planting the low temperatures prolonged maize silking-physiological maturity duration with non- proper grain black layer filling. The late-maturing maize hybrids generally obtain higher yield than the early maturing maize hybrids under early planting while early maturing maize hybrids yielded consistently across different planting dates due to a better-balanced source-sink ratio (Tsimba et al., 2013). Jiang et al. (2020) found long-season maize hybrids with the highest yield when planted before mid-June while the short -season maize hybrids are recommended to be planted after mid -June in Texas High Plains. Lindsey and Thomison (2016) reported that delayed planting resulted in an increase in agronomic optimum plant population compared to the May planting by 1300 pph, but the economic optimum plant population decreased by 3100 pph. Climate change has impacted maize optimum planting date and a 1 °C increase in mean temperature increases the length of the growing season by 10 days while the optimum planting date changed by -2+ 6 days, depending on the cultivar (Baum Mitch et al., 2020).

As demonstrated through different research studies, maize grain yield is affected by plant density, planting date, and other management practices. The climatic conditions are the main factor governing maize planting dates and may affect the crop response function to plant density and genotype. Therefore, it is critical to investigate the optimum maize plant density that maximizes grain yield and water use efficiency under local climatic conditions. The objective of this study was to determine maize planting window and optimum plant density that maximize grain yield under sprinkler irrigation at high elevations in northwestern New Mexico.

2. MATERIALS AND METHODS

2.1. Study area

Two-year field experiments were conducted from 2019 to 2020 at the Agricultural Science Center at Farmington, New Mexico State University, U.S. The experiment site is located at 36.69°N, 108.31°W, 1720 m above mean sea level and it is characterized by the semiarid climate. The long-term average annual precipitation, maximum temperature and minimum temperature at the study site are 216 mm, 17.2 °C and 2.2 °C, respectively, while maize growing season values of the same variables are 101 mm, 20.0 °C, and 10.8 °C, respectively (Djaman et al., 2018, 2020). During the experiment period, climate variables such as the maximum relative humidity (RHmax), minimum relative humidity (RHmin), average relative humidity (RHmean), minimum temperature (Tmin), maximum temperature (Tmax), average temperature (Tmean), solar radiation (Rs), and wind speed (u₂) were collected daily from an automated weather station installed at the site by the New Mexico Climate Center. Thermal unit (TU) was estimated for maize during maize growing seasons. The weather conditions for the 2019–2020 period are summarized in Figure 1. The soil at the experimental site is a well-drained Doak sandy loam with a pH 8.2 and low organic matter content (less than 1%).

2.2. Experimental design and crop management

Sequential weekly maize planting was performed at the NMSU Farmington Agricultural Science Center in 2019 and 2020. Six plant densities (54,700, 64,600, 74,600, 88,000, 101,700, and 120,100 plants/ha) were evaluated under seven planting dates in 2019 (April 23, May 1, May 7, May 14, May 22, May 30, and June 5) and in 2020 (April 21, April 30, May 7, May 18, May 27, June 3, and June 10). Hybrid maize DKC53–45RIB was the testing hybrid with a relative maturity of 103 days, growing degree units at mid-pollination of 1265 °C and black layer at 2530 °C. After chisel ripping, the plots were disked and harrowed. The experiment was set up under a split-split plot design with three replications. The main plots were attributed to the planting dates and the subplots were attributed to the plant densities. An experimental unit size was 9.14 m over 6.10 m. A John Deere 7200 two-row planter with 76-cm row spacing was used for sowing. Plots were solid set

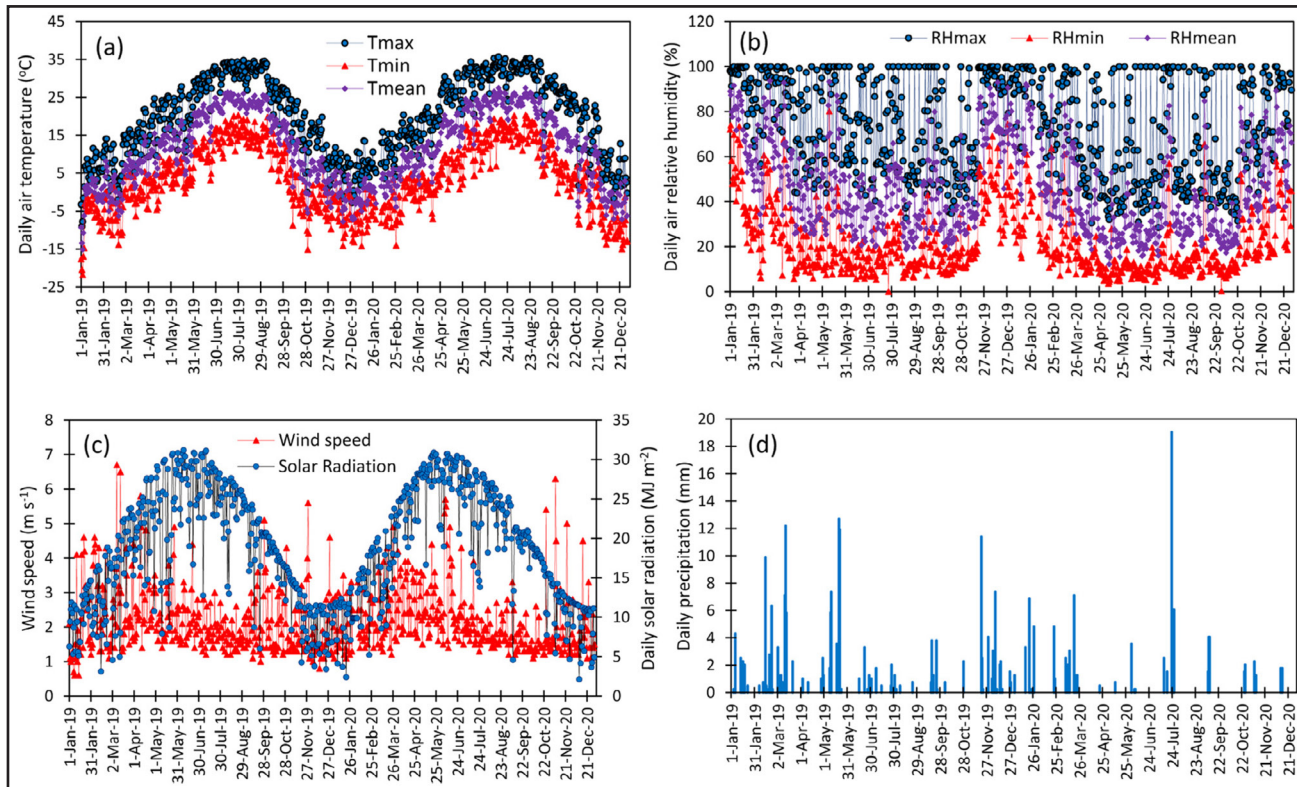


Figure 1. Weather condition during the 2019–2020 period at the experiment station: (a) air temperatures, (b) air relative humidity, (c) wing speed and solar radiation, and (d) precipitation.

sprinkler irrigated and the irrigation scheduling was based on maize actual evapotranspiration estimated by the two-step FAO approach ($ET_a = kc ETo$). Dry fertilizer was applied before planting at a rate of 56 kg ha^{-1} of the equal proportional mixture of mono-ammonium phosphate (11–52–0), potassium chloride (0–0–60), and urea (46–0–0). During maize growth phase, a total of 140 kg ha^{-1} of nitrogen in the form of liquid nitrogen (ammonium nitrate, 32–0–0) was timely applied from maize stage V4 to VT stage by fertigation. Weeds were controlled using glyphosate herbicide application at the recommended rate. Maximum plant height and leaf area index were measured at the maize plant full tasseling stage. Plant height was taken on ten plants per plot and the leaf area index was measured five times per plot using an LAI-2200C plant canopy analyzer (LI-COR Inc., Lincoln, NE, USA). At crop maturity, three central maize rows of each experimental unit were combine harvested and the grain weight and grain moisture content were measured. Plot yield was reported in Mg ha^{-1} after grain moisture adjustment to a standard grain moisture content of 14%.

2.3. Standardized Penman-Monteith reference evapotranspiration model

Daily grass-reference evapotranspiration (ETo) was computed using the standardized ASCE form of the Penman-Monteith Eq. (1):

$$ETo = \frac{0.408\Delta(Rn - G) + (\gamma Cn u_2 / (T + 273))(es - ea)}{\Delta + \gamma(1 + Cd u_2)} \quad (1)$$

where ETo is the reference evapotranspiration (mm day^{-1}), Δ is the slope of saturation vapor pressure versus air temperature curve ($\text{kPa } ^\circ\text{C}^{-1}$), Rn is the net radiation at the crop surface ($\text{MJ m}^{-2} \text{ d}^{-1}$), G is the soil heat flux density at the soil surface ($\text{MJ m}^{-2} \text{ d}^{-1}$), T is the mean daily air temperature at 1.5–2.5 m height ($^\circ\text{C}$), u_2 is the mean daily wind speed at 2 m height (m s^{-1}), es is the saturation vapor pressure at 1.5–2.5 m height (kPa), ea is the actual vapor pressure at 1.5–2.5 m height (kPa), $es - ea$ is the saturation vapor pressure deficit (kPa), γ is

the psychrometric constant ($\text{kPa}^\circ\text{C}^{-1}$), C_n and C_d are constants with values of $900^\circ\text{C mm s}^3 \text{Mg}^{-1} \text{d}^{-1}$ and 0.34sm^{-1} . The procedure developed by Allen et al. (1998) was used to compute the needed parameters.

2.4. Crop coefficients (Kc)

Maize was grown under non-limiting water and fertilizer conditions, and the standard crop coefficient curve locally developed by Sammis et al. (1985) was used in combination with the daily reference evapotranspiration for the daily maize crop actual evapotranspiration estimation. Daily values of crop evapotranspiration were summed throughout the growing season to obtain maize seasonal actual evapotranspiration. To generate the K_c curve, maize thermal units were estimated for each growing cycle and the K_c equation by Sammis et al. (1985) was applied daily Djaman et al., 2018). Eqs. (2) and (3).

$$K_c = 0.12 + 0.00168 \times TU - 2.45 \times 10^{-7} \times TU^2 - 4.37 \times 10^{-10} \times TU^3 \quad (2)$$

where K_c is the daily crop coefficient and TU is a thermal unit ($^\circ\text{C}$).

2.5. Thermal unit (TU)

Maize thermal unit is the accumulated growing degree days (GDD) that contribute to plant growth and development during the growing season and is expressed as follows:

$$TU = \sum_{i=1}^n \frac{T_{max} + T_{min}}{2} - T_{base} \quad (3)$$

where TU = thermal unit ($^\circ\text{C}$), T_{max} = maximum air temperature ($^\circ\text{C}$), T_{min} = minimum air temperature ($^\circ\text{C}$), T_{base} = base temperature threshold for maize (10°C), and n = number of days. The base temperature is the minimum threshold temperature at which plant growth starts. The maximum and minimum temperature thresholds for maize were of 30°C and 10°C , respectively. The TU value was assumed to be zero if the average daily temperature was below the base temperature because no crop growth occurs in that condition.

2.6. Actual evapotranspiration estimation (ETa)

Daily maize ET_a was estimated as the product of the daily ET_o and the corresponding crop coefficient according to the Eq. (4) proposed by Jensen (1968) and Allen et al. (1998). Maize seasonal evapotranspiration was obtained as the summation of all daily actual evapotranspiration values from crop planting to its physiological maturity.

$$ET_a = K_c \times ET_o \quad (4)$$

where ET_a = daily actual evapotranspiration (mm), K_c = daily crop coefficient, and ET_o = grass reference evapotranspiration (mm).

2.7. Irrigation water requirement (IWR)

The study site is characterized by an arid climate with not usually enough rainfall before the start of crop growing season. Therefore, pre-irrigation was practiced to facilitate crop germination and emergence. Irrigation water requirement was calculated using following Eq. (5) :

$$WR = \frac{PR + ET_a + DP + RO - Pe}{Eff} \quad (5)$$

where PR = pre-irrigation (mm), equal to the soil water holding capacity, ETa = actual evapotranspiration (mm), DP = deep percolation (mm), Ro = runoff (mm), and Pe = effective precipitation (mm), Eff = efficiency of the irrigation system (0.85). Deep percolation was estimated by the soil water balance approach using a program written in Microsoft Visual Basic (Bryant et al., 1992) and the effective precipitation was estimated according to Chen et al. (2014).

2.8. Crop water use efficiency

Crop water use efficiency (WUE) was estimated as the ratio of maize grain yield and maize seasonal evapotranspiration (Eq. (6)) (Djaman et al., 2018 ; Liang et al., 2021).

$$WUE = \frac{Yield}{Maize\ seasonal\ ETa} \quad (6)$$

where WUE is in $kg\ m^{-3}$, yield in $kg\ ha^{-1}$, and maize seasonal ETa is the seasonal cumulative ETa (mm).

2.9. Statistical analysis

The analysis of variance (ANOVA) was performed to analyze the effects of planting date and plant density on maize LAI, plant height, yield and crop water use efficiency using CoStat statistical software. Means were cross-paired and compared using LSD at 5% significance level in the case of significance of the impact of a factor (planting date, plant density) on the measured variable (plant height, LAI, grain yield, and WUE). Correlation analysis was also performed to determine the relationships between plant population and grain yield for each planting date in 2019 and 2020. Similar relationships were determined between the kernel number per maize ear and the plant densities. The coefficient of determination R^2 was used to quantify the fitness of the relationships.

3. RESULTS AND DISCUSSION

3.1. Weather conditions during the 2019 and 2020 growing seasons

Daily weather conditions during the experiment period 2019–2020 are presented in Figure 1 . The maximum, minimum, and average temperatures increased from January 1, 2019 to the maximum values mid-July and decreased thereafter to the minimum values at the end of December 2019 early January 2020. A similar trend was shown in 2020. Monthly average air temperature varied from $-1.5\ ^\circ C$ (January 2019) to $24\ ^\circ C$ in July 2019 and decreased to the lowest value of $-0.6\ ^\circ C$ in January 2020. It increased later up to $24.7\ ^\circ C$ in August and decreased to $-2.7\ ^\circ C$ in December 2020. As we started planting from April to early June, soil temperature which has a very strong correlation ($R^2 = 0.93$) with the air temperature (Figure 2) is very important for the metabolism and physiology of the seed. Average air temperature in April 2019 and April 2020 were $11.7\ ^\circ C$ and $11.6\ ^\circ C$ while average air temperature values in June 2019 and 2020 were 12.3 and $18.1\ ^\circ C$, respectively. A similar trend was observed in the soil temperature. There was a temperature drop during the May18–22 period with a snowfall on May 20, 2019. Air temperature in May 2020 was 47.2% higher than the temperature in May 2019. Overall, the weather was warmer during the 2020 growing season compared to the 2019 growing season. This was transited by the higher accumulated thermal units in 2020 compared to 2019 (Figure 3).

The trend in the daily air relative humidity looks similar in both years (Figure 1), however, the average seasonal (April-October) relative humidity was 39.2% in 2019 and 31.3%. The seasonal relative humidity in 2020 was 20.2% lower compared to the value in 2019. The crop growing season air temperature in 2020 was higher than the crop growing season air temperature in 2019 while lower seasonal relative humidity was observed in 2020 compared to the seasonal air relative humidity in 2019. The evaporative demand in 2020 was, therefore, higher than the evaporative demand in 2019. Moreover, the seasonal total precipitation was 77.3 mm in 2019 and 50.7 mm in 2020 (Figure 1). Consequently, from these weather data, crop evapotranspiration and irrigation water requirement were therefore higher in 2020 than in 2019 as shown

in Figure 4 , reference evapotranspiration was slightly higher in 2020 than in 2019. There was no significant difference in the seasonal total incoming solar radiation which was 161 MJ m⁻² in 2019 against 166.0 MJ m⁻² (Figure 1) and wind speed which averaged 2.18 m s⁻¹ and 2.19 m s⁻¹ in 2020 (Figure 1).

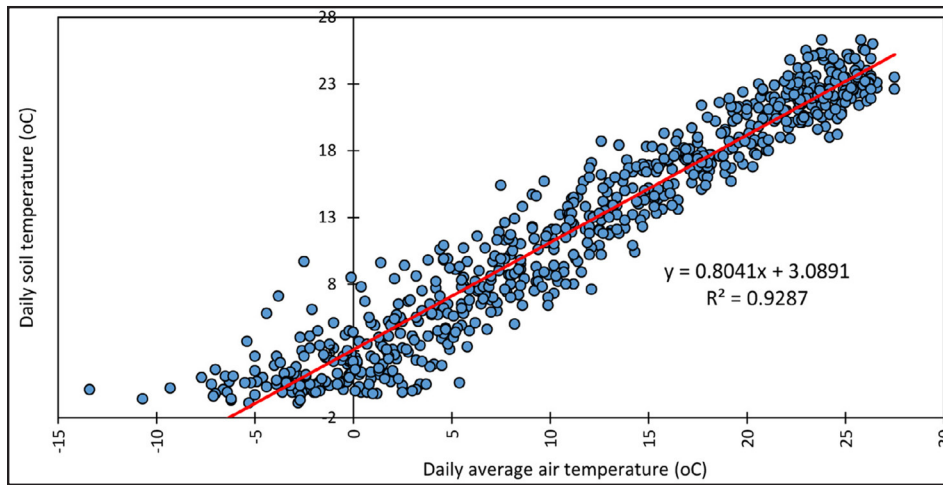


Figure 2. Relationship between mean daily air temperature and the soil temperature (average upper 10 cm layer) during the 2019–2020 period at the experiment station.

Figure 3. Maize growing degree days and thermal unit available in 2019 and 2020 at the experiment station.

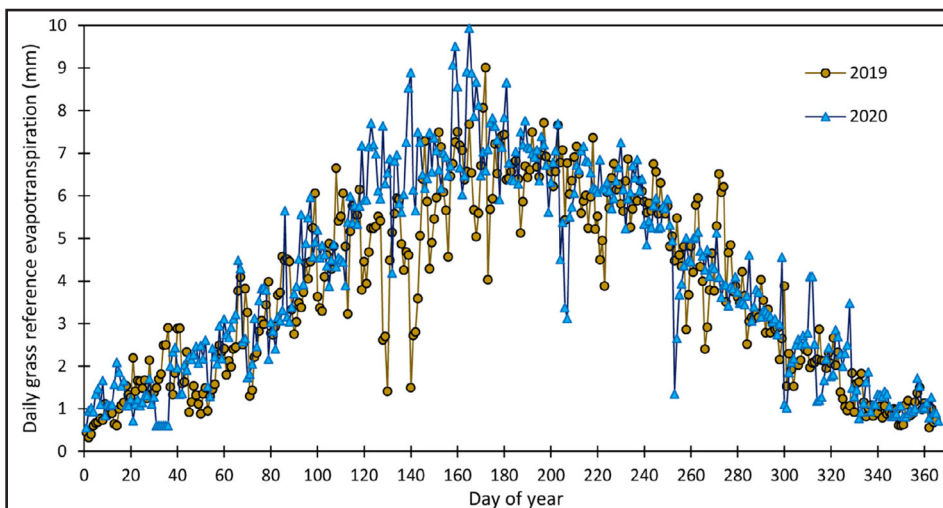
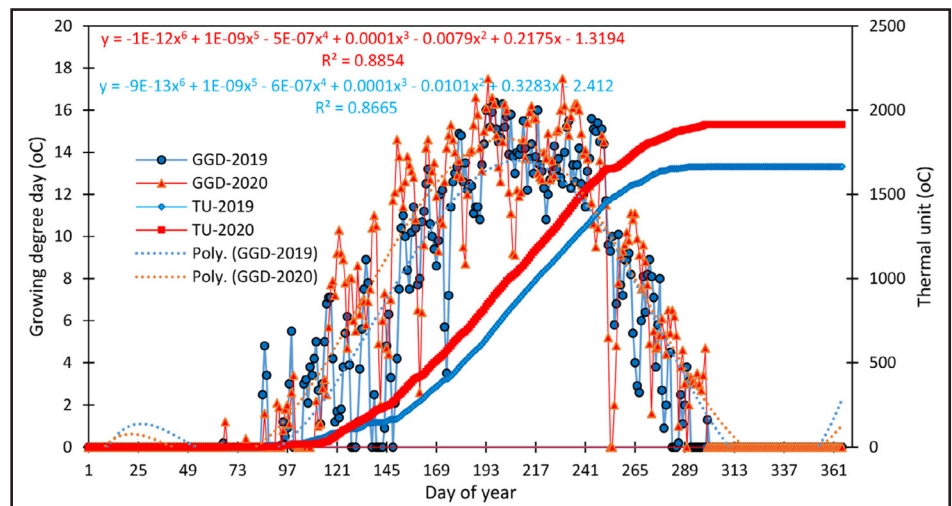


Figure 4. Variation in the daily ETo during 2019 and 2020 at the experiment station.

3.2. Effect of planting date and plant density on the growth parameters of maize

Maize emergence varied with planting date as the effect of soil and air temperature on the seed metabolism. Maize planted on April 23, May 1, May 7, May 14, May 22, May 30, and June 5 emerged on May 6, May 16, May 23, May 29, June 3, June 07, and June 11, respectively. The first two plantings (April 23, May 1, May 7) were subject to cold temperature damage due to temperature drop during May 18–22 with snowfall on May 20. However, maize plants survived as their growing point was underground and it was not impacted by the freezing air temperatures. Maize plants reached the tasseling stage on July 28, July 30, July 30, August 02, August 04, August 07, and August 09 for the respective planting dates in 2019. During the 2020 season, maize was planted on April 21, April 30, May 7, May 18, May 27, June 3, and June 10, and emerged on May 7, May 11, May 17, May 26, June 3, June 9 and June 15, respectively. In contrast to the cold event with snow around May 18–22, 2019, there was a hot desert sand dune dust storm blowing on June 6–8, 2020 and which burnt the young corn seedlings. The young seedling recovered the damage as the growing point was situated below the ground surface. Maize plants reached the tasseling stage on July 12, July 18, July 20, July 28, August 03, August 09, and August 13 for the respective planting dates in 2020. The accumulated thermal units by the April 23, May 1, May 7, May 14, May 22, May 30 and June 5 plantings were 830.0, 824.2, 803.9, 829.6, 829.1, 854.9, and 828.8 °C, respectively, and averaged 828.6 °C. The accumulated thermal units by the April 21, April 30, May 7, May 18, May 27, June 3, and June 10 plantings were 828.7, 878.4, 851.1, 866.0, 899.6, 892.9,

and 874 °C, respectively and averaged 870.1 °C, representing a 5% increase in maize plant accumulated thermal units in 2020 compared to 2019. Overall, there was a slight increase in maize plant thermal unit accumulated from the first planting to the last planting during both growing seasons.

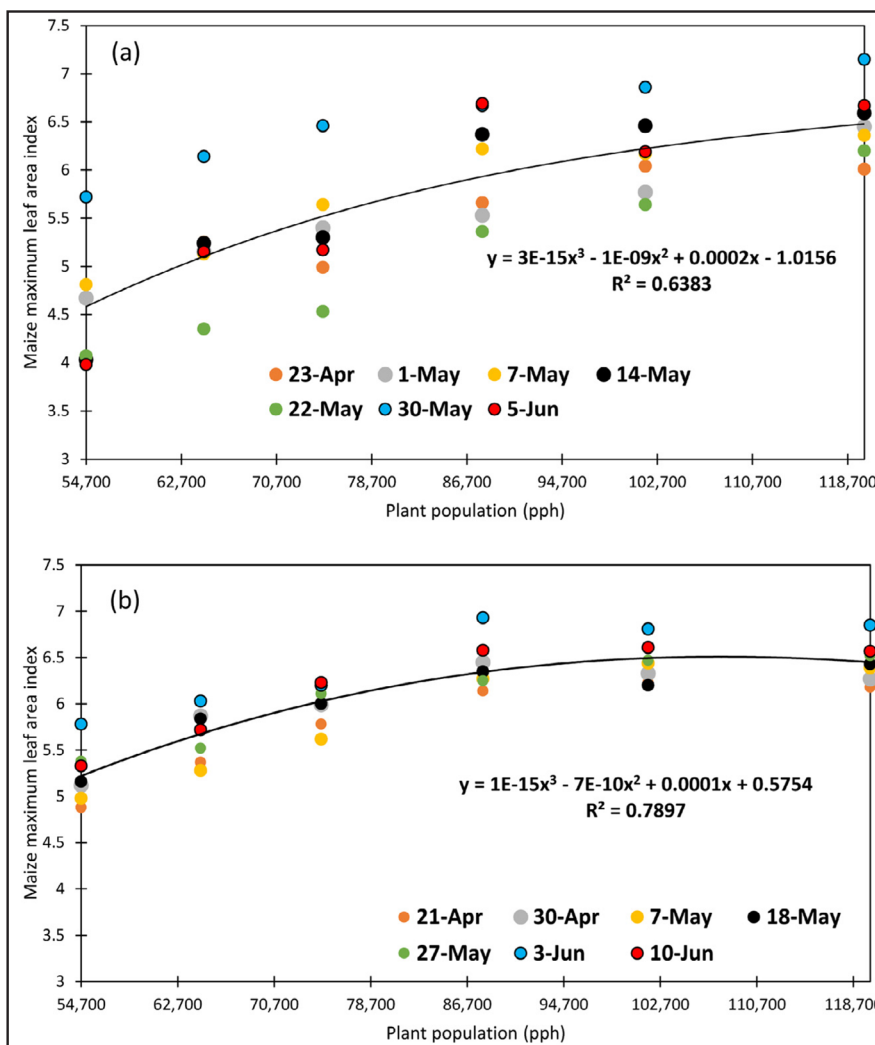


Figure 5. Relationship between maximum leaf area index and plant population in 2019 and 2020.

Maize leaf area index varied with plant densities and planting date. Leaf area index varied from 3.98 to 7.15 in 2019 (Figure 5 a) and from 4.88 to 6.93 in 2020 (Figure 5 b). While the lowest leaf area index was obtained by 54,700 pph during both growing seasons, the maximum leaf area index was obtained by 120,100 pph in 2019 and by 88,000 pph in 2020. The lower LAI under the 120,100 pph in 2020 compared to the LAI under the same density in 2019 might be due to the impact of spider mite (*Tetranychus urticae*) infestation in 2020. The 2019 growing season was cooler than the 2020 growing season and the warmer and dry conditions during July-August 2020 favored plot infestation with spider mites. The spider mites feed on the leaves, sucking out chlorophyll

from cells, which lead to leaf discoloration, and senescence with more severe impact under the high densities 101,700 and 120,100 pph and reducing LAI under those densities. The plots were treated with a miticide Zeal (Etoxazole 72%) on August 14 however, the damage was already important and the new spider mite eggs hatching reinfested and prolonged the damage. Overall during the 2019 season, the May 30 planting showed the highest leaf area index across all densities while the May 22 planting obtained the lowest leaf area index across plant densities. In 2020 growing season, the highest leaf area index was obtained under the June 3

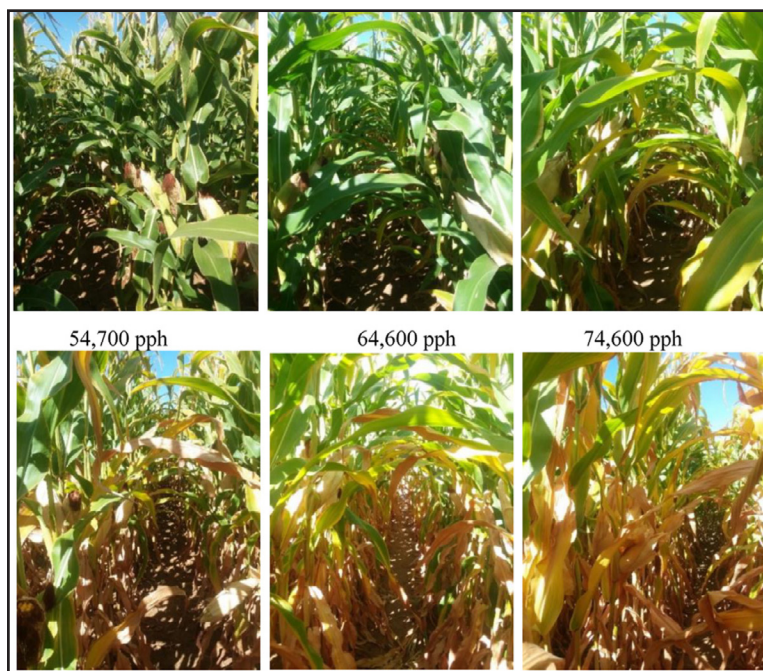


Figure 6. Differences in plant maturity and appearance of maize plants under different population treatments.



Figure 7. Impact of low temperature on June 10 planting maize plant observed on September 20, 2020.

planting and the lowest leaf area index was recorded under the May 7 planting across the densities. Maize leaf area index averaged 4.56, 5.20, 5.36, 6.07, 6.16, and 6.49 in 2019 and 5.23, 5.66, 5.99, 6.42, 6.44, and 6.46 in 2020 for the densities 54,700; 64,600; 74,600; 88,000; 101,700, and 120,200 pph, respectively. Maize leaf area index showed a quadratic correlation with the plant density with R^2 values of 0.64 in 2019 and 0.79 in 2020 (Figure 5). While there is no clear trend in maize leaf area index with delayed planting, maize leaf area index increased with plant density with the highest values at the high densities. These results contradicted the findings of Jia et al. (2018) who reported significantly higher maximum leaf area index at the low and medium plant density than the high plant density at silking stage. Timlin et al. (2014) indicated that leaf area index was dependent on plant density. In contrast, Irmak and Djaman (2016) reported no significant effect of plant density or planting date on maize plant height and leaf area index during a two-year experiment under subsurface drip irrigation in southcentral Nebraska. Maize plant growth period decreased with increasing plant density for the same planting date; plant senescence started with the highest density 120,100 pph and decreased toward the lower densities (Figure 6). With increasing plant density, a reduced amount of solar radiation is intercepted by the lower strata leaves and the utilization efficiency of radiation decreased promoting accelerated rate of leaf senescence (Borras et al., 2003 ; Liu et al., 2016). Moreover, lower leaf senescence suppressed root growth, N uptake, and altered N partition, thereby decreasing green leaf area and ultimately affecting grain yield (Li et al., 2019). The last plantings were at risk as they did not reach the crop physiological maturity before the occurrence of the early fall frost as shown in Figure 7.

Maize plant height increased with delaying planting date during both growing seasons while there were no significant differences between plant populations for the same planting date. In 2019, the first two planting dates obtained similar plant height (253.6 cm) which was lower and different from the plant height of the next 3 planting dates (May 7, May 14, May 22) with significantly similar heights (264.4 cm) and the May 30 and June 3 planting had the highest plant height (297.1 cm) (Table 1). During the 2020 growing season, the April 21 planting obtained the lowest plant height (234.8 cm), significantly lower than the April 30 and May 7 plantings (255.3 cm) (Table 1). The May 18, May 27 and June 3 plantings obtained statistically similar plant height (276.7 cm) which is higher than the previous planting plant height but significantly lower than the June planting plant height of 283.3 cm. The increase of plant height with delayed planting is a reflection of the growth rates with more available energy with the delayed planting. Daily thermal unit increased from the first plant to the last plant and continue until mid-July and decreased thereafter as shown in Figure 3. Our results are in agreement with Irmak and Djaman (2016) who reported that maize plant height was not significantly affected by plant density, however, delaying planting date significantly affected plant height as reported in the present study. In contrast, Tetio-Kagho and Gardner (1988) reported that maize plant height was significantly affected by plant density with the decrease in plant height at higher densities. Similar findings were reported by Bernhard and Below (2020).

Table 1. Maximum plant height (cm) as a function of planting dates and plant densities for the 2019 and 2020 seasons.

Plant densities	Planting dates (2019)						
	23-Apr	1-May	7-May	14-May	2-May	30-May	5-Jun
54,700	251.4 ± 5.5	260.5 ± 4.4	266.5 ± 3.7	265.6 ± 4.2	259.3 ± 8.9	296.6 ± 9.7	298.8 ± 8.3
64,600	255.3 ± 3.7	254.3 ± 8.6	265.3 ± 8.3	265.7 ± 6.6	259 ± 5.4	298.1 ± 8.6	297.3 ± 7.6
74,600	250.2 ± 5.2	254.8 ± 10.5	266 ± 6.3	265 ± 8.1	244.5 ± 7.9	297.3 ± 12.2	287.9 ± 10.4
88,000	247.4 ± 6.4	257.5 ± 8.0	268.3 ± 3.7	261 ± 5.6	270.9 ± 8.3	298.8 ± 15.6	300 ± 7.7
101,700	257.1 ± 4.6	258.8 ± 9.0	268.3 ± 6.5	269.3 ± 6.5	270.5 ± 7.8	298.1 ± 12.9	296.6 ± 6.4
120,100	251.8 ± 4.4	244.3 ± 5.7	264.1 ± 5.7	265 ± 7.5	265 ± 8.7	297.5 ± 8.9	298.1 ± 6.8
Plant densities	Planting dates (2020)						
	21-Apr	30-Apr	7-May	18-May	27-May	3-Jun	10-Jun
54,700	233.7 ± 9.9	253.4 ± 6.1	259.7 ± 9.4	278.8 ± 2.9	278.8 ± 8.5	269.9 ± 15.7	273.7 ± 9.8
64,600	237.5 ± 5.9	257.2 ± 6.7	264.8 ± 7.5	278.8 ± 5.2	278.8 ± 7.9	281.3 ± 4.2	285.8 ± 4.5
74,600	237.5 ± 8.0	251.5 ± 5.8	249.6 ± 5.8	271.8 ± 4.0	271.8 ± 10.9	271.8 ± 7.6	284.5 ± 7.5
88,000	232.4 ± 3.0	260.4 ± 3.6	252.7 ± 2.7	266.7 ± 2.6	266.7 ± 8.1	278.1 ± 7.3	284.5 ± 7.8
101,700	233.7 ± 5.3	246.4 ± 5.0	265.4 ± 4.2	285.8 ± 5.6	285.8 ± 3.2	278.8 ± 9.0	297.8 ± 7.1
120,100	233.7 ± 7.6	247.7 ± 10.3	255.3 ± 6.6	280 ± 6.5	280 ± 5.9	277.5 ± 9.1	273.7 ± 9.7

3.3. Effect of planting date and plant density on maize grain yield and yield components

The maize ear length and yield components decreased with the increasing plant population. Maize kernels per ear significantly varied with plant density and ranged from 447 to 675 in 2019 and from 375 to 0 712 in 2020. Plant density 54,700 pph obtained the highest kernels number per plant while the lowest kernel number per plant was obtained by the density 120,100 pph. Average kernels number per plant was 640 ± 29 , 625 ± 17 , 604 ± 20 , 573 ± 28 , 512 ± 15 , and 474 ± 22 kernels for the 54,700; 64,600; 74,600; 88,000; 101,70–0 and 120,100 pph in 2019, and 696 ± 17 , 662 ± 28 , 612 ± 47 , 595 ± 26 , 512 ± 37 and 450 ± 37 kernels under the respective densities in 2020. The number of kernels per plant linearly decreased as the plant population increased (Figure 8). These findings are in agreement with different findings of several studies. Jia et al. (2018) reported a decrease in maize number of kernel per row, number of kernels per ear, and kernel yield per plant with increasing plant density. Similar findings were reported by Borrás et al. (2003), Echarte et al. (2000), and Zhang et al. (2015). Yan et al. (2018) reported maize kernel number per plant that varied between 525.3 to 614 and 358.2 to 523.4 with a significant impact of sowing date and plant density on the kernel number per plant. Chen et al. (2013) indicated that kernel number accounts for most of the trend in maize grain yield components,

especially for the apical kernels, which have the lowest priority for assimilating supply. Cerrudo et al. (2020) found that across plant densities, the kernel number per plant was associated with greater prolificacy at low plant density. Echarte et al. (2000) reported decreasing trend in kernels number per plant with increasing plant density in four hybrids. Fischer and Palmer (1984) indicated that kernel number in general accounts for most of the variation in yield. Tollenaar et al. (1992) also concluded that kernel number contributed most to the difference in grain yield among hybrids released during different decades in Canada. Sangoi et al. (2002) found that plant density greatly affects the grain filling process and the yield components while Andrade et al. (2000) pointed out that kernel number is one of the most important components of maize grain yield and is the most variable factor of yield components. Different planting dates put crop growth stages to occur under different climatic conditions. From the planting to tasseling, maize plants from different planting were under different temperature conditions as temperature increased with delayed plantings. The opposite phenomenon occurred during the reproductive phase of the different plantings dates (Yan et al., 2018). Photo-synthetically active radiation interception increases with increasing maize density (Shen et al., 1993 ; Yang et al., 2010) but under high plant density, the ability of light to penetrate the lower canopy is reduced (Liu et al., 2014) and the light intensity within maize canopy decreased with increasing density (Gou et al., 2017). The radiation use efficiency is therefore reduced (Lin et al., 2016) and premature senescence of the lower leaves occurs (Borrás et al., 2003) and grain yield is significantly reduced (Borrás et al., 2003 ; Sangoi et al., 2002 ; Maddonni and Otegui, 2004).

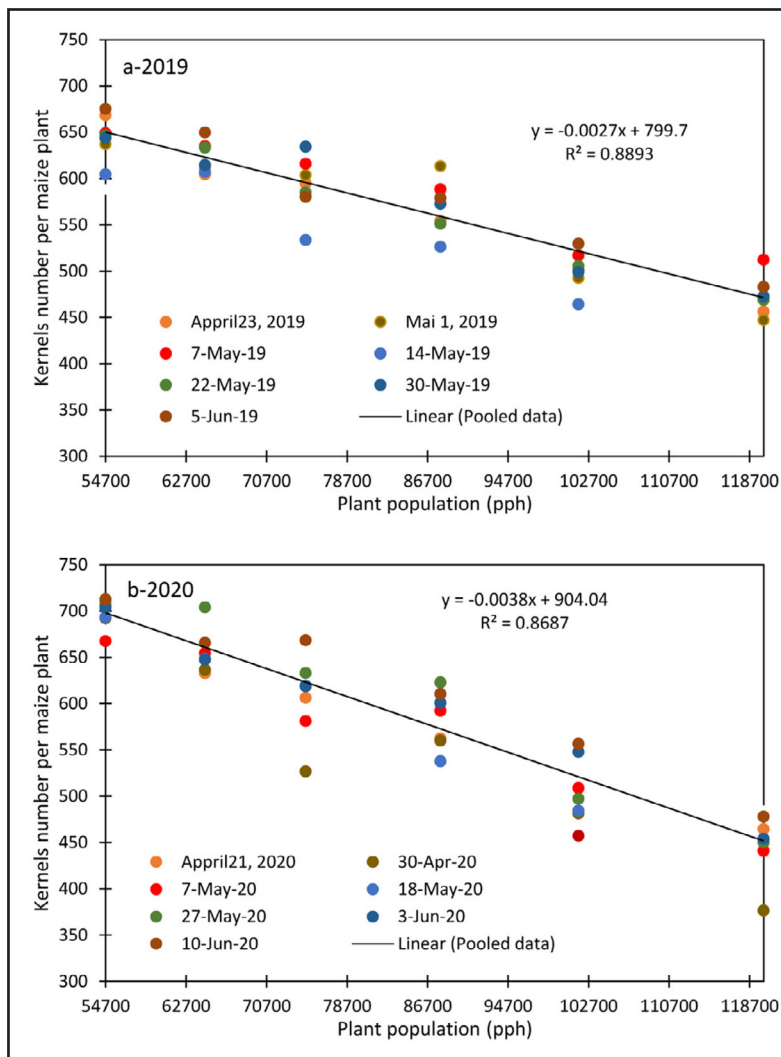


Figure 8. Relationship between maize kernel number per plant and plant density under different planting dates in 2019 and 2020.

Plant density is one of the major factors that impact crop yield and water use. Maize yield varied with plant densities and planting dates. It varied from 10.89 Mg ha⁻¹ to 16.77 Mg ha⁻¹ and from 11.87 to 17.77 Mg ha⁻¹ in 2020 (Figure 9). In both years, the lowest yield was obtained by 54,700 pph while the highest yield was obtained by 101,700 pph in 2019 and 88,000 pph in 2020. Maize grain yield showed a strong quadratic relationship with the plant density under different planting dates with R^2 varying from 0.90 to 0.99 in 2019 and from 0.73 to 0.97 in 2020 (Figure 9). For all plant densities combined, the April 23 planting registered the highest maize grain yield, and the lowest yield was registered for June 5 planting in 2019 while in 2020, the highest yield was registered for May 18 planting and the lowest yield was obtained by the April 30 planting (Figure 9). On a two-year average, the plant densities 54,700; 64,600; 74,600; 88,000; 101,700, and 120,100 pph yielded 12.64 ± 0.84 , 13.77 ± 0.73 , 14.63 ± 0.61 , 15.88 ± 0.98 , 15.64 ± 1.14 , and 14.81 ± 1.35 Mg ha⁻¹, respectively. During the 2019 season, the first three plantings obtained the best yield performance while the very last planting (June 5) obtained the lowest grain yield. Early planting in the cold spring of 2019 promoted higher yield which showed the least decline with delaying planting.

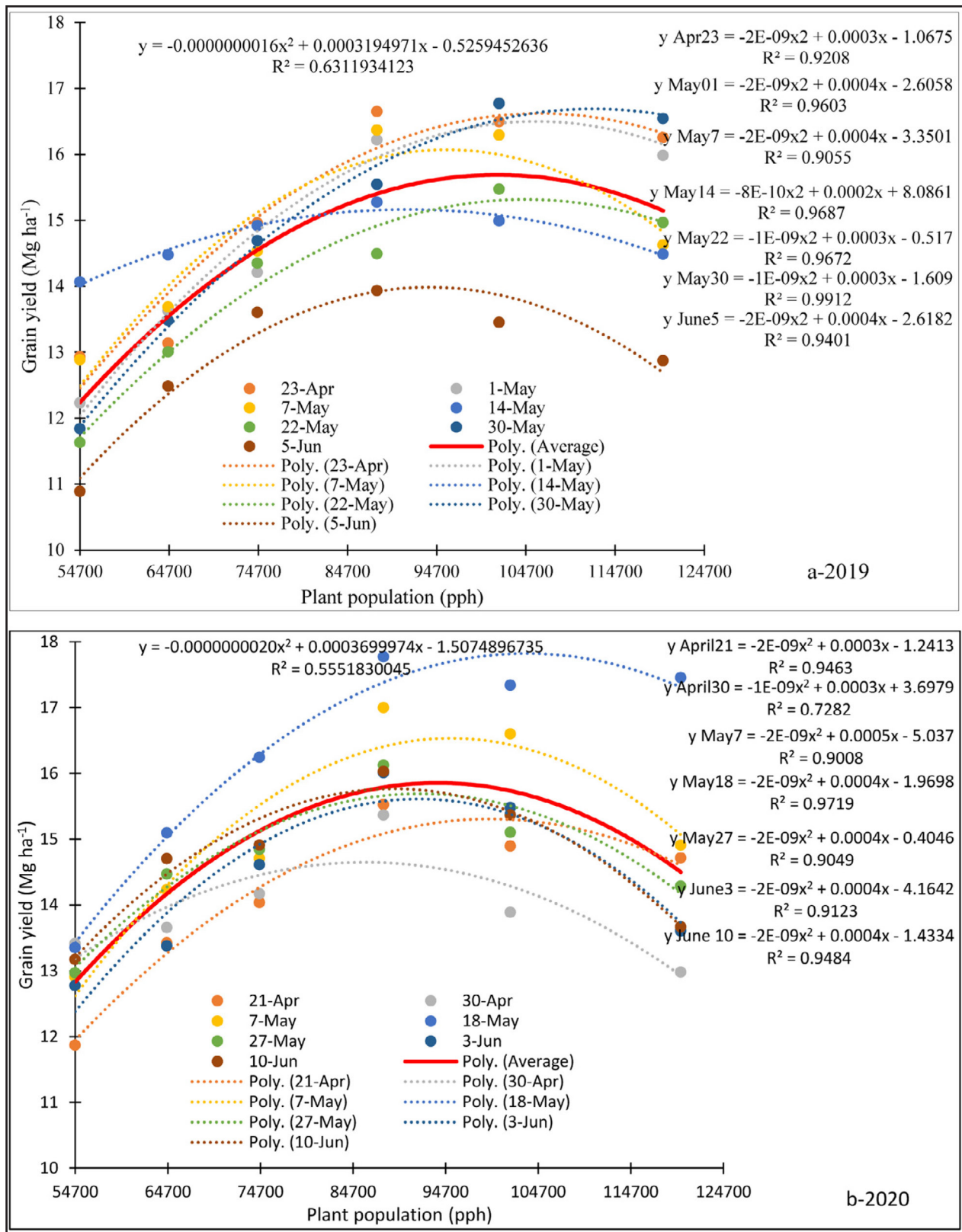


Figure 9. Relationship between maize plant population and grain yield under different planting dates in 2019 and 2020.

During the warm spring in 2020, grain yield increased from the April 21 planting up to May 18 planting and decreased thereafter until June 10 planting. The pooled data showed no significant difference between plant densities 88,000 and 101,700 pph which obtained the highest grain yield. Due to the cost of the hybrid seed, a plant density of 88,000 pph should be recommended for the hybrid maize seeding rate in the study area and the neighboring environment. From the present study, there is no clear planting window and the planting timing depends on the hardness of the spring temperature. Early planting is the best option during the cold spring while mid-May planting is revealed the optimum planting time. Crop growing might rely on the season forecasting for proper decision making. Solomon et al. (2017) suggested that the choice of maize plant densities should be based on seasonal weather forecasts to maximize opportunities for higher yields. However, as many farmers always suggested, planting during American Mother's Day week should be the last option for maize planting in Northwestern New Mexico. Two years' data combined, delaying 54,700 pph planting for one day decreases grain yield by 8.6 kg ha⁻¹, while each delay of 64,600 pph increases grain yield by 4.9 kg ha⁻¹ and each delay of 74,600 pph increases grain yield by 3.6 kg ha⁻¹. Each one-day delay in planting 88,000; 101,700; and 120,100 pph decreased grain yield by 15.8, 12.8 and 23.8 kg ha⁻¹, respectively. The results of the present study are in agreement with the findings of other studies. Westgate et al. (1997) indicated that an increase in plant density is associated with higher yield grain due to early canopy closure improving light interception and decreasing soil water evaporation. However, when the optimum density is reached, increasing density is associated with a decrease in maize grain yield as the radiation use efficiency decreases and the competition among plants for water and nutrient increases (Griesh and Yakout, 2001). Irmak and Djaman (2016) found increasing maize grain yield with an increase in plant density and the impact of planting date on grain yield varied with plant date and years in South-central Nebraska. The results of the present study are in agreement with Teasdale (1998) who reported that grain yield increased as plant density increased from 56,000 to 128,000 pph in Maryland, and Cox and Cherney (2001) who reported an increase in maize silage yield by increasing the plant density from 80,000 to 116,000 pph. In contrast, Shapiro and Wortmann (2006) reported no effect of plant density on maize grain yield beyond plant density of 61,800 pph. Similarly, Ping et al. (2008) reported a non-significant seed rate effect on maize yields in four site-years in Nebraska. Long et al. (2017) reported variation in maize optimum planting across the U.S. and found maize planting dates as 42 and 88; 89 and 106; 107 and 118; 119 and 128; and 129 and 135 days of the year for the latitude groups between 25 and 30; 30 and 35; 35 and 40; 40 and 45; and 45 and 50 °N, respectively. With the development of new hybrid maize with different plant architecture producing only one ear per plant (Gerdner and Pearce, 1985), optimum plant density that maximizes grain yield might vary with environment and even with maize hybrid. Maize optimum density was 98,800–104,500 pph across the Corn Belt region (Stanger and Lauer, 2007), 67,000–70,000 pph in the US semiarid regions (Lamm et al., 2008; Al-kaisi and Yin, 2003), and 90,000 pph in the semiarid region of China (Huang et al., 2012). Cox (1996) found that maize plant density 45,000 pph yielded 15% less than the 90,000 pph. Cooper et al. (2014) reported a positive grain yield response of drought-tolerant hybrids when the plant density increased from 30,000 to 80,000 pph.

3.4. Effect of planting date and plant density on maize water use efficiency

Maize crop water use efficiency Ranged from 1.69 to 2.57 kg m⁻³ in 2019 (Table 2) and from 1.76 to 2.71 kg m⁻³ in 2020 (Table 2). Maize WUE slightly increased with plant density and averaged 1.86, 2.02, 2.17, 2.33, 2.36 and 2.27 kg m⁻³ for 54,700; 64,600; 74,600; 88,000; 101,700 and 120,100 pph, respectively in 2019 and 1.98, 2.17, 2.27, 2.40, 2.38, and 2.23 kg m⁻³ for the respective densities in 2020. The planting dates did not significantly affect WUE. The overall WUE averaged 2.20, 2.20, 2.19, 2.20, 2.20 2.12, 2.27, and 2.00 kg m⁻³ for the successive seven planting dates in 2019 and 2.09, 2.05, 2.26, 2.47, 2.26, 2.26 and 2.40 kg m⁻³ for the successive seven planting dates in 2020, respectively. Maize WUE was 4% greater in 2020 than in 2019. Maize WUE slightly decreased with planting date in 2019 while it increased slightly with planting date in 2020. The plant density 101,700 pph obtained the highest WUE of 2.36 kg m⁻³ while the highest WUE of 2.50 kg m⁻³ was obtained by the plant density 88,000 pph in 2020. The two-year pooled data revealed an increase in maize WUE with an increase in plant density and reach the maximum under 88,000 pph and decreased with plant densities 101,700 and 120,100 pph. The plant density 88,000 pph obtained the highest WUE of 2.41 kg m⁻³ while maize WUE was 1.92, 2.09, 2.22, 2.37 and 2.24 kg m⁻³ for the plant densities 54,700; 64,600; 74,600; 101,700, and 120,100 pph, respectively. Maize WUE was reported to vary from 2.0 to 2.3 kg m⁻³, averaging 2.1 kg m⁻³, at the same research station (Djaman et al., 2018). The results of the study aligned with the findings of Irmak

Table 2. Maize water use efficiency (kg m^{-3}) as a function of plant density and planting date in 2019 and 2020 (number followed by different letters are significantly different).

Plant density	Planting dates (2019)						
	23-Apr	1-May	7-May	14-May	22-May	30-May	5-Jun
54,700	1.88 a	1.82 a	1.92 a	2.10 a	1.76 a	1.82 a	1.69 a
64,600	1.91 a	2.02 a	2.04 a	2.16 a	1.97 a	2.07 a	1.94 b
74,600	2.17 ab	2.11 a	2.16 a	2.23 a	2.17 a	2.25 ab	2.11 b
88,000	2.42 b	2.41 b	2.44 b	2.28 b	2.19 a	2.38 b	2.17 b
101,700	2.39 b	2.49 b	2.42 b	2.24 a	2.34 b	2.57 b	2.09 b
120,100	2.36 b	2.37 b	2.18 a	2.16 a	2.27 ab	2.54 b	2.00 b
Plant density	Planting dates (2020)						
	21-Apr	30-Apr	7-May	18-May	27-May	3-Jun	10-Jun
54,700	1.76 a	1.98 a	1.93 a	2.03 a	2.01 a	2.02 a	2.16 a
64,600	1.99 ab	2.01 a	2.13 a	2.30 ab	2.24 ab	2.12 a	2.41 b
74,600	2.08 ab	2.09 a	2.20 a	2.48 b	2.29 ab	2.31 ab	2.44 b
88,000	2.30 bc	2.27 b	2.55 b	2.71 c	2.49 c	2.53 b	2.63 bc
101,700	2.21 b	2.05 a	2.49 b	2.64 c	2.33 bc	2.45 b	2.52 b
120,100	2.18 ab	1.92 a	2.23 a	2.66 c	2.21 ba	2.15 a	2.24 a

and Djaman (2016) who investigated the impact of 59,300; 74,100; 88,900 pph in combination with May 4, May 16, and May 23 plantings in 2011 and April 24, May 8, and May 17 plantings in 2012, and found maize WUE varying from 2.27 to 2.81 kg m^{-3} , with no particular trends in maize WUE and planting date and plant density in Nebraska. Ren et al. (2016) reported. Maize WUE was 1.81 kg m^{-3} at 52,500 pph in dry years, 1.92 kg m^{-3} at 67,500 pph in normal years, and 2.19 kg m^{-3} at 67,500 pph in mild wet years, and 2.25 kg m^{-3} at 67,500 pph in extremely wet years. Zhang et al. (2014) reported maize maximum WUE of 2.53 kg m^{-3} under a plant density of 75,000 pph in Shanxi province in China.

4. CONCLUSION

Under variable climatic conditions of northwestern New Mexico, field experiments were carried out to quantify the effects of seven planting dates (from April 20 to June 10) and six plant densities (from 54,700 to 120,100 pph) on maize growth parameters, yield, and water use efficiency. The results showed that maize leaf area index increased with plant density and did not significantly vary with planting dates. Plant height increased with the delayed plantings while no significant variation was observed with plant density. Maize plants did not reach crop maturity before the fall first killing frost under all planting after May 25. Overall, maize yield showed a polynomial relationship with plant density under different planting dates. Maize response to plant density and planting date is therefore likely to have substantial inter-annual variability under the same management practices due to local climate variability. From the two-year experiment, plant density 88,000 pph maximized both grain yield and water use efficiency and it is, therefore, considered as the optimum plant density. The optimum maize planting window covers the period from May 7 to May 22 (126–142 days of the year) however, the early planting could be considered mostly with the long-season maize hybrids and for the large commercial maize production farm like the Navajo Agricultural Products Industry operating in the study area. Due to the inter-annual variability of the climatic conditions that may affect crop yield response to plant density and planting date, long-term research including a large range of relative maturity hybrids and expanded planting period from April 1st to June 30 is needed to determine the

optimum plant density and planting window in relation with the hybrid relative maturity date especially in the challenging years with extremely cold spring and or extremely warm spring to improve farmers' recommendation on planting date and maize relative maturity for the production sustainability and profitability.

Declaration of Competing Interest

None.

Acknowledgment

The authors would like to express their deep gratitude to New Mexico State University for supporting and providing funds.

REFERENCES

- Abendroth, L.J., Woli, K.P., Myers, A.J.W., Elmore, R.W., 2017. Yield-based corn planting date recommendation windows for Iowa. *Crop Forage Turfgrass Manag.* 3, 1–7.
- Al-Kaisi, M.M., Yin, X., 2003. Effects of nitrogen rate, irrigation rate, and plant population on corn yield and water use efficiency. *Agron. J.* 95, 1475–1482. doi: [10.2134/agronj2003.1475](https://doi.org/10.2134/agronj2003.1475).
- Allen, R.G., Pereira, L.S., Raes, D., Smith, M., 1998. Crop evapotranspiration: guide-lines for computing crop water requirements. In: *FAO Irrigation and Drainage Paper No. 56*. FAO, Rome, Italy, p. 300.
- Andrade, F.H., Uhart, S.A., Cirilo, A., 1993. Temperature affects radiation use efficiency in maize. *Field Crops Res.* 32, 17–25.
- Andrade, H.F., Otegui, M.E., Vega, C., 2000. Intercepted radiation at flowering and kernel number in maize. *Agron. J.* 92, 92–97.
- Assefa, Y., Vara Prasad, P.V., Carter, P., Hinds, M., Bhalla, G., Schon, R., Jeschke, M., Paszkiewicz, S., Ciampitti, I.A., 2016. Yield response to planting density for US modern corn hybrids: a synthesis-analysis. *Crop Sci.* 56, 2802–2817. doi: [10.2135/crop-sci2016.04.0215](https://doi.org/10.2135/crop-sci2016.04.0215).
- Baum, M.E., Archontoulis, S.V., Licht, M.A., 2019. Planting date, hybrid maturity, and weather effects on maize yield and crop stage. *Agron. J.* 111, 1–11. doi: [10.2134/agronj2018.04.029](https://doi.org/10.2134/agronj2018.04.029).
- Baum Mitch, E., Licht, M.A., Huber, I., Archontoulis, S.V., 2020. Impacts of climate change on the optimum planting date of different maize cultivars in the central US Corn Belt. *Eur. J. Agron.* 119, 126101. doi: [10.1016/j.eja.2020.126101](https://doi.org/10.1016/j.eja.2020.126101).
- Bernhard, B.J., Below, F.E., 2020. Plant population and row spacing effects on corn: plant growth, phenology, and grain yield. *Agron. J.* 112, 2456–2465.
- Beruski, G.C., Schiebelbein, L.M., Pereira, A.B., 2020. Maize yield components as affected by plant population, planting date, crop growing season and soil coverings in Brazil. *Agriculture* 10 (12), 579. doi: [10.3390/agriculture101205791](https://doi.org/10.3390/agriculture101205791).
- Berzsenyi, Z., Tokatlidis, I.S., 2012. Density-dependence rather maturity determines hybrid selection in dryland maize production. *Agron. J.* 104, 331–336. doi: [10.2134/agronj2011.0205](https://doi.org/10.2134/agronj2011.0205).
- Borras, L., Maddonni, G.A., Otegui, M.E., 2003. Leaf senescence in maize hybrids: plant population: row spacing and kernel set effects. *Field Crops Res.* 82, 13–26.
- Brekke, B., Edwards, J., Knapp, A., 2011. Selection and adaptation to high plant density in the Iowa stiffstalk synthetic maize (*Zea mays* L.) population. *Crop Sci.* 51, 1965–1972.
- Bryant, K.J., Benson, V.W., Kiniry, J.R., Williams, J.R., Lacewell, R.D., 1992. Simulating corn yield response to irrigation timings: validation of the EPIC model. *J. Prod. Agric.* 5, 237–242.
- Cassman, K.G., 2016. Long-term trajectories: crop yields, farmland, and irrigated agriculture. *Econ. Rev.* 101, 21–46.
- Cerrudo, D., Hernández, M., Tollenaar, M., Vega, C.R.C., Echarte, L., 2020. Kernel number response to plant density in tropical, temperate, and tropical × temperate maize hybrids. *Crop Sci.* 60 (1), 381–390.
- Chen, F.W., Liu, C.W., Chang, F.J., 2014. Improvement of the agricultural effective rainfall for irrigating rice using the optimal clustering model of rainfall station network. *Paddy Water Environ.* 12, 393–406.
- Chen, T., van der Werf, G.R., de Jeu, R.A.M., Wang, G., Dolman, A.J., 2013. A global analysis of the impact of drought on net primary productivity. *Hydrol. Earth Syst. Sci.* 17, 3885–3894.
- Ciampitti, I.A., Vyn, T.J., 2012. Physiological perspectives of changes over time in maize yield dependency on nitrogen uptake and associated nitrogen efficiencies: a review. *Field Crops Res.* 133, 48–67.
- Cooper, M., Gho, C., Leafgren, R., Tang, T., Messina, C., 2014. Breeding drought-tolerant maize hybrids for the US corn-belt: discovery to product. *J. Exp. Bot.* 65, 6191–6204.

- Cox, W.J., Cherney, D.J., 2001. Row spacing, plant density, and nitrogen effects on corn silage. *Agron. J.* 93 (3), 597–602. doi: [10.2134/agronj2001.933597x](https://doi.org/10.2134/agronj2001.933597x).
- Cox, W.J., 1996. Whole-plant physiological and yield responses of maize to plant population. *Agron. J.* 88 (3), 489–496.
- Dias, F.S., Rezende, W.M., Zuffo, L.T., Caixeta, D.G., Massensini, M.A., Ribeiro, J.I., De- Lima, R.O., 2019. Agronomic responses of maize hybrids to row spacing and plant population in the summer and winter seasons in Brazil. *Agronomy Journal* 111 (6), 3119–3129. doi: [10.2134/agronj2018.12.0765](https://doi.org/10.2134/agronj2018.12.0765).
- Djaman, K., Owen, C., West, M.M., Allen, S., Koudahe, K., Darapuneni, M., O'Neill, M., 2020. Relationship between relative maturity and grain yield of maize (*Zea mays* L.) hybrids in northwest New Mexico for the 2003–2019 period. *Agriculture* 10, 290.
- Djaman, K., O'Neill, M., Owen, C.K., Smeal, D., Koudahe, K., West, M., Allen, S., Lombard, K., Irmak, S., 2018. Crop evapotranspiration, irrigation water requirement and water productivity of maize from meteorological data under semiarid climate. *Water* 10 (4), 405.
- Echarte, L., Luque, S., Andrade, F.H., Sadras, V.O., Cirilo, A., Otegui, M.E., Vega, C.R.C., 2000. Response of maize kernel number to plant density in Argentinean hybrids released between 1965 and 1993. *Field Crops Res.* 68, 1–8. doi: [10.1016/S0378-4290\(00\)00101-5](https://doi.org/10.1016/S0378-4290(00)00101-5).
- Feng, L.Y., Raza, M.A., Chen, Y., Khalid, M.H.B., Meraj, T.A., Ahsan, F., Fan, Y., Du, J., Wu, X., Song, C., Liu, C., Bawa, G., Zhang, Z., Yuan, S., Yang, F., Yang, W., 2019. Narrow-wide row planting pattern improves the light environment and seed yields of intercrop species in relay intercropping system. *PLoS One* 14, e0212885.
- Fischer, K.S., Palmer, A.F.E., Goldsworthy, P.R., Fischer, N.M., 1984. Tropical maize. In: *The Physiology of Tropical Field Crops*. Wiley, New York, pp. 213–248.
- Gardner, F.P., Pearce, R.B., Mitchell, R.L., 1985. *Physiology of Crop Plants*. Ames: Iowa State University Press, p. 478.
- Gou, L., Xue, J., Qi, B., Ma, B., Zhang, W.F., 2017. Morphological variation of maize cultivars in response to elevated plant densities. *Agronomy* 109 (4), 1443–1453.
- Griesh, M.H., Yakout, G.M., Horst, W.J., et al., 2001. Effect of plant population density and nitrogen fertilization on yield and yield components of some white and yellow maize hybrids under drip irrigation system in sandy soil. *Plant Nutrition. Developments in Plant and Soil Sciences*, 92 (eds). Springer, Dordrecht doi: [10.1007/0-306-47624-X_394](https://doi.org/10.1007/0-306-47624-X_394).
- Haarhoff, S.J., Swanepoel, P.A., 2019. Narrow rows and high maize plant population improve water use and grain yield under conservation agriculture. *Agron. J.* 112, 921–931.
- Haegel, Jason, W., Becker, R.J., Henninger, A.S., Below, F.E., 2014. Row arrangement, phosphorus fertility, and hybrid contributions to managing increased plant density of maize. *Agron. J.* 106 (5), 1838–1846.
- Huang, L.J., Zhang, H., Hu, X.Y., Guo, Y.H., Li, M.S., 2012. Preliminary report on corn variety zhengdan 958 planting density. *Ningxia J. Agric. For. Sci. Technol* 53, 15–16.
- Irmak, S., Djaman, K., 2016. Effects of planting date and density on plant growth, yield, evapotranspiration, and irrigation- and evapotranspiration-yield production functions of maize (*Zea mays* L.) under subsurface drip irrigation and rainfed conditions. *Trans. ASABE* 59 (5), 1235–1256.
- Jensen, M.E., Kozlowski, T.T., 1968. Water consumption by agricultural plants. In: *Water Deficits and Plant Growth*, 2. Academic Press, New York, NY, USA, pp. 1–22.
- Jia, Q., Sun, L., Mou, H., Shahzad, A., Liu, D., Zhang, Y., Zhang, P., Ren, X., Jia, Z., 2018. Effects of planting patterns and sowing densities on grain-filling, radiation use efficiency and yield of maize (*Zea mays* L.) in semi-arid regions. *Agric. Water Manag.* 201, 287–298.
- Jiang, W., Thapa, S., Jessup, K.E., Hao, B., Hou, X., Marek, T., Becker, J., Bell, J., Xue, Q., 2020. Corn response to later than traditional planting dates in the Texas High Plains. *Crop Sci.* 60 (2), 1004–1020.
- Kucharik, C.J., 2008. Contribution of planting date trends to increased maize yields in the central United States. *Agron. J.* 100, 328–336. doi: [10.2134/agronj2007.0145](https://doi.org/10.2134/agronj2007.0145).
- Lamm, F.R., Aiken, R.M., Abou Kheira, A.A., 2008. Effect of tillage practices and deficit irrigation on corn. In: *Proceedings of the Central Plains Irrigation Conference*, Greeley, CO. Colby, KS, pp. 84–100 Available from CPIA, 760 N. Thompson.
- Li, R., Liu, P., Dong, S., Zhang, J., Zhao, B., 2019. Increased maize plant population induced leaf senescence, suppressed root growth, nitrogen uptake, and grain yield. *Agron. J.* 111 (4), 1581–1591.
- Liang, H., Yang, S., Xu, J., Hu, K., 2021. Modeling water consumption, N fates, and rice yield for water-saving and conventional rice production systems. *Soil Tillage Res.* 209, 104944. doi: [10.1016/j.still.2021.104944](https://doi.org/10.1016/j.still.2021.104944).
- Lin, P., Qi, H., Li, C., Zhao, M., 2016. Optimized tillage practices and row spacing to improve grain yield and matter transport efficiency in intensive spring maize. *Field Crops Res.* 198, 258–268.
- Lindsey, A.J., Thomison, P.R., 2016. Drought-tolerant corn hybrid and relative maturity yield response to plant population and planting date. *Agron. J.* 108, 229–242.
- Liu, J., Bu, L., Zhu, L., Luo, S., Chen, X., Li, S., 2014. Optimizing plant density and plastic film mulch to increase maize productivity and water-use efficiency in semiarid areas. *Agron. J.* 106 (4), 1138–1146.
- Liu, T., Wang, Z., Cai, T., 2016. Canopy apparent photosynthetic characteristics and yield of two spike-type wheat cultivars in response to row spacing under high plant density. *PLoS One* 11 (2), e0148582. doi: [10.1371/journal.pone.0148582](https://doi.org/10.1371/journal.pone.0148582).
- Liu, H., Huang, X., Huang, M., Yan, L., Chi, B., 2010. Effect of varieties and plant-densities to yield and WUE in dryland maize. *J. Shanxi Agric. Sci.* 38, 32–34 (in Chinese).

- Long, N.V., Assefa, Y., Schwalbert, R., Ciampitti, I.A., 2017. Maize yield and planting date relationship: a synthesis analysis for US high-yielding contest-Winner and field research data. *Front. Plant Sci.* 8, 2106. doi: [10.3389/fpls.2017.02106](https://doi.org/10.3389/fpls.2017.02106).
- Maddoni, G.A., Otegui, M.E., 2004. Intra-specific competition in maize: early establishment of hierarchies among plants affects final kernel set. *Field Crops Res.* 85, 1–13.
- Nafziger, E.D., 1994. Corn planting date and plant population. *J. Prod. Agric.* 7, 59–62.
- Nielsen, R.L., Thomison, P.R., Brown, G.A., Halter, A.L., Wells, J., Wuethrich, K.L., 2002. Delayed planting effects on flowering and grain maturation of dent corn. *Agron. J.* 94 (3), 549–558.
- Parker, P.S., Shonkwiler, J.S., Aurbacher, J., 2016. Cause and consequence in maize planting dates in Germany. *J. Agron. Crop Sci.* 203, 1–14. doi: [10.1111/jac.12182](https://doi.org/10.1111/jac.12182).
- Ping, L., Ferguson, R.B., Dobermann, A., 2008. Site-specific nitrogen and plant density management in irrigated maize. *Agron. J.* 100 (4), 1193–1204.
- Raza, M.A., Khalid, M.H.B., Zhang, X., Feng, L.Y., Khan, I., Hassan, M.J., Ahmed, M., Ansar, M., Chen, Y.K., Fan, Y.F., 2019. Effect of planting patterns on yield, nutrient accumulation and distribution in maize and soy-bean under relay intercropping systems. *Sci. Rep.* 9, 4947.
- Ren, X., Sun, D., Wang, Q., 2016. Modeling the effects of plant density on maize productivity and water balance in the loess plateau of China. *Agric. Water Manag.* 171, 40–48.
- Sammis, T.W., Mapel, C.L., Lugg, D.G., Lansford, R.R., McGuckin, J.T., 1985. Evapotranspiration crop coefficients predicted using growing-degree days. *Trans. ASAE* 28, 773–780.
- Sangoi, L., Gracietti, M.A., Rampazzo, C., Bianchetti, P., 2002. Response of Brazilian maize hybrids from different eras to changes in plant density. *Field Crops Res.* 79, 39–51.
- Shapiro, C.A., Wortmann, C.S., 2006. Corn response to nitrogen rate, row spacing, and plant density in eastern Nebraska. *Agron. J.* 98, 529–535.
- Shen, X.Y., Dai, J.Y., Hu, A.C., Gu, W.L., Zheng, B., 1993. Studies on relationship among character of canopy light interception and yield in maize populations (*Zea mays* L.). *Acta Agron. Sin.* 19, 246–252.
- Shi, Y., Qin, Y., Sun, Y., Zhu, P., Wang, J., 2008. Researches on the relationships between soil moisture and maize planting densities as well as yields. *Chin. J. Soil Sci.* 39, 792–796.
- Shrestha, J., Kandel, M., Chaudhary, A., 2018. Effects of planting time on growth, development and productivity of maize (*Zea mays* L.). *J. Agric. Nat. Resour.* 1 (1), 43–50.
- Solomon, K.F., Chauhan, Y., Zeppa, A., 2017. Risks of yield loss due to variation in optimum density for different maize genotypes under variable environmental conditions. *J. Agron. Crop Sci.* 203 (6), 519–527.
- Stanger, T.F., Lauer, J.G., 2007. Corn stalk response to plant population and the Bt-European corn borer trait. *Agron. J.* 99, 657–664. doi: [10.2134/agronj2006.0079](https://doi.org/10.2134/agronj2006.0079).
- Teasdale, J.R., 1998. Influence of corn (*Zea mays* L.) population and row spacing on corn and velvetleaf (*Abitilon theophrasti*) yield. *Weed Sci.* 46 (4), 447–453.
- Tetio-Kagho, F., Gardner, F.P., 1988. Responses of maize to plant population density: I. Canopy development, light relationships, and vegetative growth. *Agron. J.* 80, 930–935.
- Timlin, D.J., Fleisher, D.H., Kemanian, A.R., Reddy, V.R., 2014. Planting density and leaf area index effects on the distribution of light transmittance to the soil surface in maize. *Agron. J.* 106, 1828–1837.
- Tollenaar, M., Bruulsema, T.W., 1998. Effects of temperature on rate and duration of kernel dry matter accumulation of maize. *Can. J. Plant Sci.* 68, 935–940.
- Tollenaar, M., Dwyer, L.M., Stewart, D.W., 1992. Ear and kernel formation in maize hybrids representing three decades of grain yield improvement in Ontario. *Crop Sci.* 32, 432–438.
- Tsimba, R., Edmeades, G.O., Millner, J.P., Kemp, P.D., 2013. The effect of planting date on maize grain yields and yield components. *Field Crops Res.* 150, 135–144. United State Department of Agriculture-National Agricultural Statistics Service (USDA-NASS), 2020. Crop Production 2019 Summary. Washington, D.C. USDA, p. 124.
- Westgate, M.E., Forcella, F., Reicosky, D.C., Somsen, J., 1997. Rapid canopy closure for maize production in the northern US corn belt: radiation-use efficiency and grain yield. *Field Crops Res.* 49, 249–258. doi: [10.1016/S0378-4290\(96\)01055-6](https://doi.org/10.1016/S0378-4290(96)01055-6).
- Yan, P., Chen, Y., Sui, P., Vogel, A., Zhang, X., 2018. Effect of maize plant morphology on the formation of apical kernels at different sowing dates and under different plant densities. *Field Crops Res.* 223, 83–92.
- Yang, J.S., Gao, H.Y., Peng, L., Geng, L.I., Dong, S.T., Zhang, J.W., 2010. Effects of planting density and row spacing on canopy apparent photosynthesis of high-yield summer corn. *Acta Agron. Sin.* 36, 1226–1235.
- Yang, F., Liao, D., Wu, X., Gao, R., Fan, Y., Raza, M.A., Wang, X., Yong, T., Liu, W., Liu, J., Du, J., Shu, K., Yang, W., 2017. Effect of aboveground and below ground interactions on the intercrop yields in maize-soybean relay intercropping systems. *Field Crops Res.* 203, 16–23.
- Zhang, M., Song, Z.W., Chen, T., Yan, X.G., Zhu, P., Ren, J., 2015. Differences in responses of biomass production and grain-filling to planting density between spring maize cultivars. *J. Maize Sci.* 23, 57–65.
- Zhang, D., Zhang, W., Chen, Q., Huang, X., Zhang, C., 2014. Effects of planting density on plant traits and water consumption characteristics of dry-land maize. *J. Maize Sci.* 22, 102–108.

Database of Water Quality and Groundwater Elevation Within and Surrounding the Lee Acres Landfill, New Mexico, 1985–2020

Erin L. Gray and Christina L. Ferguson

U.S. Geological Survey
United States Department of the Interior

Prepared in cooperation with the Bureau of Land Management

Data Report 1154
(*Conversion Factors available at end of report*)

ABSTRACT

This report describes the background information related to and the contents of the Lee Acres-Giant Bloomfield Refinery Database (LAGBRD), which is a compilation of monitoring data collected at the Lee Acres Landfill and the Giant Bloomfield Refinery near Farmington, New Mexico. LAGBRD includes monitoring data from as early as 1985, when awareness was increasing regarding contamination from liquid waste lagoons at the landfill and fuel releases at the refinery. Water quality and groundwater elevation data from sampling locations at the landfill and the refinery are included in the database. LAGBRD was compiled in cooperation with the Bureau of Land Management, which operates the Lee Acres Landfill, in order to facilitate future studies into the characteristics of groundwater contamination and background geochemistry at the landfill and refinery sites.

INTRODUCTION

The Lee Acres Landfill, located in northwestern New Mexico approximately 6 miles east of Farmington, New Mexico, is a former 60-acre landfill that is adjacent to an unnamed arroyo approximately 1 mi above its confluence with the San Juan River (Figure 1). The landfill was operated by San Juan County from May 1962 through April 1986 on land leased from the Bureau of Land Management (BLM). The New Mexico Environment Department (NMED) detected chlorinated solvents in liquid waste lagoons at the site in 1985 (NMED, 1986). The site was placed on the National Priorities List in 1990 by the U.S. Environmental Protection Agency (EPA) because of the presence of heavy metals and volatile organic compounds in groundwater and soils surrounding the site (EPA, 2004). Since that time, the U.S. Geological Survey (USGS) has performed regular groundwater monitoring at the site in cooperation with the BLM, which oversees the site. Alluvial aquifer background concentration ranges were published in the site's remedial investigation report (Roy F. Weston, Inc., 1995), and cleanup levels for the seven contaminants of concern (COCs) at the site were set by the EPA in the site's record of decision (ROD) (EPA, 2004). The alluvial aquifer background concentration ranges for several parameters and cleanup levels for the COCs at the landfill are described in Table 1. Dissolved manganese is the only COC that is persistent in Lee Acres Landfill monitoring wells in concentrations larger than cleanup levels described in the ROD (EPA, 2004; USGS, 2021). Several monitoring

wells that continue to have elevated dissolved manganese concentrations are located on Giant Bloomfield Refinery (GBR) property, which borders the Lee Acres Landfill directly to the south (Figures 1 and 2). GBR is a former crude oil refinery that operated from 1973 to 1982. Following 1982, the site was used as a truck maintenance and dispatching headquarters for Giant Industries. In 1986, Giant Industries began remediating the site because of several historical releases of diesel fuel, crude oil, and gasoline (Geoscience Consultants, Ltd., 1988; LT Environmental, Inc., 2020).

Remediation activities at GBR have included groundwater treatment and onsite recharge of the treated water to the alluvial aquifer (Giant Industries Arizona, Inc., 1993). Groundwater treatment was discontinued in 2015, but groundwater quality, treatment system influent and effluent water quality, and groundwater elevations continue to be monitored annually at GBR. During regular groundwater monitoring, groundwater samples collected from GBR wells upgradient from historical fuel release sites have exceeded regulatory standards for manganese, iron, and chromium (LT Environmental, Inc., 2020). More investigation is required to determine the possible sources of elevated concentrations of metals at GBR wells.

Groundwater has been monitored at the Lee Acres Landfill and GBR since 1985. Several State, Federal, and private entities have been involved in groundwater sample collection at the landfill and at GBR (NMED, 1986; Geoscience Consultants, Ltd., 1988; Roy F. Weston, Inc., 1995). The long monitoring histories at the landfill and the refinery have resulted in an array of data related to these sites that exists in different locations, forms, and standards. In cooperation with the BLM, the USGS compiled these data into a single, usable database, called Lee Acres-Giant Bloomfield Refinery Database (LAGBRD), to aid future investigations into the sources of contamination at the Lee Acres Landfill and GBR.

Table 1. Alluvial aquifer background concentrations for selected parameters and cleanup levels for contaminants of concern at the Lee Acres Landfill near Farmington, New Mexico.

[The alluvial aquifer background concentrations and cleanup levels for the organic contaminants (*cis*-1,2-dichloroethene, *trans*-1,2-dichloroethene, tetrachloroethene, trichloroethene, and vinyl chloride) refer to values of raw, unfiltered water; NA, not applicable (not a contaminant of concern at the Lee Acres Landfill); ND, nondetect]

Parameter	Alluvial aquifer background concentration range (micrograms per liter) ¹	Cleanup level (micrograms per liter) ²
Total chloride	6,400 to 62,900	NA
Dissolved manganese	16.1 to 1,680	346
Dissolved nickel	ND to 10.5	200
Dissolved chromium	14.4 to 31.2	NA
Dissolved iron	ND to 2,460	NA
<i>cis</i> -1,2-Dichloroethene	ND	70
<i>trans</i> -1,2-Dichloroethene	ND	100
Tetrachloroethene (perchloroethylene [PCE])	ND	5
Trichloroethene (TCE)	NA ³	5
Vinyl chloride	ND	1

¹Alluvial aquifer background concentration ranges from the "Remedial Investigation Report for the Lee Acres Landfill" (Roy F. Weston, Inc., 1995).

²Cleanup levels from the Lee Acres Landfill record of decision (U.S. Environmental Protection Agency, 2004).

³Trichloroethene was detected in 3 of 43 alluvial aquifer background samples collected for the remedial investigation and was eliminated as a background contaminant because of the low frequency of detection (Roy F. Weston, Inc., 1995).

PURPOSE AND SCOPE

Publicly available water quality and groundwater elevation data were gathered and compiled into LAGBRD. This report explains the database structure and data fields within LAGBRD, describes the sources of data included in LAGBRD, and displays time-series plots of some of the compiled water quality data. Figures 3–7 display the locations of samples represented in LAGBRD. The database is available at <https://doi.org/10.3133/dr1154>.

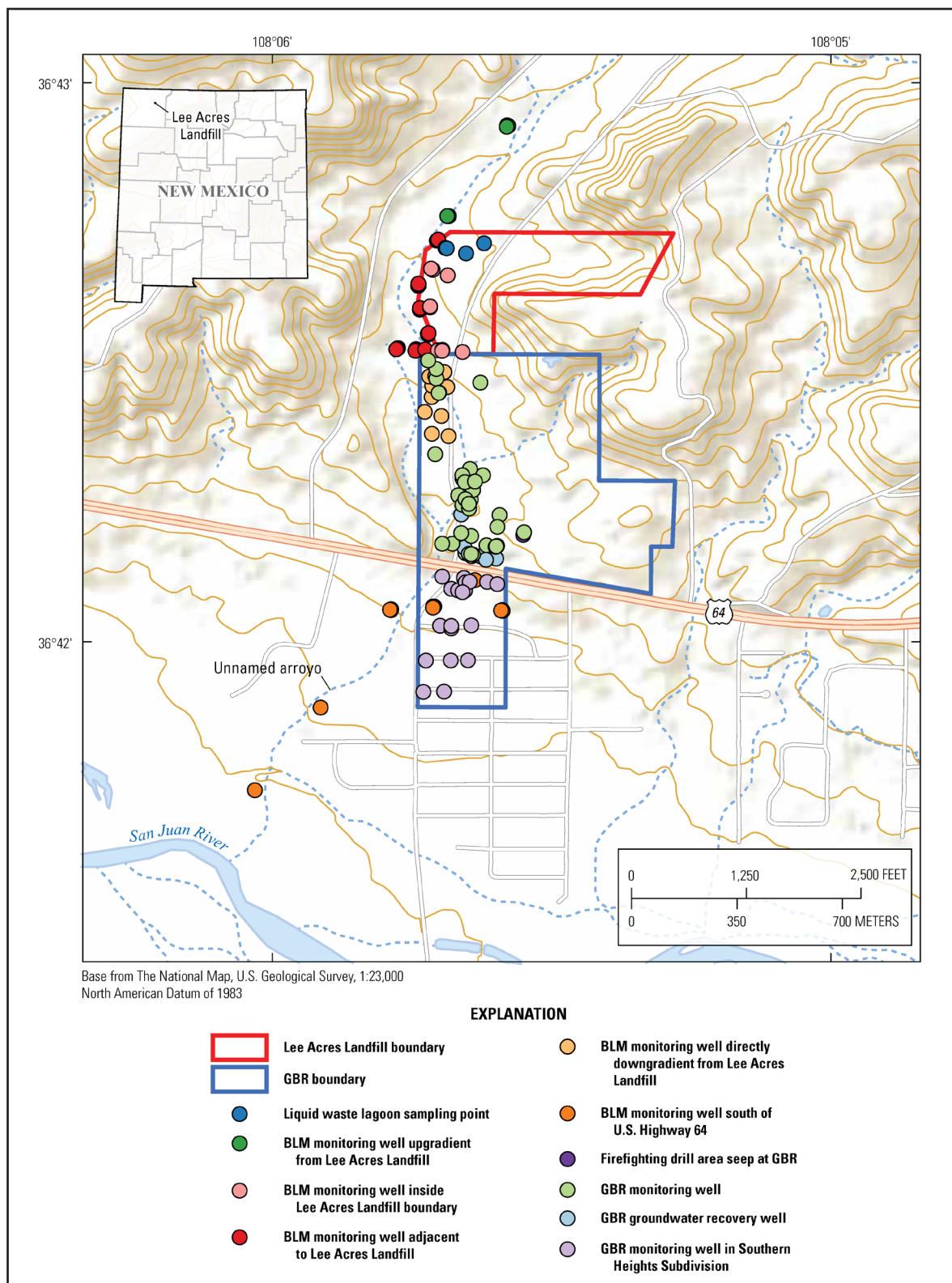


Figure 1. Locations of the Lee Acres Landfill and the Giant Bloomfield Refinery (GBR) adjacent to an unnamed arroyo approximately 1 mile above its confluence with the San Juan River near Farmington, New Mexico (Roy F. Weston, Inc., 1995; LT Environmental, Inc., 2020). Figure also shows Bureau of Land Management (BLM) and GBR monitoring locations.

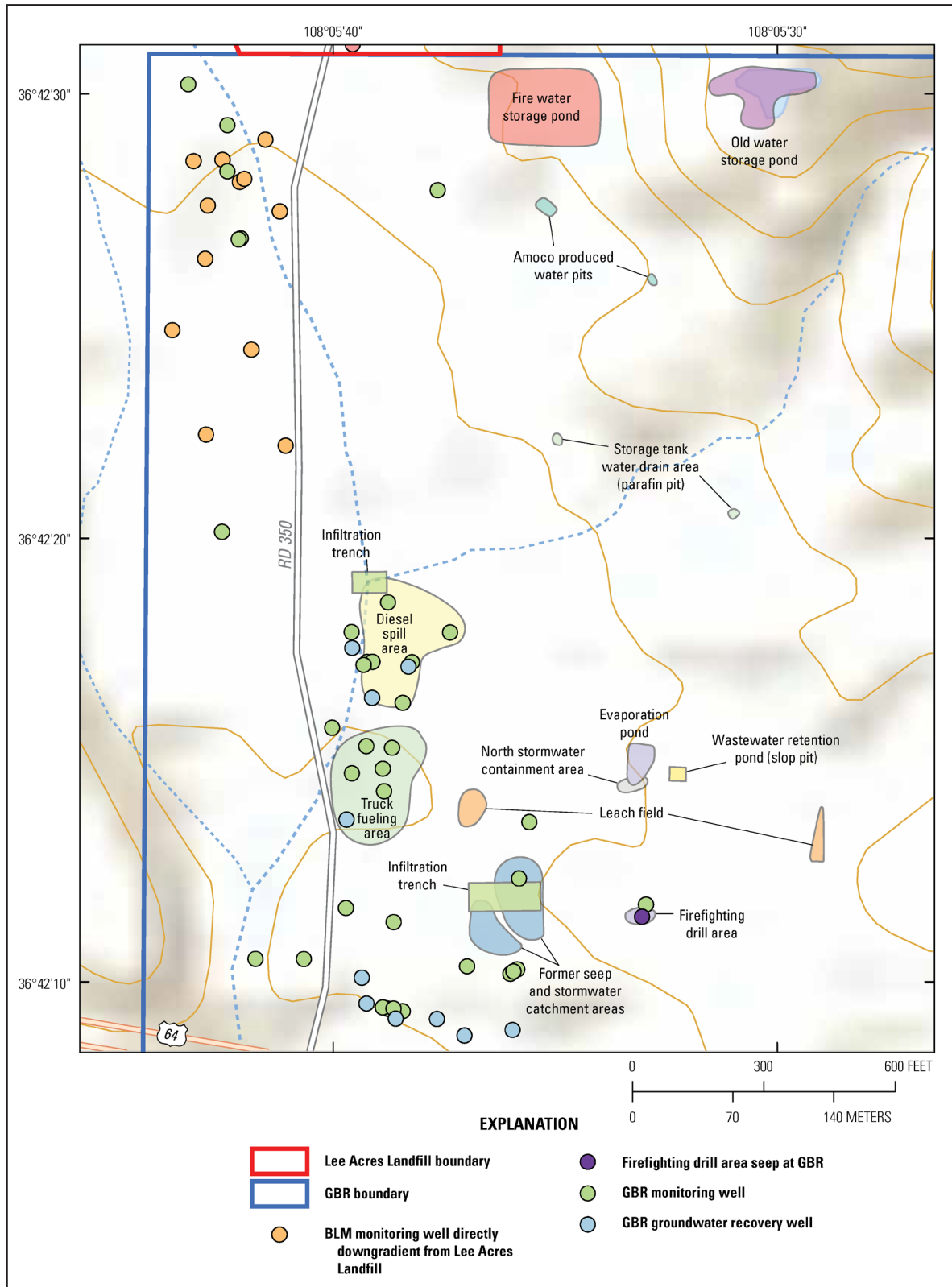


Figure 2. Locations of Bureau of Land Management (BLM) monitoring wells and other wells and surface features related to refinery operations and remediation activities near historical fuel release sites at Giant Bloomfield Refinery (GBR), located downgradient from the Lee Acres Landfill near Farmington, New Mexico (Geoscience Consultants, Ltd., 1988).

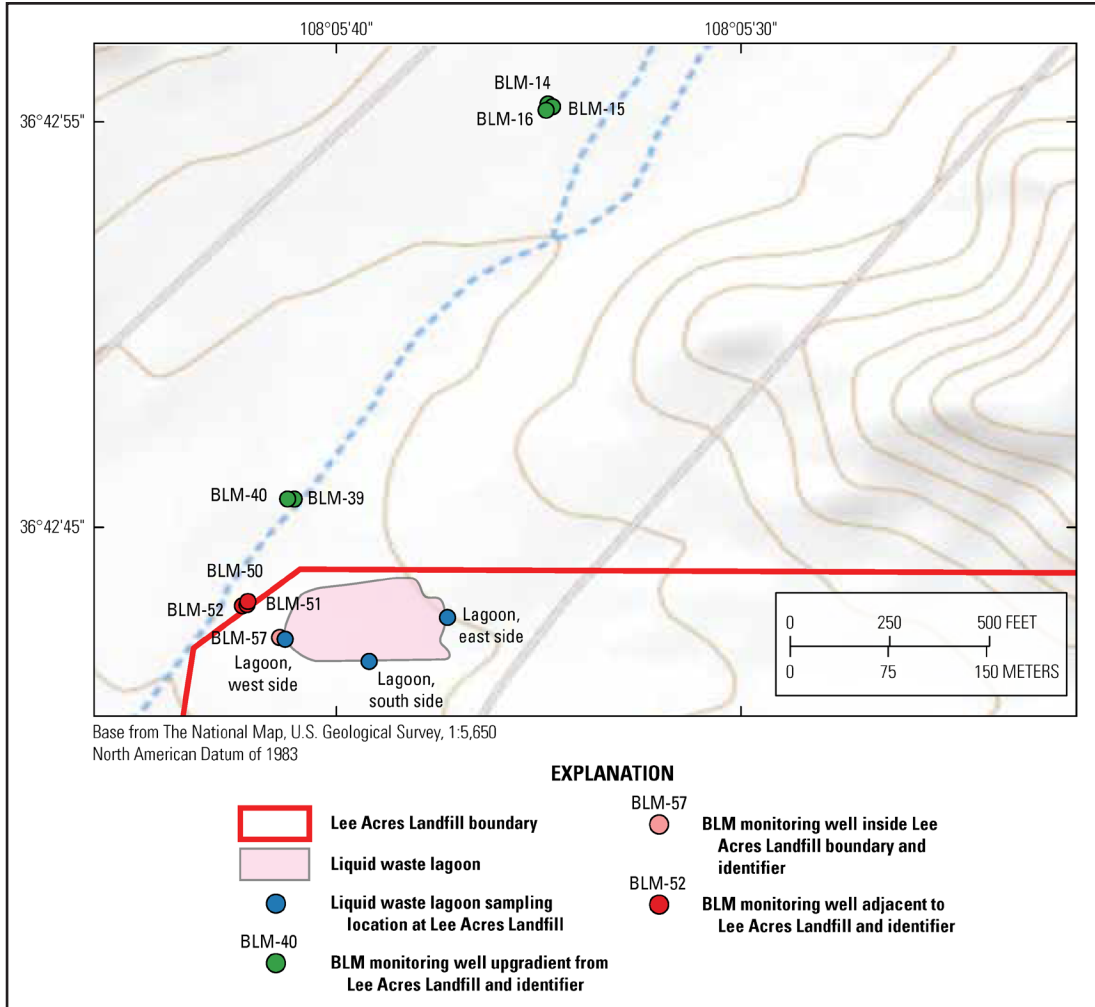


Figure 3. Locations of Bureau of Land Management (BLM) monitoring wells and liquid waste lagoon sampling locations upgradient from, within, and adjacent to the Lee Acres Landfill near Farmington, New Mexico.

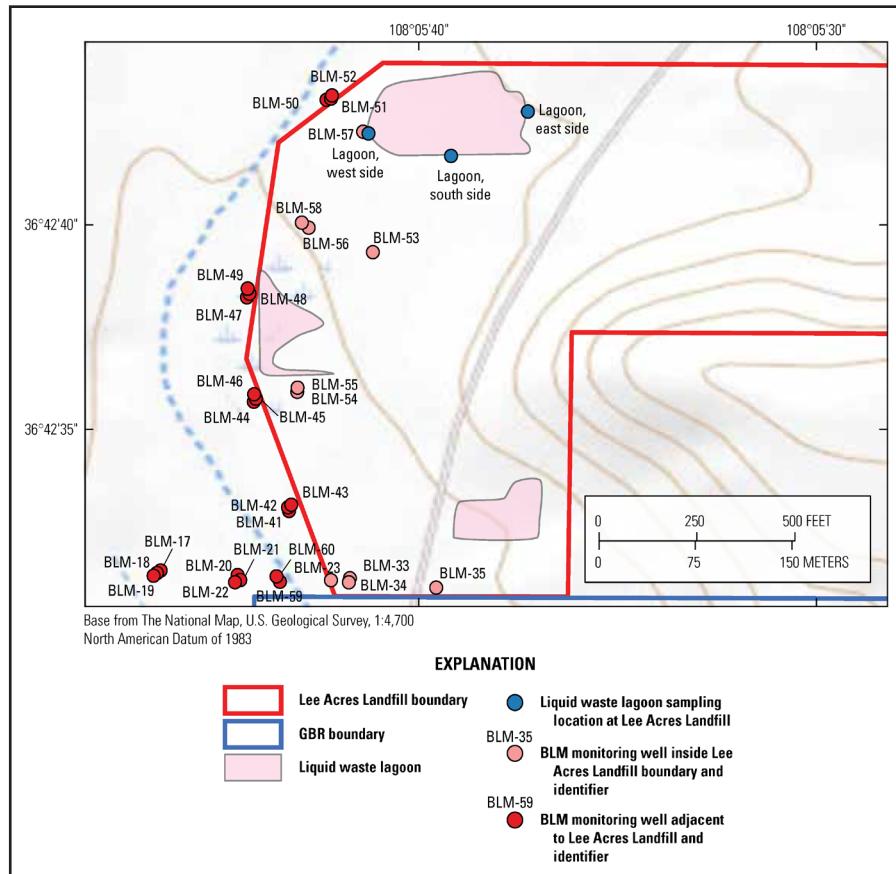


Figure 4. Locations of Bureau of Land Management (BLM) monitoring wells and liquid waste lagoon sampling locations within the boundary of and adjacent to the Lee Acres Landfill outside of the Giant Bloomfield Refinery boundary near Farmington, New Mexico.

DATABASE CHARACTERISTICS

LAGBRD is a relational database created in Microsoft Access for Office 365. The structure of the database is a modification of that used by the USGS National Water Information System (NWIS) database (USGS, 2021). Described below are summaries of the contents and structure of the relations of the tables in addition to details of data sources and quality assurance procedures of the data presented.

Database Contents and Structure

LAGBRD (available at <https://doi.org/10.3133/dr1154>) contains six related tables: "Sites," "WQ_Result," "GW_Elevation," "Remark_Cd," "Val_Qual_Cd," and "Field_Explanation."

The "Sites" table in LAGBRD contains site-level information on the locations where the water quality and groundwater elevation data contained in the database were collected. Data fields in the "Sites" table are described in Table 2 and in the "Field_Explanation" table in LAGBRD.

The "WQ_Result" table in LAGBRD contains water quality information by result (each row of the table contains information pertaining to a single result) collected from wells at the Lee Acres Landfill and GBR, liquid waste lagoons at the Lee Acres Landfill, effluent from the GBR groundwater treatment system, and a subterranean seep at GBR associated with a firefighting drill area. Data fields in the "WQ_Result" table are described in Table 3 and in the "Field_Explanation" table in LAGBRD. Each water quality result in the "WQ_Result" table is associated with a sampling location connected to the "Sites" table through the "loc_station_nm" field. Water quality parameters ("parameter_nm" field in the "WQ_Result" table) are named

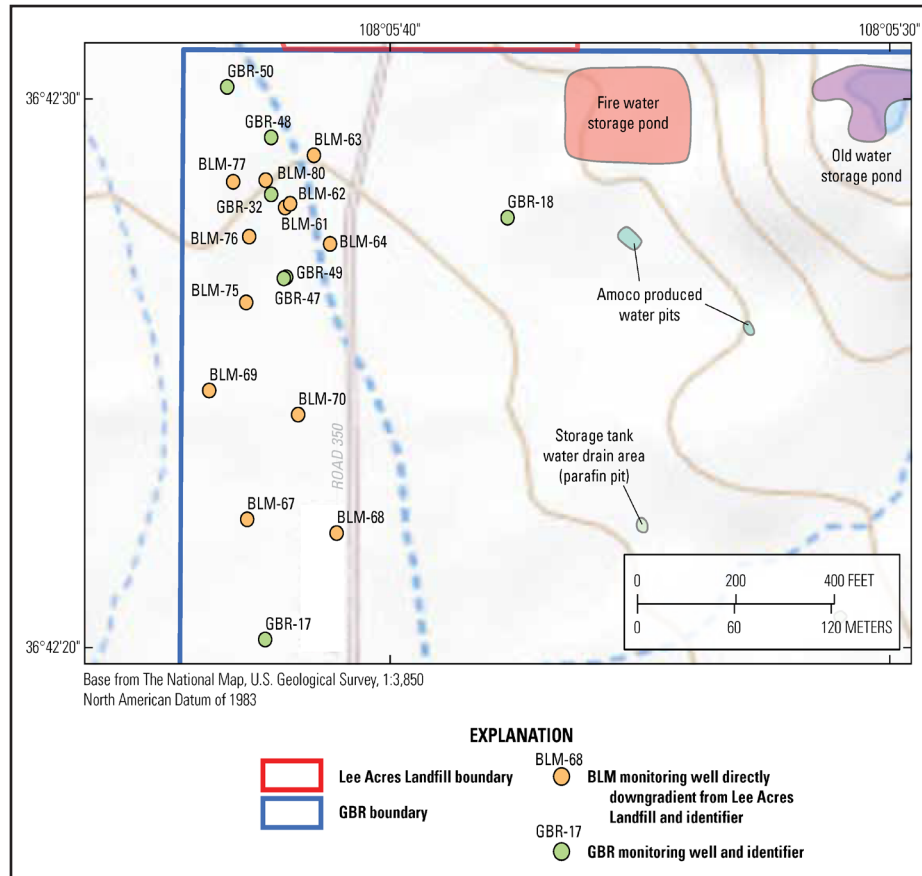


Figure 5. Locations of Bureau of Land Management (BLM) and Giant Bloomfield Refinery (GBR) monitoring wells directly downgradient from the Lee Acres Landfill near Farmington, New Mexico. These sites are all within the GBR boundary.

according to NWIS parameter naming convention. NWIS parameter names include the chemical name, a code for the sample medium (in LAGBRD, “wu” for unfiltered water, “wf” for filtered water, or “water” if it is unknown whether a sample was filtered), and sometimes additional information about the parameter, such as the sample fraction or the analytical method. The units of the result are also included in the “parameter_nm” field. Data were not always available for every field in the “WQ_Result” table because of the variations in sampling methodologies of the parties involved in groundwater monitoring at these sites. For instance, some data in LAGBRD were transcribed from tables in reports and were not accompanied by analytical laboratory reports; analytical method, reporting level, reporting level type, and result value qualifiers may not be known for such data.

The “GW_Elevation” table in LAGBRD contains groundwater elevation data from NWIS and from GBR monitoring reports. Data fields in the “GW_Elevation” table are described in Table 4 and in the “Field_Explanation” table in LAGBRD. Each groundwater elevation measurement in the “GW_Elevation” table is associated with a sampling location connected to the “Sites” table through the “loc_station_nm” field. Groundwater elevation data from annual GBR monitoring reports are presented in LAGBRD as reported, despite inconsistencies between the reported elevations and water-level measurements.

The tables “Remark_Cd” and “Val_Qual_Cd” in LAGBRD act as keys to explain the coded data in fields “remark_cd” and “val_qual_cd” in the table “WQ_Result.” The fields of tables “Remark_Cd” and “Val_Qual_Cd” are described in Table 5 and Table 6 and in the “Field_Explanation” table in LAGBRD. The “Field_Explanation” table in LAGBRD, which is also included as Table 7 in this report, provides explanations of the field names in the other tables in LAGBRD.

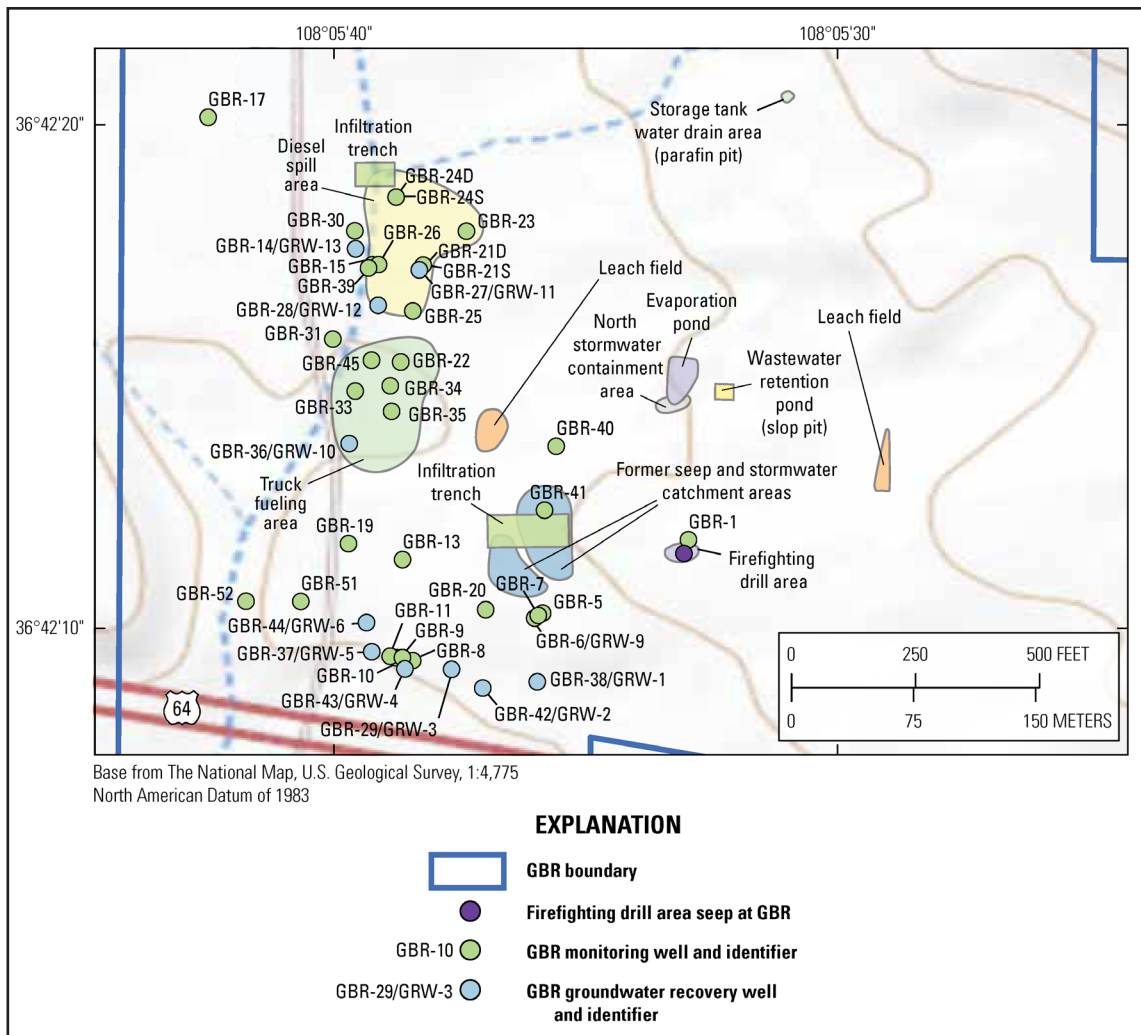


Figure 6. Locations of Giant Bloomfield Refinery (GBR) monitoring wells, GBR groundwater recovery wells (GRW), and a subterranean seep within the GBR boundary near Farmington, New Mexico.

LAGBRD also contains two regular queries, “WQ_Result_Inorganic” and “WQ_Result_Organic,” which filter the water quality results from the “WQ_Result” table into organic and inorganic parameters. Finally, LAGBRD contains two crosstab queries, “WQ_Result_Inorganic_Crosstab” and “WQ_Result_Organic_Crosstab,” which present the data contained in the by-result queries “WQ_Result_Inorganic” and “WQ_Result_Organic” in a by-sample format. The formatting of the by-sample crosstab queries makes the output of these queries useful for plotting and manipulating the data in spreadsheet applications such as Microsoft Excel, though users should be aware that these data are presented without their associated remarks and value qualifiers. Remarks and value qualifiers are contained in the “remark_cd” and “val_qual_cd” fields in the “WQ_Result” table. The by-result format of the “WQ_Result” table makes it well suited for working in programming environments such as R (R Core Team; <https://www.r-project.org/>) or Python (Python Software Foundation; <https://www.python.org/>).

Database Data Sources

Site-level information contained in the “Sites” table in LAGBRD is from a variety of sources. Site-level information on the liquid waste lagoons at the Lee Acres Landfill is from NMED (1986). Site-level information on BLM monitoring wells is from NWIS (USGS, 2021) and from the “Remedial Investigation Report for the Lee Acres Landfill” (Roy F. Weston, Inc., 1995). NWIS is also the source of information for several GBR

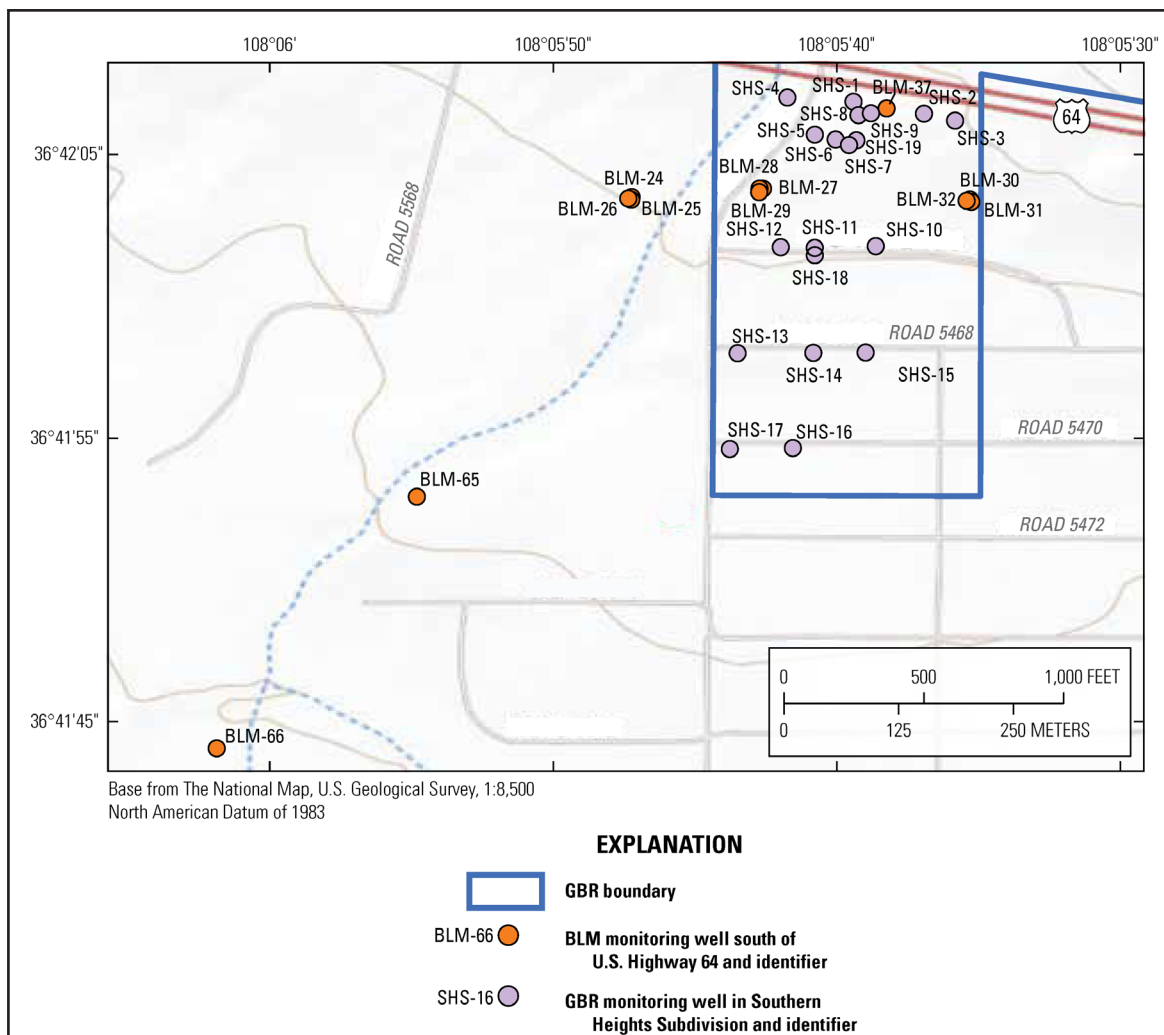


Figure 7. Locations of Bureau of Land Management (BLM) and Giant Bloomfield Refinery (GBR) monitoring wells south of U.S. Highway 64 near Farmington, New Mexico. GBR monitoring wells within the Southern Heights Subdivision (SHS) are named with an “SHS-” prefix.

monitoring wells (USGS, 2021). Information on other GBR monitoring wells, groundwater recovery wells, and the underground seep at the firefighting drill area is from that site’s discharge plan application (Geoscience Consultants, Ltd., 1988) and stage 1 abatement plan (LT Environmental, Inc., 2020). Monitoring results from the GBR treatment system do not have coordinates in LAGBRD because treatment system effluent was released to several infiltration trenches at GBR and the specific discharge location was not provided in the monitoring reports. Figure 2 displays the locations of two infiltration trenches used by GBR for the release of effluent from that site’s treatment system.

The water quality and groundwater elevation data contained in LAGBRD were collected by NMED, USGS, and private contractors on behalf of the BLM and GBR to satisfy site characterization and monitoring requirements. The field “data_src,” which is built into the “Site,” “WQ_Result,” and “GW_Elevation” tables in LAGBRD, contains the citation of the database or report from which the data originated.

All data in LAGBRD collected by the USGS originate from NWIS (USGS, 2021). Monitoring activities at the Lee Acres Landfill followed protocols described in the sampling and analysis plan for that site (Fredrick Gebhardt, USGS New Mexico Water Science Center, written commun., 2021). Other general guidelines that were followed during the collection and review of the USGS-collected water-level data in LAGBRD are

Table 2. Definitions of field names contained in the “Sites” table of the Lee Acres-Giant Bloomfield Refinery Database (LAGBRD; available at <https://doi.org/10.3133/dr1154>).

Field	Field description
USGS_site_no	U.S. Geological Survey site identification number; if blank, the site does not exist in the National Water Information System database
USGS_station_nm	U.S. Geological Survey station name; if blank, the site does not exist in the National Water Information System database
loc_station_nm	Local station name
site_type	Site type (monitoring well, Giant Bloomfield Refinery treatment system, underground seep, groundwater recovery well, or Lee Acres Landfill liquid waste lagoon)
site_assoc	The entity the site is associated with (the Lee Acres Landfill, the Giant Bloomfield Refinery, or the Southern Heights Subdivision)
lat_va	Latitude value of site in decimal degrees, if known
long_va	Longitude value of site in decimal degrees, if known
coord_datum	Latitude/longitude datum, if known
alt_va	Altitude of land-surface datum, if known
alt_datum	Altitude datum, if known
alt_acy_va	Altitude accuracy in feet, if known
hole_depth_va	Total borehole depth in feet below land-surface datum (for wells only), if known
csng_top_va	Depth to top of casing in feet below land surface (negative if top of casing is above ground) (for wells only), if known
csng_bottom_va	Depth to bottom of casing in feet below land surface (for wells only), if known
csng_dia_va	Inner diameter of the casing in inches (for wells only), if known
csng_material	Casing material (for wells only), if known
screen_top_va	Depth to the top of the screened interval in feet below land surface (for wells only), if known
screen_bottom_va	Depth to the bottom of the screened interval in feet below land surface (for wells only), if known
screen_material	Screened interval material (for wells only), if known
screen_dia_va	Screened interval diameter in inches (for wells only), if known
site_note	Notes on site-level information
data_src	Citation of data source

described in the USGS New Mexico Water Science Center internal document “Quality-Assurance Plan for Data Collection, Processing, and Archival in the New Mexico Water Science Center” (Kimberly Beisner, USGS New Mexico Water Science Center, written commun., 2020). Monitoring activities at GBR followed protocols described in the 1988 discharge plan application for that site (Geoscience Consultants, Ltd., 1988). Data from GBR reporting sources are presented in LAGBRD as reported. USGS staff did not review the data quality of the reported GBR data.

Data collected at GBR were reported to the New Mexico Oil Conservation Division (NMOCD) and are available from the online NMOCD data repository (NMOCD, 2021). Regulatory data collection and reporting protocols associated with the GBR data in LAGBRD are contained in the 1993 discharge plan for GBR (Giant Industries Arizona, Inc., 1993). Where available, GBR data in the “WQ_Result” table in LAGBRD originate from analytical laboratory results and include detailed result-level information, such as analytical method, reporting level, reporting level type, and value qualifiers.

Regular monitoring data collected by the USGS at the Lee Acres Landfill and by private contractors at GBR represent the bulk of data available in LAGBRD, but there are several other data sources. During initial site investigations, NMED collected samples from liquid waste lagoons within the Lee Acres Landfill (NMED, 1986), the results of which are included in LAGBRD. Also included in LAGBRD are groundwater quality monitoring results from the “Remedial Investigation Briefing Document for the Lee Acres Landfill” (Roy F. Weston, Inc., 1991). Sampling was performed for the landfill’s remedial investigation by Roy F. Weston, Inc., on behalf of the BLM. Finally, water quality data from groundwater wells and an underground seep from the GBR discharge plan application (Geoscience Consultants, Ltd., 1988) are included in LAGBRD. When analytical methods for water quality data are known, they are included in the “method” field of the “WQ_Result” table in LAGBRD.

Table 3. Definitions of field names contained in the “WQ_Result” table of the Lee Acres-Giant Bloomfield Refinery Database (LAGBRD; available at <https://doi.org/10.3133/dr1154>).

Field	Field description
loc_station_nm	Local station name
sample_dt	Water sample collection date, if given in the data source
sample_yr	Water sample collection year, if the exact date is not given in the data source
sample_mo_qrt	Water sample collection month or quarter, if the exact date is not given in the data source; for several samples in 1989, only the sample quarter was given
sample_dt_calc	Water sample collection date, if given in the data source, or the first day of the month or quarter the sample was collected
parameter_nm	Water quality parameter (wu, unfiltered water; wf, filtered water; water, it is unknown whether a sample was filtered)
parameter_tp	Type of water quality parameter (organic or inorganic)
method	Analytical method of the result, if known
result_va	Result value. If a sample is reported as nondetect, result value is equal to reporting level value, if available, and remark code is “<.” If a result is nondetect and a reporting level value is not available, result value is set to “ND”
remark_cd	Remark code associated with result_va, if applicable; codes explained in the table Remark_Cd in LAGBRD
val_qual_cd	Value qualifier code associated with result_va, if applicable; codes explained in the table Val_Qual_Cd in LAGBRD
rpt_lev_va	Reporting level value, if known
rpt_lev_cd	If rpt_lev_va is known, type of reporting level used in rpt_lev_va, as described in the data source
result_unit	Units of measure for result_va and rpt_lev_va
wq_note	Contains notes on result-level information
data_src	Citation of data source

TIME-SERIES PLOTS

The uniform formatting and naming of the water chemistry data contained in LAGBRD make it a useful tool for visualizing data from the Lee Acres Landfill and GBR that previously existed only in disparate sources. There are 131 sites with water quality data in LAGBRD and more than 2,100 water quality samples spanning from 1985 to 2020. Table 8 summarizes statistics that describe the water quality data in the database, including sampling start and end dates and sources of water quality data for each sampling location in the database.

The remainder of this section contains time-series plots generated from data contained in LAGBRD but is not an exhaustive display of those data. Some of the plots in this section contain many nondetect results (ND; analytes that may be present in a sample but were not detected above method detection limits) or estimated results (E; results are estimated, formerly applied to results above method detection limits but below reporting levels). Nondetect results are plotted at their reporting level and are symbolized as open diamonds, and estimated results are symbolized as open squares. The data in LAGBRD are associated with several different reporting level types. The reporting level and reporting level type are contained in the table “WQ_Result” in LAGBRD when those data are available. Because laboratory practices changed over time, and because a number of different laboratories and analytical methods were used to analyze samples from the Lee Acres Landfill and GBR, reporting levels are generally not constant for the analytes in LAGBRD. These changes in reporting level are evident in the nondetect results in the time-series plots.

Because of the large number of sites, results have been plotted in groups of sites according to site operator and location relative to the Lee Acres Landfill and GBR. Time-series plots of chloride concentration data from LAGBRD are displayed in Figures 8–14. Anion samples collected at the Lee Acres Landfill by USGS personnel were historically not filtered, and Figures 8–11 display the total, unfiltered chloride results for those samples. GBR monitoring reports do not explicitly state whether anion samples were filtered or unfiltered, and so it is unknown whether the GBR anion data in LAGBRD represent dissolved or total sample fractions. Figures

Table 4. Definitions of field names contained in the “GW_Elevation” table of the Lee Acres-Giant Bloomfield Refinery Database (LAGBRD; available at <https://doi.org/10.3133/dr1154>).

Field	Field description
loc_station_nm	Local station name
lev_dt	Water-level measurement date, if given in the data source
lev_yr	Water-level measurement year, if the exact date is not given in the data source
lev_mo	Water-level measurement month, if the exact date is not given in the data source
lev_dt_calc	Water-level measurement date, if given in the data source, or the first day of the month the water-level measurement was collected
csng_top_alt_va	Altitude of the top of casing in feet above datum, for Giant Bloomfield Refinery monitoring data
lev_va_below_land_surf	Water level in feet referenced to land-surface datum, for data downloaded from the National Water Information System database; land-surface elevation provided in the table Sites in LAGBRD
lev_va_below_csng_top	Water level in feet referenced to top of casing, for Giant Bloomfield Refinery monitoring data
lev_product_va_below_csng_top	Floating product level in feet referenced to top of casing, for Giant Bloomfield Refinery monitoring data
thickness_product_va	Floating product thickness in feet, for Giant Bloomfield Refinery monitoring data, as reported
lev_va_above_datum	Altitude of the water surface (adjusted for floating product thickness) in feet referenced to altitude datum, as reported. Altitude datum for National Water Information System sites can be found in the table Sites in LAGBRD. The altitude datum is not known for some data collected by the Giant Bloomfield Refinery
data_src	Citation of data source

Table 5. Definitions of field names contained in the “Remark_Cd” table of the Lee Acres-Giant Bloomfield Refinery Database (LAGBRD; available at <https://doi.org/10.3133/dr1154>).

Field	Field description
remark_cd	Remark code
remark_nm	Name associated with the remark code
remark_description	Description of the remark

Table 6. Definitions of field names contained in the “Val_Qual_Cd” table of the Lee Acres-Giant Bloomfield Refinery Database (LAGBRD; available at <https://doi.org/10.3133/dr1154>).

Field	Field description
val_qual_cd	Value qualifier code
val_qual_description	Description of the value qualifier code

Table 7. Definitions of field names contained in the “Field_Explanation” table of the Lee Acres-Giant Bloomfield Refinery Database (LAGBRD; available at <https://doi.org/10.3133/dr1154>).

Field	Field description
table_nm	Name of LAGBRD table in which the field is found
field_nm	Field name
field_explanation	Explanation of the field

12–14 display the chloride results in LAGBRD from GBR reports with unknown chloride fractions. The two inorganic COCs listed in the ROD (EPA, 2004) for the Lee Acres Landfill are dissolved manganese and dissolved nickel. At GBR, dissolved manganese, dissolved chromium, and dissolved iron have been detected above alluvial aquifer background concentrations (Table 1) at several monitoring wells. Time-series plots of dissolved manganese, dissolved nickel, dissolved chromium, and dissolved iron at BLM and GBR monitoring sites are displayed in Figures 15–42. Since 2011, the GBR monitoring plan has included analysis of total metals at some of their monitoring locations. Time-series plots of total metals at GBR sites are displayed in Figures 43–54. The BLM monitoring plan has not historically included analysis of total metals.

Five of the COCs described in the ROD (EPA, 2004) are organic compounds: *cis*-1,2-dichloroethene, *trans*-1,2-dichloroethene, tetrachloroethene (also called perchloroethylene or PCE), trichloroethene (also called TCE), and vinyl chloride. All results for the organic COCs in LAGBRD and discussed in this report represent raw, unfiltered water. Results for these organic COCs for BLM monitoring wells upgradient from the Lee Acres Landfill, within the landfill boundary, adjacent to the landfill, or directly downgradient from the landfill are displayed as time-series plots in Figures 55–66. Because there were few detections of organic COCs at wells south of U.S. Highway 64, time-series plots of organic COCs from that area have been omitted from this report. In the instances where there were no detections above reporting levels at a BLM well within an area, then that time-series plot has been omitted. Specifically, *trans*-1,2-dichloroethene has not been detected in any BLM well within those areas, so *trans*-1,2-dichloroethene time-series plots, which would display only reporting levels, have been omitted. Likewise, there have been no detections of trichloroethene in BLM wells upgradient from the landfill (except one suspect value reported in the remedial investigation [Roy F. Weston, Inc., 1991], which is not displayed herein), nor have there been detections of vinyl chloride in BLM wells upgradient from the landfill, adjacent to the landfill, or directly downgradient from the landfill.

Table 8. Site-level summary statistics of the water quality data within the Lee Acres-Giant Bloomfield Refinery Database (LAGBRD; available at <https://doi.org/10.3133/dr1154>). [BLM, Bureau of Land Management; RI, Lee Acres remedial investigation; USGS, U.S. Geological Survey; GBR, Giant Bloomfield Refinery; GRW, groundwater recovery well; NMED, New Mexico Environment Department; SHS, Southern Heights Subdivision]

Local station name	Site type	Water quality sampling start date (month/day/year)	Water quality sampling end date (month/day/year)	Number of water quality samples in LAGBRD	Number of individual water quality results in LAGBRD	Water quality data source(s) ¹
BLM-14	Monitoring well	12/15/1987	5/17/1990	17	197	RI
BLM-15	Monitoring well	12/15/1987	11/16/2004	31	1,159	RI, USGS
BLM-16	Monitoring well	12/16/1987	5/17/1990	16	205	RI
BLM-17	Monitoring well	12/15/1987	5/16/1990	17	196	RI
BLM-18	Monitoring well	12/15/1987	5/16/1990	17	244	RI
BLM-19	Monitoring well	12/16/1987	5/16/1990	17	203	RI
BLM-20	Monitoring well	12/15/1987	5/16/1990	17	171	RI
BLM-21	Monitoring well	12/15/1987	11/17/2004	32	1,178	RI, USGS
BLM-22	Monitoring well	12/15/1987	5/16/1990	18	220	RI
BLM-23	Monitoring well	12/16/1987	5/16/1990	17	224	RI
BLM-24	Monitoring well	12/16/1987	5/20/1990	19	166	RI
BLM-25	Monitoring well	12/16/1987	5/20/1990	17	201	RI
BLM-26	Monitoring well	12/16/1987	5/20/1990	19	186	RI
BLM-27	Monitoring well	12/16/1987	5/19/1990	17	198	RI
BLM-28	Monitoring well	12/16/1987	5/19/1990	17	197	RI
BLM-29	Monitoring well	12/16/1987	5/19/1990	17	192	RI
BLM-30	Monitoring well	12/16/1987	5/19/1990	18	224	RI
BLM-31	Monitoring well	12/16/1987	5/19/1990	17	194	RI
BLM-32	Monitoring well	12/16/1987	5/19/1990	19	225	RI
BLM-33	Monitoring well	2/8/1989	5/16/1990	7	119	RI
BLM-34	Monitoring well	2/8/1989	5/16/1990	7	103	RI

Table 8. Site-level summary statistics of the water quality data within the Lee Acres-Giant Bloomfield Refinery Database (LAGBRD; available at <https://doi.org/10.3133/dr1154>). – Continued
[BLM, Bureau of Land Management; RI, Lee Acres remedial investigation; USGS, U.S. Geological Survey; GBR, Giant Bloomfield Refinery; GRW, groundwater recovery well; NMED, New Mexico Environment Department; SHS, Southern Heights Subdivision]

Local station name	Site type	Water quality sampling start date (month/day/year)	Water quality sampling end date (month/day/year)	Number of water quality samples in LAGBRD	Number of individual water quality results in LAGBRD	Water quality data source(s) ¹
BLM-35	Monitoring well	2/8/1989	5/16/1990	7	131	RI
BLM-37	Monitoring well	5/16/1989	4/28/1990	7	179	RI
BLM-39	Monitoring well	3/1/1990	8/4/2020	56	3,946	RI, USGS
BLM-40	Monitoring well	3/1/1990	5/17/1990	3	46	RI
BLM-41	Monitoring well	3/1/1990	5/18/1990	3	40	RI
BLM-42	Monitoring well	3/1/1990	11/16/2004	17	988	RI, USGS
BLM-43	Monitoring well	3/1/1990	5/18/1990	3	39	RI
BLM-44	Monitoring well	3/2/1990	5/17/1990	3	36	RI
BLM-45	Monitoring well	3/2/1990	8/4/2020	49	3,584	RI, USGS
BLM-46	Monitoring well	3/2/1990	5/17/1990	3	38	RI
BLM-47	Monitoring well	3/3/1990	5/17/1990	3	36	RI
BLM-48	Monitoring well	3/3/1990	11/16/2004	17	971	RI, USGS
BLM-49	Monitoring well	3/3/1990	5/17/1990	3	38	RI
BLM-50	Monitoring well	3/20/1990	5/17/1990	3	47	RI
BLM-51	Monitoring well	3/20/1990	11/16/2004	17	980	RI, USGS
BLM-52	Monitoring well	3/20/1990	5/17/1990	3	36	RI
BLM-53	Monitoring well	3/21/1990	5/21/1990	3	39	RI
BLM-54	Monitoring well	3/4/1990	5/21/1990	3	53	RI
BLM-55	Monitoring well	3/4/1990	11/16/2004	17	984	RI, USGS
BLM-56	Monitoring well	3/6/1990	11/16/2004	25	1,533	RI, USGS
BLM-57	Monitoring well	3/21/1990	11/16/2004	25	1,539	RI, USGS

Table 8. Site-level summary statistics of the water quality data within the Lee Acres-Giant Bloomfield Refinery Database (LAGBRD; available at <https://doi.org/10.3133/dr1154>).—Continued
 [BLM, Bureau of Land Management; RI, Lee Acres remedial investigation; USGS, U.S. Geological Survey; GBR, Giant Bloomfield Refinery; GRW, groundwater recovery well; NMED, New Mexico Environment Department; SHS, Southern Heights Subdivision]

Local station name	Site type	Water quality sampling start date (month/day/year)	Water quality sampling end date (month/day/year)	Number of water quality samples in LAGBRD	Number of individual water quality results in LAGBRD	Water quality data source(s) ¹
BLM-58	Monitoring well	3/6/1990	5/22/1990	3	36	RI
BLM-59	Monitoring well	3/2/1990	5/18/1990	3	36	RI
BLM-60	Monitoring well	3/2/1990	8/5/2020	49	3,674	RI, USGS
BLM-61	Monitoring well	3/21/1990	5/20/1990	3	37	RI
BLM-62	Monitoring well	3/21/1990	8/5/2020	49	3,569	RI, USGS
BLM-63	Monitoring well	3/21/1990	5/20/1990	3	40	RI
BLM-64	Monitoring well	3/21/1990	5/20/1990	3	39	RI
BLM-65	Monitoring well	3/20/1990	5/20/1990	3	41	RI
BLM-66	Monitoring well	3/20/1990	5/18/1990	3	32	RI
BLM-67	Monitoring well	5/20/1998	11/18/2004	14	933	USGS
BLM-68	Monitoring well	5/20/1998	8/5/2020	41	3,184	USGS
BLM-69	Monitoring well	5/20/1998	8/5/2020	16	1,164	USGS
BLM-70	Monitoring well	5/20/1998	5/14/2003	11	730	USGS
BLM-75	Monitoring well	5/19/1998	8/5/2020	46	3,527	USGS
BLM-76	Monitoring well	5/19/1998	11/17/2004	13	875	USGS
BLM-77	Monitoring well	5/19/1998	8/5/2020	46	3,571	USGS
BLM-80	Monitoring well	12/20/2005	8/5/2020	31	2,450	USGS
Filter discharge	GBR treatment system	10/1/1993	12/1/1993	3	173	GBR
Firefighting drill area seep	Underground seep	10/24/1985	11/21/1986	4	94	GBR
Firefighting drill area seep, east	Underground seep	6/5/1986	6/5/1986	1	3	GBR
Firefighting drill area seep, west	Underground seep	10/29/1985	10/29/1985	1	2	GBR

Table 8. Site-level summary statistics of the water quality data within the Lee Acres-Giant Bloomfield Refinery Database (LAGBRD; available at <https://doi.org/10.3133/dr1154>).— Continued
 [BLM, Bureau of Land Management; RI, Lee Acres remedial investigation; USGS, U.S. Geological Survey; GBR, Giant Bloomfield Refinery; GRW, groundwater recovery well; NMED, New Mexico Environment Department; SHS, Southern Heights Subdivision]

Local station name	Site type	Water quality sampling start date (month/day/year)	Water quality sampling end date (month/day/year)	Number of water quality samples in LAGBRD	Number of individual water quality results in LAGBRD	Water quality data source(s) ¹
GBR treatment system effluent	GBR treatment system	3/14/1989	8/3/2015	132	7,233	GBR
GBR-1	Monitoring well	6/5/1986	6/5/1986	1	6	GBR
GBR-10	Monitoring well	11/21/1986	11/21/1986	1	19	GBR
GBR-11	Monitoring well	4/1/1986	8/6/2015	5	94	GBR
GBR-13	Monitoring well	4/15/1986	12/12/1989	12	343	GBR
GBR-14/GRW-13	Groundwater recovery well	10/17/1986	1/1/2001	24	1,229	GBR
GBR-15	Monitoring well	10/17/1986	1/1/2001	29	1,365	GBR
GBR-17	Monitoring well	5/29/1986	11/5/2019	71	3,538	RI, USGS, GBR
GBR-18	Monitoring well	5/9/1986	5/19/1990	9	119	RI, GBR
GBR-19	Monitoring well	10/17/1986	10/8/1992	4	102	RI, GBR
GBR-20	Monitoring well	5/9/1986	8/6/2015	5	63	GBR
GBR-21	Monitoring well	5/9/1986	5/9/1986	1	4	GBR
GBR-21D	Monitoring well	10/17/1986	8/7/2015	2	10	GBR
GBR-22	Monitoring well	5/9/1986	8/7/2015	3	14	GBR
GBR-23	Monitoring well	4/18/1986	4/18/1986	1	3	GBR
GBR-24	Monitoring well	4/18/1986	6/5/1986	3	27	GBR
GBR-24D	Monitoring well	10/17/1986	11/6/2019	45	2,710	GBR
GBR-24S	Monitoring well	11/21/1986	8/25/1988	2	34	RI, GBR
GBR-25	Monitoring well	5/9/1986	8/7/2015	3	15	GBR
GBR-26	Monitoring well	5/9/1986	8/7/2015	3	47	GBR
GBR-27/GRW-11	Groundwater recovery well	10/24/1985	11/21/1986	4	74	GBR

Table 8. Site-level summary statistics of the water quality data within the Lee Acres-Giant Bloomfield Refinery Database (LAGBRD; available at <https://doi.org/10.3133/dr1154>).— Continued
 [BLM, Bureau of Land Management; RI, Lee Acres remedial investigation; USGS, U.S. Geological Survey; GBR, Giant Bloomfield Refinery; GRW, groundwater recovery well; NMED, New Mexico Environment Department; SHS, Southern Heights Subdivision]

Local station name	Site type	Water quality sampling start date (month/day/year)	Water quality sampling end date (month/day/year)	Number of water quality samples in LAGBRD	Number of individual water quality results in LAGBRD	Water quality data source(s) ¹
GBR-28/GRW-12	Groundwater recovery well	5/29/1986	9/4/1990	3	18	GBR
GBR-29/GRW-3	Groundwater recovery well	5/30/1986	10/11/2018	32	1,979	GBR
GBR-30	Monitoring well	10/17/1986	11/6/2019	45	2,645	RI, GBR
GBR-31	Monitoring well	10/17/1986	10/15/2018	60	2,880	RI, GBR
GBR-32	Monitoring well	4/30/1987	11/5/2019	62	2,960	RI, USGS, GBR
GBR-33	Monitoring well	3/15/1989	10/8/1990	8	477	RI, GBR
GBR-36/GRW-10	Groundwater recovery well	9/4/1990	9/4/1990	1	8	GBR
GBR-37/GRW-5	Groundwater recovery well	9/4/1990	9/4/1990	1	8	GBR
GBR-38/GRW-1	Groundwater recovery well	9/4/1990	9/4/1990	1	8	GBR
GBR-39	Monitoring well	5/9/1986	10/17/1986	2	39	GBR
GBR-40	Monitoring well	6/24/1993	6/24/1993	1	13	GBR
GBR-41	Monitoring well	6/24/1993	6/24/1993	1	13	GBR
GBR-42/GRW-2	Groundwater recovery well	9/8/1989	6/1/1997	3	81	GBR
GBR-43/GRW-4	Groundwater recovery well	4/2/1990	4/8/1992	9	529	GBR
GBR-44/GRW-6	Groundwater recovery well	4/2/1990	10/12/2018	31	2,065	GBR
GBR-45	Monitoring well	10/1/1996	10/1/1996	1	37	GBR
GBR-47	Monitoring well	3/14/1989	6/13/1989	3	199	RI, GBR
GBR-48	Monitoring well	3/14/1989	11/5/2019	51	2,806	RI, USGS, GBR

Table 8. Site-level summary statistics of the water quality data within the Lee Acres-Giant Bloomfield Refinery Database (LAGBRD; available at <https://doi.org/10.3133/dr1154>).— Continued
[BLM, Bureau of Land Management; RI, Lee Acres remedial investigation; USGS, U.S. Geological Survey; GBR, Giant Bloomfield Refinery; GRW, groundwater recovery well; NMED, New Mexico Environment Department; SHS, Southern Heights Subdivision]

Local station name	Site type	Water quality sampling start date (month/day/year)	Water quality sampling end date (month/day/year)	Number of water quality samples in LAGBRD	Number of individual water quality results in LAGBRD	Water quality data source(s) ¹
GBR-49	Monitoring well	3/14/1989	11/5/2019	56	2,685	RI, USGS, GBR
GBR-5	Monitoring well	1/23/1986	1/10/1990	5	85	RI, GBR
GBR-50	Monitoring well	10/1/1989	11/5/2019	51	2,772	RI, USGS, GBR
GBR-51	Monitoring well	6/12/1989	10/11/2018	21	1,216	RI, GBR
GBR-52	Monitoring well	6/12/1989	11/5/2019	23	1,315	RI, GBR
GBR-6/GRW-9	Monitoring well	11/20/1986	6/24/1993	9	352	RI, GBR
GBR-7	Monitoring well	10/17/1986	1/9/1990	3	77	RI, GBR
GBR-8	Monitoring well	10/17/1986	8/6/2015	10	374	RI, GBR
GBR-9	Monitoring well	10/17/1986	8/25/1988	3	54	RI, GBR
Lagoon, east side	Lee Acres Landfill liquid waste lagoon	2/27/1985	2/27/1985	1	38	NMED
Lagoon, south side	Lee Acres Landfill liquid waste lagoon	5/2/1985	5/2/1985	1	42	NMED
Lagoon, west side	Lee Acres Landfill liquid waste lagoon	1/11/1985	2/27/1985	2	77	NMED
SHS-1	Monitoring well	9/6/1989	6/1/2017	6	228	RI, GBR
SHS-10	Monitoring well	1/1/1991	1/1/2005	39	1,635	GBR
SHS-12	Monitoring well	1/1/1991	1/1/2005	39	1,638	GBR
SHS-13	Monitoring well	1/1/1991	1/22/2018	40	1,706	GBR
SHS-14	Monitoring well	1/9/1992	1/22/2018	7	351	GBR
SHS-15	Monitoring well	1/1/1991	1/22/2018	30	1,328	GBR
SHS-16	Monitoring well	1/1/1991	1/22/2018	41	1,742	GBR

Table 8. Site-level summary statistics of the water quality data within the Lee Acres-Giant Bloomfield Refinery Database (LAGBRD; available at <https://doi.org/10.3133/dr1154>).—Continued
 [BLM, Bureau of Land Management; RI, Lee Acres remedial investigation; USGS, U.S. Geological Survey; GBR, Giant Bloomfield Refinery; GRW, groundwater recovery well; NMED, New Mexico Environment Department; SHS, Southern Heights Subdivision]

Local station name	Site type	Water quality sampling start date (month/day/year)	Water quality sampling end date (month/day/year)	Number of water quality samples in LAGBRD	Number of individual water quality results in LAGBRD	Water quality data source(s) ¹
SHS-17	Monitoring well	8/1/1992	1/22/2018	35	1,460	GBR
SHS-18	Monitoring well	8/10/1992	1/23/2018	8	383	GBR
SHS-19	Monitoring well	1/1/2004	1/23/2018	6	323	GBR
SHS-2	Monitoring well	9/6/1989	6/1/2017	6	192	RI, GBR
SHS-3	Monitoring well	1/1/1991	1/1/2003	26	1,134	GBR
SHS-4	Monitoring well	7/7/1992	6/1/2017	16	677	GBR
SHS-5	Monitoring well	1/15/2009	6/1/2017	2	94	GBR
SHS-6	Monitoring well	1/1/1991	1/23/2018	24	1,080	GBR
SHS-8	Monitoring well	8/1/2001	10/11/2018	11	754	GBR
SHS-9	Monitoring well	1/9/1992	11/5/2019	8	406	GBR

¹Data sources: RI, Roy F. Weston, Inc. (1995); USGS, U.S. Geological Survey (2021); GBR, data related to site investigations and regular monitoring at the Giant Bloomfield Refinery compiled in an online data repository (New Mexico Oil Conservation Division, 2021); NMED, New Mexico Environment Department (1986).

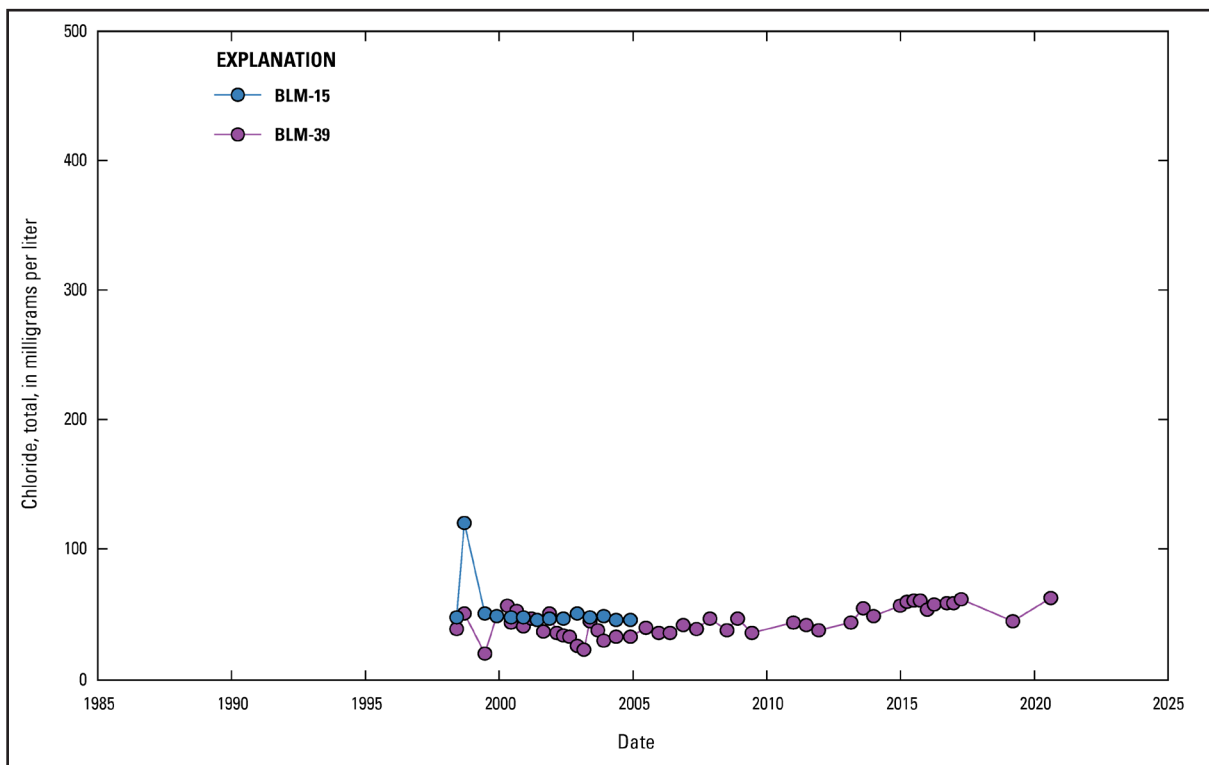


Figure 8. Total chloride concentration over time at Bureau of Land Management (BLM) monitoring wells upgradient from the Lee Acres Landfill near Farmington, New Mexico. Locations of wells are shown in Figure 3; data sources are specified in Table 8. As shown in Table 1, the alluvial aquifer background concentrations for total chloride at the Lee Acres Landfill range from 6.4 to 62.9 milligrams per liter (Roy F. Weston, Inc., 1995). Chloride is not a contaminant of concern at the Lee Acres Landfill.

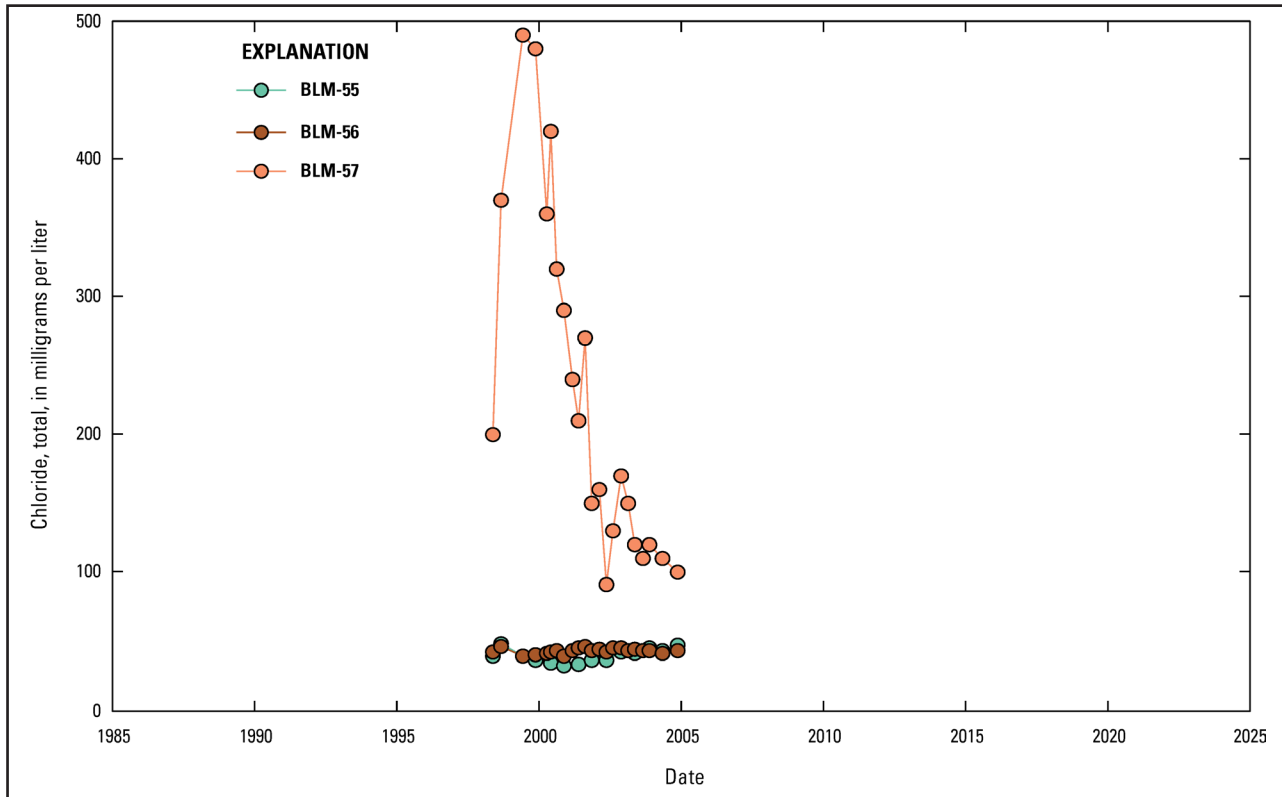


Figure 9. Total chloride concentration over time at Bureau of Land Management (BLM) monitoring wells within the boundary of the Lee Acres Landfill near Farmington, New Mexico. Locations of wells are shown in Figure 4; data sources are specified in Table 8. As shown in Table 1, the alluvial aquifer background concentrations for total chloride at the Lee Acres Landfill range from 6.4 to 62.9 milligrams per liter (Roy F. Weston, Inc., 1995). Chloride is not a contaminant of concern at the Lee Acres Landfill.

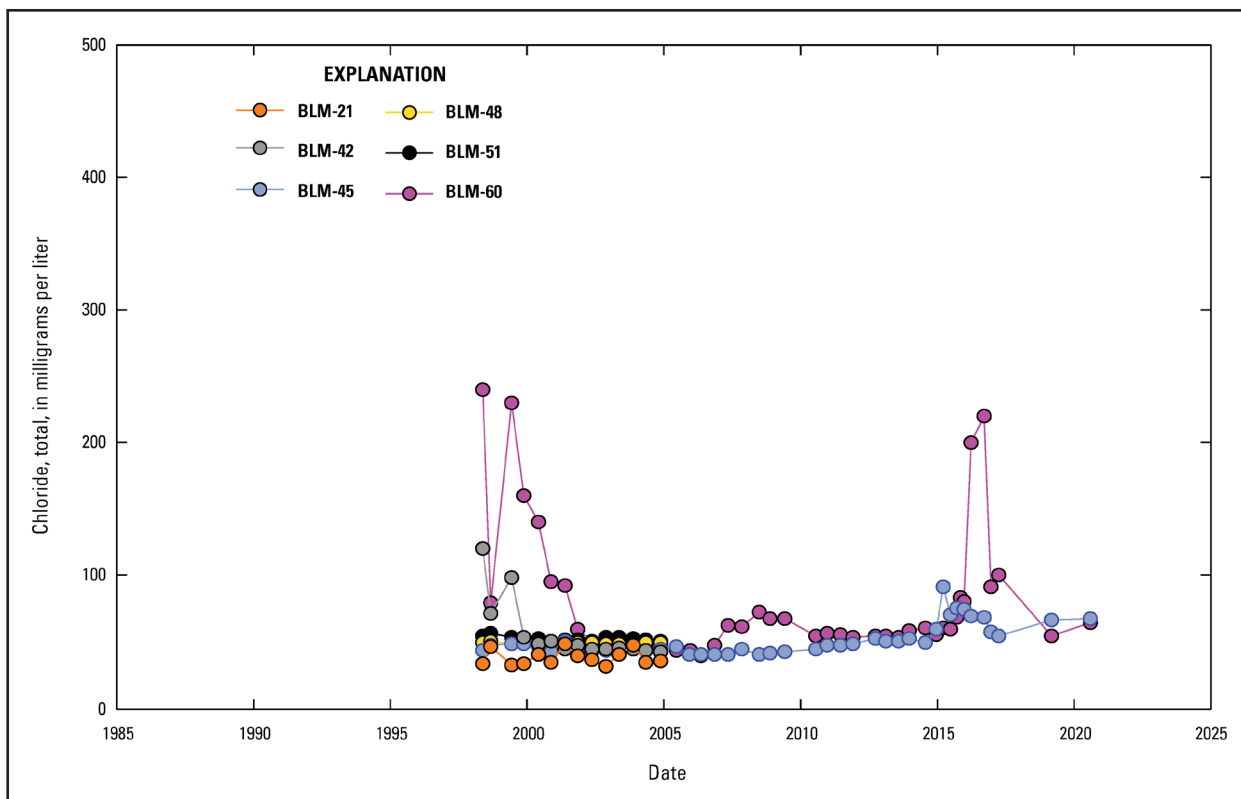


Figure 10. Total chloride concentration over time at Bureau of Land Management (BLM) monitoring wells adjacent to the Lee Acres Landfill near Farmington, New Mexico. Locations of wells are shown in Figure 4; data sources are specified in Table 8. As shown in Table 1, the alluvial aquifer background concentrations for total chloride at the Lee Acres Landfill range from 6.4 to 62.9 milligrams per liter (Roy F. Weston, Inc., 1995). Chloride is not a contaminant of concern at the Lee Acres Landfill.

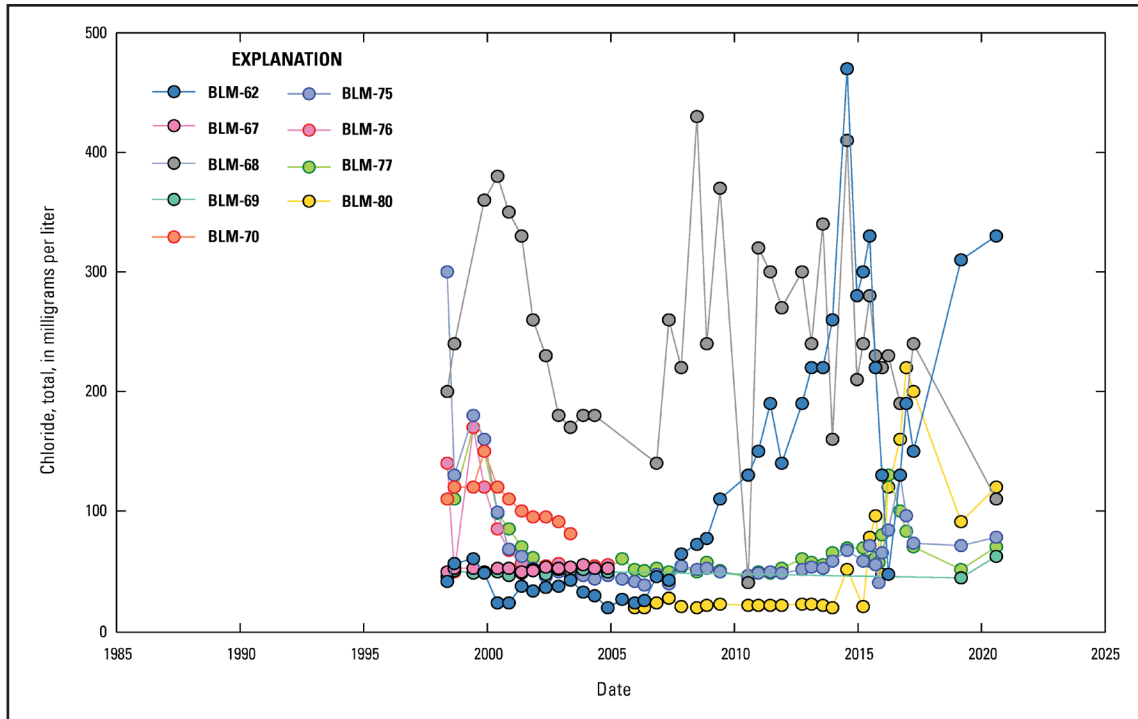


Figure 11. Total chloride concentration over time at Bureau of Land Management (BLM) monitoring wells directly downgradient from the Lee Acres Landfill near Farmington, New Mexico. Locations of wells are shown in Figure 5; data sources are specified in Table 8. As shown in Table 1, the alluvial aquifer background concentrations for total chloride at the Lee Acres Landfill range from 6.4 to 62.9 milligrams per liter (Roy F. Weston, Inc., 1995). Chloride is not a contaminant of concern at the Lee Acres Landfill.

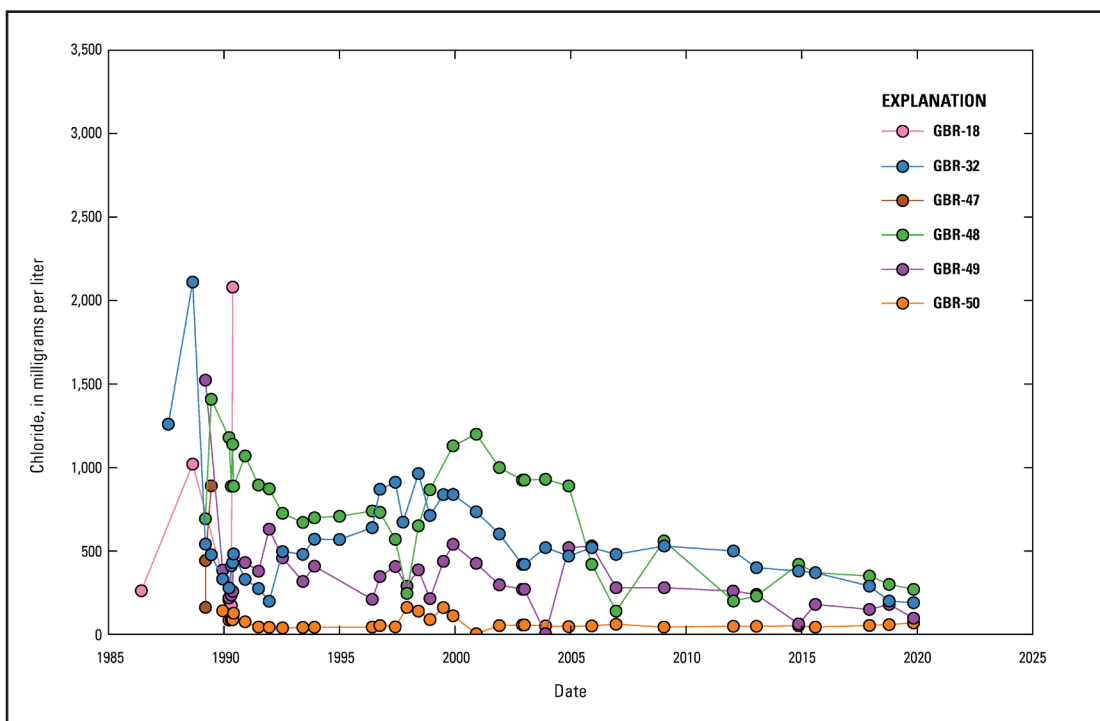


Figure 12. Chloride concentration over time at Giant Bloomfield Refinery (GBR) monitoring wells upgradient from refinery operations at GBR near Farmington, New Mexico. Locations of wells are shown in Figure 5; data sources are specified in Table 8. Whether these chloride results are total or dissolved is unknown (not reported). As shown in Table 1, the alluvial aquifer background concentrations for total chloride at the Lee Acres Landfill range from 6.4 to 62.9 milligrams per liter (Roy F. Weston, Inc., 1995). Chloride is not a contaminant of concern at the Lee Acres Landfill.

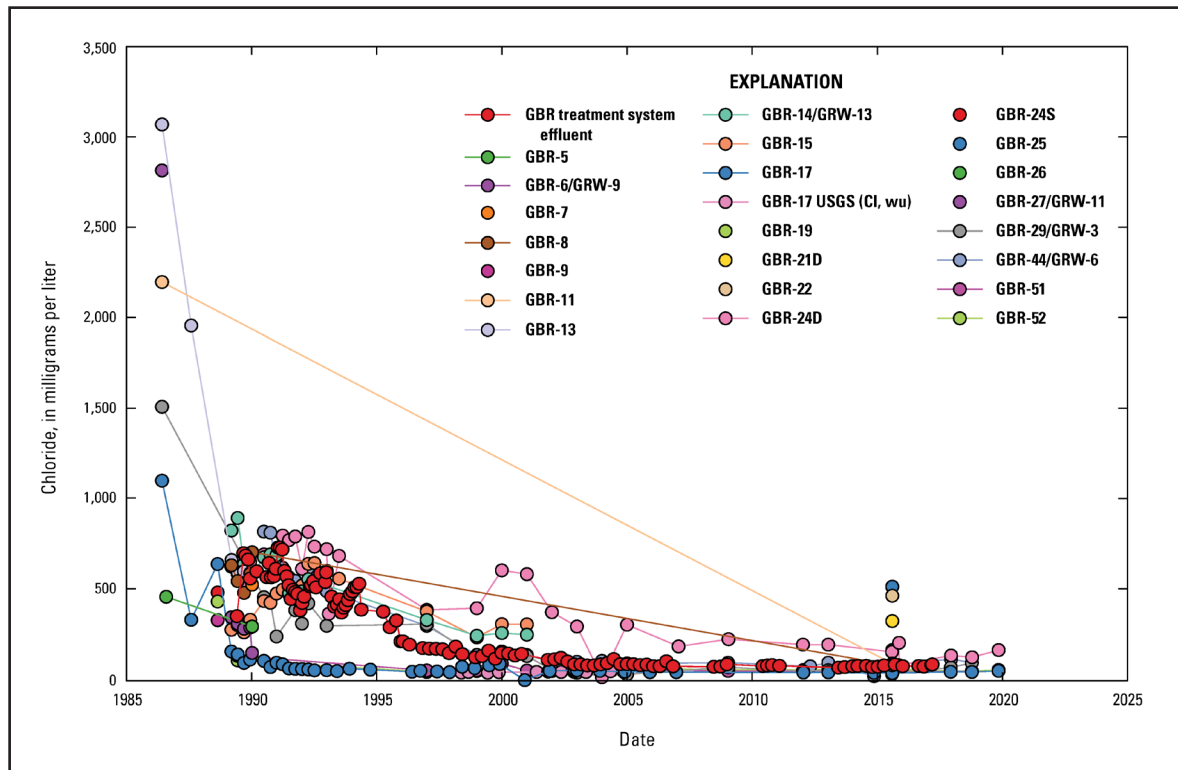


Figure 13. Chloride concentration over time at Giant Bloomfield Refinery (GBR) monitoring wells, groundwater recovery wells (GRW), and treatment system effluent near refinery operations at GBR near Farmington, New Mexico. Locations of wells and infiltration trenches, which accept the treatment system effluent, are shown in Figure 6; data sources are specified in Table 8. Whether these chloride results are total or dissolved is unknown (not reported). As shown in Table 1, the alluvial aquifer background concentrations for total chloride at the Lee Acres Landfill range from 6.4 to 62.9 milligrams per liter (Roy F. Weston, Inc., 1995). Chloride is not a contaminant of concern at the Lee Acres Landfill. Well GBR-17 was monitored by the U.S. Geological Survey (USGS) between 1998 and 2004; the results from those unfiltered samples are labeled in the Figure explanation as “GBR-17 USGS (Cl, wu).” Cl, chloride; wu, unfiltered water.

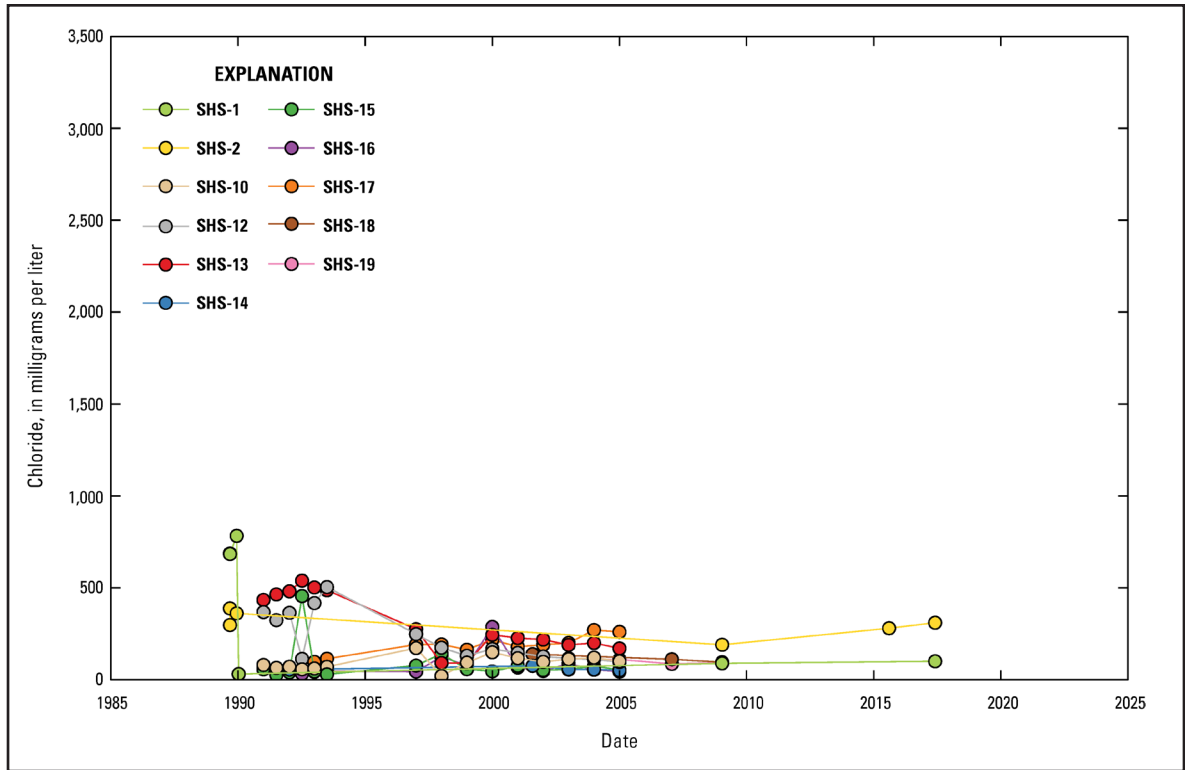


Figure 14. Chloride concentration over time at Southern Heights Subdivision (SHS) monitoring wells south of U.S. Highway 64 near Farmington, New Mexico. SHS wells were monitored by the Giant Bloomfield Refinery. Locations of wells are shown in Figure 7; data sources are specified in Table 8. Whether these chloride results are total or dissolved is unknown (not reported). As shown in Table 1, the alluvial aquifer background concentrations for total chloride at the Lee Acres Landfill range from 6.4 to 62.9 milligrams per liter (Roy F. Weston, Inc., 1995). Chloride is not a contaminant of concern at the Lee Acres Landfill.

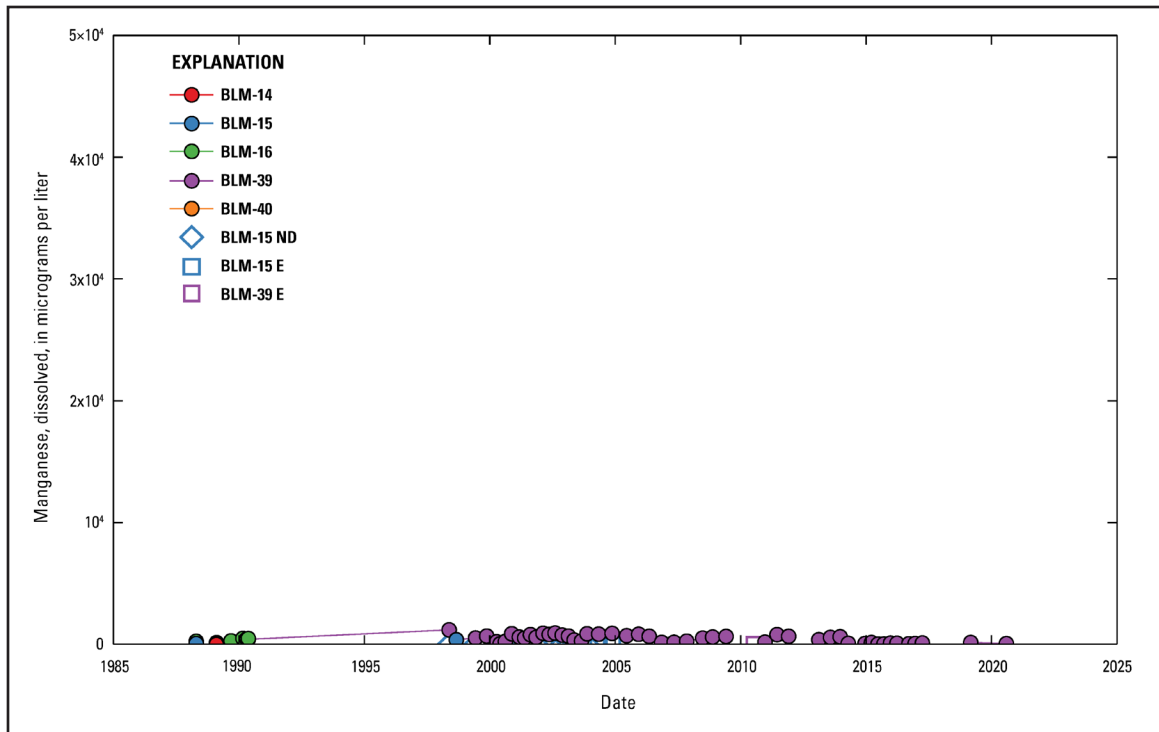


Figure 15. Dissolved manganese concentration over time at Bureau of Land Management (BLM) monitoring wells upgradient from the Lee Acres Landfill near Farmington, New Mexico. Locations of wells are shown in Figure 3; data sources are specified in Table 8. As shown in Table 1, the alluvial aquifer background concentrations for dissolved manganese at the Lee Acres Landfill range from 16.1 to 1,680 micrograms per liter (Roy F. Weston, Inc., 1995), and the cleanup level for dissolved manganese at the Lee Acres Landfill is 346 micrograms per liter (U.S. Environmental Protection Agency, 2004). ND, no detection above method detection limits; E, estimated results.

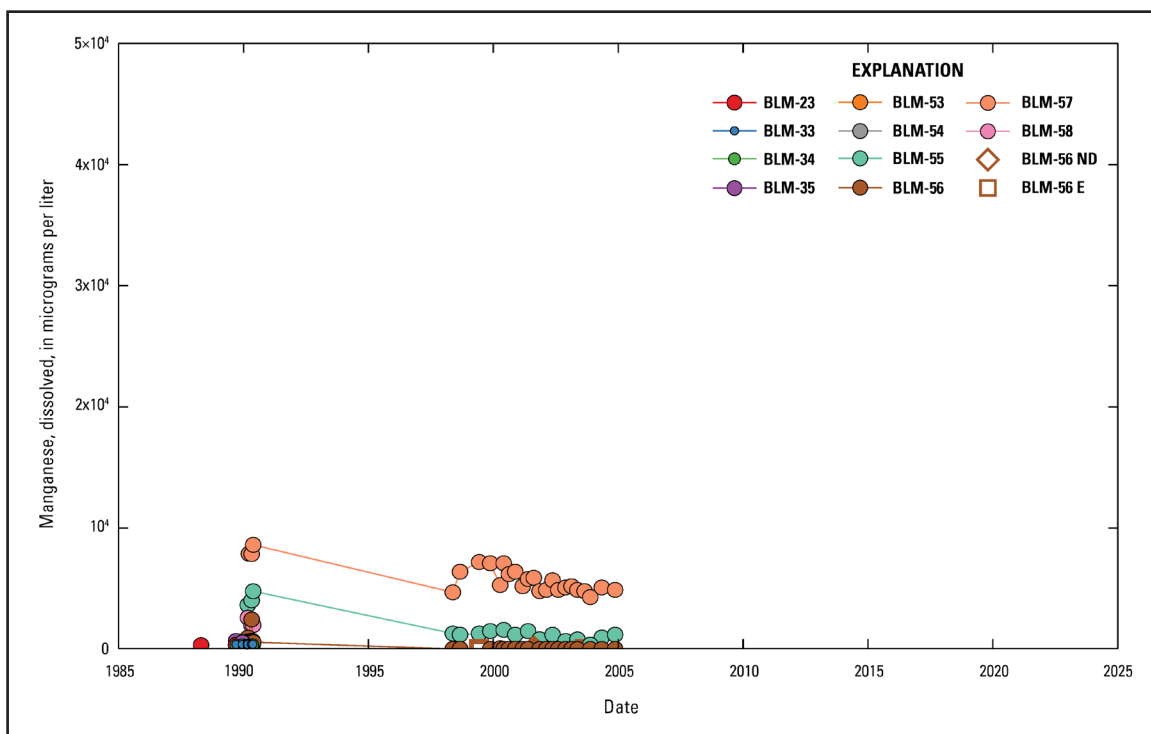


Figure 16. Dissolved manganese concentration over time at Bureau of Land Management (BLM) monitoring wells within the boundary of the Lee Acres Landfill near Farmington, New Mexico. Locations of wells are shown in Figure 4; data sources are specified in Table 8. As shown in Table 1, the alluvial aquifer background concentrations for dissolved manganese at the Lee Acres Landfill range from 16.1 to 1,680 micrograms per liter (Roy F. Weston, Inc., 1995), and the cleanup level for dissolved manganese at the Lee Acres Landfill is 346 micrograms per liter (U.S. Environmental Protection Agency, 2004). ND, no detection above method detection limits; E, estimated results.

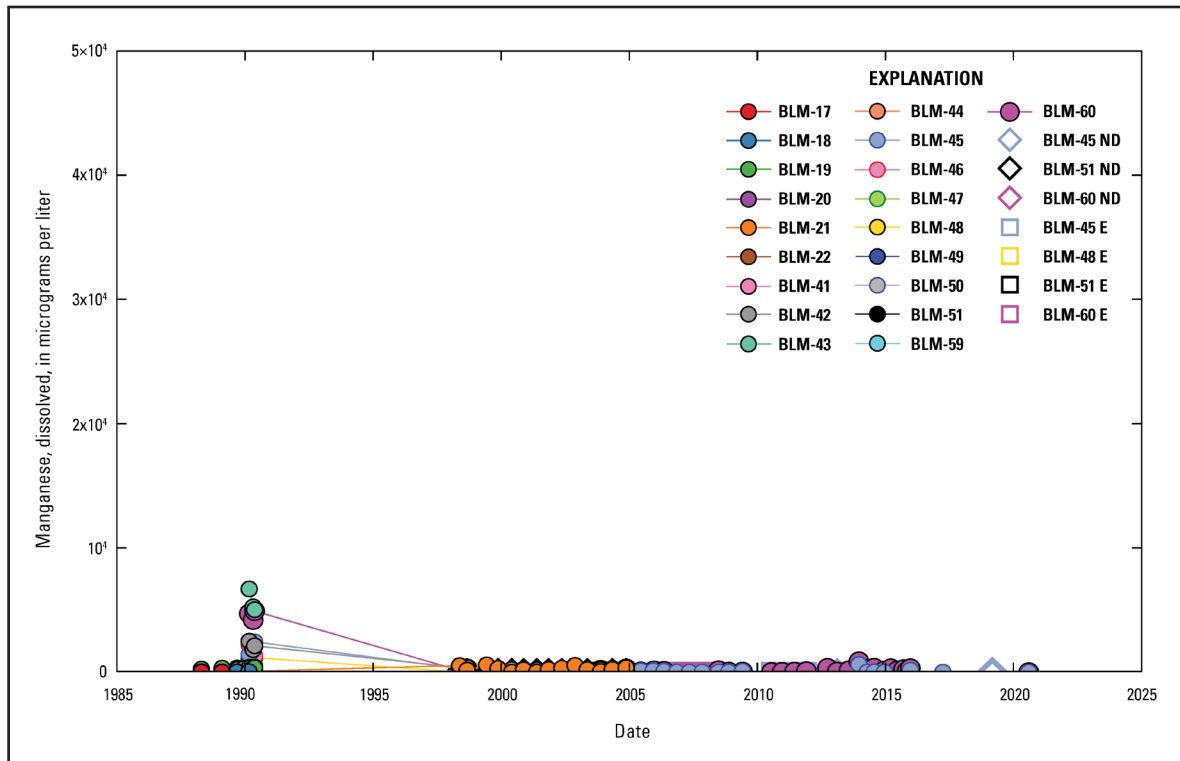


Figure 17. Dissolved manganese concentration over time at Bureau of Land Management (BLM) monitoring wells adjacent to the Lee Acres Landfill near Farmington, New Mexico. Locations of wells are shown in Figure 4; data sources are specified in Table 8. As shown in Table 1, the alluvial aquifer background concentrations for dissolved manganese at the Lee Acres Landfill range from 16.1 to 1,680 micrograms per liter (Roy F. Weston, Inc., 1995), and the cleanup level for dissolved manganese at the Lee Acres Landfill is 346 micrograms per liter (U.S. Environmental Protection Agency, 2004). ND, no detection above method detection limits; E, estimated results.

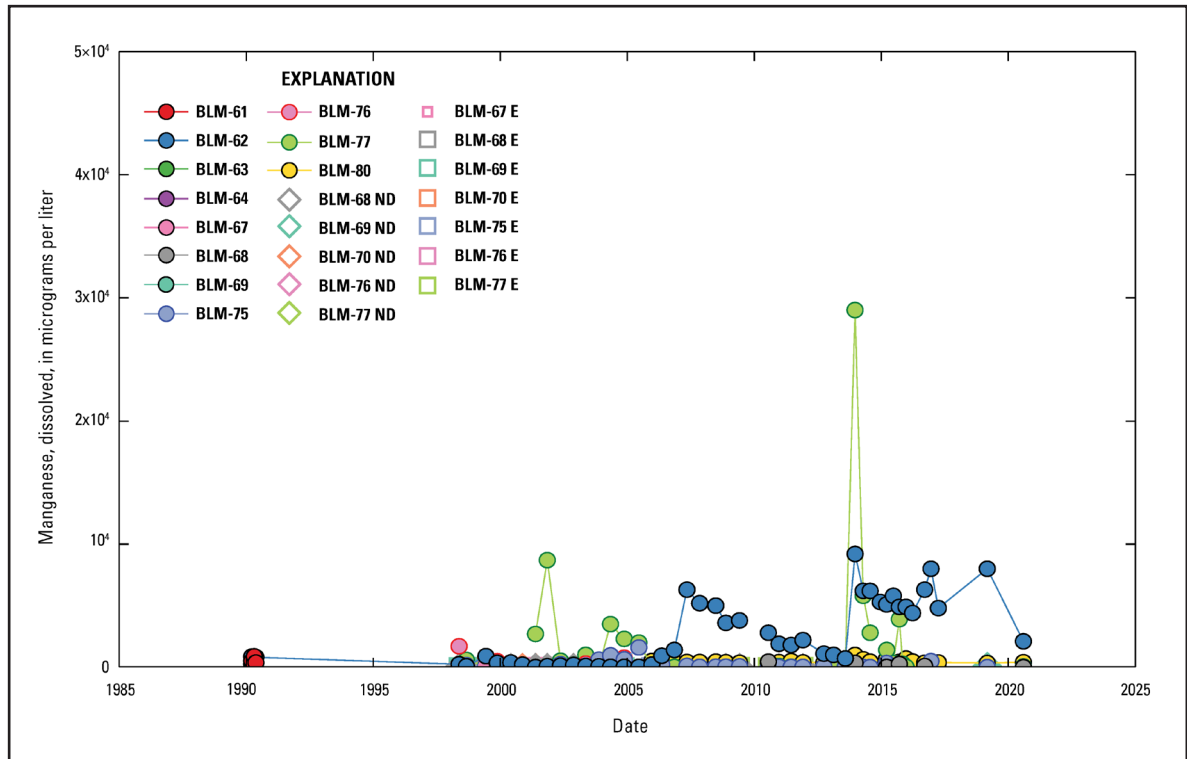


Figure 18. Dissolved manganese concentration over time at Bureau of Land Management (BLM) monitoring wells directly downgradient from the Lee Acres Landfill near Farmington, New Mexico. Locations of wells are shown in Figure 5; data sources are specified in Table 8. As shown in Table 1, the alluvial aquifer background concentrations for dissolved manganese at the Lee Acres Landfill range from 16.1 to 1,680 micrograms per liter (Roy F. Weston, Inc., 1995), and the cleanup level for dissolved manganese at the Lee Acres Landfill is 346 micrograms per liter (U.S. Environmental Protection Agency, 2004). ND, no detection above method detection limits; E, estimated results.

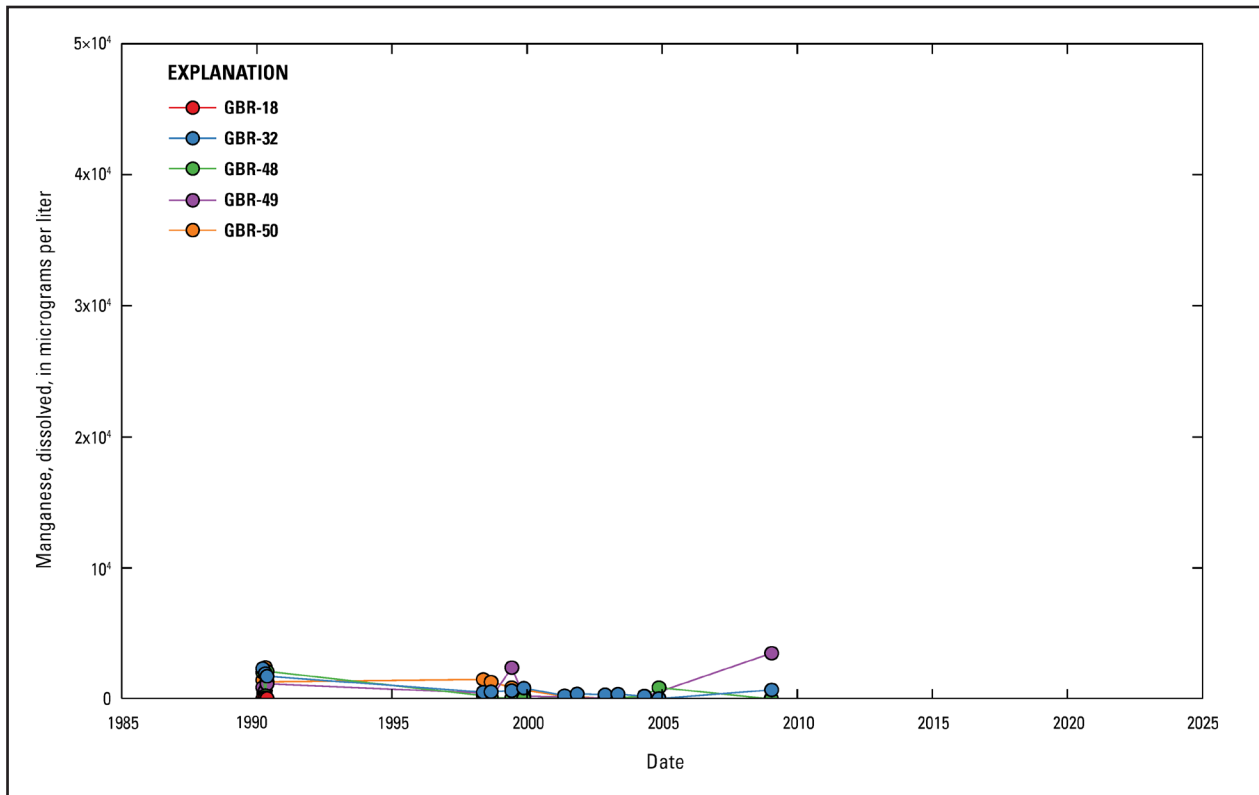


Figure 19. Dissolved manganese concentration over time at Giant Bloomfield Refinery (GBR) monitoring wells upgradient from refinery operations at GBR near Farmington, New Mexico. Locations of wells are shown in Figure 5; data sources are specified in Table 8. As shown in Table 1, the alluvial aquifer background concentrations for dissolved manganese at the Lee Acres Landfill range from 16.1 to 1,680 micrograms per liter (Roy F. Weston, Inc., 1995), and the cleanup level for dissolved manganese at the Lee Acres Landfill is 346 micrograms per liter (U.S. Environmental Protection Agency, 2004).

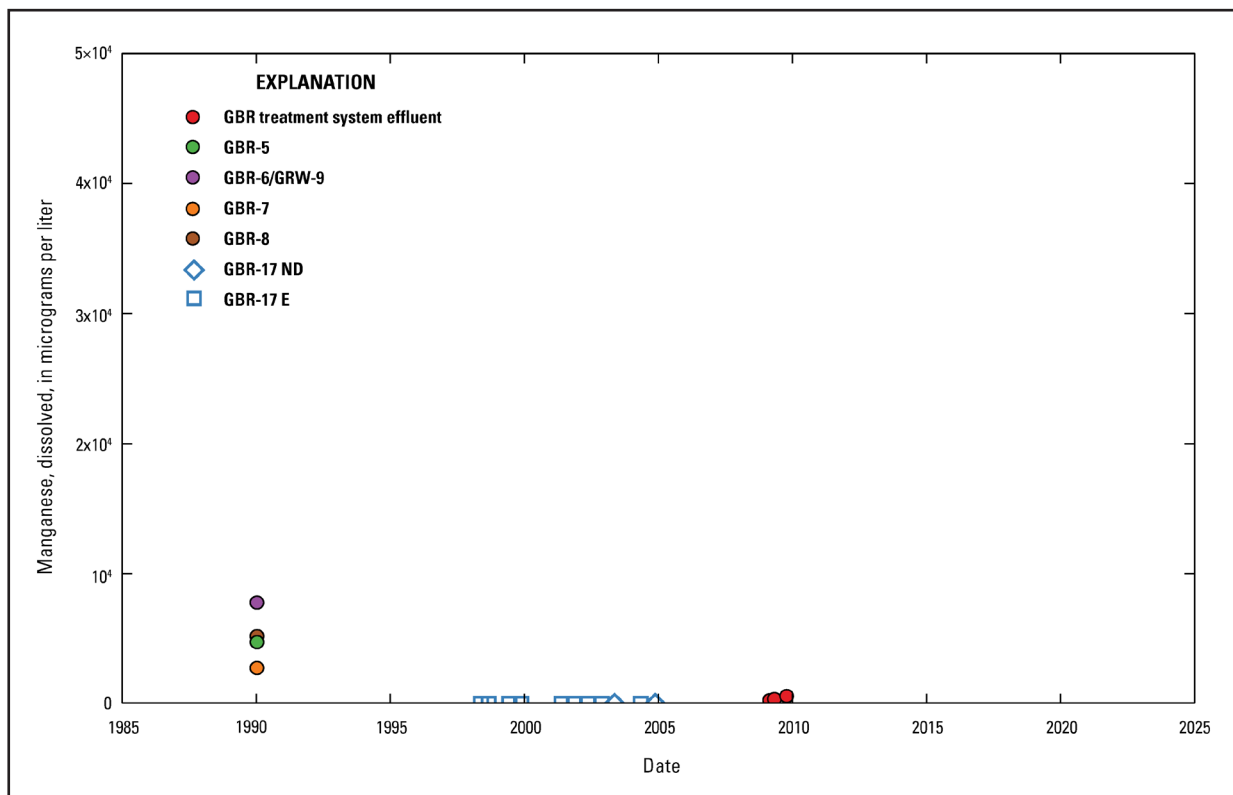


Figure 20. Dissolved manganese concentration over time at Giant Bloomfield Refinery (GBR) monitoring wells, groundwater recovery wells (GRW), and treatment system effluent near refinery operations at GBR near Farmington, New Mexico. Locations of wells and infiltration trenches, which accept the treatment system effluent, are shown in Figure 6; data sources are specified in Table 8. As shown in Table 1, the alluvial aquifer background concentrations for dissolved manganese at the Lee Acres Landfill range from 16.1 to 1,680 micrograms per liter (Roy F. Weston, Inc., 1995), and the cleanup level for dissolved manganese at the Lee Acres Landfill is 346 micrograms per liter (U.S. Environmental Protection Agency, 2004). ND, no detection above method detection limits; E, estimated results.

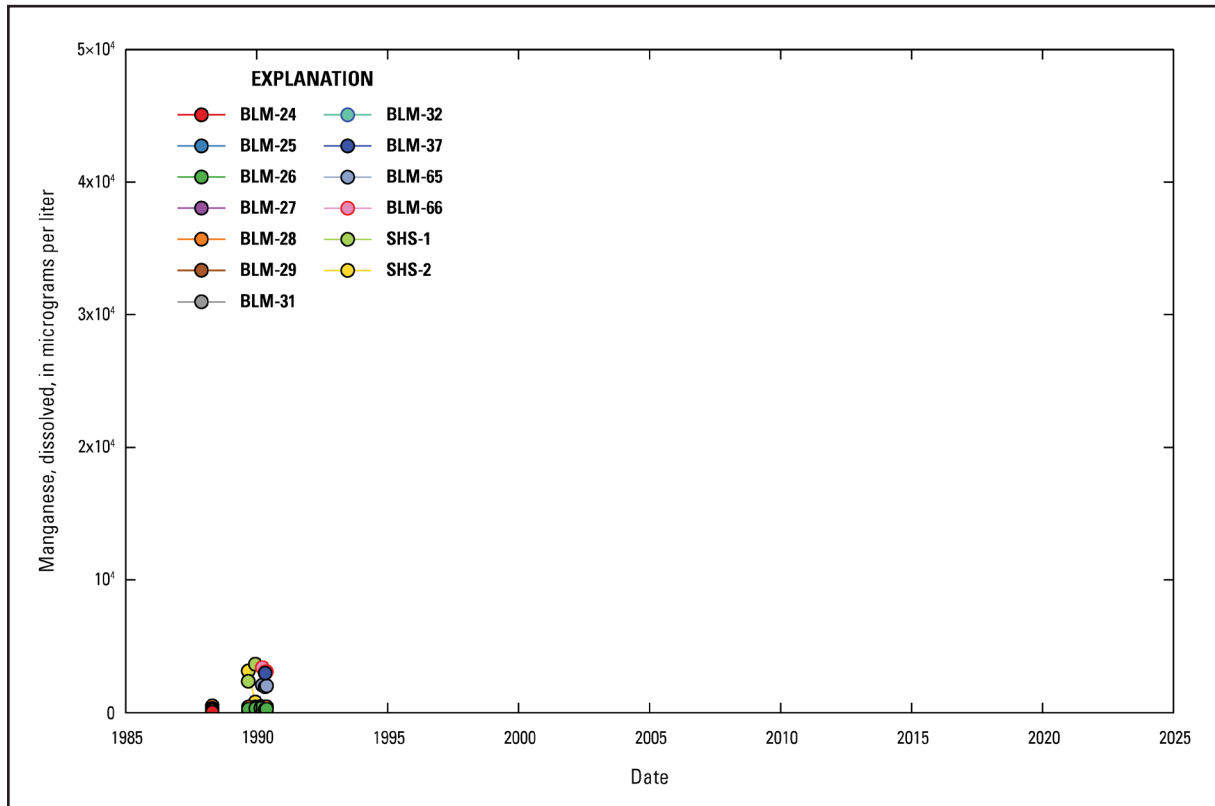


Figure 21. Dissolved manganese concentration over time at Bureau of Land Management (BLM) and Southern Heights Subdivision (SHS) monitoring wells south of U.S. Highway 64 near Farmington, New Mexico. SHS wells were monitored by the Giant Bloomfield Refinery. Locations of wells are shown in Figure 7; data sources are specified in Table 8. As shown in Table 1, the alluvial aquifer background concentrations for dissolved manganese at the Lee Acres Landfill range from 16.1 to 1,680 micrograms per liter (Roy F. Weston, Inc., 1995), and the cleanup level for dissolved manganese at the Lee Acres Landfill is 346 micrograms per liter (U.S. Environmental Protection Agency, 2004).

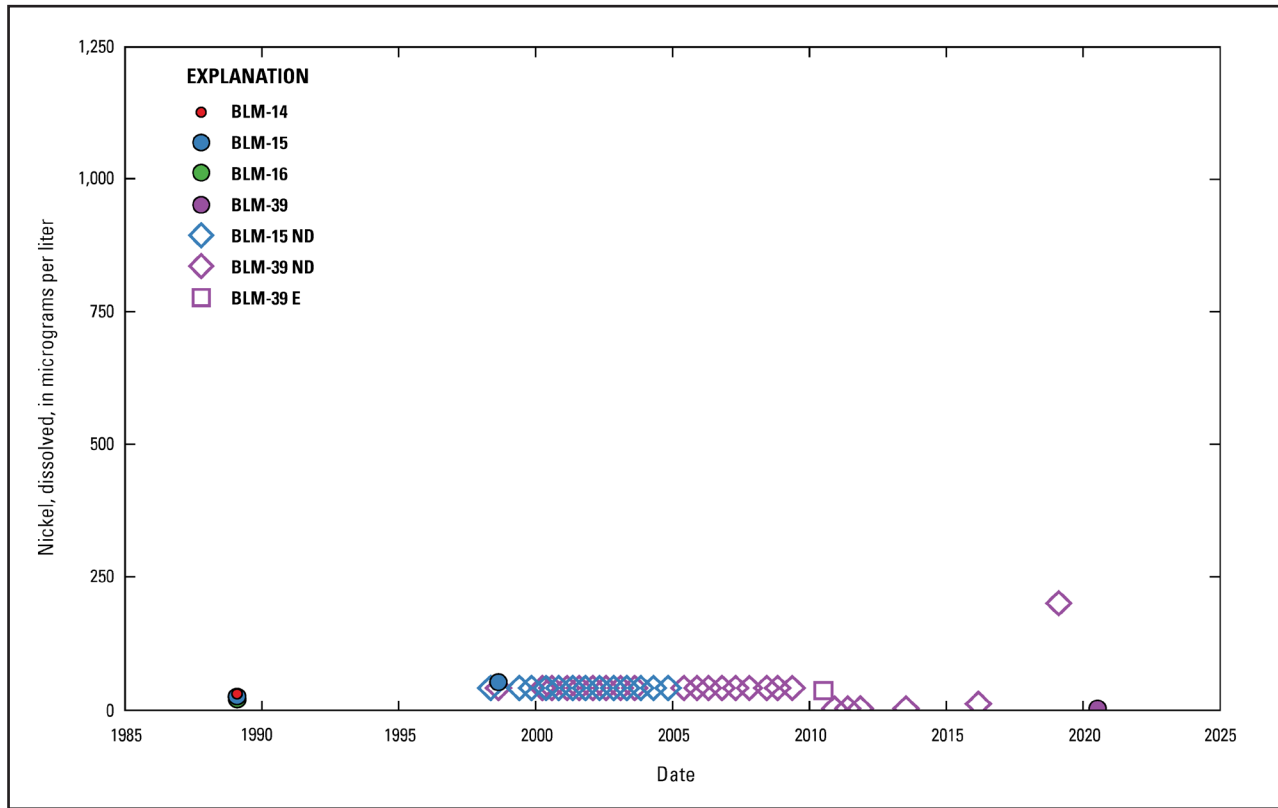


Figure 22. Dissolved nickel concentration over time at Bureau of Land Management (BLM) monitoring wells upgradient from the Lee Acres Landfill near Farmington, New Mexico. Locations of wells are shown in Figure 3; data sources are specified in Table 8. As shown in Table 1, the alluvial aquifer background concentrations for dissolved nickel at the Lee Acres Landfill range from nondetect to 10.5 micrograms per liter (Roy F. Weston, Inc., 1995), and the cleanup level for dissolved nickel at the Lee Acres Landfill is 200 micrograms per liter (U.S. Environmental Protection Agency, 2004). ND, no detection above method detection limits; E, estimated results.

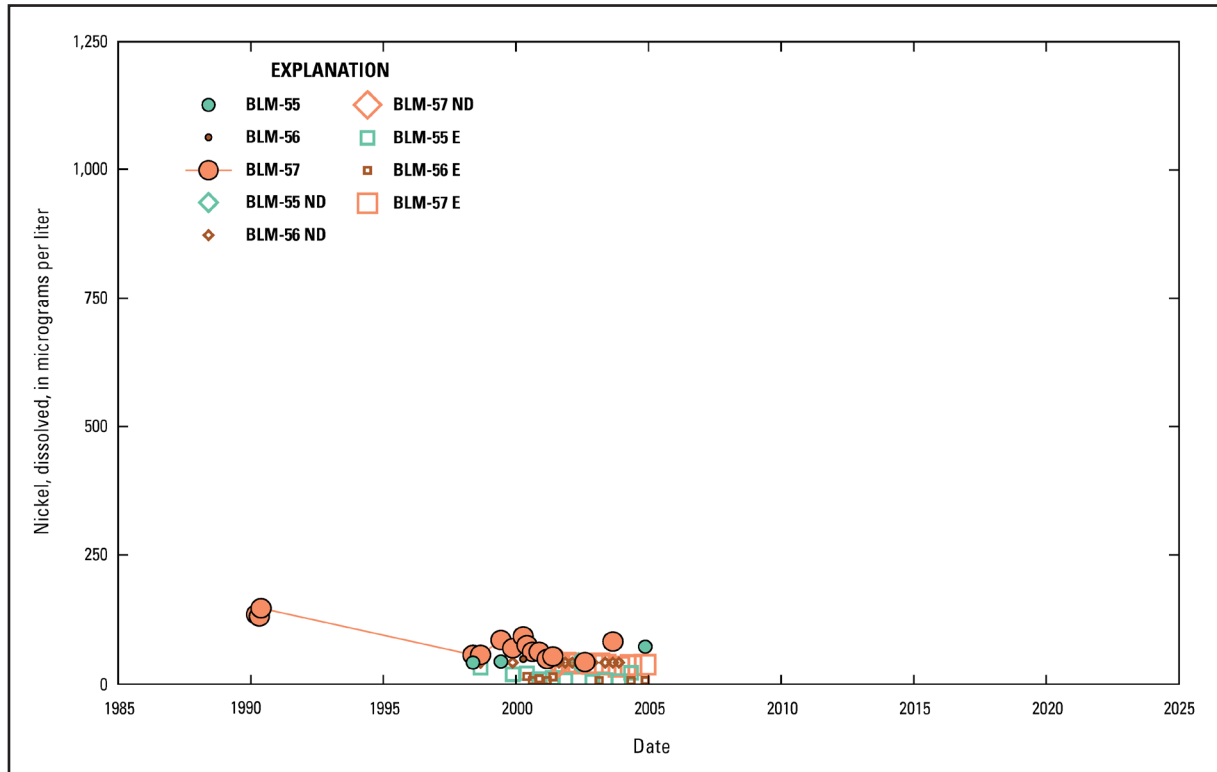


Figure 23. Dissolved nickel concentration over time at Bureau of Land Management (BLM) monitoring wells within the boundary of the Lee Acres Landfill near Farmington, New Mexico. Locations of wells are shown in Figure 4; data sources are specified in Table 8. As shown in Table 1, the alluvial aquifer background concentrations for dissolved nickel at the Lee Acres Landfill range from nondetect to 10.5 micrograms per liter (Roy F. Weston, Inc., 1995), and the cleanup level for dissolved nickel at the Lee Acres Landfill is 200 micrograms per liter (U.S. Environmental Protection Agency, 2004). ND, no detection above method detection limits; E, estimated results.

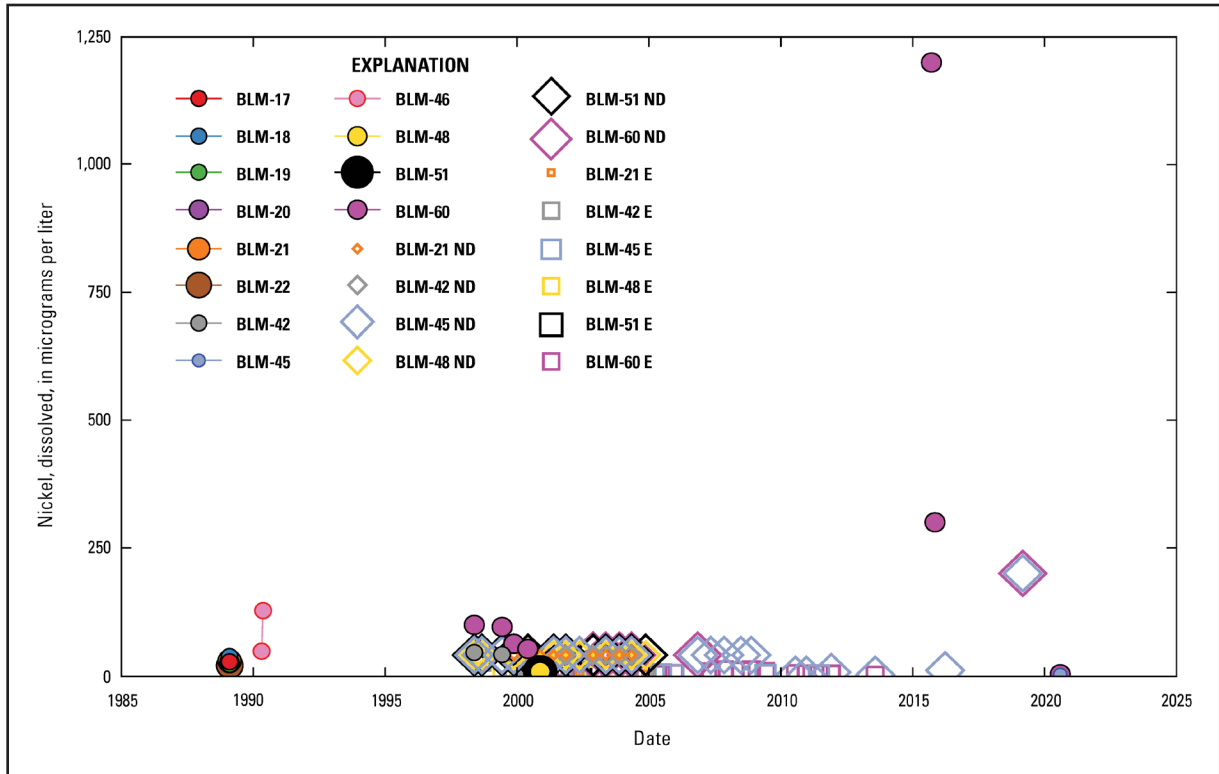


Figure 24. Dissolved nickel concentration over time at Bureau of Land Management (BLM) monitoring wells adjacent to the Lee Acres Landfill near Farmington, New Mexico. Locations of wells are shown in Figure 4; data sources are specified in Table 8. As shown in Table 1, the alluvial aquifer background concentrations for dissolved nickel at the Lee Acres Landfill range from nondetect to 10.5 micrograms per liter (Roy F. Weston, Inc., 1995), and the cleanup level for dissolved nickel at the Lee Acres Landfill is 200 micrograms per liter (U.S. Environmental Protection Agency, 2004). ND, no detection above method detection limits; E, estimated results.

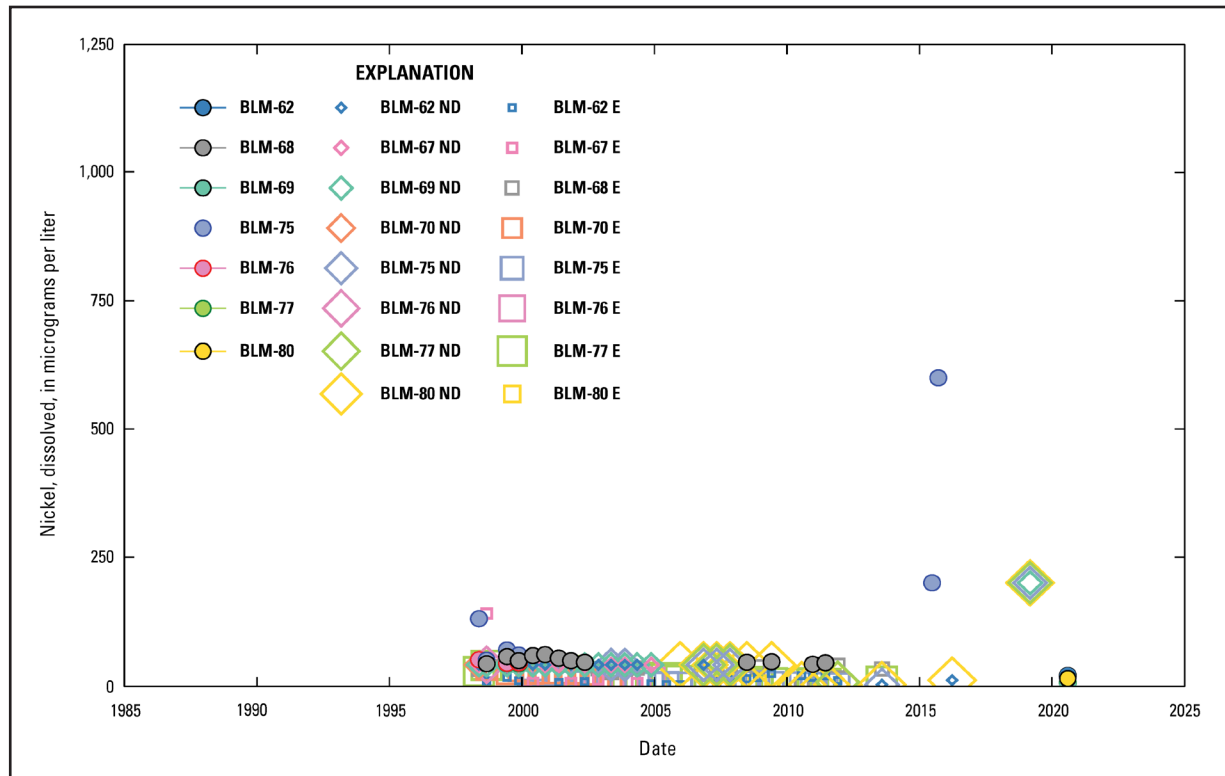


Figure 25. Dissolved nickel concentration over time at Bureau of Land Management (BLM) monitoring wells directly downgradient from the Lee Acres Landfill near Farmington, New Mexico. Locations of wells are shown in Figure 5; data sources are specified in Table 8. As shown in Table 1, the alluvial aquifer background concentrations for dissolved nickel at the Lee Acres Landfill range from nondetect to 10.5 micrograms per liter (Roy F. Weston, Inc., 1995), and the cleanup level for dissolved nickel at Lee Acres is 200 micrograms per liter (U.S. Environmental Protection Agency, 2004). ND, no detection above method detection limits; E, estimated results.

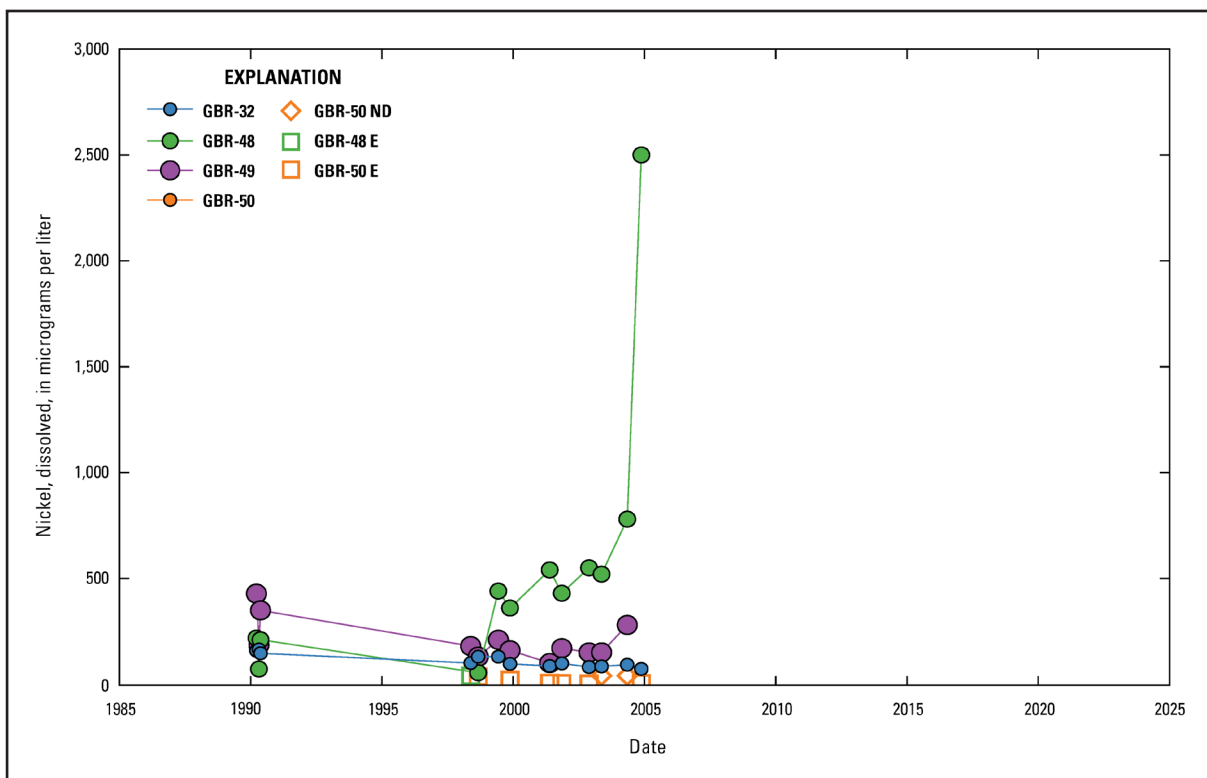


Figure 26. Dissolved nickel concentration over time at Giant Bloomfield Refinery (GBR) monitoring wells upgradient from refinery operations at GBR near Farmington, New Mexico. Locations of wells are shown in Figure 5; data sources are specified in Table 8. As shown in Table 1, the alluvial aquifer background concentrations for dissolved nickel at the Lee Acres Landfill range from nondetect to 10.5 micrograms per liter (Roy F. Weston, Inc., 1995), and the cleanup level for dissolved nickel at the Lee Acres Landfill is 200 micrograms per liter (U.S. Environmental Protection Agency, 2004). ND, no detection above method detection limits; E, estimated results.

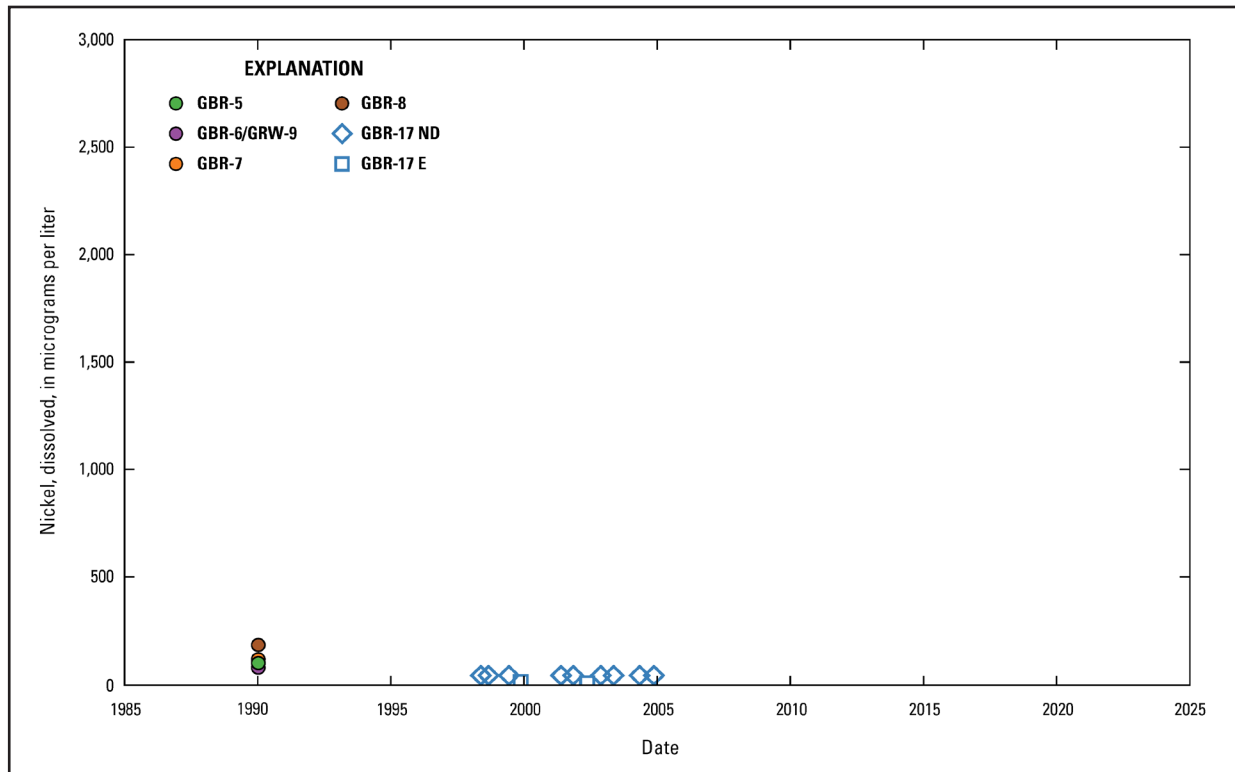


Figure 27. Dissolved nickel concentration over time at Giant Bloomfield Refinery (GBR) monitoring wells near refinery operations at GBR near Farmington, New Mexico. Locations of wells are shown in Figure 6; data sources are specified in Table 8. As shown in Table 1, the alluvial aquifer background concentrations for dissolved nickel at the Lee Acres Landfill range from nondetect to 10.5 micrograms per liter (Roy F. Weston, Inc., 1995), and the cleanup level for dissolved nickel at the Lee Acres Landfill is 200 micrograms per liter (U.S. Environmental Protection Agency, 2004). ND, no detection above method detection limits; E, estimated results.

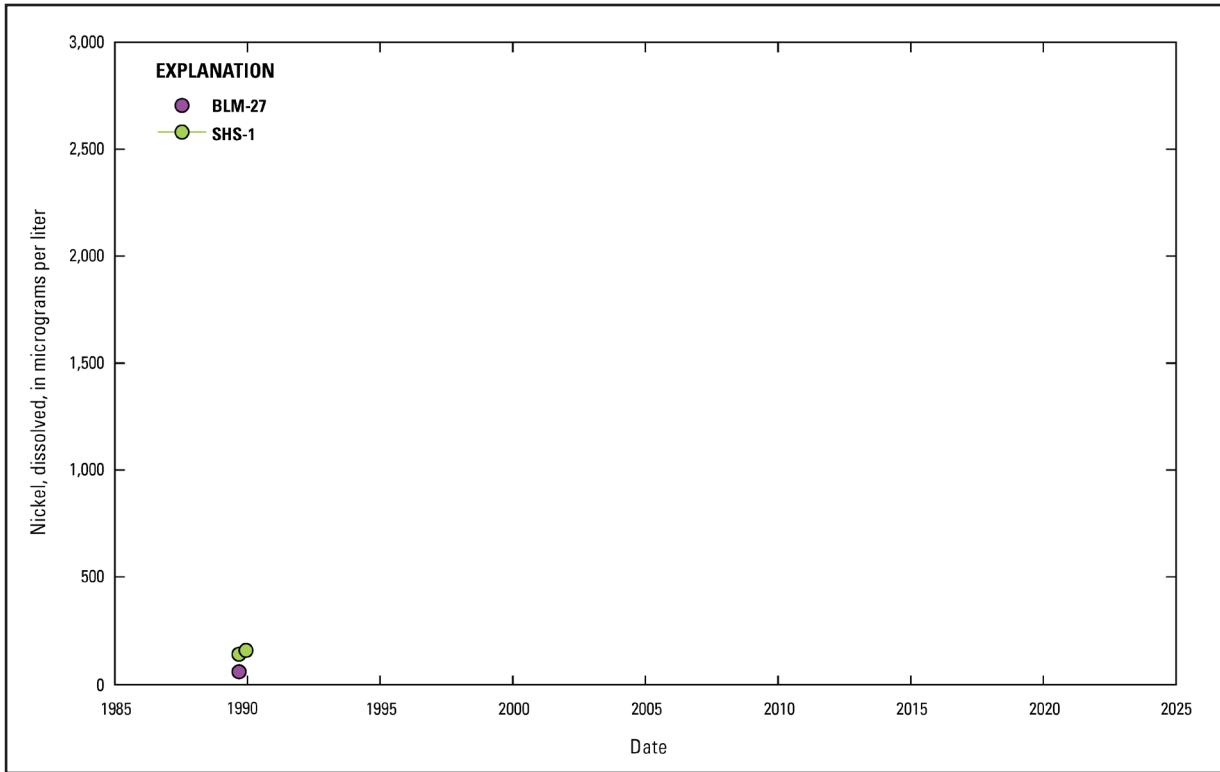


Figure 28. Dissolved nickel concentration over time at Bureau of Land Management (BLM) and Southern Heights Subdivision (SHS) monitoring wells south of U.S. Highway 64 near Farmington, New Mexico. SHS wells were monitored by the Giant Bloomfield Refinery. Locations of wells are shown in Figure 7; data sources are specified in Table 8. As shown in Table 1, the alluvial aquifer background concentrations for dissolved nickel at the Lee Acres Landfill range from nondetect to 10.5 micrograms per liter (Roy F. Weston, Inc., 1995), and the cleanup level for dissolved nickel at the Lee Acres Landfill is 200 micrograms per liter (U.S. Environmental Protection Agency, 2004).

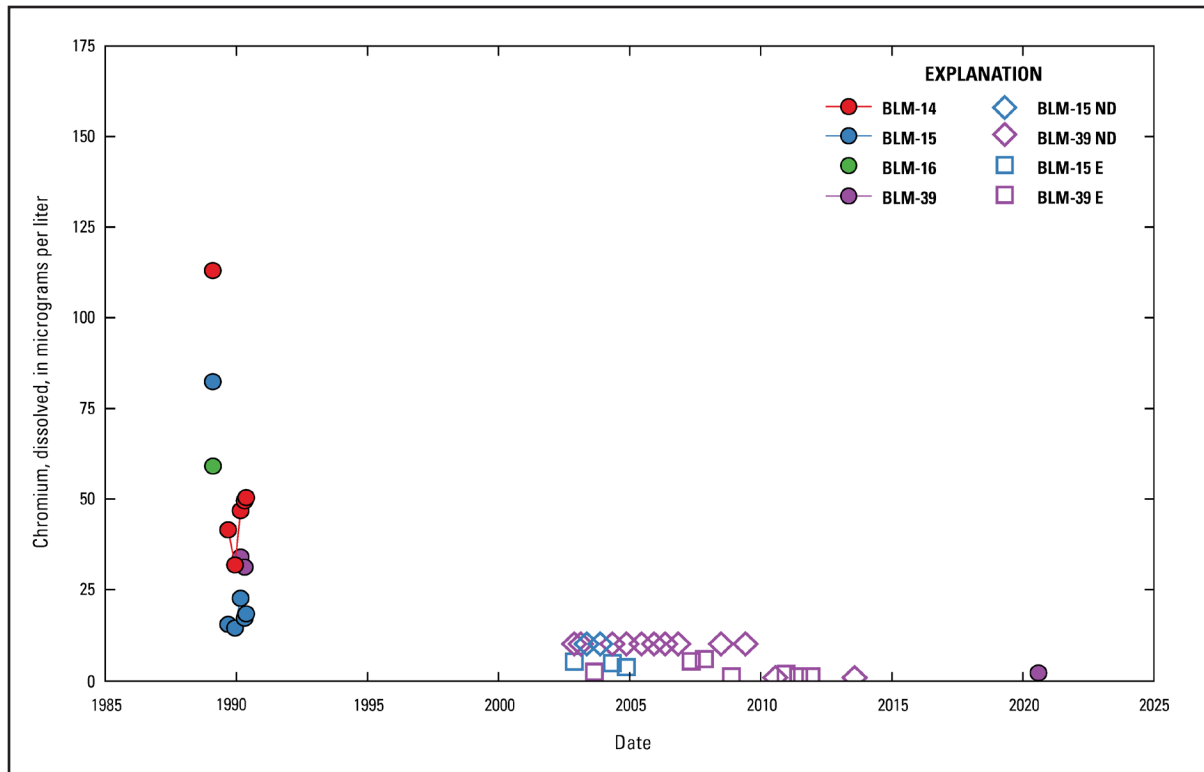


Figure 29. Dissolved chromium concentration over time at Bureau of Land Management (BLM) monitoring wells upgradient from the Lee Acres Landfill near Farmington, New Mexico. Locations of wells are shown in Figure 3; data sources are specified in Table 8. As shown in Table 1, the alluvial aquifer background concentrations for dissolved chromium at the Lee Acres Landfill range from 14.4 to 31.2 micrograms per liter (Roy F. Weston, Inc., 1995). Chromium is not a contaminant of concern at the Lee Acres Landfill. ND, no detection above method detection limits; E, estimated results.

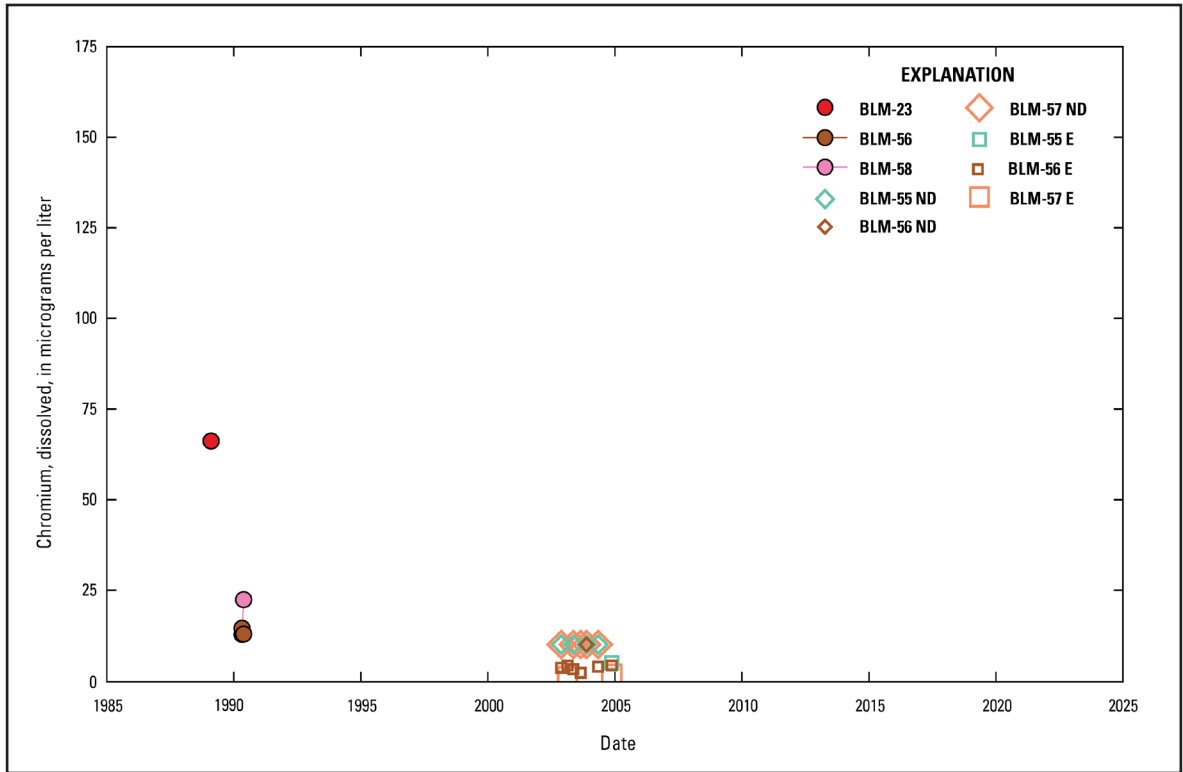


Figure 30. Dissolved chromium concentration over time at Bureau of Land Management (BLM) monitoring wells within the boundary of the Lee Acres Landfill near Farmington, New Mexico. Locations of wells are shown in Figure 4; data sources are specified in Table 8. As shown in Table 1, the alluvial aquifer background concentrations for dissolved chromium at the Lee Acres Landfill range from 14.4 to 31.2 micrograms per liter (Roy F. Weston, Inc., 1995). Chromium is not a contaminant of concern at the Lee Acres Landfill. ND, no detection above method detection limits; E, estimated results.

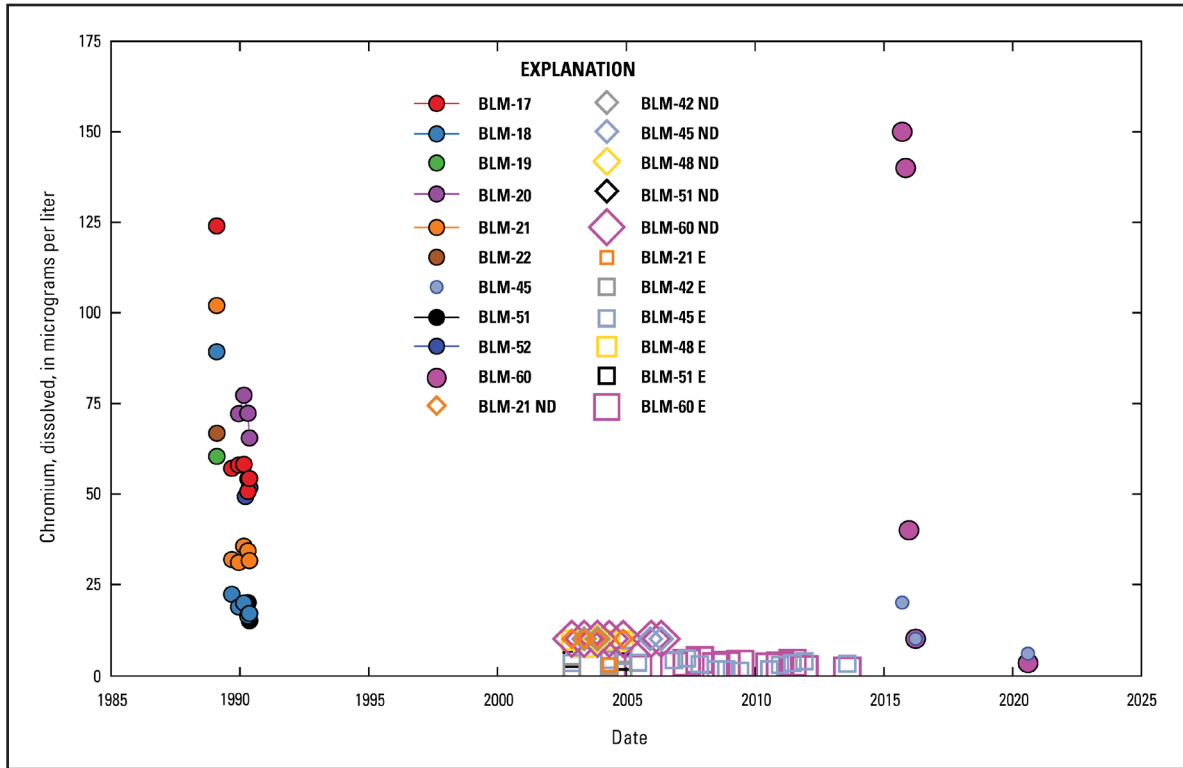


Figure 31. Dissolved chromium concentration over time at Bureau of Land Management (BLM) monitoring wells adjacent to the Lee Acres Landfill near Farmington, New Mexico. Locations of wells are shown in Figure 4; data sources are specified in Table 8. As shown in Table 1, the alluvial aquifer background concentrations for dissolved chromium at the Lee Acres Landfill range from 14.4 to 31.2 micrograms per liter (Roy F. Weston, Inc., 1995). Chromium is not a contaminant of concern at the Lee Acres Landfill. ND, no detection above method detection limits; E, estimated results.

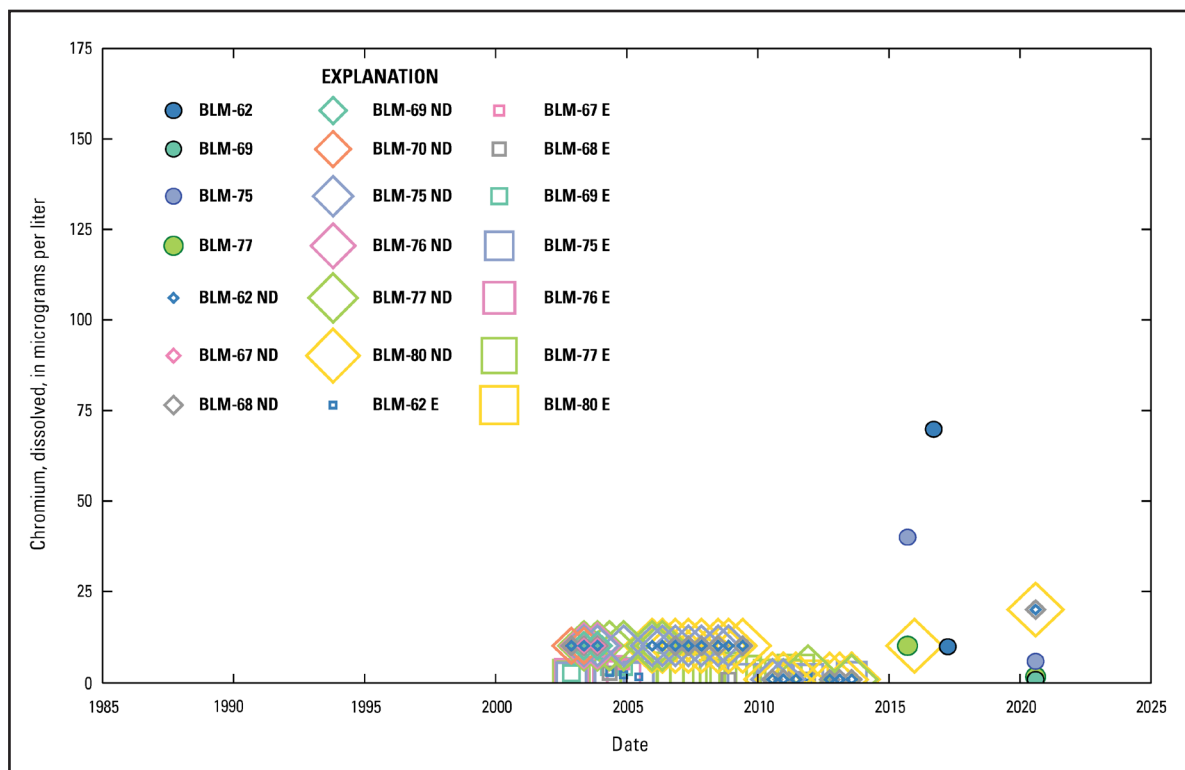


Figure 32. Dissolved chromium concentration over time at Bureau of Land Management (BLM) monitoring wells directly downgradient from the Lee Acres Landfill near Farmington, New Mexico. Locations of wells are shown in Figure 5; data sources are specified in Table 8. As shown in Table 1, the alluvial aquifer background concentrations for dissolved chromium at the Lee Acres Landfill range from 14.4 to 31.2 micrograms per liter (Roy F. Weston, Inc., 1995). Chromium is not a contaminant of concern at the Lee Acres Landfill. ND, no detection above method detection limits; E, estimated results.

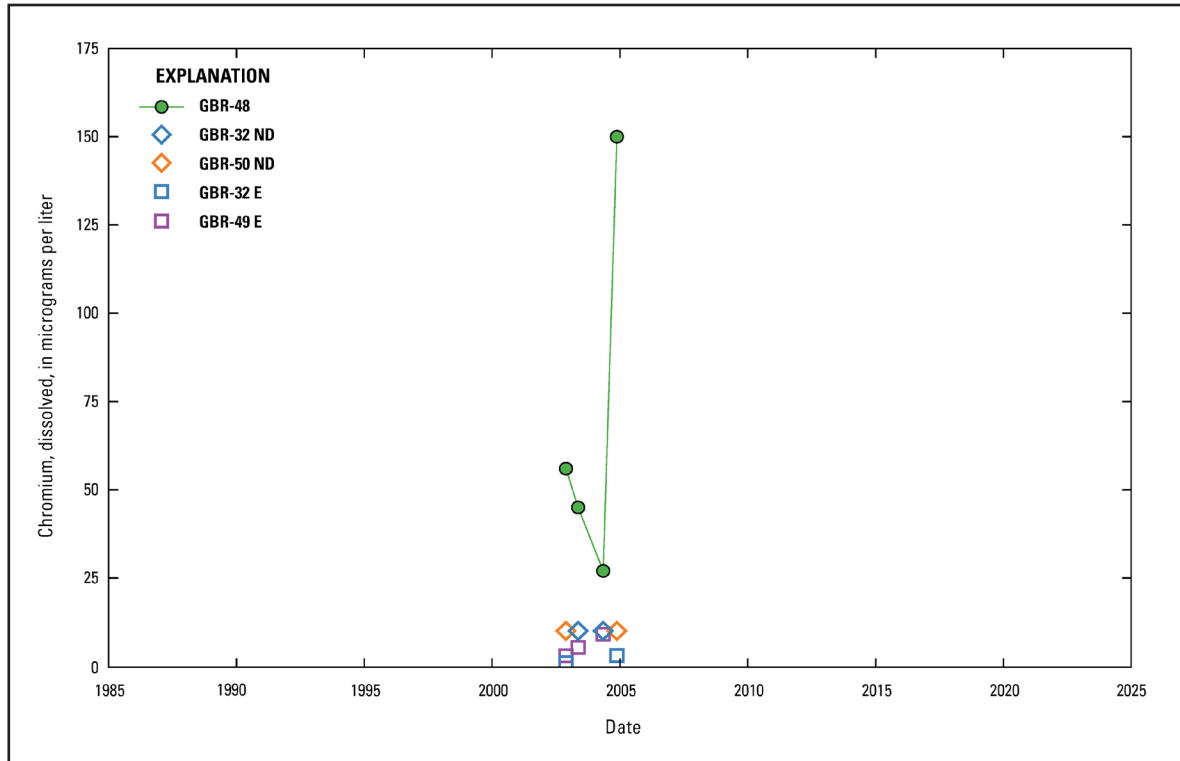


Figure 33. Dissolved chromium concentration over time at Giant Bloomfield Refinery (GBR) monitoring wells upgradient from refinery operations at GBR near Farmington, New Mexico. Locations of wells are shown in Figure 5; data sources are specified in Table 8. As shown in Table 1, the alluvial aquifer background concentrations for dissolved chromium at the Lee Acres Landfill range from 14.4 to 31.2 micrograms per liter (Roy F. Weston, Inc., 1995). Chromium is not a contaminant of concern at the Lee Acres Landfill. ND, no detection above method detection limits; E, estimated results.

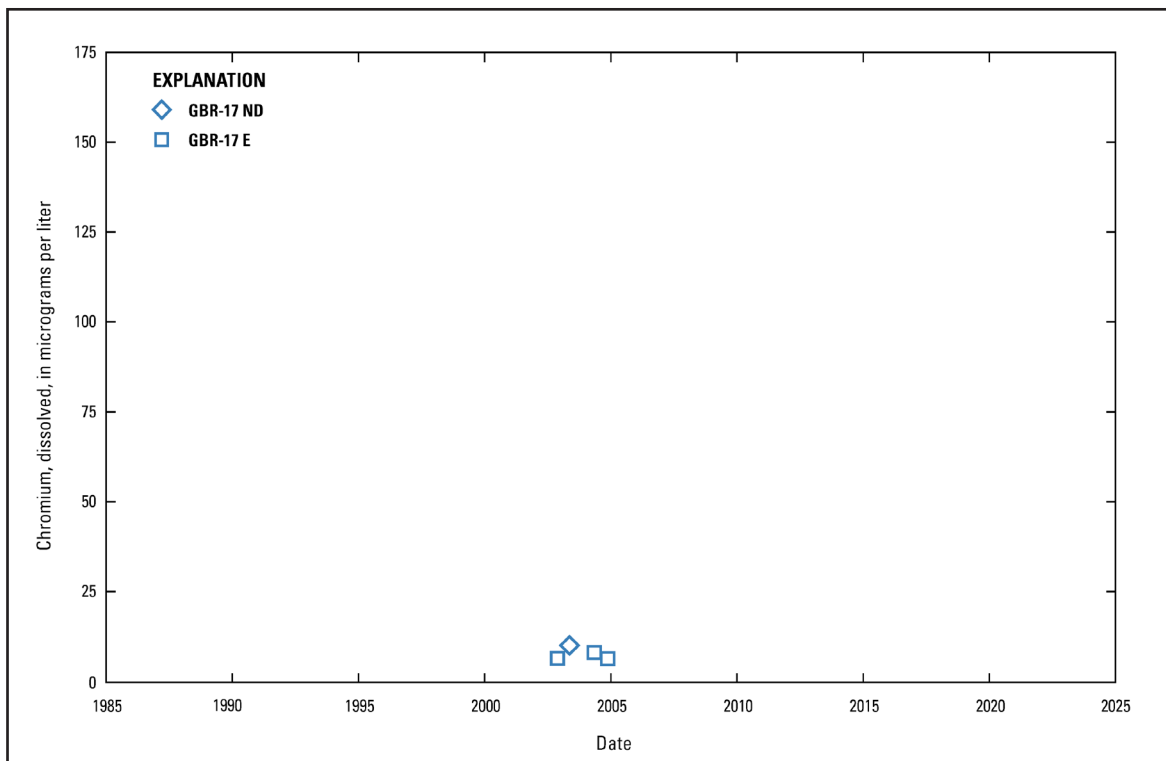


Figure 34. Dissolved chromium concentration over time at Giant Bloomfield Refinery (GBR) monitoring wells near refinery operations at GBR near Farmington, New Mexico. Locations of wells are shown in Figure 6; data sources are specified in Table 8. As shown in Table 1, the alluvial aquifer background concentrations for dissolved chromium at the Lee Acres Landfill range from 14.4 to 31.2 micrograms per liter (Roy F. Weston, Inc., 1995). Chromium is not a contaminant of concern at the Lee Acres Landfill. ND, no detection above method detection limits; E, estimated results.

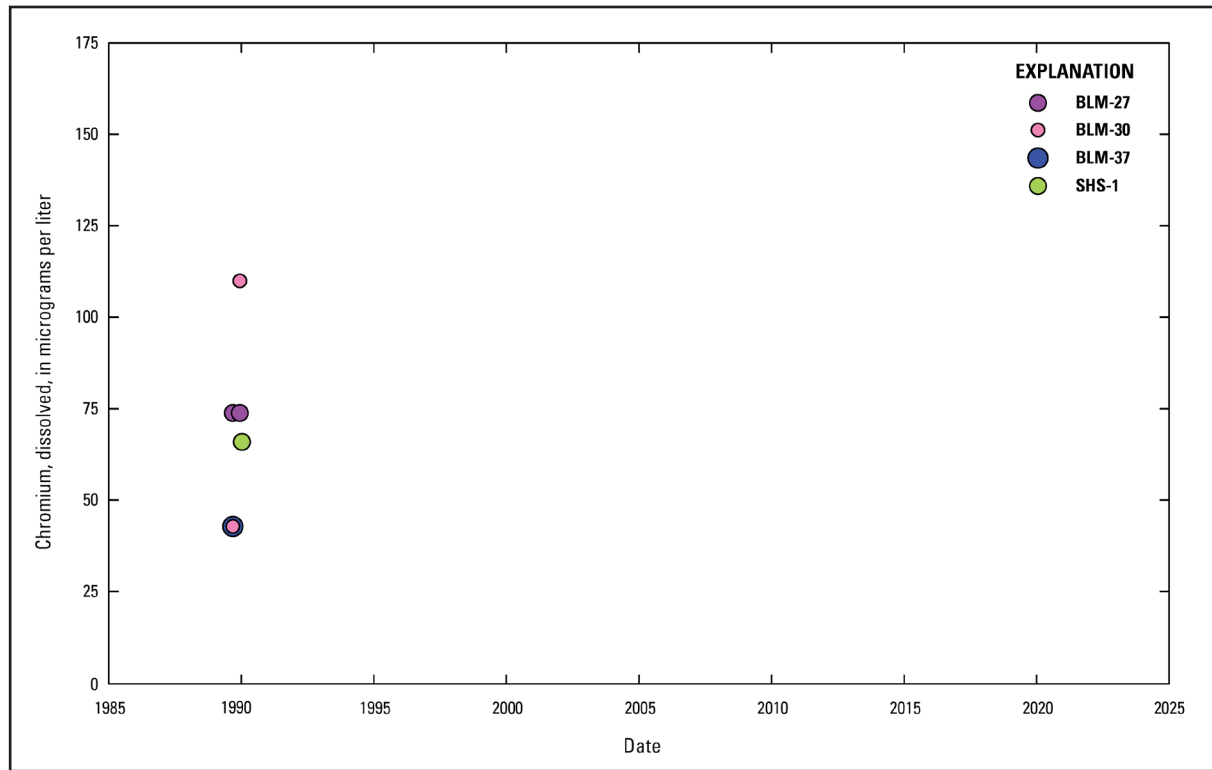


Figure 35. Dissolved chromium concentration over time at Bureau of Land Management (BLM) and Southern Heights Subdivision (SHS) monitoring wells south of U.S. Highway 64 near Farmington, New Mexico. SHS wells were monitored by the Giant Bloomfield Refinery. Locations of wells are shown in Figure 7; data sources are specified in Table 8. As shown in Table 1, the alluvial aquifer background concentrations for dissolved chromium at the Lee Acres Landfill range from 14.4 to 31.2 micrograms per liter (Roy F. Weston, Inc., 1995). Chromium is not a contaminant of concern at the Lee Acres Landfill.

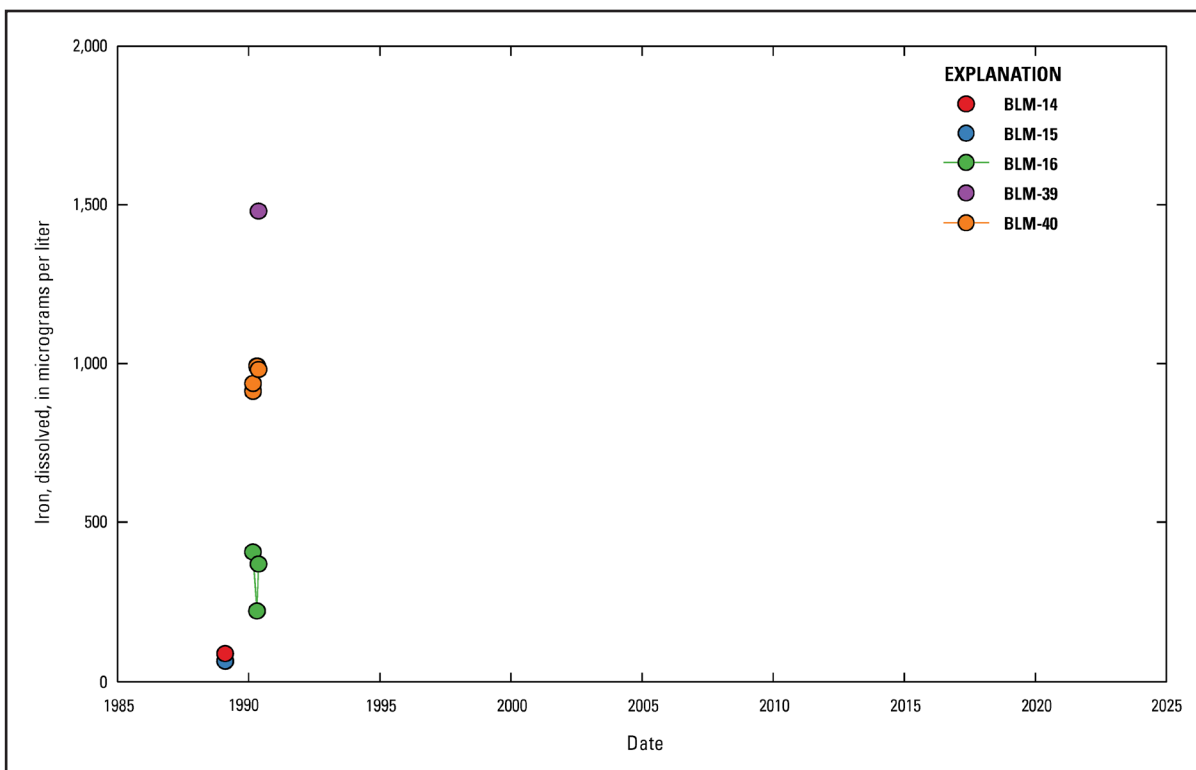


Figure 36. Dissolved iron concentration over time at Bureau of Land Management (BLM) monitoring wells upgradient from the Lee Acres Landfill near Farmington, New Mexico. Locations of wells are shown in Figure 3; data sources are specified in Table 8. As shown in Table 1, the alluvial aquifer background concentrations for dissolved iron at the Lee Acres Landfill range from nondetect to 2,460 micrograms per liter (Roy F. Weston, Inc., 1995). Iron is not a contaminant of concern at the Lee Acres Landfill.

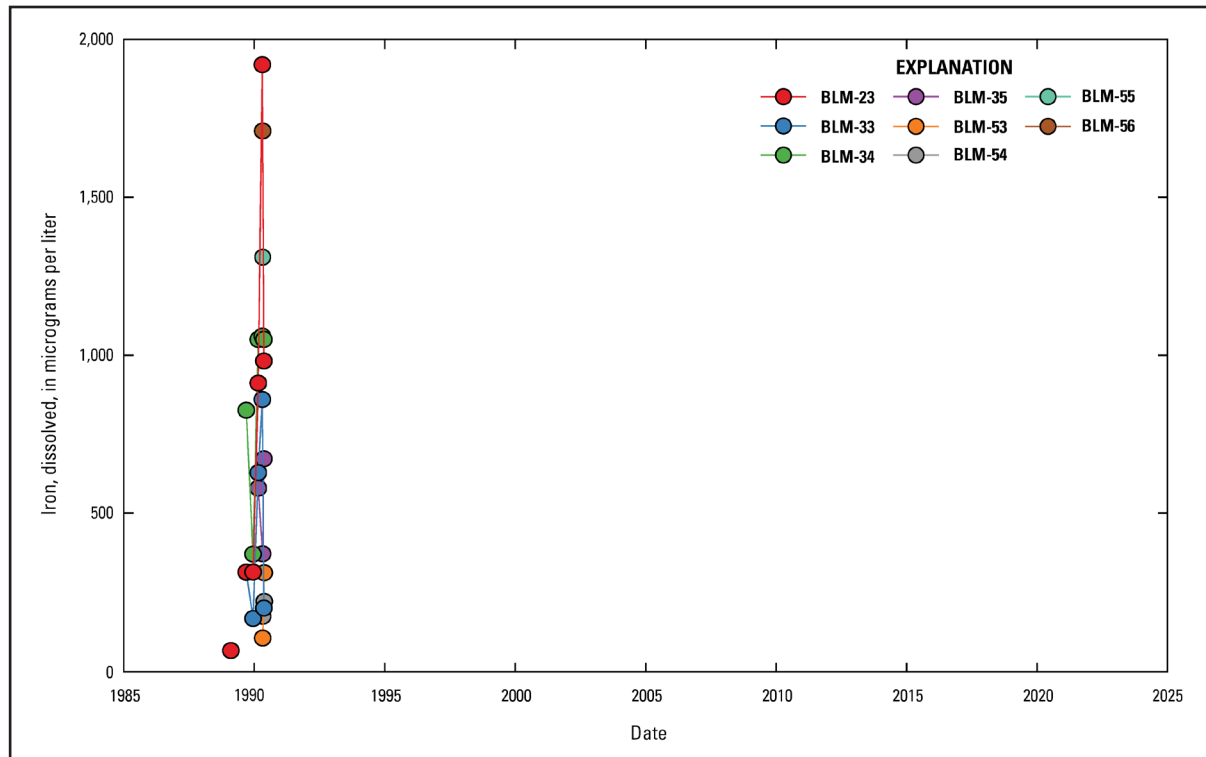


Figure 37. Dissolved iron concentration over time at Bureau of Land Management (BLM) monitoring wells within the boundary of the Lee Acres Landfill near Farmington, New Mexico. Locations of wells are shown in Figure 4; data sources are specified in Table 8. As shown in Table 1, the alluvial aquifer background concentrations for dissolved iron at the Lee Acres Landfill range from nondetect to 2,460 micrograms per liter (Roy F. Weston, Inc., 1995). Iron is not a contaminant of concern at the Lee Acres Landfill.

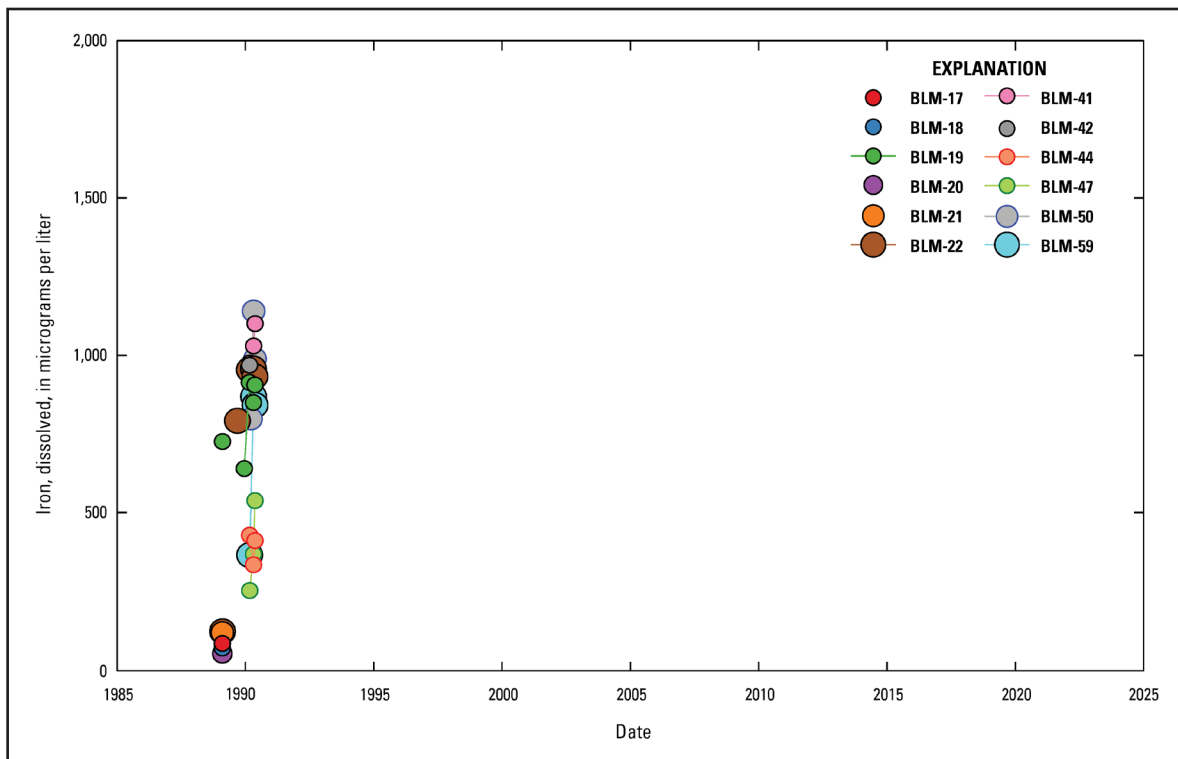


Figure 38. Dissolved iron concentration over time at Bureau of Land Management (BLM) monitoring wells adjacent to the Lee Acres Landfill near Farmington, New Mexico. Locations of wells are shown in Figure 4; data sources are specified in Table 8. As shown in Table 1, the alluvial aquifer background concentrations for dissolved iron at the Lee Acres Landfill range from nondetect to 2,460 micrograms per liter (Roy F. Weston, Inc., 1995). Iron is not a contaminant of concern at the Lee Acres Landfill.

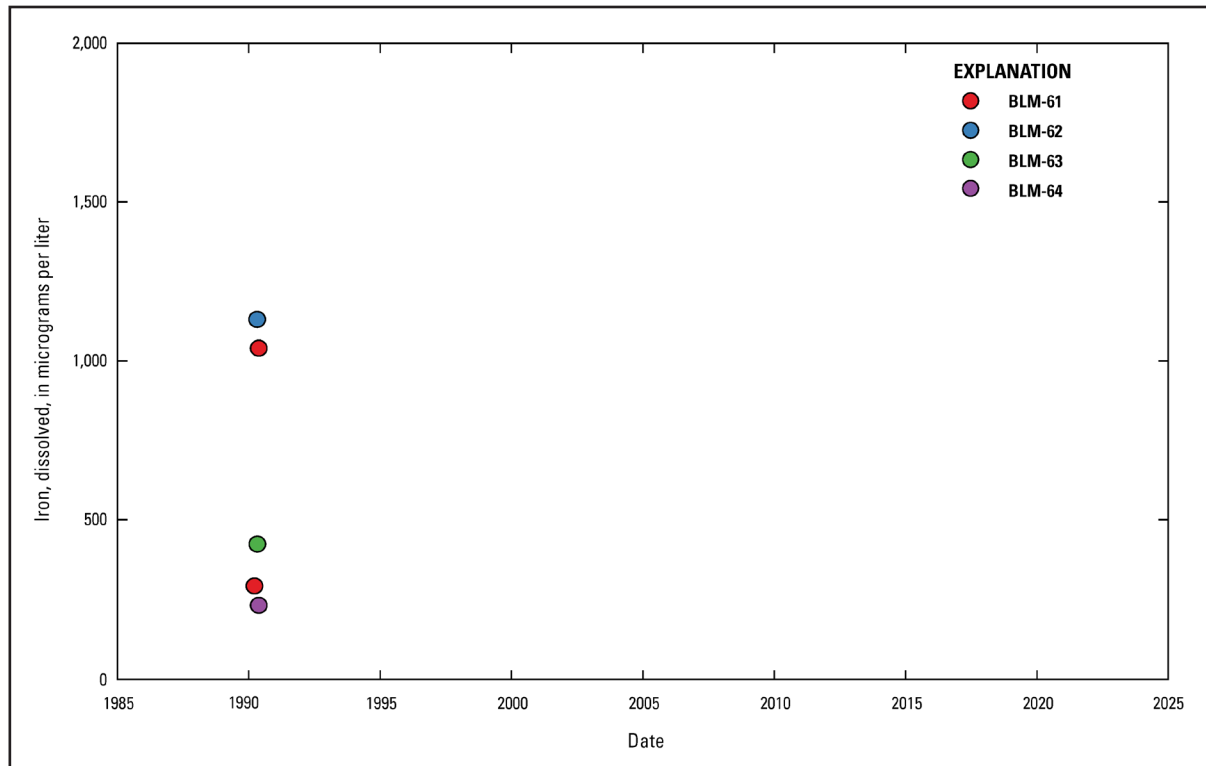


Figure 39. Dissolved iron concentration over time at Bureau of Land Management (BLM) monitoring wells directly downgradient from the Lee Acres Landfill near Farmington, New Mexico. Locations of wells are shown in Figure 5; data sources are specified in Table 8. As shown in Table 1, the alluvial aquifer background concentrations for dissolved iron at the Lee Acres Landfill range from nondetect to 2,460 micrograms per liter (Roy F. Weston, Inc., 1995). Iron is not a contaminant of concern at the Lee Acres Landfill.

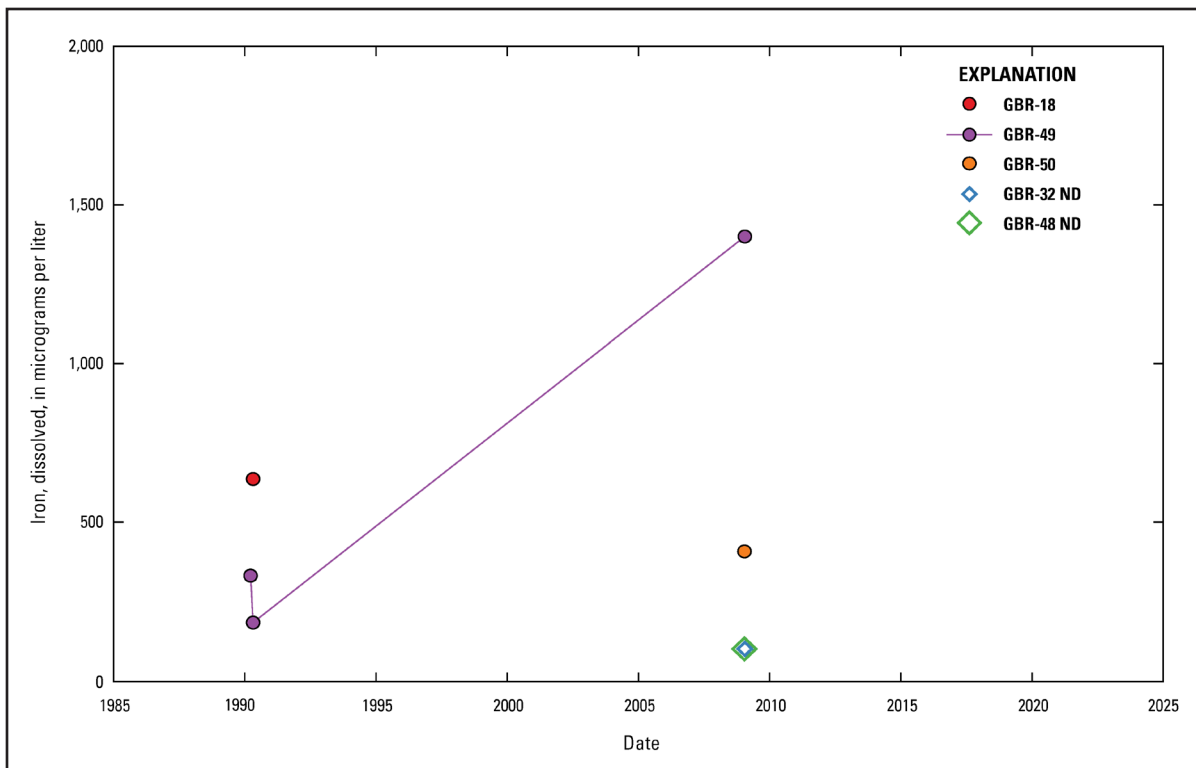


Figure 40. Dissolved iron concentration over time at Giant Bloomfield Refinery (GBR) monitoring wells upgradient from refinery operations at GBR near Farmington, New Mexico. Locations of wells are shown in Figure 5; data sources are specified in Table 8. As shown in Table 1, the alluvial aquifer background concentrations for dissolved iron at the Lee Acres Landfill range from nondetect to 2,460 micrograms per liter (Roy F. Weston, Inc., 1995). Iron is not a contaminant of concern at the Lee Acres Landfill. ND, no detection above method detection limits.

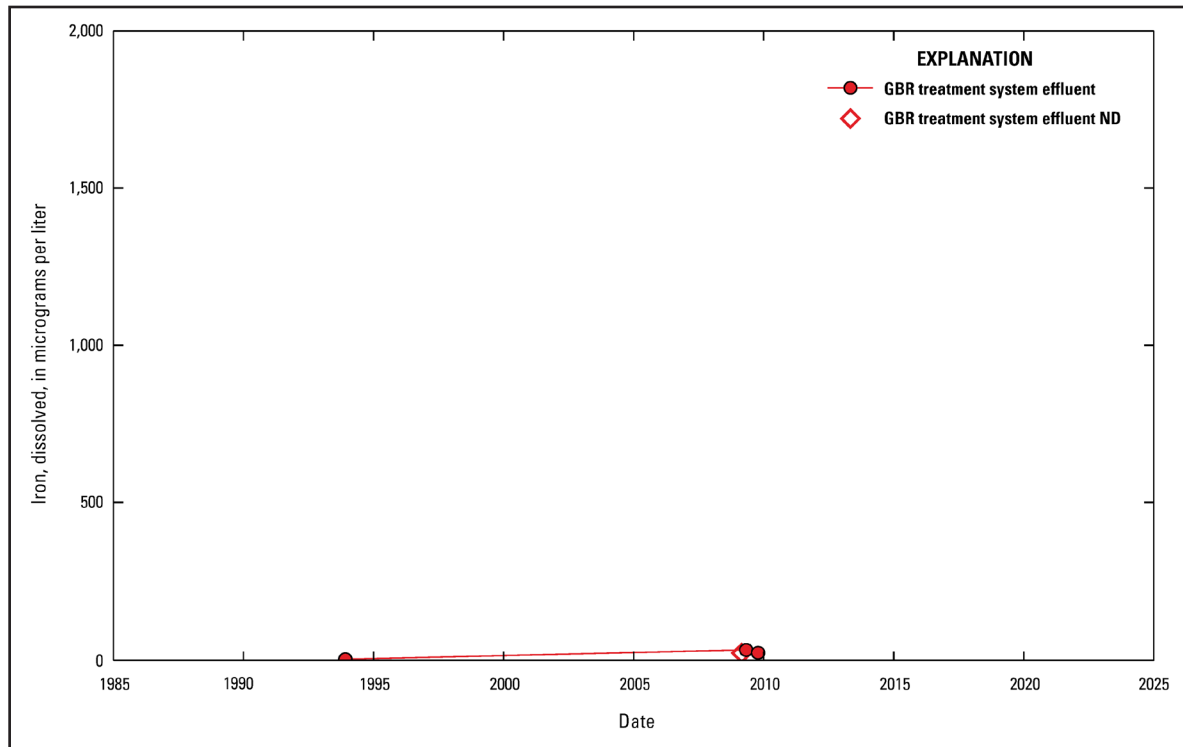


Figure 41. Dissolved iron concentration over time in Giant Bloomfield Refinery (GBR) treatment system effluent at GBR near Farmington, New Mexico. Locations of infiltration trenches, which accept the treatment system effluent, are shown in Figure 6; data sources are specified in Table 8. As shown in Table 1, the alluvial aquifer background concentrations for dissolved iron at the Lee Acres Landfill range from nondetect to 2,460 micrograms per liter (Roy F. Weston, Inc., 1995). Iron is not a contaminant of concern at the Lee Acres Landfill. ND, no detection above method detection limits.

SUMMARY OF RESULTS, 1985–2020

This section discusses the results of the BLM monitoring well data contained in LAGBRD for the analytes depicted in the time-series plots (Figures 8–66) with references to the ROD for the landfill (EPA, 2004).

BLM-14 was sampled from December 1987 to May 1990 (Table 8). At this well, there are no results for total chloride. There is only one result for dissolved manganese (Figure 15). Sampled on February 6, 1989, the dissolved manganese concentration is 8.7 micrograms per liter ($\mu\text{g/L}$). There is only one result for dissolved nickel (Figure 22): 28.9 $\mu\text{g/L}$ on February 6, 1989. Dissolved chromium concentrations range from 31.8 $\mu\text{g/L}$ (December 13, 1989) to 113 $\mu\text{g/L}$ (February 6, 1989) (Figure 29). There is only one result for dissolved iron (Figure 36): sampled on February 6, 1989, the dissolved iron concentration is 85.5 $\mu\text{g/L}$. There are no results for the organic COCs described in the ROD.

BLM-15 was sampled from December 1987 to November 2004 (Table 8). At this well, total chloride concentrations range from 45 milligrams per liter (mg/L) (May 22, 2001; May 4, 2004; and November 16, 2004) to 120 mg/L (September 1, 1998) (Figure 8). Dissolved manganese concentrations range from no detection above reporting levels (multiple dates) to 380 $\mu\text{g/L}$ on September 1, 1998 (Figure 15). Dissolved nickel results (Figure 22) all represent no detection above reporting levels except for two samples: 23.8 $\mu\text{g/L}$ on February 6, 1989, and 51 $\mu\text{g/L}$ on September 1, 1998. Dissolved chromium results range from no detection above reporting levels (multiple dates) to 82.4 $\mu\text{g/L}$ (February 6, 1989) (Figure 29). There is one result for iron, 61.9 $\mu\text{g/L}$ on February 6, 1989 (Figure 36). *cis*-1,2-Dichloroethene (Figure 55) and *trans*-1,2-dichloroethene were not detected above reporting levels. Tetrachloroethene was not detected above reporting levels except in one sample (Figure 59): 2 $\mu\text{g/L}$ on September 1, 1998. Trichloroethene was not detected above reporting levels except in one sample collected on December 15, 1987, with a concentration of 140 $\mu\text{g/L}$. This result is suspect

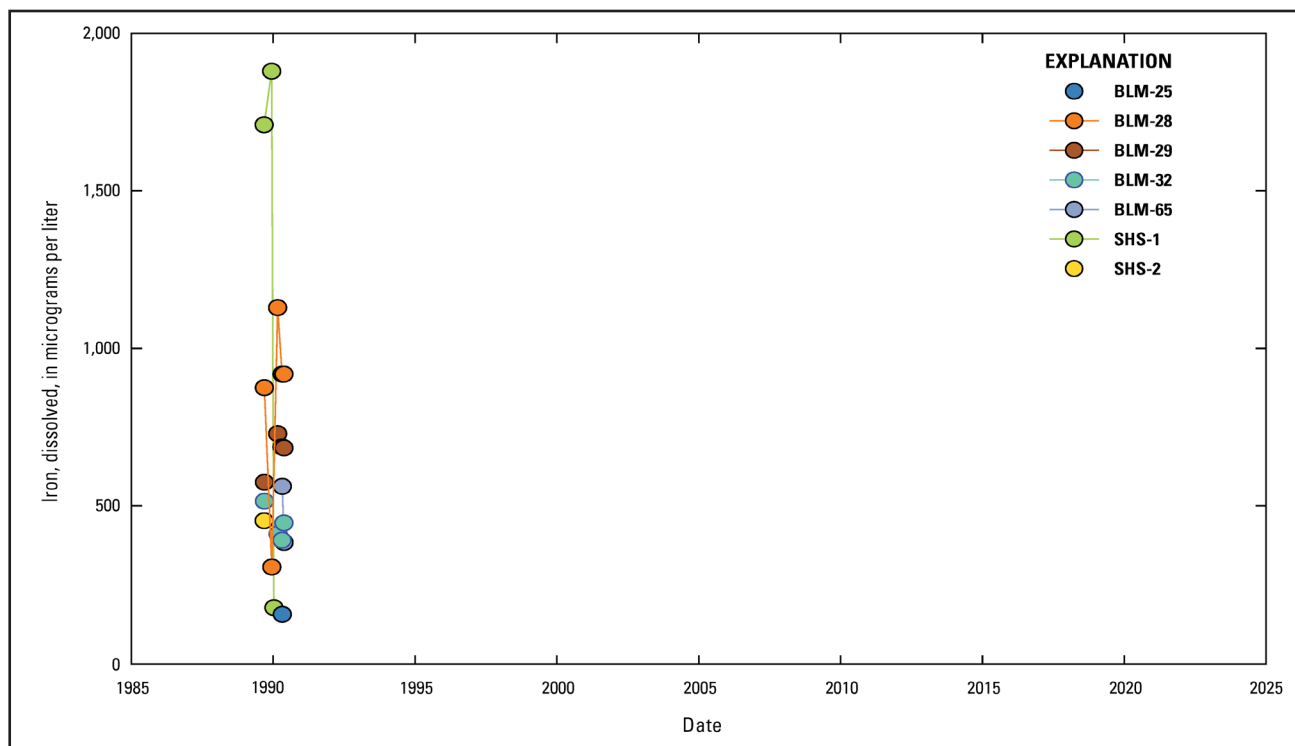


Figure 42. Dissolved iron concentration over time at Bureau of Land Management (BLM) and Southern Heights Subdivision (SHS) monitoring wells south of U.S. Highway 64 near Farmington, New Mexico. SHS wells were monitored by the Giant Bloomfield Refinery. Locations of wells are shown in Figure 7; data sources are specified in Table 8. As shown in Table 1, the alluvial aquifer background concentrations for dissolved iron at the Lee Acres Landfill range from nondetect to 2,460 micrograms per liter (Roy F. Weston, Inc., 1995). Iron is not a contaminant of concern at the Lee Acres Landfill.

and therefore omitted from the time-series plots, as BLM-15 is upgradient from the landfill and the result exceeds the highest concentration of trichloroethene detected in any other BLM well (including those within and adjacent to the landfill boundary) by an order of magnitude. Vinyl chloride was not detected above reporting levels in this area and was thus excluded from the time-series plots of concentrations.

BLM-16 was sampled from December 1987 to May 1990 (Table 8). At this well, there are no results for total chloride. Dissolved manganese concentrations range from 149 µg/L (February 9, 1989) to 504 µg/L (February 28, 1990) (Figure 15). There is one result for dissolved nickel of 18.4 µg/L on February 9, 1989 (Figure 22). There is one dissolved chromium result of 59.1 µg/L on February 9, 1989 (Figure 29). Dissolved iron concentrations range from 61.4 µg/L (February 9, 1989) to 406 µg/L (February 28, 1990) (Figure 36). The only organic COC described in the ROD that has a result is tetrachloroethene, which had a concentration of 1.3 µg/L on September 8, 1989 (Figure 59).

BLM-17 was sampled from December 1987 to May 1990 (Table 8). At this well, there are no total chloride results. There are two results for dissolved manganese (Figure 17): 17 µg/L on April 19, 1988, and 8.7 µg/L on February 6, 1989. The only result for dissolved nickel has a concentration of 26.9 µg/L on February 6, 1989 (Figure 24). Dissolved chromium concentrations range from 50.7 µg/L (April 25, 1990) to 124 µg/L (February 6, 1989) (Figure 31). There is one result for dissolved iron of 83.8 µg/L on February 6, 1989 (Figure 38). The only organic COC from the ROD is tetrachloroethene. The tetrachloroethene result, collected on December 15, 1987, is 9 µg/L (Figure 61).

BLM-18 was sampled from December 1987 to May 1990 (Table 8). At this well, there are no total chloride results. Dissolved manganese concentrations range from 16.1 µg/L (September 8, 1989) to 39.4 µg/L (February 26, 1990) (Figure 17). The two results for dissolved nickel, both collected on February 6, 1989, have

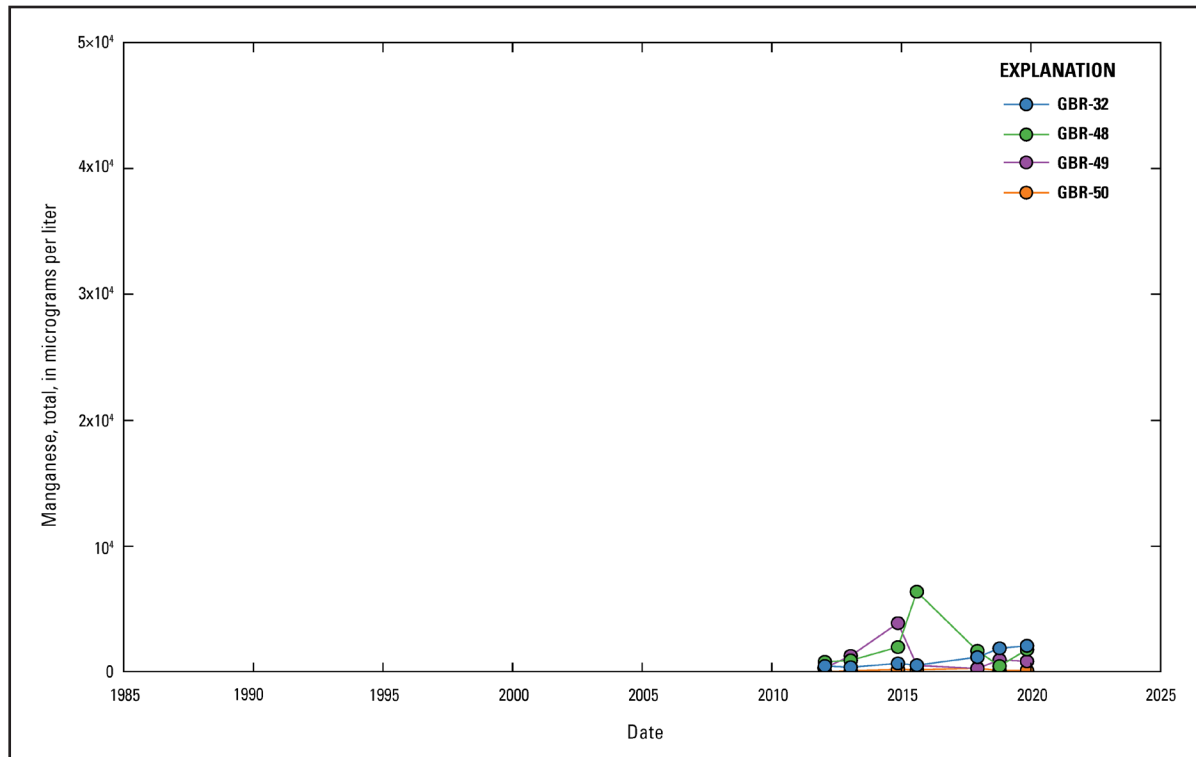


Figure 43. Total manganese concentration over time at Giant Bloomfield Refinery (GBR) monitoring wells upgradient from refinery operations at GBR near Farmington, New Mexico. Locations of wells are shown in Figure 5; data sources are specified in Table 8.

concentrations of 37.1 µg/L and 36.5 µg/L (Figure 24). Dissolved chromium concentrations range from 16.3 µg/L (April 25, 1990) to 89.3 µg/L (February 6, 1989) (Figure 31). The two results for dissolved iron were both collected on February 6, 1989, and have concentrations of 69.1 µg/L and 131 µg/L (Figure 38). There are no results for the organic COCs described in the ROD.

BLM-19 was sampled from December 1987 to May 1990 (Table 8). At this well, there are no results for total chloride. Dissolved manganese concentrations range from 225 µg/L (September 12, 1989) to 359 µg/L (May 16, 1990) (Figure 17). The only result for dissolved nickel, from February 8, 1989, has a concentration of 21.8 µg/L (Figure 24). The one result for dissolved chromium, collected on February 8, 1989, has a concentration of 60.4 µg/L (Figure 31). Dissolved iron concentrations range from 640 µg/L (December 16, 1989) to 914 µg/L (February 26, 1990) (Figure 38). There are no results for the organic COCs described in the ROD.

BLM-20 was sampled from December 1987 to May 1990 (Table 8). At this well, there are no total chloride results. The two results for dissolved manganese (Figure 17) are 79 µg/L on April 20, 1988, and 8.7 µg/L on February 6, 1989. There is one result for dissolved nickel (Figure 24): 24 µg/L on February 6, 1989. Dissolved chromium concentrations range from 65.5 µg/L (May 16, 1990) to 124 µg/L (February 6, 1989) (Figure 31). There is one result for dissolved iron (Figure 38): 51.2 µg/L collected on February 6, 1989. There are no results for the organic COCs described in the ROD.

BLM-21 was sampled from December 1987 to November 2004 (Table 8). At this well, total chloride concentrations range from 31 mg/L (November 19, 2002) to 48 mg/L (May 22, 2001) (Figure 10). Dissolved manganese concentrations range from 1.6 µg/L (May 31, 2000) to 590 µg/L (June 8, 1999) (Figure 17). Only one result for dissolved nickel was above reporting levels, collected on February 6, 1989, with a concentration of 28.4 µg/L (Figure 24). Dissolved chromium concentrations range from no detection above reporting levels (multiple dates) to 102 µg/L (February 6, 1989) (Figure 31). The only result for dissolved iron (Figure 38) is 118 µg/L on February 6, 1989. The organic COCs described in the ROD were not detected above reporting levels.

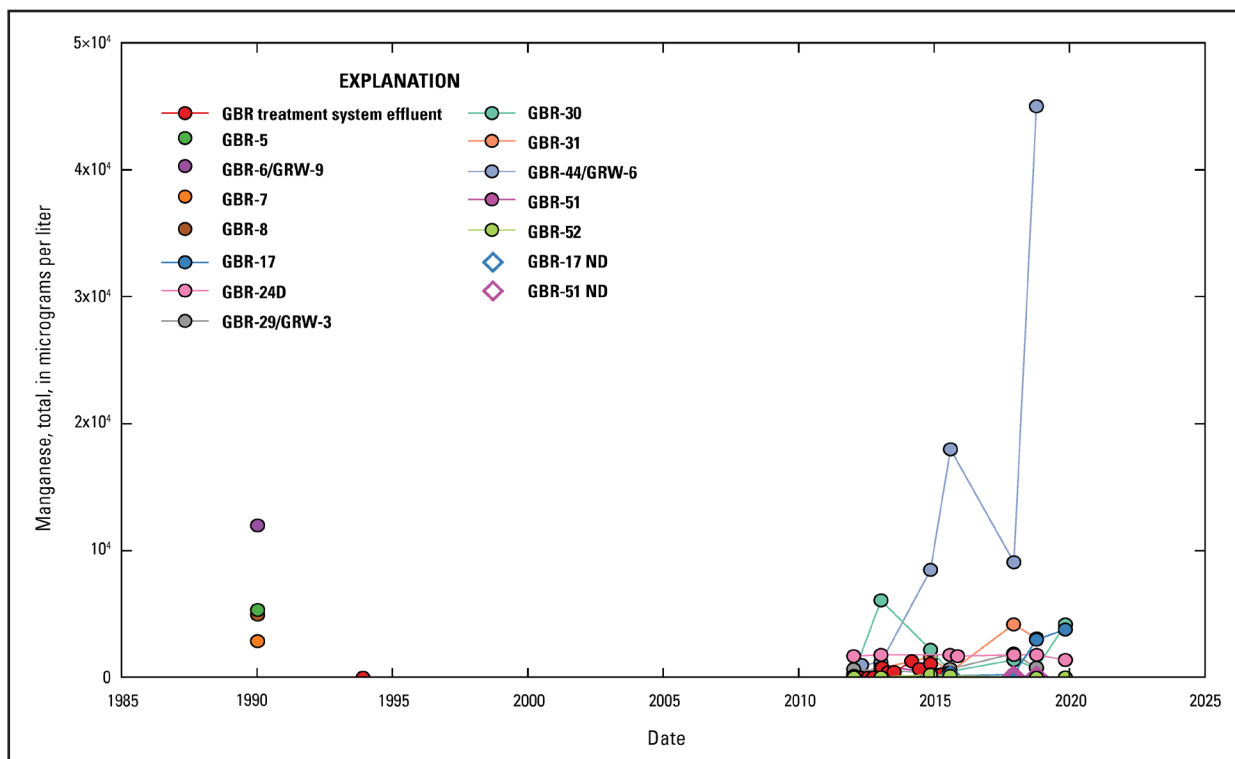


Figure 44. Total manganese concentration over time at Giant Bloomfield Refinery (GBR) monitoring wells, groundwater recovery wells (GRW), and treatment system effluent near refinery operations at GBR near Farmington, New Mexico. Locations of wells and infiltration trenches, which accept the treatment system effluent, are shown in Figure 6; data sources are specified in Table 8. ND, no detection above method detection limits.

BLM-22 was sampled from December 1987 to May 1990 (Table 8). At this well, there are no results for total chloride. Dissolved manganese concentrations range from 98 µg/L (April 20, 1988) to 376 µg/L (April 24, 1990) (Figure 17). There is one dissolved nickel result (Figure 24): 19.5 µg/L on February 9, 1989. The only result for dissolved chromium (Figure 31) is 66.8 µg/L on February 9, 1989. Dissolved iron concentrations range from 122 µg/L (February 9, 1989) to 958 µg/L (April 24, 1990) (Figure 38). There are no results for the organic COCs described in the ROD.

BLM-23 was sampled from December 1987 to May 1990 (Table 8). At this well, there are no results for total chloride or dissolved nickel. Dissolved manganese concentrations range from 339 µg/L (April 20, 1988) to 377 µg/L (April 24, 1990) (Figure 16). The only result for dissolved chromium is 66.2 µg/L on February 8, 1989 (Figure 30). Dissolved iron concentrations range from 64.3 µg/L (February 8, 1989) to 1,920 µg/L (April 24, 1990) (Figure 37). There are no results for the organic COCs described in the ROD.

BLM-24 was sampled from December 1987 to May 1990 (Table 8). At this well, there are no results for total chloride, dissolved nickel, dissolved chromium, or dissolved iron. The only result for dissolved manganese is 30 µg/L on April 21, 1988 (Figure 21). There are no results for the organic COCs described in the ROD.

BLM-25 was sampled from December 1987 to May 1990 (Table 8). At this well, there are no results for total chloride, dissolved nickel, or dissolved chromium. The only result for dissolved manganese is 47 µg/L on April 21, 1988 (Figure 21). The only result for dissolved iron is 158 µg/L on April 28, 1990 (Figure 42). The only organic COC from the ROD with results is tetrachloroethene, collected on May 20, 1990, with a concentration of 2 µg/L.

BLM-26 was sampled from December 1987 to May 1990 (Table 8). At this well, there are no results for total chloride, dissolved nickel, dissolved chromium, or dissolved iron. Dissolved manganese concentrations range

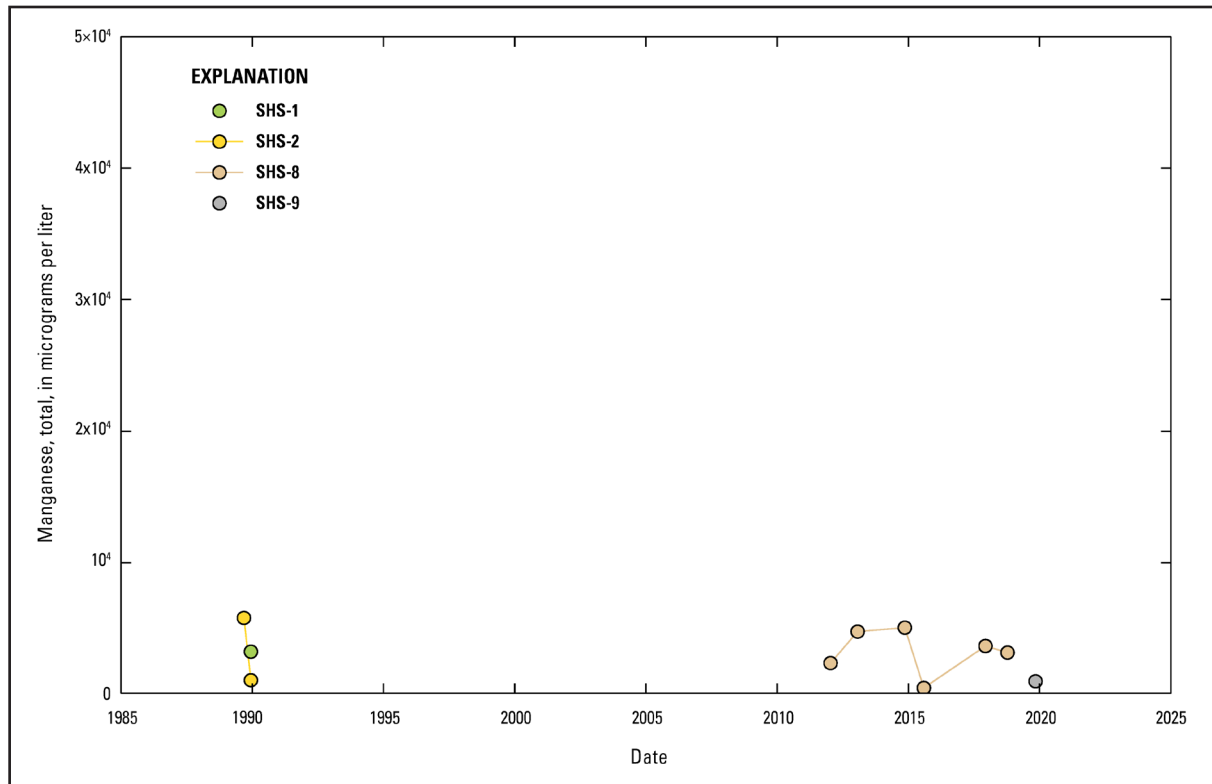


Figure 45. Total manganese concentration over time at Southern Heights Subdivision (SHS) monitoring wells south of U.S. Highway 64 near Farmington, New Mexico. SHS wells were monitored by the Giant Bloomfield Refinery. Locations of wells are shown in Figure 7; data sources are specified in Table 8.

from 182 µg/L (April 21, 1988) to 335 µg/L (February 28, 1990) (Figure 21). The only organic COC from the ROD with results is trichloroethene, which was sampled on July 19, 1988, and had a concentration of 7 µg/L.

BLM-27 was sampled from December 1987 to May 1990 (Table 8). At this well, there are no results for total chloride or dissolved iron. There are two dissolved manganese results, both collected on April 21, 1988 (Figure 21). Their values are 18 µg/L and 70 µg/L. There is one result for dissolved nickel, sampled on September 7, 1989, with a concentration of 60.2 µg/L (Figure 28). There are two results for dissolved chromium (Figure 35). Both results have the same value of 74 µg/L; one was collected on September 7, 1989, and the other was collected on December 12, 1989. There are no results for the organic COCs described in the ROD.

BLM-28 was sampled from December 1987 to May 1990 (Table 8). At this well, there are no results for total chloride, dissolved nickel, or dissolved chromium. Dissolved manganese concentrations range from 426 µg/L (December 14, 1989) to 511 µg/L (April 21, 1988) (Figure 21). Dissolved iron concentrations range from 308 µg/L (December 14, 1989) to 1,130 µg/L (February 27, 1990) (Figure 42). There are no results for the organic COCs described in the ROD.

BLM-29 was sampled from December 1987 to May 1990 (Table 8). At this well, there are no results for total chloride, dissolved nickel, or dissolved chromium. Dissolved manganese concentrations range from 307 µg/L (December 17, 1989) to 419 µg/L (February 27, 1990, and April 25, 1990) (Figure 21). Dissolved iron concentrations range from 577 µg/L (September 10, 1989) to 731 µg/L (February 27, 1990) (Figure 42). There are no results for the organic COCs described in the ROD.

BLM-30 was sampled from December 1987 to May 1990 (Table 8). At this well, there are no results for total chloride, dissolved manganese, dissolved nickel, or dissolved iron. There are two results for dissolved

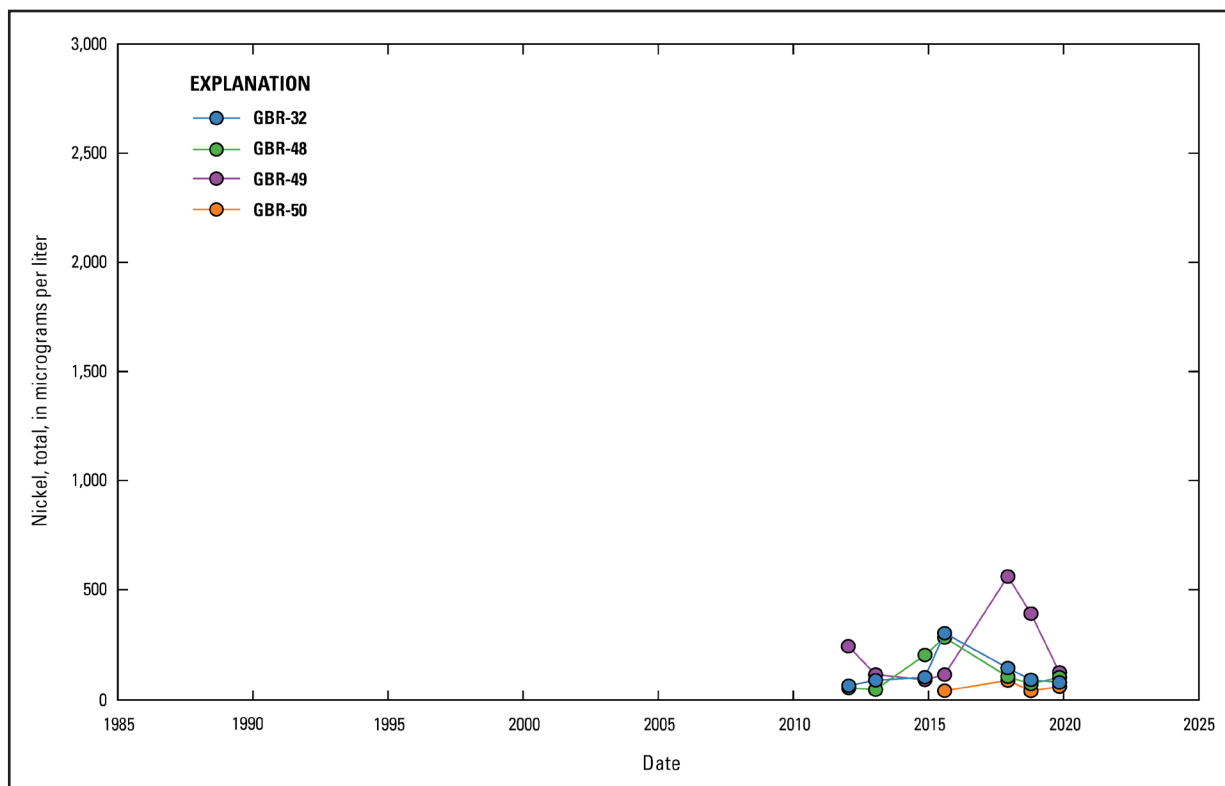


Figure 46. Total nickel concentration over time at Giant Bloomfield Refinery (GBR) monitoring wells upgradient from refinery operations at GBR near Farmington, New Mexico. Locations of wells are shown in Figure 5; data sources are specified in Table 8.

chromium (Figure 35): 43 µg/L on September 7, 1989, and 110 µg/L on December 12, 1989. There are no results for the organic COCs described in the ROD.

BLM-31 was sampled from December 1987 to May 1990 (Table 8). At this well, there are no results for total chloride, dissolved nickel, dissolved chromium, or dissolved iron. Dissolved manganese concentrations range from 136 µg/L (April 21, 1988) to 267 µg/L (May 19, 1990) (Figure 21). There are no results for the organic COCs described in the ROD.

BLM-32 was sampled from December 1987 to May 1990 (Table 8). At this well, there are no results for total chloride, dissolved nickel, or dissolved chromium. Dissolved manganese concentrations range from 283 µg/L (December 17, 1989) to 335 µg/L (April 25, 1990) (Figure 21). Dissolved iron concentrations range from 393 µg/L (April 25, 1990) to 517 µg/L (September 10, 1989) (Figure 42). There are no results for the organic COCs described in the ROD.

BLM-33 was sampled from February 1989 to May 1990 (Table 8). At this well, there are no results for total chloride, dissolved nickel, or dissolved chromium. Dissolved manganese concentrations range from 387 µg/L (September 12, 1989) to 411 µg/L (May 16, 1990) (Figure 16). Dissolved iron concentrations range from 166 µg/L (December 15, 1989) to 860 µg/L (April 24, 1990) (Figure 37). There are no results for the organic COCs described in the ROD.

BLM-34 was sampled from February 1989 to May 1990 (Table 8). At this well, there are no results for total chloride, dissolved nickel, or dissolved chromium. Dissolved manganese concentrations range from 340 µg/L (September 11, 1989, and February 26, 1990) to 372 µg/L (May 16, 1990) (Figure 16). Dissolved iron concentrations range from 370 µg/L (December 15, 1989) to 1,060 µg/L (April 24, 1990) (Figure 37). There are no results for the organic COCs described in the ROD.

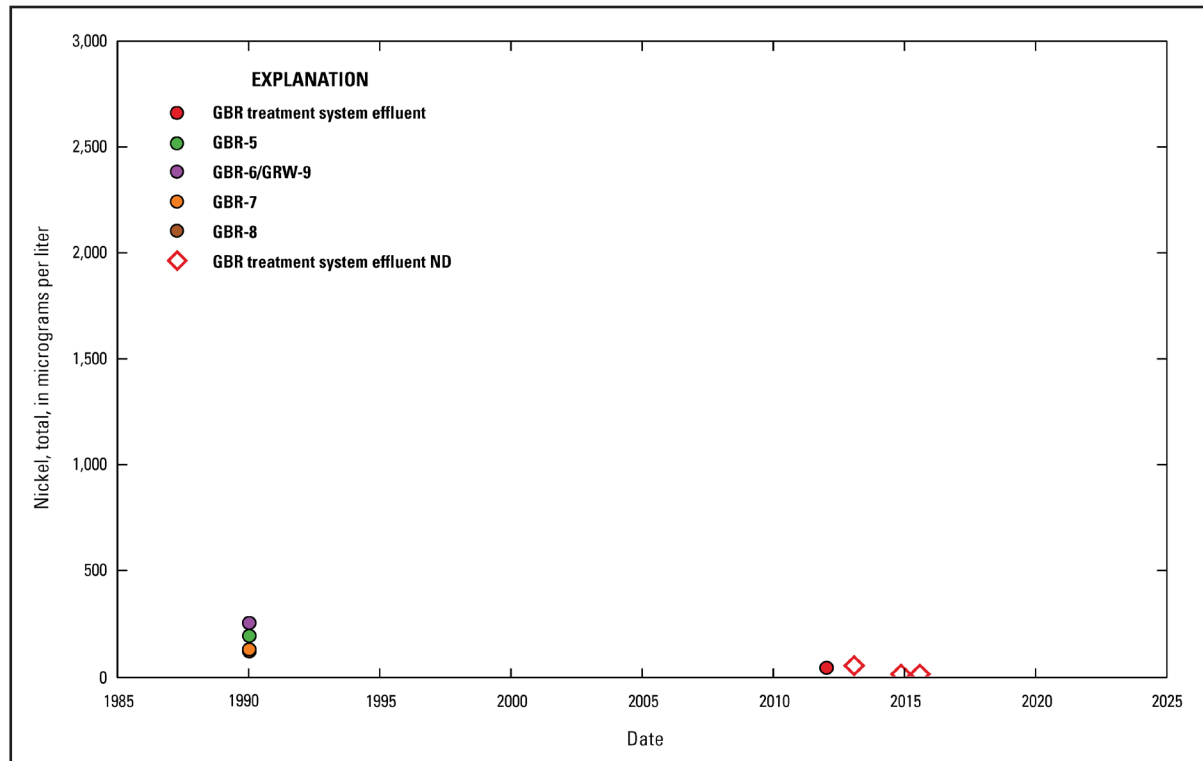


Figure 47. Total nickel concentration over time at Giant Bloomfield Refinery (GBR) monitoring wells, groundwater recovery wells (GRW), and treatment system effluent near refinery operations at GBR near Farmington, New Mexico. Locations of wells and infiltration trenches, which accept the treatment system effluent, are shown in Figure 6; data sources are specified in Table 8. ND, no detection above method detection limits.

BLM-35 was sampled from February 1989 to May 1990 (Table 8). At this well, there are no results for total chloride, dissolved nickel, or dissolved chromium. Dissolved manganese concentrations range from 570 µg/L (December 15, 1989) to 756 µg/L (September 12, 1989) (Figure 16). Dissolved iron results are from three dates: 579 µg/L on February 26, 1990; 371 µg/L on April 28, 1990; and 672 µg/L on May 16, 1990 (Figure 37). There are no results for the organic COCs described in the ROD.

BLM-37 was sampled from May 1989 to April 1990 (Table 8). At this well, there are no results for total chloride, dissolved nickel, or dissolved iron. There is only one dissolved manganese result (Figure 21): 2,980 µg/L on April 28, 1990. There is one result for dissolved chromium of 43 µg/L on September 7, 1989 (Figure 35). The only organic COC described in the ROD with results is *trans*-1,2-dichloroethene with a concentration of 3 µg/L on December 12, 1989.

BLM-39 was sampled from March 1990 to August 2020 (Table 8). At this well, total chloride concentrations range from 19 mg/L (June 8, 1999) to 62 mg/L (August 4, 2020) (Figure 8). Dissolved manganese concentrations range from no detection above reporting levels (July 23, 2010) to 1,200 µg/L (May 19, 1998) (Figure 15). Dissolved nickel concentrations range from no detection above reporting levels (multiple dates) to an estimated value of 35 µg/L (July 23, 2010) (Figure 22). Dissolved chromium concentrations range from no detection above reporting levels (multiple dates) to 34 µg/L (March 1, 1990) (Figure 29). The only result for dissolved iron is 1,480 µg/L on May 17, 1990 (Figure 36). *cis*-1,2-Dichloroethene was not detected above reporting levels except in one sample with a concentration of 0.4 µg/L on June 23, 2015 (Figure 55). All *trans*-1,2-dichloroethene results represent no detection above reporting levels. Tetrachloroethene was not detected above reporting levels except in one sample with a concentration of 1 µg/L collected on July 23, 2010 (Figure 59). Trichloroethene and vinyl chloride were not detected above reporting levels.

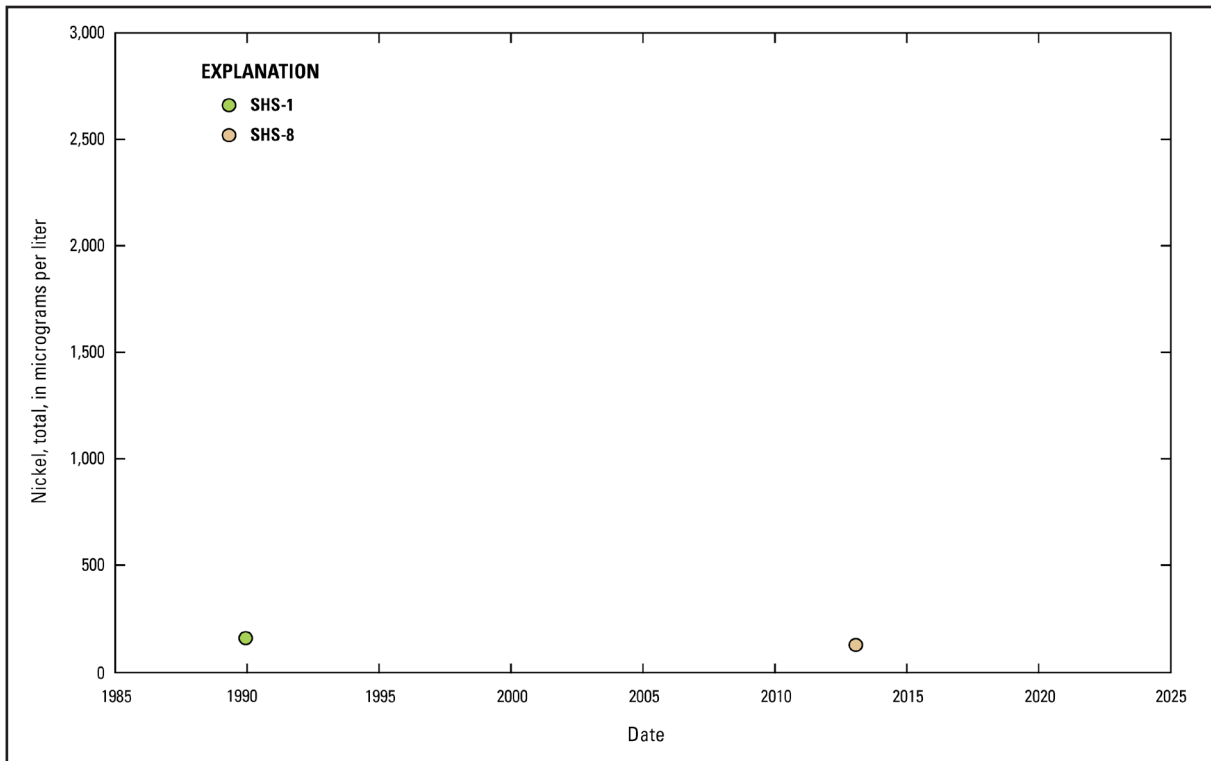


Figure 48. Total nickel concentration over time at Southern Heights Subdivision (SHS) monitoring wells south of U.S. Highway 64 near Farmington, New Mexico. SHS wells were monitored by the Giant Bloomfield Refinery. Locations of wells are shown in Figure 7; data sources are specified in Table 8.

BLM-40 was sampled from March 1990 to May 1990 (Table 8). At this well, there are no results for total chloride, dissolved nickel, or dissolved chromium. Dissolved manganese concentrations range from 426 µg/L (March 1, 1990) to 470 µg/L (April 26, 1990) (Figure 15). Dissolved iron concentrations range from 914 µg/L (March 1, 1990) to 993 µg/L (April 26, 1990) (Figure 36). There are no results for the organic COCs described in the ROD.

BLM-41 was sampled from March 1990 to May 1990 (Table 8). At this well, there are no results for total chloride, dissolved nickel, or dissolved chromium. There are three results for dissolved manganese (Figure 17): 400 µg/L on March 1, 1990; 385 µg/L on April 27, 1990; and 409 µg/L on May 18, 1990. The three results for dissolved iron (Figure 38) are 976 µg/L on March 1, 1990; 1,030 µg/L on April 27, 1990; and 1,100 µg/L on May 18, 1990. There are no results for the organic COCs described in the ROD.

BLM-42 was sampled from March 1990 to November 2004 (Table 8). At this well, total chloride concentrations range from 42 mg/L (November 16, 2004) to 120 mg/L (May 19, 1998) (Figure 10). Dissolved manganese concentrations range from 180 µg/L (May 22, 2001; November 6, 2001; May 15, 2002; and November 16, 2004) to 2,490 µg/L (March 1, 1990) (Figure 17). Dissolved nickel was not detected above reporting levels except in two samples: 45 µg/L on May 19, 1998, and 41 µg/L on June 8, 1999 (Figure 24). Dissolved chromium was not detected above reporting levels (Figure 31). The only result for dissolved iron is 969 µg/L on March 1, 1990 (Figure 38). The organic COCs described in the ROD were not detected above reporting levels.

BLM-43 was sampled from March 1990 to May 1990 (Table 8). At this well, there are no data for total chloride, dissolved nickel, dissolved chromium, or dissolved iron. There are three results for dissolved manganese (Figure 17): 6,700 µg/L on March 1, 1990; 5,260 µg/L on April 27, 1990; and 5,030 µg/L on May 18, 1990. There are no results for the organic COCs described in the ROD.

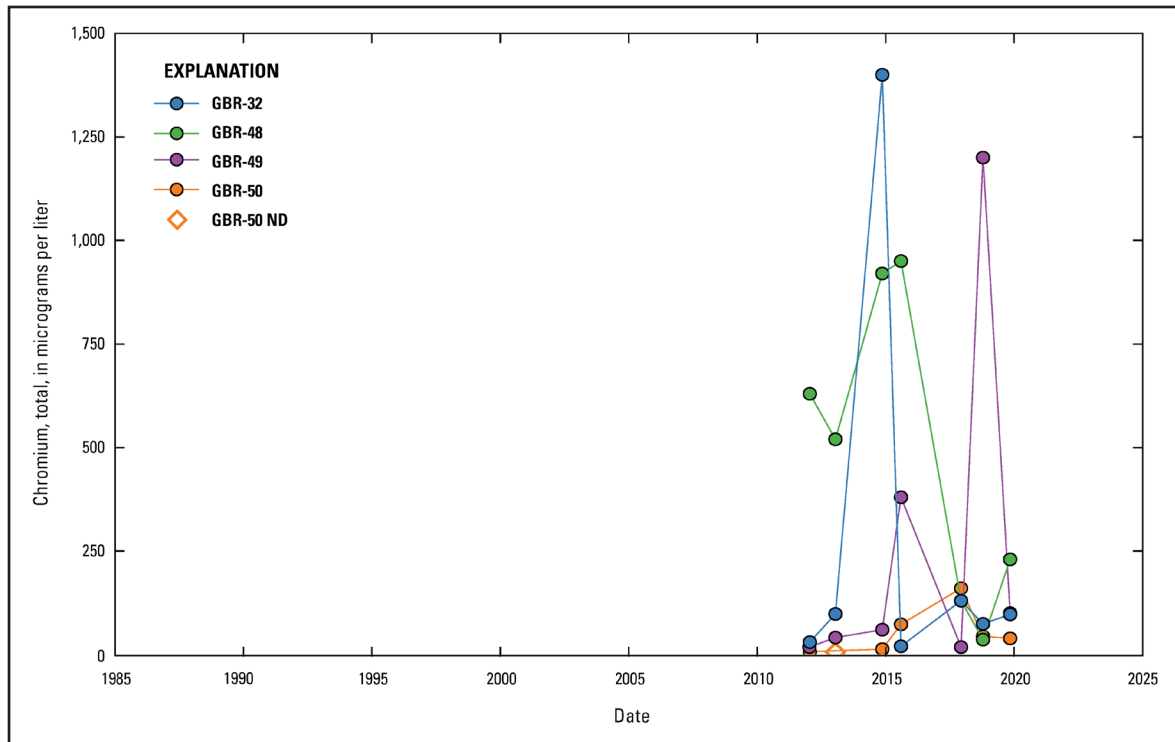


Figure 49. Total chromium concentration over time at Giant Bloomfield Refinery (GBR) monitoring wells upgradient from refinery operations at GBR near Farmington, New Mexico. Locations of wells are shown in Figure 5; data sources are specified in Table 8. ND, no detection above method detection limits.

BLM-44 was sampled from March 1990 to May 1990 (Table 8). At this well, there are no results for total chloride, dissolved nickel, or dissolved chromium. The three results for dissolved manganese (Figure 17) are 388 µg/L on March 2, 1990; 421 µg/L on April 26, 1990; and 402 µg/L on May 17, 1990. The three results for dissolved iron (Figure 38) are 428 µg/L on March 2, 1990; 334 µg/L on April 26, 1990; and 411 µg/L on May 17, 1990. There are no results for the organic COCs described in the ROD.

BLM-45 was sampled from March 1990 to August 2020 (Table 8). At this well, there are no dissolved iron results. Total chloride concentrations range from 40 mg/L (multiple dates) to 91 mg/L (March 19, 2015) (Figure 10). Dissolved manganese concentrations range from no detection above reporting levels (multiple dates) to 2,440 µg/L (May 17, 1990) (Figure 17). Dissolved nickel was not detected above reporting levels (Figure 24). Dissolved chromium concentrations range from no detection above reporting levels (multiple dates) to 20 µg/L on September 17, 2015 (Figure 31). *cis*-1,2-Dichloroethene (Figure 57) was not detected above reporting levels except in one sample with a concentration of 0.4 µg/L on June 23, 2015. The remainder of the organic COCs described in the ROD were not detected above reporting levels.

BLM-46 was sampled from March 1990 to May 1990 (Table 8). At this well, there are no results for total chloride, dissolved chromium, or dissolved iron. The three results for dissolved manganese are 2,210 µg/L on March 2, 1990; 1,100 µg/L on February 26, 1990; and 1,290 µg/L on May 17, 1990 (Figure 17). The two results for dissolved nickel are 47.5 µg/L (April 26, 1990) and 127 µg/L (May 17, 1990) (Figure 24). There are no results for the organic COCs described in the ROD.

BLM-47 was sampled from March 1990 to May 1990 (Table 8). At this well, there are no results for total chloride, dissolved nickel, or dissolved chromium. The three results for dissolved manganese are 420 µg/L on March 3, 1990; 462 µg/L on April 26, 1990; and 484 µg/L on May 17, 1990 (Figure 17). The three results for dissolved iron are 252 µg/L on March 3, 1990; 368 µg/L on April 26, 1990; and 538 µg/L on May 17, 1990 (Figure 38). There are no results for the organic COCs described in the ROD.

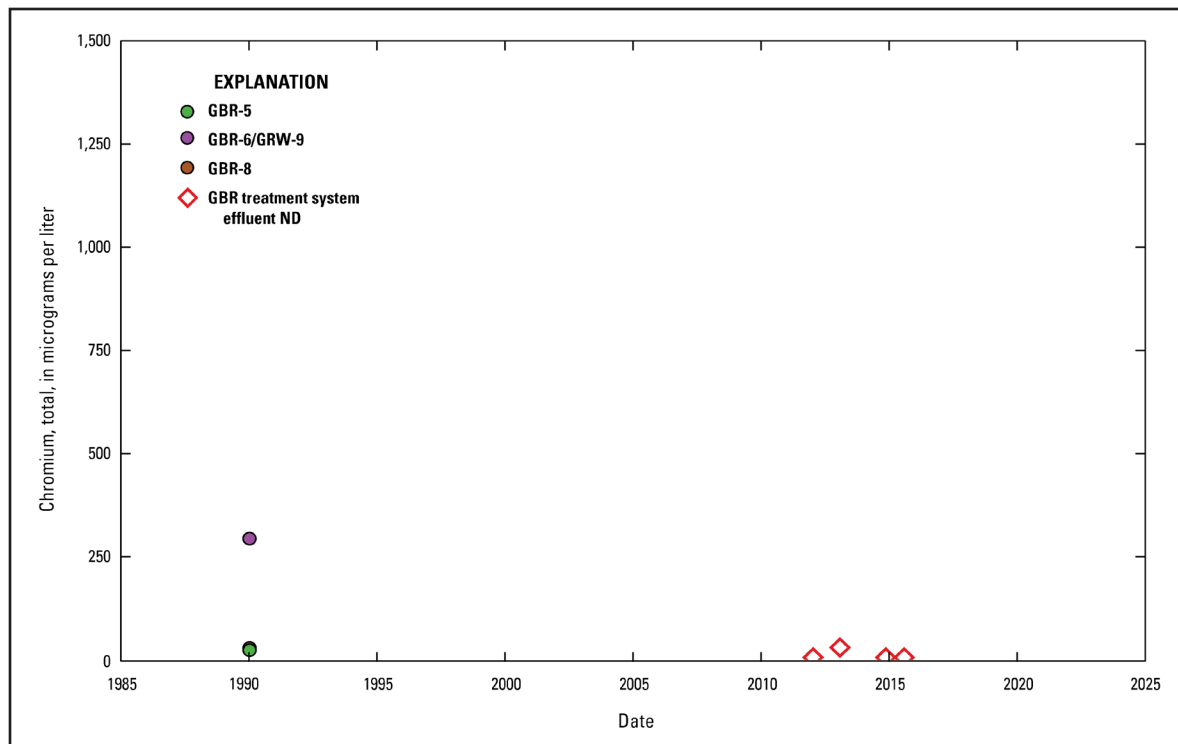


Figure 50. Total chromium concentration over time at Giant Bloomfield Refinery (GBR) monitoring wells, groundwater recovery wells (GRW), and treatment system effluent near refinery operations at GBR near Farmington, New Mexico. Locations of wells and infiltration trenches, which accept the treatment system effluent, are shown in Figure 6; data sources are specified in Table 8. ND, no detection above method detection limits.

BLM-48 was sampled from March 1990 to November 2004 (Table 8). At this well, there are no results for dissolved iron. Total chloride concentrations range from 44 mg/L on November 17, 2003, to 50 mg/L on September 1, 1998 (Figure 10). Dissolved manganese concentrations range from below reporting levels (June 8, 1999) to 1,220 µg/L (April 26, 1990) (Figure 17). Dissolved nickel was not detected above reporting levels (Figure 24). Dissolved chromium was not detected above reporting levels (Figure 31). The organic COCs described in the ROD were not detected above reporting levels.

BLM-49 was sampled from March 1990 to May 1990 (Table 8). At this well, there are no results for total chloride, dissolved nickel, dissolved chromium, or dissolved iron. There are three results for dissolved manganese (Figure 17): 1,340 µg/L on March 3, 1990; 1,470 µg/L on April 26, 1990; and 1,240 µg/L on May 17, 1990. The one result for tetrachloroethene has a value of 12 µg/L on April 26, 1990 (Figure 61). The one result for trichloroethene has a value of 9.8 µg/L on April 26, 1990 (Figure 64). There are no results for the other organic COCs described in the ROD.

BLM-50 was sampled from March 1990 to May 1990 (Table 8). At this well, there are no results for total chloride, dissolved nickel, or dissolved chromium. Dissolved manganese concentrations range from 367 µg/L on April 27, 1990, to 404 µg/L on May 17, 1990 (Figure 17). Dissolved iron concentrations range from 798 µg/L on March 20, 1990, to 1,140 µg/L on April 27, 1990 (Figure 38). There are no results for the organic COCs described in the ROD.

BLM-51 was sampled from March 1990 to November 2004 (Table 8). At this well, there are no results for dissolved iron. Total chloride concentrations range from 48 mg/L (November 16, 2000) to 56 mg/L (September 1, 1998) (Figure 10). Of the 17 dissolved manganese results, 14 represent no detection above reporting levels (Figure 17). The results representing detections are 73.4 µg/L on March 20, 1990; 33.5 µg/L on April 26, 1990; and 31.8 µg/L on May 17, 1990. Dissolved nickel was not detected above reporting levels (Figure 24). Dissolved chromium concentrations range from no detection above reporting levels (multiple dates)

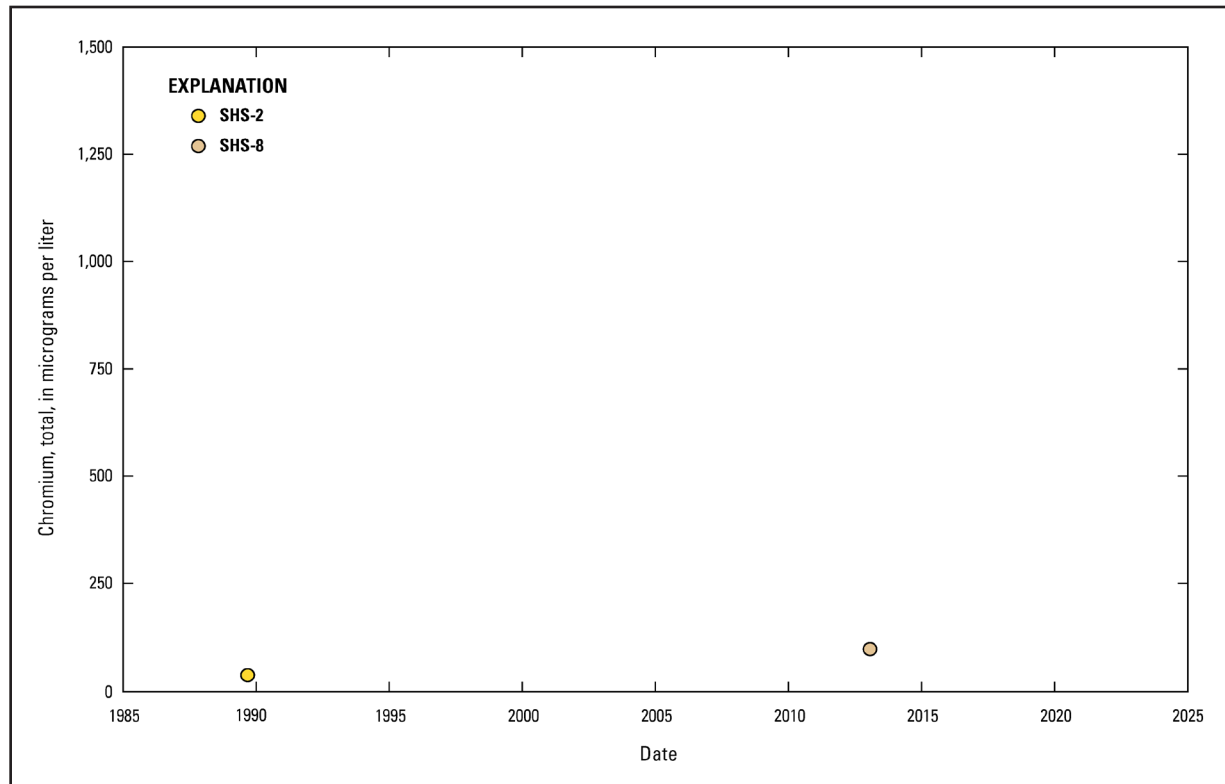


Figure 51. Total chromium concentration over time at Southern Heights Subdivision (SHS) monitoring wells south of U.S. Highway 64 near Farmington, New Mexico. SHS wells were monitored by the Giant Bloomfield Refinery. Locations of wells are shown in Figure 7; data sources are specified in Table 8.

to 20 µg/L on April 26, 1990 (Figure 31). The organic COCs described in the ROD were not detected above reporting levels.

BLM-52 was sampled from March 1990 to May 1990 (Table 8). At this well, there are no results for total chloride, dissolved manganese, dissolved nickel, or dissolved iron. The three results for dissolved chromium are 49.3 µg/L on March 20, 1990; 54.2 µg/L on April 26, 1990; and 51.8 µg/L on May 17, 1990 (Figure 31). There are no results for the organic COCs described in the ROD.

BLM-53 was sampled from March 1990 to May 1990 (Table 8). At this well, there are no results for total chloride, dissolved nickel, or dissolved chromium. The three results for dissolved manganese are 191 µg/L on March 21, 1990; 415 µg/L on April 29, 1990; and 440 µg/L on May 21, 1990 (Figure 16). There are two results for dissolved iron (Figure 37): 104 µg/L on April 29, 1990, and 311 µg/L on May 21, 1990. There are no results for the organic COCs described in the ROD.

BLM-54 was sampled from March 1990 to May 1990 (Table 8). At this well, there are no results for total chloride, dissolved nickel, or dissolved chromium. Dissolved manganese concentrations range from 417 µg/L on March 4, 1990, to 461 µg/L on May 21, 1990 (Figure 16). The two results for dissolved iron are 173 µg/L on April 29, 1990, and 220 µg/L on May 21, 1990 (Figure 37). There are no results for the organic COCs described in the ROD.

BLM-55 was sampled from March 1990 to November 2004 (Table 8). Total chloride concentrations range from 32 mg/L (November 16, 2000) to 48 mg/L (September 1, 1998) (Figure 9). Dissolved manganese concentrations range from 380 µg/L (November 19, 2003) to 4,790 µg/L (May 21, 1990) (Figure 16). Of the 14 results for dissolved nickel, 11 are below reporting levels (Figure 23). The remaining results are 40 µg/L on May 19, 1998; 42 µg/L on June 8, 1999; and 71 µg/L on November 16, 2004. Dissolved chromium was not detected above reporting levels (Figure 30). The only result for dissolved iron is 1,310 µg/L on April 29, 1990 (Figure

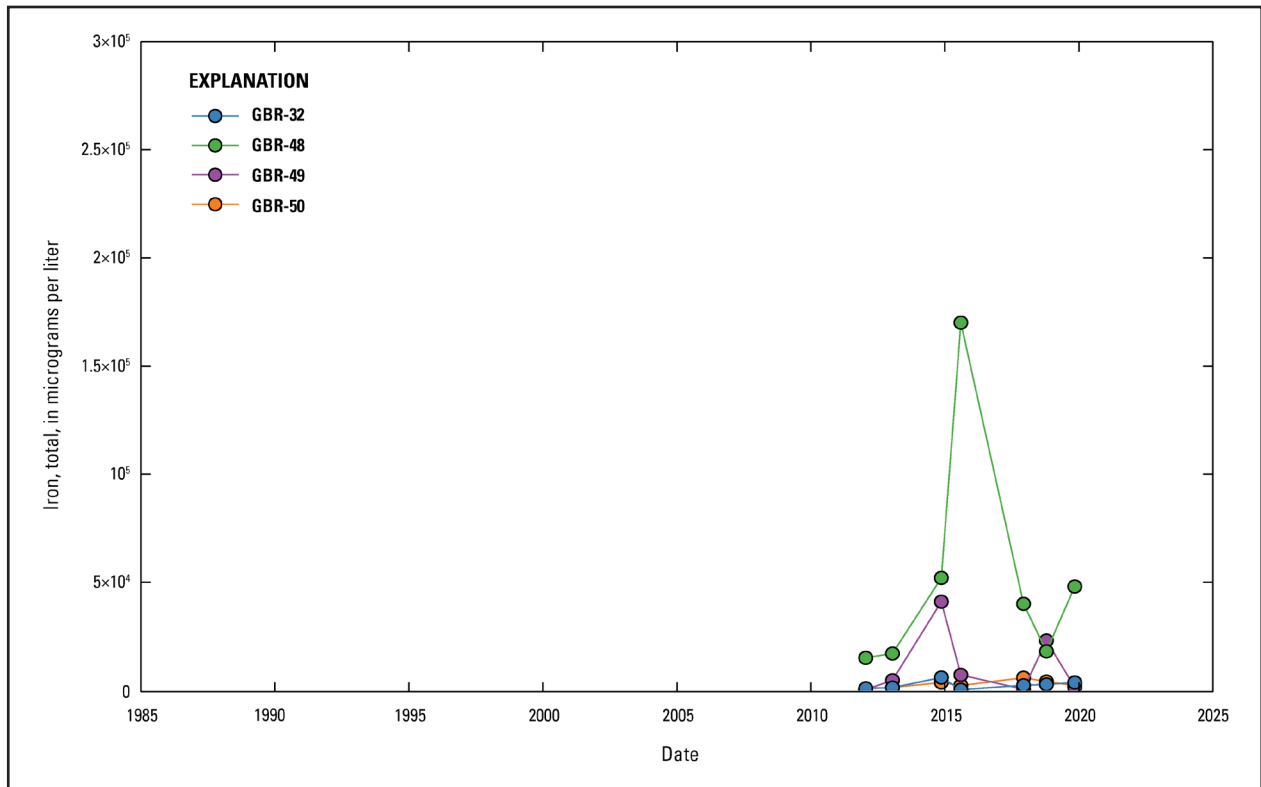


Figure 52. Total iron concentration over time at Giant Bloomfield Refinery (GBR) monitoring wells upgradient from refinery operations at GBR near Farmington, New Mexico. Locations of wells are shown in Figure 5; data sources are specified in Table 8.

37). There are 14 results for *cis*-1,2-dichloroethene (Figure 56). Twelve of those results represent no detection above reporting levels. The results above reporting levels are 20 µg/L on March 4, 1990, and 1.1 µg/L on May 19, 1998. *trans*-1,2-Dichloroethene was not detected above reporting levels. Twelve of the fourteen results for tetrachloroethene are below reporting levels (Figure 60). The two samples with tetrachloroethene results above reporting levels are 2 µg/L on April 29, 1990, and 1.7 µg/L on May 21, 1990. Trichloroethene was not detected above reporting levels except for the sample collected on April 29, 1990 (3.2 µg/L) (Figure 63). Vinyl chloride was not detected above reporting levels (Figure 66).

BLM-56 was sampled from March 1990 to November 2004 (Table 8). Total chloride concentrations range from 39 mg/L (June 8, 1999, and November 16, 2000) to 46 mg/L (September 1, 1998, and August 15, 2001) (Figure 9). Dissolved manganese concentrations range from no detection above reporting levels (multiple dates) to 2,460 µg/L (April 29, 1990) (Figure 16). Dissolved nickel was not detected above reporting levels except on April 10, 2000, when it was detected at 47 µg/L (Figure 23). Of the nine results, dissolved chromium was not detected above reporting levels in seven of the samples and was detected at 14.5 µg/L on April 29, 1990, and 12.9 µg/L on May 22, 1990 (Figure 30). There is one result for dissolved iron (Figure 37): 1,710 µg/L on April 29, 1990. Organic COCs described in the ROD were not detected above reporting levels.

BLM-57 was sampled from March 1990 to November 2004 (Table 8). At this well, there are no results for dissolved iron. Total chloride concentrations range from 91 mg/L on May 16, 2002, to 490 mg/L on June 8, 1999 (Figure 9). Dissolved manganese concentrations range from 4,300 µg/L (November 19, 2003) to 8,620 µg/L (May 22, 1990) (Figure 16). Dissolved nickel concentrations range from no detection above reporting levels (multiple dates) to 146 µg/L (May 22, 1990) (Figure 23). Dissolved chromium was not detected above reporting levels (Figure 30). Results for *cis*-1,2-dichloroethene range from no detection above reporting levels (multiple dates) to 14 µg/L (June 8, 1999) (Figure 56). *trans*-1,2-Dichloroethene and tetrachloroethene (Figure 60) were not detected above reporting levels. Trichloroethene was not detected above reporting levels among

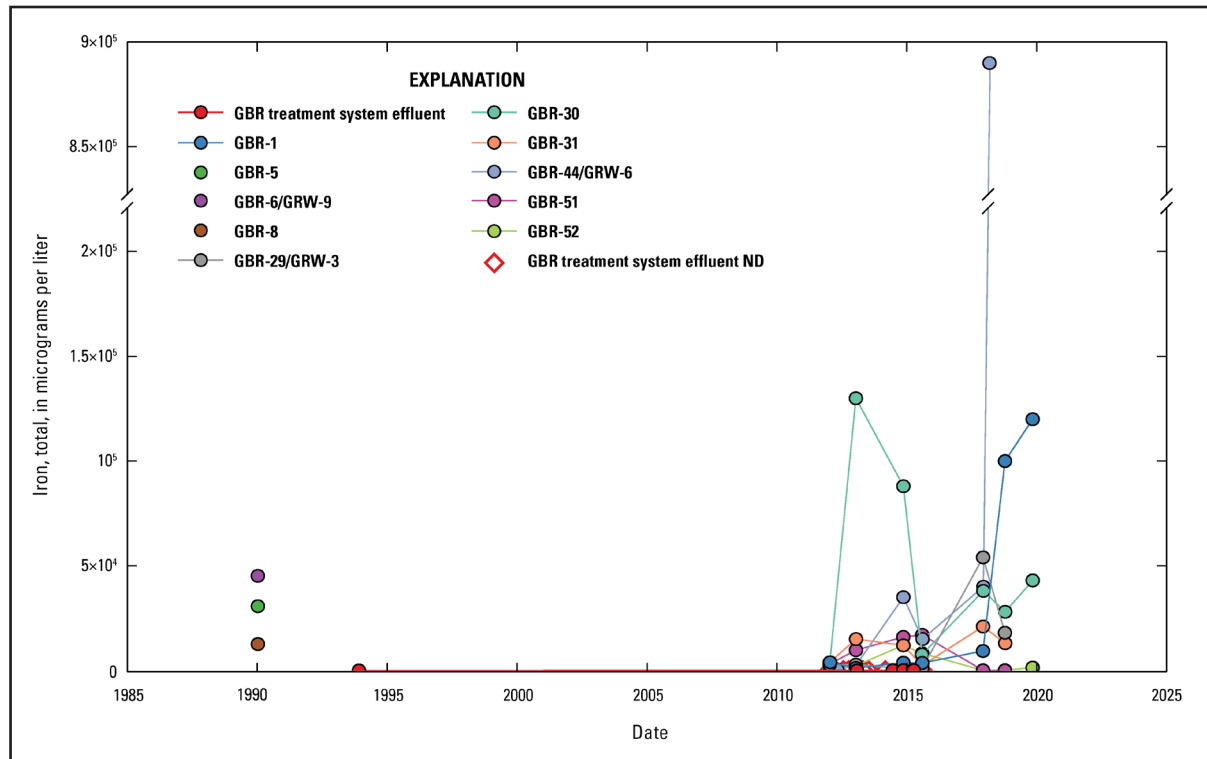


Figure 53. Total iron concentration over time at Giant Bloomfield Refinery (GBR) monitoring wells, groundwater recovery wells (GRW), and treatment system effluent near refinery operations at GBR near Farmington, New Mexico. Locations of wells and infiltration trenches, which accept the treatment system effluent, are shown in Figure 6; data sources are specified in Table 8. ND, no detection above method detection limits.

13 of the 24 samples collected (Figure 63). The remaining trichloroethene results range from 0.7 $\mu\text{g/L}$ (March 21, 1990) to 4.6 $\mu\text{g/L}$ (June 8, 1999). Of the 24 samples collected with results for vinyl chloride, vinyl chloride was not detected above reporting levels in 17 of the samples (Figure 66). The remainder of the vinyl chloride results range from 2.3 $\mu\text{g/L}$ (April 10, 2000) to 6.7 $\mu\text{g/L}$ (March 21, 1990).

BLM-58 was sampled from March 1990 to May 1990 (Table 8). At this well, there are no results for total chloride, dissolved nickel, or dissolved iron. There are three results for dissolved manganese (Figure 16): 2,610 $\mu\text{g/L}$ on March 6, 1990; 1,940 $\mu\text{g/L}$ on April 29, 1990; and 1,990 $\mu\text{g/L}$ on May 22, 1990. There are two results for dissolved chromium (Figure 30): 12.8 $\mu\text{g/L}$ on April 29, 1990, and 22.4 $\mu\text{g/L}$ on May 22, 1990. There are no results for the organic COCs described in the ROD.

BLM-59 was sampled from March 1990 to May 1990 (Table 8). At this well, there are no results for total chloride, dissolved nickel, or dissolved chromium. The three results for dissolved manganese (Figure 17) are 370 $\mu\text{g/L}$ on March 2, 1990; 358 $\mu\text{g/L}$ on April 27, 1990; and 406 $\mu\text{g/L}$ on May 18, 1990. There are three results for dissolved iron (Figure 38): 365 $\mu\text{g/L}$ on March 2, 1990; 869 $\mu\text{g/L}$ on April 27, 1990; and 842 $\mu\text{g/L}$ on May 18, 1990. There are no results for the organic COCs described in the ROD.

BLM-60 was sampled from March 1990 to August 2020 (Table 8). At this well, there are no results for dissolved iron. Total chloride results range from 39 mg/L (May 10, 2006) to 240 mg/L (May 19, 1998) (Figure 10). Dissolved manganese concentrations range from no detection above reporting levels (multiple dates) to 4,920 $\mu\text{g/L}$ (May 18, 1990) (Figure 17). Dissolved nickel concentrations range from no detection above reporting levels (multiple dates) to 1,200 $\mu\text{g/L}$ (September 17, 2015) (Figure 24). Dissolved chromium concentrations range from no detection above reporting levels (multiple dates) to 150 $\mu\text{g/L}$ (September 17, 2015) (Figure 31). All of the results for *cis*-1,2-dichloroethene are below reporting levels except for the sample collected on June 23, 2015 (0.4 $\mu\text{g/L}$) (Figure 57). All other organic COCs described in the ROD were not detected above reporting levels.

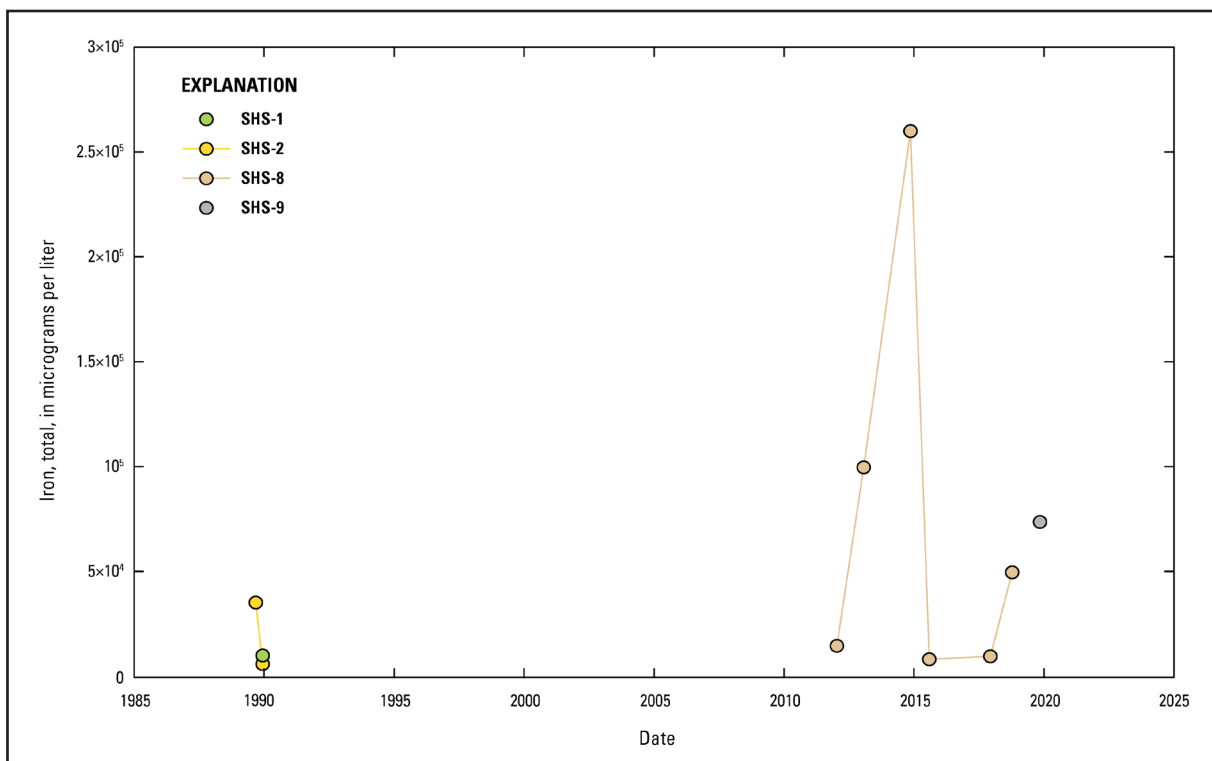


Figure 54. Total iron concentration over time at Southern Heights Subdivision (SHS) monitoring wells south of U.S. Highway 64 near Farmington, New Mexico. SHS wells were monitored by the Giant Bloomfield Refinery. Locations of wells are shown in Figure 7; data sources are specified in Table 8.

BLM-61 was sampled from March 1990 to May 1990 (Table 8). At this well, there are no results for total chloride, dissolved nickel, or dissolved chromium. There are three results for dissolved manganese (Figure 18): 512 µg/L on March 21, 1990; 882 µg/L on April 27, 1990; and 376 µg/L on May 20, 1990. There are two results for dissolved iron (Figure 39): 291 µg/L on March 21, 1990, and 1,040 µg/L on May 20, 1990. There are no results for the organic COCs described in the ROD.

BLM-62 was sampled from March 1990 to August 2020 (Table 8). At this well, total chloride concentrations range from 19 mg/L (November 17, 2004) to 470 mg/L (August 24, 2014) (Figure 11). Dissolved manganese concentrations range from 12 µg/L (May 22, 2001) to 9,200 µg/L (December 20, 2013) (Figure 18). Dissolved nickel concentrations range from no detection above reporting levels (multiple dates) to an estimated value of 19 µg/L (July 22, 2010, and June 15, 2011) (Figure 25). Dissolved chromium was not detected above reporting levels except in two samples: 70 µg/L on September 15, 2016, and 10 µg/L on March 31, 2017 (Figure 32). There is one result for dissolved iron (Figure 39): 1,130 µg/L on April 27, 1990. *cis*-1,2-Dichloroethene was not detected above reporting levels except in the sample collected on June 23, 2015 (0.4 µg/L) (Figure 58). *trans*-1,2-Dichloroethene was not detected above reporting levels. Tetrachloroethene (Figure 62) and trichloroethene (Figure 65) were not detected above reporting levels except for detections of 4 µg/L and 2 µg/L, respectively, on September 1, 1998. Vinyl chloride was not detected above reporting levels.

BLM-63 was sampled from March 1990 to May 1990 (Table 8). At this well, there are no results for total chloride, dissolved nickel, or dissolved chromium. There are three results for dissolved manganese (Figure 18): 252 µg/L on March 21, 1990; 443 µg/L on April 30, 1990; and 358 µg/L on May 20, 1990. There is one result for dissolved iron (Figure 39): 423 µg/L on April 30, 1990. There are no results for the organic COCs described in the ROD.

BLM-64 was sampled from March 1990 to May 1990 (Table 8). At this well, there are no results for total chloride, dissolved nickel, or dissolved chromium. There are three results for dissolved manganese (Figure

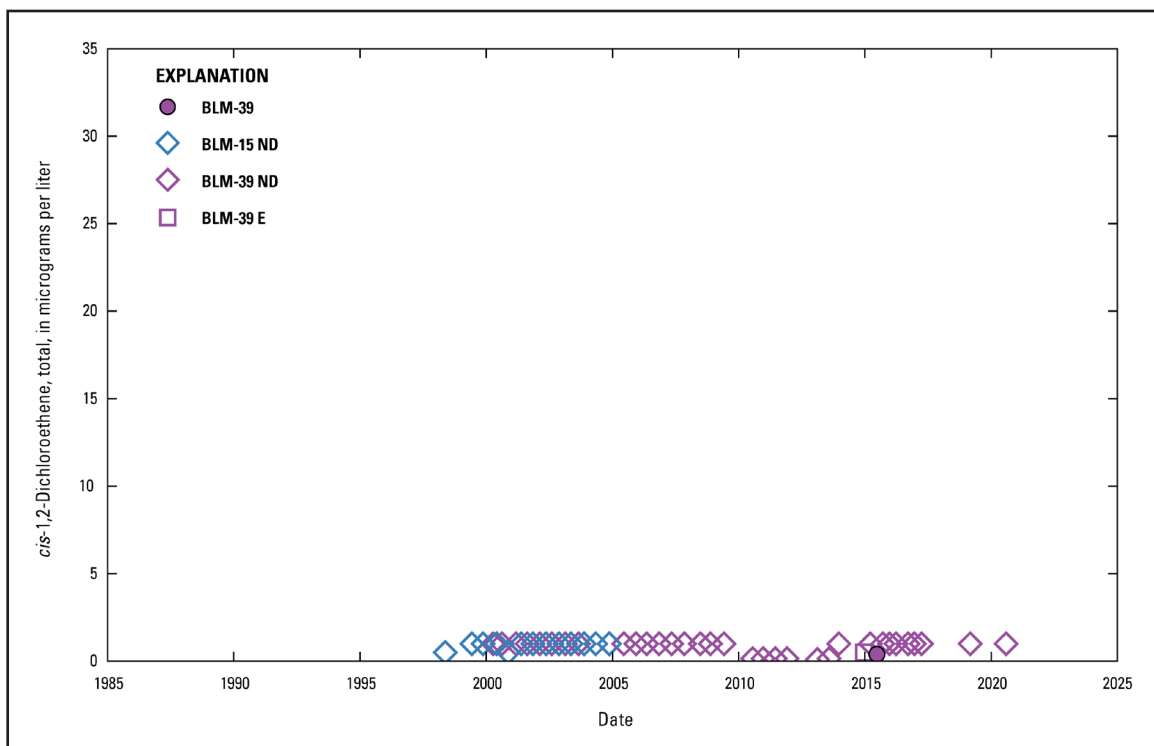


Figure 55. *cis*-1,2-Dichloroethene concentration over time at Bureau of Land Management (BLM) monitoring wells upgradient from the Lee Acres Landfill near Farmington, New Mexico. Locations of wells are shown in Figure 3; data sources are specified in Table 8. As shown in Table 1, *cis*-1,2-dichloroethene was not detected in the alluvial aquifer background samples collected at the Lee Acres Landfill (Roy F. Weston, Inc., 1995), and the cleanup level for *cis*-1,2-dichloroethene at the Lee Acres Landfill is 70 micrograms per liter (U.S. Environmental Protection Agency, 2004). ND, no detection above method detection limits; E, estimated results.

18): 462 µg/L on March 21, 1990; 739 µg/L on April 28, 1990; and 606 µg/L on May 20, 1990. There is one result for dissolved iron (Figure 39): 230 µg/L on May 20, 1990. There are no results for the organic COCs described in the ROD.

BLM-65 was sampled from March 1990 to May 1990 (Table 8). At this well, there are no results for total chloride, dissolved nickel, or dissolved chromium. There are three results for dissolved manganese (Figure 21): 2,080 µg/L on March 20, 1990; 1,940 µg/L on April 28, 1990; and 2,020 µg/L on May 20, 1990. There are two results for dissolved iron (Figure 42): 564 µg/L on April 28, 1990, and 386 µg/L on May 20, 1990. There are no results for the organic COCs described in the ROD.

BLM-66 was sampled from March 1990 to May 1990 (Table 8). At this well, there are no results for total chloride, dissolved nickel, dissolved chromium, or dissolved iron. There are three results for dissolved manganese (Figure 21): 3,400 µg/L on March 20, 1990; 3,060 µg/L on April 28, 1990; and 3,090 µg/L on May 18, 1990. There are no results for the organic COCs described in the ROD.

BLM-67 was sampled from May 1998 to November 2004 (Table 8). At this well, there are no results for dissolved iron. Total chloride concentrations range from 49 mg/L (May 20, 1998) to 55 mg/L (November 19, 2003) (Figure 11). Dissolved manganese concentrations range from no detection above reporting levels (multiple dates) to 28 µg/L (May 20, 1998) (Figure 18). Dissolved nickel concentrations range from no detection above reporting levels (multiple dates) to an estimated value of 140 µg/L (September 2, 1998) (Figure 25). Dissolved chromium was not detected above reporting levels (Figure 32). Except for trichloroethene, which was detected at 1.1 µg/L on May 6, 2004 (Figure 65), organic COCs described in the ROD were not detected above reporting levels.

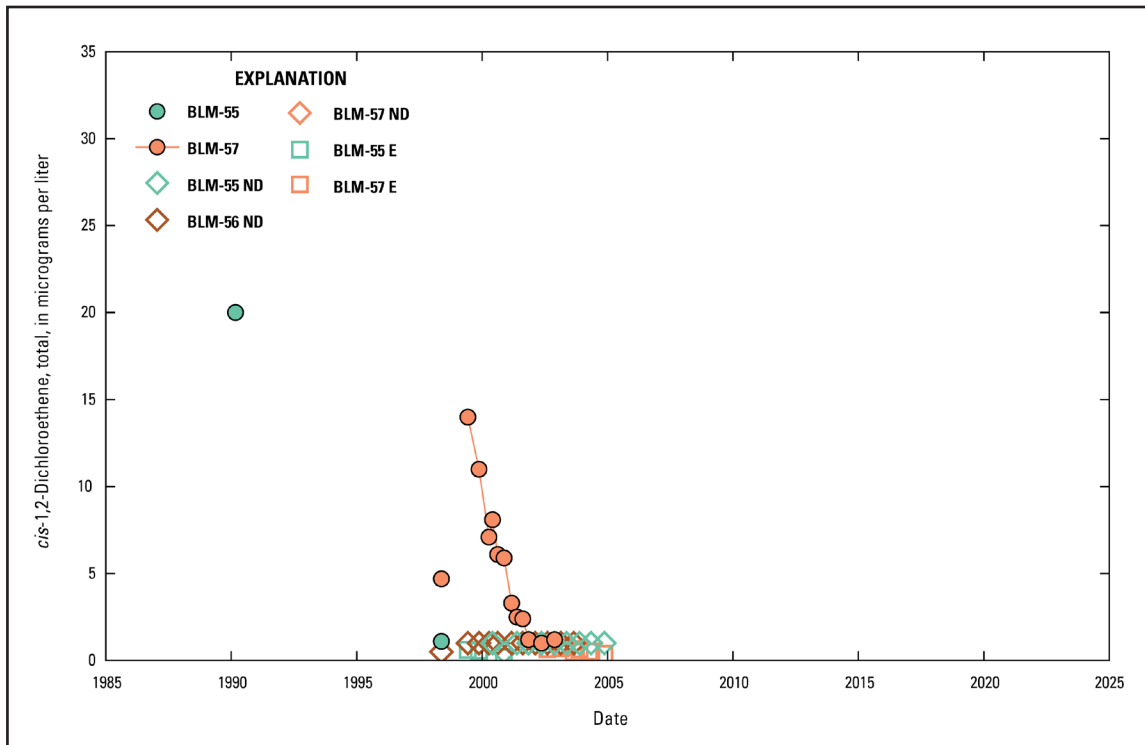


Figure 56. *cis*-1,2-Dichloroethene concentration over time at Bureau of Land Management (BLM) monitoring wells within the boundary of the Lee Acres Landfill near Farmington, New Mexico. Locations of wells are shown in Figure 4; data sources are specified in Table 8. As shown in Table 1, *cis*-1,2-dichloroethene was not detected in the alluvial aquifer background samples collected at the Lee Acres Landfill (Roy F. Weston, Inc., 1995), and the cleanup level for *cis*-1,2-dichloroethene at the Lee Acres Landfill is 70 micrograms per liter (U.S. Environmental Protection Agency, 2004). ND, no detection above method detection limits; E, estimated results.

BLM-68 was sampled from May 1998 to August 2020 (Table 8). At this well, there are no results for dissolved iron. Total chloride concentrations range from 40 mg/L (July 23, 2010) to 430 mg/L (June 26, 2008) (Figure 11). Dissolved manganese concentrations range from no detection above reporting levels (multiple dates) to 450 µg/L (July 23, 2010) (Figure 18). Dissolved nickel concentrations range from no detection above reporting levels (multiple dates) to 60 µg/L (November 15, 2000) (Figure 25). Dissolved chromium concentrations range from no detection above reporting levels (multiple dates) to an estimated value of 0.9 µg/L (June 14, 2011) (Figure 32). *cis*-1,2-Dichloroethene concentrations range from no detection above reporting levels (multiple dates) to 35 µg/L (May 20, 1998) (Figure 58). *trans*-1,2-Dichloroethene was not detected above reporting levels. The results for tetrachloroethene range from no detection above reporting levels (multiple dates) to 8 µg/L (May 20, 1998, and September 2, 1998) (Figure 62). Trichloroethene was not detected above reporting levels between December 20, 2013, and August 5, 2020 (Figure 65). Between May 20, 1998, and July 31, 2013, trichloroethene results ranged from no detection above reporting levels (multiple dates) to 3 µg/L (May 20, 1998, and September 2, 1998). Vinyl chloride was not detected above reporting levels.

BLM-69 was sampled from May 1998 to August 2020 (Table 8). At this well, there are no results for dissolved iron. Total chloride concentrations range from 44 mg/L (March 5, 2019) to 62 mg/L (August 5, 2020) (Figure 11). Dissolved manganese (Figure 18), dissolved nickel (Figure 25), and dissolved chromium (Figure 32) were not detected above reporting levels. Organic COCs described in the ROD were not detected above reporting levels.

BLM-70 was sampled from May 1998 to May 2003 (Table 8). At this well, there are no results for dissolved iron. Total chloride concentrations range from 81 mg/L (May 14, 2003) to 150 mg/L (November 18, 1999) (Figure 11). Dissolved manganese (Figure 18), dissolved nickel (Figure 25), and dissolved chromium (Figure

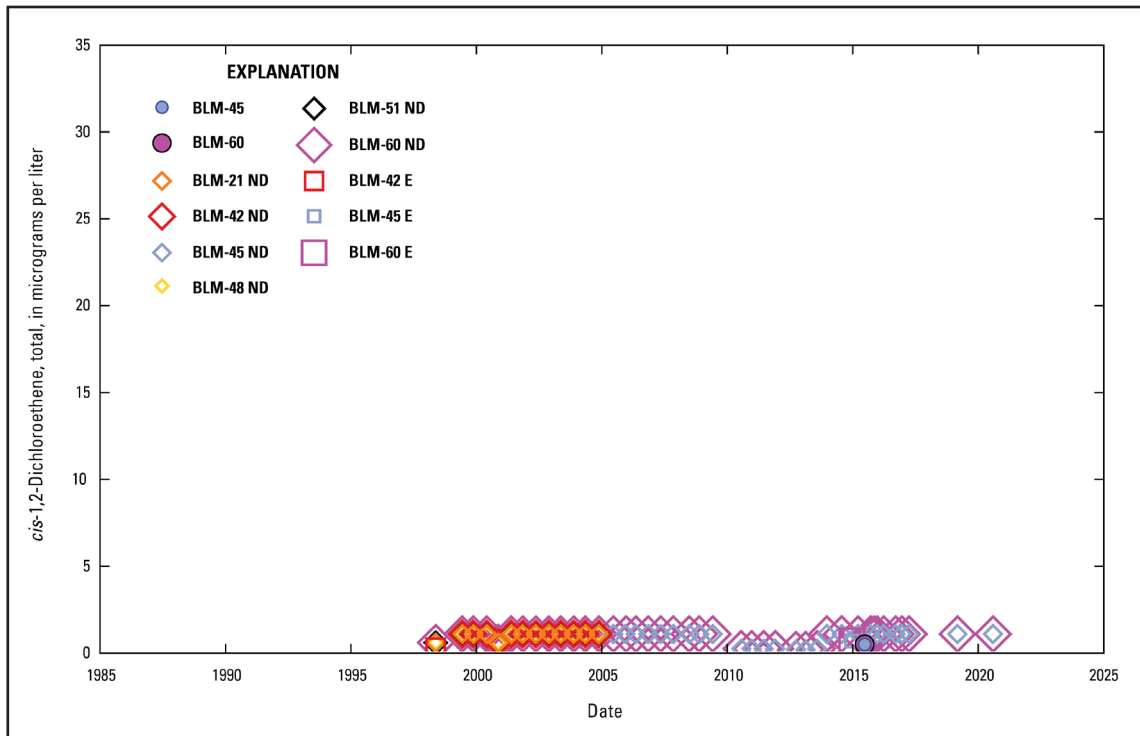


Figure 57. *cis*-1,2-Dichloroethene concentration over time at Bureau of Land Management (BLM) monitoring wells adjacent to the Lee Acres Landfill near Farmington, New Mexico. Locations of wells are shown in Figure 4; data sources are specified in Table 8. As shown in Table 1, *cis*-1,2-dichloroethene was not detected in the alluvial aquifer background samples collected at the Lee Acres Landfill (Roy F. Weston, Inc., 1995), and the cleanup level for *cis*-1,2-dichloroethene at the Lee Acres Landfill is 70 micrograms per liter (U.S. Environmental Protection Agency, 2004). ND, no detection above method detection limits; E, estimated results.

32) were not detected above reporting levels. *cis*-1,2-Dichloroethene concentrations range from no detection above reporting levels (multiple dates) to 7.1 µg/L (May 20, 1998) (Figure 58). *trans*-1,2-Dichloroethene was not detected above reporting levels. Tetrachloroethene results range from no detection above reporting levels (multiple dates) to 3 µg/L (May 20, 1998, and September 2, 1998) (Figure 62). Trichloroethene (Figure 65) and vinyl chloride were not detected above reporting levels.

BLM-75 was sampled from May 1998 to August 2020 (Table 8). At this well, there are no results for dissolved iron. Total chloride concentrations range from 38 mg/L (May 11, 2006) to 300 mg/L (May 19, 1998) (Figure 11). Dissolved manganese concentrations range from no detection above reporting levels (multiple dates) to 1,600 µg/L (June 16, 2005) (Figure 18). Dissolved nickel concentrations range from no detection above reporting levels (multiple dates) to 600 µg/L (September 17, 2015) (Figure 25). Dissolved chromium concentrations range from no detection above reporting levels (multiple dates) to 40 µg/L (September 17, 2015) (Figure 32). Results for *cis*-1,2-dichloroethene range from no detection above reporting levels (multiple dates) to 0.3 µg/L (June 23, 2015) (Figure 58). Other organic COCs described in the ROD were not detected above reporting levels.

BLM-76 was sampled from May 1998 to November 2004 (Table 8). At this well, there are no results for dissolved iron. Total chloride concentrations range from 48 mg/L (May 14, 2003) to 170 mg/L (June 9, 1999) (Figure 11). Dissolved manganese concentrations range from no detection above reporting levels (multiple dates) to 1,700 µg/L (May 19, 1998) (Figure 18). Dissolved nickel concentrations range from no detection above reporting levels (multiple dates) to 50 µg/L (May 19, 1998) (Figure 25). Dissolved chromium was not detected

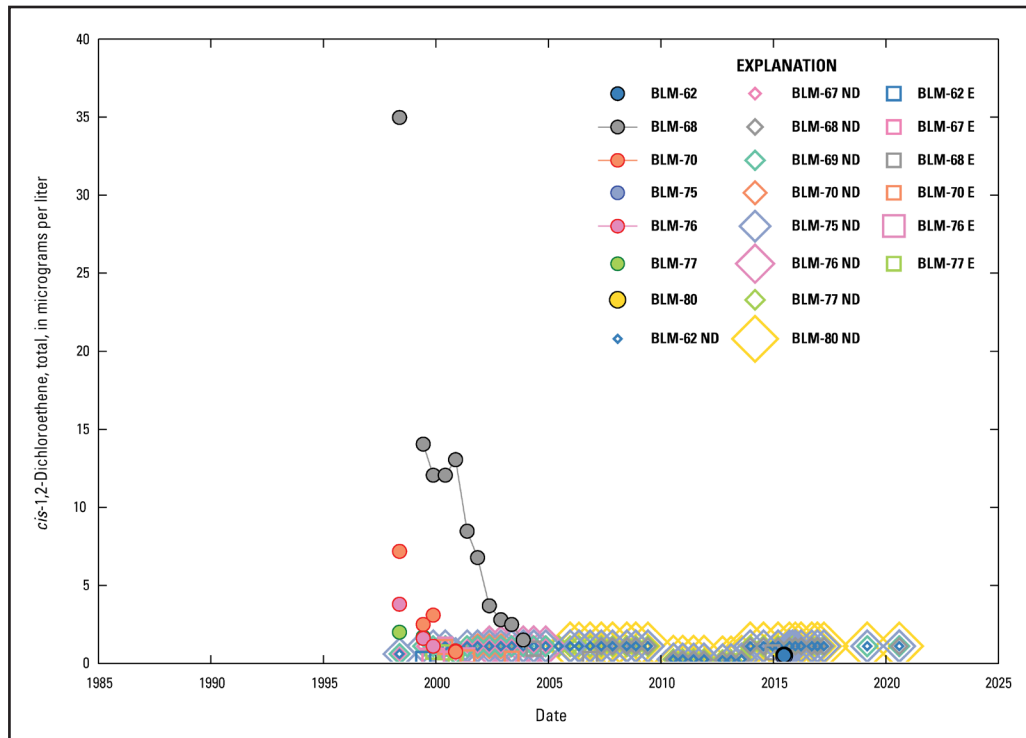


Figure 58. *cis*-1,2-Dichloroethene concentration over time at Bureau of Land Management (BLM) monitoring wells directly downgradient from the Lee Acres Landfill near Farmington, New Mexico. Locations of wells are shown in Figure 5; data sources are specified in Table 8. As shown in Table 1, *cis*-1,2-dichloroethene was not detected in the alluvial aquifer background samples collected at the Lee Acres Landfill (Roy F. Weston, Inc., 1995), and the cleanup level for *cis*-1,2-dichloroethene at the Lee Acres Landfill is 70 micrograms per liter (U.S. Environmental Protection Agency, 2004). ND, no detection above method detection limits; E, estimated results.

above reporting levels (Figure 32). Results for *cis*-1,2-dichloroethene range from no detection above reporting levels (multiple dates) to 3.7 µg/L (May 19, 1998) (Figure 58). *trans*-1,2-Dichloroethene was not detected above reporting levels. Tetrachloroethene was not detected above reporting levels except in two samples: 2 µg/L on May 19, 1998, and 1.3 µg/L on June 9, 1999 (Figure 62). Trichloroethene (Figure 65) and vinyl chloride were not detected above reporting levels.

BLM-77 was sampled from May 1998 to August 2020 (Table 8). At this well, there are no results for dissolved iron. Total chloride concentrations range from 44 mg/L (July 22, 2010) to 170 mg/L (June 8, 1999) (Figure 11). Dissolved manganese concentrations range from no detection above reporting levels (multiple dates) to 29,000 µg/L (December 19, 2013) (Figure 18). Dissolved nickel concentrations range from no detection above reporting levels (multiple dates) to 42 µg/L (June 8, 1999, and November 18, 1999) (Figure 25). Dissolved chromium concentrations range from no detection above reporting levels (multiple dates) to 10 µg/L (September 17, 2015) (Figure 32). *cis*-1,2-Dichloroethene was detected above reporting levels in only two samples (Figure 58): 1.9 µg/L on May 19, 1998, and 1.6 µg/L on June 8, 1999. *trans*-1,2-Dichloroethene was not detected above reporting levels. Tetrachloroethene concentrations range from no detection above reporting levels (multiple dates) to 2 µg/L (May 19, 1998, and September 1, 1998) (Figure 62). Trichloroethene (Figure 65) and vinyl chloride were not detected above reporting levels.

BLM-80 was sampled from December 2005 to August 2020 (Table 8). At this well, there are no results for dissolved iron. Total chloride concentrations range from 19 mg/L (December 20, 2005; May 11, 2006; June 26, 2008; and December 19, 2013) to 220 mg/L (December 15, 2016) (Figure 11). Dissolved manganese

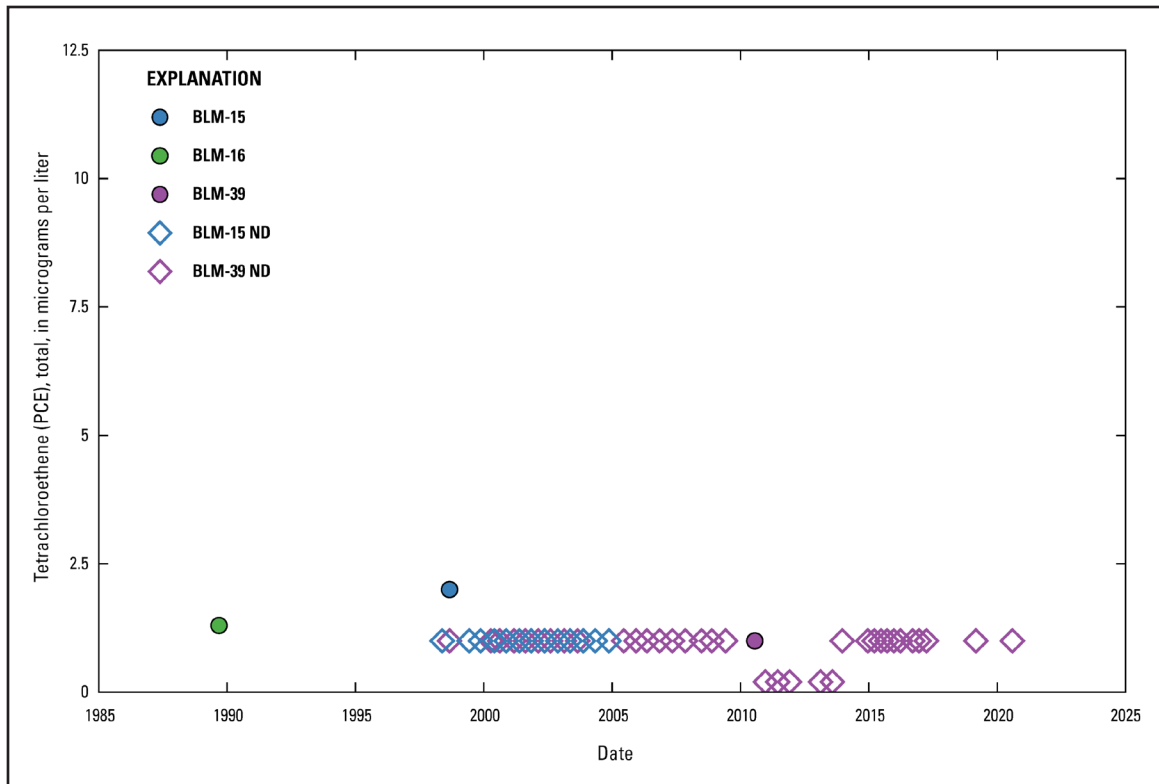


Figure 59. Tetrachloroethene (perchloroethylene [PCE]) concentration over time at Bureau of Land Management (BLM) monitoring wells upgradient from the Lee Acres Landfill near Farmington, New Mexico. Locations of wells are shown in Figure 3; data sources are specified in Table 8. As shown in Table 1, tetrachloroethene was not detected in the alluvial aquifer background samples collected at the Lee Acres Landfill (Roy F. Weston, Inc., 1995), and the cleanup level for tetrachloroethene at the Lee Acres Landfill is 5 micrograms per liter (U.S. Environmental Protection Agency, 2004). ND, no detection above method detection limits.

concentrations range from 340 µg/L (March 4, 2019) to 990 µg/L (December 19, 2013) (Figure 18). Dissolved nickel (Figure 25) and dissolved chromium (Figure 32) were not detected above reporting levels. *cis*-1,2-Dichloroethene was not detected above reporting levels except in one sample with a concentration of 0.4 µg/L on June 23, 2015 (Figure 58). Tetrachloroethene was not detected above reporting levels except in one sample with a concentration of 1 µg/L on March 25, 2016 (Figure 62). The remainder of the organic COCs described in the ROD were not detected above reporting levels.

DATABASE ADVANTAGES AND LIMITATIONS

LAGBRD is a tool that can be leveraged to provide a deeper understanding of groundwater contamination and the background geochemistry at the Lee Acres Landfill and GBR. While not an interpretive product, the data within LAGBRD could be used in future analyses, such as a comparative study of the groundwater chemistry at both sites that accounts for spatial and temporal trends. This type of study could provide insight into the sources of contamination in groundwater at these sites. A notable benefit of having water chemistry results compiled in LAGBRD is the ease with which chemical trends in groundwater could be reviewed and analyzed.

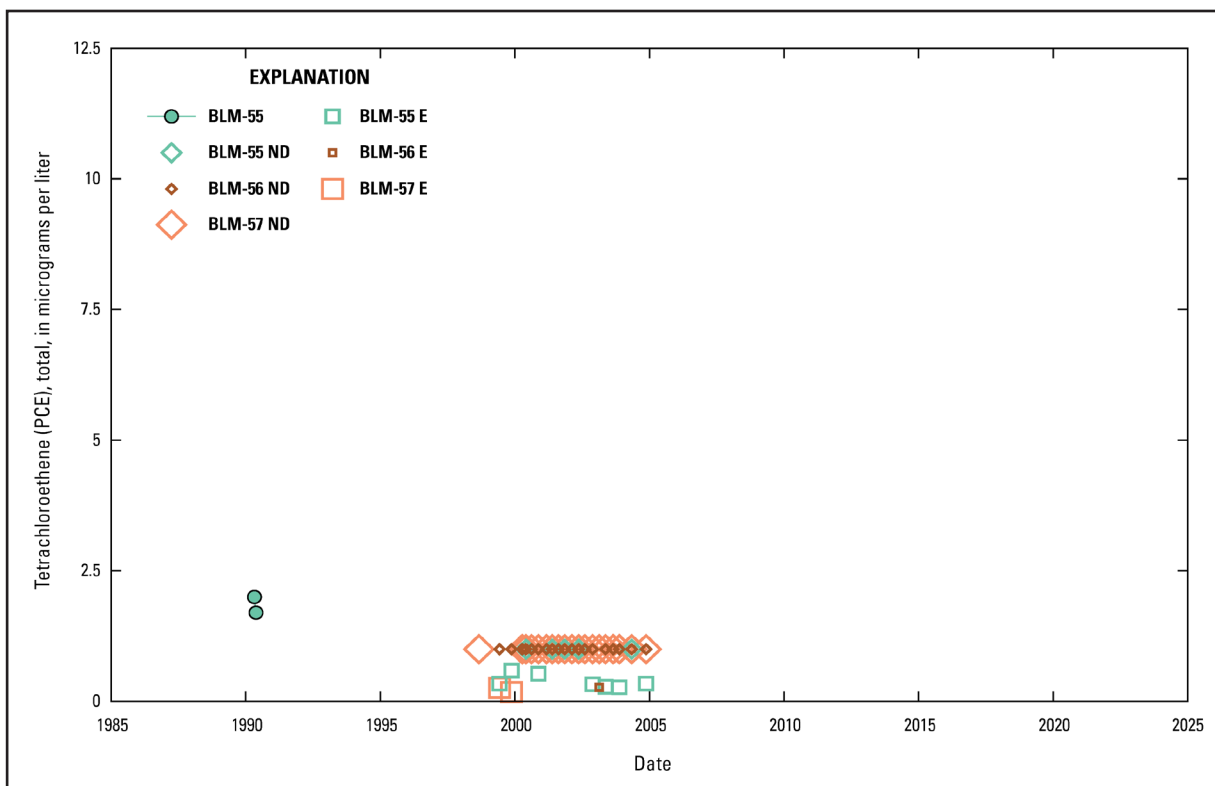


Figure 60. Tetrachloroethene (perchloroethylene [PCE]) concentration over time at Bureau of Land Management (BLM) monitoring wells within the boundary of the Lee Acres Landfill near Farmington, New Mexico. Locations of wells are shown in Figure 4; data sources are specified in Table 8. As shown in Table 1, tetrachloroethene was not detected in the alluvial aquifer background samples collected at the Lee Acres Landfill (Roy F. Weston, Inc., 1995), and the cleanup level for tetrachloroethene at the Lee Acres Landfill is 5 micrograms per liter (U.S. Environmental Protection Agency, 2004). ND, no detection above method detection limits; E, estimated results.

A difficulty encountered during the compilation of data within LAGBRD is related to the disparity among sampling methods, analytical methods, and record keeping of data from different sources. For instance, regular groundwater samples collected at the Lee Acres Landfill are analyzed for dissolved metals, whereas GBR has analyzed samples for total (unfiltered) metals since 2011; hence, these results are not comparable. Additionally, regular sampling at the Lee Acres Landfill does not include sampling and analysis of iron, a metal that is regularly detected at elevated levels at GBR. Future work could benefit from coordination of sampling protocols between the Lee Acres Landfill and GBR. Finally, manganese, which at BLM wells is the COC that consistently exceeds cleanup goals described in the ROD (EPA, 2004), is sensitive to reducing conditions (McMahon and others, 2019). The cleanup goal for manganese (Table 1) is 346 µg/L. Expanding the sampling plan at Lee Acres Landfill to include more redox sensitive species could lead to a better understanding of manganese mobility in groundwater at the Lee Acres Landfill.

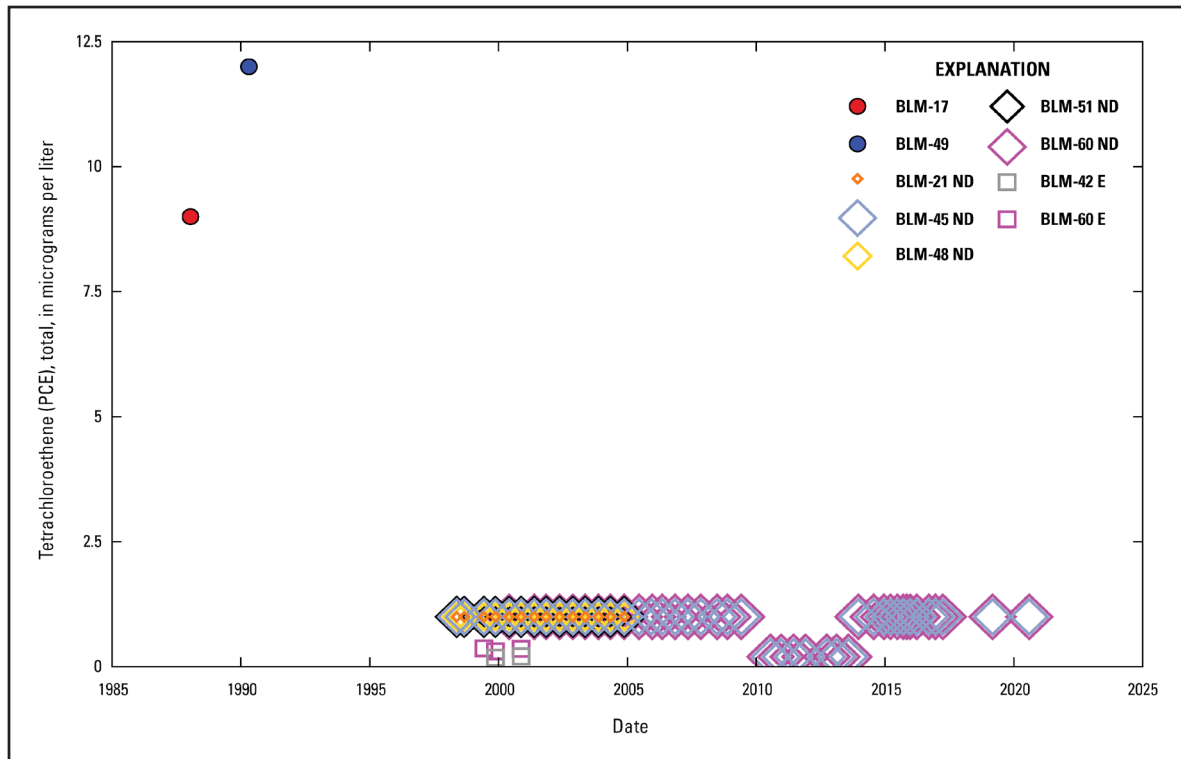


Figure 61. Tetrachloroethene (perchloroethylene [PCE]) concentration over time at Bureau of Land Management (BLM) monitoring wells adjacent to the Lee Acres Landfill near Farmington, New Mexico. Locations of wells are shown in Figure 4; data sources are specified in Table 8. As shown in Table 1, tetrachloroethene was not detected in the alluvial aquifer background samples collected at the Lee Acres Landfill (Roy F. Weston, Inc., 1995), and the cleanup level for tetrachloroethene at the Lee Acres Landfill is 5 micrograms per liter (U.S. Environmental Protection Agency, 2004). ND, no detection above method detection limits; E, estimated results.

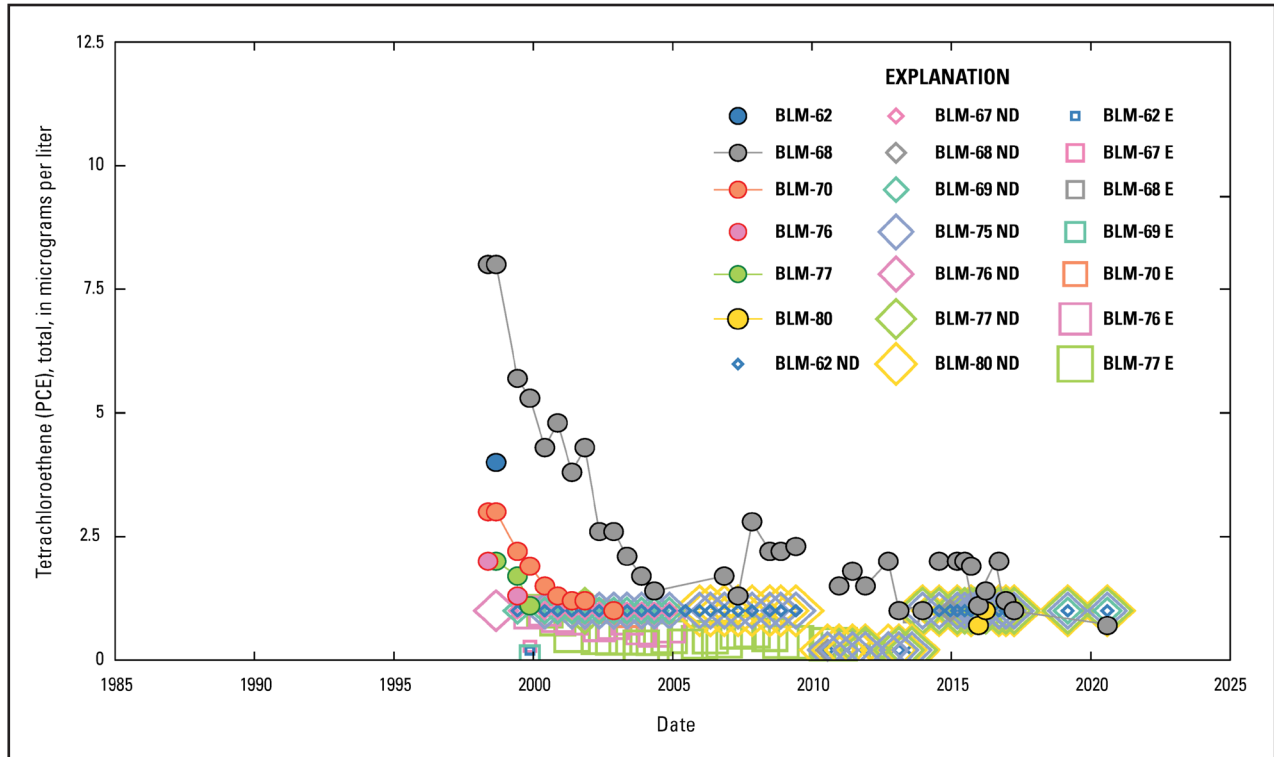


Figure 62. Tetrachloroethene (perchloroethylene [PCE]) concentration over time at Bureau of Land Management (BLM) monitoring wells directly downgradient from the Lee Acres Landfill near Farmington, New Mexico. Locations of wells are shown in Figure 5; data sources are specified in Table 8. As shown in Table 1, tetrachloroethene was not detected in the alluvial aquifer background samples collected at the Lee Acres Landfill (Roy F. Weston, Inc., 1995), and the cleanup level for tetrachloroethene at the Lee Acres Landfill is 5 micrograms per liter (U.S. Environmental Protection Agency, 2004). ND, no detection above method detection limits; E, estimated results.

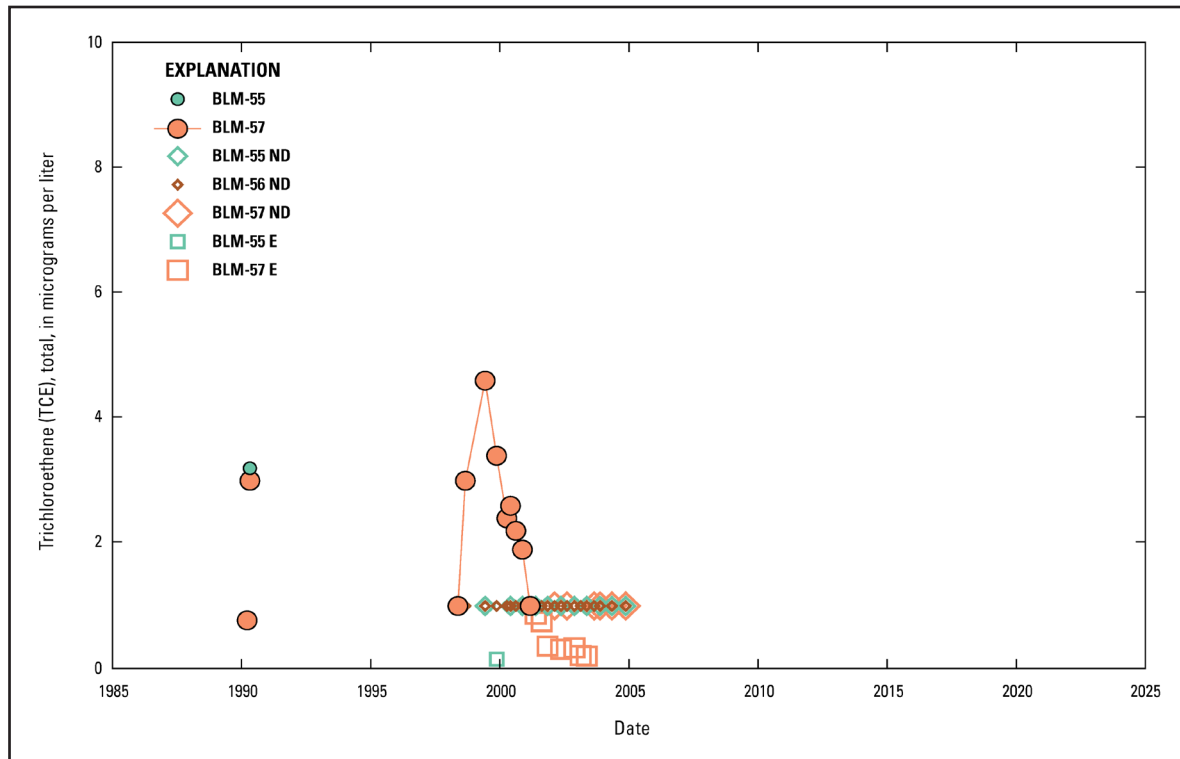


Figure 63. Trichloroethene (TCE) concentration over time at Bureau of Land Management (BLM) monitoring wells within the boundary of the Lee Acres Landfill near Farmington, New Mexico. Locations of wells are shown in Figure 4; data sources are specified in Table 8. As shown in Table 1, trichloroethene was eliminated as a background contaminant in the alluvial aquifer at the Lee Acres Landfill (Roy F. Weston, Inc., 1995), and the cleanup level for trichloroethene at the Lee Acres Landfill is 5 micrograms per liter (U.S. Environmental Protection Agency, 2004). ND, no detection above method detection limits; E, estimated results.

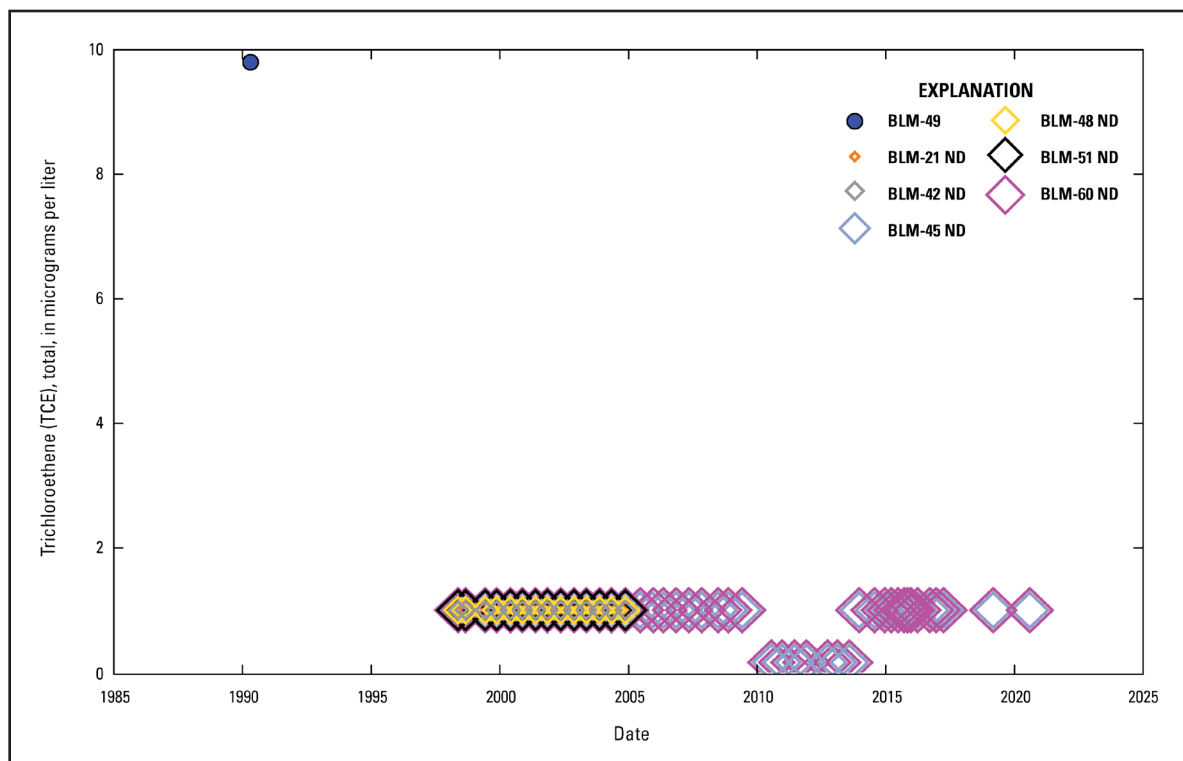


Figure 64. Trichloroethene (TCE) concentration over time at Bureau of Land Management (BLM) monitoring wells adjacent to the Lee Acres Landfill near Farmington, New Mexico. Locations of wells are shown in Figure 4; data sources are specified in Table 8. As shown in Table 1, trichloroethene was eliminated as a background contaminant in the alluvial aquifer at the Lee Acres Landfill (Roy F. Weston, Inc., 1995), and the cleanup level for trichloroethene at the Lee Acres Landfill is 5 micrograms per liter (U.S. Environmental Protection Agency, 2004). ND, no detection above method detection limits.

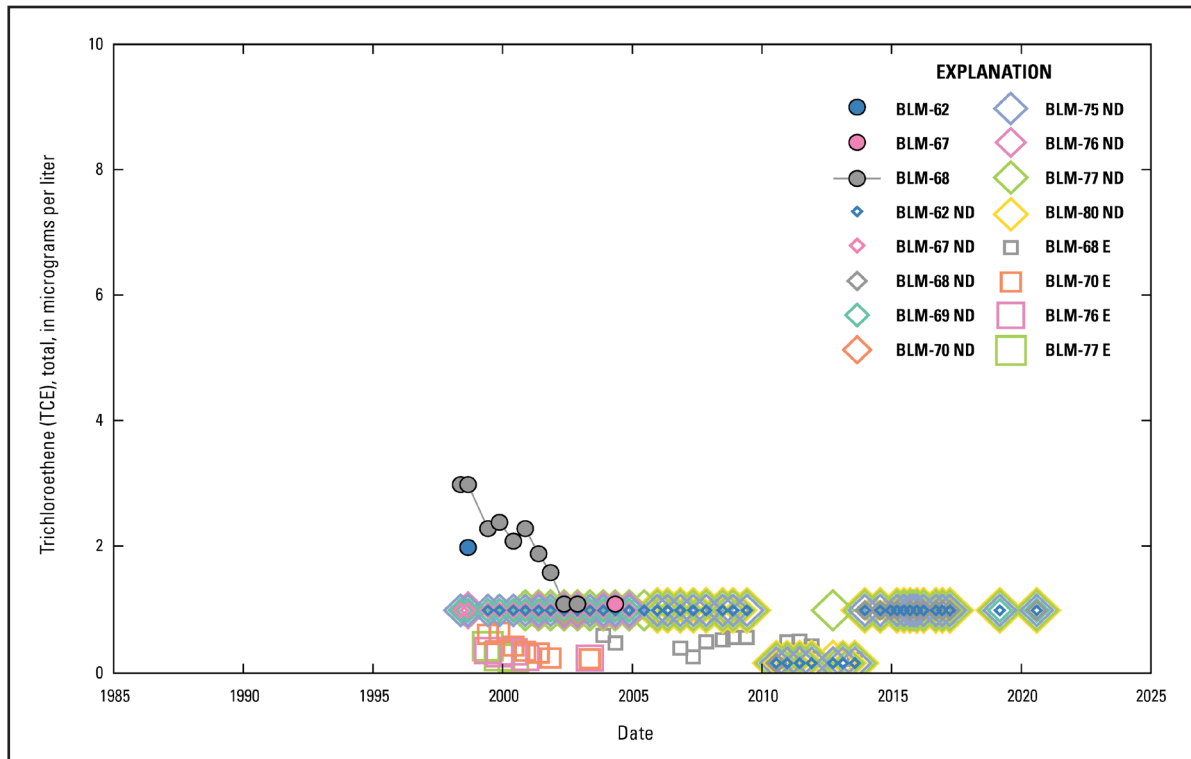


Figure 65. Trichloroethene (TCE) concentration over time at Bureau of Land Management (BLM) monitoring wells directly downgradient from the Lee Acres Landfill near Farmington, New Mexico. Locations of wells are shown in Figure 5; data sources are specified in Table 8. As shown in Table 1, trichloroethene was eliminated as a background contaminant in the alluvial aquifer at the Lee Acres Landfill (Roy F. Weston, Inc., 1995), and the cleanup level for trichloroethene at the Lee Acres Landfill is 5 micrograms per liter (U.S. Environmental Protection Agency, 2004). ND, no detection above method detection limits; E, estimated results.

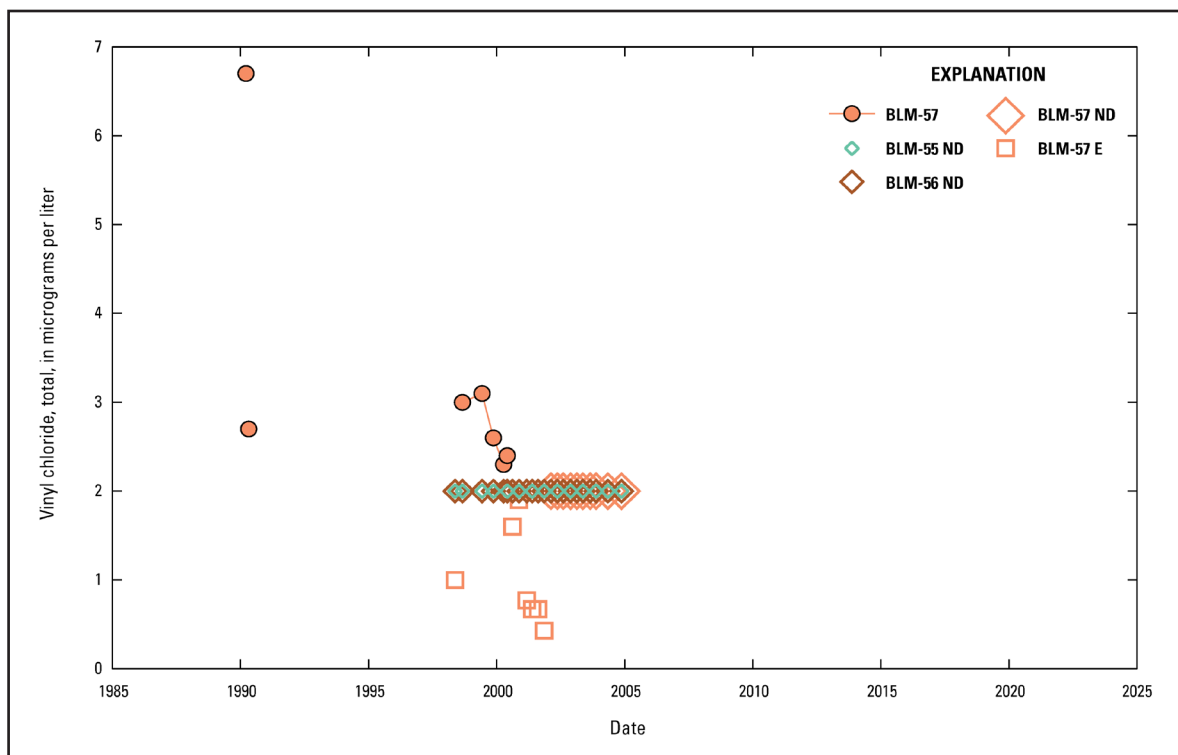


Figure 66. Vinyl chloride concentration over time at Bureau of Land Management (BLM) monitoring wells within the boundary of the Lee Acres Landfill near Farmington, New Mexico. Locations of wells are shown in Figure 4; data sources are specified in Table 8. As shown in Table 1, vinyl chloride was not detected in the alluvial aquifer background samples collected at the Lee Acres Landfill (Roy F. Weston, Inc., 1995), and the cleanup level for vinyl chloride at the Lee Acres Landfill is 1 microgram per liter (U.S. Environmental Protection Agency, 2004). ND, no detection above method detection limits; E, estimated results.

SUMMARY

At the Lee Acres Landfill and the Giant Bloomfield Refinery (GBR), near Farmington, New Mexico, the long history of groundwater monitoring and involvement of various parties have led to a variety of disparate data sources in several formats. The Lee Acres-Giant Bloomfield Refinery Database (LAGBRD) is a Microsoft Access database that is a compilation of publicly available water quality and groundwater elevation data from the Lee Acres Landfill and GBR sites that span from 1985, when awareness was increasing regarding contamination from liquid waste lagoons at the landfill and fuel releases at the refinery, to 2020. Sources of data represented in LAGBRD include the U.S. Geological Survey National Water Information System, data collected by GBR for monitoring required by the New Mexico Oil Conservation Division, and site investigation data from both the landfill and the refinery.

This report discusses the purpose and structure of LAGBRD and contains maps of sampling locations and site features at the Lee Acres Landfill and GBR. This report also contains time-series plots created using LAGBRD data including total chloride, chloride of unknown filtration status, dissolved manganese, dissolved nickel, dissolved chromium, dissolved iron, *cis*-1,2-dichloroethene, tetrachloroethene, trichloroethene, and vinyl chloride, as well as time-series plots of total manganese, total nickel, total chromium, and total iron in GBR wells where dissolved metals were not consistently measured. The Figures in this report can be used for reference by site managers to visualize the spatial and temporal relationships of data from the Lee Acres Landfill and GBR. However, this report does not interpret the data or explain why several metals continue to exceed regional background levels in monitoring wells at these sites. Dissolved manganese concentrations in several Bureau of Land Management and GBR monitoring wells downgradient from the landfill continue to be elevated relative to alluvial aquifer background concentrations. Furthermore, dissolved chromium and dissolved iron have exceeded regional background levels at several GBR wells upgradient from refinery operations. LAGBRD is a tool that can be leveraged for future work related to groundwater contamination and the background geochemistry at these sites.

ACKNOWLEDGMENTS

The authors would like to acknowledge the contributions of the Farmington Field Office of the Bureau of Land Management to this work.

REFERENCES

- Geoscience Consultants, Ltd., 1988, Discharge plan application for Giant Bloomfield Refinery, Bloomfield, NM: Montgomery & Andrews, P.A., prepared by Geoscience Consultants, Ltd., 77 p., accessed November 24, 2020, at https://ocdimage.emnrd.state.nm.us/Imaging/FileStore/santafeenvironmental/ao/b-51571/penv000gw00042_0007.pdf
- Giant Industries Arizona, Inc., 1993, Discharge plan: Farmington, New Mexico, State of New Mexico, Energy, Minerals and Natural Resources Department, Oil Conservation Division, prepared by Giant Industries Arizona, Inc., 46 p., accessed November 24, 2020, at https://ocdimage.emnrd.state.nm.us/Imaging/FileStore/santafeenvironmental/ao/b-51571/penv000gw00042_0004.pdf
- LT Environmental, Inc., 2020, Stage 1 abatement plan, former Giant Bloomfield Refinery, Bloomfield, New Mexico: Western Refining, Inc., prepared by LT Environmental, Inc., 10 p., accessed November 24, 2020, at https://ocdimage.emnrd.state.nm.us/Imaging/FileStore/santafeenvironmental/ao/20200911/penv000gw00042_09_11_2020_11_38_27.pdf
- McMahon, P.B., Belitz, K., Reddy, J.E., and Johnson, T.D., 2019, Elevated manganese concentrations in United States groundwater, role of land surface–soil–aquifer connections: *Environmental Science & Technology*, v. 53, no. 1, p. 29–38, accessed April 23, 2021, at <https://doi.org/10.1021/acs.est.8b04055>
- New Mexico Environment Department [NMED], 1986, Water-quality investigations at the Lee Acres Landfill and vicinity, San Juan County, New Mexico: Santa Fe, New Mexico, New Mexico Environment Department, 47 p.
- New Mexico Oil Conservation Division [NMOCD], 2021, OCD online imaging, administrative/environmental order search—Order number GW–40, entity Giant Bloomfield Refinery: New Mexico Oil Conservation Division web page, accessed January 21, 2021, at <https://ocdimage.emnrd.state.nm.us/imaging/AEOrderFileView.aspx?appNo=pENV000GW00042>
- Roy F. Weston, Inc., 1991, Remedial investigation briefing document for the Lee Acres Landfill: U.S. Department of the Interior Bureau of Land Management, prepared by Roy F. Weston, Inc., 269 p., accessed November 24, 2020, at https://ocdimage.emnrd.state.nm.us/Imaging/FileStore/santafeenvironmental/ao/b-51571/penv000gw00042_0017.pdf
- Roy F. Weston, Inc., 1995, Remedial investigation report for the Lee Acres Landfill, volume 1, final: U.S. Department of the Interior Bureau of Land Management, prepared by Roy F. Weston, Inc., 544 p.
- U.S. Environmental Protection Agency [EPA], 2004, Record of decision for the Lee Acres Landfill superfund site, Farmington, New Mexico: U.S. Environmental Protection Agency Region 6 Superfund Division, 92 p., accessed January 21, 2021, at <https://semspub.epa.gov/work/06/171035.pdf>
- U.S. Geological Survey [USGS], 2021, USGS water data for the Nation: U.S. Geological Survey National Water Information System database, accessed January 23, 2021, at <https://waterdata.usgs.gov/nwis/>

For more information about this report, contact

Director, New Mexico Water Science Center
U.S. Geological Survey
6700 Edith Blvd. NE
Albuquerque, NM 87113

For additional information, visit

<https://www.usgs.gov/centers/nm-water>

For more information on the USGS—the Federal source for science about the Earth, its natural and living resources, natural hazards,
and the environment—visit <https://www.usgs.gov> or call 1–888–ASK–USGS.

CONVERSION FACTORS

U.S. customary units to International System of Units		
Multiply	By	To obtain
Length		
inch (in.)	2.54	centimeter (cm)
inch (in.)	25.4	millimeter (mm)
foot (ft)	0.3048	meter (m)
mile (mi)	1.609	kilometer (km)
Area		
acre	4,047	square meter (m ²)
acre	0.4047	hectare (ha)
acre	0.4047	square hectometer (hm ²)
acre	0.004047	square kilometer (km ²)
Volume		
gallon (gal)	3.785	liter (L)
Mass		
ounce, avoirdupois (oz)	28.35	gram (g)

Temperature in degrees Celsius (°C) may be converted to degrees Fahrenheit (°F) as follows:
 $^{\circ}\text{F} = (1.8 \times ^{\circ}\text{C}) + 32.$

DATUM

Vertical coordinate information is referenced to the North American Vertical Datum of 1988 (NAVD 88) or the National Geodetic Vertical Datum of 1929 (NGVD 29), as indicated.

Horizontal coordinate information is referenced to the North American Datum of 1983 (NAD 83) or the North American Datum of 1927 (NAD 27), as indicated.

Altitude, as used in this report, refers to distance above the vertical datum.

SUPPLEMENTAL INFORMATION

Specific conductance is given in microsiemens per centimeter at 25 degrees Celsius ($\mu\text{S}/\text{cm}$ at 25 °C).

Concentrations of chemical constituents in water are given in either milligrams per liter (mg/L [parts per million]) or micrograms per liter ($\mu\text{g}/\text{L}$ [parts per billion]).

ABBREVIATIONS

BLM	Bureau of Land Management
COC	contaminant of concern
E	estimated results
EPA	U.S. Environmental Protection Agency
GBR	Giant Bloomfield Refinery
LAGBRD	Lee Acres-Giant Bloomfield Refinery Database
ND	no detection above method detection limits
NMED	New Mexico Environment Department
NMOCD	New Mexico Oil Conservation Division
NWIS	National Water Information System
ROD	record of decision
USGS	U.S. Geological Survey

Water Quality at Chaco Culture National Historical Park and the Potential Effects of Hydrocarbon Extraction

Benjamin S. Linhoff¹, Kimberly R. Beisner¹, and Zachary M. Shephard¹

¹U.S. Geological Survey, New Mexico Water Science Center, USA

Andrew G. Hunt²

²U.S. Geological Survey, Noble Gas Laboratory, USA

ABSTRACT

Study region: Chaco Culture National Historical Park (CCNHP) is in the San Juan Basin of northwestern New Mexico, U.S.A. Its only water supply is in Gallup Sandstone aquifer, stratigraphically surrounded by layers long targeted for oil and natural gas extraction.

Study focus: To assess groundwater flow direction, age, mixing between aquifers, and whether hydrocarbons extraction may affect water quality, we completed a geochemical groundwater sampling campaign. Groundwater at 11 sites was analyzed for major ions, hydrocarbon associated volatile organic carbon (VOC) compounds, noble gases, and the isotope systems $\delta^2\text{H}$, $\delta^{18}\text{O}$, $^{87}\text{Sr}/^{86}\text{Sr}$, $\delta^{13}\text{C}$, and ^{14}C .

New hydrological insights for the region: Results demonstrate that all sampled groundwaters are exceedingly old and geochemically evolved, with a median ^{14}C age of ~41,000 years before present and a north flowing path. Three lines of evidence suggest mixing between aquifers through relatively impermeable shale units and mixing with hydrocarbons: 1) noble gases are fractionated likely through mixing with connate water expelled during hydrocarbon genesis; 2) several wells—including the park’s main supply well—contained trace amounts of hydrocarbon related VOC compounds; and 3) major ion analysis shows mixing trends between aquifers. We hypothesize that cross-aquifer mixing may be facilitated through the region’s numerous hydrocarbon related boreholes. Whether our findings are the result of oil and gas extraction or represent the natural state of the aquifers will require more research.

1. INTRODUCTION

The potential effects of oil and natural gas extraction in the San Juan Basin of northwestern New Mexico, U.S.A. (Engler et al., 2015; Kelley et al., 2014; Figure 1) on Chaco Culture National Historical Park (CCNHP) have garnered national attention (e.g. Moe, 2017 and Bryan, 2023), concern from the National Park Service (NPS), and Native American tribes. Nearly 60,000 visitors a year travel to the park, many of whom stay at the park campground. Following decades of unsuccessful attempts to develop usable near-surface water sources (C. Filippone, National Park Service, written communication, 2018), a 944-m deep well (Chaco Well, Site 602; Table 1 and Figure 1) was constructed in the Gallup Sandstone aquifer in 1972. This provided the park with the first reliable drinking water source since it was established in 1907. All park visitors and some members from the surrounding community rely on this water source in the Gallup Sandstone aquifer.

Advances in unconventional hydrocarbon extraction techniques including hydrofracking (HF) have increased the potential for hydrocarbon extraction within the San Juan Basin and many other locations in the U.S.A. (U.S. Energy Information Administration, 2015). Furthermore, in the last decade, a rapid increase in hydrocarbon extraction in the San Juan Basin near CCNHP has targeted the Gallup Sandstone, Mancos Shale, and the surrounding units (Figures 1 and 2; Engler et al., 2015; Kelley et al., 2014).

The 30–60 m thick Gallup Sandstone (Stone et al., 1983) is stratigraphically between thick confining sequences of the lower-permeability Mancos Shale (Figure 2). Both the Mancos Shale and the Gallup Sandstone are in the San Juan Basin and both may contain oil or natural gas (Kelley et al., 2014). Available oil and gas well data—available through the State of New Mexico Oil Conservation Division (<https://www.emnrd.nm.gov/ocd/#gsc.tab=0>)—show that hydrocarbon wells near the park were drilled in the 1950s through 1970s and targeted the Dakota Formation, Entrada Sandstone, Gallup Sandstone, Mancos Shale, and Morrison Formation (Figures 2 and 3). This scenario, whereby the drinking water aquifer is at the same depth as targeted hydrocarbons is likely unique; in general, drinking water aquifers are shallow near-surface aquifers while hydrocarbon bearing units are hundreds or thousands of meters below land surface (Meng and Ashby, 2014). Hence, the Chaco Well may be more vulnerable to contamination from hydrocarbon extraction activities than many other locations.

During HF, hydraulic fracturing fluid (HFF) is injected into a low-permeability petroleum reservoir (such as shale) under high pressure. This fractures the rock formation horizontally and vertically, increasing permeability by orders of magnitude and mobilizing fluids, such as natural gas and oil, which are induced to flow to a well where they are extracted. HF at a single site can be economically viable for decades, and a single well can undergo HF multiple times over its life cycle (Clark et al., 2013). The process is extremely water intensive, routinely requiring 4–16 million gallons of water per well (Clark et al., 2013). Following HF, between 5% and 300% of the initial HFF volume returns to the surface as flowback water (also called produced water). This produced water may be reinjected for HF or disposed of through deep well injection, wastewater treatment facilities, storage in ponds, or released onto the ground surface or into surface waters (Clark et al., 2013; Gallegos and Varela, 2015).

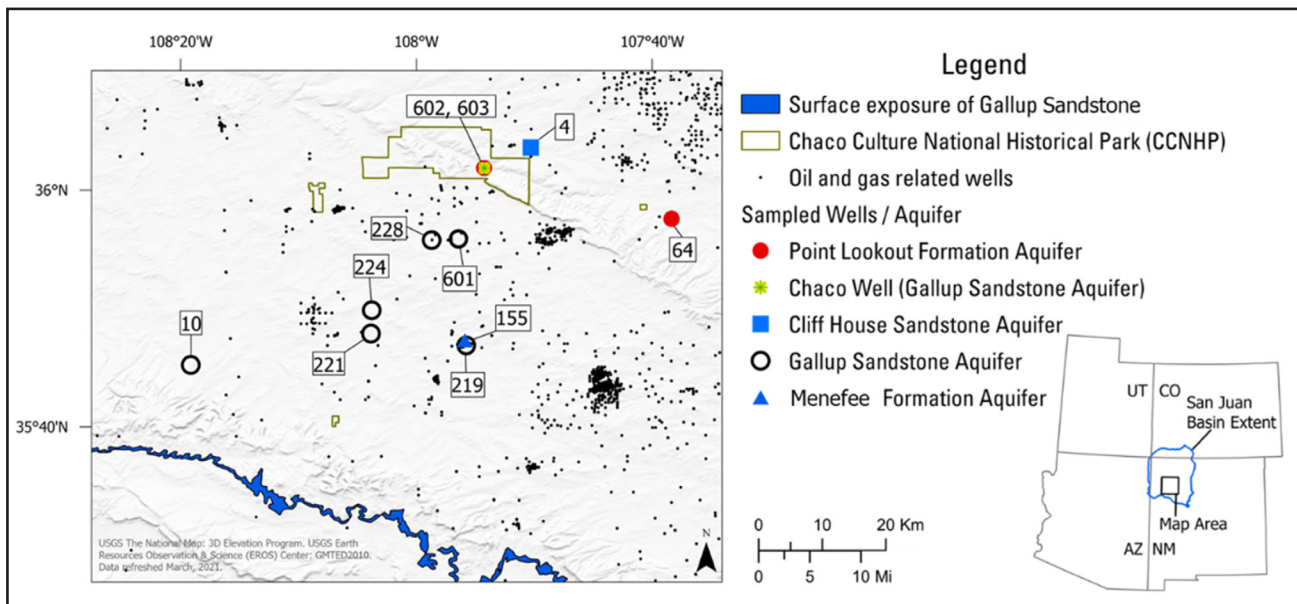


Figure 1. This map of the field area in the San Juan Basin in northwestern New Mexico shows the locations of sampled wells, their respective aquifers, surface exposure of the Gallup Sandstone, and the boundaries of Chaco Culture National Historical Park. Also shown are the locations of oil and gas related wells, most of which are inactive (oil and gas well locations and information is available through the State of New Mexico Oil Conservation Division: <https://www.emnrd.nm.gov/ocd/#gsc.tab=0>)

HFF is a mixture of water, proppants used to maintain fractures, and additives to enhance production such as lubricants, scale reducers, viscosity builders, and biocides to minimize biofouling and souring of the hydrocarbon (Mumford et al., 2018; Stringfellow et al., 2014). Self-reported chemical disclosures of fracturing fluid can be found within the FracFocus database (<https://fracfocus.org/>). Produced water generally has exceedingly high total dissolved solids (TDS; 1000–90,000 mg/L) with elevated Na^+ , CH_4 , Ba^{2+} , Br^- , B , hydrocarbons, and Ra activity (Cozzarelli et al., 2017; Cozzarelli et al., 2021; Gordalla et al., 2013; McIntosh and Ferguson, 2019; Tasker et al., 2020; Wen et al., 2021; Ziemkiewicz, Thomas, 2015). However, the composition of produced waters varies between brines and formations and is controlled by many factors. Ideally, when assessing whether groundwater is mixed with produced waters the composition of both end members is known. An additional concern is the existence of fast-flow pathways between geologic units created by the presence of uncased boreholes distributed around the San Juan Basin, many of which were used for oil and gas exploration (Lacombe et al., 1995). These boreholes as well as improperly cased or plugged boreholes have the potential to transmit fluids and gases from geologic units with high hydrostatic pressure to units with lower hydrostatic pressure (Perra, 2021). The rate at which this short-circuiting flow occurs depends on the hydrostatic pressure differences and the transmissivities of the geologic units or short circuit pathway. Short circuit fluid flow is potentially an important source of fluid migration in the region as there are many inactive oil and gas wells in the San Juan Basin (Figures 1 and 3).

The potential for contamination from hydrocarbon extraction activities to CCNHP is largely unknown due to the lack of knowledge of groundwater flow direction, geochemical evolution, flow velocity, and mixing between aquifers. Additionally, baseline water chemistry in relevant aquifers has not been defined and contamination from HFF and produced waters has not been assessed. The objectives of this work were to complete a geochemical sampling campaign at wells within and outside of CCNHP to determine baseline water chemistry, assess mixing between aquifers, determine groundwater flow directions, and to evaluate whether groundwater has been contaminated or could become contaminated from nearby hydrocarbon extraction activities. Geochemical constituents measured include major ions, noble gases, and isotope systems including strontium ($^{87}\text{Sr}/^{86}\text{Sr}$), deuterium ($\delta^2\text{H}$) and oxygen ($\delta^{18}\text{O}$) in water, and the dissolved inorganic carbon isotopes $\delta^{13}\text{C}$ and ^{14}C . We also measured volatile organic carbon (VOC) compounds including benzene, toluene, ethylbenzene, and xylene (BTEX) compounds, which are often associated with hydrocarbons.

2. METHODS

2.1. Study area

Between 850 and 1250 A.D., CCNHP (Figure 1) was the center of a sophisticated social, political, and architectural civilization with a 130,000 km² sphere of influence (NPS, 2015). Situated in a remote and arid region of northwestern New Mexico, CCNHP protects over 4000 sites—representing 10,000 years of continuous use (NPS, 2015)—including dozens of major complexes, monumental masonry, and earthen structures; many of these structures were the largest buildings in North America until the late 19th century (Lekson, 1984). CCNHP is a United Nations Educational, Scientific and Cultural Organization (UNESCO) World Heritage Site as well as an important religious site for Native Americans (<https://whc.unesco.org/en/list/353/>).

While this study focused on sampling wells screened within the Gallup Sandstone, wells were also sampled in the Point Lookout Sandstone, Menefee Formation and Cliff House Sandstone (Figure 2). The Gallup Sandstone is surrounded by the Mancos Shale and consists of sandstone, shale, and coal. The Chaco Well is located near the Gallup Sandstone's northern extent (Figure 1). The Point Lookout Sandstone is stratigraphically above the Mancos Shale and is composed largely of sandstone. The Menefee Formation, in contrast, is composed of interbedded shale, sandstone, and coal (Kelley et al., 2014). Stratigraphically above this, the Cliff House Sandstone is largely composed of sandstone. All units described above are known to contain oil or natural gas within the San Juan Basin (Brister and Hoffman, 2002).

Previous studies in the San Juan Basin found that groundwater in the Morrison Formation (stratigraphically below the Mancos Shale; Figure 2) had too little ^{14}C to effectively date, concluding that groundwater likely

recharged > 52,000 years before present (ybp; Dam, 1995). Past research has found that recharge to the Gallup Sandstone generally occurs where the unit crops out at the surface ~ 55 km to the south of the Chaco Well (Figure 1; Stone et al., 1983) and that groundwater generally flows from the south to the north through the Gallup Sandstone (Kernodle, 1996). However, more recent groundwater withdrawals and hydrocarbon extraction across the San Juan Basin may have altered groundwater flow paths.

2.2. Field sample collection

Groundwater samples were collected for water chemistry analyses from 11 wells in 2019 and 2020 following U.S. Geological Survey protocols (U.S. Geological Survey, 2021). Sites were sampled once except for wells 602 and 603, which were sampled three times for VOCs. Where possible, historical data (pre-2019) is also presented from the U.S. Geological Survey National Water Information System (NWIS; U.S. Geological Survey, 2021). Wells sampled were artesian—discharging at the surface—except for Sites 4 and 10, which were subartesian and sampled via windmill pump. pH, temperature, water temperature, specific conductance (SC), and dissolved oxygen (O₂) were measured in a flow-through cell prior to sampling at each site (Table 2). Total dissolved solids (TDS) were estimated as the sum of dissolved major ion constituents. Groundwater was discharging at the surface at all sites prior to sampling (either through windmill pump or artesian flow), hence, no purge volume was recorded. Sample bottles were filled following field parameter stabilization. Water samples were filtered through a GWV capsule 0.45 μm filter for major cations, trace elements, alkalinity, nutrients, and carbon and strontium isotopes. Samples collected for VOCs, tritium (³H), and stable isotopes were unfiltered. Major cations, trace elements, and strontium isotope samples were preserved to pH < 2 by adding ultrapure nitric acid. VOC samples were collected in triplicate 40-mL septum capped amber glass vials, filled from the bottom using a high density polyethylene tube until no air bubbles or headspace remained and then acidified to pH < 2 with 1:1 HCl:H₂O. Similarly, carbon isotope samples were collected in 1-L glass bottles filled from the bottom and allowed to flush three bottle volumes before being capped with a polycone cap with no headspace. Tritium samples were collected in 1-L poly bottles following the same bottom filling procedure and cone cap as the carbon isotope samples. Noble gas samples were collected in copper tubes in duplicate; back pressure was applied with a restrictor on the sample tubing past the copper tube to minimize bubble formation prior to sealing the samples with refrigerator clamps (Weiss, 1968). Field alkalinity was computed from titration data using the incremental equivalence method (USGS, 2021). All samples were kept below 4 °C following sample collection. Water levels at windmill sites were measured after stopping the windmill for several hours until groundwater levels were stable. At artesian sites, water levels were measured using a pressure transducer.

Table 1. This table shows the project Site Identification Number (ID) and the USGS Site number as well as location and information about the well and groundwater elevation. A * symbol is used for well depth elevation (el.) where only the hole depth was available. Abbreviations Ss and Fm stand for sandstone and formation respectively. Data from U.S. Geological Survey (2021).

Site ID	USGS Site ID	Aquifer	Latitude	Longitude	Sample Date	Water Level (m)	Site el. (m)	Groundwater el. (m)	Well Depth (m)
4	360336107501801	Cliffhouse	36.06000	-107.83834	8/28/2019	23.38	1931	1907.23	153.92
10	354514108190601	Gallup	35.75391	-108.31896	8/27/2019	48.77	2055	2006.50	393.80
219	354653107554401	Gallup	35.78141	-107.92951	5/31/2019	-8.12	1996	2004.56	350.52
221	354753108034901	Gallup	35.79807	-108.06423	5/30/2019	-16.64	1962	1978.94	504.44
224	354951108034501	Gallup	35.83085	-108.06312	5/30/2019	-20.47	1935	1955.95	1011.94 *
228	355547107584001	Gallup	35.92974	-107.97840	5/29/2019	-24.64	1945	1969.27	887.58
601	355553107562301	Gallup	35.93141	-107.94034	5/29/2019		1951	1951.02	998.22 *
602	360152107541401	Gallup (Chaco Well)	36.03111	-107.90383	8/3/2017	-55.47	1895	1950.42	941.83
155	354724107555201	Menefee fm.	35.79002	-107.93173	5/30/2019		1999	1999.49	
64	355735107382101	Point Lookout	35.95984	-107.63914	8/29/2019		1997	1997.05	511.45
603	360152107541301	Point Lookout	36.03113	-107.90423	1/29/2020	-30.11	1891	1921.40	570.59

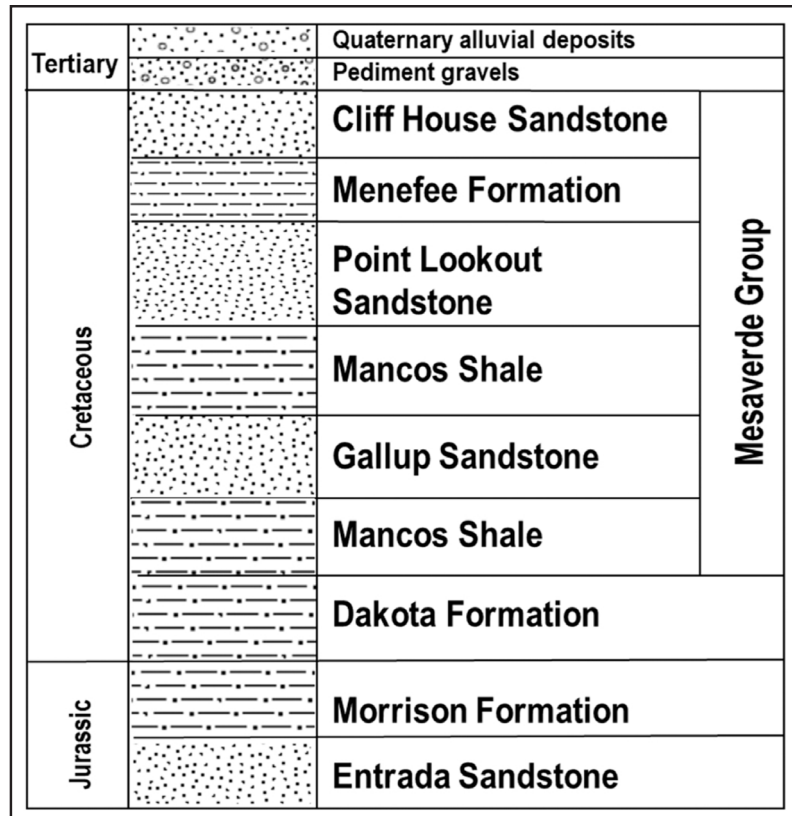


Figure 2. Stratigraphy of major geological units in the San Juan Basin. Samples for this study were collected in the Gallup Sandstone, Point Lookout Sandstone, Cliff House Sandstone, and Menefee Formation. Geologic symbols adapted from Federal Geographic Data Committee (2006).

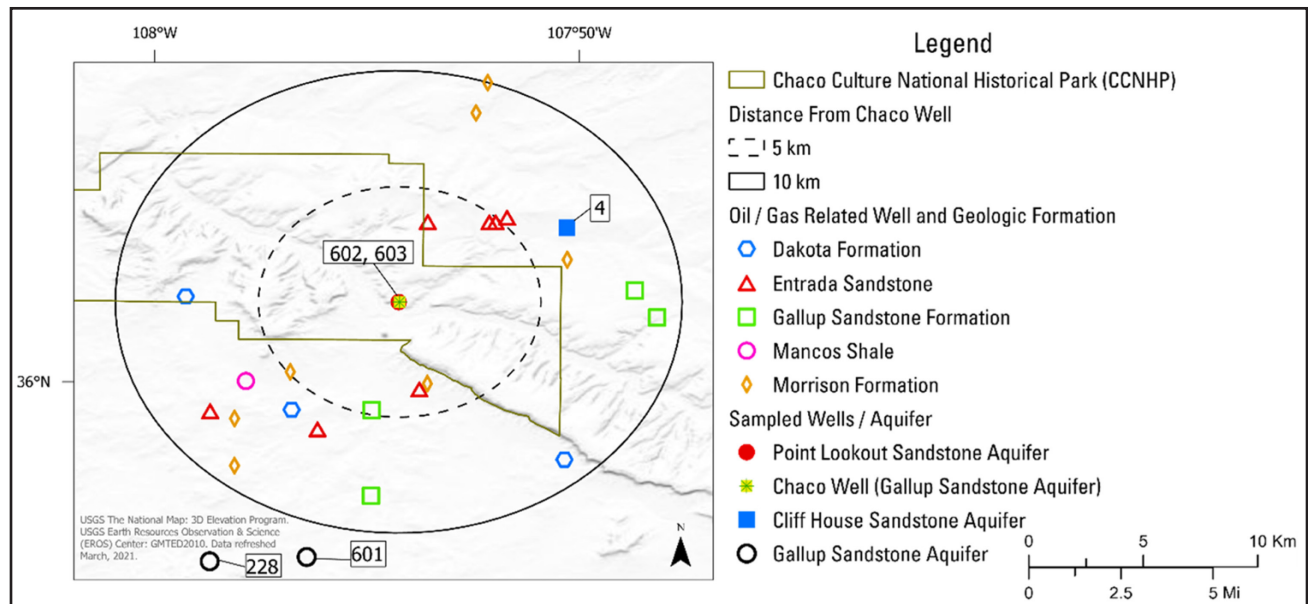


Figure 3. All known hydrocarbon related boreholes within a 10 km radius of the Chaco Well (602). Oil and gas well locations and information is available through the State of New Mexico Oil Conservation Division: <https://www.emnrd.nm.gov/ocd/#gsc.tab=0>

Table 2. Field parameters and nutrient concentrations used for this study. While this study collected samples in 2019 and 2020, historical sampling results from the USGS National Water Information System database are also provided for comparison. Data from U.S. Geological Survey (2021).

Site ID	Date	Temperature °C	SC µS/cm	TDS mg/L	Alkalinity mg/L (as CaCO3)	O2 mmol/L	pH (field) field	NH3 +NH4 mmol/L as N	NO2- mmol/L as N	NO3- mmol/L as N	NO3 +NO2 mmol/L as N	PO4 mmol/L as PO4
Median		21.2	2800	1940	302	0.009	8.5	0.055				
Mean		22.6	3151	2084	434	0.011	8.5	0.050				
4	28-03-1978	14	3000	2350			8.3				0.004	0.0003
10	28-08-2019	18.6	2930	2270	473	0.009	7.8	0.051	< 0.0001	< 0.003	< 0.003	0.0003
219	27-08-2019	21.8	1400	900	176	0.022	8.1	0.024	0.001	< 0.003	< 0.003	0.0002
221	31-05-2019	20.6	3970	2960	362	0.025	8.5	0.056	< 0.0001	< 0.003	< 0.003	0.0003
224	30-05-2019	15	1230	871	264	0.025	9	0.021	< 0.0001	< 0.003	< 0.003	0.0004
228	30-05-2019	14.2	1250	795	265	0.001	9.2	0.022	< 0.0001	< 0.003	< 0.003	0.0006
601	29-05-2019	28.1	2420	1940	225	0.006	8.6	0.057	< 0.0001	< 0.003	< 0.003	0.0003
601	21-04-1986	32.7	2900	1910	210		8.6					
601	29-05-2019	33.5	2920	1990			8.6	0.053	< 0.0001	< 0.003	< 0.003	0.0003
601	27-08-2019	33.3	2680			0.013	8.5					
602	22-04-1986	32.8	2720	1810			8.2					
602	21-10-1987	32.9	2800	2030	290		8.3	0.033	< 0.0001	< 0.003	< 0.003	0.0006
602	22-08-2017	20.5	2800	1860	302	0.003	8.7	0.059	< 0.0001	0.003	0.003	0.0003
155	28-05-2019	15.4	2800	1920	313	0.013	8.3	0.056	< 0.0001	< 0.003	< 0.003	0.0002
64	30-05-2019	15	5710	3910	379	0.003	8.5	0.075	< 0.0001	< 0.003	< 0.003	0.0002
603	29-08-2019	21.7	1750	1150	734	0.009	8.7	0.024	< 0.0001	< 0.003	< 0.003	0.0010
603	10-11-1987		5500	3270	1650		8.1	0.086	< 0.0001	< 0.003	< 0.003	0.0003
603	29-05-2019	14.5	5280	3500		0.001	8.6	0.088	< 0.0001	< 0.003	< 0.003	0.0008
603	04-06-2020	21.7	5800			0.013	8.4		< 0.0001	< 0.003	< 0.003	

2.3. Water chemistry analytical methods

Water samples were analyzed for major cations, trace elements, and nutrients by the USGS National Water Quality Laboratory (NWQL) in Denver, Colorado. Inductively coupled plasma atomic emission spectrometry was used to analyze for cations including calcium (Ca^{2+}), total iron (Fe), magnesium (Mg^{2+}), manganese (Mn^{2+}), potassium (K^+), and sodium (Na^+) (Fishman, 1993). Chloride (Cl^-), fluoride (F^-), and sulfate (SO_4^{2-}) were analyzed by ion chromatography, and dissolved silica (SiO_2) was analyzed by discrete analyzer colorimetry (Fishman and Friedman, 1989). Nitrate (NO_3^-) plus nitrite (NO_2^-) was analyzed by colorimetry (Patton and Kryskalla, 2011). Twenty-three VOC compounds were analyzed by gas chromatography/mass spectrometry (Rose et al., 2016; Connor et al., 1998). Quality assurance and quality control (QA/QC) samples include three field blank samples using certified inorganic blank water, two field blank samples with nitrogen purged organic blank water for VOC analysis, two replicate samples, and three laboratory spikes for VOC samples. Results and discussion of the QA/QC samples are presented in Supplemental Material.

Stable isotope ratios ($\delta^{18}\text{O}$ and $\delta^2\text{H}$ in H_2O) were measured at the USGS Reston Stable Isotope Laboratory in Reston, Virginia. Samples were analyzed using mass spectrometry following methods by Révész and Copley (2008). Two-sigma uncertainties are 0.2‰ for $\delta^{18}\text{O}$ and 2‰ for $\delta^2\text{H}$ reported relative to Vienna Standard Mean Ocean Water (VSMOW). Strontium (Sr) isotope ratios ($^{87}\text{Sr}/^{86}\text{Sr}$) were measured by the USGS National Research Program Laboratory in Menlo Park, California by using multi-collector mass spectrometry following methods described in Bullen et al. (1996); results were precise to 0.00002 or better at the 95-percent confidence level. Noble gases helium (He), neon (Ne), argon (Ar), krypton (Kr), and xenon (Xe) were analyzed by the USGS Noble Gas Laboratory in Lakewood, Colorado using methods described in Hunt (2015). The University of Miami Tritium Laboratory in Miami, Florida measured tritium in samples using electrolytic enrichment and gas counting, with a reporting limit of 0.3 pCi/L. Mineral saturation indexes (SI) were calculated using Geochemist's Workbench (version 15.0; Aqueous Solutions, LLC, Champaign, Illinois).

2.4. Dating groundwater using carbon isotopes

Carbon isotopes—percent modern carbon-14 (PMC) and $\delta^{13}\text{C}$ —were analyzed by the National Ocean Sciences Accelerator Mass Spectrometry (NOSAMS) at the Woods Hole Oceanographic Institution, Massachusetts using accelerator mass spectrometry. To estimate the initial ^{14}C present in these samples ($^{14}\text{C}_0$), we used the program NETPATHXL (Parkhurst and Charlton, 2008; Han and Plummer, 2016) which calculates ^{14}C using the Fontes and Garnier model (Han and Plummer, 2013). This model corrects for the effect of carbon exchange between dissolved inorganic carbon (DIC) and solid carbonate and soil, the major unknowns are the isotopic composition of solid carbonates and soil gas.

Once $^{14}\text{C}_0$ was estimated, age was determined through Eq. (1).

$$t = -\frac{5730}{\ln 2} \ln\left(\frac{^{14}\text{C}_{\text{DIC}}}{^{14}\text{C}_0}\right) \quad (1)$$

where t is the groundwater age in years, 5730 is the half-life of ^{14}C , $^{14}\text{C}_{\text{DIC}}$ is the PMC measured in the sample and $^{14}\text{C}_0$ was the initial ^{14}C present calculated through NETPATHXL assuming solid carbonate exchange is the dominant process impacting the carbon isotopes.

2.5. Noble gas solubility modeling

Noble gas composition is initially set during recharge to an aquifer and is controlled by the partial pressure of the gas phase (mole fraction multiplied by atmospheric pressure), temperature, salinity, and the amount of excess gas entrapped during recharge (e.g., Heaton and Vogel, 1981). An estimate of the initial temperature of water during recharge can be determined by the application of a solubility-based model which takes the measured noble gas compositions and fits the modeled recharge parameters to the data (Aeschbach-Hertig et al., 1999).

We utilized the closed equilibrium (CE) model developed by Aeschbach-Hertig et al. (1999) for noble gas solubility modeling and the DGMETA (Dissolved Gas Modeling and Environmental Tracer Analysis; Jurgens et al., 2020) model to resolve noble gas recharge parameters. Work by Stute and Sonntag (1992), Aeschbach-Hertig et al. (1999), Heaton and Vogle (1981), and Ballentine et al. (2002) showed that excess air components trapped during recharge can vary in composition depending on the degree of equilibration of the trapped air, gas losses, and fractionation of the original air-like component. For implementation of the CE model, measured dissolved noble gas components are compared to modeled concentration values using estimated parameters of temperature (T), initial concentration of entrapped air (Ae), and the reduction of entrapped volume by dissolution and compression, with the assumption that the water was fresh (or low salinity) and the partial pressure of the gases is associated with atmospheric pressure at the elevation of the water table (~1994 m). An error-weighted least squares fit was used to solve for free model parameters (T and Ae) by minimizing chi squared.

All data that support the results and conclusions in this study are available from U.S. Geological Survey (2021) by using the USGS Site Number in Table 1 to compile the data.

3. RESULTS

3.1. Groundwater chemistry and elevation results

In the Gallup Sandstone aquifer, groundwater elevation was highest in the south and lowest in the north implying south to north groundwater flow (Table 1); this is consistent with the findings of Kernodle (1996). SC and TDS were highest in the Menefee Formation aquifer (Well 155; 5710 $\mu\text{S}/\text{cm}$ and 3910 mg/L, respectively) and the Point Lookout Sandstone aquifer at Well 603 (Table 2). Generally, sampled wells had low O_2 concentrations (0.003–0.025 mmol/L O_2), basic pH (7.8–9.2) and low nitrogen and phosphorous (Table 2).

3.2. Noble gas and isotopic results

Noble gas concentrations—shown in Table 3—varied across the field site with Wells 228 and the Chaco Well (Gallup Sandstone aquifer) generally having the highest noble gas concentrations and Well 603 (Point Lookout Sandstone aquifer) having the lowest (with the exception of ^4He). For the seven sites sampled for noble gases, median Ne, ^4He , Ar, Kr, and Xe values were 3.49×10^{-7} , 6.99×10^{-6} , 4.53×10^{-4} , 9.4×10^{-8} , and 9.6×10^{-9} cm^3/g , respectively (Table 3).

The stable isotopes of water ($\delta^2\text{H}$ and $\delta^{18}\text{O}$) were heaviest at Well 64 (Point Lookout Sandstone aquifer) and lightest at Well 228 (Gallup Sandstone aquifer). In the Gallup Sandstone aquifer, $\delta^2\text{H}$ and $\delta^{18}\text{O}$ isotopes were light with respect to other aquifers except for Well 219 which was heavier than the other Gallup Sandstone aquifer samples (Figure 4). Well 602 (Chaco Well) had higher $^{87}\text{Sr}/^{86}\text{Sr}$ values (0.70922) than the rest of the data set (Table 4).

3.3. Groundwater age—tritium and carbon isotopes

Tritium concentrations at all sites were below the instrument detection limit ($^3\text{H} < 0.3$ pCi/L; Table 4). Carbon-14 results were very low (< 1 PMC) except for Well 10 (3.59 PMC; Table 4) in the Gallup Sandstone aquifer in the southern portion of the field area. $\delta^{13}\text{C}$ values ranged from -17.5‰ to -7.55‰ across the study area with the highest values at Well 155 (-7.55‰) and the lowest at Well 4 (-17.5‰).

The lack of detectable tritium in groundwaters likely indicates no mixing with modern waters (Table 4; Linhoff, 2022; Lindsey et al., 2019; Travis et al., 2021). In the absence of inputs from modern waters, carbon isotopes are generally useful indicators of geochemical processes and may help constrain groundwater age. Dam (1995) measured carbon isotopes in the San Juan Basin as part of a larger groundwater chemistry study; in that study, ^{14}C varied between < 0.4 PMC to 6.4 PMC and $\delta^{13}\text{C}$ varied from -7.6 to -26.1‰ in seven samples collected from the Gallup Sandstone aquifer.

When interpreting groundwater ages, chemical processes that alter the initial ^{14}C of dissolved inorganic carbon (DIC) in groundwater must be considered (Cartwright et al., 2020). A graphical method (Figure 5) developed by Han et al. (2012) and Han and Plummer (2013, 2016) was used to recognize processes that might prevent accurate assessment of whether a sample contained ^{14}C that had undergone decay. The method uses the PMC, $\delta^{13}\text{C}$, and HCO_3^- composition of a sample to determine the suitability of a groundwater for age dating. The two triangles in Figure 5 represents the “zero-age” zone; these were constructed according to Han and Plummer (2016) using soil gas $\delta^{13}\text{C}$ values of -20 and -25‰ from Dam (1995). The soil gas $\delta^{13}\text{C}$ values are based on Gallup Sandstone aquifer groundwater in the likely recharge zone south of the field site where the Gallup Sandstone crops out (Figure 1). In Figure 5, all samples plot below the zero-age region and hence are likely old groundwater that has undergone ^{14}C decay and may be dated.

Well 10 in the Gallup Sandstone was the youngest water (~23,000 ybp) followed by Well 4 (37,000 ybp) in the Cliff House Sandstone (Table 4 and Figure 2). Five samples had PMC lower than the method can accurately date and hence are assumed to be older than 52,000 ybp (Table 4). Older ages were found in the northern portion of the field area implying south to north groundwater flow. These age estimates do not take into

Table 3. Results of noble gas analyses including neon (Ne), helium-4 (^4He), argon (Ar), krypton (Kr), and xenon (Xe). Uncertainty is the published method uncertainty in Hunt (2015). Data from U.S. Geological Survey (2021).

Site ID	Date	Ne cm ³ /g	±	⁴ He cm ³ /g	±	Ar cm ³ /g	±	Kr cm ³ /g	±	Xe cm ³ /g	±
Median		3.49E-07		6.99E-06		4.53E-04		9.40E-08		9.60E-09	
Mean		3.41E-07		1.37E-05		4.40E-04		8.76E-08		8.99E-09	
219	5/31/2019	2.77E-07	5.50E-09	3.94E-06	1.87E-08	4.14E-04	8.28E-06	8.90E-08	2.60E-09	9.60E-09	2.00E-10
221	5/30/2019	3.75E-07	7.50E-09	5.54E-06	2.63E-08	4.75E-04	9.51E-06	9.80E-08	2.90E-09	1.08E-08	3.00E-10
224	5/30/2019	3.71E-07	7.40E-09	4.99E-06	2.36E-08	4.81E-04	9.63E-06	9.80E-08	2.90E-09	1.14E-08	3.00E-10
228	5/29/2019	4.18E-07	8.30E-09	1.03E-05	4.90E-08	5.06E-04	1.01E-05	1.01E-07	3.00E-09	1.11E-08	3.00E-10
602	8/22/2017	3.48E-07	5.20E-09	1.95E-05	1.61E-07	4.53E-04	7.18E-06	9.40E-08	2.10E-09	9.30E-09	4.00E-10
155	5/30/2019	3.49E-07	6.90E-09	6.99E-06	3.32E-08	4.40E-04	8.80E-06	8.50E-08	2.50E-09	8.10E-09	2.00E-10
603	5/29/2019	2.48E-07	4.90E-09	4.45E-05	2.11E-07	3.11E-04	6.23E-06	4.79E-08	1.40E-09	2.60E-09	0.00E+00

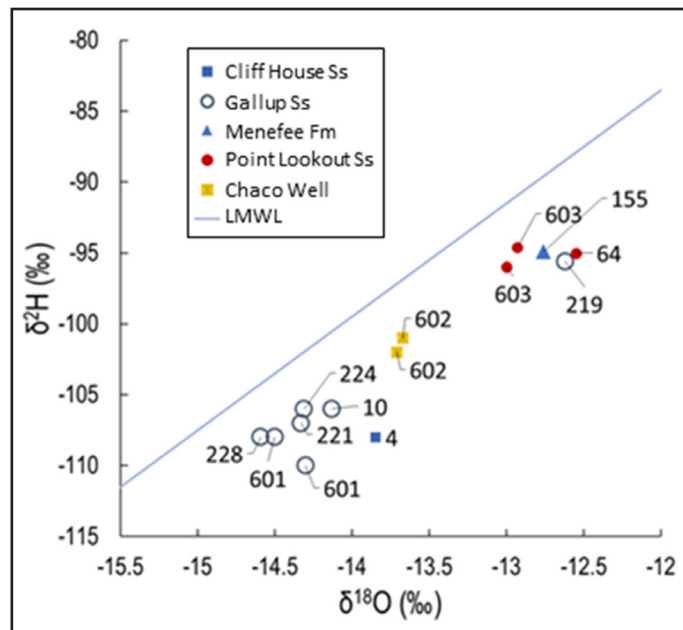


Figure 4. Results from $\delta^{18}\text{O}$ and $\delta^2\text{H}$ analyses along with the local meteoric water line (LMWL) from (Vuataz and Goff, 1986). These data may represent a shifted meteoric water line or a past drier environment (Section 4.2). Abbreviations Ss and Fm stand for Sandstone and Formation, respectively.

Table 4. Results of isotope analyses of carbon (percent modern carbon (PMC) and $\delta^{13}\text{C}$), tritium (^3H), strontium ($^{87}\text{Sr}/^{86}\text{Sr}$), deuterium ($\delta^2\text{H}$), and oxygen ($\delta^{18}\text{O}$). Also shown are estimated radiocarbon ages in years before present (ybp) of groundwater using soil gas $\delta^{13}\text{C}$ values of -20‰ and -25‰ . Five samples had radiocarbon ages greater than the method can resolve ($>52,000$ ybp). Data from U.S. Geological Survey (2021).

Site	Data	^{13}C	^{14}C	^{14}C	^{14}C	Age (-20‰ soil gas ^{13}C)	Age (-25‰ soil gas ^{13}C)	^3H	$^{87}\text{Sr}/^{86}\text{Sr}$	$\delta^2\text{H}$	$\delta^{18}\text{O}$
		‰	pmc	denormalized pmc	error pmc	ybp	ybp	(pCi/ L)		‰	‰
Median		-11.42	0.21	0.22		44865	42921		0.70848	-104	-13.8
Mean		-11.56	0.55	0.56					0.70858	-102	-13.7
4	28-08-2019	-17.48	0.78	0.79	0.06	38,688	36,832	< 0.3		-108	-13.85
10	27-08-2019	-14.19	3.59	3.64	0.07	24,266	22,380	< 0.3		-106	-14.13
219	31-05-2019	-7.85	0.15	0.15	0.05	> 52,000	> 52,000	< 0.3	0.70843	-95.6	-12.62
221	30-05-2019	-12.31	0.31	0.32	0.06	43,194	41,369	< 0.3	0.70844	-107	-14.33
224	30-05-2019	-12.56	0.37	0.38	0.05	41,905	40,087	< 0.3	0.70837	-106	-14.31
228	29-05-2019	-12.45	0.26	0.26	0.05	44,865	42,921	< 0.3	0.70862	-108	-14.59
601	21-04-1986								0.70865	-110	-14.3
601	29-05-2019									-108	-14.5
602	22-08-2017	-10.07	0.06	0.06	0.06	> 52,000	> 52,000	< 0.3		-101	-13.67
602	28-05-2019	-10.05	0.17	0.17	0.06	> 52,000	> 52,000	< 0.3	0.70922	-102	-13.71
155	30-05-2019	-7.55	0.21	0.22	0.05	42,093	40,266	< 0.3	0.70841	-94.9	-12.76
64	29-08-2019	-11.42	0.05	0.05	0.06	> 52,000	> 52,000	< 0.3		-95	-12.55
603	10-11-1987									-96	-13
603	29-05-2019	-11.23	0.1	0.1	0.05	> 52,000	> 52,000	< 0.3	0.70851	-94.6	-12.93

account potential redox reactions. All sites had relatively low dissolved O_2 concentrations as well as reduced forms of nitrogen ($\text{NH}_3 + \text{NH}_4$) and CH_4 ; this could cause an overestimate of ^{14}C ages (Han et al., 2012).

3.4. Major ion results

The major ion composition differs markedly between aquifers (Figure 6, Table 5). Notably, Mg^{2+} and Ca^{2+} are relatively high in the Cliff House Sandstone and Cl^- and HCO_3^- are elevated in groundwaters in the Point Lookout Sandstone. SO_4^{2-} , Cl^- , and Na^+ are also quite different between each aquifer with the Point Lookout Sandstone and Menefee Formation waters having elevated Na^+ and Cl^- . The Gallup Sandstone—where the Chaco Well is screened—generally has relatively low Ca^{2+} , Mg^{2+} , Cl^- and HCO_3^- with elevated SO_4^{2-} concentrations. In general, all groundwater sites in the study were near calcite and quartz equilibrium and were supersaturated (mineral saturation index (SI) > 0) with dolomite and undersaturated (SI < 0) with respect to gypsum and halite (Table 6). Both calcite and gypsum are very common secondary minerals and may be found in all rock types.

3.5. Organic compound detections

VOC were detected at five sites in the study area (Table 7). All samples with VOC detections were from the Gallup Sandstone and Point Lookout Sandstone. Four out of five of those sites had detections of multiple VOCs. This includes BTEX compounds, which are known to be associated with hydrocarbon deposits, flowback water, and many adverse health effects (Njobuenwu et al., 2005; Ziemkiewicz, Thomas, 2015; McMahon et al., 2017; Spycher et al., 2017; Ran et al., 2018; Karolyte et al., 2021). Eleven organic compounds were detected in samples from this study (Table 7). Organic compound detections were at low concentrations but were greater than the laboratory detection level. Benzene was the most frequently detected organic compound found at five sites (64, 228, 601, 602, and 603). Wells 64 and 603 had the greatest number of organic compounds detected, and these two wells are both from the Point Lookout Sandstone. Concentrations at Well 64 were generally higher than at Well 603, but both had low level concentrations. Well 602 was sampled by USGS in 2017 during a regional sampling effort for wells in the Colorado Plateaus physiographic province which included other organic compounds. Butane ($0.398 \mu\text{g/L}$) and hexane ($0.073 \mu\text{g/L}$) were detected in the 2017 sample above the laboratory detection level.

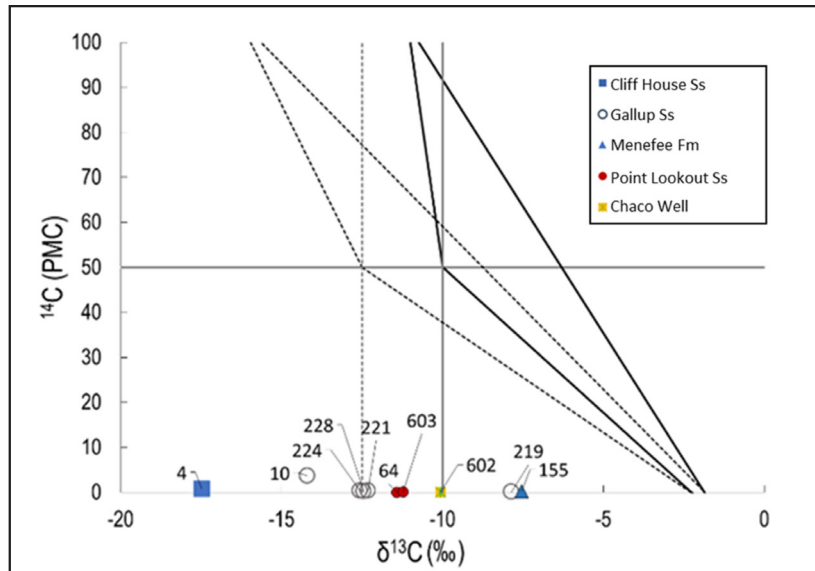


Figure 5. Samples collected in this study have very low percent modern carbon (PMC) content and variable $\delta^{13}\text{C}$ values likely reflecting very old waters with multiple pathways of geochemical evolution. In this figure, solid black lines represent the zero-age area using -20 $\delta^{13}\text{C}$ for soil gas and the dashed lines were created using -25 $\delta^{13}\text{C}$ for soil gas. According to Han and Plummer (2013), samples that plot below the zero-age triangles likely contain old carbon that may be dated.

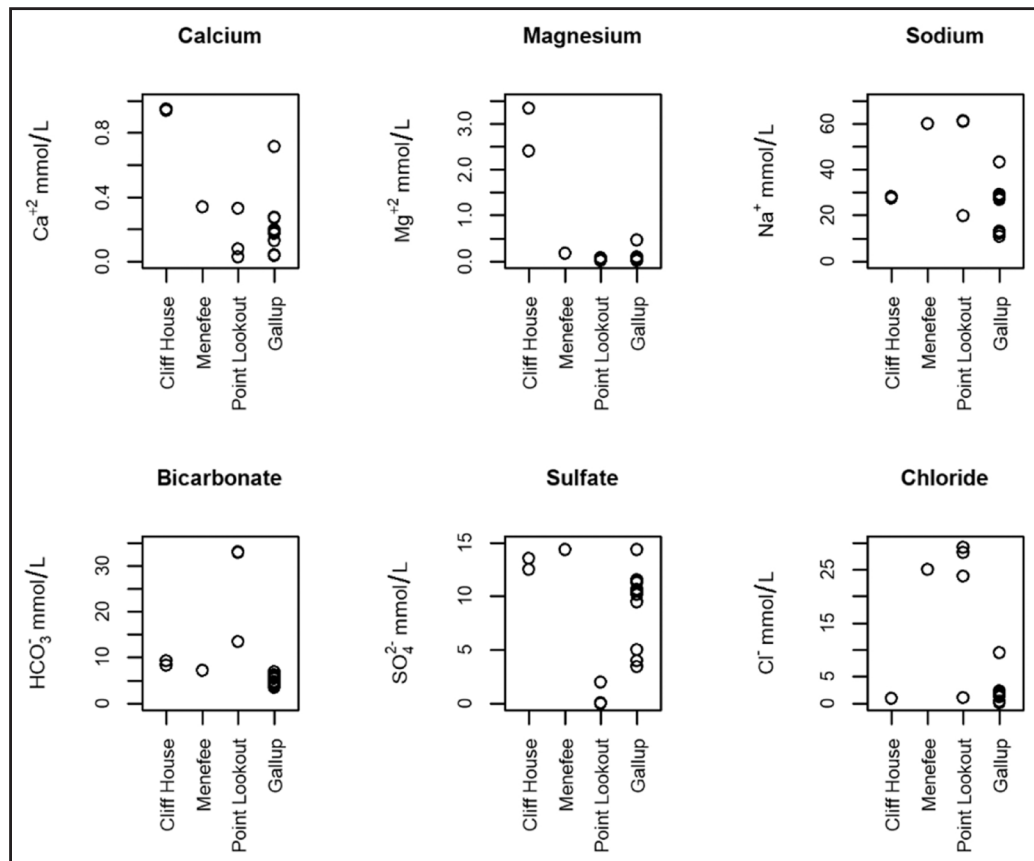


Figure 6. Major ion concentrations in mmol/L of the four aquifers sampled. Plots represent Cliff House aquifer (n = 2), Menefee Formation aquifer (n = 1), Point Lookout Sandstone (n = 3), and the Gallup Sandstone aquifer (n = 11).

Table 5. Results of major ion and total dissolved inorganic carbon (TDIC), dinitrogen (N₂), and methane (CH₄) analyses used in this study. Data from U.S. Geological Survey (2021).

Site ID	Date	HCO ₃	TDIC	Ca ²⁺	Mg ²⁺	Na ⁺	K ⁺	Cl ⁻	Br ⁻	SO ₄ ²⁻	F ⁻	SiO ₂	Ba	N ₂	CH ₄
		mmol/L	mmol/L	mmol/L	mmol/L	mmol/L	mmol/L	mmol/L	mmol/L	mmol/L	mmol/L	mmol/L (as SiO ₂)	µmol/L	mmol/L	mmol/L
Median		6.01	31.43	0.20	0.09	27.49	0.08	1.33	0.00	10.41	0.08	0.22	0.12	0.98	0.00
Mean		9.36	48.68	0.30	0.42	31.32	0.09	6.02	0.00	8.48	0.11	0.23	9.01	0.94	0.00
4	28-03-1978	8.36	42.80	0.95	3.33	27.40	0.12	0.96		13.53	0.021	0.16			
4	28-08-2019	9.29	48.76	0.94	2.40	28.10	0.09	0.89	0.0039	12.49	0.020	0.17	0.05		
10	27-08-2019	3.46	17.97	0.71	0.46	10.92	0.07	0.15	0.00059	5.01	0.026	0.19	0.18		
219	31-05-2019	6.83	35.86	0.20	0.10	43.24	0.11	9.51	0.0072	14.37	0.134	0.18	0.06	0.83	0.0053
221	30-05-2019	4.74	25.43	0.04	0.01	13.09	0.03	0.35	0.0010	3.98	0.061	0.22	0.06	1.01	0.0039
224	30-05-2019	4.46	24.72	0.04	0.01	12.05	0.03	0.38	0.0011	3.41	0.049	0.22	0.04	1.00	0.0037
228	29-05-2019	4.24	22.26	0.13	0.03	27.49	0.07	1.81	0.0015	11.24	0.041	0.27	0.12	1.10	0.0055
601	21-04-1986	3.92	20.91	0.17	0.05	29.14	0.06	2.28	0.0025	10.41	0.037	0.28	0.73		
601	29-05-2019	3.88	20.58	0.19	0.05	28.32	0.07	2.10	0.0016	11.56	0.038	0.27	0.13		
602	22-04-1986	6.15	31.53	0.27	0.09	27.40	0.08	1.33	0.0023	9.47	0.084	0.28	0.12		
602	21-10-1987	5.47	28.85	0.18	0.10	29.14	0.08	1.38	0.00088	11.45	0.084	0.27	0.12	0.97	0.0038
602	22-08-2017	5.88	30.37	0.27	0.09	26.97	0.08	1.20	0.0020	10.14	0.076	0.28	0.12	0.99	0.0032
602	28-05-2019	6.01	31.43	0.27	0.09	27.10	0.09	1.26	0.0018	10.62	0.082	0.26	0.12	0.99	0.0032
155	30-05-2019	7.26	37.85	0.34	0.17	60.03	0.16	24.93	0.0140	14.37	0.17	0.18	0.07	0.78	0.0070
64	29-08-2019	13.37	71.38	0.03	0.01	19.83	0.03	1.05	0.0039	1.99	0.33	0.24	0.40		
603	10-11-1987	32.78	168.5	0.07	0.07	60.90	0.14	23.69	0.0044	0.048	0.18	0.22	72.82		
603	29-05-2019	32.99	168.3	0.33	0.07	61.33	0.18	29.05	0.0161	0.0026	0.46	0.20	60.15	0.83	0.0053

Table 6. Calculated mineral saturation indexes.

Site ID	Date	Dolomite	Quartz	Talc	Calcite	Gypsum	Halite
4	28-03-1978	3.21	0.19	4.19	0.85	-1.38	-6.36
4	28-08-2019	2.18	0.22	0.91	0.41	-1.39	-6.38
10	27-08-2019	1.45	0.28	1.18	0.35	-1.63	-7.49
219	31-05-2019	1.15	0.22	0.79	0.25	-2.06	-5.18
221	30-05-2019	0.64	0.26	1.85	0.06	-3.01	-7.05
224	30-05-2019	0.91	0.22	2.66	0.26	-3.04	-7.04
228	29-05-2019	0.43	0.39	0.90	0.01	-2.25	-6.07
601	21-04-1986	0.68	0.42	1.49	0.13	-2.13	-5.94
601	29-05-2019	0.67	0.39	1.32	0.15	-2.06	-5.99
602	21-10-1987	0.48	0.42	-0.05	-0.10	-2.08	-6.16
602	22-08-2017	1.68	0.40	2.82	0.59	-1.95	-6.25
602	28-05-2019	0.92	0.39	0.40	0.21	-1.93	-6.23
155	30-05-2019	1.64	0.22	1.55	0.48	-1.89	-4.63
64	29-08-2019	0.53	0.34	-0.46	0.07	-3.49	-6.41
603	10-11-1987	1.35	0.33	-1.21	0.18	-4.90	-4.63
603	29-05-2019	2.80	0.26	1.21	1.24	-5.61	-4.54

4. DISCUSSION

4.1. Noble Gases

Dissolved noble gases are often useful in deciphering groundwater recharge sources and temperature, as well as assessing past mixing with hydrocarbons and groundwater age (Aeschbach-Hertig et al., 1999; Ballentine et al., 2002; Byrne et al., 2020; Heaton and Vogle 1981; Solder et al., 2020; Stute and Sonntag, 1992). Noble gas concentrations (Table 3) could not be fitted to the CE model using DGMETA (Jurgens et al., 2020) based on probable elevation and mean annual temperature parameters for the area. This inability to fit using likely recharge parameters assumes groundwater followed simple recharge into the aquifer and that no further noble gas partitioning occurred post isolation from the atmosphere. Hence, estimating the recharge temperature of groundwater across the field area using noble gases is not possible.

In groundwater, the heavier noble gases (Kr and Xe) are typically enriched relative to the light gases (He and Ne), however in this study, in all sampled sites the light noble gases were enriched relative to the heavier noble gases. No samples plot close to estimated air saturated water (ASW) or trend with air addition (excess air) from ASW (as the CE model would predict) (Figure 7). Instead, the lower FXe values indicate a depletion in Xe concentrations relative to ^{36}Ar , and the FNe values show enrichment of Ne relative to ^{36}Ar . This failure of the CE model to fit the recharge parameters to the measured data is due to partitioning of the light and heavy noble gas compositions. One way this partitioning can occur is in the presence of a hydrocarbon phase in the subsurface. During groundwater mixing with a hydrocarbon phase, the solubility differences between hydrocarbons and groundwater preferentially partitions the heavy noble gases into the hydrocarbon phase; this process leaves the resulting groundwater depleted in the heavy and enriched in the light noble gases. This type of noble gas fluid phase partitioning can be modeled by simple Rayleigh fractionation of the noble gas components between the two fluid phases driven by the differences of solubility between phases (Ballentine et al., 2002).

We used a Rayleigh fractionation model of ASW (15 °C, 1,994-m elevation) encountering and losing noble gas components to a hydrocarbon phase using solubility coefficients for light oil (Kharaka and Specht, 1988) and water solubility coefficients (Crovetto et al., 1982) at an equilibration temperature of 30 °C. The fractionation trend (green dashed line in Figure 7) begins with little change near the ASW value and progresses with greater partitioning and the loss of the heavier gases to the oil component. The calculations for Ne and Xe partitioning were made relative to the amount of Ar lost from the groundwater to the oil fraction (P-Ar 0.5 indicates 50% loss of the Ar component from the groundwater to the oil). The sample data remain offset from the Rayleigh fractionation modeled composition of oil/water interaction and ASW; this is likely explained as a mixture of ASW containing a partitioned oil/water component (mixing lines A and B in Figure 7).

During the genesis of hydrocarbons from kerogen in a source rock, the compounds produced in the early stages of hydrocarbon formation interact with connate water trapped in the system to produce groundwaters that follow the trend of the oil/water partitioning from an air saturated source water. With ongoing hydrocarbon maturation, some amount of the connate groundwater present during the early stage of hydrocarbon formation is lost from the source rock (Bryne et al., 2020). These hydrocarbon waters presumably migrate to permeable units surrounding the source rock, forming a mix of ASW compositions and hydrocarbon water that is characteristic of mixing line B (Figure 7). In noble gas samples taken from the Gallup Sandstone, Menefee Formation, and Point Lookout Sandstone aquifers, a large component of partitioned noble gas compositions sourced from the Mancos Shale seems to be mixed with an ASW component in the aquifers. The actual mixing could be ASW with some excess air and groundwater that is marginally fractionated with hydrocarbon groundwater (mixing line A in Figure 7). Alternatively, the mixing could be through a much greater component of ASW with less excess air mixed with a much more partitioned component sourced from the hydrocarbon bearing shale (mixing line B in Figure 7). The sample from the Point Lookout Sandstone (Well 603) is closest to the Rayleigh fractionation modeled values for water/oil partitioning and could in fact lie on the trend by adjusting the modeling temperature to 80 °C instead of 30 °C. As discussed below (Section 4.4), mixing with hydrocarbons could be facilitated by improperly cased boreholes in the region (Figure 3 and 10).

4.2. Stable isotopes of oxygen and hydrogen

$\delta^{18}\text{O}$ and $\delta^2\text{H}$ results are shifted to the right of the local meteoric water line (LMWL; $\delta^2\text{H}=8 \delta^{18}\text{O} + 12.5$, Vuataz and Goff, 1986) and may define a different meteoric water line or a past drier environment (Figure 4). This result was repeated in Phillips et al. (1986) and Walvoord et al. (1999) who also found a right shift in the $\delta^{18}\text{O}$ and $\delta^2\text{H}$ isotopes in San Juan Basin groundwaters. Most Gallup Sandstone groundwaters sampled in our study have $\delta^{18}\text{O}$ values about 2‰ lighter than samples collected in the Cliff House Sandstone and Menefee Formation (Table 4). This could be driven by Gallup Sandstone recharge in the mountains south of the field area and lower elevation recharge in other formations. In Phillips et al. (1986), a relationship was found between ^{14}C and $\delta^{18}\text{O}$ whereby older groundwater was generally isotopically lighter than younger groundwater suggesting cooler climates during the Pleistocene. In the current study, older (>40,000 ybp) estimated ^{14}C ages are associated with heavier $\delta^{18}\text{O}$ and $\delta^2\text{H}$ values (Table 4). Although data are very limited, this could indicate some amount of climate warming between 40,000 and 20,000 ybp.

4.3. Geochemical evolution of groundwater

Groundwaters chemically evolve through time and over distances (Fisher and Mullican, 1997); in this field area, they have had a long time to evolve (Section 3.3). Young groundwaters tend to have Ca-HCO_3 type water because carbonate minerals weather fastest imparting Ca^{2+} and HCO_3^- ions. As calcite and dolomite saturation is reached, dissolution of silicate and gypsum minerals contribute SO_4^{2-} and Na^+ and Ca^{2+} and Mg^{2+} are exchanged for adsorbed Na^+ . This geochemical evolution of groundwater produces Na-HCO_3 and Na-SO_4 type waters over long flow paths and time scales (Fisher and Mullican, 1997). All groundwater sites in this study are near calcite equilibrium and are supersaturated with dolomite and undersaturated with respect to gypsum (Table 6). A Piper diagram (Figure 8) shows that the dominant cation in all groundwaters is sodium (Na^+); wells screened in the Point Lookout Sandstone are Na-HCO_3 type waters and the rest of the sampled sites have Na-SO_4 type water. This analysis suggests that groundwater in the Cliff House Sandstone is the least geochemically evolved and the Menefee Formation and Point Lookout Sandstone are the most geochemically evolved. In this section, we will show that Gallup Sandstone contains groundwater both relatively young at the southernmost sampling points (for the San Juan Basin) and highly geochemically evolved in the eastern and northern portion of the field area. Furthermore, there is evidence of mixing between aquifers.

If Ca^{2+} , Mg^{2+} , SO_4^{2-} , and HCO_3^- are largely from the dissolution of calcite, dolomite, and gypsum, then these ions should be charge balanced, but they are not. In Figure 9A, a ratio of 1:1 between $\text{Ca}^{2+} + \text{Mg}^{2+}$ and $\text{SO}_4^{2-} - \text{HCO}_3^-$ would indicate mineral weathering of carbonates or gypsum. Instead, all waters plot below this line meaning that Na^+ —the only other major cation—must balance the excess negative charge. All sites have molal ratios of Na^+ to Cl^- that exceed one (Figure 9B). A ratio approximately equal to one would indicate halite

Table 7. Volatile organic carbon (VOC) compounds were detected at five sampled sites. Concentrations are in µg/L. Toluene was below the detection limit at all sites. Data from U.S. Geological Survey (2021).

Analyte	Well 602 (Chaco Well)					Well 64		Well 603		
	29-05-2019	27-08-2019	22-08-2017	28-05-2019	29-08-2019	04-06-2020	29-08-2019	29-05-2019	28-08-2019	04-06-2020
Benzene	0.072	0.044	0.044	0.049	0.054	0.044	1.08	< 0.026	0.019	< 0.026
Ethylbenzene	0.014	< 0.036	< 0.036	< 0.036	< 0.036	< 0.036	0.122	< 0.036	0.015	0.011
Naphthalene	< 0.26	< 0.26	< 0.26	< 0.26	< 0.26	< 0.26	0.17	< 0.26	< 0.26	< 0.26
1,2,3,4 Tetramethylbenzene	< 0.1	< 0.01	-	< 0.01	< 0.01	< 0.01	0.05	< 0.01	< 0.01	< 0.01
o-Xylene	< 0.032	< 0.032	< 0.032	< 0.032	< 0.032	< 0.032	0.502	0.018	0.021	0.019
m-Xylene plus p-Xylene	< 0.08	0.05	< 0.08	< 0.08	< 0.08	< 0.08	0.05	0.04	0.04	0.03
2-Ethyltoluene	< 0.032	< 0.032	-	< 0.032	< 0.032	< 0.032	0.051	< 0.032	< 0.032	< 0.032
1,2,3 Trimethylbenzene	< 0.06	< 0.06	-	< 0.06	< 0.06	< 0.06	0.099	0.012	0.023	< 0.06
Isopropylbenzene	< 0.042	< 0.042	-	< 0.042	< 0.042	< 0.042	0.021	< 0.042	< 0.042	< 0.042
n-propylbenzene	< 0.036	< 0.036	< 0.036	< 0.036	< 0.036	< 0.036	0.01	< 0.036	< 0.036	< 0.036
1,2,4 Trimethylbenzene	< 0.032	0.019	< 0.032	< 0.032	< 0.032	< 0.032	< 0.032	0.024	0.039	0.021

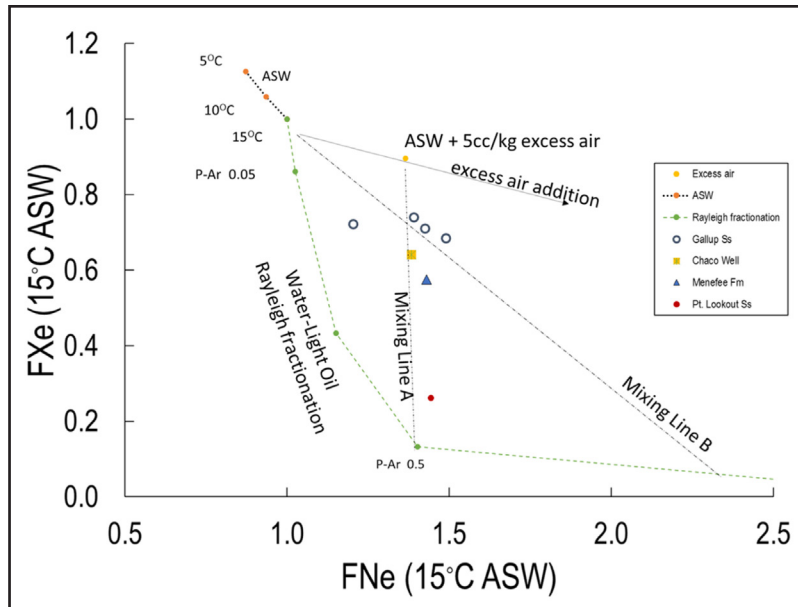


Figure 7. Plot of FXe versus FNe. F values are defined as $C_{\text{sample}}/^{36}\text{Ar}$ of the sample normalized to $\text{CASW}/^{36}\text{Ar}$ of fresh air saturated water (ASW) at 1,994-m elevation and 15 °C where C is the noble gas concentration. Note the propagated error is smaller than sample symbols. Green dots and the corresponding dashed line represent a water-light oil partition Rayleigh fractionation model done with ASW at 15 °C and at equilibration with oil at 30 °C. The yellow dot with corresponding arrow labeled excess air addition represents ASW with 5cc/kg air addition. The burnt orange dots show ASW values at equilibrium with indicated temperatures. Mixing Line A represents mixing among ASW with excess air and groundwater slightly fractionated through interactions with hydrocarbons. Mixing Line B represents mixing between a much greater component of ASW with less excess air that is mixed with a much more partitioned component sourced from the shale. The point P-Ar 0.5 indicates a 50% loss of the Ar component from the groundwater to the oil.

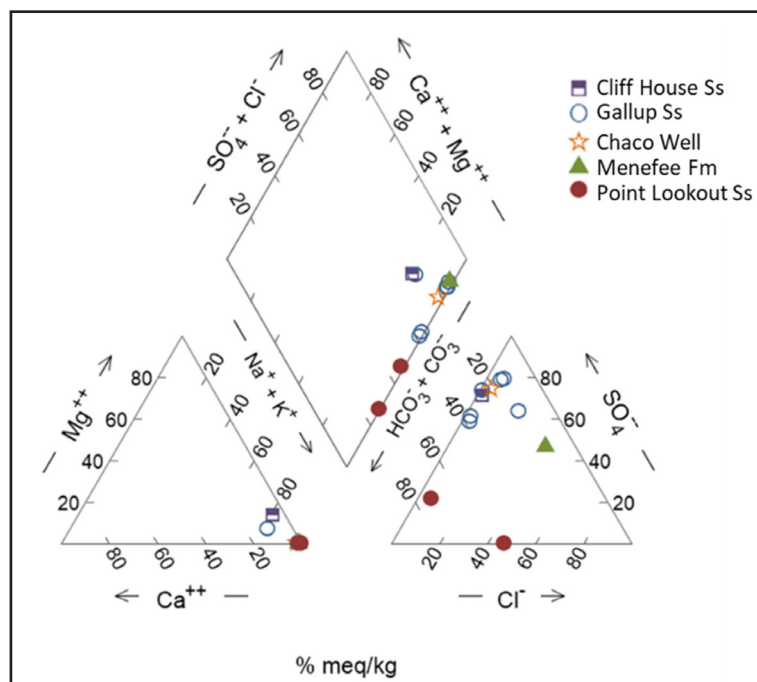


Figure 8. Piper diagram showing major ion composition and geochemical water types of the aquifers sampled for this study. Abbreviations Ss and Fm stand for Sandstone and Formation, respectively.

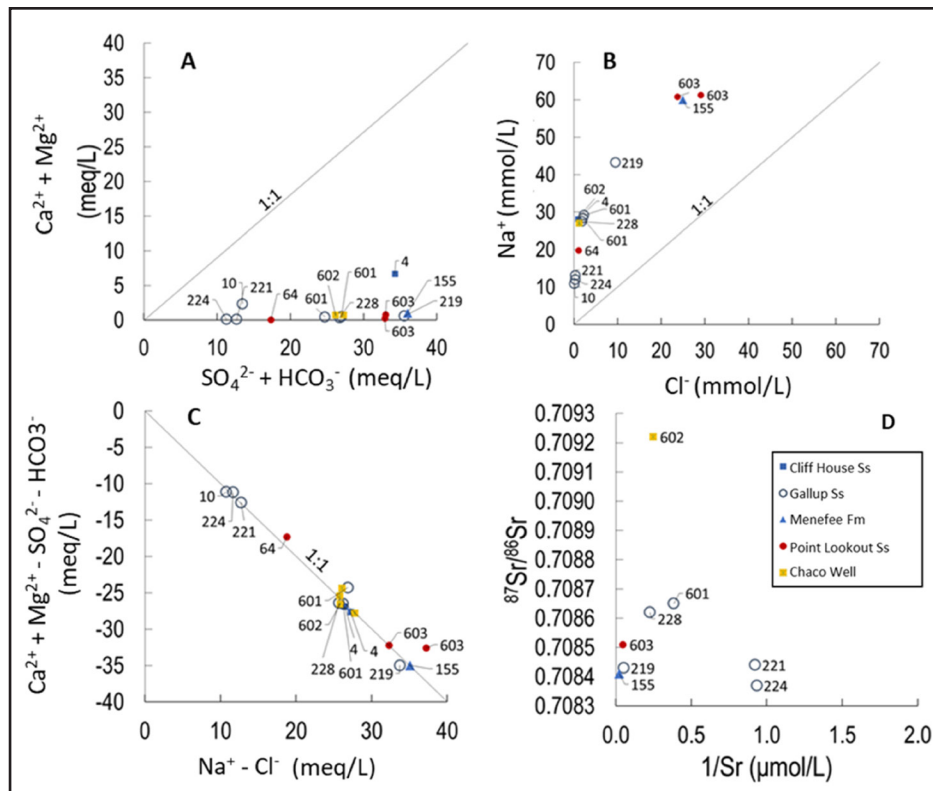


Figure 9. Major ion and $^{87}\text{Sr}/^{86}\text{Sr}$ relationships used to decipher the geochemical evolution of groundwater. Samples show evidence of increasing geochemical evolution and silicate weathering along a flow path from the south to the north.

dissolution while a ratio greater than one generally indicates Na^+ released from silicate weathering or cation exchange for Ca^{2+} and Mg^{2+} (Meybeck, 1987). Hence, in these samples, silicate weathering or cation exchange is likely contributing Na^+ . Groundwater samples collected from the Menefee Formation and Point Lookout Sandstone are the only sites where Cl^- makes up a substantial portion of the anion balance. To test the importance of cation exchange, the relationships between $\text{Na}^+ - \text{Cl}^-$ and $\text{Ca}^{2+} + \text{Mg}^{2+} - \text{SO}_4^{2-} - \text{HCO}_3^-$ were examined (Figure 9C). In this scenario, $\text{Na}^+ - \text{Cl}^-$ (meq/L) represents the amount of Na^+ gained or lost from halite dissolution. $\text{Ca}^{2+} + \text{Mg}^{2+} - \text{SO}_4^{2-} - \text{HCO}_3^-$ represents the amount of Ca^{2+} and Mg^{2+} gained or lost relative to gypsum, calcite, and dolomite dissolution. If cation exchange is a dominant and controlling process, the relationship between these parameters will be linear with a slope of -1 (Fisher and Mullican, 1997). Figure 9C shows that all groundwater samples plot along a straight line ($R^2=0.97$) with a slope of -0.96 . Hence, Ca^{2+} and Mg^{2+} ions have been exchanged for Na^+ through cation exchange. Gypsum dissolution also explains the relatively high SO_4^{2-} concentrations in many of the sampled groundwaters. In summary, groundwater in the field area is geochemically evolved with ions largely coming from cation exchange and gypsum dissolution. From this information, we infer that among wells in the Gallup Sandstone, wells from the southwest part of the field area (Wells, 10, 221, and 224) are the least geochemically evolved and wells 601, 602, and 228 to the north are more geochemically evolved. This is consistent with south to north groundwater flow as indicated by groundwater elevations (Table 1) and ^{14}C ages (Table 4). Well 219 also appears to be more geochemically evolved than other wells in the Gallup Sandstone though it is in the southern part of the field area; as discussed below (Section 4.4), this well is likely affected by mixing with adjacent aquifers.

In general, little variation in $^{87}\text{Sr}/^{86}\text{Sr}$ values was observed with the exception of Well 602, the Chaco Well, which had a higher $^{87}\text{Sr}/^{86}\text{Sr}$ value (Figure 9D). It is presently unclear why the ratio was higher at this site, though higher $^{87}\text{Sr}/^{86}\text{Sr}$ ratios in groundwater are generally associated with greater weathering of potassium and rubidium rich minerals such K-feldspar and biotite (Cartwright et al., 2007).

4.4. Mixing between aquifers

Mixing between aquifers may be facilitated through improperly cased or plugged hydrocarbon wells in the region. The Chaco Well (Well 602) and Well 603 have 22 inactive hydrocarbon wells within 10 km and seven within 5 km (Figure 3). Wells 155 and 219 have 24 hydrocarbon related boreholes wells within 1 km, all of which are drilled to the Menefee Formation, Morrison Formation, and to unknown depths (Figure 10). Although these hydrocarbon wells are inactive, some could be conduits for vertical groundwater movement through relatively impermeable units such as the Mancos Shale (Kernodle, 1996; Lacombe et al., 1995).

A mixing line can be inferred from lower to higher concentrations of Na^+ versus Cl^- between Well 10 in the Gallup Sandstone and Wells 603 and 155 in the Point Lookout Sandstone and Menefee Formation, respectively (Figure 9B). When examining HCO_3^- and SO_4^{2-} concentrations against Na^+ (Figures 11A and 11B), two divergent mixing pathways are seen, one towards Na-SO_4 type waters and the other towards Na-HCO_3 type waters. Again, the younger Well 10 (~23,000 ybp) is the more dilute end member and Wells 603 (>52,000 ybp) and 155 (~41,000 ybp) being the second and third end members with varying SO_4^{2-} and HCO_3^- concentrations. These geochemical plots show that well 155, screened in the Menefee Formation and Well 603, screened in the Point Lookout Sandstone, represent distinct end members in the dataset. The low SO_4^{2-} at Well 603 could be indicative of SO_4 reduction as this site which also had the highest $\text{NH}_3 + \text{NH}_4$ concentrations (Tables 2 and 5). Waters in the Gallup Sandstone and Cliff House Sandstone appear to be mixing with waters in the Menefee Formation instead of the Point Lookout Sandstone.

Cl^-/Br^- ratios are often used to help differentiate different water sources and infer sources of produced water (Davis et al., 1998; Ziemkiewicz, Thomas, 2015). For example, groundwaters with Cl^-/Br^- molar ratios > 2500 are likely mixing with brine (Davis et al., 1998) while produced waters may carry excess Br^- potentially lowering the Cl^-/Br^- ratio (Tasker et al., 2020; Ziemkiewicz, Thomas, 2015). In this study, Cl^-/Br^- molar ratios varied between 229.8 and 5,409.1 with the lowest and highest values coming from Well 4 (Cliff House Sandstone) and Well 603 (Point Lookout Sandstone), respectively. In Figure 11 C, Cl^-/Br^- ratios are highest for Wells 155 and 603 screened in the Menefee Formation and Point Lookout Sandstone, respectively. As evidenced by the noble gas results (Section 3.1), water in Well 603 may be mixing with shale connate waters expelled during hydrocarbon formation. Water from Well 155 may also be mixing with a brine water.

Vertical mixing between aquifers is known to occur in the San Juan Basin, generally with low rates through shale beds and higher leakage rates in localized areas associated with faults and fractures (Stone et al., 1983); furthermore, vertical gradients were found in this study which could help induce mixing (Table 1). Mixing between aquifers is evident between geochemical end members represented by the youngest (Section 3.2) and most dilute Gallup Sandstone sample collected (Well 10) and the much more saline Well 155 (Menefee Formation) and Well 603 (Point Lookout Sandstone); this also could include mixing between an unsampled aquifer deeper in the region. Well 219, screened in the Gallup Sandstone, is geochemically similar to Well 155 in all geochemical figures including the carbon isotopes (Figure 5), $\delta^{18}\text{O}$ and $\delta^2\text{H}$ (Figure 4), strontium isotopes (Figure 9D), and major ion chemistry (Figures 6, 8, 9, and 11). The Chaco Well appears to be intermediate between the Gallup Sandstone and the Menefee Formation and Cliff House Sandstone end members. The direction of mixing in the basin is likely from deeper to shallower depths as indicated by the groundwater level measurements (Table 1); it is possible that deeper unsampled groundwaters moving vertically through formations or through improperly cased boreholes are strongly influencing groundwater chemistry. This may be the case in Wells 219 (Gallup Sandstone aquifer) and 155 (Menefee Formation) where the many nearby inactive hydrocarbon boreholes (Figure 10) could have facilitated vertical mixing and groundwater chemistry homogenization.

Implications of this research is that while groundwater movement is slow, vertical mixing between aquifers is likely occurring despite the less permeable Mancos Shale that separates the Gallup Sandstone and the surrounding aquifers. This mixing could be augmented through the many boreholes drilled throughout the field area (Figures 3 and 10). Hence, contaminants from hydrocarbon extraction activities in the San Juan Basin may travel between aquifers and could be affecting water quality in the Gallup Sandstone aquifer.

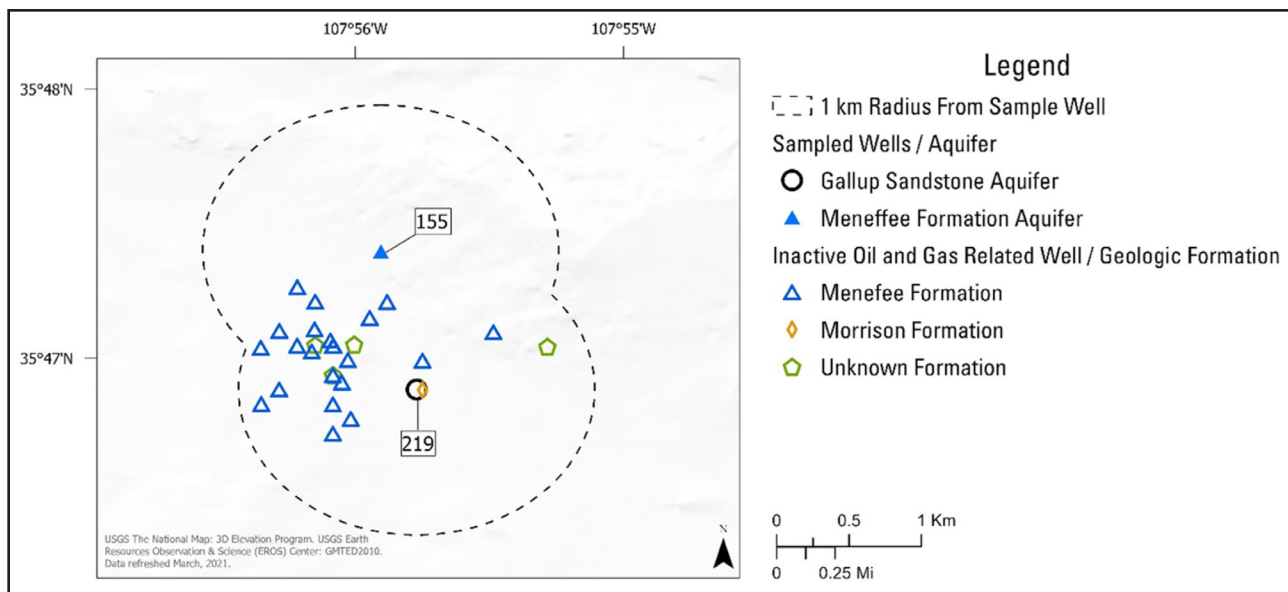


Figure 10. All known hydrocarbon related boreholes within a 1-km radius of Wells 155 and 219. Oil and gas well locations and information is available through the State of New Mexico Oil Conservation Division: <https://www.emnrd.nm.gov/ocd/#gsc.tab=0>

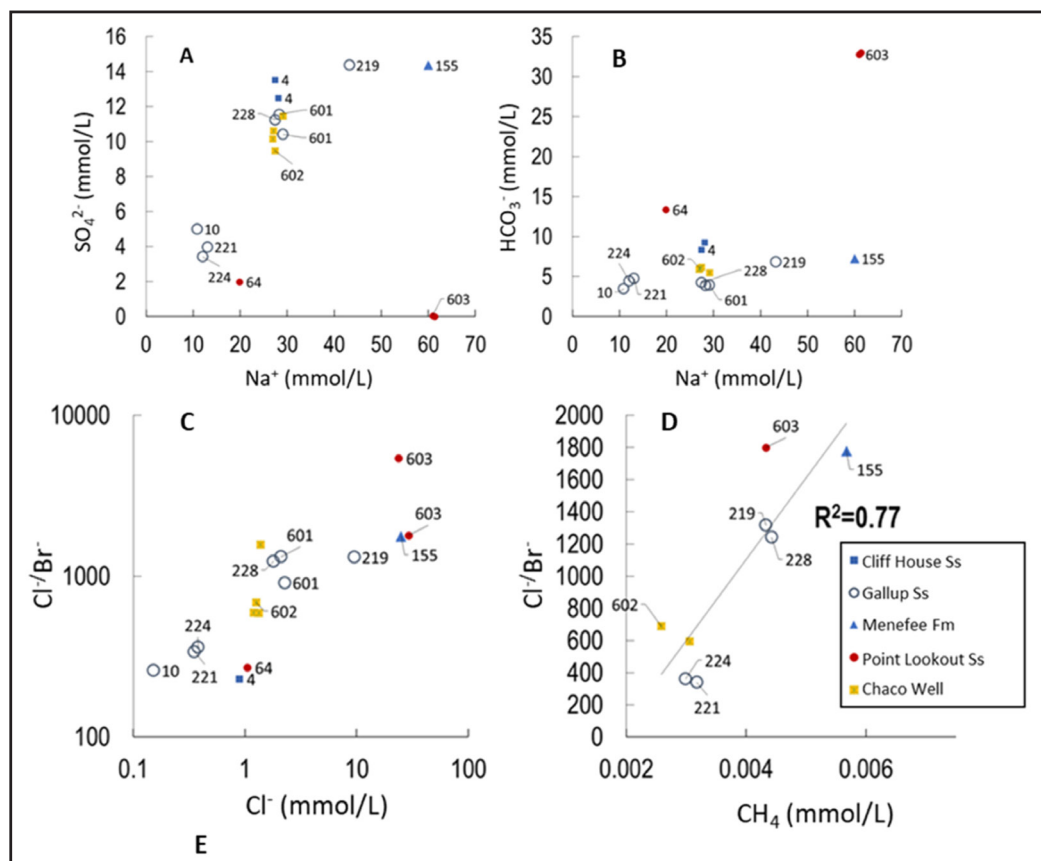


Figure 11. Plots A and B: Sulfate versus Na^+ and HCO_3^- versus Na^+ in sampled groundwaters. These plots demonstrate that well 603, 155, and 10 represent three end members in the hydrochemical dataset. Plots C and D: molar ratios of Cl^-/Br^- versus Cl^- and methane (CH_4) concentrations.

4.5. Detections of hydrocarbon related compounds and the possibility of contamination from hydrocarbon extraction activities

Though naturally occurring, BTEX and other VOC detections may be explained by leakage from improperly cased or failed casings of nearby oil and gas wells (Figures 3 and 10). For example, Chaco Well is 5 km directly north from an inactive hydrocarbon borehole drilled into the Gallup Sandstone aquifer. Given the age of the hydrocarbon well (1956), groundwater flow directions (south to north), and the conductivity of the Gallup Sandstone aquifer (111 m/y; Kernodle, 1996), it is possible that contaminants could have migrated vertically through the borehole and then horizontally ~7 km towards the Chaco Well.

The three Gallup Sandstone aquifer wells with VOC detections were located on the north and east side of the study area downgradient of Gallup Sandstone wells with no VOC detections. The downgradient water may represent older more evolved groundwater that has had more interaction with hydrocarbon deposits or leakage through boreholes from adjacent stratigraphic units with hydrocarbon deposits.

In addition to evidence from noble gas analyses which suggests influence from connate water expelled from shale during hydrocarbon formation (Section 4.1), Well 603 had highly elevated barium (Ba; 60–73 $\mu\text{mol/L}$; Table 5), relatively high Cl^- (28.21–29.05 mmo/L), and bromide (0.0125–0.0161 mmol/L). These elements are commonly present in high concentrations in oil field brines and shale waters (Barbot et al., 2013; Hudak and Wachal, 2001; Ziemkiewicz, Thomas, 2015). Notably, the Cl^-/Br^- molar ratio changed from 5409 to 1799 between 1987 and 2019 at Well 603 and in 2019, the well contained trace VOC detections. The drop in Cl^-/Br^- is consistent with a new source of Br rich brine water though TDS did not change appreciably. CH_4 concentrations were also significantly correlated to the Cl^-/Br^- ratio (Figure 11D), a finding that could implicate a similar source for high Cl^-/Br^- and CH_4 . However, both CH_4 and high Cl^-/Br^- ratios often have natural origins and could indicate mixing with a CH_4 containing shale water (Davis et al., 1998; Li et al., 2016; Ziemkiewicz, Thomas, 2015). Furthermore, the Point Lookout Sandstone aquifer waters had high CH_4 and low SO_4 potentially indicating in situ methanogenesis. Further work could measure stable H and C isotopes of CH_4 to help distinguish methane sources (Bernard et al., 1976).

This study did not examine synthetic chemicals that could confirm direct effect from hydrocarbon extraction activities. Further work to determine whether hydrocarbon extraction activities such as HF are affecting drinking water resources in the San Juan Basin and at CCNHP could sample for synthetic organic compounds such as diethylene glycol and per- and polyfluoroalkyl substances (PFAS). The U.S. Environmental Protection Agency reported diethylene glycol in groundwater near an extensive shale gas operation in Pavillion, Wyoming (Di Giulio et al., 2011). PFAS are extremely recalcitrant compounds—often termed forever chemicals—that are used in large quantities during hydrocarbon extraction (Glüge et al., 2020; Meng et al., 2021). In a recent study of groundwater and soils near oil fields, substantially higher concentrations of PFAS were observed downgradient of oil fields compared to upgradient (Meng et al., 2021). Further work pairing these synthetic compounds with noble gas, major ion, VOC, and isotope analyses could help determine the sources of VOCs found in groundwater at CCNHP and the greater San Juan Basin. Despite the extensive amount of hydrocarbon extraction taking place, geochemical groundwater data in the region is sparse; further work studying the effect of hydrocarbon extraction on water quality and quantity in the San Juan Basin could fill some of these knowledge gaps.

5. CONCLUSIONS

Despite the large number of hydrocarbon extraction wells in the San Juan Basin, very little is known of the groundwater chemistry, flow directions, or the potential impact oil and gas related wells could have on drinking water sources. This work shows that mixing between aquifers, even through the relatively impermeable Mancos Shale (Kernodle, 1996), is possible and may be facilitated through the numerous inactive oil and gas related boreholes in the region. Given groundwater conductivity through the Gallup Sandstone aquifer (111 m/y; Kernodle, 1996), it is possible that contaminants from nearby oil and gas wells targeting and not targeting the Gallup Sandstone could nevertheless migrate vertically and then, over the course of years to decades, move to the main drinking water source at CCNHP (Well 602, Chaco Well).

Furthermore, the lack of modern water in the sampled aquifers indicates that any water extraction will not be replaced by modern recharge.

Several lines of evidence suggest groundwater contamination from nearby oil and gas extraction activity is possible or has occurred. First, noble gas results imply mixing with waters that have interacted with hydrocarbons (Section 4.1); second, the presence of VOCs—including BTEX compounds—also indicates interaction with hydrocarbon fluids; lastly, mixing between aquifers is supported by major ion and isotopic geochemical analyses. This study establishes baseline geochemistry and groundwater flow direction (from south to north) for seldom sampled aquifers in the San Juan Basin that can serve to compare with future studies.

Whether the mixing and presence of VOC compounds is naturally occurring or is facilitated through oil and gas related boreholes will require further investigation. Further work could endeavor to analyze groundwater for synthetic chemicals used during HF (Mumford et al., 2018) especially at the Chaco Well (Gallup Sandstone) and Well 603 (Point Lookout Sandstone). Further study could also benefit from sampling produced and flowback water from active oil and gas wells to help determine the organic compounds and geochemistry that could help trace produced waters. Additional work could also seek to measure the stable isotopes of CH₄ to help determine the sources of CH₄ in the aquifer (McIntosh et al., 2018).

CRedit AUTHORSHIP CONTRIBUTION STATEMENT

Benjamin S. Linhoff: Project conceptualization, methodology, formal analysis, investigation, resources, writing original draft, writing review and editing, visualization of figures, supervision of project staff, project administration, and funding acquisition; **Kimberly R. Beisner:** Project methodology, formal analysis, writing original draft, editing final draft, and validation of data; **Andrew G. Hunt:** Formal analysis, writing original draft; **Zachary M. Shephard:** Writing original draft, writing review and editing, visualization.

DECLARATION OF COMPETING INTEREST

The authors declare the following financial interests/personal relationships which may be considered as potential competing interests: Benjamin Linhoff, Kim Beisner, Andrew G. Hunt, Zach Shephard reports financial support was provided by U.S. Geological Survey.

DATA AVAILABILITY

All data used are available through the U.S. Geological Survey National Water Information System Database: <https://waterdata.usgs.gov/nwis>

ACKNOWLEDGMENTS

This work would not have been possible without help from the Navajo Nation who provided access to wells on Navajo land and helped with well site selection, database sharing, and personnel field support. We would also like to thank the USGS field technicians who worked hard to diligently collect groundwater samples and groundwater levels in a remote setting. Johanna Blake assisted with graphical abstract design. We greatly appreciated input from our NPS collaborators during proposal development and throughout the project. Finally, we would also like to thank the many reviewers who substantially improved this work. This work was funded through the USGS-NPS Water-Quality Partnership program. Any use of trade, firm, or product names is for descriptive purposes only and does not imply endorsement by the U.S. Government.

APPENDIX A. SUPPORTING INFORMATION

Supplementary data associated with this article can be found in the online version at doi: [10.1016/jejr.2023.101430](https://doi.org/10.1016/jejr.2023.101430)

REFERENCES

- Aeschbach-Hertig, W., Peeters, F., Beyerle, U., Kipfer, R., 1999. Interpretation of dissolved atmospheric noble gases in natural waters. *Water Resour. Res.* v. 35 (9), 2779–2792.
- Ballentine, C.J., Burgess, R., Marty, B., 2002. Tracing Fluid Origin, Transport and Interaction in the Crust. In: Porcelli, D., Ballentine, C.J., Wieler, R. (Eds.), *Noble Gases in Geochemistry and Cosmochemistry*. Mineralogical Society of America, Washington D.C., pp. 481–538
- Barbot, E., Vidic, N.S., Gregory, K.B., Vidic, R.D., 2013. Spatial and temporal correlation of water quality parameters of produced waters from Devonian-age shale following hydraulic fracturing. *Environ. Sci. Technol.* v. 47 (6), 2562–2569.
- Bernard, B.B., Brooks, J.M., Sackett, W.M., 1976. Natural gas seepage in the Gulf of Mexico. *Earth Planet. Sci. Lett.* 31 (1), 48–54.
- Briser, B.S., and G.K. Hoffman. 2002. Fundamental geology of San Juan Basin energy resources. Pages 21–25 in B.S. Briser and L.G. Price, editors. *New Mexico's energy, present and future: policy, production, economics, and the environment*. Decision Makers Field Conference 2002. New Mexico Bureau of Geology and Mineral Resources, Socorro, New Mexico. <http://geoinfo.nmt.edu/publications/guides/decisionmakers/2002/> (Accessed 27 January 2023).
- Bryan, S., 2023, Court: US needs to consider effects of drilling near Chaco, Associated Press, <https://apnews.com/article/politics-united-states-government-bureau-of-land-management-climate-and-environment-business-f4aaa217511adc62cac313d0ea5bd0f5> (Accessed 4 February 2023).
- Bullen, T.D., Krabbenhoft, D., Kendall, C., 1996. Kinetic and mineralogic controls on the evolution of groundwater chemistry and $87\text{Sr}/86\text{Sr}$ in a sandy silicate aquifer, v. 60. *Geochimica et Cosmochimica Acta*, northern Wisconsin, USA, pp. 1807–1821. [https://doi.org/10.1016/0016-7037\(96\)00052-X](https://doi.org/10.1016/0016-7037(96)00052-X)
- Byrne, D.J., Barry, P.H., Lawson, M., Ballentine, C.J., 2020. The use of noble gas isotopes to constrain subsurface fluidflow and hydrocarbon migration in the East Texas Basin. *GCA* 268, 186–208.
- Cartwright, I., Weaver, T., Petrides, B., 2007. Controls on $87\text{Sr}/86\text{Sr}$ ratios of groundwater in silicate-dominated aquifers, v. 246. *Chemical Geology*, SE Murray Basin, Australia, pp. 107–123.
- Cartwright, I., Currell, M.J., Cend'on, D.I., Meredith, K.T., 2020. A review of the use of radiocarbon to estimate groundwater residence times in semi-arid and arid areas. *J. Hydrol.* 580, 124247.
- Clark, C.E., Horner, R.M., Harto, C.B., 2013. Life cycle water consumption for shale gas and conventional natural gas. *Environ. Sci. Technol.* v. 47 (20), 11829–11836.
- Connor, B.F., Rose, D.L., Noriega, M.C., Murtagh, L.K., and Abney, S.R., 1998, *Methods of Analysis by the U.S. Geological Survey National Water Quality Laboratory — Determination of 86 Volatile Organic Compounds in Water by Gas Chromatography/Mass Spectrometry, Including Detections Less Than Reporting Limits*, U.S. Geological Survey Open-File Report 97–829, 78p, <https://nwql.usgs.gov/pubs/OFR/OFR-97-829.pdf>
- Cozzarelli, I.M., Skalak, K.J., Kent, D.B., Engle, M.A., Bentham, A., Mumford, A.C., Haase, K., Farag, A., Harper, D., Nagel, S.C., Iwanowicz, L.R., 2017. Environmental signatures and effects of an oil and gas wastewater spill in the Williston Basin, North Dakota. *Sci. Total Environ.* 579, 1781–1793.
- Cozzarelli, I.M., Kent, D.B., Briggs, M., Engle, M.A., Bentham, A., Skalak, K.J., Mumford, A.C., Jaeschke, J., Farag, A., Lane Jr, J.W., Akob, D.M., 2021. Geochemical and geophysical indicators of oil and gas wastewater can trace potential exposure pathways following releases to surface waters. *Sci. Total Environ.* 755, 142909.
- Crovetto, R., Fernandez-Prini, R., Japas, M.L., 1982. Solubilities of inert gases and methane in H_2O and in D_2O in the temperature range of 300 to 600 K. *The J. Chem. Phys.* 76 (2), 1077–1086.
- Dam, W.L., 1995. *Geochemistry of ground water in the, Dakota, and Morrison aquifers, San Juan Basin*, 94. *Water-Resources Investigations Report*, New Mexico, p. 4253.
- Davis, S.N., Whittemore, D.O., Fabryka-Martin, J., 1998. Uses of chloride/bromide ratios in studies of potable water. *Ground Water* v. 36 (2), 338–350.
- Di Giulio D.C., Wilkin R.T., Miller C., Oberley G., 2011, *Investigation of Ground Water Contamination near Pavillion, Wyoming*. U.S. Environmental Protection Agency Report 2011 <http://www.epa.gov/region8/superfund/wy/pavillion/>
- Engler, T., W., Kelley, S., Cather, M., 2015, *Reasonable foreseeable development (RFD) for northern New Mexico*: New Mexico Bureau of Geology and Mineral
- Federal Geographic Data Committee [prepared for the Federal Geographic Data Committee by the U.S. Geological Survey], 2006, *FGDC Digital Cartographic Standard for Geologic Map Symbolization*: Reston, Va., Federal Geographic Data Committee Document Number FGDC-STD-013–2006, 290 p., 2 plates.
- Fisher, S.R., Mullican, W.F.I., 1997. Hydrochemical evolution of sodium-sulfate and sodium-chloride groundwater beneath the northern Chihuahuan Desert, v. 5. *Hydrogeology Journal*, Trans-Pecos, Texas, USA.
- Fishman, M.J., and Friedman, L.C., 1989, *Methods for determination of inorganic substances in water and fluvial sediments*: U.S. Geological Survey Techniques of Water-Resources Investigations, book 5, chap. A1, 545 p., <https://doi.org/10.3133/twri05A1>
- Fishman, M.J., ed., 1993, *Methods of analysis by the U.S. Geological Survey National Water Quality Laboratory—Determination of inorganic and organic constituents in water and fluvial sediments*: U.S. Geological Survey Open File Report 93–125, 217 p., at <https://doi.org/10.3133/of93125>
- Gallegos, T.J., and Varela, B.A., 2015, *Data Regarding Hydraulic Fracturing Distributions and Treatment Fluids, Additives, Proppants, and Water Volumes Applied to Wells Drilled in the United States from 1947 through 2010*: US Geological Survey Data Series 868, p. 11.

- Glüge, J., Scheringer, M., Cousins, I.T., Dewitt, J.C., Goldenman, G., Herzke, D., Lohmann, R., Ng, C.A., Trier, X., and Wang, Z., 2020, An overview of the uses of perand polyfluoroalkyl substances (PFAS): 2345–2373 p.
- Gordalla, B.C., Ewers, U., Frimmel, F.H., 2013. Hydraulic fracturing: a toxicological threat for groundwater and drinking-water? *Environ. Earth Sci.* 70 (2013), 3875–3893. <https://doi.org/10.1007/s12665-013-2672-9>
- Han, L.F., Plummer, L.N., 2016. A review of single-sample-based models and other approaches for radiocarbon dating of dissolved inorganic carbon in groundwater. *Earth-Sci. Rev.* 152, 119–142.
- Han, L.F., Plummer, L.N., Aggarwal, P., 2012. A graphical method to evaluate predominant geochemical processes occurring in groundwater systems for radiocarbon dating. *Chem. Geol.* 318–319, 88–112. <https://doi.org/10.1016/j.chemgeo.2012.05.004>
- Han, L.-F., Plummer, L.N., 2013. Revision of Fontes & Garnier’s model for the initial ^{14}C content of dissolved inorganic carbon used in groundwater dating. *Chem. Geol.* v. 351, 105–114. <https://doi.org/10.1016/j.chemgeo.2013.05.011>
- Heaton, T.H.E., Vogel, J.C., 1981. “Excess air” in groundwater. *J. Hydrol.* v. 50, 21–216.
- Hudak, P.F., Wachel, D.J., 2001. Effects of brine injection wells, dry holes, and plugged oil/gas wells on chloride, bromide, and barium concentrations in the Gulf Coast Aquifer, southeast Texas, USA. *Environ. Int.* v. 26 (7–8), 497–503.
- Hunt, A.G., 2015, Noble Gas Laboratory’s standard operating procedures for the measurement of dissolved gas in water samples: U.S. Geological Survey Techniques and Methods, book 5, chap. A11, 22 p., <https://doi.org/10.3133/tm5A11>
- Jurgens, B.C., B’ohlke, J.K., Haase, K., Busenberg, E., Hunt, A.G. and Hansen, J.A., 2020. DGMETA (version 1)—Dissolved gas modeling and environmental tracer analysis computer program (No. 4-F5). US Geological Survey.
- Karolyte, R., Barry, P.H., Hunt, A.G., Kulongoski, J.T., Tyne, R.L., Davis, T.A., Wright, M.T., McMahon, P.B., Ballentine, C.J., 2021. Noble gas signatures constrain oilfield water as the carrier phase of hydrocarbons occurring in shallow aquifers in the San Joaquin Basin, USA. *Chem. Geol.* 584 <https://doi.org/10.1016/j.chemgeo.2021.120491>
- Kelley, S., Engler, T., Cather, M., Pokorny, C., Yang, C., Mamer, E., Hoffman, G., Wilch, J., Johnson, P., Zeigler, K., 2014. Hydrologic Assessment of Oil and Gas Resource Development of the Mancos Shale in the San Juan Basin. N. Mex. N. Mex. Bur. Geol. Miner. Resour. Open-file Rep. 566.
- Kernodle, J.M., 1996, Hydrogeology and steady-state simulation of ground-water flow in the San Juan Basin, New Mexico, Colorado, Arizona, And Utah: U. S. Geological Survey Water-Resources Investigation Report 95–4187, <https://doi.org/10.3133/wri954187>
- Kharaka, Y.K., Specht, D.J., 1988. The solubility of noble gases in crude oil at 25–100C. *Appl. Geochem.* 3 (2), 137–144.
- Lacombe, S., Sudicky, E.A., Frappe, S.K., Unger, A.J.A., 1995. Influence of leaky boreholes on cross-formational groundwater flow and contaminant transport. *Water Resour. Res.* 31 (8), 1871–1882. <https://doi.org/10.1029/95WR00661>
- Lekson, S.H., 1984. Great Pueblo architecture of Chaco Canyon, Joan Mathien and Randall H. Mcguire. Southern Illinois Univ. Press, Carbondale, pp. 243–269.
- Li, J., Li, X., Wang, X., Li, Y., Wu, K., Shi, J., Yang, L., Feng, D., Zhang, T., Yu, P., 2016. Water distribution characteristic and effect on methane adsorption capacity in shale clay. *Int. J. Coal Geol.* 159, 135–154.
- Lindsey, B.D., Jurgens, B.C., and Belitz, K., 2019, Tritium as an indicator of modern, mixed, and premodern groundwater age: U.S. Geological Survey Scientific Investigations Report 2019–5090, 18 p., <https://doi.org/10.3133/sir20195090>
- Linhoff, B., 2022. Deciphering natural and anthropogenic nitrate and recharge sources in arid region groundwater. *Sci. Total Environ.*, 157345 <https://doi.org/10.1016/j.scitotenv.2022.157345>
- McIntosh, J.C., Ferguson, G., 2019. Conventional oil—the forgotten part of the water-Energy nexus. *Groundwater* 57 (5), 669–677. <https://doi.org/10.1111/gwat.12917>
- McIntosh, J.C., Hendry, M.J., Ballentine, C., Haszeldine, R.S., Mayer, B., Etiopie, G., Elsner, M., Darrah, T.H., Prinzhofer, A., Osborn, S., Stalker, L., 2018. A critical review of state-of-the-art and emerging approaches to identify fracking-derived gases and associated contaminants in aquifers. *Environ. Sci. Technol.* 53 (3), 1063–1077.
- McMahon, P.B., Barlow, J.R.B., Engle, M.A., Belitz, K., Ging, P.B., Hunt, A.G., Jurgens, B.C., Kharaka, Y.K., Tollett, R.W., Kresse, T.M., 2017. Methane and benzene in drinking-water wells overlying the Eagle Ford, Fayetteville, and Haynesville Shale hydrocarbon production areas. *Environ. Sci. Technol.* 51, 6727–6734.
- Meng, Q., Ashby, S., 2014. Distance: a critical aspect for environmental impact assessment of hydraulic fracking. *Extr. Ind. Soc.* 1 (2014), 124–126.
- Meng, Y., Yao, Y., Chen, H., Li, Q., Sun, H., 2021. Legacy and emerging per- and polyfluoroalkyl substances (PFASs) in Dagang Oilfield: Multimedia distribution and contributions of unknown precursors. *J. Hazard. Mater.* v. 412 (no. January).
- Meybeck, M., 1987. Global chemical weathering of surficial rocks estimated from river dissolved loads. *Am. J. Sci.* v. 287, 401–428.
- Moe, R., 2017, The Treasures of Chaco Canyon Are Threatened by Drilling: The New York Times. <https://www.nytimes.com/2017/12/01/opinion/chaco-canyonnew-mexicodrilling.htm>
- Mumford, A.C., Akob, D.M., Klinges, J.G., Cozzarelli, I.M., 2018. Common hydraulic fracturing fluid additives alter the structure and function of anaerobic microbial communities. *Appl. Environ. Microbiol.* 84, e02729–17. <https://doi.org/10.1128/AEM.02729-17>
- National Park Service (NPS), 2015, Foundation Document Chaco Culture National Historical Park New Mexico, https://www.nps.gov/CCNHP/getinvolved/upload/CCNHP_FD_PRINT.pdf
- Njobuenwu, D.O., Amadi, S.A., Ukpaka, P.C., 2005. Dissolution rate of BTEX contaminants in water. *Can. J. Chem. Eng.* 83, 985–989.
- Parkhurst, D.L., and Charlton, S.R., 2008, NetpathXL—An Excel® interface to the program NETPATH: U.S. Geological Survey Techniques and Methods 6–A26, 11 p.

- Patton, C.J., and Kruskalla, J.R., 2011, Colorimetric determination of nitrate plus nitrite in water by enzymatic reduction, automated discrete analyzer methods: U.S. Geological Survey Techniques and Methods, book 5, chap. B8, 34 p., <https://doi.org/10.3133/tm5B8>
- Perra, C., A., 2021, Investigating cross formational flow of fluids through oil and gas wells in Alberta and Saskatchewan, Canada, Thesis, Department of Civil, Geological and Environmental Engineering, University of Saskatchewan, Saskatoon, Canada, 157 pp.
- Phillips, F.M., Peeters, L., Tansey, M., 1986. Paleoclimatic inferences from an isotopic investigation of groundwater in the central San Juan Basin, no. 26. Quaternary Research, New Mexico, pp. 179–193.
- Ran, J., Qiu, H., Sun, S., Tian, L., 2018. Short-term effects of ambient benzene and TEX (toluene, ethylbenzene, and xylene combined) on cardiorespiratory mortality in Hong Kong. *Environ. Int.* 117, 91–98.
- Révész, K., and Coplen, T.B., 2008, Determination of the $\delta^2\text{H}/1\text{H}$, of water—RSIL lab code 1574: U.S. Geological Survey Techniques and Methods, book 10, chap. C1, 27 p., at <https://doi.org/10.3133/tm10C1>
- Rose, D.L., Sandstrom, M.W., and Murtagh, L.K., 2016, Determination of heat purgeable and ambient purgeable volatile organic compounds in water by gas chromatography/mass spectrometry: U.S. Geological Survey Techniques and Methods, book 5, chap. B12, 61 p., <https://doi.org/10.3133/tm5B12>
- Solder, J.E., Beisner, K.R., Anderson, J., Bills, D.J., 2020. Rethinking groundwater flow on the South Rim of the Grand Canyon, USA: characterizing recharge sources and flow paths with environmental tracers. *Hydrogeol. J.* 28 (5), 1593–1613. <https://doi.org/10.1007/s10040-020-02193-z>
- Spycher, B.D., Lupatsch, J.E., Huss, A., Rischewski, J., Schindera, C., Spoerri, A., Vermeulen, R., Kuehni, C.E., Swiss Paediatric Oncology Group and Swiss National Cohort Study Group, 2017. Parental occupational exposure to benzene and the risk of childhood cancer: a census-based cohort study. *Environ. Int.* 108, 84–91.
- Stone, W.J., Lyford, F.P., Frenzel, P.F., Mizell, N.H., and Padgett, E.T., 1983, Hydrogeology and water resources of San Juan Basin, New Mexico: Socorro, New Mexico Bureau of Mines and Mineral Resources Hydrologic Report 6, 70p.
- Stringfellow, W.T., Domen, J.K., Camarillo, M.K., Sandelin, W.L., Borglin, S., 2014. Physical, chemical, and biological characteristics of compounds used in hydraulic fracturing. *J. Hazard. Mater.* 275, 37–54. <https://doi.org/10.1016/j.jhazmat.2014.04.040>
- Stute, M., Sonntag, C., 1992. Paleotemperatures derived from noble gases dissolved in groundwater in relation to soil temperature. In: Staff, I.A.E.A. (Ed.), *Isotopes of Noble Gases as Tracers in Environmental Studies*. IAEA, Vienna, pp. 111–122.
- Tasker, T.L., Warner, N.R., Burgos, W.D., 2020. Geochemical and isotope analysis of produced water from the Utica/Point Pleasant Shale, Appalachian Basin. *Environ. Sci.: Process. Impacts* 22 (5), 1224–1232. <https://doi.org/10.1039/d0em00066c>
- Travis, R.E., Bell, M.T., Linhoff, B.S. and Beisner, K.R., 2021. Utilizing multiple hydrogeologic and anthropogenic indicators to understand zones of groundwater contribution to water-supply wells near Kirtland Air Force Base Bulk Fuels Facility in southeast Albuquerque, New Mexico (No. 2021–5076). US Geological Survey, <https://doi.org/10.3133/sir20215076>
- U.S. Energy Information Administration, 2015. Annual Energy Outlook 2015. . *Integr. Int. Energy Anal.* 1, 1–244 [https://doi.org/DOE/EIA-0383\(2013\)](https://doi.org/DOE/EIA-0383(2013))
- U.S. Geological Survey. (2021). USGS water data for the Nation: U.S. Geological Survey National Water Information System database, accessed [2/15/2021], at <https://doi.org/10.5066/F7P55KJN>
- Vuataz, F.D., Goff, F., 1986. Isotope geochemistry of thermal and nonthermal waters in the Valles Caldera, Jemez Mountains, northern New Mexico. *J. Geophys. Res.: Solid Earth* 91 (B2), 1835–1853.
- Walvoord, M.A., Pegram, P., Phillips, F.M., Person, M., Kicft, T.L., Fredrickson, J.K., Mckinley, J.P., Swenson, J.B., 1999. Groundwater flow and geochemistry in the southeastern San Juan Basin: implications for microbial transport and activity. *Water Resour. v.* 35 (5), 1409–1424.
- Weiss, R.F., 1968. Piggyback sampler for dissolved gas studies on sealed water samples. *Deep-Sea Res. v.* 15, 695–699.
- Wen, T., Liu, M., Woda, J., Zheng, G., Brantley, S.L., 2021. Detecting anomalous methane in groundwater within hydrocarbon production areas across the United States. *Water Res.* 200, 117236 <https://doi.org/10.1016/j.watres.2021.117236>
- Ziemkiewicz, P.F., Thomas, He, Y., 2015. Evolution of water chemistry during Marcellus Shale gas development: a case study in West Virginia. *Chemosphere v.* 134, 224–231.

Studies of Animas River Watershed Bacterial Communities as Water Quality Indicators and their Relationship to the Aquatic Food Web

Jennifer L. Lowell¹

¹Department of Public Health, Fort Lewis College, CO

Holly D. Vandever²

²UNM Health Sciences Center Office for Diversity, Equity & Inclusion,
University of New Mexico, NM

April Sandman³

³Southwestern Colorado Area Health Education Center, CO

ABSTRACT

Bacteria are an integral part of river ecosystem functioning. Bacterial communities in and on river sediments respond rapidly to environmental stressors, revert to healthy patterns when stressors are removed, and are closely connected to benthic macroinvertebrates (BMI), the gold standard of stream bioindicators. We assessed the potential for microbiomes to serve as additional water quality indicators in mining-impacted streams. Sediments were sampled from five sites in the Animas River Watershed and microbiome composition was compared among sites, to metal concentrations, pH, and BMI diversity indices using a Kruskal-Wallis H-test and UniFrac distance metric. Results revealed significant differences in microbiome diversity among sites ($p = 0.001$) according to pH, arsenic (As), and copper (Cu) concentrations. Overall, microbiomes from neutral pH sites were significantly more diverse than those from acidic sites ($p < 0.01$) regardless of metal concentrations. BMI and bacterial diversity were correlated. Microbiomes could prove valuable as biomonitoring tools.

BACKGROUND

Microbiomes are foundational to aquatic ecosystems and contribute to overall water quality and ecosystem health (Roberto et al. 2018; Gweon et al. 2020). Those within stream sediment biofilms decompose organic matter, cycle nutrients, and degrade contaminants (Battin et al. 2007; Simon et al. 2002; Kowalczyk et al. 2016). However, metal contamination can severely impact microbiome diversity, function, and membership (Yang et al. 2006; Wang et al. 2018; Liao et al. 2019). Studies showed that hyporheic microbiomes responded to metal contamination within one week and stabilized to fluvial heavy-metal contamination at concentrations as low as 9 ppm for As and lead (Pb) respectively, and to 32.2 ppm for zinc (Zn) in as little as eight weeks. Conversely, when the selective pressures of metals were removed, bacteria reverted just as quickly to communities resembling those in healthy systems (Feris et al. 2004). Minimal metal bioavailability reduces microbial respiration and stream nitrification (Carlisle et al. 2005; Yang et al. 2006). Metals also affect microbiome community membership increasing subphyla gammaproteobacteria and decreasing betaproteobacteria with metal exposure (Feris et al. 2003).

Furthermore, microbiomes may provide insight into the trophic cascade and food web vulnerabilities introduced by metal contamination. Studies of inter-taxa communities examining BMIs as consumers, and microbes as decomposers or prey, demonstrated several correlations with bacteria and macroinvertebrates that reflected the connectivity between the two communities (Kim et al. 2008). A study in central Colorado comparing the effects of leaf litter decomposition by microbes and invertebrate shredders showed negative correlations in both microbial respiration, shredder biomass, and diversity when compared to Zn concentrations (Carlisle and Clements 2005). The close association of microbiomes with stream sediments, nutrient utilization at small spatial scales, ubiquity, BMIs, and rapid responses to the introduction and removal of metals, make microbiomes promising candidates for water quality assessment (Wolff et al. 2021).

Historically, microbiome analysis techniques have been labor intensive, required specialized equipment, and lacked sensitivity for the detection of less abundant bacterial groups (Feris et al. 2004; Lowell et al. 2009). Technologies like Next Generation Sequencing, used to analyze human and environmental microbiomes (Schuster 2008), have significantly advanced analyses making their inclusion in water quality assessment a more realistic option. However, more complete comparisons of microbiomes to currently accepted stream health indicators such as BMIs are needed. The objectives of the study herein were to 1) determine if microbiomes from metal impacted streams differed significantly from less impacted streams, and 2) whether metal induced changes in microbiome diversity correlated to changes in BMI diversity. Evaluating microbiome responses to metal impacts could provide an additional tool for evaluating stream health.

STUDY AREA

Historic mining activities during the last century in the Rocky Mountain Region, western USA have produced non-point source acid mine drainage (AMD) from mine adits and waste rock piles scattered throughout mountainous terrain making remediation difficult (United States Environmental Protection Agency 2017). The Bonita Peak Mining District (BPMD), located within the confines of the Animas River Watershed, CO, USA has undergone historic and ongoing releases of metal laden water from mining operations for over a century. Most have occurred in the Mineral Creek, Cement Creek and Upper Animas drainages, which converge into the Animas River near Silverton, Colorado (United States Environmental Protection Agency 2017) (Figure 1). The BPMD consists of 48 distinct mines and was added to the Superfund National Priority List in 2017 following the Gold King Mine spill in August 2015. The Animas River flows south through Durango, CO, the Southern Ute Indian Reservation, and then to New Mexico where it meets the San Juan River. Downstream communities, including those on the Navajo Nation, are dependent on these waters for drinking, irrigation, livestock, and recreation.

METHODS

Sampling

Sediments were sampled at a 5 cm depth at five sites: the Koehler mine settling pond, which discharges effluent into Mineral Creek, two sites in Cement Creek, Town Park, Silverton, CO, and two sites at Baker's Bridge in the Animas River north of Durango, CO (Figure 1). The Koehler mine site was chosen because of its unique elevated As levels compared to other sites that mostly lack As but contain elevated iron (Fe), Zn, and Cu. The Silverton Town Park sites were sampled to represent the physical and chemical properties of Cement Creek both upstream and just before it converges with the Animas River. Baker's Bridge sites were sampled as comparison sites that are relatively unimpacted by AMD compared to those sites near Silverton. Five replicates were sampled at each site for a total of 25 samples. Sediment was transported on ice to the laboratory where As, Fe, Zn, Cu, and Pb concentrations were measured using a GOYOJO XRF Spectrum Analyzer according to EPA Method 6200. Temperature, pH, and dissolved oxygen were measured at each site using a YSI Pro Plus multimeter (Yellow Springs, OH). Average *Ephemeroptera*, *Plecoptera*, and *Trichoptera* (EPT) richness and BMI Shannon's diversity index (SDI) for BMIs measured between 2014–2016 from Baker's Bridge and Cement Creek (Roberts 2017) were compared to microbiome diversity indices to test for correlations between microbiomes and BMIs. EPT taxa are generally considered to be sensitive to degraded

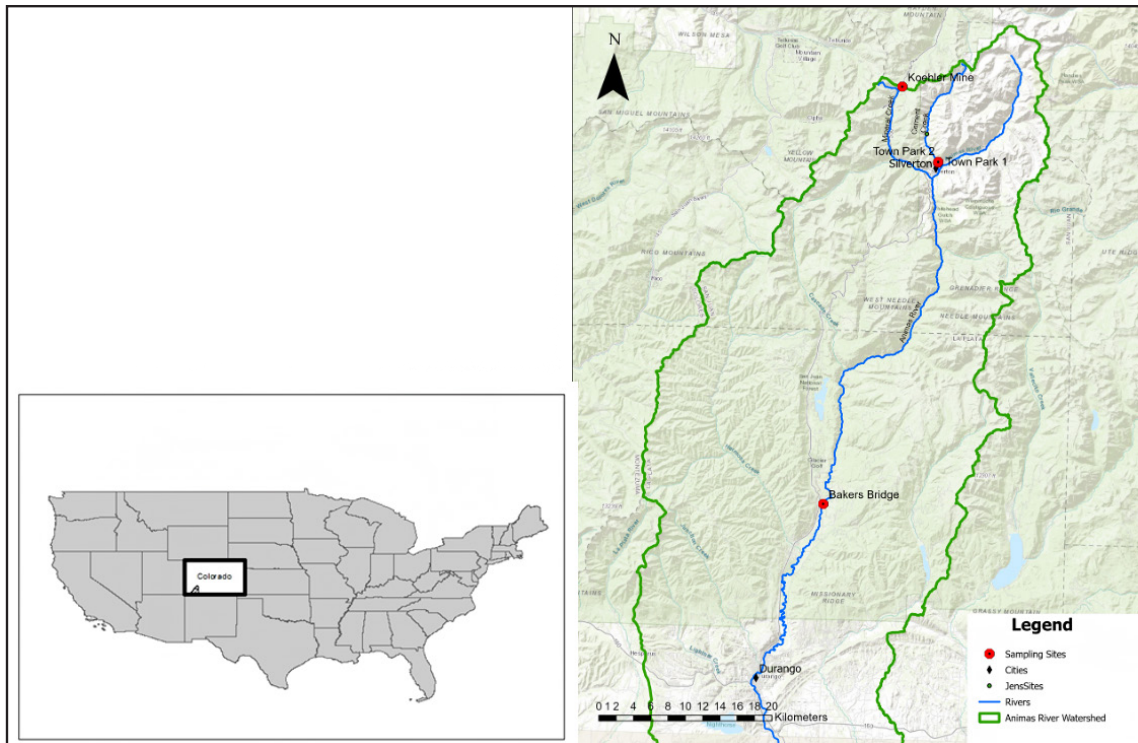


Figure 1. Map of sampling sites in CO, U.S.A. Sites with red circles denote sample locations. Baker's Bridge sites were sampled approximately 100 m apart but are represented by one point due to map scale.

water quality, including elevated metals, while SDI measures overall species diversity and evenness of a community (Roberts 2017).

DNA Extraction

Total community DNA was extracted from 0.5 gm sediment using the MoBio Power Soil Kit® (Carlsbad, CA). Extracted DNA was shipped to the University of Colorado Anschutz Medical Campus in Aurora, CO for sequencing. The V4 region of the 16S rRNA gene was amplified using the 515f/806r primer set (Caporaso et al. 2012) and 5PRIME HotMaster Taq DNA polymerase (Quantabio) according to the Earth Microbiome Project (www.earthmicrobiome.org) protocol. Amplified DNA was quantified using the Invitrogen PicoGreen assay (Carlsbad, CA) and equal amounts of DNA from each sample was pooled. The complete pool was sequenced using a V2 2x250 kit on the Illumina MiSeq platform (San Diego, CA) at the University of Colorado Cancer Center, Genomics and Microarray Core Facility.

Microbial Community and Statistical Analysis

Sequences were analyzed with the Quantitative Insights Into Microbial Ecology 2 (QIIME2) software (Bolyen et al. 2019). Merged reads were assigned to samples based on barcodes and truncated by removing the barcode and primer sequences. The DADA2 pipeline was then applied as a quality control measure to remove chimeric sequences and filter any phiX reads present in marker gene Illumina sequence data. Quality plots of demultiplexed sequences revealed high quality scores of initial and distal base reads for a final sequence length of 250 bp. Sequence alignments were generated using the mafft plugin in QIIME2, and highly variable positions were masked. FastTree was used to generate a phylogenetic tree from sequence alignments. Midpoint rooting was applied, and the resulting tree was used in downstream phylogenetic diversity analyses. Reads were rarefied to 40,391 sequences per sample and alpha-diversity was determined with Faith's Phylogenetic Diversity and Pielou's Evenness. Bacterial community diversity and BMI diversity were compared using Faith's Phylogenetic Diversity Index. Weighted UniFrac measures were applied according to

(Lozupone et al. 2010) to measure beta-diversity and generate principal coordinate analysis (PCoA) plots. This method measures the phylogenetic distance between samples based on abundance and relatedness of shared and unshared operational taxonomic units (OTUs). Taxonomic composition of the samples was determined using a Naive Bayes classifier trained on the Greengenes 13_8 99% OTUs according to QIIME2 to generate taxa tables and plots. Mean relative taxon abundance was calculated and compared between sites by merging metadata with QIIME2 taxon tables in R (version 2023.12.0). Phyla that made up less than 4% of the overall community abundance were collapsed into a category named "Other." Stacked bar charts were generated using ggplot2.

RESULTS

Environmental Data

Sites varied in metal concentrations and abiotic factors (Table 1). Most notably, Koehler mine discharge contained high levels of As, while As was not detectable in samples from Cement Creek or the Animas River. Iron concentrations ranged from 19,538 to 30,069 ppm in Cement Creek and the Animas River sites but was not detectable in the Koehler mine discharge samples. The biggest difference in between site variation was seen in pH. The sites influenced by AMD and metals were acidic (pH 4.02–4.36) compared to downstream sites on the Animas River at Baker's Bridge, which were neutral (pH 7.15). Concentrations of Zn, Cu, and Pb and temperature and dissolved oxygen varied somewhat between sites with ranges from 23.9–447, 21–138, and 76.2–301 ppm respectively (Table 1).

Table 1. Site locations and sediment variable measures. Metal concentrations are in ppm. ND: Not detected.

Location	As	Fe	Zn	Cu	Pb	pH	Temp (°C)	DO (mg/L)
Town Park 1	ND	3069	23.9	0	76.2	4.36	9.5	0.8
Town Park 2	37	39350	83	21	202	4.02	10	0.9
Bakers Bridge 1	ND	24061	447	60	215	7.15	7.2	0.9
Bakers Bridge 2	ND	19538	321	40	113	7.15	7.6	0.8
Koehler Mine Pond	7123	ND	ND	138	301	4.07	5.3	1.3

Overview of the Illumina sequencing dataset

In total, approximately 4,330,687 raw sequence reads of the 16S rRNA gene spanning the hyper variable V4 region were obtained from 25 sediment samples. After filtering the low-quality reads and chimeras, a total of 3,402,419 valid reads (average read length 255 bp) consisting of 14,389 OTUs were used for subsequent downstream analyses.

Taxonomic Profile and Abundance

Altogether, 173 phyla were recovered from the 25 sediment samples. However, the general taxonomic pattern was mainly driven by differences in the abundances of seven major taxonomic groups. The majority of these reads were affiliated with members of the *Proteobacteria*, followed by *Cyanobacteria*, *Acidobacteriota*, *Bacteroidetes*, and *Verrucomicrobia* (Figure 2).

Proteobacteria abundance among all sites ranged from 51.7–58.9% of phyla detected and appeared evenly distributed among sites. *Acidobacteriota*, *Bacteroidetes*, and *Verrucomicrobia*, were more elevated in the Baker's

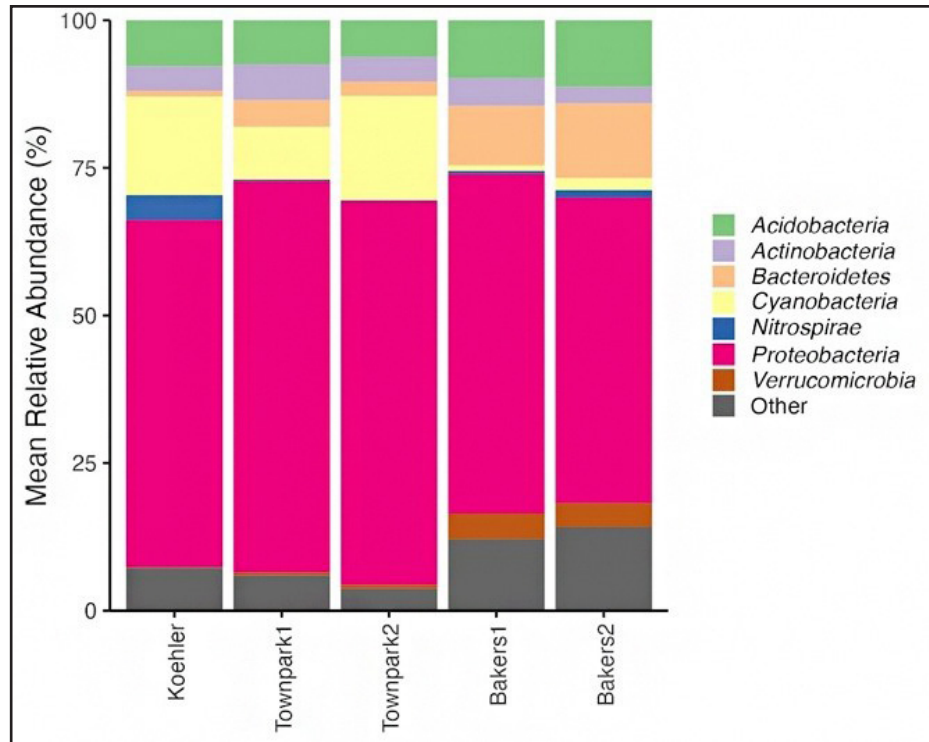


Figure 2. The seven major phyla driving taxonomic variation between sites. Phyla in the “Other” category each made up < 4% of the total community and were collapsed into one bin.

Bridge sediments (9.8–11.3%, 10.1–12.6%, and 4.2%, respectively) as compared to the Koehler mine and the Town Park sites (6.2–7.8%, 0%, .9–4.5%, and 1–2%, respectively). However, Cyanobacteria were more abundant in the Koehler and Town Park sites, ranging from 9–18%, while abundance was only 1–2% at the Baker’s Bridge sites.

Greater taxonomic resolution revealed that within the *Proteobacteria* phylum, bacterial classes differed considerably across sites. *Alphabacteria* ranged from 18.6–27.7% across sites, except Koehler mine, where abundance dropped to 12%. *Betaproteobacteria* were the most consistent class among sites with a relative abundance ranging from 20.4–29.2%. However, *Betaproteobacteria* in the acidic sites consisted almost entirely of *Gallionella*, and, to a lesser degree, *Methylophiales*, and two uncharacterized *Betaproteobacterial* OTUs. *Betaproteobacteria* in the neutral pH sites were much more diverse, consisted of more than ten different sub taxa, and were much more evenly distributed. *Gammaproteobacteria* were most abundant in acidic environments and accounted for 19% of Koehler mine bacteria and around 8–9% at the two Town Park sites. Most was attributed to *Xanthomonadales*, which was rarely detected in downstream sites. In fact, *Gammaproteobacteria* abundance dropped to only 2.2% and 2.1% at Baker’s Bridge sites one and two, respectively. Conversely, *Deltaproteobacteria* were more abundant in the neutral pH Baker’s Bridge sites (8–9%), but made up < 1% at the acidic Koehler and Town Park sites. While *Cyanobacteria* were more prominent in the Koehler and Town Park sites, it was interesting to note that *Stramenopiles* (algae), which share similarity genetic similarity with cyanobacterial 16S rRNA were also abundant.

While initially the *Acidobacteria* overall appeared more likely associated with the Baker’s Bridge sites, greater taxonomic resolution revealed that one class of *Acidobacteria* in the family *Acidobacteriaceae* was more abundant in acidic sites (7%), but made up only < 1% in the neutral pH sites. Meanwhile *Acidobacteria* abundance in the neutral Baker’s Bridge sites was much more diverse and attributed to the *Holophagae*, *Acitobacteria-6*, and *Acidobacteria RB41*. Additionally, *Saprosirae* from the *Bacteroidetes* phylum, preferred neutral conditions. Overall, the most abundant sub taxa (order) in the neutral pH Baker’s Bridge sites were *Burkholderiales*, *Rhizobiales*, *Saprosirales*, *Myxococcales*, and *Sphingomonadales*, while *Gallionellales*,

Rhodospirillales, and *Stramenopiles* (algae), *Xanthomonadales*, and *Acidobacteriales* dominated the acidic Koehler mine and Town Park sites.

Alpha Diversity: Relationship Between Microbial Community Structure and the Environment

Faith's diversity index was used to compare microbiome diversity to sediment pH and metal concentrations. The Koehler mine microbiome was the least diverse of the sites and significantly so when compared with pH and As ($p < 0.01$). Arsenic levels in Koehler mine sediments exceeded 7000 ppm, an extreme concentration compared to other sites (Table 1). When compared to pH, microbiome communities from Koehler mine and Town Park (pH ~4.0) were significantly less diverse ($p < 0.01$) than those from Baker's Bridge (pH 7.0) (Figure 3). However, while diversity was more diminished in Koehler sediments, Faith's diversity indices measured from Koehler and Town Park sediment microbiomes were not significantly different when compared with pH. Overall, as pH dropped, bacterial diversity decreased (Figure 3). Interestingly, sites with intermediate Cu concentrations had more diverse microbiomes than those on either end of the Cu concentration range (Figure 3). Iron concentrations did not appear to influence microbial diversity as much as pH and As. For example, Koehler mine, where diversity was the lowest, had undetectable Fe concentrations, but low pH and high As concentrations. Baker's Bridge sites, which supported the most diverse microbial communities, had Fe concentrations of around 22,000 ppm on average. Zinc concentrations compared to microbiome diversity showed similar patterns in that the most diverse sites had higher Zn concentrations than sites with the lowest diversity. However, those sites were also characterized by a neutral pH. Likewise, according to Peilou's evenness scores, which measures species distribution, the sites with acidic pH had significantly lower scores than those with neutral pH. High As concentrations were also associated with lower evenness scores in the Koehler mine site. And sites with intermediate Cu concentrations had more evenly distributed communities than did those on either end of Cu concentration range.

BMI

Our results suggested that as BMI diversity increases among less metal-impacted sites, so does bacterial diversity. Our two Baker's Bridge sites, which were significantly more diverse than those from mining-impacted sites, correlated to the high EPT richness and SDI scores measured in Fall 2016 (Roberts, SW, 2017). Conversely, sites where EPT readings were undetectable along Cement Creek correlated with our lowest bacterial diversity samples. Although BMIs were not sampled concurrently with bacterial communities, BMI data collected by Mountain Studies Institute (Roberts 2017) and (Scott Roberts, personal communication) were from the same or similar sites collected at the same time of year (Fall). Nevertheless, while these data suggested that BMI, EPT, and SDI fluctuations correlated with those of bacterial communities, results should be considered preliminary (Figure 4).

Beta Diversity

Community beta-diversity was calculated using weighted UniFrac distances. The pair-wise distance matrix using PCoA suggested that around 80% of the community differences were explained by Axis 1 while Axis 2 explained only around 8.9% (Figure 5). The variation demonstrated on Axis 1 was most profound between samples from the acidic Koehler mine and Town Park (pH ~4) sites, and those from Baker's Bridge (pH 7.15). Variation between Koehler mine and Town Park samples was apparent mainly on Axis 2. The PCoA, combined with taxa abundance and alpha diversity measures, led us to hypothesize that community variation is primarily driven by pH, and secondarily by the combination of metals and their concentrations—most notably Arsenic.

DISCUSSION

Lotic bacterial communities are sensitive and respond rapidly to metal contamination (Kevin P Feris et al. 2004). Our results suggested that microbiomes impacted by metals and resultant acidic environments were notably less diverse than those downstream near Baker's Bridge. Unifrac and Faith's diversity measures

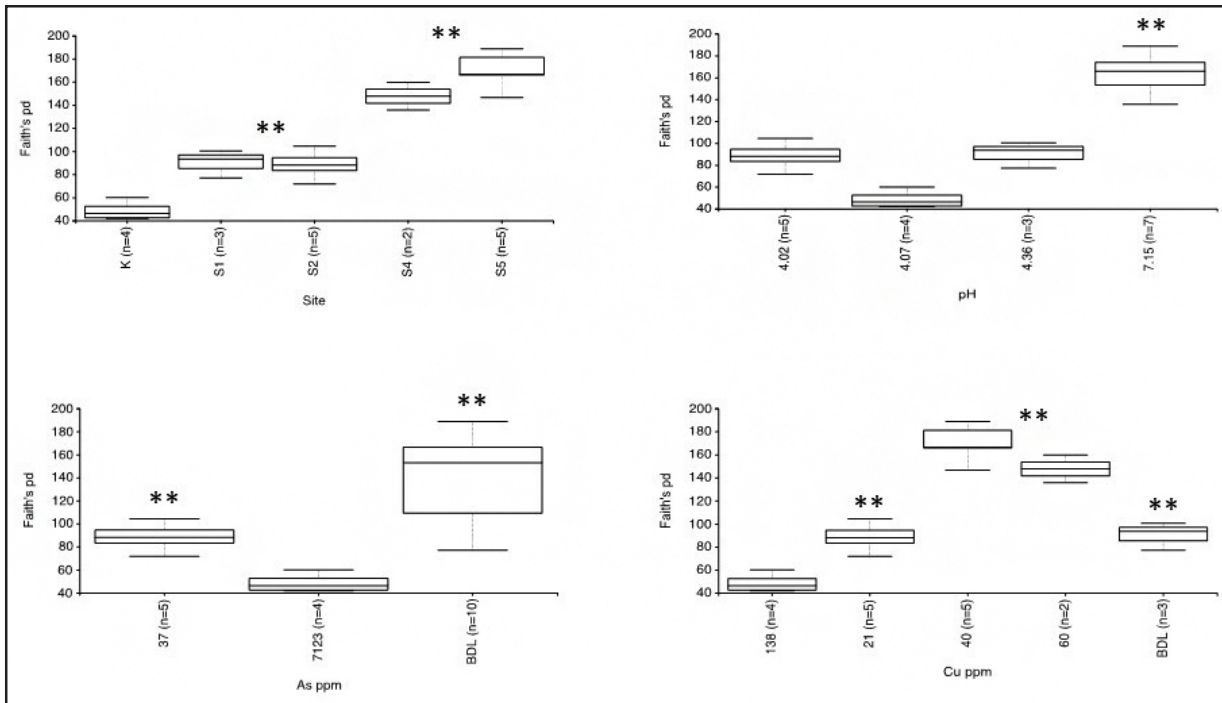


Figure 3. Faith's diversity box plots. ** denotes pairwise comparisons demonstrating significant differences ($p < 0.01$) in microbiome community diversity between sites, differing pH of ~4.0 and ~7.0, and As and Cu concentrations. K, Koehler mine; S1, Town Park 1; S2, Town Park 2; S4, Baker's Bridge 1; S5, Baker's Bridge 2.

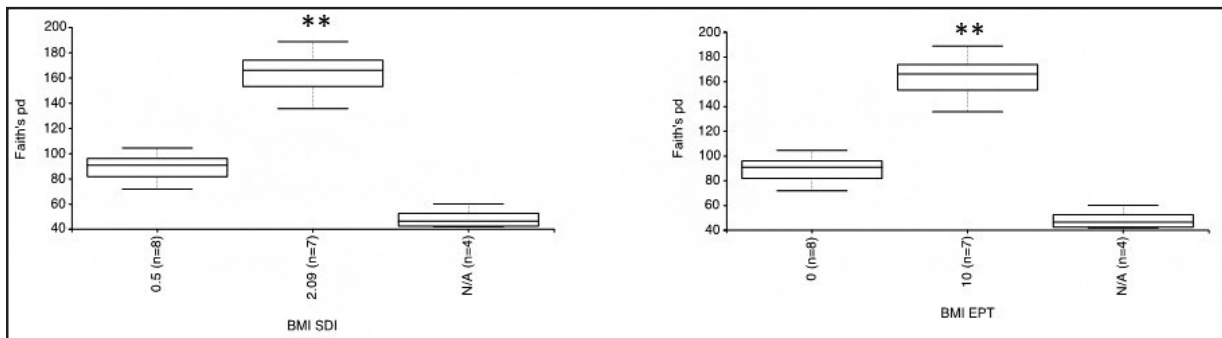


Figure 4. BMI diversity indices comparing bacterial community diversity to BMI diversity. ** denotes pairwise comparisons demonstrating significant differences ($p < 0.01$). BMI; Benthic macroinvertebrate, SDI; Shannon's diversity index, EPT; *Ephemeroptera*, *Plecoptera*, and *Trichoptera*.

strongly suggested that diversity was more likely reduced by the influence of AMD leading to acidic pH than the combination of total metals present, while metals affected bacterial membership. This finding is similar to those of (Wolff et al. 2021) where microbiome membership differed among different metal concentrations while pH was the main driver of diversity differences. Nevertheless, subtle community differences were apparent in the high As concentration Koehler mine site, and with fluctuating Cu concentrations. Four main takeaways can be noted that favor microbiomes as water quality indicators for metal contamination and subsequent remediation steps. 1) Communities in acidic environments that were often associated with metal contamination were markedly less diverse than those in neutral conditions. Clear differences in bacterial taxa produced community fingerprints representative of each environment. Taxa, including Order *Rhizobiales*, *Saprospirales*, *Burkholderiales*, *Myxococcales*, and *Sphingomonadales*, were more abundant in the Baker's Bridge



Figure 5. PCoA of weighted Unifrac microbial community distances between sites. Axis 1 explains 80.08% of the variation among sites. Baker's Bridge samples are highly dissimilar to Koehler or the Town Park sites.

sites. These taxa are plant and soil associated microbes found in healthy functioning lotic ecosystems (Wang et al. 2022) often in consortia with biofilms. Taxa associated with the BPMD sites and under the influence of AMD consisted of Order *Gallionellales*, *Rhodospirillales*, *Xanthomonadales*, *Acidobacteriales* and *Stramenopiles*. Not surprisingly, *Gallionellales* and *Acidobacteriales* are associated with Fe and Cu oxidation and dissolution (Fabisch et al. 2016; Lear et al. 2009). Previous studies have also identified *Gallionellales* as an important bacterial group in AMD environments (Fabisch et al. 2016). Interestingly, acidic sites, which tend to contain low biomass and are by nature oligotrophic, were dominated by photosynthesizers like *Xanthomonadales*, *Stramenopiles*, and *Cyanobacteria*. 2) In addition to being more diverse, taxa detected in the neutral sites were much more evenly distributed. Abundance in acidic sites was skewed towards *Gammaproteobacteria* and *Cyanobacteria*, which diminished taxa evenness. 3) Although pH drove most of the differences in microbiome diversity between sites, signatures for differing metals were detected. While the Koehler mine and Town Park site microbiomes were more similar to each other than to the Baker's Bridge sites, there were notable differences in *Gammaproteobacteria* and *Xanthomonadales* abundance in the Koehler mine site. Studies suggested that *Xanthomonadales* potentially reduces As(V) in a natural wetland (Deng et al. 2022). Given the elevated levels of As within Koehler mine site sediments, it makes sense that As reducers would be dominant at this site. 4) While bacterial diversity fluctuated between BPMD influenced and downstream sites, it also correlated with BMI diversity indices. This is interesting because BMIs and bacteria maintain important symbiotic relationships in aquatic food webs. While this correlation was expected, data to support this provide additional evidence that microbiome changes at the base of the food web may be tied to BMI responses. Furthermore, microbiome taxa and diversity that are indicative of AMD and metals provide additional information regarding the impacts of metal contamination on streams ecosystems. Microbiomes should be considered for future assessments of stream health.

ACKNOWLEDGEMENTS

I would like to thank the Southwestern Water Conservation District for funding support; Dr. Cathy Lozupone and Nichole Nusbacher, University of Colorado Anschutz Medical Campus, for assistance with Illumina sequencing; Dr. Joslynn Lee and Aaron Shiffer for assistance with QIIME2 software; and Kirstin Brown, Colorado Division of Reclamation, Mining and Safety and Scott Roberts, Mountain Studies Institute, for helpful discussions about the Bonita Peak Mining District, sampling guidance, and proposal comments.

REFERENCES

- Battin, Tom J, William T Sloan, Staffan Kjelleberg, Holger Daims, Ian M Head, Tom P Curtis, and Leo Eberl. 2007. "OPINION: Microbial Landscapes: New Paths to Biofilm Research." www.nature.com/reviews/micro
- Bolyen, Evan, Jai Ram Rideout, Matthew R. Dillon, Nicholas A. Bokulich, Christian C. Abnet, Gabriel A. Al-Ghalith, Harriet Alexander, et al. 2019. "Reproducible, Interactive, Scalable and Extensible Microbiome Data Science Using QIIME 2." *Nature Biotechnology*. Nature Publishing Group. <https://doi.org/10.1038/s41587-019-0209-9>
- Caporaso, J. Gregory, Christian L. Lauber, William A. Walters, Donna Berg-Lyons, James Huntley, Noah Fierer, Sarah M. Owens, et al. 2012. "Ultra-High-Throughput Microbial Community Analysis on the Illumina HiSeq and MiSeq Platforms." *ISME Journal* 6 (8). <https://doi.org/10.1038/ismej.2012.8>
- Carlisle, Daren M., and William H. Clements. 2005. "Leaf Litter Breakdown, Microbial Respiration and Shredder Production in Metal-Polluted Streams." *Freshwater Biology* 50 (2): 380–90. <https://doi.org/10.1111/J.1365-2427.2004.01323.X>
- Clements, William H, Daren M Carlisle, James M Lazorchak, Philip C Johnson, and Philip C Johnson3. 2000. "Heavy Metals Structure Benthic Communities in Colorado Mountain Streams." *Ecological Applicationis* 10 (2): 626–38.
- Deng, Jinmei, Tangfu Xiao, Wenjun Fan, Zengping Ning, and Enzong Xiao. 2022. "Relevance of the Microbial Community to Sb and As Biogeochemical Cycling in Natural Wetlands." *Science of the Total Environment* 818. <https://doi.org/10.1016/j.scitotenv.2021.151826>
- Fabisch, M., G. Freyer, C. A. Johnson, G. Büchel, D. M. Akob, T. R. Neu, and K. Küsel. 2016. "Dominance of 'Gallionella Capsiferiformans' and Heavy Metal Association with Gallionella-like Stalks in Metal-Rich PH 6 Mine Water Discharge." *Geobiology* 14 (1). <https://doi.org/10.1111/gbi.12162>
- Feris, Kevin P, Philip W Ramsey, Matthias Rillig, Johnnie N Moore, James E Gannon, and William E Holben. 2004. "Determining Rates of Change and Evaluating Group-Level Resiliency Differences in Hyporheic Microbial Communities in Response to Fluvial Heavy-Metal Deposition." *APPLIED AND ENVIRONMENTAL MICROBIOLOGY* 70 (8): 4756–65. <https://doi.org/10.1128/AEM.70.8.4756-4765.2004>
- Gweon, Hyun S, Michael J Bowes, Heather L Moorhouse, Anna E Oliver, Mark J Bailey, Michael C Acreman, and Daniel S Read. 2020. "Contrasting Community Assembly Processes Structure Lotic Bacteria Metacommunities along the River Continuum." <https://doi.org/10.1111/1462-2920.15337>
- Kim, Byunghyuk, Se Eun Lee, Mi Young Song, Jung Hye Choi, Soon Mo Ahn, Kun Seop Lee, Eungchun Cho, Tae Soo Chon, and Sung Cheol Koh. 2008. "Implementation of Artificial Neural Networks (ANNs) to Analysis of Inter-Taxa Communities of Benthic Microorganisms and Macroinvertebrates in a Polluted Stream." *Science of the Total Environment* 390 (1): 262–74. <https://doi.org/10.1016/J.SCITOTENV.2007.09.009>
- Kowalczyk, Agnieszka, Oliver R. Price, Christopher J. van der Gast, Christopher J. Finnegan, Roger A. van Egmond, Hendrik Schäfer, and Gary D. Bending. 2016. "Spatial and Temporal Variability in the Potential of River Water Biofilms to Degrade P-Nitrophenol." *Chemosphere* 164 (December):355–62. <https://doi.org/10.1016/J.CHEMOSPHERE.2016.08.095>
- Lear, Gavin, Dev Niyogi, Jon Harding, Yimin Dong, and Gillian Lewis. 2009. "Biofilm Bacterial Community Structure in Streams Affected by Acid Mine Drainage." *Applied and Environmental Microbiology* 75 (11). <https://doi.org/10.1128/AEM.00274-09>
- Liao, Hehuan, Kai Yu, Yanhua Duan, Zigong Ning, Binrui Li, Leiyu He, and Chongxuan Liu. 2019. "Profiling Microbial Communities in a Watershed Undergoing Intensive Anthropogenic Activities." *Science of the Total Environment* 647 (January):1137–47. <https://doi.org/10.1016/j.scitotenv.2018.08.103>
- Lowell, Jennifer L, Nathan Gordon, Dale Engstrom, Jack A Stanford, William E Holben, and James E Gannon. n.d. "Habitat Heterogeneity and Associated Microbial Community Structure in a Small-Scale Floodplain Hyporheic Flow Path." Accessed March 29, 2022. <https://doi.org/10.1007/s00248-009-9525-9>
- Lozupone, Catherine, Manuel E Lladser, Dan Knights, Jesse Stombaugh, and Rob Knight. 2010. "UniFrac: An Effective Distance Metric for Microbial Community Comparison." *The ISME Journal* 5:169–72. <https://doi.org/10.1038/ismej.2010.133>
- Roberto, Alescia A., Jonathon B. Van Gray, and Laura G. Leff. 2018. "Sediment Bacteria in an Urban Stream: Spatiotemporal Patterns in Community Composition." *Water Research* 134 (May):353–69. <https://doi.org/10.1016/j.watres.2018.01.045>
- Roberts, Scott. 2017. "Animas River 2017 Benthic Macroinvertebrate Assessment." Durango.
- Schuster, Stephan C. 2008. "Next-Generation Sequencing Transforms Today's Biology." *NATURE METHODS SPECIAL FEATURE | COMMENTARY* 5 (1). <https://doi.org/10.1038/NMETH1156>
- Simon, Meinhard, Hans Peter Grossart, Bernd Schweitzer, and Helle Ploug. 2002. "Microbial Ecology of Organic Aggregates in Aquatic Ecosystems." *Aquatic Microbial Ecology* 28 (2): 175–211. <https://doi.org/10.3354/AME028175>
- United States Environmental Protection Agency. 2017. "BONITA PEAK MINING DISTRICT UNINCORPORATED, CO." Superfund National Priorities List. 2017.
- Wang, Jing, Marc Peipoch, Xiaoxiao Guo, and Jinjun Kan. 2022. "Convergence of Biofilm Successional Trajectories Initiated during Contrasting Seasons." *Frontiers in Microbiology* 13. <https://doi.org/10.3389/fmicb.2022.991816>
- Wang, Lan, Jing Zhang, Huilin Li, Hong Yang, Chao Peng, Zhengsong Peng, and Lu Lu. 2018. "Shift in the Microbial Community Composition of Surface Water and Sediment along an Urban River." *Science of the Total Environment* 627 (June):600–612. <https://doi.org/10.1016/j.scitotenv.2018.01.203>
- Yang, Yuangen, C. D. Campbell, L. Clark, C. M. Cameron, and E. Paterson. 2006. "Microbial Indicators of Heavy Metal Contamination in Urban and Rural Soils." *Chemosphere* 63 (11): 1942–52. <https://doi.org/10.1016/J.CHEMOSPHERE.2005.10.009>

Deep Resistivity Geophysics of the San Juan–Silverton Caldera Complex, San Juan County, Colorado (USA)

**Brian D. Rodriguez, Douglas B. Yager, Eric D. Anderson, Bennett E. Hoogenboom,
Robert L. Runkel, Bruce D. Smith, and Maria Deszcz-Pan**

U.S. Geological Survey, Denver Federal Center,
Denver, Colorado, USA

ABSTRACT

Magnetotelluric (MT) and audiomagnetotelluric (AMT) data are used to better understand the subsurface geology and mineral resources in the San Juan–Silverton caldera complex located near Silverton, Colorado, western United States, as part of the extensive southern Rocky Mountains volcanic field that covers much of southwestern Colorado and northern New Mexico. Seven MT and AMT profiles of varying lengths image resistivity structure to depths of ~5 km. The AMT inversion models characterize geophysical responses of near-surface lithologies, structures, and mineralized systems and also help corroborate airborne electromagnetic data at shallow levels. The MT inversion models extend our depth of investigation from near the surface to great depths (~5 km) and help to form hypotheses about roots of the hydrothermal plumbing that fed shallower mineralized systems. Subsurface high resistivities occur beneath intermediate-composition lava flows and Proterozoic units. Subsurface moderate to low-resistivity values may reflect hydrothermal plumbing that served as flow paths for mineralizing fluids and metallic ore formation. The model interpretations presented in this study could be utilized in remediation planning or mineral resource applications. The methods used could be applied to other watersheds with similar volcanic environments containing acid-generating historical mines or hydrothermally altered and mineralized source rocks.

INTRODUCTION

The southern Rocky Mountains volcanic field (Figure 1) is host to multiple silicic calderas that represent the tops of silicic batholiths that intruded a voluminous intermediate-composition volcanic pile covering much of southwestern Colorado and northern New Mexico, western United States (Lipman and Bachmann, 2015). This geologic setting provides a natural laboratory for using magnetotelluric geophysical techniques for investigating shallow (0–0.3 km) and deep (0.3–5 km) resistivity of lithologies, volcano-tectonic structures, mineralization, ancient hydrothermal plumbing, and modern groundwater plumbing. During caldera formation, ring faults fractured the crust to several kilometers depth and intersected crustal magma reservoirs that vented to the surface and erupted extensive ash-flow tuffs. Dynamic volcanic processes along the caldera margins caused radial fractures to form (Varnes, 1963) as well as megabreccia blocks composed of older rocks comprising the caldera roof rocks that collapsed into the calderas upon eruption (Lipman, 1984). Contemporaneous structures developed during caldera formation and post-caldera collapse structures such as those formed over resurgent domes served as hydrothermal flow paths for mineralizing fluids (Casadevall

and Ohmoto, 1977). The focus of this study is the Paleogene San Juan–Silverton caldera complex (Yager and Bove, 2007), which is centered near Silverton, Colorado, and comprises the San Juan and nested Silverton calderas (Figure 1A). A caldera complex is defined in Cole et al. (2005) as spatially associated nested or overlapping calderas of different ages.

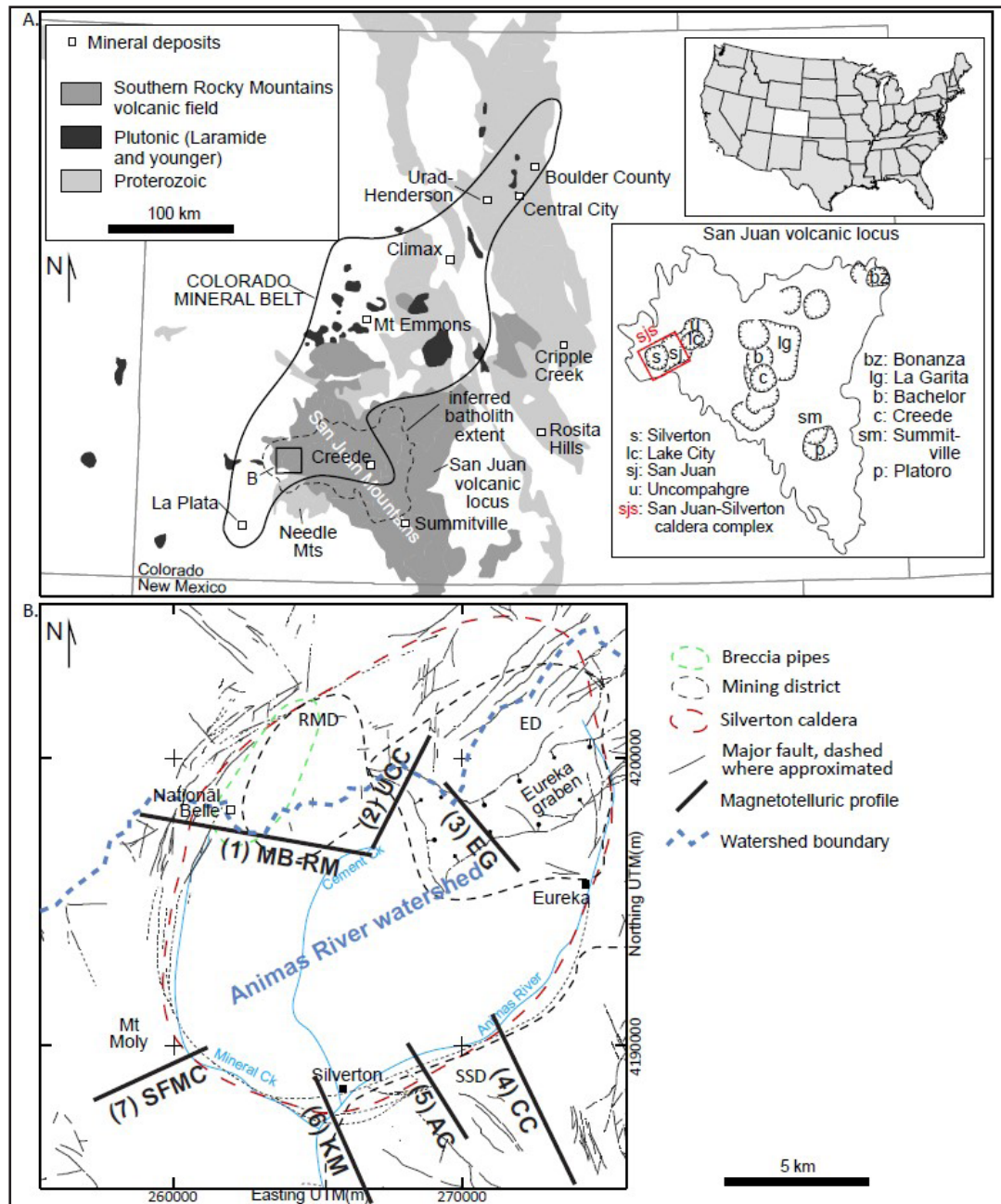


Figure 1. Generalized geologic map of Colorado and structural map of the Silverton caldera in southwest Colorado, USA. (A) Geologic map (modified from Tweto and Sims, 1963) shows Colorado Mineral Belt and mineral deposits. State of Colorado is highlighted in the inset USA index map. San Juan volcanic locus inset map shows ignimbrite calderas (modified from Lipman, 2007). (B) Structural map of the Silverton caldera (modified from Bove et al., 2007b) shows caldera and graben structures, mining districts, and breccia pipes. Mining district abbreviations: ED—Eureka mining district; RMD—Red Mountain mining district; SSD—south Silverton mining district. Magnetotelluric profile abbreviations: MB- RM—Mineral Basin– Red Mountain; UCC—upper Cement Creek; EG—Eureka graben; SFMC—South Fork Mineral Creek; KM—Kendall Mountain; AC—Arrastra Creek; CC—Cunningham Creek. UTM—Universal Transverse Mercator (North American Datum of 1983).

Volcanic rocks in the Silverton, Colorado, area have been subjected to hydrothermal fluids that altered the primary rocks to a secondary mineral assemblage and precipitated metallic minerals, which were historically mined in the area from the late 1870s to the 1990s (Burbank and Luedke, 1969; Bove et al., 2007a, 2007b; Casadevall and Ohmoto, 1977; Varnes, 1963). Minerals such as pyrite weather and dissolve in the presence of oxygen and water to form sulfuric acid, which leaches metals from host rocks. Alteration halos on intrusion margins can impact water quality where groundwater interacts with sulfide-bearing rocks and can also generate acidic drainage. The water that forms due to acid rock weathering can contain relatively high concentrations of dissolved metals that lead to measurable changes in fluid resistivity (Campbell and Fitterman, 2000; Lesmes and Friedman, 2005). This allows bulk resistivity contrasts to be detected and imaged by electromagnetic geophysical methods and mapped in the subsurface. Areas of saturated clay-size minerals, such as smectite, chlorite, illite, kaolinite, pyrophyllite, biotite, and iron oxide (Fulginiti, 2020; Ito and Wagai, 2017), that are originally introduced during hydrothermal alteration events can also be imaged by electromagnetic methods.

The structural evolution of caldera environments such as the San Juan–Silverton caldera complex (Figure 1A) can provide the volcano-tectonic architecture for mineralizing fluids. Where caldera faults are unfilled by secondary minerals, they can serve as pathways for mineralizing fluids that deposit economic minerals during hydrothermal activity. Permeable caldera structures are groundwater flow paths for the modern-day hydrologic plumbing system. Where caldera faults are filled with metallic minerals, the structures may display low resistivity. If quartz, other silicates, and/or non-silicate gangue minerals filled the caldera faults, the structures would be highly resistive. Structures that are filled by metallic or gangue minerals, especially quartz, can act as a hydrologic barrier to groundwater flow (Caine et al., 1996; McDougal et al., 2007; Smith et al., 2007).

This study was designed to investigate major structural features covering a wide geographic distribution of the caldera complex. In addition to having good coverage of many parts of the calderas, this study investigated resistivity responses at multiple depths. The audiomagnetotelluric (AMT) and magnetotelluric (MT) geophysical methods that were applied in this study were used to image electrical resistivity of surficial deposits and bedrock in a hydrothermally altered and mineralized caldera setting. The AMT method allowed investigation of resistivity of Quaternary sediments and fractured bedrock near the surface to ~300 m depth (MT data analysis in the Supplemental Material¹). Imaging of deeper levels of the crust from ~300 m depth to ~5 km depth with the MT method allowed inferences regarding the resistivity of deeper lithologies of rocks that infill and underlie the entire San Juan–Silverton caldera complex. Data collected by the U.S. Geological Survey (USGS) help in the formation of hypotheses regarding the post-caldera collapse hydrothermal plumbing system and modern groundwater locations. Scientists have been pondering for a long time the distribution of subsurface lithology within the Silverton caldera. Doe et al. (1979) is one example where the researchers did not have certainty about subsurface lithology within the calderas. Our data can be used to inform hypotheses about the subsurface lithologies, strengthened with existing surface mapping.

Extensive Pleistocene glaciation and subsequent fluvial erosion of the San Juan–Silverton caldera complex has exposed multiple alteration types associated with different levels of porphyry-style mineralized systems (Bove et al., 2007b; Sillitoe, 2010). Sillitoe (2010) discussed the spatial relationships of alteration types associated with a porphyry-style mineralized system. In general, a silicic lithocap and highly sulfur-rich alteration occur near the top of the porphyry system, and moderately sulfur-rich epithermal polymetallic veins occur at mid-depths above a deeper-seated mineralized porphyry intrusive. Characteristic alteration mineral assemblages that are imaged with geophysics in this study occur in each part of the porphyry system (Bove and Yager, 2007; Ringrose, 1982; Sillitoe, 2010).

¹ Supplemental Material. Magnetotelluric data analysis: Includes introductions to electrical rock properties and the magnetotelluric method, data processing approach, profile model construction, inversion parameters, and topographic effects. Please visit <https://doi.org/10.1130/GEOS.S.25301791> to access the supplemental material, and contact editing@geosociety.org with any questions.

Approximately 700 m of topographic relief from the mountain tops to the valley bottoms has revealed shallow and deep levels of the porphyry systems. This provides an exceptional natural laboratory for investigating porphyry-style mineralization events. The epithermal and porphyry $\text{Co} \pm \text{Au} \pm \text{Mo}$ environments within the porphyry copper system generally span the upper few kilometers of crust (Sillitoe, 2010). Such geometry makes the porphyry copper system difficult to map with continuous data sets. However, modification from post-ore tectonics can reveal shallow and deep environments, providing more complete surface exposures to the system (e.g., Ann-Mason porphyry copper deposit, Nevada, USA; Dilles and Einaudi, 1992).

MT data have been successfully used to image subsurface electrical resistivity contrasts in caldera environments. Studies have shown MT data to be applicable to interpretations of groundwater reservoirs of intracaldera fill, mineralized structures, and areas of hydrothermal alteration. At Las Cañadas caldera, Tenerife, Canary Islands, the MT method was used to image zones of low resistivity associated with groundwater aquifers in porous, post-caldera volcanics within the caldera (Pous et al., 2002). The MT data at Las Cañadas caldera were also used to image and reconstruct caldera collapse geometry (Coppo et al., 2008; Piña-Varas et al., 2015). MT studies at Long Valley caldera, California, western United States, were used to investigate the hydrothermal source for hot, shallow circulating fluids (Peacock et al., 2016). In addition to groundwater and caldera structural geometry, active geothermal systems have been imaged (Aizawa et al., 2009; Di Giuseppe et al., 2017; Hogg et al., 2018; Santos et al., 2006; Siniscalchi et al., 2017). The MT method has also been applied to extinct, altered and mineralized caldera environments. A MT study of the Bursum caldera, New Mexico, imaged a resistive, silicified and mineralized vein zone with an adjacent lower-resistivity alteration halo (Senterfit et al., 1996). The MT method was utilized at Questa caldera in northern New Mexico to image the caldera ring-fault margin as well as zones of low resistivity associated with inferred areas of hydrothermally altered rocks and stockwork molybdenum mineralization (Long, 1985).

MT data were collected in this study for interpretation of subsurface changes in resistivity related to bedrock lithologies, caldera structures, mineralization, and hydrothermal alteration as well as overburden and modern groundwater. The MT method is useful for interpreting causes of low-resistivity signatures where groundwater in volcanic rocks might have higher specific conductance in areas of acid rock weathering. We imaged electromagnetically, utilizing the MT method, multiple styles of alteration and mineralization, representing multiple depths in the crust.

Specific questions addressed in this study include:

- What is the electrical resistivity of hydrothermally altered and mineralized systems, and what can electromagnetic data reveal about an ancient hydrothermal plumbing system?
- Can the tops of granitic batholiths that underpin the silicic calderas be imaged?
- Can groundwater aquifers be imaged, and can this information be used to interpret hydrology and physical properties of a modern hydrologic plumbing system?
- What is the resistivity of near-surface, highly fractured rocks compared with deeper, more sparsely fractured bedrocks?
- What is the resistivity of vein structures and caldera faults?
- What is the resistivity of Quaternary sediments?

The questions addressed have direct application to mineral deposit research in caldera settings in the study area and in other caldera settings having similar magmatic, volcano-tectonic, and mineralization characteristics. Application of shallow electromagnetic data has implications for understanding the resistivity of modern groundwater that are pertinent to multiple legacy mines being remediated as part of cleanup efforts in the Bonita Peak mining district Superfund area. The Superfund area (all National Priority List sources are listed in U.S. Environmental Protection Agency, 2016) encompasses much of the Silverton caldera and includes the drainages of South Fork Mineral Creek, Arrastra Creek, and Cunningham Creek along the

Silverton caldera margin. This study applies inverse modeling to MT data to better understand the resistivity beneath the San Juan–Silverton caldera complex at a depth of investigation and scale not realized in previous studies.

GEOLOGIC SETTING

In the western San Juan Mountains, early Proterozoic metasediments, metavolcanics, and quartzites form the basement rocks (Gonzales and Van Schmus, 2007). These Proterozoic rocks are unconformably overlain by a sedimentary sequence of Paleozoic, Mesozoic, and Cenozoic sedimentary rocks (Figure 2). Within the study area, most of these older rocks are overlain, crosscut, or buried by a thick sequence of mainly Eocene, Oligocene, and Miocene volcanic and intrusive rocks (Bove et al., 2001; Gonzales, 2015; Lipman et al., 1976; Lipman and McIntosh, 2008). The oldest igneous rocks are 35–30 Ma intermediate-composition volcanic rocks of the San Juan Formation. The San Juan Formation represents the initiation of volcanism in the southern Rocky Mountains volcanic field. The San Juan Formation and subsequent eruptives cover much of southwestern Colorado and parts of northern New Mexico (Lipman and Bachmann, 2015). The early intermediate-composition volcanic and volcanoclastic rocks were erupted or eroded from central vent volcanoes likely similar to those seen today in the Cascade Range of the Pacific Northwest, United States. The volcanic deposits coalesced, covering an area of ~25,000 km² (Lipman et al., 1970). Within the area of this study, San Juan Formation rocks are exposed mainly north and west of Mineral Creek (Figure 2).

Silicic Caldera Cycle of Volcanism and Volcano-Tectonic Framework

An episode of silicic volcanism followed deposition of the San Juan Formation. Several ash-flow tuffs derived from western San Juan Mountains caldera-forming eruptions are preserved as a sequence of layered units near the headwaters of Middle Fork Mineral Creek, Porphyry Gulch, and Mineral Basin located west of Mineral Creek (Figure 2). The silicic calderas most relevant to this study are the 28.2 Ma San Juan and nested 27.6 Ma Silverton calderas, referred to in this study as the San Juan–Silverton caldera complex. The San Juan caldera's eruptive volume (1000 km³) is about two orders of magnitude greater than that of the Silverton caldera (75 km³) (Lipman, 2007; Lipman and Bachmann, 2015). The intracaldera Eureka Member of the Sapinero Mesa Tuff (Figure 2, unit Tse) that ponded within the San Juan caldera is the principal ash-flow unit traversed in this geophysical study. The topographic margin of the San Juan caldera is well defined south of the Animas River in headwater basins such as in Cunningham Creek (Figure 2), where Paleogene volcanics of the caldera cycle are in abrupt contact with older Proterozoic crystalline basement rocks, Paleozoic sedimentary units, and San Juan Formation volcanoclastic rocks (Yager and Bove, 2007, their plate 1). Caldera faults associated with the Silverton caldera are prominent structural features and have been mapped along Mineral Creek in a zone extending from Red Mountain Pass to south of Middle Fork Mineral Creek and along the upper Animas River east of Silverton (Figure 2) (Lipman and Bachmann, 2015; Steven and Lipman, 1976; Yager and Bove, 2007). The Silverton caldera has a slightly oval morphology in map view and is elongate toward the northeast with a dimension of ~17 km × 13 km. Incision of the major drainages occurs along caldera-bounding faults, and the arcuate drainage pattern formed by Mineral Creek and the upper Animas River demarcates the Silverton caldera margins.

The mapped caldera faults and structural topographic features can generally be categorized as belonging to four groups: (1) an arcuate zone of caldera ring faults that define the Silverton caldera structural margin, (2) radial faults that trend northwest-southeast along the northern and southern caldera margins, (3) northeast-to northwest-trending graben-related faults that developed over a resurgent dome within the caldera complex, and (4) the topographic margin of the San Juan caldera (Varnes, 1963; Casadevall and Ohmoto, 1977; Yager and Bove, 2007). Caldera faults extend as much as several kilometers in depth (Lipman, 1984).

San Juan Formation lavas were down-dropped along normal faults during caldera formation when caldera ring faults formed along the western Silverton caldera structural margin. The caldera faults mapped in Mineral Basin are north-to northeast-trending features that may penetrate the crust from the surface to several kilometers depth (Lipman, 1984; Luedke and Burbank, 2000, their plate 1, cross section A-A') and may have been conduits for hydrothermal fluids and magmatic intrusions. Fisher and Leedy (1973) recognized the inferred structural control of dacitic intrusions and breccia deposits in the Red Mountain mining district

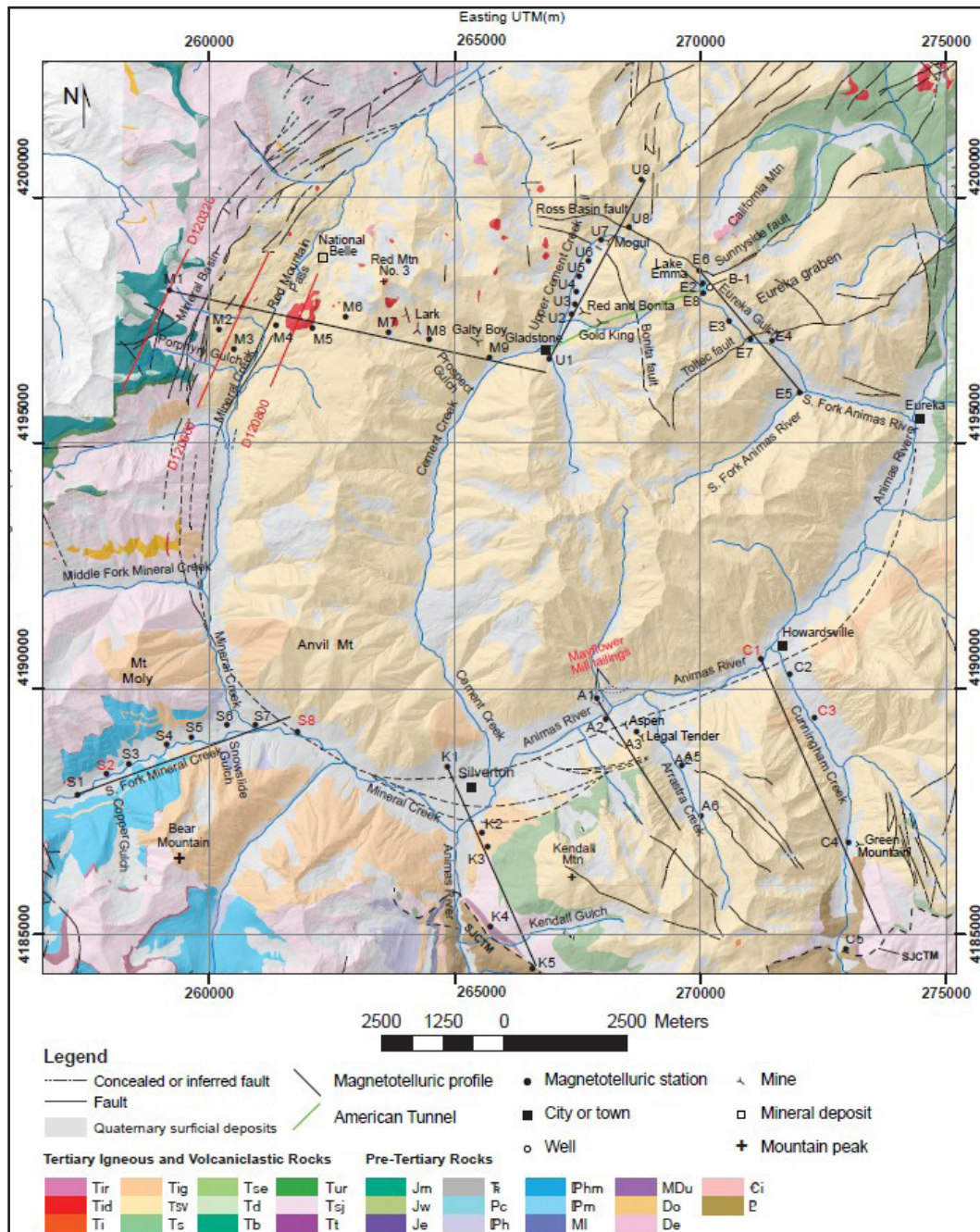


Figure 2. Generalized geologic map of part of the Animas River watershed and vicinity, Silverton area, southwestern Colorado, USA (modified from Yager and Bove, 2007). Black bold number labels represent audiomagnetotelluric (AMT) and magnetotelluric (MT) stations (red number labels are AMT- only stations). Straight black lines are profile projections of AMT and MT profile models. Red lines (D120320, D120600, and D120800) are 2019 airborne electromagnetic flight lines (Hoogenboom et al., 2022a). Straight green line is American Tunnel. SJCTM—San Juan caldera topographic margin; Tir—rhyolite; Tid—dacite intrusions; Ti—intrusions; Tig—Sultan Mountain stock; Tsv—Silverton Volcanics; Ts—Sapinero Mesa Tuff; Tse—Eureka Member of Sapinero Mesa Tuff; Td—Dillon Mesa Tuff; Tb—Blue Mesa Tuff; Tur—Ute Ridge Tuff; Tsj—San Juan Formation; Tt—Telluride Conglomerate; Jm—Morrison Formation; Jw—Wanakah Formation; Je—Entrada Sandstone; —Dolores Formation; Pc—Cutler Formation; h—Hermosa Formation; hm—Hermosa and Molas Formations (undivided); m—Molas Formation; MI—Leadville Limestone; MDu—Leadville and Ouray Limestones (undivided); Do—Ouray Limestone; De—Elbert Formation; i—Ignacio Quartzite; P—Proterozoic rocks (undifferentiated). UTM—Universal Transverse Mercator (North American Datum of 1983).

(Figure 1B) on structures that formed along the Silverton caldera margin. These structures may also be zones of weakness in the bedrock that are modern groundwater flow paths. Paleoproterozoic basement rocks and the overlying Paleozoic, Mesozoic, and Eocene–Oligocene volcanic rocks, including those of the San Juan Formation, down-dropped as megabreccia blocks along the caldera structural wall (Luedke and Burbank, 2000, their plate 1, cross sections A-A' and C-C'). These older rocks were concealed beneath the San Juan–Silverton caldera complex by later volcanic rocks as part of the caldera cycle of volcanism (Luedke and Burbank, 2000, their plate 1, cross section C-C'; Yager and Bove, 2007).

The San Juan caldera topographic margin features are of interest from a shallow groundwater perspective due to contrasting lithologies that have developed along the caldera wall. Contrasting lithologies occur where intracaldera Silverton Volcanics lavas overlie San Juan Formation volcanoclastic rocks. Rock textural contrasts occur where fragmental mesobreccia and megabreccia formed along the caldera wall as ash-flow tuff comingled with caldera wall-rock fragments. Megabreccia occurs along the northwestern Silverton caldera ring-fault zone (Figure 2, near station M4) and along the southern San Juan caldera margin in upper Cunningham Creek where Paleozoic rocks overlie down-dropped Proterozoic basement (Figure 2, near C5). Mesobreccia occurs along the eastern slopes of Cunningham Creek (Figure 2, near C3) and along the San Juan caldera margin south of Silverton (Figure 2, near K4 and K5). The contrast in lithology from more competent Proterozoic basement wall rocks outward from the caldera topographic margin to inward toward the caldera core consisting of fragmental breccia, intracaldera tuff, and layered lavas of the Silverton Volcanics may provide surfaces or zones for groundwater flow.

Silverton Volcanics lavas that are predominantly intermediate in silica composition and subsidiary silicic lavas infilled the caldera collapse area to a thickness of >1 km after ignimbrite eruption (Lipman et al., 1973; Lipman, 1976b; Yager and Bove, 2007). Silverton Volcanics lavas are the most pervasive lithology exposed in the study area, and volcanic accumulations are centered on the core of the caldera complex.

The intracaldera lavas that infilled the calderas were subsequently domed, forming an apical graben (Eureka graben). The Eureka graben is a complex structure that has been described as “boot shaped” (Casadevall and Ohmoto, 1977). The eastern part of the “leg” of the boot-shaped structure comprises northeast-trending faults (Sunnyside and Toltec faults) that extend for ~5 km toward the northeastern part of the caldera complex. Intracaldera Silverton Volcanics have been down-dropped along the graben faults against older intracaldera ash flows of the San Juan caldera. The top “foot” of the structure in the western part of the Eureka graben consists of an ~3-km-long northwest-trending structure known as the Ross Basin fault that intersects the Sunnyside fault in upper Eureka Gulch near Sunnyside Saddle and extends into Ross Basin. The “sole” of the boot is an ~4-km-long northwest-trending structure in upper Cement Creek known as the Bonita fault. Some structures within the Eureka graben were highly mineralized with base and precious metals and were mined from near the surface in Eureka Gulch to as much as 600 m vertical extent in the Sunnyside mine workings (Casadevall and Ohmoto, 1977).

Hydrothermal Alteration and Mineralization Events

Hydrothermal events have altered the primary mineralogy of the rocks within the San Juan and Silverton calderas. An alteration map modified from Bove et al. (2007a) is shown in Figure 3. Secondary mineral assemblages formed when hydrothermal fluids from igneous intrusions heated and permeated the surrounding rocks, altering the primary mineralogy. In places, hydrothermal fluids transported and precipitated sulfide minerals such as pyrite. The acid generated from the weathering of these sulfide-bearing assemblages can leach metals from rocks and produce waters with moderate to high specific conductance in the pore space of igneous host rocks, causing lower bulk electrical resistivity as observed in geophysical data (Campbell and Fitterman, 2000).

A relatively low-temperature, caldera-related episode of propylitic alteration (Figure 3) is pervasive throughout the caldera and in the entire upper Animas River watershed (Figure 1B) (Bove et al., 2007b; Burbank, 1960). The secondary minerals, including calcite that formed during propylitic alteration, can supply acid-neutralizing capacity and be a source of some alkalinity (Yager et al., 2008). The propylitic assemblage was overprinted by higher-temperature alteration events associated with igneous intrusions and stocks in an

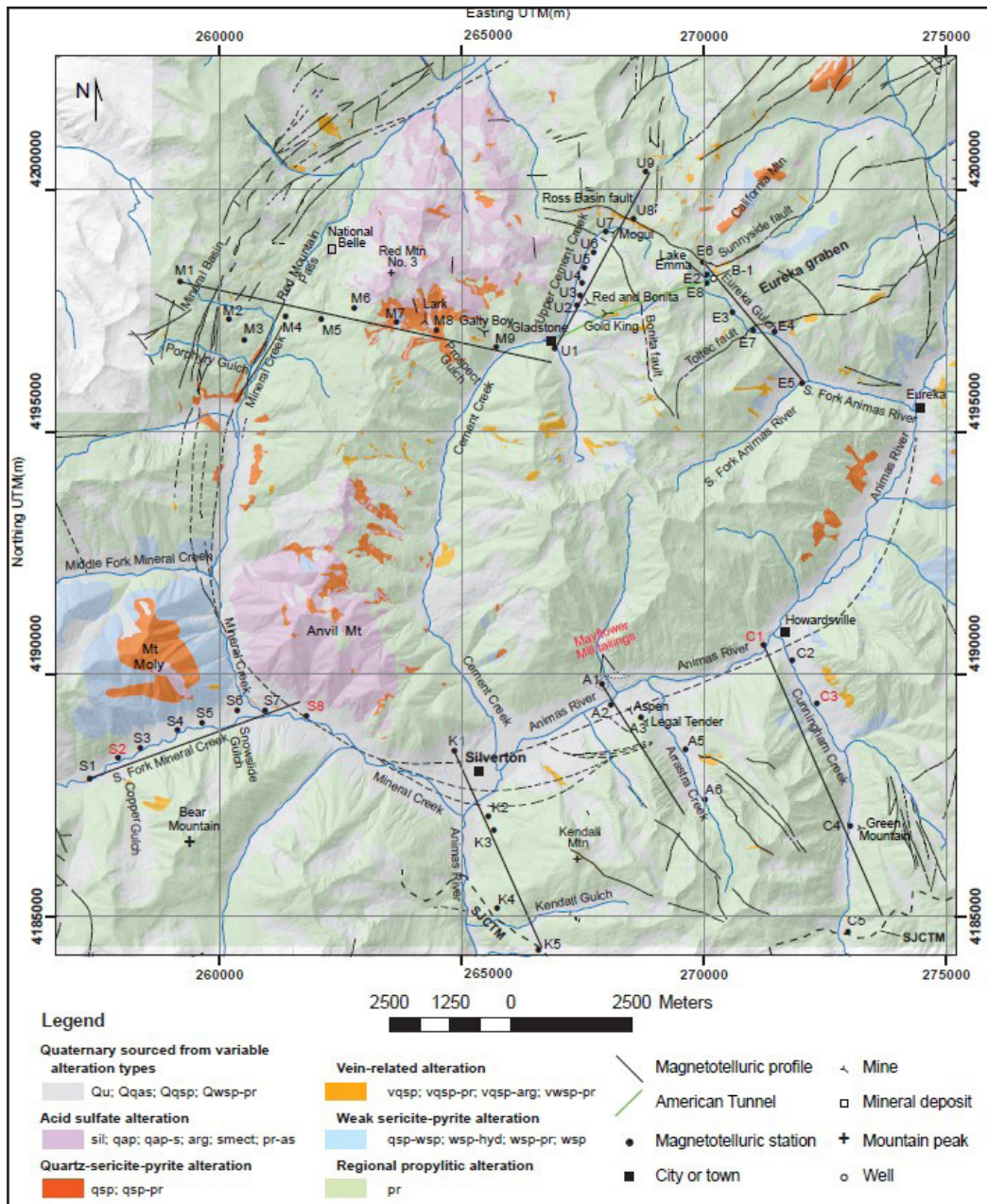


Figure 3. Alteration map showing major faults of the Animas River watershed headwaters near Silverton, southwestern Colorado (modified from Bove et al., 2007a). Black bold number labels represent audiomagnetotelluric (AMT) and magnetotelluric (MT) stations (red number labels are AMT only stations). Straight black lines are profile projections of AMT and MT profile models. Straight green line is American Tunnel. Other symbols are as in Figure 2. Quaternary surficial deposits include: Qu—undifferentiated Quaternary units, including talus and landslide deposits from altered rocks; Qqas—quartz- alunite- pyrophyllite; Qqsp—quartz- sericite- pyrite; Qwsp- pr—weak sericite-pyrite (WSP) and propylitic. Bedrock acid sulfate suite includes: sil—silicified; qap—quartz- alunite- pyrophyllite (QAP); qap- s—predominantly QAP with lesser quartz- sericite- pyrite; arg—argillic; smect—smectitic; pr- as—mixed propylitic and acid sulfate. Bedrock pervasive quartz- sericite- pyrite alteration includes: qsp—quartz- sericite- pyrite (QSP); qsp- pr—mix of QSP and propylitic altered rocks. Bedrock vein- related alteration includes: vqsp—vein- related zones of QSP; vqsp- pr—vein QSP mixed with lesser propylitic; vqsp- arg—vein QSP grading into argillic; vwsp- pr—vein- related zones of WSP mixed with propylitic. Bedrock weak sericite- pyrite alteration includes: qsp- wsp—mix of QSP and WSP altered rock; wsp- hyd—mix of WSP and hydrothermal propylitic; wsp- pr—mixed WSP and propylitic; wsp—weak sericite- pyrite. Bedrock regional propylitic suite includes: pr—propylitic. UTM—Universal Transverse Mercator (North American Datum of 1983); SJCTM—San Juan caldera topographic margin.

area covering ~12% of the study area (Yager et al., 2013). The important alteration assemblages in the caldera listed in order of increasing alteration intensity and temperature are: propylitic, weak sericite-pyrite (WSP), quartz-sericite-pyrite (QSP), vein QSP, and acid sulfate. WSP, QSP, vein QSP, and acid sulfate alteration are all potential acid generators due to the presence of pyrite. The higher-temperature, intense alteration types have abundant clay or clay-sized minerals (Bove et al., 2002) that can decrease the electrical resistivity. For a detailed discussion of alteration types, see Bove et al. (2007b).

The mineral deposits within the caldera have been mined for metallic minerals formed as part of the mineralizing systems of the Red Mountain mining district (Fisher and Leedy, 1973), Eureka mining district (Casadevall and Ohmoto, 1977), and south Silverton mining district (Figure 1B) (Varnes, 1963). Dates determined on intrusions and associated alteration and mineralization document the multiple episodes and styles of mineralization. The mineral deposits have been partially exhumed due to uplift and weathering, exposing multiple levels of porphyry-style mineralization events.

Deposits in the Red Mountain mining district are characterized by acid sulfate alteration and chimney-shaped breccia deposits hosted in Silverton Volcanics that contain ores of silver-lead-zinc in the shallower levels to copper-gold in the deeper levels (Fisher and Leedy, 1973; Gonzales and Larson, 2017). Sanidine and biotite from dacite porphyry intrusions that are spatially associated with mineralized breccias and that likely were the heat source for mineralization yield slightly discordant K-Ar dates of 24.0 ± 0.7 Ma and 21.9 ± 0.6 Ma, respectively (Hon and Mehnert, 1983).

Mineralization associated with the Eureka and south Silverton mining districts are characterized by QSP (vein) alteration and epithermal polymetallic vein mineralization, dominantly composed of ores of copper-lead-zinc-silver-gold. Ages of mineralization in the Eureka mining district (Sunnyside mine) are estimated to be between 16.6 and 13 Ma. These ages are based on Rb-Sr isotope data determined on altered rocks within the mineralized system (Casadevall and Ohmoto, 1977). Mineralization ages in the Eureka mining district overlap ages of mineralization of the south Silverton mining district (Shenandoah-Dives mine) that were determined from concordant zircon and sphene fission-track dates to be 17–16 Ma (Casadevall and Ohmoto, 1977). Due to the limited age determinations from relatively imprecise methods and lack of suitable datable material from vein-related altered rock, more work is necessary to better understand the timing and genetic similarities of mineralization in the Eureka and south Silverton mining districts. Ages of Eureka mining district ore bodies were estimated to be between 16.6 and 13.0 Ma (Casadevall and Ohmoto, 1977). Concordant sphene and zircon fission-track dates from the Shenandoah-Dives mine in the south Silverton mining district were determined to be 16 to 17 Ma (Casadevall and Ohmoto, 1977).

Minor tungsten and gold telluride minerals were mined in several of the polymetallic vein deposits (Belser, 1956; Burbank and Luedke, 1969; Koch, 1990). Low-grade porphyry copper-molybdenum mineralization along the western margin of the caldera complex occurs west of Mineral Creek between the subbasins of South Fork Mineral Creek and Middle Fork Mineral Creek (Figure 3). The copper-molybdenum deposit is associated with granitoid stocks ranging in age from 25.9 ± 0.6 Ma to 25.2 ± 0.6 Ma (K-Ar from biotite) (Jackson et al., 1980). The copper-molybdenum deposit has a zoned alteration assemblage consisting of QSP and minor acid sulfate–WSP (hydrothermal)–propylitic extending outward from the intrusive rocks (Bove et al., 2007b; Ringrose et al., 1986).

GEOPHYSICAL METHODS

Airborne electromagnetic (AEM) data collected in 2019 have been analyzed, modeled, interpreted, and reported in related papers (Hoogenboom et al., 2022a, 2022b), while aeromagnetic data collected in 1999 (Figure 4) have been analyzed, interpreted, and reported (Anderson et al., 2018; Smith et al., 2007). The USGS collected MT data in July 2018 and July 2019 (Cox et al., 2021; Reitman et al., 2019, 2021a, 2021b) along seven profiles that cross the structural margin of the Silverton caldera (Figure 2) and along two profiles within the caldera itself. The major magnetic trends in Figure 4 reveal that the alignment of each MT profile is sub-perpendicular to these trends except for the MT profile along upper Cement Creek (Figure 2). The MT depth of investigation extends the resistivity imaging of the 2019 AEM survey to ~5 km depth (Figures 5–11).

Resistivity inversions of the 2019 AEM survey were examined for flight lines in close proximity to USGS AMT stations. One example of a coincident flight line with an AMT profile illustrates an area where the resistivity inversions of the AEM and AMT surveys were in general agreement (Figure 12).

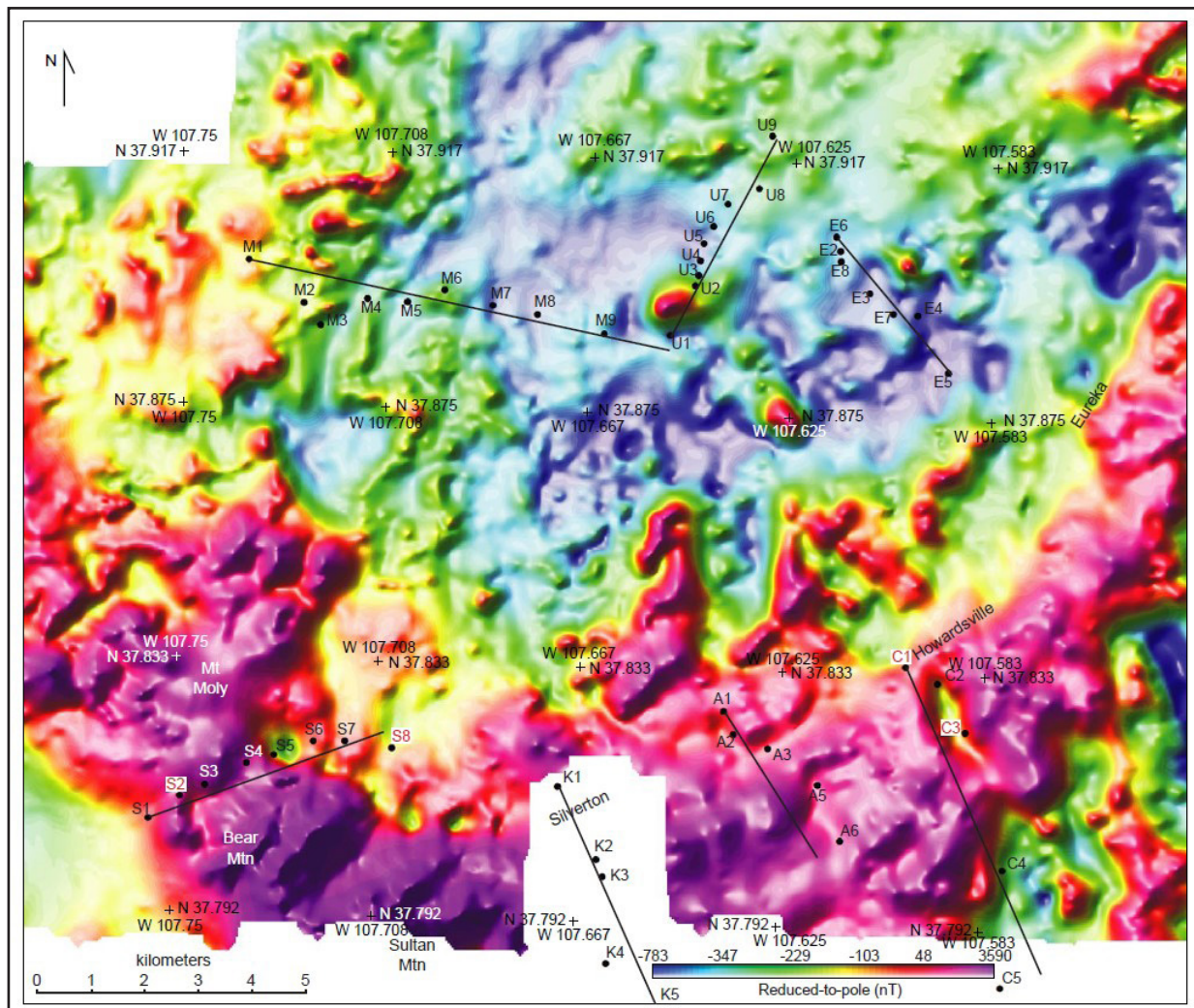


Figure 4. Reduced-to-pole magnetic anomaly map over the Silverton caldera. Warm colors indicate magnetic highs, cool colors indicate magnetic lows. Arcuate magnetic high in the south follows the caldera-bounding structures (Figure 1B) and is interpreted to be sourced in the Sultan Mountain stock that crops out in the southwest and intermittently along the southern margin (Figure 2). Central magnetic low indicates that much of the caldera infill volcanic rocks have low magnetic response, which may be due in part to magnetite destructive hydrothermal alteration (Anderson et al., 2022). Solid black circles with labels represent audiomagnetotelluric (AMT) and magnetotelluric (MT) stations. Red number labels are AMT-only stations. Straight black lines are profile projections of AMT and MT profile models.

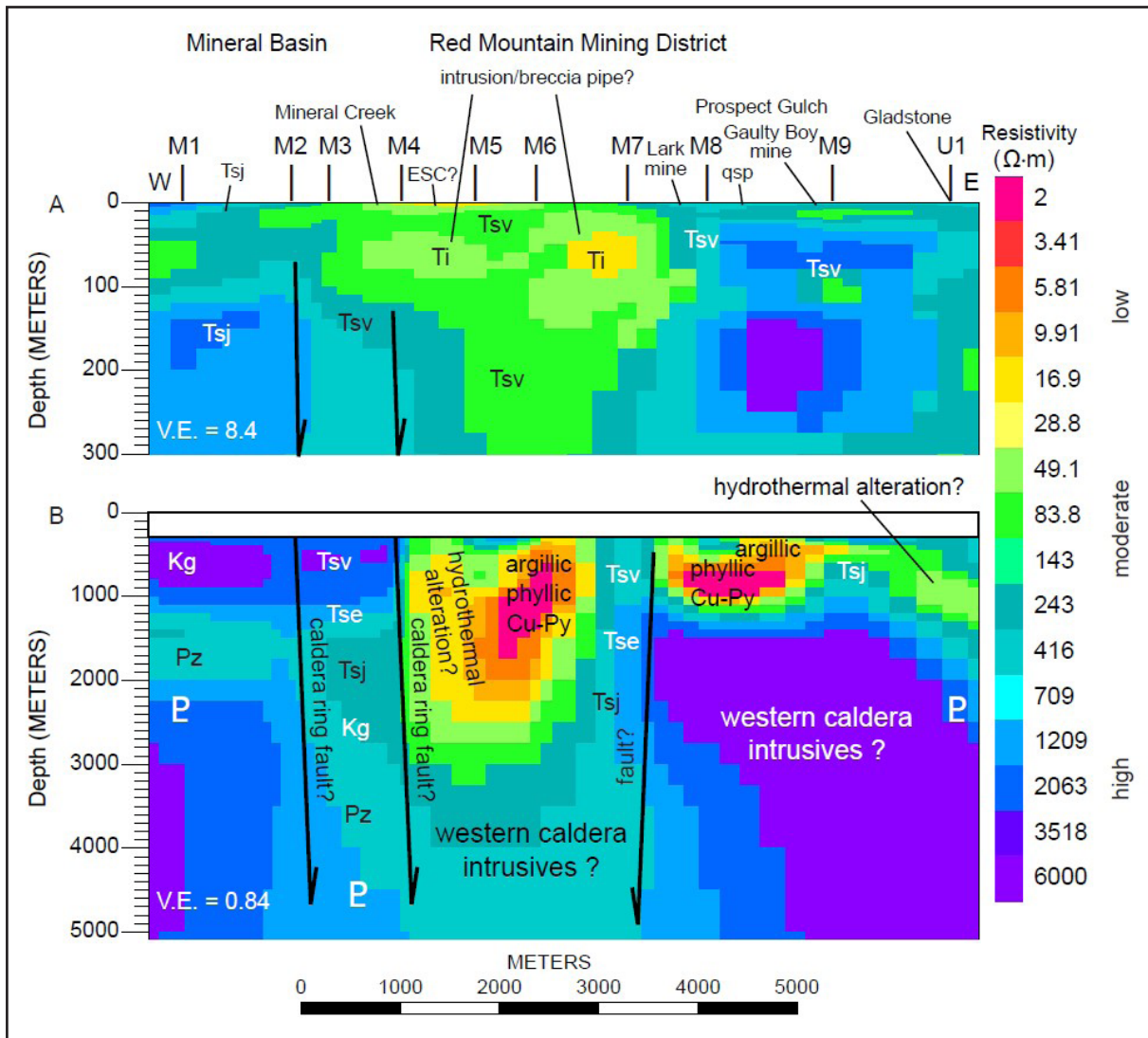


Figure 5. Magnetotelluric resistivity section across Mineral Basin and Red Mountain mining district (Figure 1) with interpreted geologic units and faults (Figure 2). Black number labels at top of profile represent projected locations of magnetotelluric (MT) and audiomagnetotelluric (AMT) stations. Ti—intrusions; Tsv—Silverton Volcanics; Tse—Eureka Member of Sapinero Mesa Tuff; Tsj—San Juan Formation; Kg—Cretaceous granodiorite; Pz—Paleozoic rocks (undifferentiated); P—Proterozoic rocks (undifferentiated); qsp—quartz-sericitopyrite alteration. Top panel (A) is AMT model showing depths from 0 to 300 m with vertical exaggeration (V.E.) ~8.4. ESC—elevated specific conductance. Bottom panel (B) is MT model showing depths from 0 to 5000 m with vertical exaggeration ~0.84. Cu-Py—copper-pyrite.

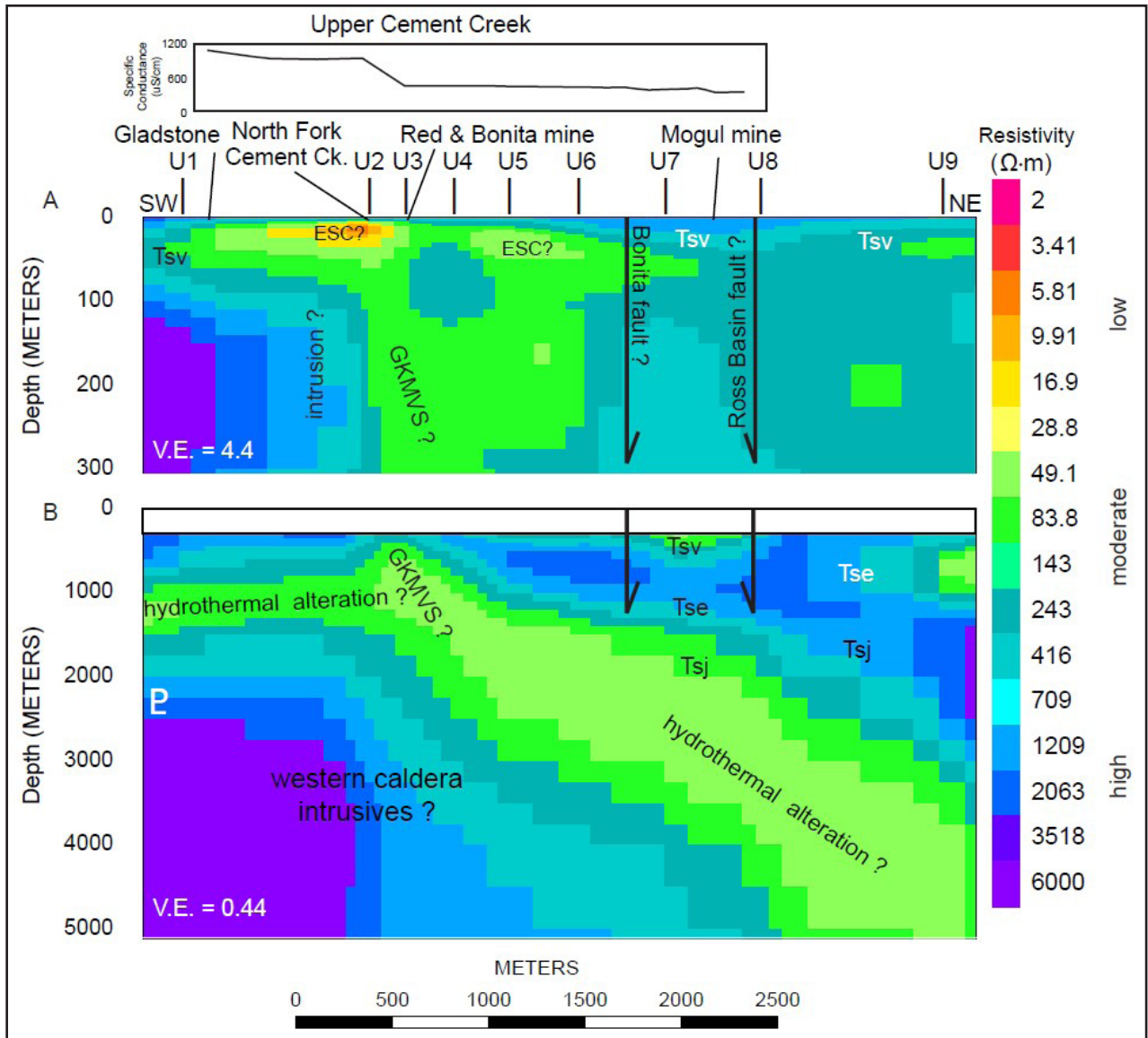


Figure 6. Magnetotelluric resistivity section along upper Cement Creek (Figure 1) with interpreted geologic units and faults (Figure 2). Black number labels at top of profile represent projected locations of magnetotelluric (MT) and audiomagnetotelluric (AMT) stations. Tsv—Silverton Volcanics; Tse—Eureka Member of Sapinero Mesa Tuff; Tsj—San Juan Formation; P—Proterozoic rocks (undifferentiated). Top panel (A) is AMT model showing depths from 0 to 300 m with vertical exaggeration (V.E.) ~4.4, with top plot of specific conductivity sampled from stream flow within upper Cement Creek from September 2019 (Runkel et al., 2022). ESC—elevated specific conductance. Bottom panel (B) is MT model showing depths from 0 to 5000 m with vertical exaggeration ~0.44. GKMVS—Gold King mine vein systems.

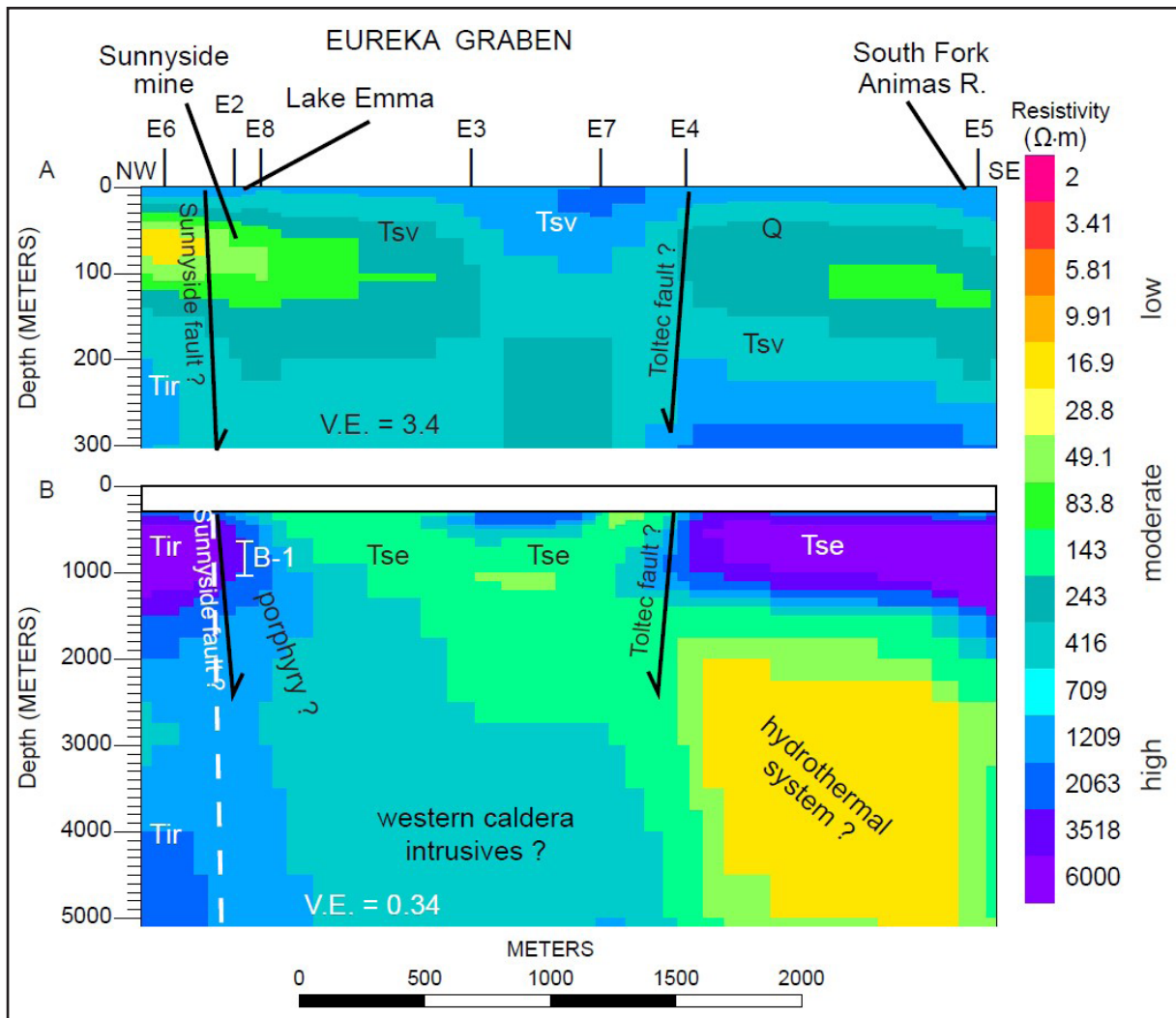


Figure 7. Magnetotelluric resistivity section across Eureka graben (Figure 1) with interpreted geologic units and faults (Figure 2). White dashed line is interpreted intrusion boundary. Black number labels at top of profile represent projected locations of magnetotelluric (MT) and audiomagnetotelluric (AMT) stations. Q—Quaternary surficial deposits; Tir— rhyolite; Tsv—Silverton Volcanics; Tse—Eureka Member of Sapinero Mesa Tuff. Top panel (A) is AMT model showing depths from 0 to 300 m with vertical exaggeration (V.E.) ~3.4. Bottom panel (B) is MT model showing depths from 0 to 5000 m with vertical exaggeration ~0.34. Vertical line labeled B-1 is well with drill core reported in Casadevall and Ohmoto (1977).

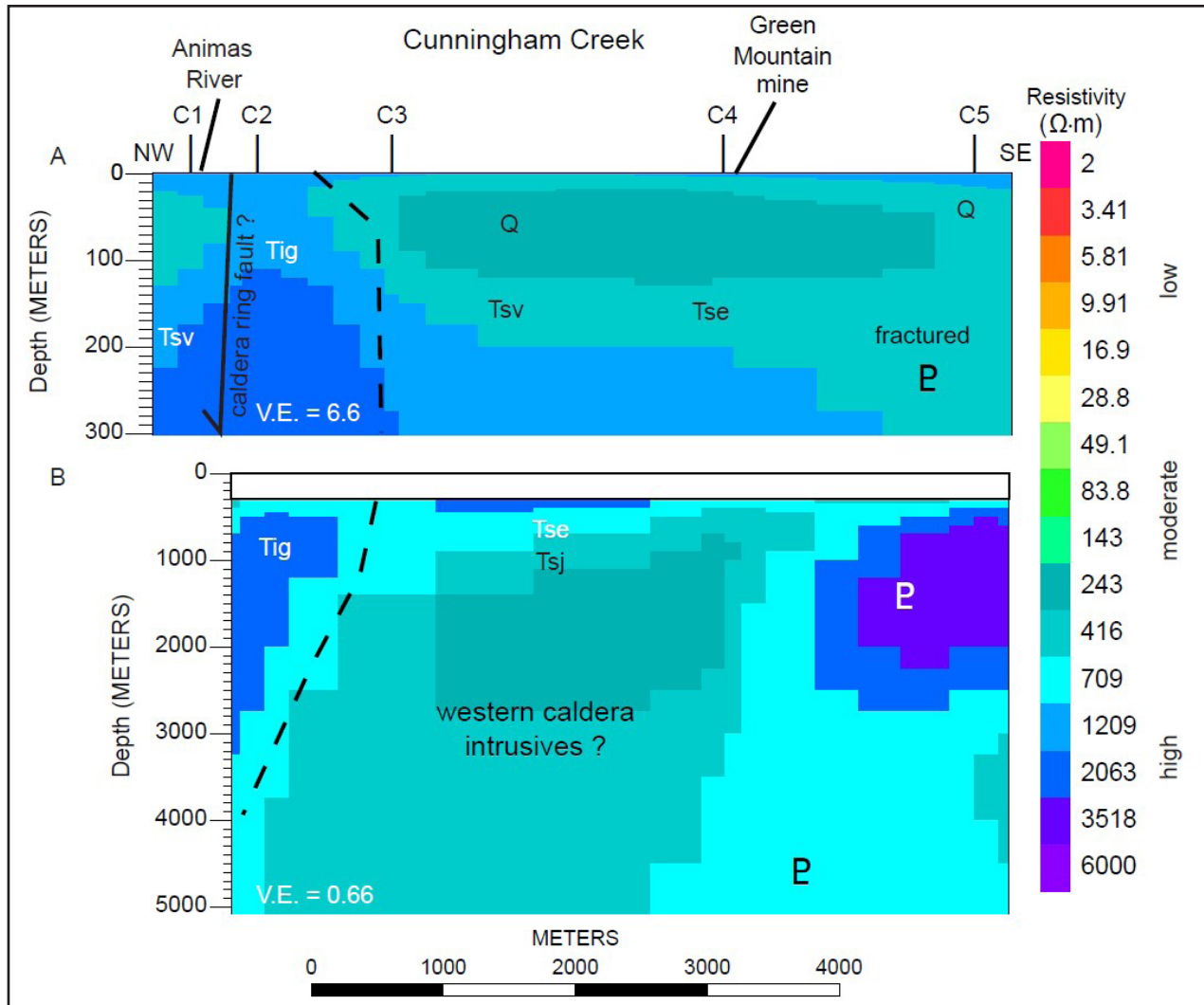


Figure 8. Magnetotelluric resistivity section along Cunningham Creek (Figure 1) with interpreted geologic units and faults (Figure 2). Black dashed line is interpreted intrusion boundary. Black number labels at top of profile represent projected locations of magnetotelluric (MT) and audiomagnetotelluric (AMT) stations. Q—Quaternary surficial deposits; Tig—Sultan Mountain stock; Tsv—Silverton Volcanics; Tse—Eureka Member of Sapinero Mesa Tuff; Tsj—San Juan Formation; P—Proterozoic rocks (undifferentiated). Top panel (A) is AMT model showing depths from 0 to 300 m with vertical exaggeration (V.E.) ~6.6. Bottom panel (B) is MT model showing depths from 0 to 5000 m with vertical exaggeration ~0.66.

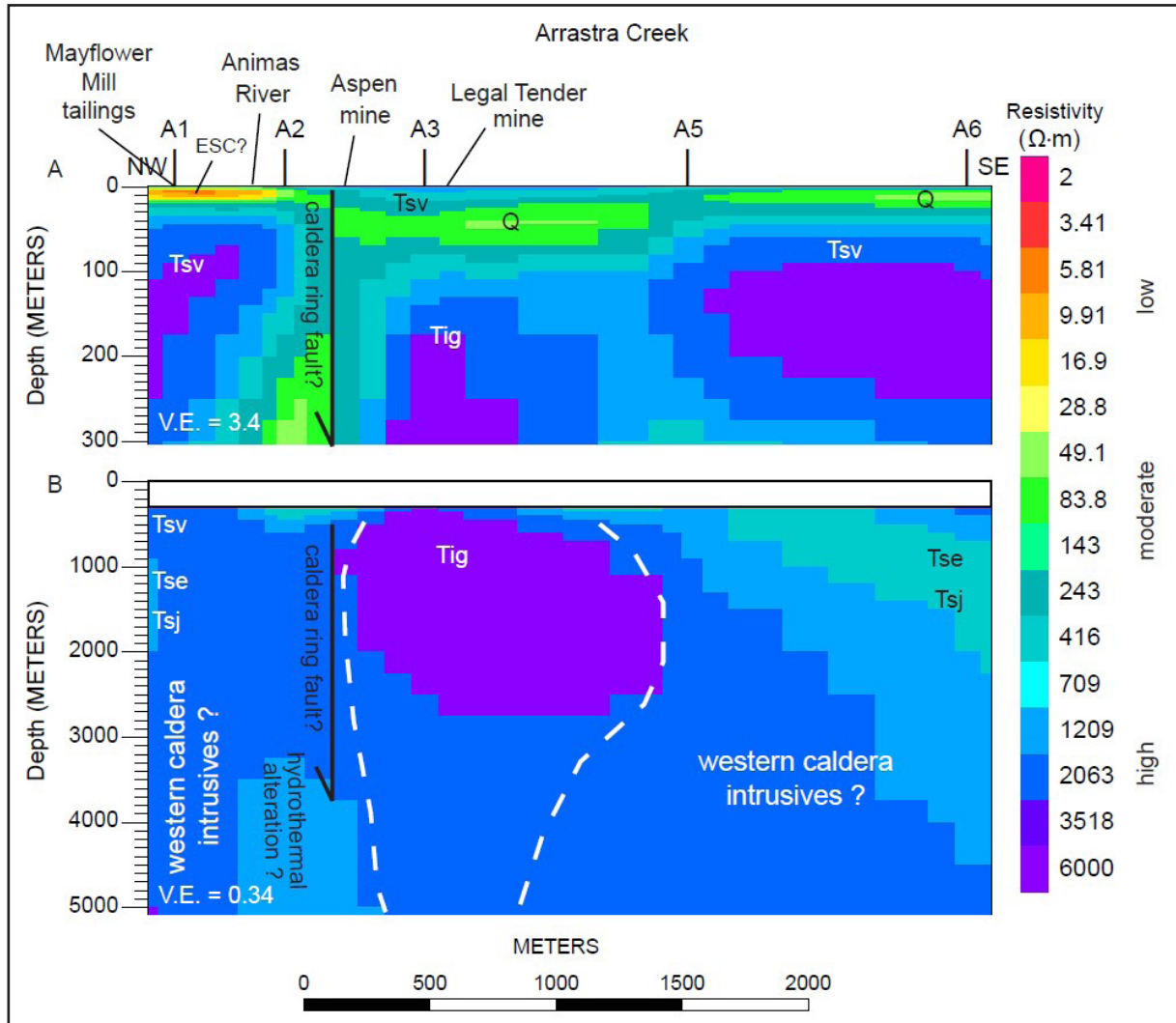


Figure 9. Magnetotelluric resistivity section along Arrastra Creek (Figure 1) with interpreted geologic units and faults (Figure 2). White dashed line is interpreted intrusion boundary. Black number labels at top of profile represent projected locations of magnetotelluric (MT) and audiomagnetotelluric (AMT) stations. Q—Quaternary surficial deposits; Tig—Sultan Mountain stock; Tsv—Silverton Volcanics; Tse—Eureka Member of Sapinero Mesa Tuff; Tsj—San Juan Formation. Top panel (A) is AMT model showing depths from 0 to 300 m with vertical exaggeration (V.E.) ~3.4. ESC—elevated specific conductance. Bottom panel (B) is MT model showing depths from 0 to 5000 m with vertical exaggeration ~0.34.

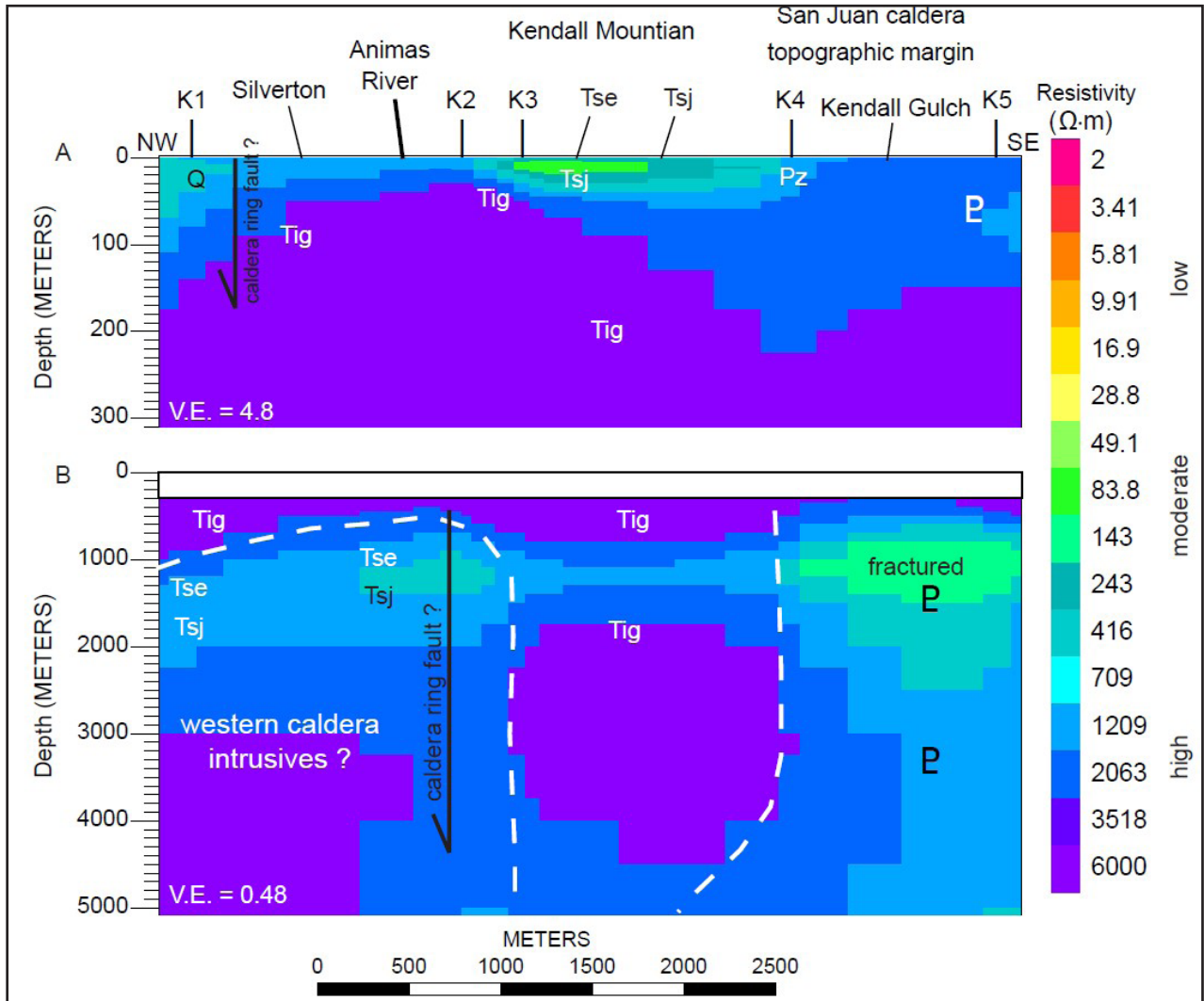


Figure 10. Magnetotelluric resistivity section across Kendall Mountain (Figure 1) with interpreted geologic units and faults (Figure 2). White dashed line is interpreted intrusion boundary. Black number labels at top of profile represent projected locations of magnetotelluric (MT) and audiomagnetotelluric (AMT) stations. Q—Quaternary surficial deposits; Tig—Sultan Mountain stock; Tse—Eureka Member of Sapinero Mesa Tuff; Tsj—San Juan Formation; Pz—Paleozoic rocks (undifferentiated); P—Proterozoic rocks (undifferentiated). Top panel (A) is AMT model showing depths from 0 to 300 m with vertical exaggeration (V.E.) ~4.8. Bottom panel (B) is MT model showing depths from 0 to 5000 m with vertical exaggeration ~0.48.

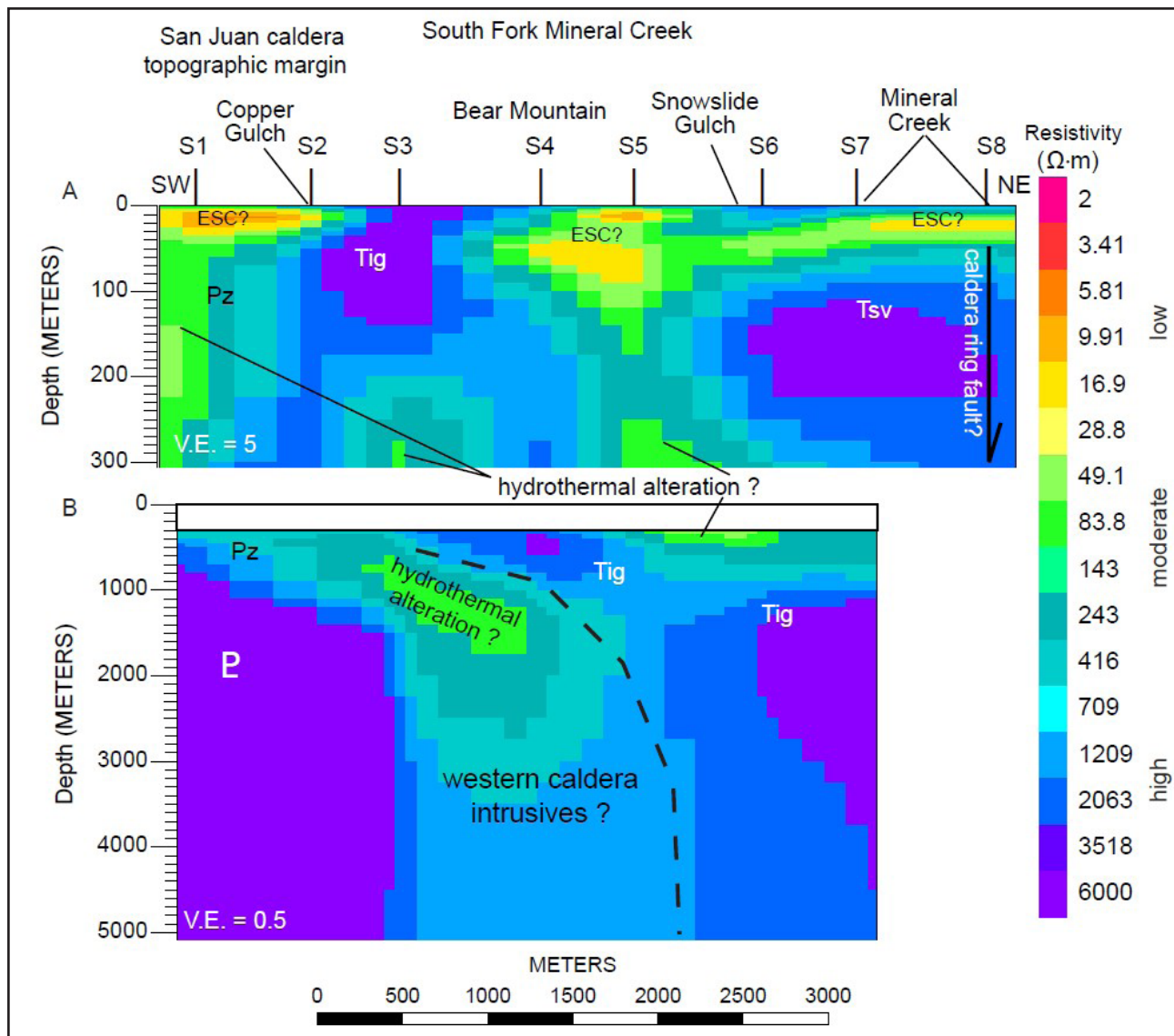


Figure 11. Magnetotelluric resistivity section along South Fork Mineral Creek (Figure 1) with interpreted geologic units and faults (Figure 2). Black dashed line is interpreted intrusion boundary. Black number labels at top of profile represent projected locations of magnetotelluric (MT) and audiomagnetotelluric (AMT) stations. Tig—Sultan Mountain stock, Pz—Paleozoic rocks (undifferentiated), P—Proterozoic rocks (undifferentiated). Top panel (A) is AMT model showing depths from 0 to 300 m with vertical exaggeration (V.E.) ~5. ESC—elevated specific conductance; Tsv—Silverton Volcanics. Bottom panel (B) is MT model showing depths from 0 to 5000 m with vertical exaggeration ~0.5.

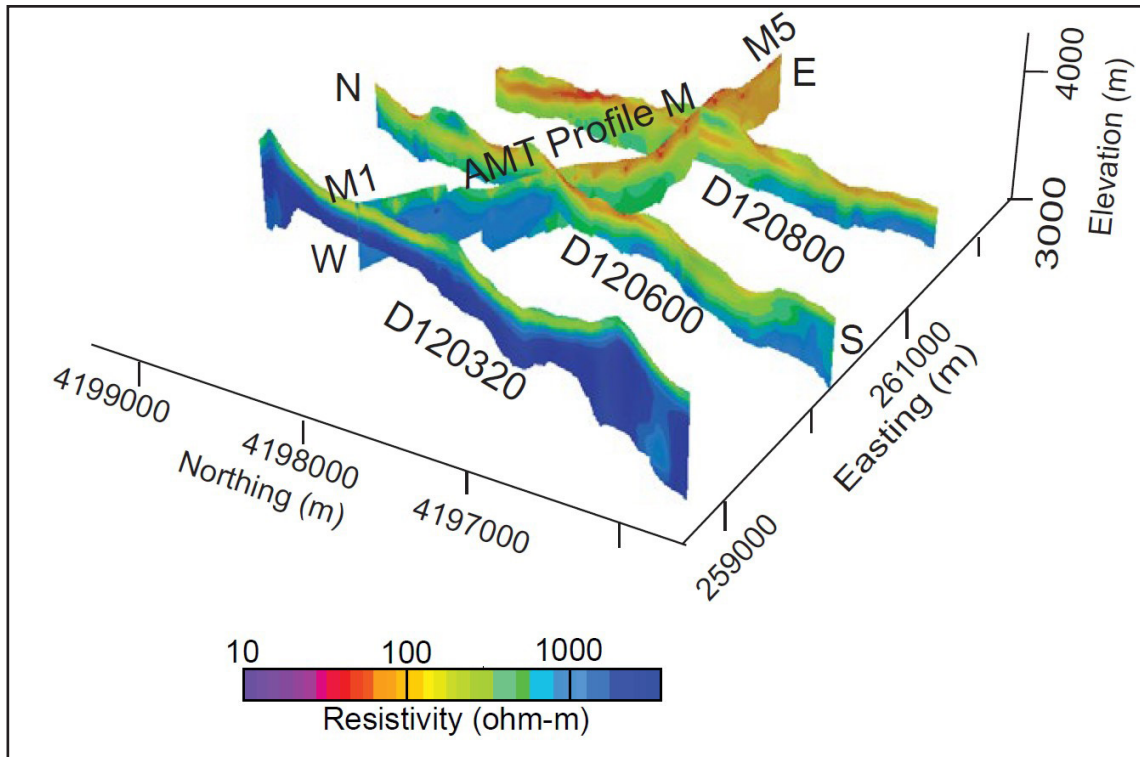


Figure 12. Intersection of Mineral Basin audiomagnetotelluric (AMT) profile M inversion section (Figure 5A) with three nearby sub-perpendicular airborne electromagnetic flight line (D120320, D120600, and D120800) inversion sections showing profile depths from 0 to 300 m. M1 and M5 labels are AMT stations (Figure 2). Northing and easting distances are in World Geodetic System 1984 Universal Transverse Mercator (UTM) coordinates.

The MT method is a ground-based electromagnetic technique that investigates subsurface electrical resistivity (inverse of conductivity) at depths of tens of meters to tens of kilometers (Vozoff, 1991). The MT method measures time variations in Earth's electric and magnetic fields. Worldwide lightning activity and geomagnetic micropulsations from solar wind-charged particles interacting with Earth's magnetosphere provide the main source of signal used by the audiomagnetotelluric (AMT) and MT methods, respectively (see magnetotelluric data analysis in the Supplemental Material [see footnote 1] for details).

Electrical properties of rocks and sediments vary depending on (1) the resistivity, porosity, and saturation of the host rock and (2) the fluid resistivity, which can vary by four to five orders of magnitude (Davis and Annan, 1989). The resistivity of the host rock varies depending on minerals present. Altered volcanic rocks commonly contain replacement minerals that have electrical resistivities that are only a tenth of those in minerals in unaltered surrounding rocks (Nelson and Anderson, 1992). Rocks that have been hydrothermally altered to clays exhibit low resistivity (Goldie, 2000; Locke et al., 1999), especially when wet. Water-saturated clay-rich alluvium, marine shale, and other mudstones normally have very low resistivity, ranging from 1–3 to 10–30 ohm-meters ($\Omega\cdot\text{m}$). Freshwater-saturated, unconsolidated, terrestrial alluvial sediments commonly have very low to moderately low resistivity (2–70 $\Omega\cdot\text{m}$). Sediments containing conglomerate and coarse, clean sand possess higher electrical resistivities (tens of ohm-meters); silty sand and siltstone have lower values of resistivity (<10 $\Omega\cdot\text{m}$). In situ measurements of electrical resistivity from central New Mexico (Deszcz-Pan et al., 2000) show that coarser-grained sediments, such as gravels and clean sands, commonly have moderately low resistivity (tens of ohm-meters). Similar in situ resistivity measurements for sands and gravels are reported elsewhere in North America (Alger, 1971; Gilson et al., 2000).

Unaltered, disconnected fractured igneous rocks are normally highly resistive and typically possess resistivity values of a few hundred to thousands of ohm-meters. Carbonate rocks are moderately to highly resistive (hundreds to thousands of ohm-meters), with the range dependent upon their fluid content, porosity, fracturing, and impurities. Metamorphic rocks that do not contain graphite are also moderately

to highly resistive (hundreds to thousands of ohm-meters). Resistivity may be low ($<100 \Omega\cdot\text{m}$) along fault zones that were fractured enough to have once hosted fluids, generally water or brine, from which conductive minerals were deposited. Higher subsurface temperatures decrease fluid viscosity and cause greater mobility of ions in the fluids, therefore reducing rock resistivity (Hallenburg, 1998). The rocks and sediments in this study area contain varying percentages of clay and sulfide minerals, both of which have a negative correlation with measured bulk resistivity.

The USGS collected MT data along seven profiles (Figures 1 and 2) ranging from 3 km to 8 km in length: (1) across the northwestern structural margin of the Silverton caldera in Mineral Basin and traversing south of Red Mountain Number 3 peak within the Silverton caldera, (2) within the caldera along upper Cement Creek near the Gold King mine, (3) within the caldera in Eureka graben, (4) across the southeastern margin of the caldera along Cunningham Creek, (5) across the southeastern margin of the caldera along Arrastra Creek, (6) across the southern margin of the caldera along the western margin of Kendall Mountain, and (7) across the southwestern margin of the caldera along South Fork Mineral Creek. Station spacing was determined based on investigating the caldera structural margins and on logistics of site access. Profiles across the caldera wall allow investigation of the geometry of intracaldera fill and degree of permeability of the ring fracture zone. A profile across the resurgent core of the caldera complex and across an apical graben permits investigation of resistivity response of mineralized segments of graben faults. AMT profiles characterize geophysical responses of near-surface lithologies, structures, and mineralized systems and help to corroborate AEM data at shallow levels (Hoogenboom et al., 2022).

Multiple physical factors in MT analyses were considered in this study to address possible uncertainties in resistivity model results (magnetotelluric data analysis in the Supplemental Material). First, we culled the processed AMT and MT data (Figures S1 and S2 in the Supplemental Material) employing the highest coherencies and lowest skews and also removing data outliers to mitigate data that were significantly affected by noise. Second, given that the caldera setting in the survey area is a three-dimensional (3-D) geologic structure, we assumed that the MT and AMT measurements would have a 3-D electromagnetic response. Also, the calculated phase tensor skew angle (Caldwell et al., 2004; Chave and Jones, 2012) from the field MT data indicated a primarily dominant 3-D electromagnetic response (Figure S4). In modeling these data, large-scale biases in model depths or resistivities are possible in two-dimensional (2-D) resistivity models that invert or attempt to fit the transverse electric mode if 3-D effects are present. The overall AMT and MT data in this study area were definitely 3-D to strongly 3-D for about three-fourths of frequencies inverted (Figure S4).

Three-dimensional effects are suppressed by modeling the transverse magnetic (TM) mode if along-profile coordinates are used, such as in this study. Two-dimensional modeling of fixed-axis, TM-mode data across 3-D low resistivities can yield remarkably accurate resistivity cross sections. TM-mode data have low sensitivity to the effects of excess currents caused by the finite electrical strike of 3-D resistivity structures (Wannamaker, 1999). The observed TM data at each MT station were inverted for resistivity structure using unconstrained 2-D resistivity inversion models (Mackie et al., 1997; Rodi and Mackie, 2001), constrained only by any permissible resistivity values and structure required by the MT data at each site. In a 3-D geologic structural environment, certain model features in the 2-D profile inversions may be offprofile features that are projected along the given 2-D profile. Also, thickness of low-resistivity zones may be less than the what TM-only inversions produce, given that there is a tendency for downward smearing of conductance from an overlying low-resistivity region, caused by both the model regularization employed in the inversion and the inherent low resolution of MT data for the base of low-resistivity features (magnetotelluric data analysis in the Supplemental Material).

Initial model assumptions and 2-D finite-element grids employed are described in the Supplemental Material. Data misfit plots indicate good agreement between modeled and observed culled data (Figures S1 and S2). Although data misfit is good, any large gaps in the culled observed data add uncertainty to the thickness of modeled resistivity features.

RESULTS

The 2-D MT inversions show crustal resistivity structure to depths of ~5 km (Figures 5–11). With the MT method, we are investigating to depth multiple hydrothermal events related to a porphyry copper system that is already exposed at the surface through caldera-forming processes and erosion (Ringrose et al., 1986). While the precise depths of the porphyry-style mineralization being imaged with the MT method is uncertain, the Sillitoe (2010) porphyry system model provides a guide for interpreting relative depths of mineralization. The mineralized system ranges from shallow levels (including the acid sulfate National Belle mine; Figures 1B and 2), to mid-levels (epithermal polymetallic vein mineralization, south Silverton mining area, Sunnyside mine, and Eureka mining district; Figures 1B and 2), and finally to the deeper levels south of Mount Moly (Figure 1B). Mount Moly, peak elevation 12,442 ft (U.S. Geological Survey, 1955), is an informal name for the hydrothermally altered peak located west of highway 550, between South Fork and Middle Fork Mineral Creek. We have more certainty in geologic unit names and formations at shallow levels where surface mapping shows us what we are imaging; at deeper levels, interpretations become less certain and additional data from mine mapping and drill holes would be necessary to confirm them, but those data are not readily available. One drill hole from a groundwater study in upper Prospect Gulch near Red Mountain Number 3 peak (Johnson et al., 2011) has abundant clay alteration (to 56 wt%) that corresponds to moderate resistivity shown in the AMT model in Figure 5. The low resistivity shown in Figure 5 west of the Lark mine at 50 to 100 m depth could be caused by high clay contents near MT station M7. Another factor influencing interpretations of subsurface resistivities in the inversions (Figures 5–11) is the conductive overprint of buried hydrothermal alteration that may exist below some of the MT profiles. The conductive overprint would lower resistivities for any given geologic unit when compared with resistivities in areas absent of significant hydrothermal alteration.

Northwestern Caldera Structural Margin, Mineral Basin and Red Mountain Profile

For the northwestern structural margin of the Silverton caldera in Mineral Basin and over Red Mountain Number 3 within the Silverton caldera, the approximately east-west MT profile (Figures 1–3 and 5) reveals moderate to high resistivities in the upper few hundred meters (Figure 5A) for mapped San Juan Formation intermediate volcanics near MT station M1, west of a mapped Silverton caldera ring fault. The ring fault may have been a barrier to hydrothermal fluid flow, which would have prevented rocks west of the structure from becoming more highly altered and, as a result, caused them to have generally higher resistivities. East of the ring fault, resistivities are lower (Figure 5A), indicating that the units may be more permeable, where meteoric groundwater may be present and infiltrating along the ring-fault structures to depth, and possibly more highly propylitized subsurface rocks when compared with higher-resistivity rocks west of the ring fault. A mapped ring fault between stations M2 and M3 correlates to a resistivity structure between stations M2 and M3, which we image as lower resistivities on the east side of the caldera ring fault and interpret as a down-dropped block beneath station M3 (Figure 5B). Further east, another mapped caldera ring fault separates the moderately resistive rocks beneath station M3 from lower-resistivity rocks between stations M4 and M7 beneath the Red Mountain mining district (Figure 5B). Low resistivity associated with hydrothermal alteration has been reported in other studies, such as Allis (1990), Hoschke (2008), Irvine and Smith (1990), and Mitchinson et al. (2013). This 3-km-wide low-resistivity zone extends from a few hundred meters depth to ~3 km depth and may reflect hydrothermally altered rocks within or adjacent to the breccia deposits. Moderately low resistivities occur in the upper few hundred meters near a mapped dacite intrusion and associated breccia pipe near station M5 (Figure 5A). High resistivity associated with quartz silica has been reported in other studies, such as Allis (1990), Goldie (2000), Hoschke (2008), Hoschke and Sexton (2005), Irvine and Smith (1990), and Locke et al. (1999). More electrically resistive material, likely quartz, overlies the zone of lower resistivity and armors the breccia pipe in our study area. Silicification in the upper part of the hydrothermal breccias was commonly observed in the field.

The shallow low-resistivity zone in the upper 15 m beneath MT station M4 (Figure 5A) may indicate water with elevated specific conductance in the near surface. A low-resistivity zone occurs in the upper hundred meters near another mapped breccia pipe near station M7 (Figure 5A), while a moderately high-resistivity zone occurs in the upper few hundred meters near the Lark mine (Figure 2). This resistive zone appears to be a few hundred meters thick. Below the resistive zone near the Lark mine at station M8, and also below

station M6, a low-resistivity zone (Figure 5B) could be part of a zoned acid sulfate alteration assemblage with an argillic or QSP alteration (Hübert et al., 2016), similar to alteration patterns of porphyry copper systems (Sillitoe, 2010) that have argillic and phyllic components (Figure 5B). Alteration at depth could be similar to what we see at the surface in upper Prospect Gulch (Figure 2). Drill holes UPG and MPG in upper Prospect Gulch have significant clay alteration in the upper 40 m (Bove et al., 2007c) that is consistent with low resistivity between station M7 and the Lark mine. The alteration in this area is pervasive and clay minerals prevalent, which could be causing low bulk resistivity imaged at deeper depths. Alteration is zoned outward in upper Prospect Gulch in some places from silicified masses, to argillic, to quartz-alunite-pyrophyllite, to quartz-sericite-pyrite, and to propylitic (Bove et al., 2007a).

At the eastern end of this MT profile (Figure 5) near Gladstone (Figure 2), shallow low-resistivity rocks below a few hundred meters depth (Figure 5B) may also be related to hydrothermal plumbing that served as pathways for mineralizing fluids and metal precipitation during later ore formation. Hydrothermal plumbing may be responsible for mineralization at the nearby Galty Boy mine (Figure 2) north of MT station M9 and the Gold King mine east of the MT profile. High resistivities below this low-resistivity zone on the eastern end of the MT profile and high resistivities below 2 km depth at the western end of the profile are interpreted to represent Proterozoic rocks. Moderately high resistivities (400–1200 $\Omega\cdot\text{m}$) below a few kilometers depth in the center of the profile we interpret to represent Paleozoic and Proterozoic rocks intruded by western caldera plutons of the San Juan batholith (Drenth et al., 2012; Lipman and Bachmann, 2015) based on the imaged resistivity structure east of the caldera ring faults.

Upper Cement Creek Profile

The upper Cement Creek profile is located entirely within the Silverton caldera and passes near the Gold King, Red and Bonita, and Mogul mines. The south-southwest–north-northeast MT profile (Figures 1–3 and 6) reveals a low-resistivity zone (2–50 $\Omega\cdot\text{m}$) whose top is at ~100 m depth near the Gold King mine vein system (Figure 6A). This low-resistivity zone continues northeasterly along the profile and deepens northeast of the Bonita fault, reaching a depth of ~5 km northeast of the Ross Basin fault and may reflect rocks hydrothermally altered by hydrothermal plumbing. Similar low-resistivity zones were observed in other studies that were attributed to conduits for hydrothermal fluids (Allis, 1990; Hoschke, 2008; Irvine and Smith, 1990; Mitchinson et al., 2013). In this instance, the low-resistivity zones may be imaging pathways for metal-bearing fluids responsible for ore formation near the Gold King and Red and Bonita mines (Figure 2).

The shallow low-resistivity zone in the upper 100 m between MT stations U1 and U6 (label ESC in Figure 6A) may be associated with a zone of water with moderate to high specific conductance. Specific conductivity (inverse of resistivity) measurements (Figure 6) collected in upper Cement Creek reveal higher resistivities north of the projection of the Red and Bonita mine to ~250 m north of the Mogul mine and lower resistivities south of the Red and Bonita mine (Figure 2).

The AMT image (Figure 6A) reveals low resistivities in the upper few meters south of the Red and Bonita mine that correspond with mapped seeps (Runkel et al., 2022). A low-resistivity zone north of the Red and Bonita mine is interpreted to represent water with moderate to high specific conductance that may be part of a deeper groundwater system to the north. It is possible that geomorphology controls and constricts groundwater flow near the Red and Bonita mine where, south of that point, the valley narrows. Shallow groundwater, having moderate to high specific conductance, may be accumulating in surficial sediments near North Fork Cement Creek and Red and Bonita mine. Near the Mogul mine, groundwater having higher specific conductance might be dispersed in a larger area because the valley is wider and less constricted compared to downstream. High-resistivity rocks in the upper few kilometers northeast of MT station U8 (Figure 6B) may be volcanics (units Tsv, Tse, and Tsj) that are less altered than the low-resistivity rocks near the Gold King mine. In the upper 100 m, the Bonita fault may be acting as a hydrologic barrier to groundwater flow as indicated by low-resistivity zones, which we interpret as groundwater with elevated specific conductance south of the Bonita fault.

A concealed subsurface intrusion may exist south of MT station U2 based on the shallow high resistivity (Figure 6A) and a local magnetic high (Figure 4). High resistivities were determined (>1000 $\Omega\cdot\text{m}$) below 3

km depth on the southwestern end of the MT profile (Figure 6B) that we interpret to represent Proterozoic rocks. In the southern half of the profile, moderately high to high resistivities (200–6000 $\Omega\cdot\text{m}$) below a few kilometers depth we interpret to represent Proterozoic rocks intruded by western caldera plutons of the San Juan batholith based on the imaged resistivity structure.

Eureka Graben Profile

The Eureka graben profile is also located entirely within the Silverton caldera, and the northwest-southeast MT profile (Figures 1–3 and 7) reveals a shallow low-resistivity zone in the upper 100 m near MT stations E6, E2, and E8 (Figure 7A) that corresponds to shallow workings of the Sunnyside mine near Lake Emma. Below 100 m depth beneath Lake Emma (Figure 2), the rocks are moderately resistive, which we infer to represent an annealed quartz-rich zone (Allis, 1990; Goldie, 2000; Hoschke, 2008; Hoschke and Sexton, 2005; Irvine and Smith, 1990; Locke et al., 1999). Another buried (below ~1 km depth) low-resistivity zone between stations E3 and E7 within the Eureka graben (Figure 7B) may reflect hydrothermally altered rocks from hydrothermal plumbing (Allis, 1990; Hoschke, 2008; Irvine and Smith, 1990; Mitchinson et al., 2013) that served as pathways for metal-rich fluids during ore formation related to the nearby Sunnyside mine vein systems in the upper few hundred meters at the northwestern end of the MT profile. The dip of the inferred Sunnyside fault (Figure 2) is interpreted to follow the anomalous trend between deep high resistivities (>2000 $\Omega\cdot\text{m}$) imaged below station E6 and moderately high resistivities (<2000 $\Omega\cdot\text{m}$) imaged southeast of station E6 and is not constrained by subsurface geologic evidence. An area of low resistivity below stations E4 and E5 at depths greater than 2000 m (Figure 7B) may be associated with the hydrothermally altered margin of a possible intrusion that trends northeast, as mapped in California Mountain (Figure 2) northeast of our profile, that domed the area underlying the Eureka graben. The mapped Toltec fault (Figure 2) appears to separate resistive rock on the footwall and less-resistive rock on the hanging wall. The dip of the inferred Toltec fault is also an interpretation and is not constrained by subsurface geologic evidence. High resistivities (>2000 $\Omega\cdot\text{m}$) below 100 m depth on the northwestern end of the MT profile are interpreted to represent intrusive rocks (unit Tir). Moderately high resistivities (400–1200 $\Omega\cdot\text{m}$) below a few kilometers depth in the center of the profile we interpret to represent western caldera intrusions of the San Juan batholith. The inferred intrusives are not as resistive as the interpreted intrusives along the other MT profiles, which may be due in part to the degree of alteration and replacement minerals present (see Geophysical Methods section above).

Southeastern Caldera Structural Margin, Cunningham Creek Profile

For the southeastern structural margin of the Silverton caldera along Cunningham Creek, the north-northwest–south-southeast MT profile (Figures 1–3 and 8) reveals a resistive zone at the northwestern end of the MT profile, beneath MT station C2, interpreted to represent an intrusion near the structural margin of the Silverton caldera along the caldera ring fault. This inferred intrusion (unit Tig) is mapped at the surface both northeast and southwest of Cunningham Creek (Luedke and Burbank, 2000; Yager and Bove, 2007). The high-resistivity zone inferred to represent the intrusion also correlates with the arcuate magnetic high that is all along the southern margin of the caldera (Figure 4). The high-resistivity zone (>500 $\Omega\cdot\text{m}$) below a few hundred meters depth at the southeastern end of the profile (Figure 8B) we interpret to represent Proterozoic rocks mapped near station C5 along the topographic margin of the San Juan caldera. The moderate-resistivity zone in the upper few hundred meters (Figure 8A) may also be Proterozoic but fractured and saturated. In the center of the profile, high resistivities (>500 $\Omega\cdot\text{m}$) near the surface correlate with mapped intermediate lavas, but below 1 km depth, moderate resistivities (200–400 $\Omega\cdot\text{m}$) may indicate western caldera intrusives of the San Juan batholith. The inferred intrusives are not as resistive as the interpreted intrusives along the other MT profiles, which may be due in part to the degree of alteration and replacement minerals present.

Southeastern Caldera Structural Margin, Arrastra Creek Profile

For the southeastern structural margin of the Silverton caldera along Arrastra Creek, the northwest-southeast MT profile (Figures 1–3 and 9) reveals very resistive rocks southeast of the Aspen mine (Figure 9) that we interpret to be an intrusion of the Sultan Mountain stock (unit Tig) that follows the southern structural caldera

margin, supported by the presence of an arcuate magnetic high along the southern margin of the caldera (Figure 4) and the inferred location of the caldera ring fault (Figure 2). This interpretation is consistent with granitoid intrusives occurring along several parts of the southern Silverton caldera ring-fault zone (Varnes, 1963, his plate 1; Yager and Bove, 2007, their plate 1). Shallow resistivities between stations A2 and A3 in the upper few hundred meters (Figure 9A) along the caldera ring fault are lower than those of adjacent inferred Silverton Volcanics (unit Tsv) to the northwest and the inferred Sultan Mountain stock to the southeast. The lower resistivity may be associated with rocks along the ring fault that are more permeable, where meteoric groundwater may be present and infiltrating along the ring-fault structures to depth. Less-resistive zones below 3 km depth (Figure 9B) northwest of the inferred caldera ring fault and near the Aspen mine may reflect hydrothermally altered rocks that were formed from hydrothermal fluids and metal deposition along hydrothermal plumbing (Allis, 1990; Hoschke, 2008; Irvine and Smith, 1990; Mitchinson et al., 2013) that served as flow paths for metallic mineralization.

The shallow (0–50 m) low-resistivity zone (Figure 9A) near the Aspen mine may be attributed to water with elevated specific conductance in surficial deposits. At the northwestern end of the MT profile, resistive rocks in the upper kilometer are interpreted to be Silverton Volcanics (unit Tsv) that are mapped just northwest of MT station A1, while the very low-resistivity rocks in the upper 15 m are interpreted to indicate water with high specific conductance within the Mayflower Mill tailings (Figure 2). This area of low resistivity is also perched above the Animas River, so it seems unlikely that lower-resistivity shallow groundwater is attributed to flow from the south in Arrastra Creek toward the Mayflower Mill tailings, at least along this part of the profile. Shallow resistivities beneath station A2 in the upper 15 m near the Aspen mine were moderately low, which we interpret to indicate water with moderate specific conductance when compared to the elevated specific conductance values that are inferred below station A1. Below 1 km depth, an ~1-km-thick zone of moderately resistive rocks is interpreted to represent down-dropped intracaldera tuffs (units Tse and Tsj) on the hanging-wall side of the caldera ring fault. High resistivities (1200–2000 $\Omega\cdot\text{m}$) below 2 km depth at the northwestern end of the MT profile and also in the center of the profile are interpreted to represent western caldera intrusives of the San Juan batholith.

Southern Caldera Structural Margin, Profile along the Western Edge of Kendall Mountain

Along the southern structural margin of the Silverton caldera, near the western edge of Kendall Mountain, the north-northwest–south-southeast MT profile (Figures 1–3 and 10) reveals resistive ($>1000 \Omega\cdot\text{m}$) rocks in the upper 0.6 km. The southeastern end of the profile correlates with nearby mapped undivided Proterozoic rocks (unit) west of the MT profile and at MT station K5. Mississippian rocks (unit MDu) are mapped at the surface at station K4, and San Juan Formation volcanoclastic rocks (unit Tsj) are mapped at the surface between stations K3 and K4 (Figures 2 and 10A). At the southern end of the profile, a moderately low-resistivity zone appears from ~0.6 to ~2 km depth along the San Juan caldera topographic margin that the profile intersects obliquely. The resistivity image appears more resistive in the upper 0.6 km where it is likely dry, given that station K5 is ~0.6 km higher in elevation than the Animas River, which is offset to the west of the MT profile. Another less-resistive zone at depth (0.5 to 1 km depth), also ~1 km thick (Figure 10B), appears beneath Silverton and the Animas River that may be associated with down-dropped rocks of units Tse and Tsj. Resistive rocks in the upper kilometer at the northern end of the MT profile correlate with mapped intrusions of the Sultan Mountain stock (unit Tig) beneath stations K1, K2, and K3 and correlate with the arcuate magnetic high that is all along the southern margin of the caldera (Figure 4). Shallow resistivities in the upper few hundred meters (Figure 10A) near the ring fault are high, indicating low permeability for rocks along the ring fault.

High resistivities (2000–10,000 $\Omega\cdot\text{m}$) below 2 km depth at the northwestern end of the MT profile we interpret to be related to the western caldera intrusives of the San Juan batholith, whereas moderately high resistivities (400–2000 $\Omega\cdot\text{m}$) below 2 km depth at the southeastern end of the MT profile we interpret to represent Proterozoic rocks.

Southwestern Caldera Structural Margin, South Fork Mineral Creek Profile

For the southwestern structural margin of the Silverton caldera along South Fork Mineral Creek, the west-southwest–east-northeast MT profile (Figures 1–3 and 11) reveals a lower-resistivity zone at ~250 m depth near MT station S5 (Figure 11A) that we interpret to represent QSP altered rocks (Hubert et al., 2016). Below this lower-resistivity zone are high-resistivity rocks between stations S3 and S7 (Figure 11B) that correlate with mapped intrusions of the Sultan Mountain stock (unit Tig) northwest and southeast of the MT profile. The high-resistivity rocks also correlate with the arcuate magnetic high that is all along the southern margin of the caldera (Figure 4). Shallow low resistivities imaged beneath stations S1 and S2 and stations S4–S8 in the upper 20–50 m (Figure 11A) may indicate water with moderate to high specific conductance. In contrast, shallow resistivities imaged beneath stations S3 and S4 are high, which we interpret to represent a hydraulic barrier.

All along the profile there are alluvial fans that formed at the base of Mount Moly, derived from weathered areas of QSP, quartz-alunite-pyrophyllite (QAP), and a mix of WSP and hydrothermal propylitic (WSP-hyd) alteration. For the very shallow low-resistivity zones in the upper 50 m of the model, fans sourced from sericitically altered areas on the mountain could be a cause of the less-resistive lithologies. The deeper low resistivity beneath MT stations S1 (100–200 m depth) and S5 (250–300 m depth) (Figure 11A) could be attributed to a younger phase of the Sultan Mountain stock (Bove et al., 2001; Gonzales, 2015; Jackson et al., 1980; Ringrose, 1982) that is associated with alteration and weak mineralization (Allis, 1990; Hoschke, 2008; Irvine and Smith, 1990; Mitchinson et al., 2013) on and possibly adjacent to Mount Moly. Moderate resistivities in the upper few hundred meters at the southwestern end of the profile correlate (Figure 11A) with mapped Paleozoic rocks north and south of the profile. Below the inferred intrusions of the Sultan Mountain stock is a less-resistive zone (Figure 11B) that may reflect hydrothermally altered rocks from hydrothermal plumbing that served as pathways that may have provided metals during later ore formation related to nearby prospects and mines on Bear Mountain between Copper Gulch and Snowslide Gulch (Figure 2). Resistive (>1000 $\Omega\cdot\text{m}$) rocks below 1 km depth on the southwestern end of the MT profile we interpret to be Proterozoic. Moderately high resistivities (1200 $\Omega\cdot\text{m}$) in the center of the profile we interpret to represent Proterozoic rocks intruded by western caldera intrusives of the San Juan batholith. This is where the San Juan caldera ring-fault zone would have likely penetrated the crust but has been obliterated by multiple episodes of post-caldera collapse granitoid intrusives.

DISCUSSION

The San Juan–Silverton caldera complex provides an exceptional laboratory for investigating shallow to deep levels of a caldera complex and post-collapse resurgence, alteration, and mineralization. MT data collected in this study demonstrate that these data can be used to augment field mapping studies to image the geometry and lithologic contrasts in caldera margins and intracaldera fill. These data can extend observations to the subsurface and build on the work of previous workers such as Lipman (1976a) who, from detailed field mapping, synthesized how caldera geometry and the structural architecture develop during and after caldera formation.

This study was designed in part after the Las Cañadas study at Tenerife, which successfully applied the MT method to investigating the structure and hydrogeology of a caldera (Pous et al., 2002). However, in contrast to studies at Las Cañadas caldera, which also applied the MT method to imaging an active geothermal system (Piña-Varas et al., 2014) which our study area lacks, the goals of this study focused on imaging lithologies, caldera structures, modern groundwater locally affected by acid rock drainage, and the hydrothermal plumbing system and related mineralization.

The interpretations presented here are non-unique because multiple physical and chemical properties within the lithologies that were imaged using the MT method could result in similar electromagnetic responses. For example, interconnected sulfides could have a similar low-resistivity response (Hubert et al., 2016) compared

with abundant, saturated clay-size minerals (Goldie, 2000; Locke et al., 1999). In addition, conductive water attributed to acidic weathering could also cause a low-resistivity response. Interpretations described herein are based on the current knowledge of mapped geology, structure, and alteration as well as knowledge of mineral deposits. A drill hole in upper Prospect Gulch and mineralogy from X-ray diffraction analysis helped to corroborate areas of moderately low resistivity that were associated with abundant clay alteration. Additional drill hole data could be useful to further confirm subsurface interpretations and some inferences that were made in other areas. The interpretations discussed provide working hypotheses of possible subsurface lithologies and associated electromagnetic responses.

The geologic deposits, lithologies, and structural and intrusive events pertinent to geophysical data and interpretations as part of this study and described in the following sections include: (1) paleoproterozoic rocks and the overlying sedimentary sections that formed the roof of the caldera complex and that caved into the calderas during caldera ring-fault formation; (2) the sequence of 35–30 Ma intermediate-composition lavas and related volcanoclastics (San Juan Formation); (3) caldera ring faults and other caldera-related structures along caldera structural margins; (4) post-collapse volcanism consisting of intermediate lavas and volcanoclastic rocks (Burns and Henson Members and pyroxene andesite of the Silverton Volcanics) infilling the San Juan caldera depression (Lipman et al., 1973); (5) multiple episodes of igneous intrusions, hydrothermal alteration, and mineralization (Bove et al., 2007a, 2007b); and (6) Pleistocene glaciation, erosion, and deposition of Quaternary sediments that cover much of the area in the form of moraines, colluvium, landslides, alluvial fans, and alluvial terraces (Blair et al., 2002; Yager and Bove, 2007).

Resistivity and Imaging of Lithologies

MT imaging of lithologies along the caldera margins and within the calderas in this study allowed subsurface inferences to be made regarding caldera processes and intracaldera lithologies (Figure 13). MT data were effective in imaging geologic units of varying age and composition from Proterozoic crystalline basement rocks and overlying Paleozoic sedimentary units to early intermediate Paleogene volcanics in which the calderas formed. Each of these pre-caldera units has contrasting resistivities that were imaged by the MT method. The southern San Juan caldera margin in Arrastra Creek and Cunningham Creek is an example where MT data allow inferences of subsurface lithology within the calderas. In upper Cunningham Creek, there is an abrupt change from Silverton Volcanics to older Paleozoic and Early Proterozoic rocks exposed south of the San Juan caldera topographic margin. MT data in this area (Figures 2 and 8) permit inferences of where Proterozoic country rocks were down-dropped (Figure 8, unit) along the oversteepened San Juan caldera topographic margin. Paleogene volcanics and intracaldera fill (Figure 8, units Tsv, Tse, and Tsj) tend to have lower resistivity compared to what is interpreted as Proterozoic terrain near the caldera margin.

Implications for Imaging Hydrothermal Alteration and Mineralization

MT imaging of hydrothermal alteration within the calderas in this study allowed subsurface inferences to be made regarding hydrothermal alteration and mineralization (Figure 13). An example of how MT data helped in forming hypotheses about caldera processes and hydrothermal alteration and mineralization events is demonstrated along the northwestern Silverton caldera structural margin (Figures 2 and 5). Fisher and Leedy (1973) suggested that the emplacement of mineralized breccia deposits and coeval dacitic to rhyolite intrusions was strongly controlled by the northerly trending Silverton caldera ring-fault zone (Figure 2). One hypothesis is that the Silverton caldera structural margin was part of the hydrothermal plumbing architecture that focused hydrothermal fluids along the north-south structural margin and may have been a lateral barrier to hydrothermal flow that prevented alteration west of Mineral Creek. This interpretation is generally consistent with larger areas of more intensely altered rocks being focused and more prevalent east of the structural margin in the Red Mountain mining district, near Ohio Peak, and south along Anvil Mountain (Bove et al., 2007a). The Red Mountain mining district consists of pervasively altered rocks of an epithermal system (Bove et al., 2007b; Larsen and Cross, 1956) and porphyry copper system (Gilzean, 1984).

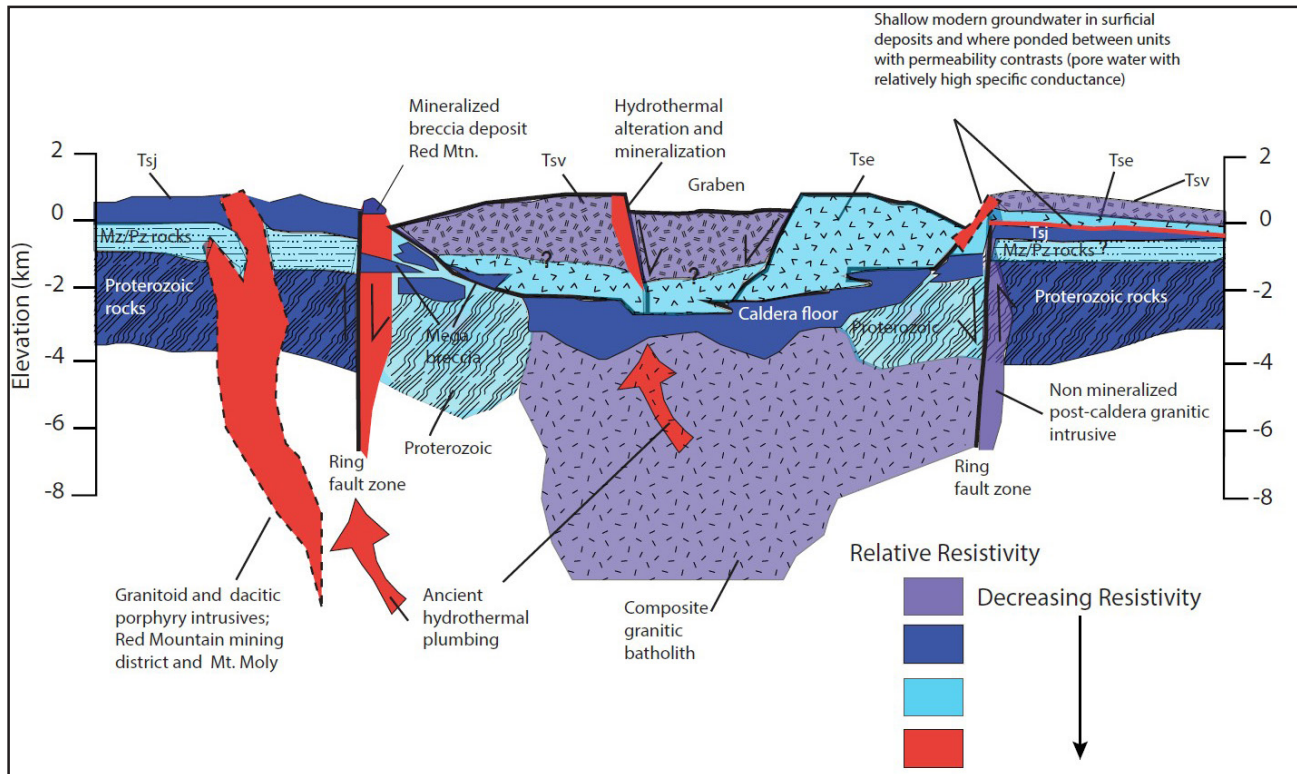


Figure 13. Schematic diagram showing caldera structures, lithologies, hydrothermal plumbing, modern groundwater zones, and resistivity imaged by magnetotellurics in this study. Figure is modified from Lipman (1984) based on subsurface resistivity signatures. Subsurface features, while somewhat speculative, are interpreted using surface geologic mapping, locations of intrusive centers, and knowledge of mineral deposits at depth (Casadevall and Ohmoto, 1977; Luedke and Burbank, 2000; Varnes, 1963; Yager and Bove, 2007). Tsj—San Juan Formation; Tsv—Silverton Volcanics; Tse—Eureka Member of Sapinero Mesa Tuff; Mz/Pz—Mesozoic–Paleozoic.

MT data helped image down-dropped megabreccia blocks of older San Juan Formation within the Silverton caldera (Figure 5B). These features were observed to have offsets and contrasting resistivities that could be used to show displacement of the blocks that occurred during caldera formation. Later silicic intrusions utilized the ring-fracture zone and other caldera-related structures near the Eureka graben during their emplacement, and associated hydrothermal fluids deposited silver-lead-zinc in the upper levels to coppergold in the lower zones (Casadevall and Ohmoto, 1977; Fisher and Leedy, 1973). The MT method was successful in imaging resistivity lows associated with hydrothermal alteration (Allis, 1990; Hoschke, 2008; Irvine and Smith, 1990) that likely contain abundant clay-size alteration minerals (Goldie, 2000; Locke et al., 1999) that formed during the mineralization events (Figure 5B) (Bove et al., 2007b). In addition, resistivity lows could be caused by interconnected sulfides (Hubert et al., 2016) that are characteristic of the ore mined in the breccia deposits (Gonzales and Larson, 2017).

AMT data may be imaging mineralization horizontally adjacent to 40–120 m of vertical mine workings in the upper part of the Sunnyside mine (Casadevall and Ohmoto, 1977). Between ~40 m and 100 m, there is a zone of relatively low resistivity that may be due to interconnected sulfides along the Sunnyside vein structure (Figure 7A). This is the area where at the surface, massive base-metal sulfides are exposed, which led to the initial discovery of the Sunnyside mine deposit (Bird, 1986). Alternatively, oxidation and weathering along near-surface veins could be causing water with relatively high specific conductance to form that could be reducing resistivity. Abundant clay alteration is not commonly prevalent along veins of the Sunnyside mine, which would, if present, be a cause of low resistivity. This area of low resistivity is also near where on 8 June 1974, mining was commencing when deposits below the mine breached former Lake Emma and caused the mine to be flooded. Less-competent and permeable rock that is possibly saturated with meteoric water where the upper workings of the mine were initially flooded could be contributing to lower bulk resistivity.

Some of the areas imaged as having low resistivity under and near former Lake Emma are where the mine pool has filled the Sunnyside mine workings (Figure 7A, near stations E2 and E8). A series of bulkheads was emplaced in the lower workings of the American Tunnel between 1996 and 2003 as part of a remediation strategy to reduce metal loading to Cement Creek (Walton-Day et al., 2021). The American Tunnel was initially constructed around the beginning of the 20th century to provide access below workings of the Gold King mine. It was greatly extended as a long-haul tunnel in 1959 to drain the Sunnyside mine workings and to provide access to ore in the Sunnyside mine. After the bulkheads were emplaced, the Sunnyside mine was flooded and water filled the mine workings. It is possible that rocks adjacent to the mine pool are also saturated, especially where fractures or faults are present. Where mine pool water has a high specific conductance, this could be a cause of low resistivity in some areas, but a higher spatial resolution with more closely spaced MT stations would be required to help address this question. AEM data when used in combination with MT data could aid in possibly imaging the mine pool.

MT data may also be imaging alteration associated with a mineralized system near the Gold King mine in upper Cement Creek. Resistivity lows were imaged at shallow levels to as much as 5 km depth (Figure 6). This resistivity low occurs where the predominant northwest-trending Gold King mine vein system, with a known lateral extent of 1 km (Koch, 1990), would intersect a possible concealed fault on trend with the northerly trending Cement Creek. Cement Creek has a very linear trend in the area west of the predominant Gold King mine vein system (Figure 2), and, while speculative, there appears to be a possible Proterozoic basement structural control for concealed hydrothermal alteration at depth. A northerly structural trend that penetrates Proterozoic basement in the southwestern United States is discussed in Marshak et al. (2000; their figure 1). The Gold King vein system, if it continues beneath Cement Creek, is buried beneath the alluvial valley fill. A moderate-resistivity low occurs near AMT station U7 between 30 and 60 m depth (Figure 6A) and could be associated with alteration or water having moderate specific conductance along the Bonita fault. This suggests that the Bonita fault may be permeable in this area. Northeast of the Ross Basin fault, a resistivity low between 3 and 5 km depth may be imaging alteration associated with hydrothermal plumbing at depth (Figure 6B). Examining geologic and alteration map data showed that less electrically resistive areas correlated with hydrothermally altered terrain, whereas more electrically resistive areas correlated with either weakly altered or propylitically altered terrains.

Imaging of the Caldera Ring-Fault Zones and Topographic Margin

MT imaging of the caldera ring-fault zones along the caldera margins and along the topographic margins (Figures 5, 8, 10, and 11) in this study allowed subsurface inferences to be made regarding caldera processes that developed during intrusive events (Figure 13). MT profiles that crossed different parts of the caldera complex were fundamental in addressing whether ring-fracture zones and topographic margins are zones of high permeability for hydrothermal fluids or for modern groundwater. One of the best examples of the Silverton caldera ring-fault zone being a zone of possible high permeability near the surface is seen in Figure 9. South of the Animas River, a zone of relatively low resistivity extends from the surface to >300 m. Outcrops of the ring-fault zone near AMT station A2 (Figure 9) are highly fractured and weakly mineralized. Groundwater with moderate to high specific conductance that infiltrated along the fault zone is one potential cause of low resistivity. Clay mineralization is also a potential cause, but it is not prevalent at the surface. Alternatively, fault gouge containing clay-size material could be present and cause a lower resistivity.

The Silverton caldera ring-fault zone has variable resistivity, indicating that where the structure was resistive (e.g., the western end of Mineral Basin and Red Mountain, Cunningham Creek, Kendall Mountain, and South Fork Mineral Creek MT profiles), quartz mineralization could be a cause of higher resistivity as has been noted in other studies (Allis, 1990; Goldie, 2000; Hoschke, 2008; Hoschke and Sexton, 2005; Irvine and Smith, 1990; Locke et al., 1999). Where silicification permeated the ring fault, this could form a hydrologic dam that is impermeable to present-day lateral fluid flow of groundwater. Perhaps the best example where an impermeable dam might have formed is near the western Silverton caldera ring-fault zone along Mineral Creek (Figures 2 and 5). Lithologies east of the caldera ring-fault zone are highly altered over large areas, indicating they were permeated by hydrothermal fluids. In contrast, lithologies west of Mineral Creek, north of the Mount Moly intrusive center, are generally resistive. A possible cause for contrasting resistivities east and west of the ring-fault zone is a hydrologic barrier that prevented hydrothermal fluids from flowing

westward and focused fluids within the Silverton caldera to the east. Variable and late silicification along the ring-fault zone may have annealed the structures and made them impermeable to fluid flow, preventing flooding by hydrothermal fluids in much of the western study area.

In addition to the caldera ring-fault zone, the topographic margin of the San Juan caldera is of interest from a groundwater perspective. The caldera margins consist of fragmental material that caved into the caldera as landslide deposits along the oversteepened caldera margins (Yager and Bove, 2007) and could be a permeable flow path for modern groundwater. Along the southern San Juan caldera topographic margin below MT station K5 (Figure 10), a zone of relatively low resistivity between ~0.6 and 2 km depth was imaged that, while speculative, could be caldera-wall, water-saturated landslide deposits. An electrically resistive block of dry Proterozoic crystalline rocks overlies the zone of less-resistive, wet, fragmental caldera wall rocks.

Imaging of Resurgent Caldera Features and Intrusions

MT imaging within the calderas in this study allowed subsurface inferences to be made regarding resurgent caldera features and intrusions that developed during intrusive events (Figure 13). Post-caldera collapse resurgence within the caldera complex caused apical graben fractures to form that were flow paths for mineralizing fluids (Burbank and Luedke, 1969; Casadevall and Ohmoto, 1977). The MT method provided an opportunity to image the resistivity structure below the resurgently domed caldera core. Resurgent doming inflation events are attributed to multiple, shallow magmatic pulses that remain below the crust in many felsic caldera systems (Acocella, 2019). The process of resurgent doming was suggested by Acocella (2019) to represent a continuum of magmatic emplacement events with episodes of inflation and deflation and incremental growth of the magmatic system being driven by shallow plutons or intrusions. MT data were used to image the possible magmatic system responsible for doming of the San Juan–Silverton caldera complex beneath the Eureka graben. Moderately low resistivity (~50–150 $\Omega\cdot\text{m}$) is imaged by MT data at ~1–3 km depth under the graben (Figures 2 and 7B). The resistivity low (Figure 7B) observed beneath the graben is consistent with those of mineralized plutons in other areas. Hernández Pardo et al. (2012) used the induced polarization electromagnetic geophysical technique to identify resistive unmineralized and less-resistive but mineralized intrusions as part of a porphyry system at the southern end of the mid-Cauca gold belt in Colombia. Previously, Casadevall and Ohmoto (1977) used drill core (label B-1 in Figures 2 and 7B) observations to suggest a porphyry deposit at depth. The resistivity low (~20–50 $\Omega\cdot\text{m}$) below ~2 km depth in Figure 7B (between MT stations E4 and E5) shows an area of possible sulfides (Hubert et al., 2016) and hydrothermal plumbing (Allis, 1990; Hoschke, 2008; Irvine and Smith, 1990; Mitchinson et al., 2013) that may represent the remnants or roots of a porphyry system at depth. We speculate that this low-resistivity zone, perhaps strongly influenced by hyper-saline brines, may be imaging part of a hydrothermal system associated with a porphyry intrusion at depth. The resistivity lows contrast with more resistive and presumably less-highly altered country rock that is distant from the hydrothermal conduit or the more highly mineralized parts of a concealed porphyry system beneath the resurgent dome. In addition, the geometry of the resistivity low could indicate a magmatic conduit that was used during pulsed magmatic inflation events that accompany resurgent doming that have been described in other similar volcanic systems (Acocella, 2019; Gilmer et al., 2021). The MT data also provide a glimpse into the deeper crustal lithologies and may be imaging the source areas for granitic plutons that underpin the multiple calderas of the southern Rocky Mountains volcanic field (Drenth et al., 2012; Lipman and Bachmann, 2015). Moderately high resistivities (500–1000 $\Omega\cdot\text{m}$) below a few kilometers depth in the southwestern half of the upper Cement Creek profile (Figure 6) and beneath the Eureka graben (Figure 7) and Cunningham Creek (Figure 8), respectively, are a few examples that we interpret to represent western caldera intrusions of the San Juan batholith.

Geoenvironmental and Modern Groundwater Implications and Hypotheses

AMT imaging of the shallow subsurface along the caldera margins and within the calderas in this study allowed subsurface inferences to be made regarding environmental and modern groundwater implications and hypotheses (Figure 13). A fundamental question addressed by the MT data is: Can modern groundwater be imaged? This information could be useful to land management agencies as they address issues pertinent to cleanup of the Bonita Peak mining district Superfund sites. In one area of specific interest, centered on

the Gold King and Red and Bonita mines, AMT data imaged a low-resistivity zone that thickens from a few meters in the southwest near Gladstone to ~80 m toward the northeast near the Red and Bonita mine (Figure 6A). This zone of relatively low resistivity may represent water with moderate to high specific conductance that accumulated in alluvial valley-fill sediments. Groundwater seeps have been mapped along Cement Creek in this area and bog iron deposits have formed below the Red and Bonita mine waste pile, an indication of the acidic weathering that has been ongoing in the area and that would result in groundwater having moderate to high specific conductance.

A zone of low resistivity that extends from the surface to ~30 m depth occurs below MT station A1 (Figure 9A) on the Mayflower Mill tailings, suggesting water with moderate to high specific conductance within the weathered tailings pile. Moderate-resistivity signatures are present near the surface adjacent to the Aspen mine, although lower resistivity occurs between depths of ~10 and 50 m. The zone of low resistivity continues southward toward the Legal Tender mine, suggesting that AMT data are imaging relatively low-resistivity Quaternary colluvium. The possible shallow groundwater features near each Bonita Peak mining district Superfund site would need to be interpreted on a case-by-case basis. MT data combined with geologic information, either from existing or new field studies at each site, could be useful in interpretations of the observed resistivity responses and possible causes. The AMT method appears to be effective, especially when combined with AEM data in interpreting resistivity responses that may be attributed to acid rock and acid mine weathering. Conversely, where known weakly propylitic rocks are mapped at the surface and where resistivity inversions reveal resistive rock in the subsurface could suggest zones rich in calcite that can supply acid-neutralizing capacity.

CONCLUSION

Magnetotellurics were applied to characterize the electromagnetic response of lithologies within a hydrothermally altered caldera setting. Prior MT studies of caldera environments primarily involved active geothermal systems, but few have focused on extinct caldera environments. Data and interpretations from this study revealed that although no active geothermal system is present, inferences could be made about the hydrothermal system applicable to future mineral assessment. In addition, present-day groundwater is evident in the resistivity inversion results. Mapping of groundwater can help to inform land managers responsible for assessing legacy mine sites in the Bonita Peak mining district Superfund area. The MT data can be useful in assessing where low-bulk-resistivity signatures in Quaternary alluvium and colluvium deposits occur that are attributed to water having relatively high specific conductance. These low-resistivity signatures could help to inform where acidic drainage may be a long-term source of metals and acidity to groundwater that could confound remediation efforts. Conversely, where higher bulk resistivity in surficial deposits persists could be an indication of where groundwater may be less affected by acidic drainage and where remediation efforts have a higher chance of success. Additional data from drill holes, ground-based electromagnetic methods, downhole geophysical logging, and groundwater sampling and analysis, if available, could augment interpretations based solely on MT data. Prior comprehensive studies involving geologic framework and alteration mapping investigations in the study area provide a backbone for interpreting the MT data in a way that might not be as possible in other mineralized caldera environments studied using the MT method. While this MT study is not totally unique, its study area is arguably one of the most well-studied caldera settings in the United States that employs the MT method in such a comprehensive way.

The model interpretations presented in this study could be utilized in remediation planning or mineral resource applications. The methods used in this study could be applied to other watersheds with similar volcanic environments containing acid-generating historical mines or source rocks.

The study was designed to investigate major structural features covering a wide geographic distribution of the caldera complex. In addition to having good coverage of many parts of the calderas, this study investigated resistivity responses at multiple depths. AMT data characterized geophysical responses of groundwater, near-surface lithologies, structures, and mineralized systems and also helped corroborate AEM data at shallow levels. The MT data were useful to extend our depth of investigation from near the surface

to depths of ~5 km, which helped in forming hypotheses about roots of the hydrothermal plumbing that fed shallower mineralized systems.

This study was also useful for deciphering the complex caldera geometry that developed along the caldera wall during eruption and caldera formation. Several MT profiles identified pre-caldera wall rocks that were offset along normal faults and down-dropped into the caldera. Examining geologic and alteration map data showed that less electrically resistive areas correlated with hydrothermally altered terrain, whereas more electrically resistive areas correlated with either weakly altered or propylitically altered terrains. AMT data were effective in helping to identify where meteoric groundwater may be present within caldera faults and areas of unconsolidated materials around the Gold King mine and Mayflower Mill tailings. The MT profiles suggest that the Silverton caldera structural and topographic margins may be zones of possible high permeability along some segments, where low-resistivity groundwater formed near the surface in surficial deposits and infiltrated the ring-fault structures in the upper 0.5 km. Parts of the ring fault are more resistive, suggesting lower permeability along those sections of the structure. Higher resistivities encountered along caldera ring-fault segments may be attributed to annealing by vein quartz. MT profiles collected across caldera faults, vein structures, and mineralized systems were used to probe the deeper parts of the mineralized system. Shallow resistivity may help to refine interpretations of modern groundwater locations, especially when compared with electromagnetic survey data.

ACKNOWLEDGMENTS

This work supported by the Mineral Resources Program of the U.S. Geological Survey (USGS) and by the ASARCO Trust. MT field support was provided by T. Jesse and E. Hartson (Western Colorado University), P. Weigel (Fort Lewis College), J. Bennett (Kent Denver High School), and R. Holmes (Montana State University). Colorado Department of Public Health and Environment, ASARCO Trust, and Kinross Gold Corporation provided access to sites important to this study. Reviews by USGS colleagues T. Casadevall and M. Guzman have improved this report. We are also indebted to USGS colleagues A. Angulo and A. Gilmer for providing geologic names and geological reviews, respectively. We are equally in debt to I. Ferguson, Professor of Geophysics, University of Manitoba, and an anonymous Geological Society of America reviewer for providing especially helpful geophysical reviews. Last, but not least, we acknowledge the great honor and incredible privilege it was to have worked with Bruce Smith (deceased), a great colleague and friend, who always had a positive attitude, sage advice, and caring fellowship that he so freely bestowed on everyone he met. Any use of trade, firm, or product names is for descriptive purposes only and does not imply endorsement by the U.S. Government.

MEMORIAL NOTE FROM AUTHORS

Bruce D. Smith was a geophysicist with the U.S. Geological Survey (1974-2017), a Scientist Emeritus from 2017 until his death in 2022, and a lifetime member of the Geological Society of America. He specialized in airborne geophysical surveys and contributed to numerous environmental projects. Bruce was always so positive and full of ideas. He was one of the kindest, thoughtful, and resilient persons we have ever known. The world is better place because of him. Bruce's complete GSA Memorial is available at <https://www.geosociety.org/GSA/gsa/pubs/memorials.aspx>

REFERENCES

- Acocella, V., 2019, Bridging the gap from caldera unrest to resurgence: *Frontiers in Earth Science*, v. 7, <https://doi.org/10.3389/feart.2019.00173>
- Aizawa, K., Ogawa, Y., and Ishido, T., 2009, Groundwater flow and hydrothermal systems within volcanic edifices: Delineation by electric self-potential and magnetotellurics: *Journal of Geophysical Research: Solid Earth*, v. 114, B01208, <https://doi.org/10.1029/2008JB005910>
- Alger, R.P., 1971, Interpretation of electric logs in fresh water wells in unconsolidated formations: *Transactions of the Society of Professional Well Log Analysts 7th Annual Logging Symposium*, May 9–11, 1966, Houston, Texas, 24 p., <https://doi.org/10.1515/acgeo-2016-0063>
- Allis, R.G., 1990, Geophysical anomalies over epithermal systems: *Journal of Geochemical Exploration*, v. 36, p. 339–374, [https://doi.org/10.1016/0375-6742\(90\)90060-N](https://doi.org/10.1016/0375-6742(90)90060-N).
- Anderson, E.D., Deszcz-Pan, M., Yager, D.B., and Smith, B.D., 2018, High resolution helicopterborne magnetic and electromagnetic survey Eureka Graben area, Colorado September 1999: U.S. Geological Survey data release, <https://doi.org/10.5066/F75D8R1W>
- Anderson, E.D., Yager, D.B., Deszcz-Pan, M., Hoogenboom, B.E., Rodriguez, B.D., and Smith, B.D., 2022, Geophysical data provide three dimensional insights into porphyry copper systems in the Silverton caldera, Colorado, USA: *Ore Geology Reviews*, v. 152, <https://doi.org/10.1016/j.oregeorev.2022.105223>
- Belser, C., 1956, Tungsten potential in the San Juan area, Ouray, San Juan, and San Miguel Counties, Colorado: U.S. Bureau of Mines Information Circular 7731, 18 p.
- Bird, A.G., 1986, *Silverton Gold: The Story of Colorado's Largest Gold Mine*: Allan G. Bird, 152 p.
- Blair, R.W., Jr., Yager, D.B., and Church, S.E., 2002, Surficial geologic maps along the riparian zone of the Animas River and its headwater tributaries, Silverton to Durango, Colorado, with upper Animas River watershed gradient profiles: U.S. Geological Survey Digital Data Series DDS-71, 5 p., 12 plates, <https://doi.org/10.3133/ds71>
- Bove, D.J., Hon, K., Budding, K.E., Slack, J.F., Snee, L.W., and Yeoman, R.A., 2001, Geochronology and geology of late Oligocene through Miocene volcanism and mineralization in the western San Juan Mountains, Colorado: U.S. Geological Survey Professional Paper 1642, 30 p., <https://doi.org/10.3133/pp1642>
- Bove, D.J., Eberl, D.D., McKarty, D.K., and Meeker, G.P., 2002, Characterization and modeling of illite crystal particles and growth mechanisms in a zoned hydrothermal deposit, Lake City, Colorado: *American Mineralogist*, v. 87, p. 1546–1556, <https://doi.org/10.2138/am-2002-11-1204>
- Bove, D.J., Yager, D.B., Mast, M.A., and Dalton, J.B., 2007a, Alteration map showing major faults and veins and associated water-quality signatures of the Animas River watershed headwaters near Silverton, southwest Colorado: U.S. Geological Survey Scientific Investigations Map 2976, 18 p. pamphlet, 1 plate, scale 1:24,000, <https://doi.org/10.3133/sim2976>
- Bove, D.J., Mast, M.A., Dalton, J.B., Wright, W.G., and Yager, D.B., 2007b, Major styles of mineralization and hydrothermal alteration and related solid- and aqueous-phase geochemical signatures, in Church, S.E., von Guerard, P., and Finger, S.E., eds., *Integrated Investigations of Environmental Effects of Historical Mining in the Animas River Watershed*, San Juan County, Colorado: U.S. Geological Survey Professional Paper 1651, p. 161–230, <https://doi.org/10.3133/pp1651>
- Bove, D.J., Johnson, R.H., and Yager, D.B., 2007c, Mineralogy from cores in Prospect Gulch, San Juan County, Colorado: U.S. Geological Survey Open-File Report 2007-1095, 82 p., <https://doi.org/10.3133/ofr20071095>
- Burbank, W.S., 1960, Pre-ore propylitization, Silverton Caldera, Colorado, in *Short Papers in the Geological Sciences: Geological Survey Research 1960*: U.S. Geological Survey Professional Paper 400-B, p. B12–B13, <https://doi.org/10.3133/pp400B>
- Burbank, W.S., and Luedke, R.G., 1969, Geology and ore deposits of the Eureka and adjoining districts, San Juan Mountains, Colorado: U.S. Geological Survey Professional Paper 535, 73 p., <https://doi.org/10.3133/pp535>
- Caine, J.S., Evans, J.P., and Forster, C.B., 1996, Fault zone architecture and permeability structure: *Geology*, v. 24, p. 1025–1028, [https://doi.org/10.1130/0091-7613\(1996\)024<1025:FZAAPS>2.3.CO;2](https://doi.org/10.1130/0091-7613(1996)024<1025:FZAAPS>2.3.CO;2).
- Caldwell, T.G., Bibby, H.M., and Brown, C., 2004, The magnetotelluric phase tensor: *Geophysical Journal International*, v. 158, p. 457–469, <https://doi.org/10.1111/j.1365-246X.2004.02281.x>
- Campbell, D.L., and Fitterman, D.V., 2000, Geoelectrical methods for investigating mine dumps, in *ICARD 2000: Proceedings from the Fifth International Conference on Acid Rock Drainage*: Littleton, Colorado, Society for Mining, Metallurgy, and Exploration, v. II, p. 1513–1524.
- Casadevall, T., and Ohmoto, H., 1977, Sunnyside Mine, Eureka mining district, San Juan, Colorado: *Geochemistry of gold and base metal ore deposition in a volcanic environment: Economic Geology*, v. 72, p. 1285–1320, <https://doi.org/10.2113/gsecongeo.72.7.1285>
- Chave, A.D., and Jones, A.G., 2012, *The Magnetotelluric Method: Theory and Practice*: Cambridge, UK, Cambridge University Press, 552 p., <https://doi.org/10.1017/CBO9781139020138>
- Cole, J.W., Milner, D.M., and Spinks, K.D., 2005, Calderas and caldera structures: A review: *Earth-Science Reviews*, v. 69, p. 1–26, <https://doi.org/10.1016/j.earscirev.2004.06.004>
- Coppo, N.P., Schnegg, P.A., Heise, W., Falco, P., and Costa, R., 2008, Multiple caldera collapses inferred from the shallow electrical resistivity signature of the Las Cañadas caldera, Tenerife, Canary Islands: *Journal of Volcanology and Geothermal Research*, v. 170, p. 153–166, <https://doi.org/10.1016/j.jvolgeores.2007.09.013>

- Cox, E.M., Rodriguez, B.D., Bloss, B.R., and Yager, D.B., 2021, Magnetotelluric sounding data in the Silverton Caldera complex, Colorado, 2018: U.S. Geological Survey data release, <https://doi.org/10.5066/P9OVM0AE>
- Davis, J.L., and Annan, A.P., 1989, Ground-penetrating radar for high-resolution mapping of soil and rock stratigraphy: *Geophysical Prospecting*, v. 37, p. 531–551, <https://doi.org/10.1111/j.1365-2478.1989.tb02221.x>
- Deszcz-Pan, Maria, Rodriguez, B.D., Doucette, J.P., Godbout, Michel, Williams, J.M., Sawyer, D.A., Stone, B.D., and Grauch, V.J.S., 2000, Digital airborne time domain electromagnetic data from surveys over Cochiti Pueblo, Rio Puerco, and Rio Rancho, New Mexico: U.S. Geological Survey Open-File Report 00-502 (CD-ROM), <https://doi.org/10.3133/ofr00502>
- Di Giuseppe, M.G., Troiano, A., and Carlino, S., 2017, Magnetotelluric imaging of the resurgent caldera on the island of Ischia (southern Italy): Inferences for its structure and activity: *Bulletin of Volcanology*, v. 79, no. 85, <https://doi.org/10.1007/s00445-017-1170-4>
- Dilles, J.H., and Einaudi, M.T., 1992, Wall-rock alteration and hydrothermal flow paths about the Ann-Mason porphyry copper deposit, Nevada: A 6-km vertical reconstruction: *Economic Geology*, v. 87, p. 1963–2001, <https://doi.org/10.2113/gsecongeo.87.8.1963>
- Doe, B.R., Steven, T.A., Delevaux, M.H., Stacey, J.S., Lipman, P.W., and Fisher, F.S., 1979, Genesis of ore deposits in the San Juan volcanic field, southwestern Colorado: Lead isotope evidence: *Economic Geology*, v. 74, p. 1–26, <https://doi.org/10.2113/gsecongeo.74.1.1>
- Drenth, B.J., Keller, G.R., and Thompson, R.A., 2012, Geophysical study of the San Juan Mountains batholith complex, southwestern Colorado: *Geosphere*, v. 8, p. 669–684, <https://doi.org/10.1130/GES00723.1>
- Fisher, F.S., and Leedy, W.P., 1973, Geochemical characteristics of mineralized breccia pipes in the Red Mountain district, San Juan Mountains, Colorado: U.S. Geological Survey Bulletin 1381, 43 p., <https://doi.org/10.3133/b1381>
- Fulignati, P., 2020, Clay minerals in hydrothermal systems: *Minerals (Basel)*, v. 10, <https://doi.org/10.3390/min10100919>
- Gilmer, A.K., Thompson, R.A., Lipman, P.W., Vazquez, J.A., and Souders, A.K., 2021, Postcaldera intrusive magmatism at the Platoro caldera complex, Southern Rocky Mountain volcanic field, Colorado, USA: *Geosphere*, v. 17, p. 898–931, <https://doi.org/10.1130/GES02242.1>
- Gilson, E.W., Nimeck, G., Bauman, P.D., and Kellett, R., 2000, Groundwater exploration in prairie environments, in Powers, M.H., Ibrahim, A.-B., and Cramer, L., eds., *Symposium on the Application of Geophysics to Environmental and Engineering Problems Proceedings*, Arlington, Virginia, February 2000: Wheat Ridge, Colorado, Environmental and Engineering Geophysical Society, p. 955-959, https://doi.org/10.3997/2214-4609-pdb.200.2000_109
- Gilzean, M.N., 1984, The nature of the deep hydrothermal system, Red Mountain district, Silverton, Colorado [M.S. thesis]: Berkeley, University of California, 69 p.
- Goldie, M.K., 2000, A geophysical case history of the Yanacocha gold district, northern Peru: *Society of Exploration Geophysicists Technical Program Expanded Abstracts*, v. 2000, p. 750–753, <https://doi.org/10.1190/1.1816178>
- Gonzales, D.A., 2015, New U-Pb zircon and ⁴⁰Ar/³⁹Ar age constraints on the late Mesozoic to Cenozoic plutonic record in the western San Juan Mountains: *Mountain Geologist*, v. 52, no. 2, p. 5–42, <https://doi.org/10.31582/rmag.mg.52.2.5>
- Gonzales, D.A., and Larson, R.A., 2017, An overview of the mineral deposits of the Red Mountain mining district, San Juan Mountains, Colorado, in Karlstrom, K.E., Gonzales, D.A., Zimmerer, M.J., Heizler, M., and Ulmer-Scholle, D.S., eds., *The Geology of the Ouray-Silverton Area: New Mexico Geological Society 68th Annual Field Conference Guidebook*, p. 133–140, <https://doi.org/10.56577/FFC-68.133>
- Gonzales, D.A., and Van Schmus, W.R., 2007, Proterozoic history and crustal evolution in southwestern Colorado: Insight from U/Pb and Sm/Nd data: *Precambrian Research*, v. 154, p. 31–70, <https://doi.org/10.1016/j.precamres.2006.12.001>
- Hallenburg, J.K., 1998, *Non-Hydrocarbon Methods of Geophysical Formation Evaluation*: Boca Raton, Florida, Lewis Publishers, 265 p.
- Hernández Pardo, O., Greta, C., Alexander, E., Iraida, M., and Pintor, B., 2012, Geophysical exploration of disseminated and stockwork deposits associated with plutonic intrusive rock: A case study on the eastern flank of Colombia's western cordillera: *Earth Sciences Research Journal*, v. 16, p. 11–23.
- Hogg, C., Kiyani, D., Rath, V., Byrdina, S., Vandemeulebrouck, J., Revil, A., Viveiros, F., Carmo, R., Silva, C., and Ferreira, T., 2018, 3-D interpretation of short-period magnetotelluric data at Furnas Volcano, Azores Islands: *Geophysical Journal International*, v. 213, p. 371–386, <https://doi.org/10.1093/gji/ggx512>
- Hon, K., and Mehnert, H.A., 1983, Compilation of revised ages of volcanic units in the San Juan Mountains, Colorado—Recalculated K-Ar age determinations using the IUGS constants: U.S. Geological Survey Open-File Report 83-668, 14 p., <https://doi.org/10.3133/ofr83668>
- Hoogenboom, B.E., Deszcz-Pan, M., Anderson, E.D., Rodriguez, B.D., Smith, B.D., and Yager, D.B., 2022a, Airborne electromagnetic and magnetic survey data, Silverton, Colorado, 2019 (ver. 2.0): U.S. Geological Survey data release, <https://doi.org/10.5066/P92IADBP>
- Hoogenboom, B.E., Rodriguez, B.D., Yager, D.B., Anderson, E.D., Deszcz-Pan, M., and Smith, B.D., 2022b, Electromagnetic data for subsurface imaging of Arrastra Gulch, San Juan County, Colorado: Implications for land-use management decisions: *Geological Society of America Abstracts with Programs*, v. 54, no. 5, <https://doi.org/10.1130/abs/2022AM-379056>
- Hoschke, T., 2008, Geophysical signatures of copper-gold porphyry and epithermal gold deposits, in Spencer, J.E., and Tittley, S.R., eds., *Ores and Orogenesis: Circum-Pacific Tectonics, Geologic Evolution, and Ore Deposits: Arizona Geological Society Digest 22*, p. 85–100.
- Hoschke, T., and Sexton, M., 2005, Geophysical exploration for epithermal gold deposits at Pajingo, North Queensland, Australia: *Exploration Geophysics*, v. 36, p. 401–406, <https://doi.org/10.1071/EG05401>
- Hübert, J., Lee, B.M., Liu, L., Unsworth, M.J., Richards, J.P., Abbassi, B., Cheng, L.Z., Oldenburg, D.W., Legault, J.M., and Rebaglatti, M., 2016, Three-dimensional imaging of a Ag-Au-rich epithermal system in British Columbia, Canada, using airborne z-axis tipper electromagnetic and ground-based magnetotelluric data: *Geophysics*, v. 81, no. 1, p. B1–B12, <https://doi.org/10.1190/geo2015-0230.1>

- Irvine, R.J., and Smith, M.J., 1990, Geophysical exploration for epithermal gold deposits: *Journal of Geochemical Exploration*, v. 36, p. 375–412, [https://doi.org/10.1016/0375-6742\(90\)90061-E](https://doi.org/10.1016/0375-6742(90)90061-E)
- Ito, A., and Wagai, R., 2017, Global distribution of clay-size minerals on land surface for biogeochemical and climatological studies: *Scientific Data*, v. 4, 170103, <https://doi.org/10.1038/sdata.2017.103>
- Jackson, S.E., Harmon, R.S., Lux, D., Rice, C.M., and Ringrose, C.M., 1980, Isotopic geochemistry and chronology of porphyry-style mineralization near Ophir, San Juan Mountains, Colorado: *Geological Society of America Abstracts with Programs*, v. 12, p. 454.
- Johnson, R.H., Yager, D.B., and Johnson, H.D., 2011, Geochemical data from waters in Prospect Gulch, San Juan County, Colorado, that span pre-and post-Lark Mine remediation: U.S. Geological Survey Open-File Report 2011-1316, 4 p., <https://doi.org/10.3133/ofr20111316>
- Koch, B.C., 1990, Origin of the Gold King-Davis epithermal gold lode, Silverton caldera, Colorado [Ph.D. thesis]: Golden, Colorado School of Mines, 291 p., <https://repository.mines.edu/handle/11124/172219>
- Larsen, E.S., Jr and Cross, W., 1956, Geology and petrology of the San Juan region, southwestern Colorado: U.S. Geological Survey Professional Paper 258, 303 p., <https://doi.org/10.3133/pp258>
- Lesmes, D.P., and Friedman, S.P., 2005, Relationships between the electrical and hydrogeological properties of rocks and soils, in Rubin, Y., and Hubbard, S.S., eds, *Hydrogeophysics*: Dordrecht, Netherlands, Springer, p. 87–128, https://doi.org/10.1007/1-4020-3102-5_4
- Lipman, P.W., 1976a, Caldera-collapse breccias in the western San Juan Mountains, Colorado: *Geological Society of America Bulletin*, v. 87, p. 1397–1410, [https://doi.org/10.1130/0016-7606\(1976\)87<1397:CBITWS>2.0.CO;2](https://doi.org/10.1130/0016-7606(1976)87<1397:CBITWS>2.0.CO;2)
- Lipman, P.W., 1976b, Geologic map of the Lake City caldera area, western San Juan Mountains, southwestern Colorado: U.S. Geological Survey Miscellaneous Investigations Series Map I-962, scale 1:48,000, <https://doi.org/10.3133/i962>
- Lipman, P.W., 1984, The roots of ash-flow calderas in western North America: Windows into the tops of granitic batholiths: *Journal of Geophysical Research: Solid Earth*, v. 89, p. 8801–8841, <https://doi.org/10.1029/JB089iB10p08801>
- Lipman, P.W., 2007, Incremental assembly and prolonged consolidation of Cordilleran magma chambers: Evidence from the Southern Rocky Mountain volcanic field: *Geosphere*, v. 3, p. 42–70, <https://doi.org/10.1130/GES00061.1>
- Lipman, P.W., and Bachmann, O., 2015, Ignimbrites to batholiths: Integrating perspectives from geological, geophysical, and geochronological data: *Geosphere*, v. 11, p. 705–743, <https://doi.org/10.1130/GES01091.1>
- Lipman, P.W., and McIntosh, W.C., 2008, Eruptive and noneruptive calderas, northeastern San Juan Mountains, Colorado: Where did the ignimbrites come from?: *Geological Society of America Bulletin*, v. 120, p. 771–795, <https://doi.org/10.1130/B26330.1>
- Lipman, P.W., Steven, T.A., and Mehnert, H.H., 1970, Volcanic history of the San Juan Mountains, Colorado, as indicated by potassium-argon dating: *Geological Society of America Bulletin*, v. 81, p. 2329–2352, [https://doi.org/10.1130/0016-7606\(1970\)81\[2329:VHOTSJ\]2.0.CO;2](https://doi.org/10.1130/0016-7606(1970)81[2329:VHOTSJ]2.0.CO;2)
- Lipman, P.W., Steven, T.A., Luedke, R.G., and Burbank, W.S., 1973, Revised volcanic history of the San Juan, Uncompahgre, Silverton, and Lake City calderas in the western San Juan Mountains, Colorado: *Journal of Research of the U.S. Geological Survey*, v. 1, p. 627–642 <https://pubs.usgs.gov/publication/70161990>
- Lipman, P.W., Fisher, F.S., Mehnert, H.H., Naeser, C.W., Luedke, R.G., and Steven, T.A., 1976, Multiple ages of mid-Tertiary mineralization and alteration in the western San Juan Mountains, Colorado: *Economic Geology*, v. 71, p. 571–588, <https://doi.org/10.2113/gsecongeo.71.3.571>
- Locke, C.A., Johnson, S.A., Cassidy, J., and Mauk, J.L., 1999, Geophysical exploration of the Puhipuhi epithermal area, Northland, New Zealand: *Journal of Geochemical Exploration*, v. 65, p. 91–109, [https://doi.org/10.1016/S0375-6742\(98\)00067-3](https://doi.org/10.1016/S0375-6742(98)00067-3)
- Long, C.L., 1985, Regional audiomagnetotelluric study of the Questa caldera, New Mexico: *Journal of Geophysical Research: Solid Earth*, v. 90, p. 11,270–11,274, <https://doi.org/10.1029/JB090iB13p11270>
- Luedke, R.G., and Burbank, W.S., 2000, Geologic map of the Silverton and Howardsville quadrangles, southwestern Colorado: U.S. Geological Survey Geologic Investigations Series Map I-2681, scale 1:24,000, <https://doi.org/10.3133/i2681>
- Mackie, R.L., Rieven, S., and Rodi, W.L., 1997, Users manual and software documentation for two-dimensional inversion of magnetotelluric data: Cambridge, Massachusetts Institute of Technology, Earth Resources Laboratory Cambridge, 10 p.
- Marshak, S., Karlstrom, K., and Timmons, J.M., 2000, Inversion of Proterozoic extensional faults: An explanation for the pattern of Laramide and Ancestral Rockies intracratonic deformation, United States: *Geology*, v. 28, p. 735–738, [https://doi.org/10.1130/0091-7613\(2000\)28<735:IOPEFA>2.0.CO;2](https://doi.org/10.1130/0091-7613(2000)28<735:IOPEFA>2.0.CO;2)
- McDougal, R.R., McCafferty, A.E., Smith, B.D., and Yager, D.B., 2007, Topographic, geophysical, and mineralogical characterization of geologic structures using a statistical modeling approach, in Church, S.E., von Guerard, P., and Finger, S.E., eds., *Integrated Investigations of Environmental Effects of Historical Mining in the Animas River Watershed, San Juan County, Colorado*: U.S. Geological Survey Professional Paper 1651, p. 647–687, <https://doi.org/10.3133/pp1651>
- Mitchinson, D.E., Enkin, R.J., and Hart, C.J.R., 2013, Linking porphyry deposit geology to geophysics via physical properties: Adding value to Geoscience BC geophysical data: *Geoscience BC Technical Report 2013-14*, 116 p., <https://cdn.geosciencebc.com/projectdata/GBCReport2013-14/GBCReport2013-14.pdf>
- Nelson, P.H., and Anderson, L.A., 1992, Physical properties of ash flow tuff from Yucca Mountain, Nevada: *Journal of Geophysical Research: Solid Earth*, v. 97, no. B5, p. 6823–6841, <https://doi.org/10.1029/92JB00350>
- Peacock, J.R., Mangan, M.T., McPhee, D., and Wannamaker, P.E., 2016, Three-dimensional electrical resistivity model of the hydrothermal system in Long Valley caldera, California: *Geophysical Research Letters*, v. 43, p. 7953–7962, <https://doi.org/10.1002/2016GL069263>

- Piña-Varas, P., Ledo, J., Queralt, P., Marcuello, A., Bellmunt, F., Hidalgo, R., and Messeiller, M., 2014, 3-D magnetotelluric exploration of Tenerife geothermal system (Canary Islands, Spain): *Surveys in Geophysics*, v. 35, p. 1045–1064, <https://doi.org/10.1007/s10712-014-9280-4>
- Piña-Varas, P., Ledo, J., Queralt, P., Marcuello, A., Bellmunt, F., Ogaya, X., Pérez, N., and Rodriguez-Losada, J.A., 2015, Vertical collapse origin of Las Cañadas caldera (Tenerife, Canary Islands) revealed by 3-D magnetotelluric inversion: *Geophysical Research Letters*, v. 42, p. 1710–1716, <https://doi.org/10.1002/2015GL063042>
- Pous, J., Heise, W., Schnegg, P.-A., Muñoz, G., Martí, J., and Soriano, C., 2002, Magnetotelluric study of the Las Cañadas caldera (Tenerife, Canary Islands): Structural and hydrogeological implications: *Earth and Planetary Science Letters*, v. 204, p. 249–263, [https://doi.org/10.1016/S0012-821X\(02\)00956-1](https://doi.org/10.1016/S0012-821X(02)00956-1)
- Reitman, J., Rodriguez, B.D., and Brown, P.J., 2019, Audiomagnetotelluric sounding data in the Silverton Caldera complex, Colorado, 2018: U.S. Geological Survey data release, <https://doi.org/10.5066/P9PPQJ8>
- Reitman, J., Rodriguez, B.D., Brown, P.J., and Yager, D.B., 2021a, Audiomagnetotelluric sounding data in the Silverton Caldera complex, Colorado, 2019: U.S. Geological Survey data release, <https://doi.org/10.5066/P9F68AQP>
- Reitman, J., Rodriguez, B.D., Brown, P.J., and Yager, D.B., 2021b, Magnetotelluric sounding data in the Silverton Caldera complex, Colorado, 2019: U.S. Geological Survey data release, <https://doi.org/10.5066/P92HEP1K>
- Ringrose, C.R., 1982, Geology, geochemistry, and stable isotope studies of a porphyry-style hydrothermal system, west Silverton district, San Juan Mountains, Colorado [Ph.D. thesis]: Aberdeen, Scotland, University of Aberdeen, 257 p., 19 plates.
- Ringrose, C.R., Harmon, R.S., Jackson, S.E., and Rice, C.M., 1986, Stable isotope geochemistry of a porphyry-style hydrothermal system, West Silverton District, San Juan Mountains, Colorado, U.S.A: *Applied Geochemistry*, v. 1, p. 357–373, [https://doi.org/10.1016/0883-2927\(86\)90021-1](https://doi.org/10.1016/0883-2927(86)90021-1)
- Rodi, W.L., and Mackie, R.L., 2001, Nonlinear conjugate gradients algorithm for 2-D magnetotelluric inversion: *Geophysics*, v. 66, p. 174–187, <https://doi.org/10.1190/1.1444893>
- Runkel, R.L., Petach, T.N., Cowie, R.M., Bowen, I., McCleskey, R.B., Dymant, S., Rock, N., and Qi, S.L., 2022, Synoptic sampling data from upper Cement Creek near Gladstone, Colorado, October 2012, September 2019, and September 2020: U.S. Geological Survey data release, <https://doi.org/10.5066/P9QO264O>
- Santos, F.A., Trota, A., Soares, A., Luzio, R., Lourenço, N., Matos, L., Almeida, E., Gaspar, J.L., and Miranda, J.M., 2006, An audio-magnetotelluric investigation in Terceira Island (Azores): *Journal of Applied Geophysics*, v. 59, p. 314–323, <https://doi.org/10.1016/j.jappgeo.2005.2.001>
- Senterfit, R.M., Ratté, J.C., Kamilli, R.J., and Klein, D.P., 1996, Audiomagnetotelluric study of the Bursum caldera and Mogollon mining district, southwest New Mexico: U.S. Geological Survey Open-File Report 96-37, 34 p., <https://doi.org/10.3133/ofr9637>
- Sillitoe, R.H., 2010, Porphyry copper systems: *Economic Geology*, v. 105, p. 3–41, <https://doi.org/10.2113/gsecongeo.105.1.3>
- Siniscalchi, A., Tripaldi, S., Romano, G., D'Auria, L., Improta, L., and Petrillo, Z., 2017, Audiomagnetotellurics-Magnetotelluric (AMT-MT) survey of the Campi Flegrei inner caldera: *Geophysical Research Abstracts*, v. 19, <https://meetingorganizer.copernicus.org/EGU2017/EGU2017-17080.pdf>
- Smith, B.D., McDougal, R.R., Deszcz-Pan, M., and Yager, D.B., 2007, Helicopter electromagnetic and magnetic surveys, in Church, S.E., von Guerard, P., and Finger, S.E., eds., *Integrated Investigations of Environmental Effects of Historical Mining in the Animas River Watershed*, San Juan County, Colorado: U.S. Geological Survey Professional Paper 1651, p. 231–254, <https://doi.org/10.3133/pp1651>
- Steven, T.A., and Lipman, P.W., 1976, Calderas of the San Juan volcanic field, southwestern Colorado: U.S. Geological Survey Professional Paper 958, 35 p., <https://doi.org/10.3133/pp958>
- Tweto, O., and Sims, P.K., 1963, Precambrian ancestry of the Colorado mineral belt: *Geological Society of America Bulletin*, v. 74, p. 991–1014, [https://doi.org/10.1130/0016-7606\(1963\)74\[991:PAOTCM\]2.0.CO;2](https://doi.org/10.1130/0016-7606(1963)74[991:PAOTCM]2.0.CO;2)
- U.S. Environmental Protection Agency, 2016, Bonita Peak Mining District NPL Sources and Other Possible Sources Map (Labeled), EPA ID 1777520, <https://semspub.epa.gov/work/08/1777520.pdf> (last accessed February 2022).
- U.S. Geological Survey, 1955, USGS 1:24000-scale Quadrangle for Silverton, CO 1955: U.S. Geological Survey, <https://www.sciencebase.gov/catalog/item/5a8a3cfce4b00f54eb3e7dcf> (last accessed February 2024).
- Varnes, D.J., 1963, Geology and ore deposits of the South Silverton mining area, San Juan County, Colorado: U.S. Geological Survey Professional Paper 378-A, 56 p., <https://doi.org/10.3133/pp378A>
- Vozoff, K., 1991, The magnetotelluric method, in Nabighian, M.N., ed., *Electromagnetic Methods in Applied Geophysics: Volume 2, Application*, Part A and Part B: Society of Exploration Geophysicists Investigations in Geophysics 3, v. 2, p. 641–711, <https://doi.org/10.1190/1.9781560802686.ch8>
- Walton-Day, K., Mast, M.A., and Runkel, R.L., 2021, Water-quality change following remediation using structural bulkheads in abandoned draining mines, upper Arkansas River and upper Animas River, Colorado USA: *Applied Geochemistry*, v. 127, <https://doi.org/10.1016/j.apgeochem.2021.104872>
- Wannamaker, P.E., 1999, Affordable magnetotellurics: Interpretation in natural environments, in Oristaglio, M., and Spies, B., eds., *Three-Dimensional Electromagnetics: Society of Exploration Geophysicists Geophysical Developments Series 7*, p. 349–374, <https://doi.org/10.1190/1.9781560802154.ch22>

- Yager, D.B., and Bove, D.J., 2007, Geologic framework, in Church, S.E., von Guerard, P., and Finger, S.E., eds., *Integrated Investigations of Environmental Effects of Historical Mining in the Animas River Watershed, San Juan County, Colorado*: U.S. Geological Survey Professional Paper 1651, p. 107–140, <https://doi.org/10.3133/pp1651>
- Yager, D.B., Choate, L., and Stanton, M.R., 2008, Net acid production, acid neutralizing capacity, and associated mineralogical and geochemical characteristics of Animas River watershed igneous rocks near Silverton, Colorado: U.S. Geological Survey Scientific Investigations Report 2008-5063, 63 p., <https://doi.org/10.3133/sir20085063>
- Yager, D.B., Johnson, R.H., Rockwell, B.W., and Caine, J.S., 2013, A GIS and statistical approach to identify variables that control water quality in hydrothermally altered and mineralized watersheds, Silverton, Colorado, USA: *Environmental Earth Sciences*, v. 70, p. 1057–1082, <https://doi.org/10.1007/s12665-013-2229-y>

Groundwater Flow Model Investigation of the Vulnerability of Water Resources at Chaco Culture National Historical Park Related to Unconventional Oil and Gas Development

Zachary M. Shephard¹, Andre B. Ritchie¹, and Benjamin S. Linhoff¹

¹United States Geological Survey
United States Department of the Interior

John J. Lunzer²

²Montana Department of Natural Resources & Conservation

Report prepared in cooperation with the National Park Service

*Scientific Investigations Report 2023–5097
(Conversion Factors available at end of report)*

ABSTRACT

Chaco Culture National Historical Park (CCNHP), located in northwestern New Mexico, protects the greatest concentration of Chacoan historical sites in the American Southwest. Geologically, CCNHP is located within the San Juan structural basin, which consists in part of complex Cretaceous stratigraphy and hosts a variety of energy resources. As part of a larger study to investigate the vulnerability of water resources at CCNHP related to oil and natural gas extraction activities, a MODFLOW groundwater model of the Mancos Shale and Gallup Sandstone units was created by the U.S. Geological Survey, as a part of a cooperative study with the National Park Service, to assess advective groundwater flow paths and traveltimes. The model determined that groundwater flow directions currently trend from south-southeast to north-northwest within the vicinity of CCNHP, groundwater traveltime through the Gallup Sandstone ranges from thousands to tens of thousands of years, and traveltime through the Mancos Shale may range from millions to tens of millions of years. The capture zone of the main CCNHP well (referred to as the “Chaco well”) extends to the south-southeast and ranges in width from approximately 1 to 12 miles, depending on pumping rate. Eighteen inactive hydrocarbon related wells are located within the capture zone and within 10 kilometers of the Chaco well. Given model estimates of traveltimes of groundwater in the Gallup Sandstone aquifer, advective groundwater transport to the Chaco well would take approximately 430 years from the nearest inactive hydrocarbon related wells. Differencing of historical and modern-day potentiometric surfaces of the Gallup Sandstone indicate a drop in groundwater levels between 34 and 96 feet within the CCNHP boundaries. Hydraulic fracturing, simulated as increased hydraulic conductivity zones, decreased groundwater traveltimes (from millions to thousands of years) and acted as permeable pathways from the Mancos Shale to the Gallup Sandstone.

INTRODUCTION

Chaco Culture National Historical Park (CCNHP) is in the Four Corners region of the United States in northwestern New Mexico (Figure 1) and preserves a major center of Ancestral Puebloan culture dating between 850 and 1250 A.D. CCNHP covers an area of approximately 53 square miles, and within CCNHP, the National Park Service (NPS) protects over 4,000 sites, which is the greatest concentration of Chacoan historical sites in the American Southwest (NPS, 2015). Today, CCNHP is a United Nations Educational, Scientific, and Cultural Organization (UNESCO) World Heritage Site as well as an important ceremonial site for the Navajo and Pueblo peoples. The park attracts approximately 60,000 visitors per year, many of whom stay overnight in the park campgrounds. Geologically, the park is located within the San Juan structural basin, a Late Cretaceous-Paleogene age structural depression on the eastern edge of the Colorado Plateau that hosts a variety of energy resources, including oil and natural gas, uranium, and coal (Stone and others, 1983). Major aquifers in the region include generally confined sandstones of Paleogene, Cretaceous, and Jurassic age (Stone and others, 1983). The NPS constructed a 3,100-foot (ft)-deep well (referred to hereafter as the “Chaco well”) into the Cretaceous Gallup Sandstone aquifer (Figure 2) in 1972 to provide the park with its first reliable drinking water source, following unsuccessful attempts to develop usable near-surface water sources (Colleen Filippone, National Park Service, oral commun., 2018). In the subsurface beneath CCNHP, the 100- to 200-ft-thick Gallup Sandstone is stratigraphically located between thick confining sequences of lower-permeability Mancos Shale. The Mancos Shale and Gallup Sandstone have been subject to both conventional and unconventional oil and gas development, including hydraulic fracturing (HF) (Engler and others, 2015). This study by the U.S. Geological Survey (USGS), in cooperation with NPS, was initiated largely in response to growing public concern about how current and future oil and gas development may negatively influence the drinking water source at CCNHP. The study is complemented by a geochemical analysis of groundwater age, groundwater flow directions, and potential mixing between aquifers (Linhoff and others, 2023).

This study involved (1) the development of a MODFLOW numerical groundwater model to assess groundwater flow directions and traveltimes through the Gallup Sandstone and Mancos Shale surrounding the CCNHP and (2) the creation of potentiometric surfaces in the Gallup Sandstone to assess groundwater drawdown within the water bearing unit in the vicinity of CCNHP. Model results are presented to delineate the area contributing flow to the Chaco well from the source area (otherwise known as the capture zone), assess groundwater travel-times of captured water, and develop simple scenarios simulating potential future oil and gas development. These tools and analyses are needed to inform the NPS about the susceptibility of the drinking water supply at CCNHP to potential contamination of HF fluids and depletion of water through water extraction. This work may serve as a template for studies examining drinking water resources that are susceptible to contamination in oil and gas producing areas.

PURPOSE AND SCOPE

This report documents the investigation of the vulnerability of water resources at CCNHP related to unconventional oil and gas development. Specifically, the report documents the following:

1. creation of updated potentiometric surfaces of the Gallup Sandstone to inform the groundwater model and to assess the change in hydraulic head (head) between historical and modern timeframes;
2. development of a numerical model to assess groundwater flow directions in the region; and
3. application of the model and simulations, including
 - a. delineation of the area contributing flow to the Chaco well from the source area (the capture zone);
 - b. estimation of advective groundwater flow traveltimes of water captured by the Chaco well; and
 - c. simulation of potential influence of HF by altering hydraulic conditions in the Mancos Shale to evaluate the effect on particle pathways, traveltimes, and potential influence on the Chaco well.

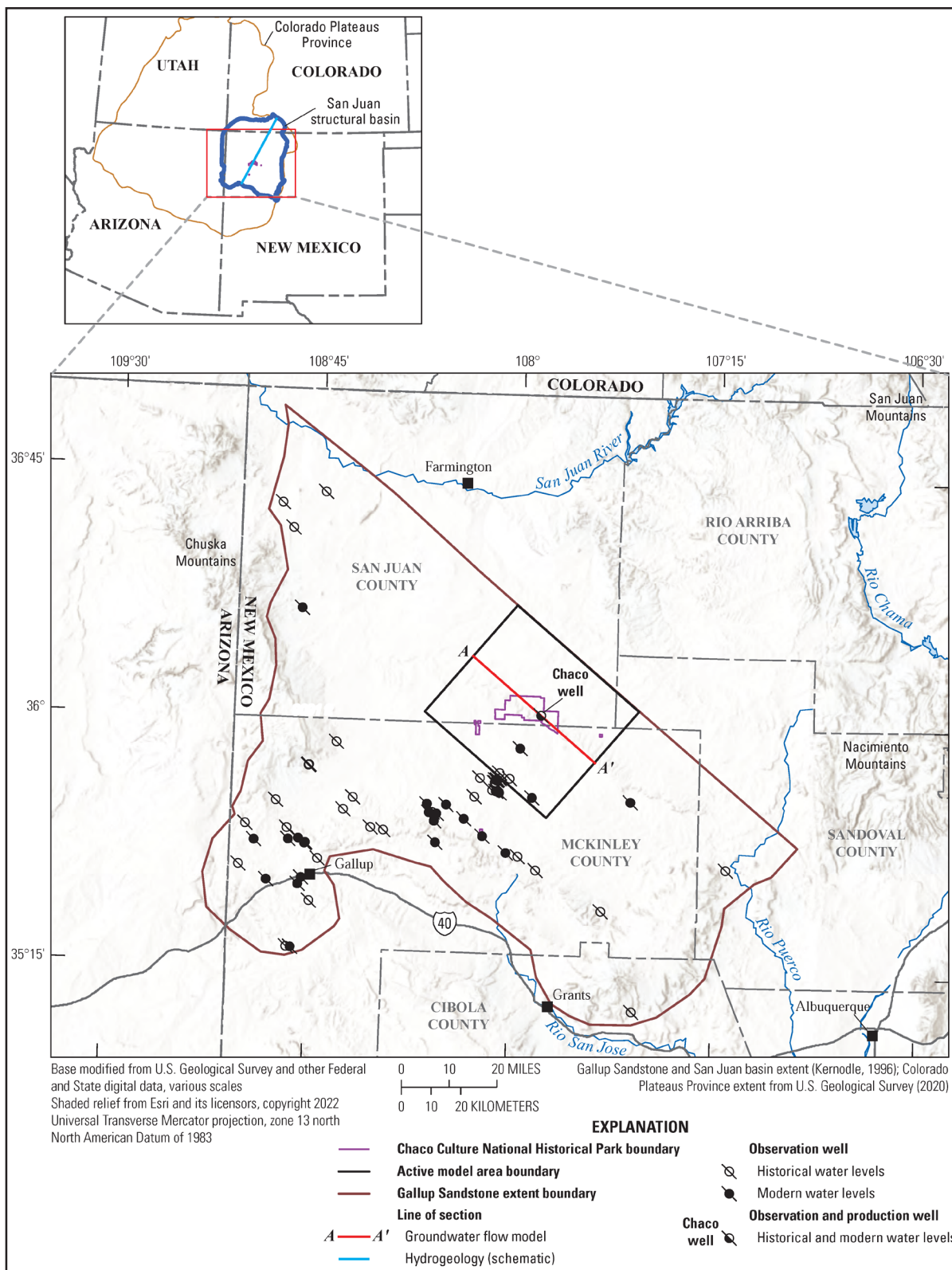


Figure 1. Study area, plan view of the active groundwater flow model area, and groundwater level observation points used in model calibration and potentiometric surface development. The Gallup Sandstone extent map unit represents the surface and subsurface extent of the unit.

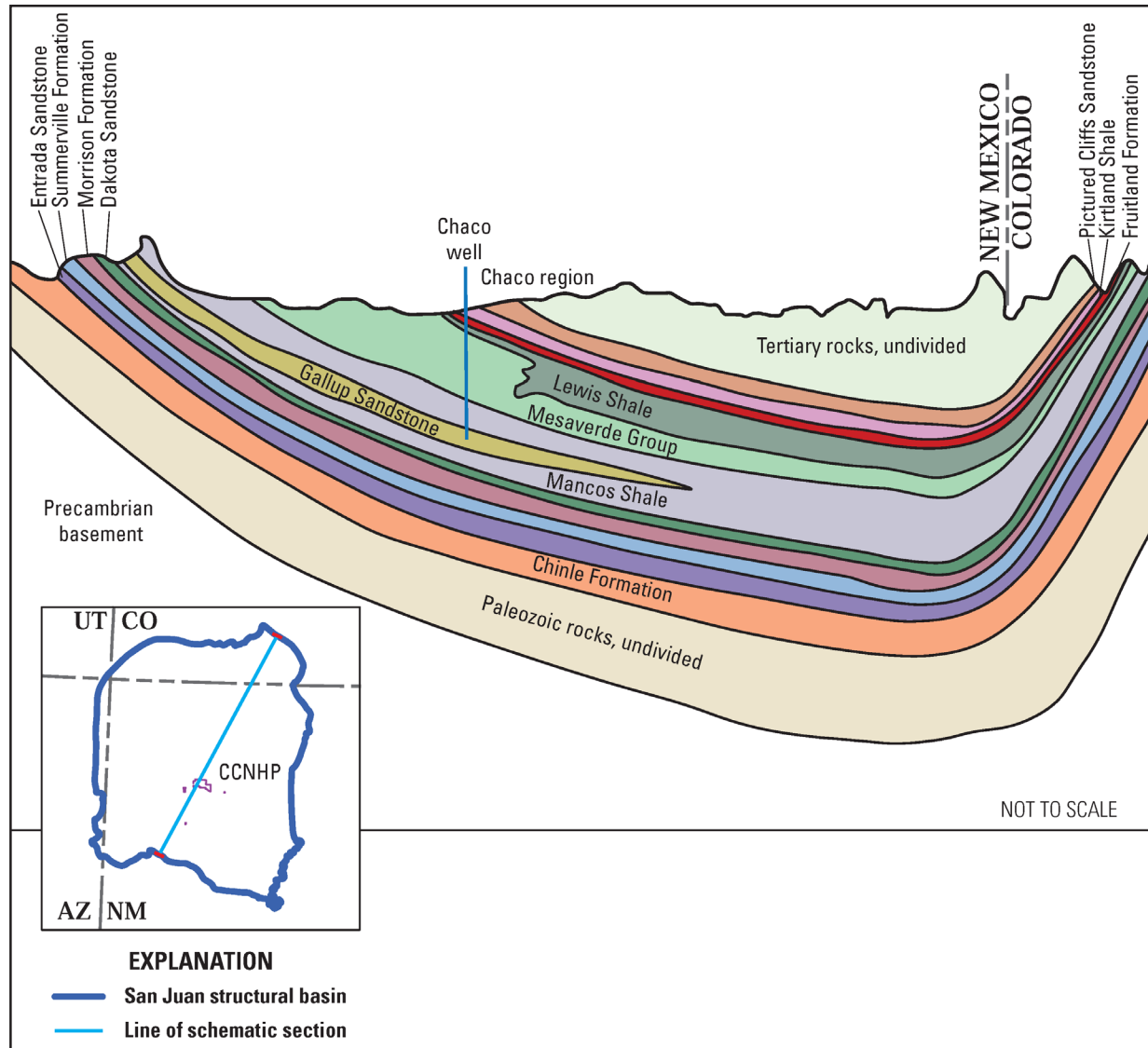


Figure 2. Schematic geologic cross section of the San Juan structural basin (modified from Stone and others, 1983). CCNHP, Chaco Culture National Historical Park.

HYDROGEOLOGIC FRAMEWORK

The San Juan structural basin has been studied for over a century, and major hydrogeologic framework summaries of the San Juan structural basin include Stone and others (1983), Kernodle (1996), and Craig (2001). The San Juan structural basin is an asymmetric, structural depression located primarily in the east-central portion of the Colorado Plateaus Province (Figure 1), and the regional aquifer is the part of the structural basin that contains rocks of Triassic through Paleogene age (Craig, 2001). The Chaco well is screened within the Cretaceous Gallup Sandstone, which is stratigraphically located between two tongues of lower-permeability Mancos Shale, both Cretaceous in age (Figure 2). San Juan structural basin Cretaceous stratigraphy is complex, consisting of sedimentary deposits from the Western Interior Seaway that formed between about 100 and 65 million years ago (Stone and Others, 1983). Other Cretaceous units overlying the Mancos Shale include parts of the Mesaverde Group, including the Cliff House Sandstone of Mesaverde Group (hereafter “Cliff House Sandstone”), the Menefee Formation of Mesaverde Group (hereafter “Menefee Formation”), and the Point Lookout Sandstone of Mesaverde Group (hereafter “Point Lookout Sandstone”) (Figure 2). The Mancos Shale is underlain by Jurassic sedimentary deposits, and it intertongues with the Dakota Sandstone.

The Gallup Sandstone is generally a fine- to medium-grained lithic arkose that ranges in thickness from 93 to 700 ft, pinching out to the northeast (Figure 1). The northeastern extent of the Gallup Sandstone coincides with the northeastern groundwater-model boundary. The Mancos Shale consists of gray to black shale and claystone, with discontinuous calcareous siltstone and sandstone. The main body of the Mancos Shale in the northern part of the basin reaches a maximum thickness of about 2,300 ft (Stone and others, 1983). In the vicinity of CCNHP, the Gallup Sandstone and Mancos Shale both generally dip to the northeast and range in thickness from 100 to 200 ft and from 600 to 1,300 ft, respectively. Recharge to the Gallup Sandstone generally occurs where the unit crops out to the south of CCNHP, although it has been noted that leakage may occur locally between adjacent Cretaceous units (Stone and others, 1983). Mixing between the Gallup Sandstone aquifer and surrounding units was confirmed by Linhoff and others (2023). Wells in the region are commonly under pressure, meaning there are artesian and free flowing wells. At least three artesian wells screened in the Gallup Sandstone south of CCNHP within the modeled domain are currently free flowing at the surface (Linhoff and others, 2023).

OIL AND GAS DEVELOPMENT IN THE SAN JUAN STRUCTURAL BASIN

Oil and gas were originally discovered in the San Juan structural basin around 1910 (Parker and Others, 1977). By the early 2000s, most existing Mancos Shale and Gallup Sandstone oil and gas development was approaching depletion, producing marginally economic amounts of oil through conventional drilling (Engler and others, 2015). However, recent technological advances, including HF, and the success of other shale plays in the United States brought about renewed interest in the Mancos/Gallup play in the San Juan structural basin. Horizontal well development in the Mancos Shale started in 2010 and quickly gained traction (Engler and others, 2015; U.S. Energy Information Administration, 2015). This increase in HF has targeted both the Gallup Sandstone, which provides the park's only water supply, and the Mancos Shale that confines the Gallup Sandstone. Horizontal drilling may extend at depth for more than a mile (Kelley and others, 2014), and although drilling has primarily occurred outside of CCNHP boundaries, the distance between the park's water supply and HF activity is unknown.

During the HF process, water mixed with sand and chemical additives is injected into low-permeability petroleum reservoirs under high pressure to fracture the rock. These fractures increase permeability by orders of magnitude and mobilize fluid such as natural gas, allowing for easier extraction. The sand contained in the fluid aids in holding the fractures open. The fracturing fluid generally flows back to the surface, where it is either reinjected into the subsurface or is stored in ponds on the surface and is later treated, although some of the fracturing fluid is unrecoverable and remains in the formation (Clark, and others, 2013; Gallegos and Varela, 2015). Self-reported chemical disclosures of fracturing fluid can be found within the FracFocus database (<https://fracfocus.org/>). Water used in hydraulic fracturing for vertical wells drilled in the San Juan structural basin averages between 105,000 and 207,000 gallons per well, and horizontal wells average approximately 1 million gallons per well (Kelley and others, 2014).

Potential water quality impairment from HF operations can stem from stray gas migration in aquifers of gas phase hydrocarbon via leaking well casings and surface spills of extracted fluids that can contaminate shallow aquifers (Vengosh and others, 2014). Additionally, overextraction of water resources used for HF can lead to groundwater depletion, water shortages, and changes in the direction of groundwater flow (Gregory and others, 2011; Clark and others, 2013). Although surface spills and leaking well casings are typically cited as the most likely contamination source, subsurface flow of HF fluids from reinjection or nonrecoverable HF fluids have the potential to negatively affect groundwater quality. Previous modeling efforts to assess the risks of HF fluid migration in other study areas have ranged in complexity and have indicated several key processes relating to driving forces and pathways of flow (Birdsell and others, 2015). Realistic and comprehensive assessment of HF fluid migration could include processes such as topographically driven flow, overpressure in shale reservoirs, buoyancy of HF fluids, and increased pressure in shale from HF fluid injection (Myers, 2012; Gassiat and others, 2013; Kissinger and others, 2013). Permeable pathways, such as faults, fractures, or abandoned wells, can act as conduits for HF fluid to cross geologic formations, even when the separation between shale gas reservoirs and groundwater aquifers is large (U.S. Department of Energy, 2009; Birdsell and others, 2015). Additionally, HF fluid migration is a multiphase flow problem, so multiphase

flow effects may also need to be accounted for, such as capillary imbibition and reduced relative permeability, which can inhibit upward migration of fluid and reduce the ability of one fluid to migrate in the presence of another fluid phase (Byrnes, 2011; Engelder, 2012).

Given the 3,100-ft depth of the screened interval of the Chaco well at CCNHP and the large thickness of the overlying confining stratigraphic units, contamination of the CCNHP water source is more likely to be caused by HF fluid migration than through surface spills. Groundwater flow directions in the Gallup Sandstone have not been assessed recently (Frenzel and Lyford, 1982; Kernodle, 1996), meaning that current (2023) advective groundwater flow pathways and groundwater travel times to the CCNHP well are uncertain. Thus, little is known about the proximity of source water in the Chaco well to HF operations. Additionally, with limited recharge to the Gallup Sandstone aquifer, the Chaco well may be at risk of groundwater shortages in the aquifer from extraction of water resources from oil and gas development and general water use in the region (Vengosh and others, 2014).

CLIMATE AND WATER USE IN THE REGION

The climate near CCNHP is semiarid, with a total precipitation normal of approximately 11 inches per year between 1991 and 2020. Precipitation is typically greatest during the late summer and early fall between July and September, when average monthly totals are greater than 1.25 inches. Mean maximum temperatures range from approximately 40 degrees Fahrenheit (°F) in the winter months to 88 °F in midsummer months. Mean minimum temperatures range from approximately 19 °F in the winter to 58 °F in the midsummer (NOAA, 2023).

The San Juan structural basin lies partly within several New Mexico counties, including Rio Arriba, Sandoval, Cibola, McKinley, and San Juan Counties (Figure 1). The population of these counties combined is approximately 411,000 people as of the year 2020 (U.S. Census Bureau, 2020). The population density is quite low, ranging from approximately 6 to 40 people per square mile. The closest population centers include the Farmington, N. Mex., area, and the Gallup, N. Mex., area, which include over 60,000 and 20,000 people, respectively, as of the year 2020.

Water used for mining in all five counties of the San Juan structural basin totaled approximately 1,200 acre-feet (acre-ft) (3.91×10^8 gallons) in 2015, and approximately 10 percent of that usage was reported as oil and gas related, with a vast majority coming from groundwater. Total water use of Cibola, Rio Arriba, and Sandoval Counties was 7,872, 132,493, and 62,836 acre-ft, respectively. CCNHP lies near the boundary of San Juan and McKinley Counties. San Juan County relies almost primarily on surface water from the Lower Colorado River Basin for general water use. Groundwater use for domestic, livestock, mining (including water used in oil and gas production) and public water supply use totaled approximately 1,800 acre-ft in 2015 (Magnuson and others, 2019). Groundwater use makes up less than 1 percent of the total water use (374,567 acre-ft) in the county, the remainder coming from surface-water sources. Water use in McKinley County totaled 10,243 acre-ft in 2015, and more than 98 percent of the water used was groundwater. Irrigated agriculture in the county was sourced from surface water. Public water supply use totaled approximately 3,600 acre-ft, all from groundwater. Domestic self-supplied water use totaled approximately 3,200 acre-ft, and livestock use totaled approximately 100 acre-ft. Power generation water use totaled 2,834 acre-ft, all from groundwater.

PREVIOUS MODELING EFFORTS

Several modeling efforts in the San Juan structural basin have been conducted with various focuses and scale, many of which are summarized in Stewart (2018). That report also documents a numerical modeling study that used particle tracking to identify the timing of groundwater recovery and potential pathways for groundwater transport of metals that may be leached from stored coal combustion byproducts.

Efforts that included numerical modeling of the Gallup Sandstone aquifer are summarized here. Frenzel and Lyford (1982) created a finite-difference steady-state model of the San Juan structural basin and modeled several major aquifers, including the Gallup Sandstone aquifer. Model-derived steady-state potentiometric heads for the Gallup Sandstone aquifer indicated groundwater flows south-southeast to northwest below the CCNHP, with a general upward vertical flow gradient throughout the modeled area. However, specifically below the CCNHP, the model predicted a downward hydraulic gradient between the Gallup Sandstone aquifer and underlying Jurassic Entrada Sandstone of the San Rafael Group, implying a downward gradient through intervening Cretaceous and Jurassic layers, and an upward gradient between the Gallup Sandstone aquifer and overlying Cretaceous layers, including the Cliff House Sandstone, Menefee Formation, and Point Lookout Sandstone. Kernodle (1996) computed steady-state heads for the Gallup Sandstone aquifer that indicate a general groundwater flow direction from the southeast to the northwest. Kernodle (1996) also indicated that there are distinct head differences between the Gallup Sandstone aquifer and Dakota Sandstone aquifer and between the Gallup Sandstone aquifer and Point Lookout Sandstone aquifer in the San Juan structural basin that suggest a very large isolating thickness of the upper and lower Mancos Shale. These studies did not, however, explicitly assess groundwater flow paths to the Chaco well or investigate specific HF scenarios and their potential influence on the Chaco well.

METHODS

Water-Level Measurements

Water-level measurements for the construction of the updated potentiometric surface were collected following standard USGS field procedures (Tables 1 and 2; Cunningham and Schalk, 2011). Measurements were made by various means, including steel tape, electronic tape, and pressure transducers when wells were under enough hydrostatic pressure for their potentiometric surfaces to be above the land surface. Data used to create the new potentiometric surface are stored in the USGS National Water Information System (U.S. Geological Survey, 2022) and include geographic coordinates (longitude, latitude, and land surface elevation) and depth-to-groundwater measurements relative to land surface for each of the monitoring sites. Depth-to-groundwater measurements were converted to groundwater elevation by subtracting depth-to-groundwater measurements from land surface elevation. Adjusted and reported elevations in Tables 1 and 2 are given relative to the North American Vertical Datum of 1988 (NAVD 88). The accuracy of groundwater levels used in this report is related to the methods used to measure land surface elevation and depth to groundwater at each monitoring site. Groundwater levels typically have an accuracy ranging from plus or minus (\pm) 0.01 to ± 1 ft (U.S. Geological Survey, 2022). Some datum discrepancies (for example, usage of the National Geodetic Vertical Datum of 1929 instead of NAVD 88) during analysis of data have led to errors in water level data as great as -3.7 ft in 65 percent of the historical groundwater level measurements and 69 percent of the modern groundwater level measurements. However, these errors are small relative to other sources of error.

Potentiometric-Surface Construction (Kriging)

The potentiometric surfaces of the Gallup Sandstone were developed using a kriging spatial interpolation algorithm (Ritchie and Pepin, 2020). This methodology uses a dataset that includes geographic coordinates and groundwater elevations from wells located within the study area, identified as the surface and subsurface extent of the Gallup Sandstone (Figure 1; Kernodle, 1996). These data are used to develop a semivariogram model of the correlation versus distance relation, which in turn is used by the kriging algorithm to estimate groundwater elevations throughout the study area. The kriging workflow was developed in the R programming language (R Core Team, 2019). This workflow used the “ObsNetwork” package, a spatial optimization algorithm (Fisher, 2013). ObsNetwork uses a geostatistical technique known as universal kriging to interpolate the groundwater elevation at unmeasured sites within the study area. The general implementation of this workflow involves (1) spatial trend modeling, (2) semivariogram development, and (3) kriged surface development and assessment.

Table 1. Observation sites and groundwater elevation for the modern potentiometric surface. IDates shown as month/day/year. Latitude and longitude shown in decimal degrees, referenced to the North American Datum of 1983. ID, identification; ft, foot; NAVD 88, North American Vertical Datum of 1988; NGVD 29, National Geodetic Vertical Datum of 1929; NA, data not applicable]

Site ID	Latitude	Longitude	Groundwater elevation (ft)	Date of measurement	Datum	Datum error (ft)	Adjusted/reported NAVD 88 groundwater elevation
362005108483101	36.33467	-108.80863	5,818.87	12/13/2019	NGVD 29	-3.2	5,822.05
360152107541401	36.03111	-107.90383	6,399.00	8/3/2017	NAVD 88	NA	NA
355547107584001	35.92974	-107.97840	6,460.85	5/15/2019	NGVD 29	-3.4	6,464.26
354951108034501	35.83085	-108.06312	6,417.15	5/15/2019	NGVD 29	-3.4	6,420.52
354753108034901	35.79807	-108.06423	6,492.60	5/15/2019	NGVD 29	-3.4	6,496.02
354738108030401	35.79391	-108.05173	6,437.06	5/15/2019	NGVD 29	-3.4	6,440.49
354653107554401	35.78141	-107.92951	6,576.64	5/15/2019	NGVD 29	-3.5	6,580.19
354630107334401	35.77489	-107.56322	6,540.48	5/28/2019	NAVD 88	NA	NA
354514108190601	35.75391	-108.31896	6,582.94	2/24/2016	NGVD 29	-3.4	6,586.36
354511108145201	35.75318	-108.24775	6,396.31	3/28/2019	NAVD 88	NA	NA
354347108175001	35.72933	-108.29818	6,624.29	3/28/2019	NAVD 88	NA	NA
354342108184001	35.72833	-108.31111	6,630.54	1/9/2020	NGVD 29	-3.5	6,634.04
354332108165501	35.72557	-108.28264	6,645.14	3/28/2019	NAVD 88	NA	NA
354243108104701	35.71194	-108.18028	6,658.42	1/8/2020	NGVD 29	-3.5	6,661.93
354211108172201	35.70264	-108.29119	6,662.59	3/28/2019	NAVD 88	NA	NA
353939108063501	35.66086	-108.11034	6,707.59	5/30/2019	NAVD 88	NA	NA
353816108170101	35.63778	-108.28417	6,941.84	3/7/2019	NGVD 29	-3.7	6,945.55
353814108473001	35.63722	-108.79222	6,091.00	2/21/2019	NGVD 29	-3.1	6,094.07
353800108494501	35.63342	-108.82978	6,145.62	2/24/2016	NGVD 29	-3.1	6,148.76
353742108572901	35.62869	-108.95650	6,622.19	3/22/2019	NGVD 29	-3.3	6,625.51
353722108460601	35.62278	-108.76889	5,943.00	2/1/2019	NGVD 29	-3.1	5,946.12
353645108011501	35.61228	-108.02172	6,791.70	3/27/2019	NAVD 88	NA	NA
353106108463501	35.51833	-108.77694	6,189.30	5/15/2016	NGVD 29	-3.1	6,192.43
353032108541901	35.50922	-108.90600	6,314.22	3/22/2019	NGVD 29	-3.2	6,317.46
352955108471801	35.49850	-108.78881	6,297.09	3/22/2019	NGVD 29	-3.1	6,300.24
351853108482701	35.30728	-108.80797	7,017.07	2/24/2016	NGVD 29	-3.4	7,020.45

Table 2. Observation sites and groundwater elevation for the historical potentiometric surface. [Dates shown as month/day/year. Latitude and longitude shown in decimal degrees, referenced to the North American Datum of 1983. ID, identification; ft, foot; NAVD 88, North American Vertical Datum of 1988; NGVD 29, National Geodetic Vertical Datum of 1929; NA, data not applicable]

Site ID	Latitude	Longitude	Groundwater elevation (ft)	Date of measurement	Datum	Datum error (ft)	Adjusted/reported NAVD 88 groundwater elevation
364117108440501	36.68806	-108.73537	5,289.40	2/25/1955	NGVD 29	-3.1	5,292.48
363907108534301	36.65195	-108.89593	5,436.50	9/23/1954	NGVD 29	-3.2	5,439.73
363436108510501	36.57667	-108.85204	5,538.78	6/13/1985	NGVD 29	-3.2	5,542.00
362005108483101	36.33467	-108.80863	5,818.48	11/10/1983	NGVD 29	-3.2	5,821.66
360152107541401	36.03111	-107.90383	6,469.54	3/8/1989	NAVD 88	NA	NA
355558108394301	35.93279	-108.66258	6,100.00	2/11/1974	NGVD 29	-3.2	6,103.21
355140108453901	35.86113	-108.76148	6,118.00	11/6/1963	NGVD 29	-3.3	6,121.29
355133108454701	35.85918	-108.76370	6,120.00	10/14/1964	NAVD 88	NA	NA
355113108030501	35.85363	-108.05201	6,485.50	1/20/1977	NGVD 29	-3.4	6,488.87
355014108030905	35.83724	-108.05312	6,460.00	1/16/1977	NGVD 29	-3.4	6,463.37
355014108005001	35.83724	-108.01451	6,531.10	1/26/1977	NGVD 29	-3.4	6,534.54
355012108080101	35.83669	-108.13423	6,441.30	9/22/1977	NGVD 29	-3.4	6,444.71
355000108033201	35.83335	-108.05951	6,462.90	2/9/1977	NGVD 29	-3.4	6,466.27
354958108035901	35.83280	-108.06701	6,389.90	3/31/1988	NGVD 29	-3.4	6,393.27
354927108041001	35.82419	-108.07007	6,369.27	4/28/1986	NGVD 29	-3.4	6,372.65
354924108035401	35.82335	-108.06562	6,411.07	11/8/1989	NGVD 29	-3.4	6,414.45
354921108040001	35.82252	-108.06729	6,398.49	10/15/1985	NGVD 29	-3.4	6,401.87
354803108043901	35.80085	-108.07812	6,686.10	2/1/1977	NGVD 29	-3.4	6,689.49
354753108034901	35.79808	-108.06423	6,484.20	3/30/1988	NGVD 29	-3.4	6,487.62
354738108030401	35.79391	-108.05173	6,533.00	10/7/1977	NGVD 29	-3.4	6,536.43
354647108083601	35.77974	-108.14396	6,577.50	1/20/1977	NGVD 29	-3.5	6,581.00
354600108354001	35.76669	-108.59508	6,407.00	8/1/1973	NGVD 29	-3.0	6,410.05
354514108190601	35.75391	-108.31896	6,593.81	10/31/1989	NGVD 29	-3.4	6,597.23
354500108525601	35.75057	-108.88065	6,338.20	1/28/1960	NGVD 29	-3.3	6,341.53
354347108175001	35.72933	-108.29818	6,643.10	6/12/1979	NAVD 88	NA	NA
354346108374401	35.72946	-108.62953	5,945.00	10/15/1958	NGVD 29	-3.1	5,948.07
354342108184001	35.72833	-108.31111	6,629.00	1/8/1977	NGVD 29	-3.5	6,632.50
354332108165501	35.72557	-108.28264	6,654.05	6/28/1985	NAVD 88	NA	NA
354243108104701	35.71194	-108.18028	6,634.34	6/26/1985	NGVD 29	-3.5	6,637.85
354211108172201	35.70264	-108.29119	6,670.08	6/28/1985	NAVD 88	NA	NA

Table 2. Observation sites and groundwater elevation for the historical potentiometric surface. — Continued
 [Dates shown as month/day/year. Latitude and longitude shown in decimal degrees, referenced to the North American Datum of 1983. ID, identification; ft, foot; NAVD 88, North American Vertical Datum of 1988; NGVD 29, National Geodetic Vertical Datum of 1929; NA, data not applicable]

Site ID	Latitude	Longitude	Groundwater elevation (ft)	Date of measurement	Datum	Datum error (ft)	Adjusted/reported NAVD 88 groundwater elevation
354039108313203	35.67752	-108.52619	6,680.82	11/2/1989	NGVD 29	-3.4	6,684.18
354038108592601	35.67724	-108.99120	6,651.00	6/7/1962	NAVD 88	NA	NA
354015108284001	35.67085	-108.47841	6,708.05	10/31/1989	NGVD 29	-3.3	6,711.40
354004108500801	35.66780	-108.83620	6,405.72	5/8/1985	NGVD 29	-3.2	6,408.89
353816108170101	35.63778	-108.28417	6,953.10	10/31/1989	NGVD 29	-3.7	6,956.81
353800108494501	35.63342	-108.82978	6,342.00	5/11/1981	NGVD 29	-3.1	6,345.14
353730108455602	35.62502	-108.76620	6,183.18	1/19/1979	NAVD 88	NA	NA
353722108460601	35.62278	-108.76889	5,961.30	11/1/1989	NGVD 29	-3.1	5,964.42
353645108011501	35.61228	-108.02172	6,803.65	10/31/1989	NAVD 88	NA	NA
353608107583501	35.60225	-107.97701	6,920.11	7/17/1986	NAVD 88	NA	NA
353440108430401	35.57780	-108.71842	6,588.00	5/25/1956	NAVD 88	NA	NA
353429107121301	35.57475	-107.20421	6,307.22	11/13/1989	NAVD 88	NA	NA
353342107543201	35.56169	-107.90951	7,039.00	10/22/1964	NAVD 88	NA	NA
353312109003701	35.55335	-109.01092	6,496.00	10/27/1967	NAVD 88	NA	NA
352657108444001	35.44919	-108.74508	6,536.00	8/30/1957	NAVD 88	NA	NA
352632107394801	35.44225	-107.66395	6,498.10	7/23/1986	NAVD 88	NA	NA
351830108492301	35.30836	-108.82370	6,932.40	10/19/1960	NAVD 88	NA	NA
350823107322801	35.13976	-107.54172	6,682.95	5/6/1987	NAVD 88	NA	NA

Spatial trend modeling addresses the kriging assumption that the mean value of the data being estimated does not change when shifted in space. Groundwater elevations typically have spatial trends that violate this assumption. To correct for this, a trend model is subtracted from the groundwater elevations, and the semivariogram and kriged surface are developed for the residuals. The trend is added back to the kriged surface to acquire the final kriged groundwater-elevation estimates.

For the semivariogram development, empirical and theoretical semivariograms were developed for the new surface. Semivariance for all pairs of monitoring sites are calculated as one-half the variance of the difference between the residual groundwater elevations at the sites. The empirical variogram is computed by grouping the semivariance values into bins based on the distance (lag) between monitoring site pairs and averaging the semivariance values within each bin. Kriging relies on a continuous theoretical semivariogram that is fit to the empirical variogram. This fitting process requires the consideration of semivariogram shape, which is strongly influenced by three components called the nugget, sill, and range. The nugget is the semivariance value at a lag of zero, which typically is related to noise in the data and is user specified by visual inspection. The sill is the semivariance value at which the mean semivariance stops changing with increasing distance. The range is the distance at which the sill is reached and indicates the distance over which data are correlated. Circular, exponential, gaussian, linear, and spherical models were all considered in fitting the theoretical semivariogram.

For the kriged surface development and assessment, universal kriging was used to interpolate groundwater elevation and quantify uncertainty associated with the interpolated values. Interpolation was performed at a uniform grid size measuring 500 by 500 ft. The grid resolution was chosen to be smaller than the minimum distance between sites and the groundwater model grid size.

Leave-one-out cross validation was used to test the performance of the theoretical semivariogram model (Fisher, 2013). This method removes each measurement point from the dataset one by one and estimates the groundwater elevation at the removed site by using the theoretical semivariogram model developed for the entire dataset to kriging with the remaining data. The estimation error from this method is calculated as the difference between the observed and estimated groundwater elevation at the omitted site.

Kriging is advantageous because it produces measurements of uncertainty associated with the estimates of water-level elevation. Uncertainty is presented as standard error, or the square root of the estimated variance (Fisher, 2013). Standard error is essentially a scaled version of the distance to the nearest measurement point, meaning standard error is zero at the water level observation points, given a nugget of zero, and increases with distance.

Potentiometric surfaces were kriged for both modern data (data range between 2016 and 2020, Table 1) and for historical data (data range between 1954 and 1989, Table 2). These new potentiometric surfaces were used to derive drawdown maps and calibrate the groundwater model. Drawdown was calculated as the difference between the two kriged potentiometric surfaces.

GROUNDWATER NUMERICAL MODEL

The following sections describe the model and its capabilities in detail. However, many of the complex fluid flow processes described in the “Introduction” section, as well as a detailed accounting of both natural and human-made permeable pathways and potential for stray gas migration along leaking well casings, are outside of the scope and intended complexity of this project.

Description of Numerical Groundwater Flow Model

The numerical groundwater flow model (“model”) (Shephard and others, 2023) was constructed using MODFLOW-2005 version 1.12.0 (Harbaugh, 2005), a well-documented and commonly used three-dimensional finite-difference groundwater flow model developed by the USGS that simulates steady and nonsteady flow in irregularly shaped flow systems. The MODFLOW code was executed in part in Groundwater Vistas (GWV) version 6 (Rumbaugh and Rumbaugh, 2011), a graphical user interface that can run source code for several different groundwater models and particle tracking simulators. GWV also has

built-in visualization functions as well as calibration and sensitivity analysis functions. The model was also run directly from the MODFLOW-2005 program executable for various runs and simulations. MODPATH version 7.2.001 (Pollock, 2016), a USGS particle tracking model for MODFLOW also executed in GWV and directly from the program executable, was used to assess relative groundwater flow paths and traveltimes within the constructed MODFLOW model.

Spatial and Temporal Discretization

The active model area is a rectangle measuring approximately 25 x 31 miles (mi), approximately centered around CCNHP (Figure 1). These model dimensions were chosen to ensure that pumping operations inside or outside of the proposed model domain produce minimal changes in the potentiometric surface at the model boundaries. The grid cells are 1,500 by 1,500 ft, and the model grid consists of 119 rows and 104 columns. Cell size was determined on the basis of layer thicknesses (described in the “Model Layer Description” methods section). Given the relatively small thicknesses of the Gallup Sandstone in the model domain, the Mancos Shale model layers were split into multiple layers of smaller cells to avoid the creation of relatively thin cells in the Gallup Sandstone in MODFLOW. The grid is rotated approximately 50.3 degrees counterclockwise from grid north to align with the general direction of groundwater flow and the geographic extent of the Gallup Sandstone (Kernodle, 1996).

The model simulates steady-state conditions relative to the modern potentiometric surface in the Gallup Sandstone (see the “Water-Level Measurements” methods section). Under steady-state conditions, the potentiometric surface does not change with time. The results presented in this study comparing the historical and modern potentiometric surfaces in the Gallup Sandstone indicate that the hydrologic system is not in steady state. However, construction of a model with time-varying inflows and outflows was beyond the scope of this study. A model of this type could change in response to well injection and extraction of water resources over time. Incorporation of time-varying flows into further versions of the model may be useful to understand the temporal dynamics of influences on the Chaco well.

Model Layer Descriptions

The model domain features one Gallup Sandstone layer and two main Mancos Shale units. The model specifically only simulates the deep groundwater system of these units below CCNHP and does not simulate flow in shallower aquifers or groundwater flow of the entire San Juan structural basin or greater region. The upper and lower Mancos Shale units within the model domain each range from 600 to 1,300 ft in thickness, whereas the Gallup Sandstone ranges from 100 to 200 ft in thickness. Large differences in thickness between adjacent layers could cause potential issues when running MODFLOW. To account for this, the Mancos Shale units are split into multiple layers so that no layer is drastically thicker than the Gallup Sandstone layer. The upper and lower Mancos Shale model units consist of 5 layers each, which together with the Gallup Sandstone layer, compose a total of 11 model layers. The upper Mancos Shale bottom geometry was assumed to be the same as the Gallup Sandstone top geometry. The top geometry for the upper Mancos Shale unit was derived from available structural data (Kernodle and others, 1989) on the top elevation of the Point Lookout Sandstone, the stratigraphic unit that overlies the upper Mancos Shale in the model domain. Using well log data, a relative thickness of the Point Lookout Sandstone in the model domain was estimated. This thickness was subtracted from structural top data of the Point Lookout Sandstone to construct the elevation and geometry of the top of the Upper Mancos Shale. The Gallup Sandstone layer was constructed using available data on the elevation of the structural top of the unit from Kernodle and others (1989). These data were digitized using a geographic information system (GIS) and then brought into the model to produce the top geometry.

The thickness of the Gallup Sandstone was based on available well log data. This thickness was subtracted from the structural top of the Gallup Sandstone to produce the bottom geometry for the layer. The lower Mancos Shale unit top geometry was assumed to be the same as the bottom of the Gallup Sandstone. The bottom geometry for the lower Mancos Shale unit was estimated from the available structural data from

Kernodle and others (1989) describing the top of the Dakota Sandstone, the stratigraphic unit located below the lower Mancos Shale.

Hydrologic Boundaries

The northeast boundary was simulated as a no-flow boundary because updated potentiometric surfaces of the Gallup Sandstone and additional references to previously published surfaces (Frenzel and Lyford, 1982; Kernodle, 1996) show that this boundary is roughly parallel to groundwater flow. Additionally, this boundary is the northeasternmost extent of the Gallup Sandstone where it pinches out, also justifying it as a no-flow boundary. The northwest boundary was simulated as a constant head boundary in the Gallup Sandstone layer, set to the head of the modern potentiometric surface. The southeast and southwest boundaries were simulated as flux-in boundaries in the Gallup Sandstone layer. Fluxes into the model were initially estimated from the hydraulic gradient, cell thickness, and initial hydraulic conductivity of the layer and were later calibrated (described in the “Calibration and Sensitivity Analysis” section). The model top and bottom were simulated as no flow boundaries because, as noted in previous work, flow into and out of the top and bottom of the Mancos Shale was assumed to be insignificant. There is generally no recharge to the Gallup Sandstone in this region from precipitation or surface water, indicated by the old age of the water (Linhoff and others, 2023) and the isolating thickness of the Mancos Shale (Stone and others, 1983).

Calibration and Sensitivity Analysis

Groundwater model calibration was conducted by matching simulated and observed heads. Calibration targets were created by extracting values from a GIS raster of the modern potentiometric surface derived from data collected for this study. These values were extracted at evenly spaced intervals throughout the model. A spacing of 20,000 ft was used for extraction points, which produced 69 evenly spaced points in the domain at a relatively high density for the size of the model area. For the calibration process, the hydraulic heads extracted at these points were used as the observed values, which were compared to the model simulated values at these points in the Gallup Sandstone (model layer 6).

Calibration and uncertainty analysis were carried out manually in GWV and automatically using the model-independent Parameter ESTimation (PEST) and uncertainty analysis program (Doherty, 2018a, b). PEST is a commonly used program for automatic environmental model calibration and uncertainty analysis. The program implements traditional parameter estimation approaches on the basis of a few parameters by running a model as many times as needed while adjusting parameters to reach a best fit between the simulated and observed data by minimizing weighted least squares errors. Parameter ranges for PEST input were set on the basis of the same literature values used in the manual calibration process (Table 3). Adjustments to parameter values during calibration were based on the ability of model simulated heads, which were extracted from the model using the Head-Observation package (Hill and others, 2000), to reproduce the heads extracted from the modern potentiometric surface. Head observation weights within PEST were applied to give equal importance to each head observation. Model files, including those used for PEST calibration, can be found in the model archive associated with this report (Shephard and others, 2023).

Parameter inputs for the model and parameter calibration ranges were determined through values reported in previous works. A summary of available data is provided in Tables 3 and 4. Primarily, the parameters altered during the calibration process were the vertical and horizontal hydraulic conductivity and the flux rates into the model, simulated as wells in MODFLOW. Specific yield and storativity were not calibrated because the model was run as steady state. Porosity was estimated from literature values for use in MODPATH, but it was not calibrated. However, this report does provide groundwater traveltime analysis for a range of porosity values. Parameters in the 10 Mancos Shale layers and single Gallup Sandstone layer were calibrated independently. The upper and lower Mancos Shale were treated as separate homogeneous and anisotropic zones, although they were calibrated at the same time with the same parameters. The flux-in boundary along the southwest and southeast parts of the model was divided evenly into three sections along the southwest and southeast boundaries, for a total of six reaches that simulated the boundary condition of groundwater flux into the model.

Table 3. Hydraulic properties of Mancos Shale and Gallup Sandstone from previous works.
 [Small hydraulic conductivity values are shown in E notation. ft/d, foot per day; %, percent; --, data not available]

Unit	Hydraulic conductivity (ft/d)		Porosity (%)	Source
	Horizontal	Vertical		
Mancos Shale	1.0 E-4	1.0 E-4	--	Kernodle, 1996
Mancos Shale	8.64 E-4–8.64 E-3	8.64 E-8	--	Frenzel and Lyford, 1982
Mancos Shale	--	--	3.5–4.25	U.S. Energy Information Administration, 2015
Gallup Sandstone	1	2.0 E-3	--	Kernodle, 1996
Gallup Sandstone	0.1–0.14	1.4 E-5	--	Frenzel and Lyford, 1982
Gallup Sandstone	--	--	3–8	Stone and others, 1983
Gallup Sandstone	--	--	3.9–27.2	Reneau and Harris, 1957

Sensitivity Analysis

A model sensitivity analysis of various model input parameters was conducted to identify the parameters that have the greatest influence on model performance. The sensitivity analysis presented in this report was conducted following model calibration; however, an initial sensitivity analysis was also conducted (not reported) to determine which model parameters should be calibrated. The sensitivity analysis was conducted using the auto-sensitivity function in GWV. Parameter values were varied by ± 50 percent of the calibrated model parameter in 10 increments, resulting in 11 model runs that vary a single parameter 10 percent between each run, including the initial calibrated parameters. This process is repeated for each parameter of interest. For each of these model runs, the absolute residual mean (RM) between the observed and simulated data is calculated and plotted against the incremental parameter values. These RM plots are used to assess the sensitivity of each model parameter from a magnitude and rate of change perspective. The model parameters used in the sensitivity analysis were the horizontal and vertical conductivities of the Mancos Shale and Gallup Sandstone layers, and the flux-in boundary for the Gallup Sandstone model layer. For vertical and horizontal hydraulic conductivities, the parameters for all 10 Mancos Shale model layers were changed at the same time to assess Mancos Shale parameter sensitivity, and the Gallup Sandstone hydraulic conductivity was changed independently of the Mancos Shale, during different sensitivity runs. The sensitivity of the flux-in boundaries of each reach of the Gallup Sandstone was tested separately, resulting in six separate sensitivity analyses for the flux-in boundary. Additionally, the constant head boundary sensitivity was tested.

Model Application and Simulations

The calibrated model was used to simulate the groundwater flow paths of water that reach the Chaco well, and how proximity of potential HF operations to the Chaco well capture zone may influence the Chaco well. Modeling simulations primarily made use of forward and reverse particle tracking using MODPATH. The model and the scenarios only consider advective groundwater transport effects of potential conductivity changes caused by HF. Four simulations carried out following model calibration are described here.

Simulation 1. Capture-Zone Assessment

Capture zones for the Chaco well were assessed for the calibrated model using forward particle tracking. Particles were released in each cell along the southwest and southeast boundary of the model in all 11 layers of the model, given that the groundwater flux into the model occurs along these boundaries in the Gallup

Sandstone layer. Particles were considered to be captured by the Chaco well if the end point of the particle shared the same cell as the Chaco well. The captured particle travel paths were then used to assess the extent of the capture zone. Two Chaco well pumping rates were tested: 1,200 cubic feet per day (ft³/d), the reported maximum pumping rate (Martin, 2005) and the rate used during model calibration, and 10,000 ft³/d to represent a hypothetical increase in future pumping rates that likely exceed the future increase in water usage. The capture zones for the two separate pumping rates became the basis for the remaining model scenario analysis.

Simulation 2. Travel-Time Analysis

Minimum and maximum particle traveltimes from the model boundary to the Chaco well were assessed by altering the porosity of the Gallup Sandstone and Mancos Shale layers to the maximum and minimum literature values (Table 3). Traveltimes were estimated through forward tracking of particles released along the flux-in boundary of the Gallup Sandstone layer and at the model domain boundary of the Mancos Shale layers of the model until their capture by the Chaco well at a pumping rate of 1,200 ft³/d. The model runs used the calibrated hydraulic conductivity and flux boundaries and only altered the porosity. The porosity values that were used for model scenario runs are described as the low and high porosity values in Table 4.

Table 4. Model hydrologic input range and initial value to be used in modeling.
[Small hydraulic conductivity values are shown in E notation. ft/d, foot per day; %, percent].

Unit	Value type	Hydraulic conductivity (ft/d)		Porosity (%)
		Horizontal	Vertical	
Mancos Shale	Low value	1.0 E-4	8.64 E-8	3.5
Mancos Shale	Initial value	8.64 E-4	1.0 E-4	4
Mancos Shale	High value	8.64 E-2	1.0 E-4	4.25
Gallup Sandstone	Low value	0.1	1.4 E-5	3
Gallup Sandstone	Initial value	1	2.0 E-3	15
Gallup Sandstone	High value	5	2.0 E-3	27.2

Simulation 3. Potential Influence of Hydrologic Fracturing-Maximum Depth and Hydraulic Conductivity

Limited literature exists on how to assess the direction, length, and cross-sectional area of HF fracture zones, and specific locations or zones for potential future HF operations are currently unknown. For this scenario, large changes to the Mancos Shale layers were made to simulate the maximum distance and depth that altering the hydraulic conductivity through HF could potentially influence the Chaco well. For model simulations to represent potential HF operations, the horizontal and vertical hydraulic conductivity of each Mancos Shale layer was systematically varied individually by several orders of magnitude. Specifically, for each scenario model run, horizontal and vertical conductivities for each Mancos Shale layer were altered individually, the model was executed, and then the particles were tracked in reverse to record groundwater flow paths from model cells in layer 6 (Gallup Sandstone) surrounding the Chaco well to the boundaries of the model. This was done by incrementally altering the horizontal and vertical conductivities in each layer separately by an order of magnitude from 10E-3 to 10E+3. The location of the particles through time and space were logged during the tracking simulation. If the particle passed through the altered Mancos Shale layer, this was seen as an indication that fracturing in that particular layer and location could lead to advective groundwater flow from that layer to the Chaco well. This analysis was repeated for the 1,200 and 10,000 ft³/d pumping rates, resulting in a total of 180 model runs. The placement of the particles for reverse tracking was based on the previously determined capture zones.

Simulation 4. Potential Influence of Hydrologic Fracturing-Zones Forward Tracking, Two Pumping Rates, Two Hydraulic Conductivities

In simulation 3, hydraulic conductivity values were changed for entire layers representing Mancos Shale. In simulation 4, more localized changes to the Mancos Shale hydraulic conductivity were simulated. Potential future placement of HF wells is unknown, but this scenario provides a representative hypothetical example. Hydraulic conductivities in parameter zones within and adjacent to the capture zones determined in simulation 1 were increased to simulate hypothetical HF wells. These circular hypothetical HF zones were assigned a 10,000-ft radius to represent possible horizontally drilled distances and the zone of influence of an individual fracturing well (Meng, 2015). The zones were chosen specifically to be either within the two previously defined capture zones (Chaco well pumping rates of 1,200 and 10,000 ft³/d) or outside of the two capture zones. The model was run with Chaco well pumping rates of 1,200 and 10,000 ft³/d. For either scenario, the horizontal and vertical hydraulic conductivities were altered in the zones in layer 4 to 1 foot per day (ft/d) and 100 ft/d, respectively, resulting in a total of four separate model runs. These two values were used, given the uncertainty of the magnitude of hydraulic conductivity change caused by HF. Forward tracking was implemented by releasing particles in each of the cells occupying the zones and tracking their flow paths. A representative schematic of the 11 model layers and altered hydraulic conductivity values is shown in Figure 3.



Figure 3. Conceptual depiction of hydraulic conductivity changes in hydraulic fracturing simulations within model layers.

RESULTS

In the following sections, results from the potentiometric surface kriging, model calibration, model sensitivity analysis, and simulation particle tracking are described. Also addressed are uncertainty and potential error in the results.

POTENTIOMETRIC-SURFACE RESULTS

After testing different linear and polynomial models of potentiometric-surface trend, a first-order linear trend model ($R^2 = 0.50$, median residual = 15.07) was removed from the modern potentiometric surface groundwater elevation data to allow for the kriging workflow to operate under the assumption of stationarity. The trend formula used is expressed below:

$$z(S) = \beta_0 + \beta_1 x(S) + \beta_2 y(S) \quad (1)$$

where

- $z(S)$ is median groundwater elevation at point S , in feet above NAVD 88;
- β_0 is deterministic unknown trend coefficient, in feet above NAVD 88;
- β_i are deterministic unknown trend coefficients, in dimensionless units ($i = 1$ through 2);
- $x(S)$ is easterly coordinate at point S , in feet; and $y(S)$ is northerly coordinate at point S , in feet.
- $y(S)$ is northerly coordinate at point S , in feet.

The theoretical semivariogram for the modern data was modeled as spherical, with no nugget, a sill of 53,009 ft, and a range of 43,566 ft. The bin width used to compute the empirical semivariogram was set to 5,000 ft because it yielded the most readily identifiable semivariogram curvature, and the spatial distance to which monitoring site pairs were included in the semivariance estimates was set at 38,500 ft, or approximately half the maximum distance between data locations. The R-squared fit between the theoretical and the empirical variogram was 0.4.

The modern (2016–20) interpolated potentiometric surface indicates that the groundwater elevation was highest in the southeast, sloping toward the San Juan River in the northwest (Figure 4). The surface shown in figure 4 was created with a grid cell size of 500 by 500 ft. For the entire interpolated surface, which is composed primarily of the area outside of the model domain, the mean estimation error for the leave-one-out cross validation was 28.8 ft, which is less than 10 percent of total head drop across the model domain. However, the minimum error was -203.1 ft and the maximum error was 383.9 ft, and ideally both would be close to zero. This range in error is comparably large relative to that within the model domain, with the minimum error being 56.6 ft and the maximum error being 68.9 ft, showing little spatial heterogeneity of error across the model domain. The correlation between observed and predicted groundwater elevations from leave-one-out cross validation was high ($R^2 = 0.85$), and the correlation between predicted and residual was low ($R^2 = -0.22$), indicating that the estimation error is independent of the magnitude of the estimated groundwater elevation from cross validation and that stationarity may be assumed for the residual groundwater elevations used for kriging (Fisher, 2013).

The same potentiometric surface interpolation was conducted for the historical surface (Figure 5), where the newest data from 1954 to 1989 for each site were used to assess the potentiometric surface before oil and gas development (U.S. Geological Survey, 2022). The two surfaces were differenced to assess the change in potentiometric surface after the onset, initiation, and (or) presence of oil and gas development. The linear trend model for the historical surface had an R^2 of 0.73 and a median residual of -8.1 ; the same first-order trend equation was applied to the historical surface (eq. 1).

The variogram for the historical kriged surface used an exponential model, a range of 17,315 ft, a sill of 49,449 ft, and no nugget. The spatial distance to which monitoring site pairs were included in the semivariance estimates was set at 51,933 ft, or approximately half the maximum distance between data locations. The R^2 fit between the theoretical and the empirical variogram was 0.29. A uniform grid cell size for the historical surface was also 500 by 500 ft. The leave-one-out cross validation mean error was 7.7 ft, and the correlation between observed and predicted values was 0.90, with a correlation of predicted and residual of -0.09 , which validates the underlying assumptions of the kriging model.

Standard error was highest near the outer areas of the Gallup Sandstone extent for both the modern and historical kriged surfaces where observed data were sparse (Figures 6 and 7). For the modern surface, standard error was particularly great in the northwestern (greater than $>$] 450 ft) and southeastern ($>$ 800 ft) corners where data points were scant (Figure 6). Observation data in the historical surface had better spatial distribution, although standard error reached $>$ 300 ft along the northeastern extent of the Gallup Sandstone (Figure 7). The kriged surfaces, as well as the drawdown maps, have great uncertainty in regions where data are sparse. The error leads to potential physical interpretation errors in areas where recharge occurs along the southern portion of the Gallup Sandstone where it crops out at the surface. Potentiometric surfaces need to be considered in context with the standard error data and maps. However, standard error was generally less within the model domain, ranging between 10 and 463.5 ft in the modern surface and 11.3 and 300.5 ft in the historical surface. Values are highest in the northeastern part of the active model area where there is increased

uncertainty because of sparse data. This area is generally downgradient from the Chaco well and near the edge of the Gallup Sandstone extent. Standard error was least near the southwestern part of the active model area where observation point density was greatest. Near the Chaco well itself, standard error approached zero. Additional error and variation in the kriged surfaces could be due to short term pumping effects and seasonal effects, as data were collected at various times of the year.

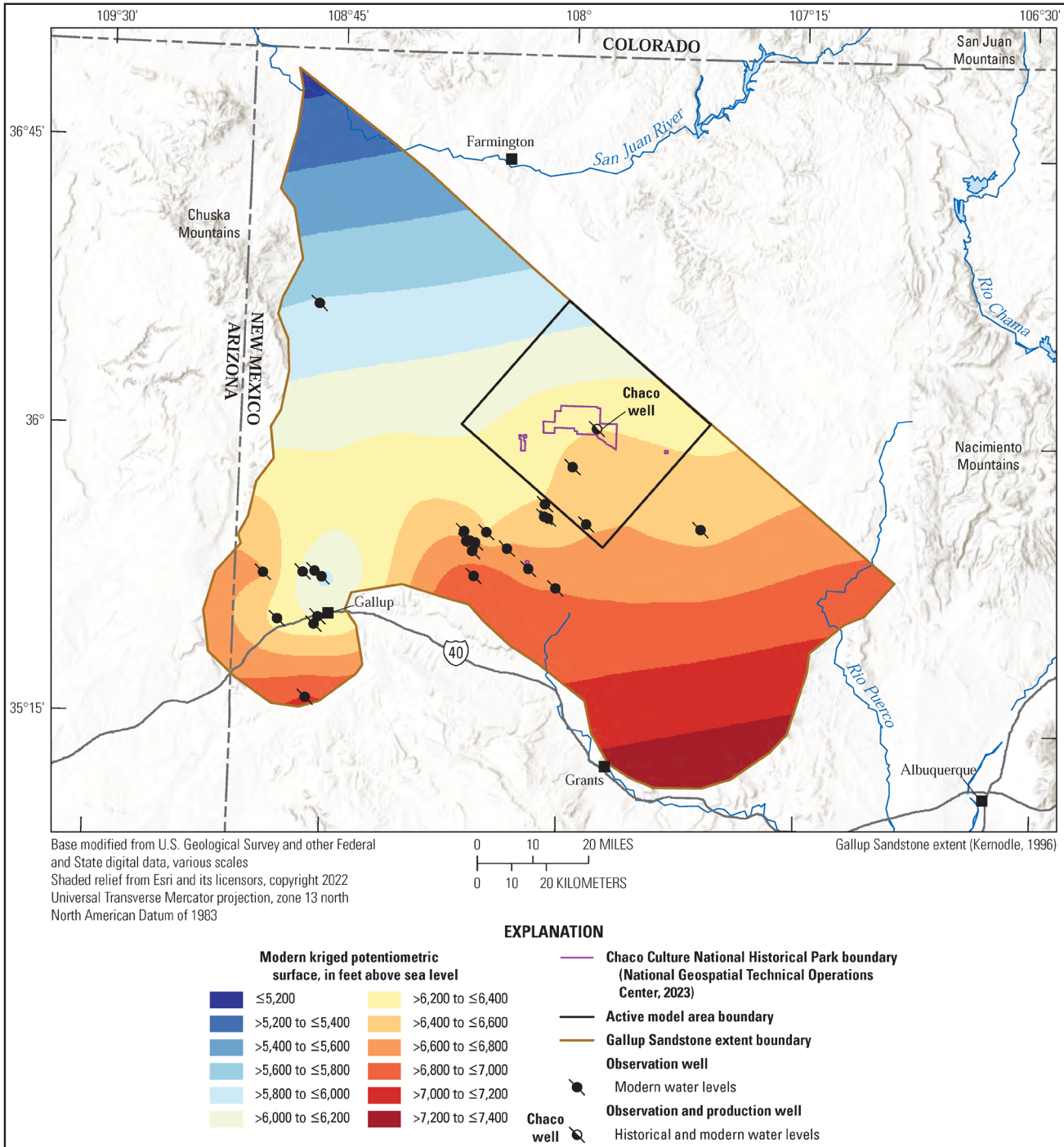


Figure 4. Modern (2016–20) kriged potentiometric surface and groundwater level observation points. Wells are screened in the Gallup Sandstone.

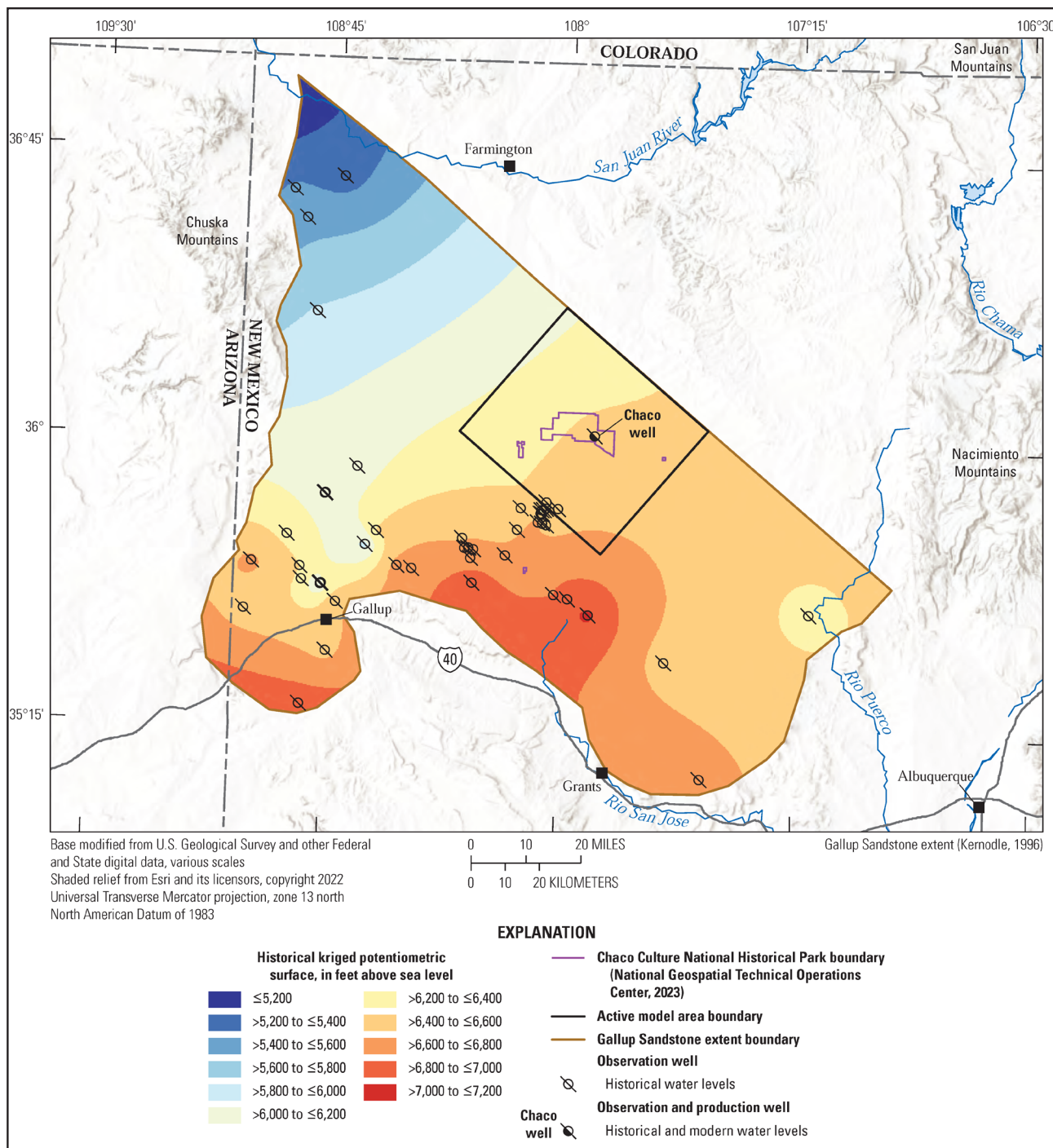


Figure 5. Historical (1954–89) kriged potentiometric surface and groundwater level observation points. Wells are screened in the Gallup Sandstone.

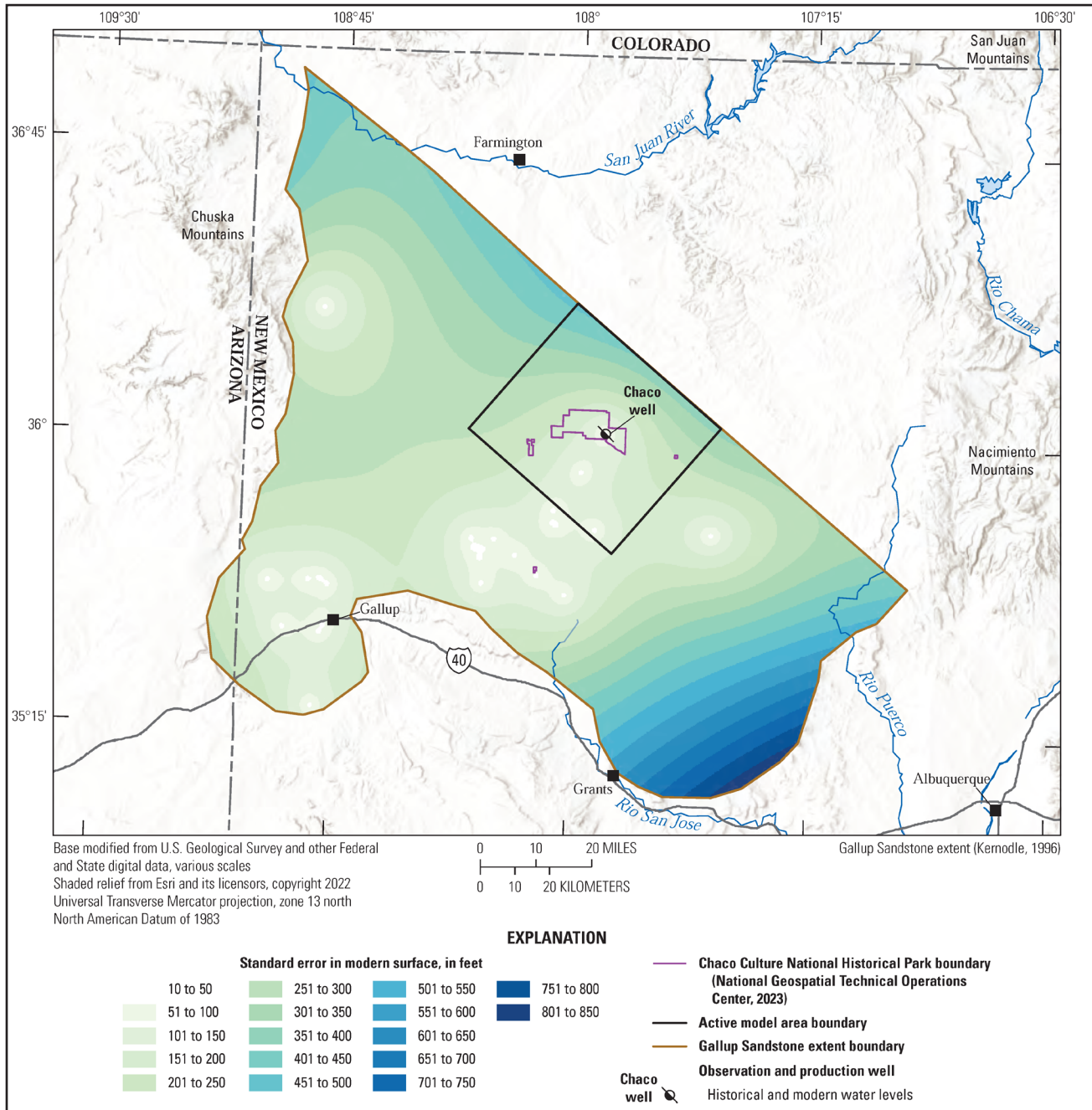


Figure 6. Modern kriged potentiometric surface standard error.

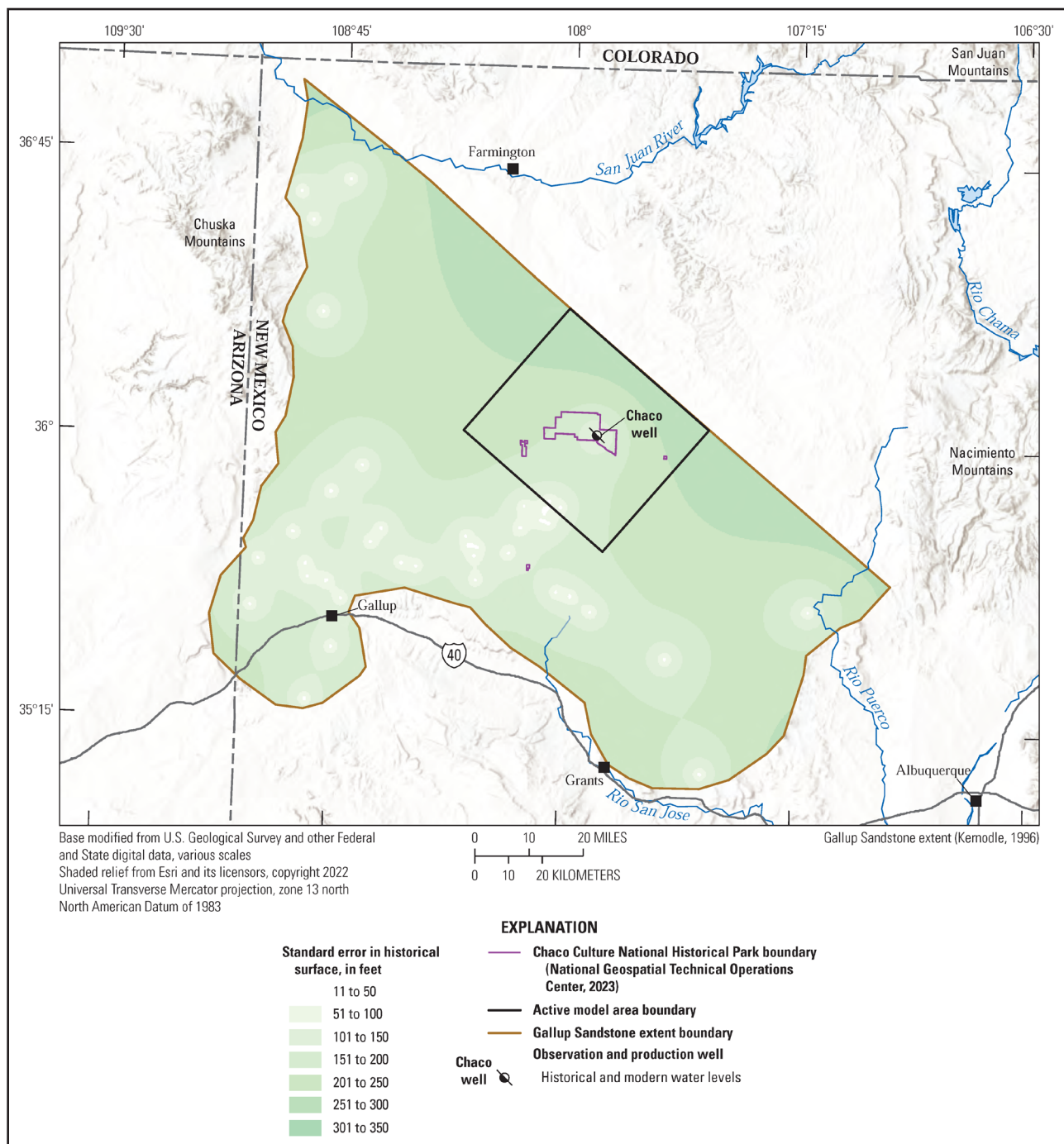


Figure 7. Historical kriged potentiometric surface standard error.

The drawdown surface is calculated as the modern surface minus the historical surface. Drawdown values ranged from -250 to 9 ft across the model domain, with a mean value of -90 ft (standard deviation 60 ft), indicating a general drop in the potentiometric surface elevation between the historical and modern potentiometric surfaces across the study area (Figure 8). Drawdown was not calculated for this report beyond the active model area because of large interpolation error, especially in the southeastern portion of the Gallup Sandstone in the modern potentiometric surface (Figure 6). Standard error of either surface should be taken into consideration when interpreting changes in the potentiometric surface. Direct water-level observations of the Chaco well indicate that head decreased by 70.5 ft between March 1989 and August 2017 (U.S. Geological Survey, 2022). The increase in potentiometric surface elevation in the southeastern portion of the active model area could be due to interpolation error.

The decreases in potentiometric surface elevation were generally greater in the northern and northeastern parts of the active model area, whereas the increases in elevation occurred near the southern and southeastern parts of the active model area. Head change values within the CCNHP boundaries ranged between -34 and -96 ft (mean -65 ft, standard deviation 12 ft). The greatest groundwater elevation decline values tended to be in the northeastern part of the primary CCNHP area and in the western detached part of the CCNHP. Groundwater elevation decline could be an artifact of interpolation error, although physical explanations could include reduction in recharge from areas outside of the active model area, water extraction for public and domestic water supply, or water used in power production, given that these are the most common uses of groundwater in the counties near CCNHP (Magnuson and others, 2019). Other causes could be related to nearby hydrocarbon extraction sites, mines, or pumping directly at CCNHP, although these activities are documented to draw relatively less water than those activities previously stated.

Carbon isotope and noble gas dating indicate groundwater in the Gallup Sandstone at CCNHP is exceptionally old, likely >52,000 years before present, which indicates limited recharge within the active model area (Linhoff and others, 2023). Although drawdown is likely due to multiple factors, the cause was not specifically investigated as part of this study.

MODEL CALIBRATION AND SENSITIVITY ANALYSIS RESULTS

The following sections describe the model calibration results, as well as a sensitivity analysis that followed model calibration. An initial sensitivity analysis (not reported) was conducted to inform which parameters should be calibrated.

Model Calibration

Horizontal and vertical hydraulic conductivity values in the Mancos Shale and Gallup Sandstone and groundwater flux into the model were calibrated using modern head observations (Table 5). The calibrated parameters are determined as being best fit by PEST, assuming the constant head boundary is equal to the head of the modern potentiometric surface in those model cells. Calibration ranges used as input for PEST were determined from well logs and literature sources (Tables 2–4). Calibrated PEST hydraulic conductivity values in the Mancos Shale (horizontal hydraulic conductivity [HK] approximately [~] 0.0001 ft/d, vertical hydraulic conductivity [VK] ~0.0001 ft/d) were almost identical to parameters reported in Kernodle (1996) (HK = 0.0001 ft/d, VK = 0.0001 ft/d). HK was slightly lower than reported by Frenzel and Lyford (1982) (HK = 0.000864–0.00864 ft/d), but vertical hydraulic conductivity in this study was higher (Frenzel and Lyford [1982] reported VK = 0.000000864 ft/d). Horizontal hydraulic conductivity in the Gallup Sandstone in this study (HK ~0.41 ft/d) was in-between the values of Kernodle(1996) (HK = 1 ft/d) and Frenzel and Lyford (1982) (HK = 0.1–0.14 ft/d), and vertical hydraulic conductivity was identical to that of Kernodle (1996) (VK = 0.002 ft/d).

The model was calibrated to the updated modern surface hydraulic heads (described in the “Calibration and Sensitivity Analysis” section), where calibration targets were extracted from an overlain grid at 20,000 ft intervals from the kriged modern potentiometric surface. Total model mass balance errors were very small (0.01 percent), and the model successfully converged with head change and residual convergence criteria of 0.001 ft and 1 ft³/d, respectively, using the Preconditioned Conjugate-Gradient solver. The mean

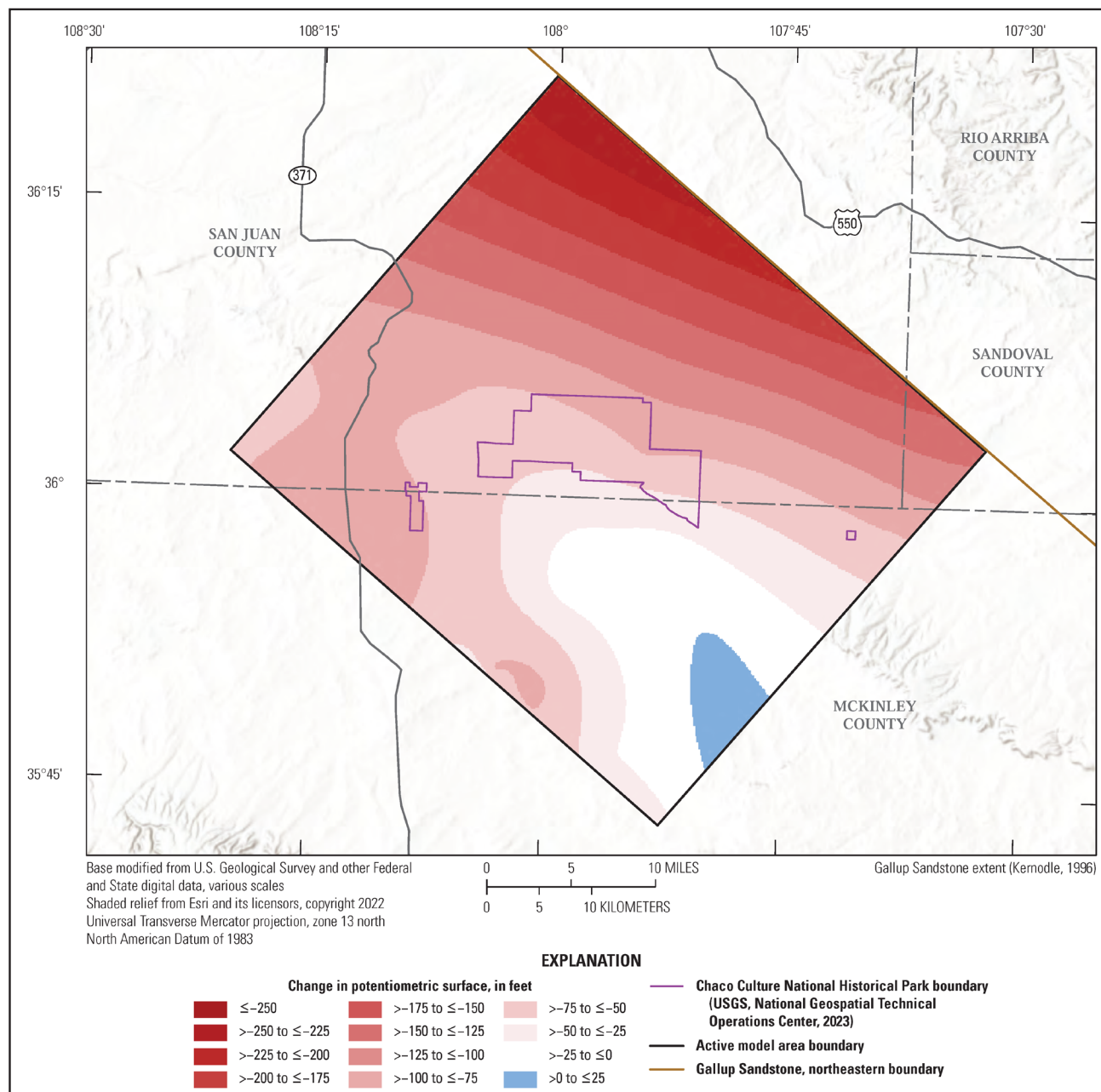


Figure 8. Change in the potentiometric surface from historical (1954–89) to modern (2016–20) conditions. Negative and positive values indicate decreasing and increasing elevation, respectively, from the historical to modern potentiometric surface.

residual (simulated minus observed) of the model was 2 ft, and the absolute residual mean was 33 ft, which is less than 5 percent of the total head drop across the active model area (~730 ft). The standard deviation of residuals was 42 ft. The minimum residual was -82 ft, and the maximum residual was 106 ft. Previously published models in the vicinity of this study area reported residuals of as much as 150 ft between model-derived potentiometric surface and observed head as “good fit,” given the total range of heads in the study area (Frenzel and Lyford, 1982), although some residuals were not reported (Kernodle, 1996). The R^2 between the simulated and observed head values was 0.93, indicating good agreement between simulated and observed values (Figure 9). However, comparison of the linear fit of the simulated against observed values, as well as the plot of the residuals versus observed values, indicate a slight tendency to overpredict at lower

Table 5. Calibrated groundwater model parameter dataset.

[Unit refers to the geologic unit represented by the model layer. Reach refers to the model flux-in reach, which was divided into six equal length parts along the southwest and southeast model boundaries. ft/d, foot per day; ft³/d, cubic foot per day; NA, not applicable]

Unit/reach	Hydraulic conductivity (ft/d)		Flux in (ft ³ /d)
	Horizontal	Vertical	
Mancos Shale	0.0001	0.0001	NA
Gallup Sandstone	0.41	0.002	NA
Gallup Sandstone/1	NA	NA	114
Gallup Sandstone/2	NA	NA	41
Gallup Sandstone/3	NA	NA	129
Gallup Sandstone/4	NA	NA	305
Gallup Sandstone/5	NA	NA	56
Gallup Sandstone/6	NA	NA	85

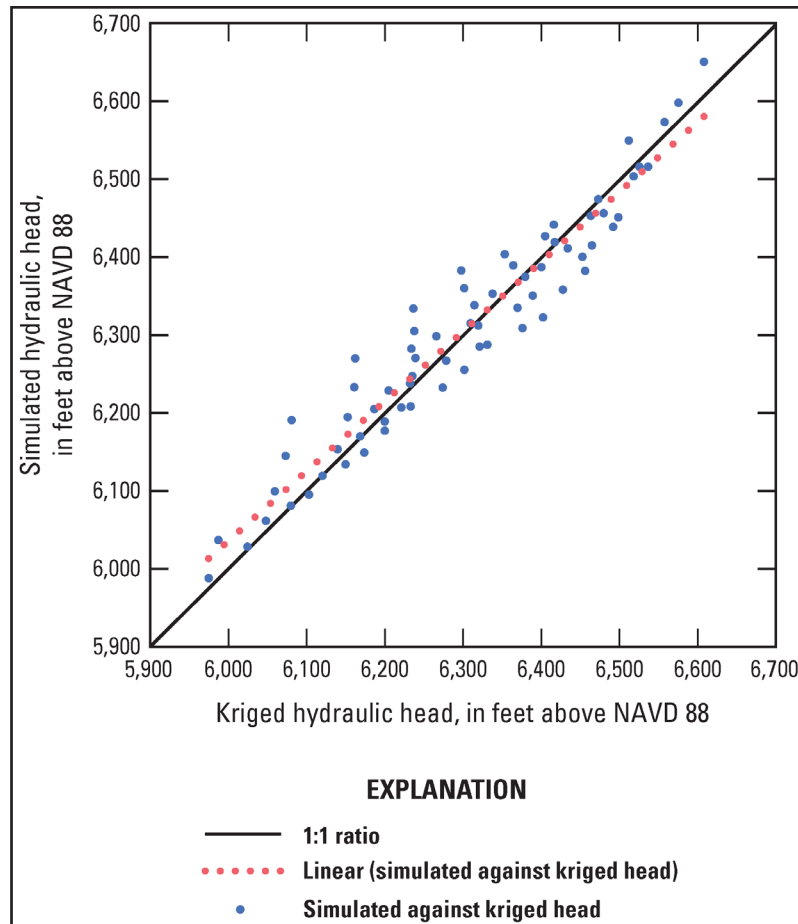


Figure 9. Kriged (observed) hydraulic head versus model simulated head and calibration target data comparison. NAVD 88, North American Vertical Datum of 1988.

observed head values and a slight tendency to underpredict at higher observed head values (kriged head versus residuals $R^2 = 0.14$, slope = -0.10) (Figures 9 and 10).

Though RMs are generally low, there is some spatial heterogeneity among residual values (Figure 11). Residuals are generally most positive (>50 ft) along the northeast boundary of the active model area, near the extent of the Gallup Sandstone, and most negative just south of CCNHP (less than -50 ft). Large residuals could be due to kriging interpolation error. Residuals generally are closest to zero (-10 to 10 ft) along the northwest boundary, which is a constant head boundary, and scattered elsewhere between areas of higher residuals.

Numerical groundwater models are simplified representations of natural systems, and these spatial biases are likely an artifact of the actual spatial heterogeneity of the vertical and hydraulic conductivity. The model treats the Mancos Shale and Gallup Sandstone layers as spatially homogeneous for the purpose of simplicity and because of the lack of data or other evidence to populate the model heterogeneously.

Several additional factors contribute to model uncertainty, including model error associated with the groundwater-level measurements and the standard error of the modern kriged surface (Figure 6). Parameter ranges for calibration were based largely on previously reported values (Table 3), which were determined either physically or through parameters previously calibrated for earlier models, which also have uncertainty and various limitations. MODPATH, which was used to generate simulated groundwater flow paths, potentially yields simplified flow paths or uncertain traveltimes because it considers only advective groundwater flow and ignores preferential flow features and dispersive flow features of water-bearing formations (Baca, 1999). Additionally, subsurface features such as faults and anthropogenic preferential pathways such as abandoned well casings were not represented. Pumping wells other than the Chaco well were not included because of a lack of data but were assumed individually to have negligible influence because of their smaller pumping volumes. As noted earlier, there may be up to 10,000 acre-ft of groundwater used in McKinley County per year. The model simulations in this report are simplistic representations of how HF operation may influence subsurface processes and advective groundwater flow paths and thus may neglect other complex HF influences, as described in the "Introduction" section (Birdsell and others, 2015).

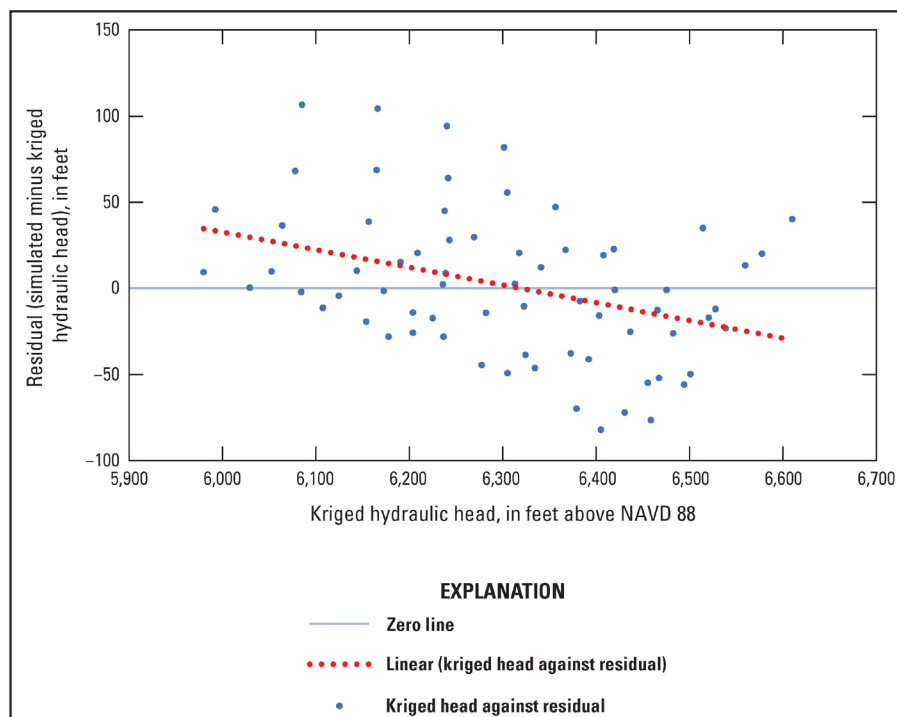


Figure 10. Kriged (observed) hydraulic head versus residuals (model simulated hydraulic head minus kriged hydraulic head). NAVD 88, North American Vertical Datum of 1988.

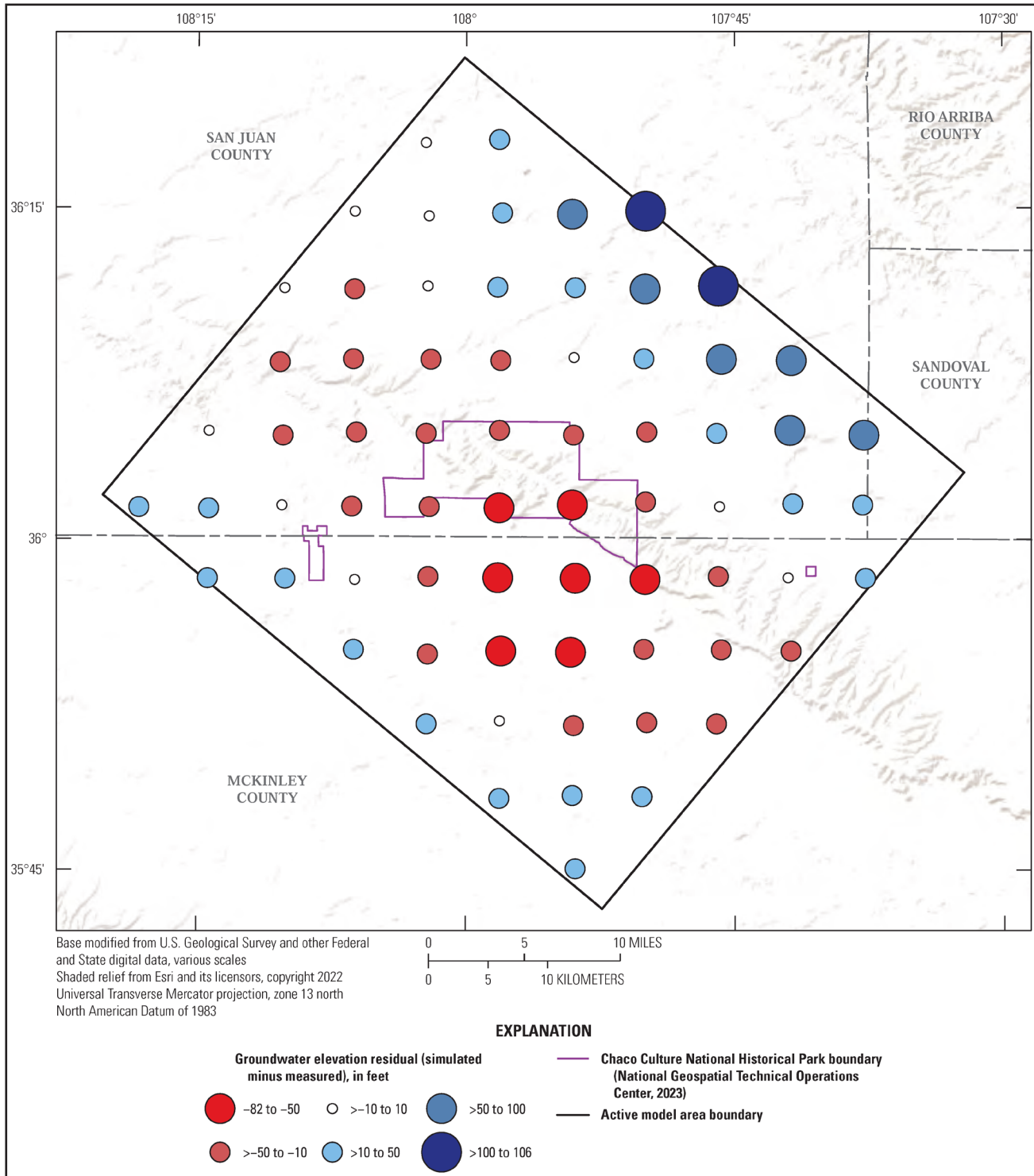


Figure 11. Spatial distribution of groundwater elevation residuals (simulated hydraulic head minus observed hydraulic head) for the calibrated groundwater flow model.

Sensitivity Analysis

Sensitivity analysis results are plotted as a percentage of parameter change from the calibrated parameter value versus the RM between simulated and observed heads (Figure 12A–C). The parameters included in the sensitivity analysis were horizontal and vertical hydraulic conductivities of the Mancos Shale and Gallup Sandstone model layers and the fluxes into the Gallup Sandstone. The sensitivity of particle traveltimes to porosity is discussed in the “Traveltimes” section of this report.

For hydraulic conductivity, only the HK RM in the Gallup Sandstone had high sensitivity (Figure 12B). The Gallup HK RM ranges from approximately 33 to 243 ft. The VK in the Gallup Sandstone as well as the HK and VK of the Mancos Shale are generally insensitive. Flux-in for reaches 3 and 4 were the most sensitive of the six flux-in parameters (Figure 12C). The reach 3 RM ranges from approximately 33 to 44 ft, and reach 4 ranges from 33 to 65 ft. The constant head boundary was found to be the most sensitive parameter in the entire sensitivity analysis, with the RM ranging from 33 to 3,033 ft (Figure 12A).

The Mancos Shale VK and HK have lower sensitivity, and as a result, altering the hydraulic conductivity through HF may have a lesser impact on model performance than initially anticipated. Reaches 3 and 4 are located along the steepest head gradient of the model, so the greater rate of change in RM for these reaches makes sense, because they contribute greater amounts of flux into the model than other reaches. The constant head boundary is the most sensitive parameter but also has the most quantitatively uncertain results through kriged standard error.

SIMULATION RESULTS

General Flow Directions and Gradients

Flow directions in the model are largely a function of head gradient derived from the modern kriged potentiometric surface, which may be subject to interpolation error. The flow directions and behavior in the model are also in part a function of the specified model boundaries. Water generally enters the model through the flux-in boundary along the southwest and southeast boundaries, flows parallel along the northeast boundary, and exits the model along the northwest boundary. Previously published potentiometric head contours (Frenzel and Lyford, 1982; Kernodle, 1996) are in relative agreement with this study in terms of gradient direction but are not digitized and are difficult to quantitatively compare with new results (Stewart, 2018). However, the hydraulic gradients in this study in the vicinity of the CCNHP (minimum and maximum values range ~730 ft) tend to be steeper (greater range) compared to previous contour maps of head (Kernodle, 1996), potentially from increased or continued groundwater extraction from the Gallup Sandstone aquifer, coupled with limited aquifer recharge.

For most of the active model area, flow vectors in cross section view indicate that groundwater tends to flow horizontally between model cells, with limited mixing between the Mancos Shale and Gallup Sandstone layers. However, model results indicate slight vertical mixing of water between the Mancos Shale and the Gallup Sandstone, primarily near the Chaco well where pumping is occurring (Figure 13A, B). Hydraulic head is lowered substantially in the model cells near the Chaco well, especially those cells extending vertically to the top and bottom of the active model area. This change in hydraulic gradient causes groundwater to flow from the Mancos Shale layers to the Gallup Sandstone layer, and the gradient increases when the pumping rate is increased from the reported 1,200 ft³/d to the theoretical 10,000 ft³/d. The model framework did not account for all pumping wells in the area and does not have the available data to account for potential abandoned or compromised wells that could act as permeable pathways between the Mancos Shale and Gallup Sandstone or other surrounding units (Birdsell and others, 2015). These gradients and pathways presumably exist elsewhere in the model domain, which could promote additional vertical mixing between the Gallup Sandstone and Mancos Shale layers.

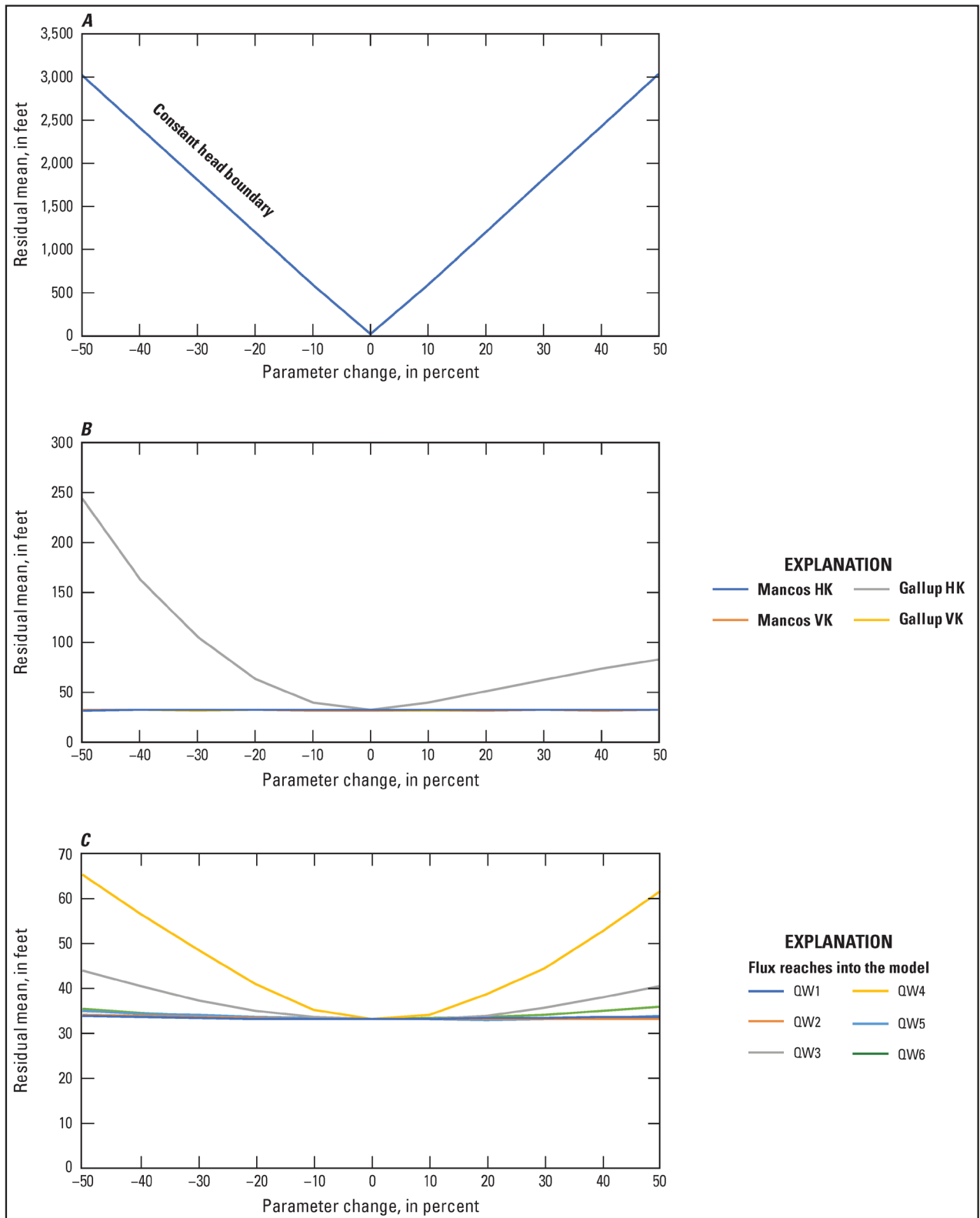


Figure 12. Sensitivity analysis (residual mean versus change in calibrated parameter value) for A, constant head boundary, B, horizontal hydraulic conductivity (HK) and vertical hydraulic conductivity (VK), C, model flux-in. Flux-in boundary definitions: QW1, Gallup Sandstone/1; QW2, Gallup Sandstone/2; QW3, Gallup Sandstone/3; QW4, Gallup Sandstone/4; QW5, Gallup Sandstone/5; QW6, Gallup Sandstone/6.

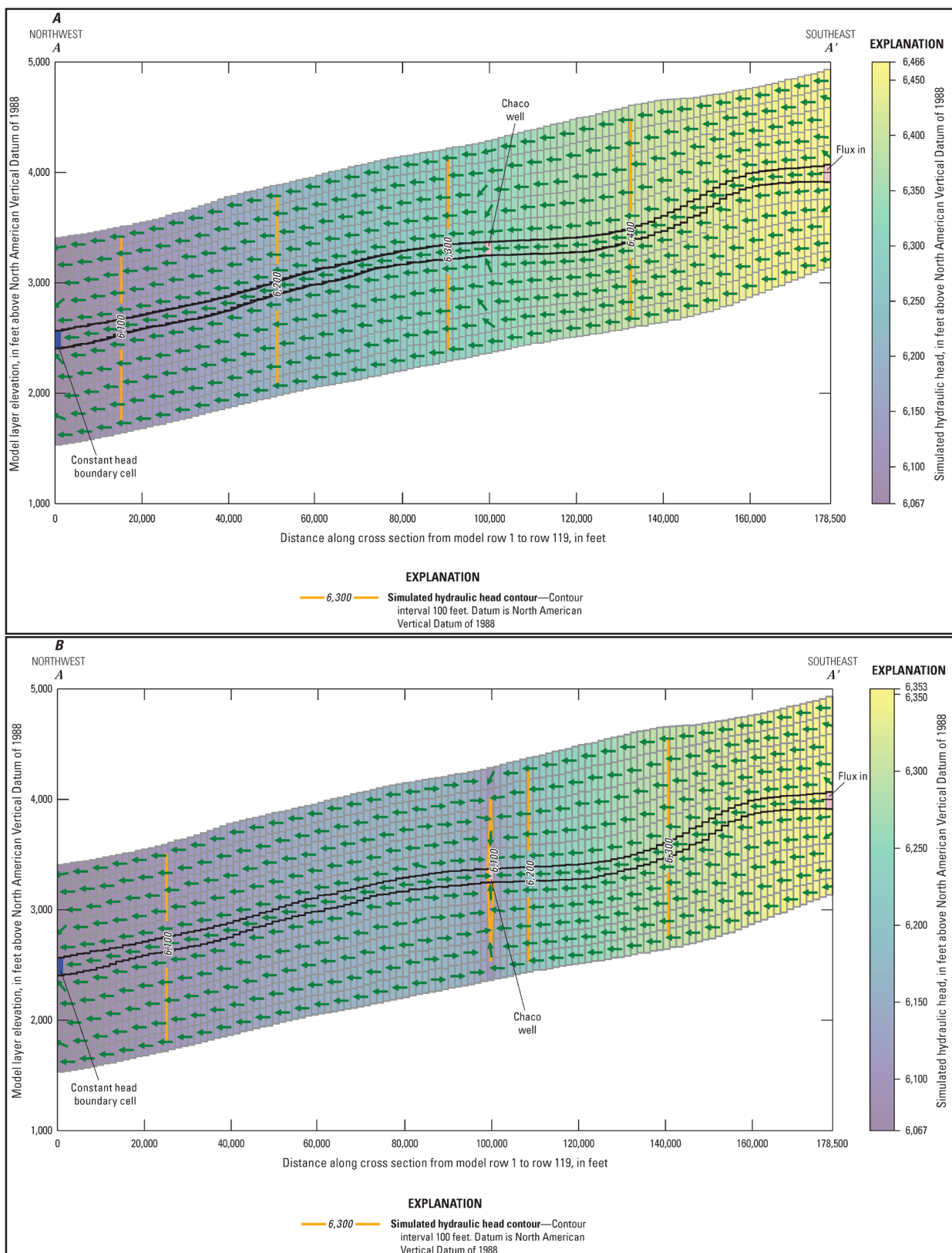


Figure 13 (A and B). Cross-sectional view (A–A', Figure 1) of groundwater flow model through model column 55 containing Chaco well (row 67) pumping rates of A, 1,200 cubic feet per day, and B, 10,000 cubic feet per day. Arrows are not scaled to the magnitude of flux and only indicate the direction of simulated flow.

Capture Zones

Capture zones were assessed by forward tracking particles placed along the flux-in boundary of the model domain until their capture by the Chaco well. Capture zones for the hypothetical Chaco well pumping rate of 10,000 ft³/d are shown in figure 14A, B in two-dimensional space and are depicted in three-dimensional space by the color of the pathways. These are representative figures of particles released in model layers 5 and 7 (Mancos Shale), representing average depths approximately 125 ft above and 175 ft below the Gallup Sandstone, respectively. The capture zone for either pumping rate tends to originate at the southeast flux-in boundary and take an arched northwest-trending path through the model until the particles are captured. Increasing the pumping rate substantially increases the capture zone width. The average width of the capture zone is approximately 1 mi for the 1,200 ft³/d pumping rate (not shown) and approximately 12 mi for the 10,000 ft³/d pumping rate.

A total of 2,442 particles were released in all 11 model layers in each cell along the southwest and southeast flux-in boundaries. Of these particles, 41 and 387 were captured by the well at pumping rates of 1,200 and 10,000 ft³/d, respectively. The remaining particles did not pass through or terminate in the cell containing the Chaco well. Particle traveltimes ranged between approximately 28,500 and 34.2 million years for captured particles at a pumping rate of 1,200 ft³/d and between approximately 24,300 and 76.4 million years at a pumping rate of 10,000 ft³/d. The longer traveltimes for the larger pumping rate are due to the resulting larger capture zone that is created. Carbon isotope dating of water from three Gallup Sandstone wells within the modeled domain indicated an age range from ~43,000 to >52,000 years before present, the latter being greater than the method can resolve (Linhoff and others, 2023). Although these sampled waters travel from an unknown recharge area, and the active model area only occupies a portion of the basin, the order of magnitude of ages and traveltimes suggest a level of consistency and accuracy between both methods. These traveltimes are theoretical and dependent on running the model in steady-state simulation until all particles reach their endpoint at the calibrated parameter set and initially determined assumed porosity values (Table 6). Traveltimes are calculated for a range of porosity values suggested in the literature (examined in the “Traveltimes” section).

Particles released in layer 5 primarily remained in the upper Mancos Shale layers (layers 2–4) stratigraphically above the Gallup Sandstone and did not reach the Gallup Sandstone until they were within 1,500 ft of the Chaco well. Similarly, the particles released in layer 7 remained in the lower Mancos Shale layers (layers 7–10) stratigraphically below the Gallup Sandstone and did not reach the Gallup Sandstone until they were within 1,500 ft of the Chaco well. These particle tracking pathways indicate that mixing between the Gallup Sandstone and Mancos Shale likely occurs primarily near pumping wells or near very permeable pathways such as compromised well casings or fractured rock.

Traveltimes

Two additional model runs were conducted that used the calibrated model parameters and Chaco well pumping rate of 1,200 ft³/d with the minimum and maximum porosity values for the Mancos Shale and Gallup Sandstone from the literature (Table 4; Martin, 2005) to assess potential minimum and maximum groundwater traveltimes. Similar to the process for capture zones, a total of 2,442 particles were released in all 11 model layers in each cell along the southwest and southeast flux-in boundaries and forward tracked in steady-state simulation. Traveltimes are generally slower with higher porosity, given that flow paths are less tortuous, and fluid velocity through a porous media is mathematically expressed as Darcy flux divided by the porosity. For minimum porosity values, traveltimes ranged from approximately 5,700 years to 30 million years. For maximum porosity values, traveltimes ranged between approximately 52,000 years and 36.3 million years. The minimum traveltimes reflect particles that originated in and primarily flowed through the Gallup Sandstone, whereas maximum values reflect particles that originated in and primarily flowed through the Mancos Shale.

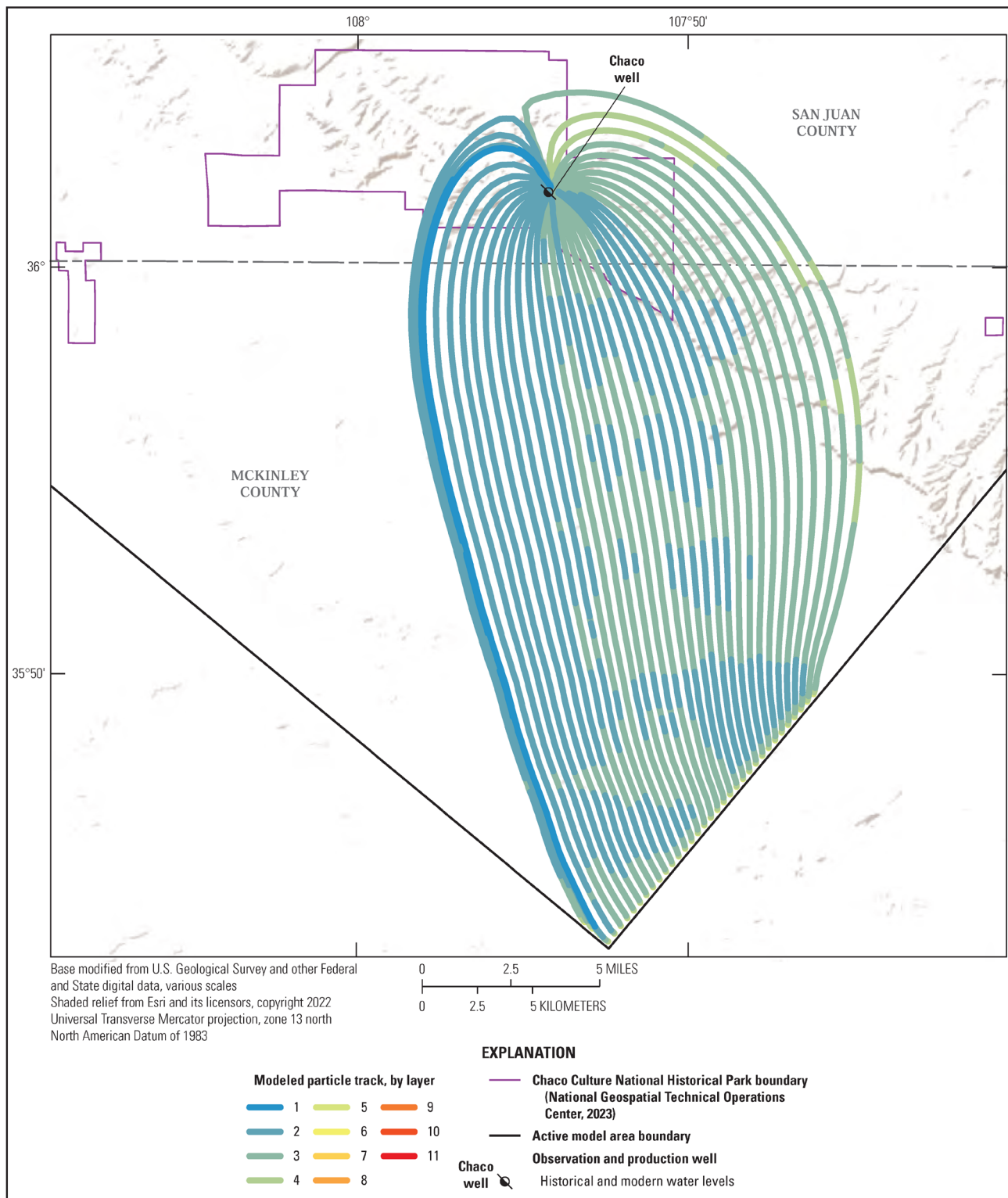


Figure 14. Chaco well groundwater capture zone, determined by particle tracking paths of well-captured particles for a pumping rate of 10,000 cubic feet per day for particles released in A, model layer 5, and B, model layer 7.

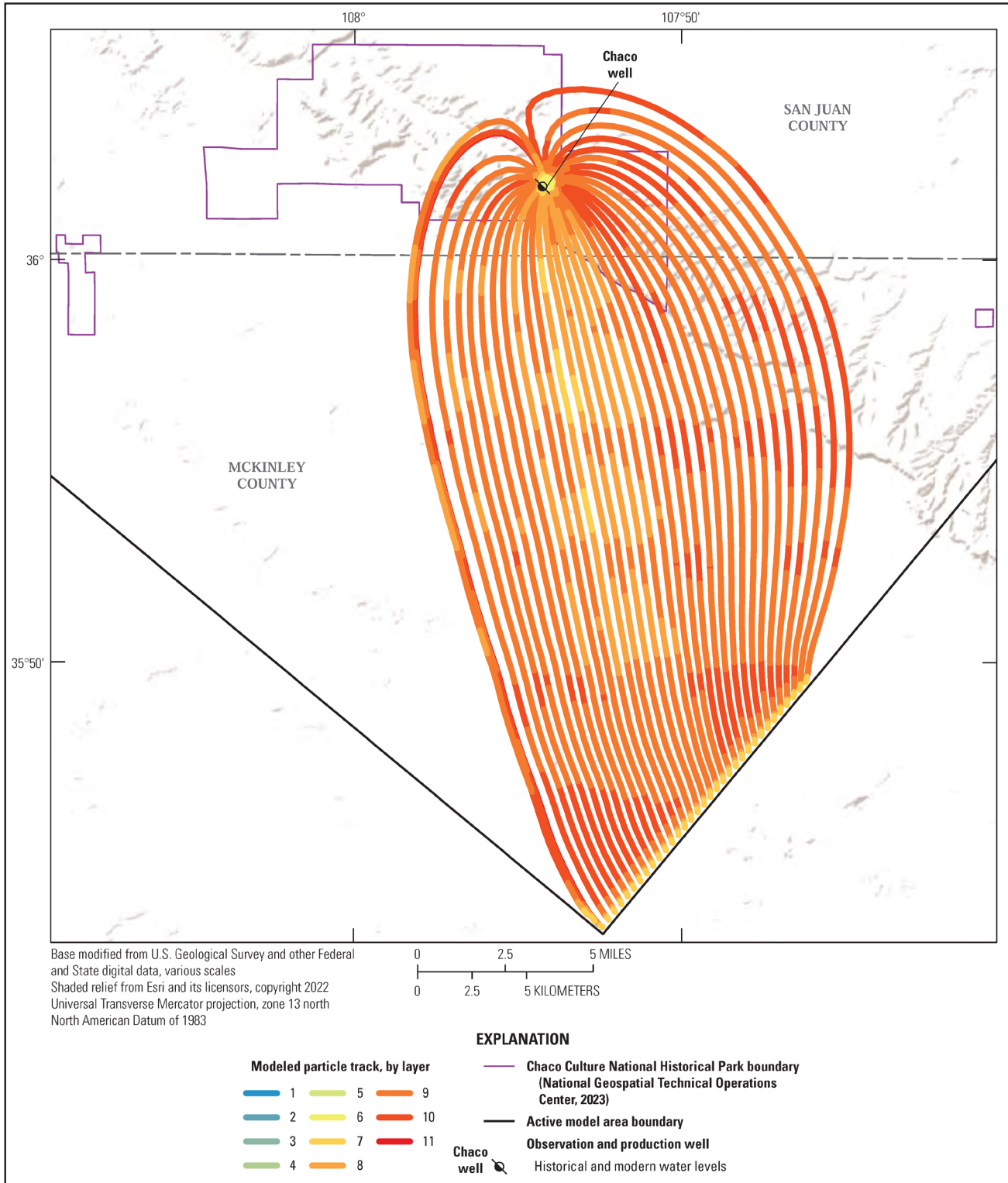


Figure 14. Chaco well groundwater capture zone, determined by particle tracking paths of well-captured particles for a pumping rate of 10,000 cubic feet per day for particles released in A, model layer 5, and B, model layer 7.—Continued

Table 6. Indicated particle travel or nontravel through individual model layers for selected hydraulic conductivities and Chaco well pumping rates.
 [ft, foot; ft/d, foot per day; ft³/d, cubic foot per day; x, particle passes through layer; --, particle does not pass through layer; /, Gallup Sandstone layer unaltered].

Layer	Average depth below top of Upper Mancos Shale (ft)	Standard deviation of depth (ft)	Horizontal and vertical hydraulic conductivity (ft/d)							
			0.001	0.01	0.1	1	10	100	1,000	
Chaco well pumping rate of 1,200 ft ³ /d										
1	182	25	--	--	--	--	--	--	--	--
2	362	49	--	--	--	--	--	--	x	x
3	543	73	--	--	--	--	--	x	x	x
4	724	98	--	--	--	--	--	x	x	x
5	905	122	--	--	--	x	x	x	x	x
6	1,031	123	/	/	/	/	/	/	/	/
7	1,202	113	--	--	--	x	x	x	x	x
8	1,372	105	--	--	--	--	x	x	x	x
9	1,543	100	--	--	--	--	x	x	x	x
10	1,713	98	--	--	--	--	--	x	x	x
11	1,883	100	--	--	--	--	--	--	--	--
Chaco well pumping rate of 10,000 ft ³ /d										
1	182	25	--	--	--	x	x	x	x	x
2	362	49	--	--	--	x	x	x	x	x
3	543	73	--	--	--	x	x	x	x	x
4	724	98	--	--	--	x	x	x	x	x
5	905	122	--	--	x	x	x	x	x	x
6	1,031	123	/	/	/	/	/	/	/	/
7	1,202	113	--	--	x	x	x	x	x	x
8	1,372	105	--	--	--	x	x	x	x	x
9	1,543	100	--	--	--	x	x	x	x	x
10	1,713	98	--	--	--	x	x	x	x	x
11	1,883	100	--	--	--	x	x	x	x	x

These simulated values represent traveltimes from the boundary of the active model area, not total traveltimes from the time water enters the subsurface. Water typically enters the Gallup Sandstone from surface outcrops far to the south and southeast of the Chaco well and the active model area (Stone and others, 1983), meaning traveltimes to the Chaco well are longer than those determined by the model. However, computed model traveltimes for minimum porosity values and the assumed additional travel from outside of the active model area are consistent with computed carbon isotope ages of samples collected in the Gallup Sandstone within the modeled domain (43,000 to >52,000 years before present; Linhoff and others, 2023).

Hydraulic Fracturing Scenarios

Several scenarios representing different HF operations were investigated (Table 6). Hydraulic conductivities of each Mancos Shale layer were altered individually by several orders of magnitude to simulate the maximum distance and depth that potential HF-induced changes in hydraulic conductivity could potentially influence the Chaco well. In Table 6, each row represents a model layer (Mancos Shale = layers 1–5, 7–11; Gallup Sandstone = layer 6), and each column represents the hydraulic conductivity assigned to simulate potential HF operation. For each scenario model run, Mancos Shale layer hydraulic conductivity (horizontal and vertical) was altered separately by layer (one layer per model run), the model was executed, and then

particles were tracked in reverse to record their path in space and time from model cells surrounding the Chaco well. If a particle passed through the altered Mancos Shale layer, this was an indication that HF operation in that particular layer could potentially influence the Chaco well. This simulation was conducted for Chaco well pumping rates of 1,200 and 10,000 ft³/d.

For the 1,200 ft³/d pumping rate, increased HK and VK in the Mancos Shale began to influence the Chaco well when hydraulic conductivity reached 1 ft/d, which is five orders of magnitude above the hydraulic conductivity determined through model calibration (HK and VK ~0.0001 ft/d). Hydraulic conductivity has been determined to change by three to five orders of magnitude from HF in laboratory settings (Gehne and Benson, 2019). Model results indicate that if HF alters hydraulic conductivity by less than five orders of magnitude, there will be no influence on the Chaco well. For a hydraulic conductivity of 1 ft/d, only the first Mancos Shale layers above and below the Gallup Sandstone (layers 5 and 7) influenced flow to the Chaco well, and for hydraulic conductivities above 10 ft/d, three layers above and below the Gallup Sandstone influenced flow to the Chaco well (layers 3–5 and 7–9). For hydraulic conductivities of 100 ft/d or more, four layers above and below the Gallup Sandstone influenced flow to the Chaco well (layers 2–5 and 7–10). However, the top and bottom layers of the model (layers 1 and 11) did not pass any particles that were captured by the Chaco well for any hydraulic conductivity values (as much as 1,000 ft/d) at the 1,200-ft³/d pumping rate.

For the 10,000-ft³/d pumping rate, flow to the Chaco well began to be influenced by high HK and VK in the Mancos Shale layers at a hydraulic conductivity of 0.1 ft/d, and more layers above and below the Gallup Sandstone began to influence flow to the Chaco well. At hydraulic conductivities of 1 ft/d or more, all of the layers above and below the Gallup Sandstone influenced water flowing to the Chaco well.

Changing the horizontal and vertical hydraulic conductivities of the entire layer may have a different effect on the behavior of subsurface flow than changing them in smaller, isolated areas. Changing the hydraulic conductivity of the Mancos Shale over an entire model layer to values above the Gallup Sandstone hydraulic conductivity may promote flow through the Mancos Shale layers, rather than promoting the movement of water from the Mancos Shale to the Gallup Sandstone. This behavior may not be indicative to how HF may influence flow pathways and travel times. Altering the hydraulic conductivity in small areas in the Mancos Shale layers, similar to how an HF well may alter hydraulic conductivity, effectively creates preferential pathways for groundwater flow between the Mancos Shale and the Gallup Sandstone.

For example, figure 15A, B shows the pathlines and starting locations in layer 4 for the particles captured by the Chaco well that originated from smaller areas (having a radius of about 10,000 ft) of altered hydraulic conductivity to emulate HF fracture zones. These particles passed vertically through the Mancos Shale, reached the Gallup Sandstone, and continued to pass through the Gallup Sandstone before reaching the Chaco well. Altering the hydraulic conductivity allowed groundwater to reach the Gallup Sandstone earlier than it otherwise would have and ultimately decreased the travel times to the Chaco well. This behavior occurred at modeled hydraulic conductivities of 1 and 100 ft/d, which suggests that a substantial change in hydraulic conductivity in a small area of the Mancos Shale may provide preferential pathways for groundwater travel to the Gallup Sandstone. These scenarios were run for both Chaco well pumping scenarios (1,200 and 10,000 ft³/d). Particles placed in smaller altered zones within the original capture zone (with original calibrated model parameters based on known, present-day, or observed conditions) in horizontal space (Figure 15A, B) were also captured by the Chaco well. Particles placed outside of the original capture zone (in horizontal space) were still not captured by the well, indicating that changes in hydraulic conductivity have limited influence on advective flow pathways outside of the HF zone.

These emulated HF zones decreased groundwater travel times from the Mancos Shale to the Gallup Sandstone by providing increased hydraulic conductivity and preferential pathways between the layers. Mean travel times for particles captured by the Chaco well that originated in altered HF zones were approximately 14,300 years for Chaco well pumping rates of 10,000 ft³/d compared to 18.5 million years for unaltered zones. The decrease in travel time was primarily due to the HF zones changing the travel paths of the particles directly into the Gallup Sandstone.

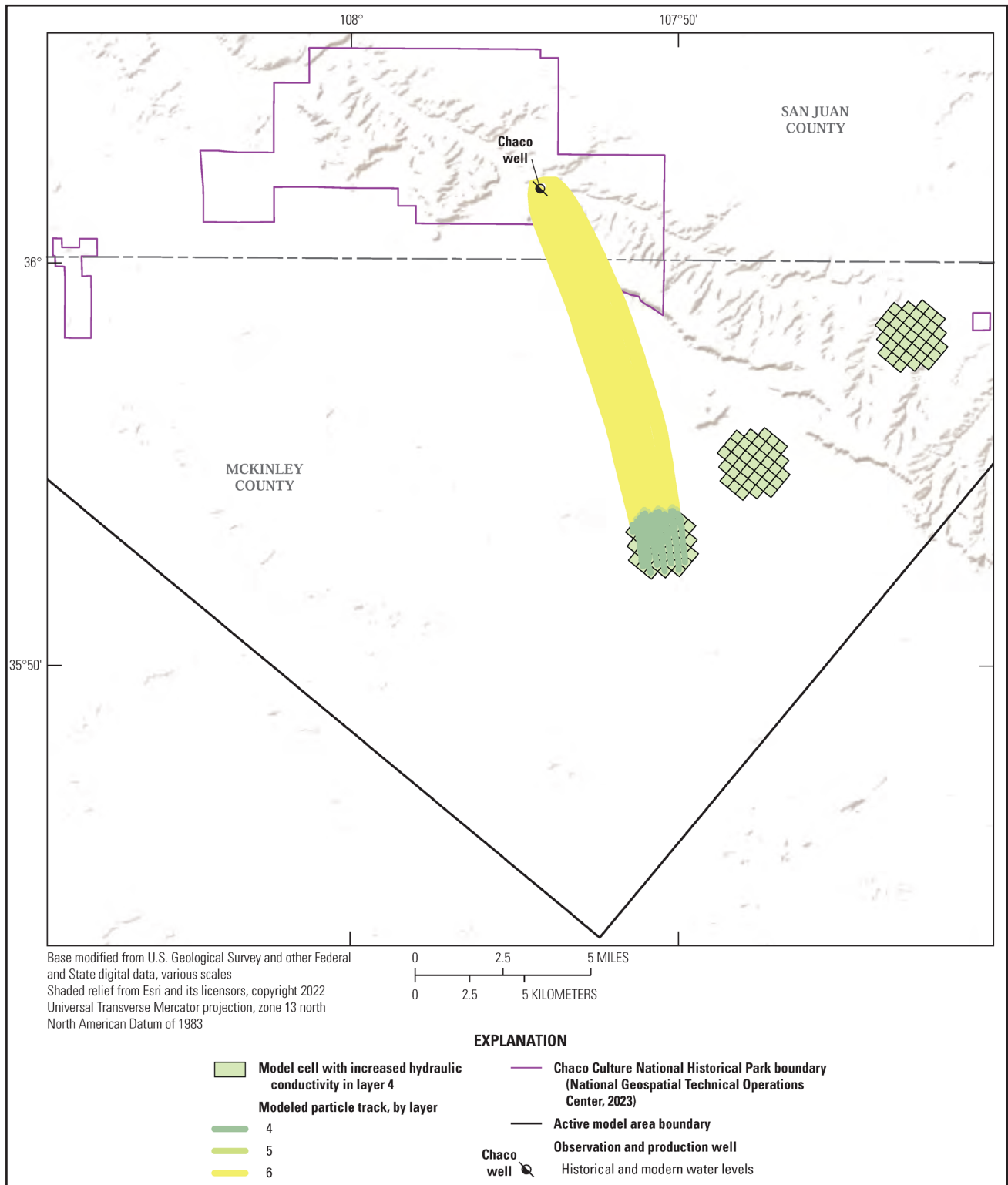


Figure 15. Particle pathways for particles released in select zones in model layer 4 at a hydraulic conductivity of 1 foot per day and a pumping rate of A, 1,200 cubic feet per day, and B, 10,000 cubic feet per day.

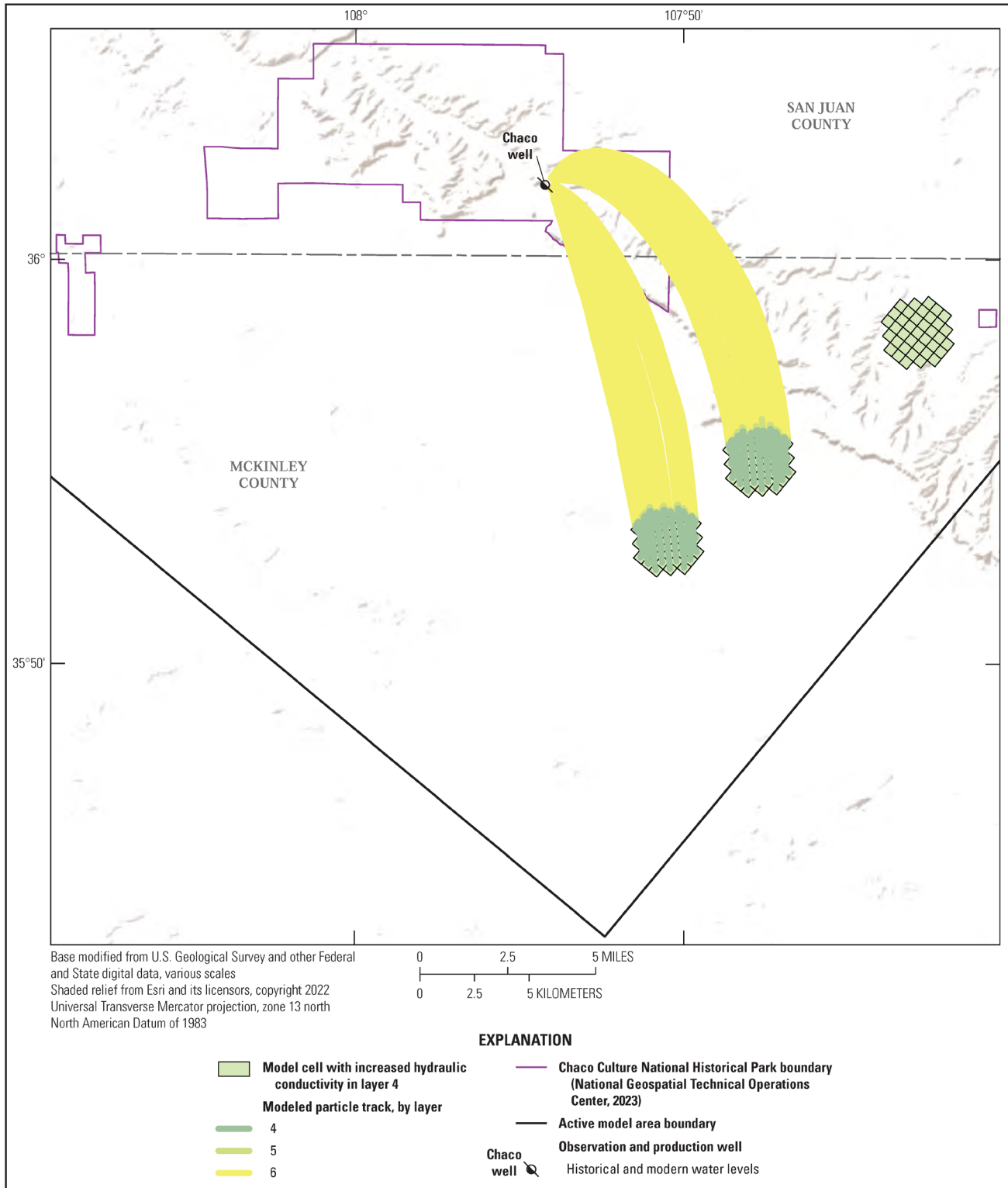


Figure 15. Particle pathways for particles released in select zones in model layer 4 at a hydraulic conductivity of 1 foot per day and a pumping rate of A, 1,200 cubic feet per day, and B, 10,000 cubic feet per day.—Continued

DISCUSSION OF POTENTIAL CHACO WELL CONTAMINATION

Potential water quality impairment from HF operations can result from stray gas phase hydrocarbon migration in aquifers via leaking well casings and surface spills of extracted fluids that can contaminate shallow aquifers (Vengosh and others, 2014). Given the low hydraulic conductivities and confining thickness of the Mancos Shale, as well as the depth of the Chaco well, it is unlikely that contamination of the Gallup Sandstone aquifer could occur from surface spills. However, vertical mixing between aquifers is possible through improper casing or plugging of hydrocarbon wells in the region. Stone and others (1983) noted that leakage may occur locally between adjacent Cretaceous units, generally at low rates through shale beds and greater rates in localized areas associated with faults and fractures. This vertical mixing could introduce hydrocarbon related compounds and could be increased by hydrocarbon extraction activities.

The groundwater model indicates mixing between the Mancos Shale and Gallup Sandstone aquifers. A companion study to this report found several lines of evidence for vertical mixing between the Gallup Sandstone aquifer and surrounding aquifers, as well as groundwater chemistry influenced by hydrocarbons (Linhoff and others, 2023). First, noble gas analysis suggested mixing with hydrocarbon influenced groundwater. Second, hydrocarbon associated volatile organic compounds including benzene, toluene, ethylbenzene, and xylene were found at low levels in the Gallup Sandstone aquifer—including in the Chaco well. Lastly, mixing between aquifers was identified through major ion and isotopic geochemical analysis (Linhoff and others, 2023). Further investigation could help determine whether interaquifer mixing and the presence of volatile organic compounds is naturally occurring or related to oil and gas activity.

Several inactive oil and gas related wells were identified within the Chaco well capture zone in the Gallup Sandstone, Entrada Sandstone, Dakota Sandstone, and Morrison Formation (Figure 16; Linhoff and others, 2023). Seven and 22 inactive hydrocarbon wells were identified within 5 and 10 kilometers of the Chaco well, respectively (Figure 16; Linhoff and others, 2023). Eighteen inactive hydrocarbon related wells are located within the capture zone and within 10 kilometers of the Chaco well. Given the initial porosity values from Table 4 in the Gallup Sandstone aquifer, simulated advective groundwater transport to the Chaco well is estimated to be approximately 430 years from the nearest inactive hydrocarbon related wells. If some of these inactive hydrocarbon related wells were improperly cased or plugged, they could potentially act as conduits for vertical groundwater movement through relatively impermeable units such as the Mancos Shale (Kernodle, 1996).

Combined modeling and geochemical results imply that contaminants from hydrocarbon extraction activities in the San Juan structural basin could travel between aquifers and could affect water quality in the Gallup Sandstone aquifer. Although further investigation, including examination of well completion and integrity, would be necessary to determine if contamination is actually facilitated, inactive oil and gas related wells found within the Chaco well capture zone could be sources of contamination for the Chaco well via vertical mixing of hydrocarbon bearing waters and Gallup Sandstone aquifer waters. Potential contamination at Chaco well may depend on three factors:

- Groundwater travel times through these geologic units are slow, so the distance a contaminant needs to travel to reach the Chaco well may influence the potential for drinking water contamination.
- The proximity of oil and gas related wells to the Chaco well (both horizontally and with respect to the unit they are completed in) may facilitate vertical mixing and decrease groundwater travel times.
- In the Chaco well groundwater capture zone, contaminants that originate upgradient of the Chaco well may have greater potential for drinking water contamination than those that originate downgradient of the Chaco well.

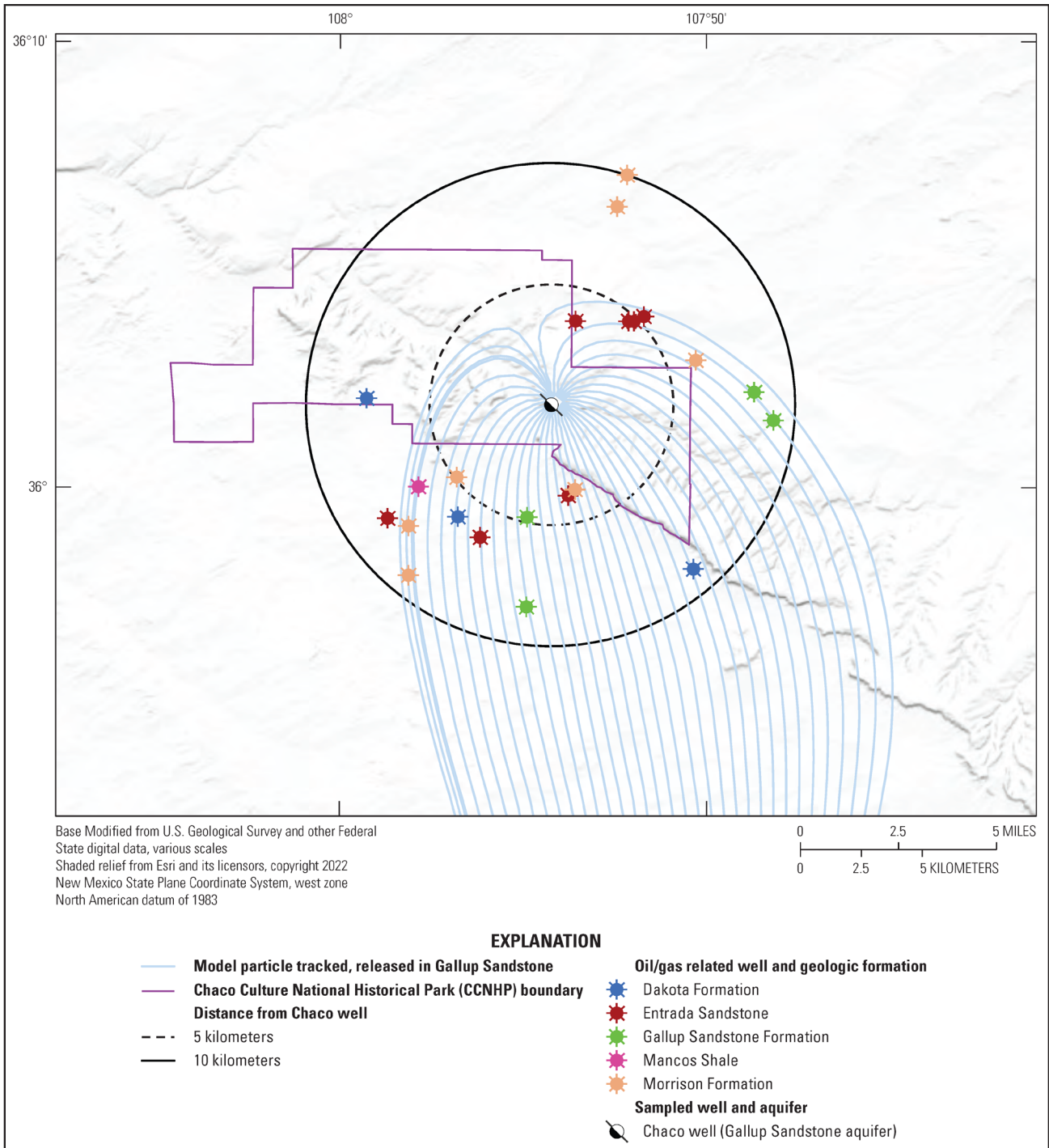


Figure 16. Inactive and plugged oil and gas wells within 5 and 10 kilometers of the Chaco well, with modeled particle pathways for particles released in the Gallup Sandstone aquifer unit. The Chaco well pumping rate is 10,000 cubic feet per day in this simulation. Figure adapted, and oil and gas related well data sourced, from Linhoff and others (2023).

LIMITATIONS AND FURTHER MODEL DEVELOPMENT

Although numerical groundwater modeling is a useful tool, there are limitations to the analysis documented herein. Additional groundwater level observations would reduce the standard error of the interpolated potentiometric surfaces. This error leads to potential errors in physical interpretation in areas where recharge occurs along the southern portion of the Gallup Sandstone where it crops out at the surface. Potentiometric surfaces need to be considered within the context of the standard error data and maps. Model performance could also be improved if the model was provided with more data on the spatial heterogeneity of hydrologic characteristics of the subsurface. Such data could include additional boreholes to refine basin lithology, nested piezometers to refine vertical groundwater gradients, and a greater density of groundwater-level measurements with closer temporal proximity.

The focus of the model scenarios was to observe particle pathways and capture zones of groundwater to the Chaco well and to visually present specific areas where HF operations could increase advective transport toward the Chaco well. This model could serve as a starting point to build a more comprehensive model that includes a detailed accounting of existing oil and gas wells, including depth, integrity, and any injections, to assess whether steady-state flow paths intersect any of these oil and gas features and to assess the potential traveltimes from these features to the Chaco well. Comprehensive assessment of HF fluid migration could include processes such as topographically driven flow, overpressure in shale reservoirs, buoyancy of HF fluids, and the increased pressure in shale from HF fluid injection. Additionally, a comprehensive model could include a detailed accounting of permeable pathways such as faults, fractures, or abandoned wells and the inclusion of more complicated multiphase flow effects, such as capillary imbibition and reduced relative permeability. Ultimately, transport mechanisms beyond advective transport, to which this report is limited, should be considered for a comprehensive study. In this study, only flow through the deep portions of the Gallup Sandstone and Mancos Shale was modeled. Although vertical hydraulic gradients between aquifers have been explored in previous studies, the substantial changes in potentiometric surface observed in this study could indicate changes in either horizontal or vertical flow paths and mixing between other aquifers. New models (potentially built by adapting the model produced for this study), could simulate additional aquifers in the San Juan structural basin using the same approach, or existing San Juan models could be adapted to new boundary conditions with the intent of assessing the amount of mixing occurring between subsurface layers. Additionally, new comprehensive San Juan structural basin models could be run for a transient time period if an accounting of various flux estimates could be determined. Finally, a detailed accounting of pumping rates and recharge in the Gallup Sandstone could be conducted to assess the cause of the declining head.

SUMMARY AND CONCLUSIONS

Through drawdown analysis and MODFLOW groundwater modeling, this study sought to determine the potential risk of hydraulic fracturing (HF) to the main drinking water well at Chaco Culture National Historical Park (CCNHP), located in northwestern New Mexico. The Gallup Sandstone of the San Juan structural basin is a confined aquifer that supplies drinking water to CCNHP and is stratigraphically located between thick, low-permeability layers of Mancos Shale. The San Juan structural basin, including the Mancos Shale, has been the subject of renewed interest in oil and gas development within the past decade. “Unconventional” reservoirs can cost-effectively produce gas, primarily through special recovery processes and technology. Unconventional methods of extraction including HF are being implemented in the Mancos Shale. Although the main CCNHP well is screened at a depth of 3,100 feet (ft) and is unlikely to be influenced by surface spills associated with extracted HF fluids, increased hydraulic conductivity caused by HF, migration of unextracted HF fluids and leaking well casings, and overextraction of water resources have the potential to negatively influence water quality and water availability for CCNHP.

New potentiometric surfaces kriged from observed historical and modern water-level measurements in the Gallup Sandstone indicate that potentiometric head has decreased by approximately 34–96 ft within the CCNHP prior to the unconventional oil and gas development in 2019. Direct water-level observations of the Chaco well indicate that head decreased by 70.5 ft between March 1989 and August 2017. The cause of this

drawdown was not investigated, although this finding indicates depletion of water resources for CCNHP. In general, the modeling indicates that groundwater in the Gallup Sandstone travels from south-southeast to north-northwest within the active model area and through CCNHP.

In some groundwater systems, the loss in aquifer storage from pumping is balanced by increased recharge and (or) decreased discharge to surface water or evapotranspiration. However, because of the depth and isolating thickness of the Mancos Shale, there is likely limited recharge to the Gallup Sandstone besides where surface outcrops are near the unit boundary. Traveltimes through the Gallup Sandstone range from thousands to tens of thousands of years through the active model area depending on the pumping rate and chosen subsurface porosity values. Groundwater traveltimes through the Mancos Shale are very long, on the order of tens of millions of years. Hence, because of the age and the very slow groundwater traveltimes, modern groundwater recharge should not be expected to replace groundwater drawdown observed in the study area. Capture zone maps created by the model in this study may help indicate when compromised well casings and HF activity are within the advective groundwater flow paths to the CCNHP main well and may lead to negative water quality influence on the CCNHP drinking water supply. Eighteen inactive hydrocarbon related wells are located within the capture zone and within 10 kilometers of the Chaco well. Given model estimates of traveltimes of groundwater in the Gallup Sandstone aquifer, advective groundwater transport to the Chaco well would take approximately 430 years from the nearest inactive hydrocarbon related wells.

Model simulations indicated that increased hydraulic conductivity from fracturing activity could decrease groundwater traveltimes (from millions to thousands of years) between the Mancos Shale and the Chaco well by creating preferential flow pathways between the Mancos Shale and the Gallup Sandstone. Comprehensive modeling scenarios that capture the complexities of HF fluid migration could aid the assessment, and improve our understanding, of the absolute vulnerability of the Chaco well to HF activity.

ACKNOWLEDGMENTS

This work was funded through the U.S. Geological Survey (USGS)-National Park Service Water Quality Program. The work was made possible with help from the Navajo Nation and assistance from USGS technicians. This work was also significantly improved by the suggestions of reviewers.

REFERENCES

- Baca, E., 1999, On the misuse of the simplest transport model: *Ground Water*, v. 37, no. 4, p. 483, accessed March 23, 2023, at <https://doi.org/10.1111/j.1745-6584.1999.tb01128.x>
- Birdsell, D.T., Rajaram, H., Dempsey, D., and Viswanathan, H.S., 2015, Hydraulic fracturing fluid migration in the subsurface—A review and expanded modeling results: *Water Resources Research*, v. 51, no. 9, p. 7159–7188, accessed March 23, 2023, at <https://doi.org/10.1002/2015WR017810>
- Byrnes, A.P., 2011, Role of induced and natural imbibition in frac fluid transport and fate in gas shales in Technical Workshops for Hydraulic Fracturing Study, Arlington, Virginia, March 28–29, 2011, [Proceedings]: U.S. Environmental Protection Agency, 28 p., accessed March 23, 2023, at <https://www.epa.gov/sites/default/files/documents/roleofinducedandnaturalimbibitioninfracfluid.pdf>
- Clark, C.E., Horner, R.M., and Harto, C.B., 2013, Life cycle water consumption for shale gas and conventional natural gas: *Environmental Science & Technology*, v. 47, no. 20, p. 11829–11836.
- Craig, S.D., 2001, Geologic framework of the San Juan structural basin of New Mexico, Colorado, Arizona, and Utah, with emphasis on Triassic through Tertiary rocks: U.S. Geological Survey Professional Paper 1420, 70 p., accessed September 21, 2023, at <https://doi.org/10.3133/pp1420>
- Cunningham, W.L., and Schalk, C.W., comps., 2011, Groundwater technical procedures of the U.S. Geological Survey: U.S. Geological Survey Techniques and Methods, book 1, chap. A1, 151 p. [Also available at <https://pubs.usgs.gov/tm/1a1/>]
- Doherty, J., 2018a, PEST model-independent parameter estimation user manual part 1—PEST, SENSAN and global optimisers (7th ed.): Queensland, Australia, Watermark Numerical Computing, 364 p.
- Doherty, J., 2018b, PEST model-independent parameter estimation user manual part 2—PEST utility support software (7th ed.): Queensland, Australia, Watermark Numerical Computing, 257 p.

- Engelder, T., 2012, Capillary tension and imbibition sequester frack fluid in Marcellus gas shale: Proceedings of the National Academy of Sciences of the United States of America, v. 109, no. 52, article E3625, 1 p., accessed March 23, 2023, at <https://doi.org/10.1073/pnas.1216133110>
- Engler, T.W., Kelley, S., and Cather, M., 2015, Reasonable foreseeable development (RFD) for northern New Mexico, New Mexico: New Mexico Bureau of Geology and Mineral Resources Open-File Report 567, 39 p.
- Fisher, J.C., 2013, Optimization of water-level monitoring networks in the eastern Snake River Plain aquifer using a kriging-based genetic algorithm method: U.S. Geological Survey Scientific Investigations Report 2013–5120, DOE/ID–22224, 74 p., accessed October 23, 2018, at <https://doi.org/10.3133/sir20135120>
- Frenzel, P.F., and Lyford, F.P., 1982, Estimates of vertical hydraulic conductivity and regional ground-water flow rates in rocks of Jurassic and Cretaceous age, San Juan Basin, New Mexico and Colorado: U.S. Geological Survey Water-Resources Investigations Report 82–4015, 67 p., accessed March 23, 2023, at <https://doi.org/10.3133/wri824015>
- Gallegos, T.J., and Varela, B.A., 2015, Data regarding hydraulic fracturing distributions and treatment fluids, additives, proppants, and water volumes applied to wells drilled in the United States from 1947 through 2010: U.S. Geological Survey Data Series 868, 11 p.
- Gassiat, C., Gleeson, T., Lefebvre, R., and McKenzie, J., 2013, Hydraulic fracturing in faulted sedimentary basins—Numerical simulation of potential contamination of shallow aquifers over long time scales: Water Resources Research, v. 49, no. 12, p. 8310–8327, accessed March 23, 2023, at <https://doi.org/10.1002/2013WR014287>
- Gehne, S., and Benson, P.M., 2019, Permeability enhancement through hydraulic fracturing—Laboratory measurements combining a 3D printed jacket and pore fluid over-pressure: Scientific Reports, v. 9, no. 1, article 12573, accessed March 23, 2023, at <https://doi.org/10.1038/s41598-019-49093-1>
- Gregory, K.B., Vidic, R.D., and Dzombak, D.A., 2011, Water management challenges associated with the production of shale gas by hydraulic fracturing: Elements (Quebec), v. 7, no. 3, p. 181–186.
- Harbaugh, A.W., 2005, MODFLOW-2005, the U.S. Geological Survey modular ground-water model—The Ground-Water Flow Process: U.S. Geological Survey Techniques and Methods, book 6, chap. A16 [variously pagged].
- Hill, M.C., Banta, E.R., Harbaugh, A.W., and Anderman, E.R., 2000, MODFLOW-2000, the U.S. Geological Survey modular ground-water model—User guide to the Observation, Sensitivity, and Parameter-Estimation Processes and three post-processing programs: U.S. Geological Survey Open-File Report 00–184, 210 p.
- Kelley, S., Engler, T., Cather, M., Pokorny, C., Yang, C., Mamer, E., Hoffman, G., Wilch, J., Johnson, P., and Zeigler, K., 2014, Hydrologic assessment of oil and gas resource development of the Mancos Shale in the San Juan Basin, New Mexico: New Mexico Bureau of Geology and Mineral Resources Open-File Report 566, 65 p.
- Kernodle, J.M., 1996, Hydrogeology and steady-state simulation of ground-water flow in the San Juan Basin, New Mexico, Colorado, Arizona, and Utah: U.S. Geological Survey Water-Resources Investigation Report 95–4187, 117 p., accessed March 23, 2023, at <https://pubs.er.usgs.gov/publication/wri954187>
- Kernodle, J.M., Levings, G.W., Craig, S.D., and Dam, W.L., 1989, Hydrogeology of the Gallup Sandstone in the San Juan structural basin, New Mexico, Colorado, Arizona, and Utah: U.S. Geological Survey Hydrologic Investigations Atlas HA–720–H, 2 sheets.
- Kissinger, A., Helmig, R., Ebigbo, A., Class, H., Lange, T., Sauter, M., Heitfeld, M., Klunker, J., and Jahnke, W., 2013, Hydraulic fracturing in unconventional gas reservoirs—Risks in the geological system, part 2: Environmental Earth Sciences, v. 70, no. 8, p. 3855–3873.
- Linhoff, S.B., Beisner, K.R., Hunt, A.G., and Shephard, Z.M., 2023, Water quality at Chaco Culture National Historical Park and the potential effects of hydrocarbon extraction: Journal of Hydrology: Regional Studies, v. 47, article 101430, 20 p., <https://doi.org/10.1016/j.ejrh.2023.101430>
- Magnuson, M.L., Valdez, J.M., Lawler, C.R., Nelson, M., and Petronis, L., 2019, New Mexico water use by categories 2015: New Mexico State Engineer Office Technical Report 55.
- Martin, L., 2005, A general description of the hydrogeology, water supply wells, groundwater monitoring, and potential threats to groundwater resources of Chaco Culture National Historical Park, New Mexico: National Park Service Technical Report RPS/NRWRD/NRTR–2005/325, 60 p.
- Meng, Q., 2015, Spatial analysis of environment and population at risk of natural gas fracking in the State of Pennsylvania, USA: Science of The Total Environment, v. 515–516, p. 198–206, accessed March 23, 2023, at <https://doi.org/10.1016/j.scitotenv.2015.02.030>
- Myers, T., 2012, Potential contaminant pathways from hydraulically fractured shale to aquifers: Ground Water, v. 50, no. 6, p. 872–882, accessed March 23, 2023, at <https://doi.org/10.1111/j.1745-6584.2012.00933.x>
- National Oceanic and Atmospheric Administration, [NOAA], 2023, NowData-NOAA online weather data: National Oceanic and Atmospheric Administration database accessed March 23, 2023, at <https://www.nws.noaa.gov/climate.php/xmaxis.php%3fwfo=abq>
- National Park Service [NPS], 2015, Foundation document Chaco Culture National Historical Park—New Mexico: National Park Service, 40 p., accessed March 23, 2023, at https://www.nps.gov/chcu/getinvolved/upload/CHCU_FD_PRINT.pdf
- Parker, J.M., Riggs, E.A., and Fisher, W.L., 1977, Oil and gas potential of the San Juan Basin, in Fassett, J.E., James, H.L., and Hodgson, H.E., eds., New Mexico Geological Survey Twenty-Eighth Field Conference, September 14–17, 1977, Guidebook: Socorro, N. Mex., New Mexico Geological Society, p. 227–241.
- Pollock, D.W., 2016, User guide for MODPATH version 7—A particle-tracking model for MODFLOW: U.S. Geological Survey Open-File Report 2016–1086, 35 p., accessed September 21, 2023, at <https://doi.org/10.3133/ofr20161086>
- R Core Team, 2019, R—A language and environment for statistical computing: Vienna, Austria, R Foundation for Statistical Computing, accessed August 13, 2019, at <https://www.R-project.org/>

- Reneau, W.E., Jr., and Harris, J.D., Jr., 1957, Reservoir characteristics of cretaceous sands of the San Juan Basin: Durango, Colo., Four Corners Geological Society Guidebook, p. 40.
- Ritchie, A.B., and Pepin, J.D., 2020, Optimization assessment of a groundwater-level observation network in the Middle Rio Grande Basin, New Mexico (ver. 2, December 2020): U.S. Geological Survey Scientific Investigations Report 2020–5007, 113 p., accessed March 23, 2023, at <https://doi.org/10.3133/sir20205007>
- Rumbaugh, J.O., and Rumbaugh, D.B., 2011, Tutorial manual for groundwater vistas (ver. 6): Reinholds, Pa., Environmental Simulations, Inc., 258 p.
- Shephard, Z.M., Ritchie, A.B., Linhoff, B.S., and Lunzer, J.J., 2023, MODFLOW-2005 and MODPATH models in support of groundwater flow model investigation of water resources at Chaco Culture National Historical Park: U.S. Geological Survey data release, <https://doi.org/10.5066/P98LTTER>
- Stewart, A.M., 2018, Hydrologic assessment and numerical simulation of groundwater flow, San Juan Mine, San Juan County, New Mexico, 2010–13: U.S. Geological Survey Scientific Investigations Report 2017–5155, 94 p., accessed March 23, 2023, at <https://doi.org/10.3133/sir20175155>
- Stone, W.J., Lyford, F.P., Frenzel, P.F., Mizell, N.H., and Padgett, E.T., 1983, Hydrogeology and water resources of San Juan Basin, New Mexico: Socorro, N. Mex., Bureau of Mines and Mineral Resources Hydrologic Report 6, 70 p.
- U.S. Census Bureau, 2020, QuickFacts—New Mexico: U.S. Census Bureau, accessed March 23, 2023, at <https://www.census.gov/quickfacts/fact/table/US/PST045222>
- U.S. Department of Energy, 2009, Modern shale gas development in the United States—A primer: U.S. Department of Energy, Office of Fossil Energy, National Energy Technology Laboratory, prepared by Ground Water Protection Council, Oklahoma City, Oklahoma, and ALL Consulting, Tulsa, Okla., 116 p.
- U.S. Energy Information Administration, 2015, Annual energy outlook 2015: Washington, D.C., Office of Integrated and International Energy Analysis, 154 p., accessed March 23, 2023, at <https://www.nrc.gov/docs/ML1617/ML16172A121.pdf>
- U.S. Geological Survey, 2022, National Water Information System: U.S. Geological Survey database, accessed March 23, 2023, at <https://nm.water.usgs.gov/infodata>
- Vengosh, A., Jackson, R.B., Warner, N., Darrah, T.H., and Kondash, A., 2014, A critical review of the risks to water resources from unconventional shale gas development and hydraulic fracturing in the United States: Environmental Science & Technology, v. 48, no. 15, p. 8334–8348.

DATUM

Vertical coordinate information is referenced to the North American Vertical Datum of 1988 (NAVD 88) and the National Geodetic Vertical Datum of 1929 (NGVD 29).

Horizontal coordinate information is referenced to the American Datum of 1983 (NAD 83).

Elevation, as used in this report, refers to distance above the vertical datum.

ABBREVIATIONS

CCNHP	Chaco Culture National Historical Park
GIS	geographic information system
GWV	Groundwater Vistas
HF	hydraulic fracturing
HK	horizontal hydraulic conductivity
NPS	National Park Service
RM	residual mean
UNESCO	United Nations Educational, Scientific and Cultural Organization
USGS	U.S. Geological Survey
VK	vertical hydraulic conductivity

Conversion Factors

U.S. customary units to International System of Units

Multiply	By	To obtain
Length		
foot (ft)	0.3048	meter (m)
mile (mi)	1.609	kilometer (km)
Area		
square mile (mi ²)	2,590	square kilometer (km ²)
Volume		
gallon (gal)	3.785	liter (L)
gallon (gal)	0.003785	cubic meter (m ³)
gallon (gal)	3.785	cubic decimeter (dm ³)
cubic foot (ft ³)	28.32	cubic decimeter (dm ³)
cubic foot (ft ³)	0.02832	cubic meter (m ³)
acre foot (acre ft)	0.001233	cubic meter (m ³)
Flow rate		
inch per day (in/d)	2.54	centimeter per day (cm/d)
inch per year (in/yr)	2.54	centimeter per year (cm/yr)
foot per day (ft/d)	0.3048	meter per day (m/d)
cubic foot per day (ft ³ /d)	0.02832	cubic meter per day (m ³ /d)
gallon per day (gal/d)	0.003785	cubic meter per day (m ³ /d)
Hydraulic conductivity		
foot per day (ft/d)	0.3048	meter per day (m/d)

International System of Units to U.S. customary units

Multiply	By	To obtain
kilometer (km)	0.6214	mile (mi)

Temperature in degrees Fahrenheit (°F) may be converted to degrees Celsius (°C) as follows:

$$^{\circ}\text{C} = (^{\circ}\text{F} - 32) / 1.8.$$

For more information about this report, contact

Director, New Mexico Water Science Center

U.S. Geological Survey

6700 Edith Blvd. NE

Albuquerque, NM 87113

For additional information, visit

<https://www.usgs.gov/centers/nm-water>

For more information on the USGS—the Federal source for science about the Earth, its natural and living resources, natural hazards, and the environment—visit <https://www.usgs.gov> or call 1-888-ASK-USGS.

The Need for Constructing Endangered Fish Habitats that Conform to Climate-driven Flow Changes in a Western U.S. River

Richard A. Valdez¹

¹SWCA Environmental Consultants,
Logan, Utah, USA

Colleen Cunningham², Ali Effati²

²New Mexico Interstate Stream Commission,
Santa Fe, New Mexico, USA

Deborah L. Freeman³

³Trout Raley Montañó Freeman Sinor Thompson P.C.,
Denver, Colorado, USA

ABSTRACT

Warmwater fish habitat in the San Juan River of the southwestern United States has been reduced by over 30% as a result of water depletion, reservoir inundation, and cold-water dam releases combined with drought-related changes in hydrology. This reduction and a suite of other factors have contributed to declines in native fish populations including the federally endangered Colorado Pikeminnow (*Ptychocheilus lucius*) and Razorback Sucker (*Xyrauchen texanus*). Conservation efforts for these species include determining flow needs; protecting, managing, and augmenting habitats; and stocking hatchery fish. But the young of stocked fish have low survival due largely to a paucity of nursery habitat not being reformed and maintained under current conditions. Flow recommendations for Navajo Dam releases designed to mimic the river's natural hydrograph have not been met due to water shortages, and the desired outcomes of increased channel complexity and enhanced fish habitat have not been observed. Forecasted hydrology that includes ongoing drought shows that achieving the flow targets through further dam reoperations is unlikely. Mechanical construction of early life-stage habitats is a highly recommended complement to flow management for offsetting the effects of flow reduction and habitat loss. Habitats with features that are effective and resilient under a range of flows are important in counterbalancing the effects of climate change.

1. INTRODUCTION

Restoring and creating riverine habitats that inundate under reduced flow regimes to support targeted life stages of fishes is a strategy for enhancing populations of imperiled species in altered rivers worldwide (Petts, 1998; Thoms & Sheldon, 2000; Wilby et al., 2010). Drought has exacerbated human-altered flows in western United States (U.S.) rivers, further reducing flow magnitude and lessening the efficacy of natural and constructed fish habitats (Beechie et al., 2012; Jaeger et al., 2014). Declining catchment runoff in regulated rivers could further reduce the effectiveness of environmental flows that have lower priority in most years

(Pennock et al., 2022). These conditions have prompted the need to design and mechanically construct sites at varying elevations that inundate at reduced and managed flows as part of an overall conservation strategy for imperiled fish species (BioWest, 2005; Chen & Olden, 2017; Large & Petts, 1994; Valdez et al., 2019).

The San Juan River of the southwestern U.S. has undergone substantial geomorphic and hydrologic changes with consequent effects on ecological processes and native fish populations. The San Juan is a major tributary of the Colorado River that forms one of the three major subbasins of the Upper Colorado River Basin (upper basin; Figure 1), contributing about 15% of flow volume (Bennett et al., 2019). Dams and water diversions in the San Juan control floods and provide irrigation and domestic water supplies such that present water uses combined with climate change have resulted in annual flow reductions of about 30% below historical levels (Bennett et al., 2019). These flow reductions have led to channel narrowing, reduced in-channel fish habitats, and reduced lateral connectivity with floodplains. Also, reservoir inundation of the lower reach and cold hypolimnetic dam releases in the upper reach have left only about 362 km of warmwater fish habitat that supports small numbers of native fishes (Holden, 2000), including two species protected under the Endangered Species Act, the Colorado Pikeminnow (CPM; *Ptychocheilus lucius*) and Razorback Sucker (RBS; *Xyrauchen texanus*).

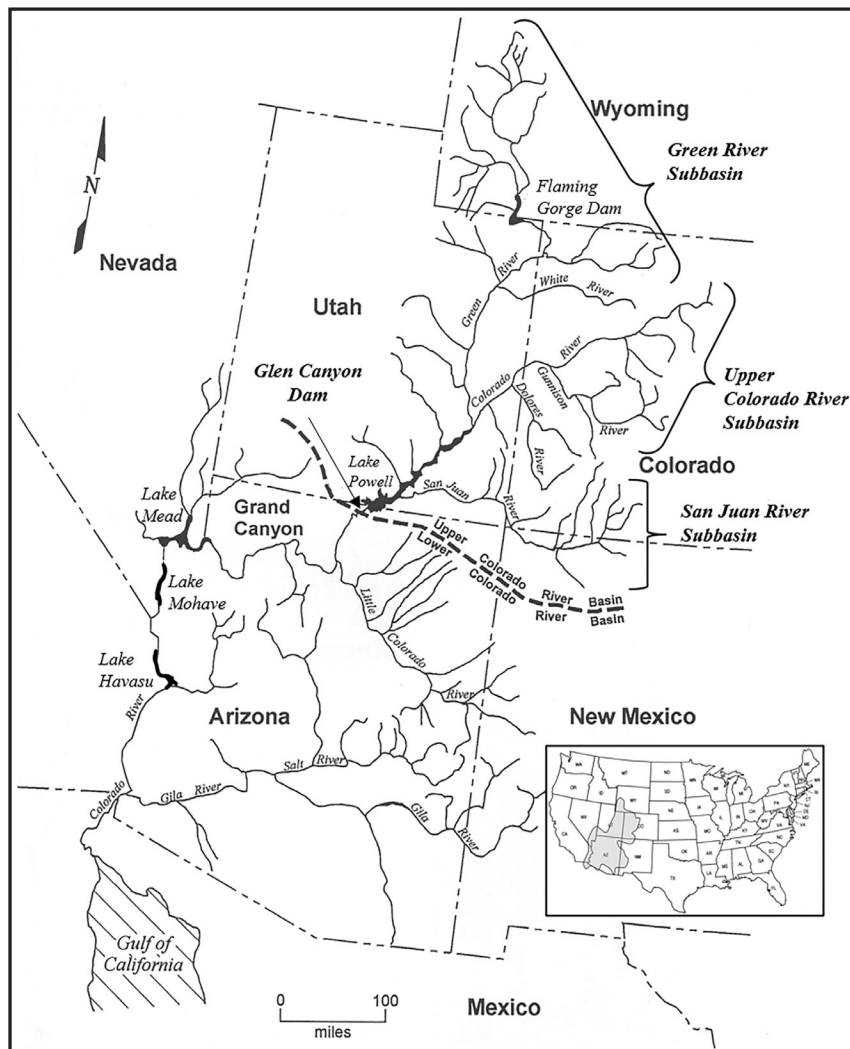


Figure 1. Map of the Colorado River and the three major subbasins of the upper basin.

The San Juan River Basin Recovery Implementation Program (SJRIP) was established in 1992 to protect and recover the CPM and RBS in the San Juan River, while water development proceeds in compliance with applicable federal and state laws (www.coloradoriverrecovery.org). Conservation of these species includes research to determine species flow needs, and protection, management, and augmentation of habitats (SJRIP, 2016). These conservation efforts have struggled to address the flow-to-habitat relationships that provide river flows necessary to sustain various life stages of these species. Flow recommendations in 1999 formulated releases from Navajo Dam to mimic the natural hydrograph for the benefit of the endangered and native fish species in the available warmwater habitat (Holden, 1999). In the ensuing 15 years, these flow targets were not regularly met, and the expected levels of channel complexity and enhanced native fish habitat were not observed. Subsequent evaluation of the flow recommendations showed that further modifying dam releases could slightly increase the ability to meet the flow targets, but it was unlikely that the recommendations could be met with the existing and forecasted hydrology under ongoing drought and climate change conditions (SJRIP, 2018a).

Seven years of research (1991–1997) found low numbers of wild CPM and no RBS in the San Juan River (Holden, 2000), and hatchery fish have been stocked since 1994 to augment the populations. Some stocked fish are reproducing but survival of the young of both species is low (USFWS, 2018, 2020) largely because of a paucity of nursery habitat that is not being reformed and maintained by present flows (Barkalow et al., 2020; Farrington et al., 2020). To augment and enhance fish habitats, the SJRIP is designing and constructing riverine features that will support early life stages of the species (Bliesner & Lamarra, 2007; Keller-Bliesner Engineering, 2018).

This paper explores the historical and present condition of fish habitats in the San Juan River and proposes large-scale construction of early life-stage habitat, with sites designed to become inundated at available river flows, as one tool to support conservation of CPM and RBS. We compare the San Juan River with other river reaches used by CPM and RBS to contextualize habitat design and construction appropriate for the contemporary San Juan. A number of factors contribute to low survival and recruitment of CPM and RBS in the San Juan River—including low numbers of spawning adults (Diver & Wilson, 2018), encroachment of fish habitats by non-native vegetation (Bassett, 2015), predation and competition from non-native fishes (Franssen et al., 2015), high emigration of young (Cathcart et al., 2017, 2018), and a paucity of available rearing habitat (Farrington et al., 2020)—all of which are being explored by the SJRIP (SJRIP, 2016). We recommend that mechanical construction of early life-stage habitats be implemented to complement flow management in the San Juan River given the present geomorphic state of the river and the reduced flow from ongoing drought.

2. THE SAN JUAN RIVER

2.1 Historical zoogeographical setting

Understanding the zoogeographical setting of the Colorado River is important in understanding the historical and contemporary ecological roles of the principal tributaries and their habitats in the life histories of the CPM and RBS. Geological evidence suggests that the Upper Colorado River has been in its present course for more than 5 million years and historically flowed into one or more closed basins south of the upper end of present-day Grand Canyon (Luchitta, 1990). About 5 million years ago (late Miocene/early Pliocene), the river began carving its way through the Colorado Plateau forming the Grand Canyon, and the upper basin joined with the more dispersed streams of the lower basin in the last 2–3 million years (McKee et al., 1967). Fish species that evolved primarily in the upper basin (including the CPM) were mostly large riverine forms, and those that evolved in the lower basin (likely the RBS) were associated with small streams and lacustrine habitats (Miller, 1961; Minckley et al., 1986).

2.1.1 *Colorado Pikeminnow*

Archeological evidence suggests that the CPM evolved as a highly migratory piscivore that ranged from tributaries of the upper basin as far downriver as the estuarine zone in the Gulf of California (Miller, 1961). Biochemical genetics show evidence of multiple stocks of CPM in tributaries of the upper basin with genetic

panmixia indicating constant interchange of genes among the stocks or subpopulations (Morizot et al., 2002). This hypothesis of multiple interconnected stocks is supported by long-distance movements and strong fidelity of adults in contemporary subpopulations to particular tributaries and reflects the development of powerful selection mechanisms that evolved over thousands of years (Irving & Modde, 2000; Tyus, 1990).

The CPM that used the San Juan River historically were likely one stock that inhabited the mainstem Colorado River through Glen Canyon and spawned in the San Juan, similar to the portion of the contemporary Green River population that resides in the mainstem and spawns in the tributary Yampa River (Bestgen et al., 2007). The disruption of migratory pathways by dams and the loss of large reaches of habitat to reservoir inundation starting with Hoover Dam in 1935 likely triggered the decline of the San Juan stock of CPM, as well as others in the lower basin. The few remaining wild fish in the San Juan River likely represent a remnant stock of fish persisting as long-lived adults with periodic successful reproduction, but these fish presently lack the full complement of habitats otherwise found in rivers with self-sustaining populations (USFWS, 2020).

2.1.2 Razorback Sucker

Contemporary collections and taxonomic analyses of RBS indicate historical long-term residence in interconnected lake habitats formed by lava flow dams in western Grand Canyon in the last 1.8 million years and by melting Pleistocene glaciers in the last 12,000–15,000 years (Hubbs & Miller, 1953; McKee et al., 1967; Minckley et al., 1986). At least 13 major lava dams impounded the Colorado River through the Grand Canyon with some persisting at least 250,000 years before eroding (Rugg & Austin, 1998). These dams created a series of large lakes, with the most recent ~400,000 years ago. Shoreline deposits show that the largest dam at Lava Falls Rapid impounded a lake 90 m above the high-water level of present-day Lake Powell and backed water for a distance of over 480 km to Moab, Utah (Duffield, 1997).

The evolution of the RBS is likely closely linked to these early and extensive lacustrine habitats of the lower basin. The present diversity of mitochondrial DNA in RBS from Lake Mohave is remarkably high, indicating that the contemporary population is comprised of direct descendants of a large, diverse, panmictic population that historically inhabited the lower basin. Whereas populations in the upper basin are less diverse and possess fewer unique genotypes, suggesting that the RBS thrived in the early lakes and abundant floodplains of the lower basin before dispersing to other parts of the Colorado River system (Dowling et al., 1996).

The evolutionary history of the RBS helps to explain its contemporary predisposition to riverside floodplains and lacustrine environments. The species has been able to survive and reproduce in artificial reservoirs in the last 85 years (lakes Mohave, Havasu, and Mead) before experiencing sharp declines due to predation of young by non-native fishes and a lack of early life-stage habitats (USFWS, 2018). The evolutionary and genetic evidence indicate that the RBS requires floodplain-like nursery habitats that are absent from the contemporary San Juan River. The numbers of young RBS hatched in the San Juan River are low likely in part to a paucity of nursery floodplain habitat. However, there is some recruitment in low water years when low velocities and warm water temperatures provide some shallow-water habitats (Barkalow et al., 2020).

Spawning habitat may also be limited for the RBS in the San Juan River. A high level of hybridization with the Flannelmouth Sucker (*Catostomus latipinnis*) (23.7% of larvae and 100% of juveniles) may be due to small numbers of RBS spawning with aggregations of Flannelmouth Sucker in limited habitat (Mussmann et al., 2022). Notably, survival of the young hybrids appears higher than that of young RBS (Mussmann et al., 2022), indicating different and distinct habitat needs.

2.2 The contemporary San Juan River

Changes in land and water uses in the last century have reduced overall San Juan River flows and narrowed and simplified the river channel (Bennett et al., 2018, 2019). Man-made reservoirs have also inundated reaches of riverine habitat important to the CPM and RBS. Glen Canyon Dam and Navajo Dam were completed in 1963, and by the mid-1980s, Lake Powell had inundated the lower 87 km of river, Navajo Reservoir had inundated 43 km of the upper river, and Navajo Dam releases had cooled the river 69 km downriver to the

Animas River confluence (Figure 2). These changes reduced potential range and habitat of the CPM and RBS in the San Juan by about 31%, from about 523 to 362 km (Animas River confluence down to Lake Powell inflow near Clay Hills; Holden, 2000). Lake Powell also inundated the mainstem Colorado River for about 145 km upriver and 110 km downriver of the San Juan River confluence, eliminating much of the connecting mainstem habitat that was likely occupied by CPM and RBS. When lake elevation is below about 1097 m, deltaic sediments are exposed and a waterfall forms at Piute Farms Canyon, creating a barrier about 87 km upriver of the historical Colorado River confluence that prevents fish that move downriver from returning upriver (Cathcart et al., 2018). The Piute Farms waterfall is not a feature of the historical river, having been formed as the river carved a new channel through Lake Powell sediments during 1989–1995 and 2001–present.

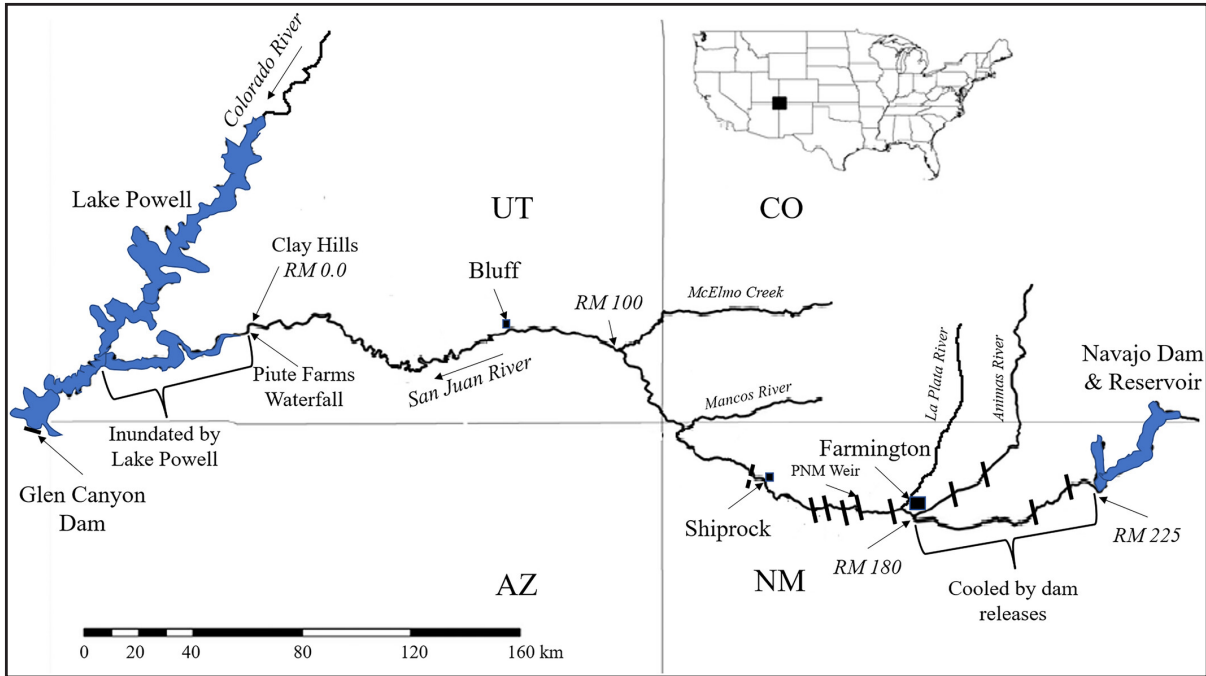


Figure 2. Map of the San Juan River from Navajo Dam downriver to the Lake Powell inflow, with river miles (RM) as distances upriver from Clay Hills near the Lake Powell inflow.

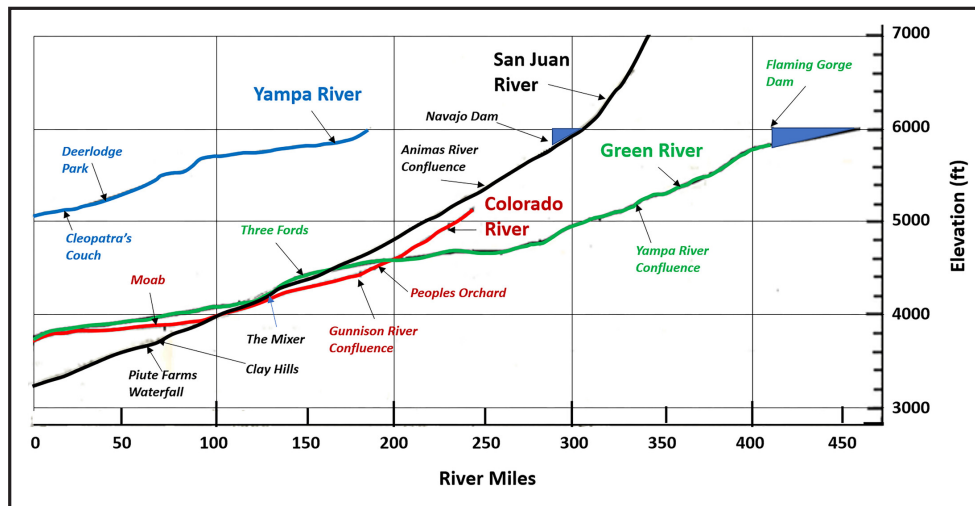


Figure 3. Channel gradients of the San Juan, Green, Yampa, and Colorado rivers. Gradients of individual rivers from Google Earth. Profiles and locations are color coded.

Of the three recovery units of CPM (USFWS, 2002a), the San Juan River has the least available longitudinal habitat. Wild populations of CPM remain in about 1754 km of the two other subbasins, including 1278 km in the Green River and 476 km in the Upper Colorado River (Miller, 2014). These reaches are considerably longer than the 362 km of habitat available in the contemporary San Juan River. The San Juan also has the steepest channel gradient of any major tributary used by CPM and RBS. For the 362 km of river from the confluence with the Animas River to Lake Powell, mean gradient is 1.91 m/km and maximum is 4.0 m/km (Holden, 1999), whereas mean gradients of the Green and Colorado rivers are 1.26 and 1.42 m/km, respectively (Figure 3). The San Juan is narrower, steeper, and shallower than the Green and Upper Colorado rivers. This geomorphology, combined with non-native vegetation anchoring the shorelines, limits the formation of backwaters used as nursery habitats by young CPM and the nursery floodplains used by young RBS. Historical photographs of the lower San Juan River and the mainstem Colorado River through Glen Canyon (Inskip, 1995) provide evidence that before these areas were inundated by Lake Powell, they contained low-gradient, sand-bed channels with backwaters and tributary inflows characteristic of nursery habitats used by CPM and RBS in other rivers.

2.3 Flow recommendations

The 1991 Biological Opinion for the Animas-La Plata Project, a water project in southwestern Colorado and northwestern New Mexico, contained a reasonable and prudent alternative (RPA) identified by the U.S. Fish and Wildlife Service (USFWS) to avoid the likelihood of jeopardizing the CPM and RBS. The RPA included a 7-year research period, reoperation of Navajo Dam, and a commitment by the U.S. Bureau of Reclamation (USBR) and others to develop and implement the SJRIP (USFWS, 1991). This opinion reflected the USFWS's belief that the small numbers of wild CPM and RBS in the San Juan River represented historical populations that had declined because of human alteration of the hydrology, and that these species could be recovered in the San Juan by restoring its flow and habitat (Gosnell, 2001).

By the mid-1990s, it was estimated that the population of wild CPM in the San Juan River was less than 100 individuals and possibly fewer than 50 (Holden, 1999). The RPA's research period (1991–1997) was intended to quantify relationships of flow to fish habitat, but direct relationships were not derived primarily because only 22 young and 13 adult CPM and no RBS were collected (Holden, 2000). To augment the existing populations and to better understand habitat use and flow needs, nearly six million young hatchery CPM and over 200,000 juvenile and adult RBS were stocked in the San Juan from 1994 to 2020.

In 1999, the SJRIP adopted year-round flow recommendations for the San Juan River that biologists thought would benefit the native fishes (Holden, 1999). The flow recommendations were designed to provide water at specified times, quantities, and durations while maintaining the authorized purposes of Navajo Dam. The primary high flow targets were flow rate (e.g., 5000 ft³/s [142 m³/s]), minimum duration (e.g., 14 days), and annual frequency (e.g., 33% of years). Secondary targets addressed maximum duration between occurrences (e.g., not to exceed 6 years without reaching 97% of target flow). It was assumed that flow targets would be met if the future hydrology of the San Juan River was statistically the same as the modeled period of record (1929–1993), but the ensuing hydrology was drier than the modeled period and the flow targets were not met (SJRIP, 2018a).

Drought in the San Juan River subbasin resulted in less available water than the modeled period of record, reducing the ability to achieve the higher primary and secondary flow targets. Aside from continual dam releases to maintain base flows, the only high releases were of short duration, and these impeded the ability to recover reservoir storage and further decreased the availability of water for future long-duration releases and elevated baseflows (SJRIP, 2018a). During this period of drought, there was a general deterioration of desirable backwater and secondary channel habitats that was attributed to the lower flows, associated dam operations, and increasing impacts of non-native vegetation that stabilized the river banks and reduced habitat complexity (Lamarra & Lamarra, 2016).

Following a review of the 1999 flow recommendations and new water calculations in 2014, an adjustment was made to the dam operating rules under a new decision tree. This adjustment revealed that it was unlikely

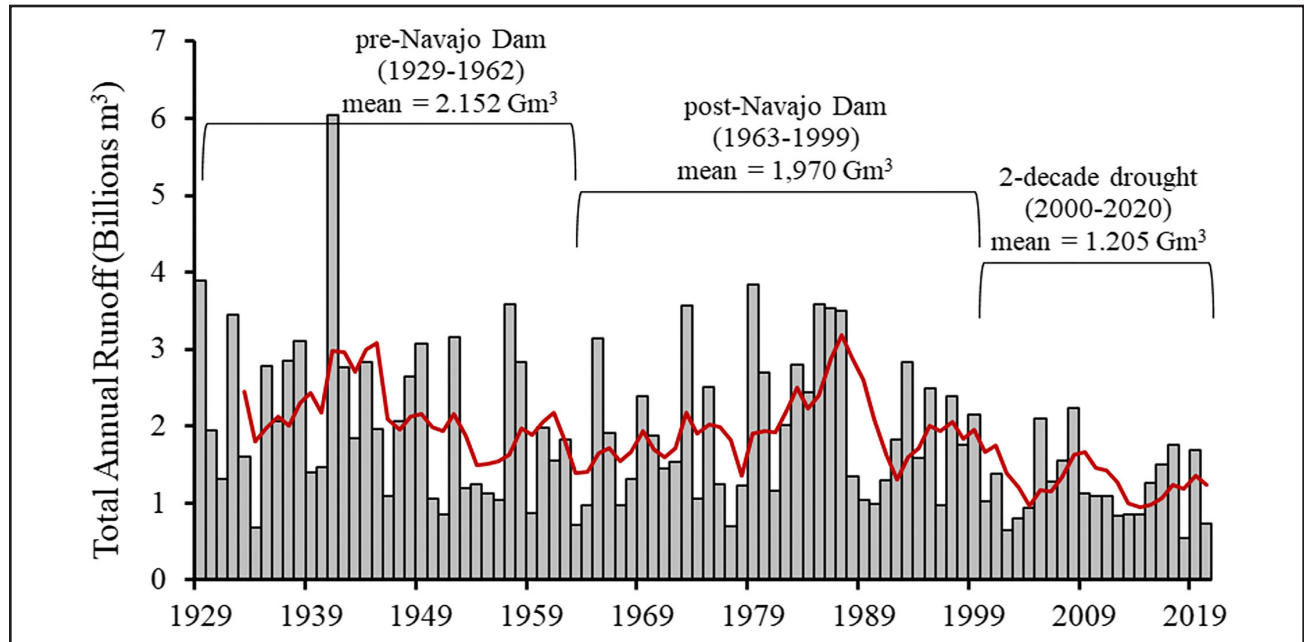


Figure 4. Total annual runoff volume (gray bars) and 5-year moving average (solid line) in billions of cubic meters (Gm³) for the San Juan River near Bluff, Utah (USGS #09379500), 1929–2020. Average annual volumes are shown for 1929–1962, 1963–1999, and 2000–2020.

the recommendations could be met under the existing and forecasted hydrology that included drought and climate change (SJRIP, 2018a).

2.4 Influence of drought and climate change on river hydrology

2.4.1 Historical drought

Dam construction and water projects have decreased the flow of the San Juan River since the early 20th century, and prolonged drought has exacerbated water supply shortages in the last two decades (Figure 4). The present drought in the Colorado River has persisted since 2000 with the period from 2000 through 2020 as the driest 21-year period in more than 100 years of record-keeping, and one of the driest in the past 1200 years based on paleohydrology data (USBR, 2021). Average monthly discharge near Bluff, UT (U.S. Geological Survey [USGS] #09379500) was 2409 ft³/s (68 m³/s) for the period before construction of Navajo Dam (1929–1962) and 2205 ft³/s (62 m³/s) for the period after construction (1963–1999). Persistent drought in the 21st century (2000–2020) has further reduced flow at Bluff to an average discharge of 1348 ft³/s (38 m³/s) for a 44% decline from the pre-dam period. Average annual water volume has decreased from 1,745,200 acre-ft (2.152 Gm³) in 1929–1962 to 976,957 acre-ft (1.205 Gm³) in 2000–2020, also a 44% decline.

2.4.2 Impacts of climate change on hydrology

Studies of the present and future effects of climate change on the Colorado River system, and specifically the San Juan River subbasin, show the likelihood of a continued decline in water supplies. A multi-model framework analysis found that the subbasin could experience significant disruptions to water deliveries (–12% to –48% for the drier models) and shortages of 53%–73% that exceed manageable thresholds, potentially affecting the subbasin as well as other regions that receive water and energy from the San Juan River (Bennett et al., 2019).

Hydrologic modeling (Precision Water Resources Engineering, 2020) also shows that climate change impacts to overall water supplies for Navajo Reservoir and the San Juan River could range from 2% to 8% increases in

a mid-low impact scenario (25 percentile impacts observed from over 200 projections) to significant decreases of 21%–26% in a mid-high impact scenario (75 percentile). A center impact scenario (50 percentile) suggests decreases ranging 10%–16% for the period extending to the year 2050, with slightly higher impacts to the year 2070. While these results show the possibility of increasing overall water supplies under some climate projections, the downward trends of the center impact scenario and most other projections are a strong signal for decreasing future water supplies in the San Juan River subbasin.

These modeling scenarios also show that average annual Navajo Dam outflows could decrease significantly, with the center impact scenario showing decreases of 19% in the 2050 time period and 23% in the 2070 period, while the mid-high impact scenario shows a 33% decrease (Precision Water Resources Engineering, 2020). This translates to a frequency of achieving the high flow targets (spring peak releases) in only about 25% of years under the center impact scenario and about 15% of years under the mid-high impact scenario. Modeling also suggests that Navajo Reservoir spring peak inflows could shift to earlier in the year by about 3 weeks for the 2050 period and by about another week for the 2070 period, potentially changing the timing of available water for spring high flow releases. These analyses confirm the low likelihood of achieving the higher targets of the flow recommendations into the future.

2.5 Channel simplification

Reductions in channel area and island numbers have occurred in recent decades in the San Juan River. This is in contrast to studies that show a fairly consistent and diverse channel geomorphology for the San Juan River in the early 1900s. Two studies using aerial imagery (Bassett, 2015; Bliesner & Lamarra, 2000) found that island area in the mid-1930s was similar at about 1619 and 1862 ha, respectively, a difference of 15%. Channel area was just over 5868 ha compared to less than 5787 ha, a difference of 1.8%, and the number of islands was 616 compared to 865. Channel and island areas were relatively consistent between the two studies, but island counts varied probably because different criteria were used to define islands and a different scale was used during feature digitization.

Annual mapping has documented large decreases in island counts and channel area throughout the Colorado River system starting in the mid-1900s, including the San Juan River subbasin. The most common mechanisms for island losses appear to be the closing off of secondary channels by vegetation encroachment and sedimentation, and abandonment by downcutting of the main channel (Bassett, 2015). In the 1930s, riverine vegetation was primarily stands of cottonwoods but by 1994, non-native vegetation accounted for 67% of all riparian vegetation that was primarily invasive Russian olive (*Elaeagnus angustifolia*) and tamarisk (*Tamarix* spp.) (Bliesner & Lamarra, 2000). These vegetative changes together with altered flow regimes led to channel simplification of the San Juan, where habitats essential to native fishes are less prevalent. Significant decreases in low-velocity habitats were seen in the mid-1990s and early 2000s that further contributed to the decline of the native fishes (Holden, 1999). These geomorphic changes reduced the areas of backwaters, embayments, and secondary channels in the San Juan River that provide low-velocity habitats for larvae and young fishes, including CPM and RBS (Farrington et al., 2020).

3. DISCUSSION

There was general acknowledgment at the onset of the SJRIP of the low numbers of wild CPM and RBS and the limited quantity and quality of key native fish habitats in the San Juan River (Gosnell, 2001; Holden, 1999). Members of the SJRIP embraced flow management as the key conservation paradigm to support and enhance the habitat features needed for reestablishing self-sustaining populations of these species in the San Juan. Flow recommendations were designed to mimic the natural hydrograph through releases from Navajo Dam, with the assumption that flow targets would benefit the native fishes and continually reshape and diversify the habitat. The 7-year research period that preceded the flow recommendations was unable to unambiguously derive flow-to-habitat relationships for the San Juan River because the low numbers of wild CPM and the absence of RBS precluded direct measures of habitat use. The high flow targets were not met due to ongoing drought and fish habitat continued to degrade through channel simplification and increased

substrate embeddedness. To better understand species habitat use, and to augment the populations, nearly six million hatchery CPM and RBS were stocked in the San Juan from 1994 to 2020.

Notwithstanding this substantial stocking, survival and recruitment of wild-produced fish beyond their first year of life have been low (USFWS, 2018, 2020), and studies show a bottleneck limiting development to adulthood (SJRIP, 2018b). Reproduction of CPM has been documented annually since 2013 with increasing catches of larval fish over time, but recruitment beyond the first year of life is limited (Farrington et al., 2020). Similarly, the population of RBS in the San Juan is comprised primarily of stocked fish and although there is annual reproduction, there is little evidence of survival and recruitment of young (Barkalow et al., 2020). A population viability analysis for CPM concluded that based on present survival and recruitment rates, the San Juan population would be extirpated in about 30 years (approximate species longevity) following cessation of stocking (Miller, 2014), revealing the low viability of the population in the absence of stocking.

Studies show that young CPM and RBS use low-velocity habitats in the San Juan River, including backwaters and side channels (e.g., Farrington et al., 2020). These habitats are not common features of the San Juan (Lamarra & Lamarra, 2016) and they occur in lower abundances than in the Green and Upper Colorado rivers (Miller, 2014), where wild populations of these species are self-sustaining. Low survival and recruitment of wild-produced CPM and RBS in the San Juan River appear to be inextricably linked to the paucity of suitable backwaters and the absence of riverside floodplains. One of the working hypotheses developed by the SJRIP to explain identified recruitment bottlenecks for CPM and RBS is that “availability of rearing habitats affects rates of recruitment” (SJRIP, 2018b). A comprehensive conservation strategy for these endangered fishes should include affirmative management to develop and enhance suitable rearing habitats as a complement to flow management and other efforts in view of this recruitment bottleneck.

Table 1. Habitats of Colorado Pikeminnow and Razorback Sucker by life stage in occupied rivers (Green and Upper Colorado) compared to the San Juan River (USFWS, 2002a, 2002b).

Life stage	Green and Upper Colorado rivers	San Juan River
Colorado Pikeminnow		
Adult movement and migration	<ul style="list-style-type: none"> Green: long-distance movements by wild adults to spawning sites (up to 950km roundtrip); high fidelity for sites Upper Colorado: more dispersed movements to various sites 	<ul style="list-style-type: none"> Long-distance movements by stocked adults to suspected spawning sites Downriver movement results in fish dropping below Piute Farms waterfall with no upriver return, except for assisted translocation
Spawning sites	<ul style="list-style-type: none"> Known spawning sites on cobble/gravel bars in high gradients River gradients of 0.0016, 0.0010, and 0.0015 	<ul style="list-style-type: none"> Known spawning area on cobble/gravel bar in high gradient River gradient of 0.0015
Drift corridors	<ul style="list-style-type: none"> Larvae drift from spawning sites to sand backwaters Distances of 69-208, 48-204, and 191-294km 	<ul style="list-style-type: none"> No defined larval drift corridors Most larvae found in lower reaches Evidence of drift of ~160km
Larval nurseries	<ul style="list-style-type: none"> Sand backwaters in low-gradient reaches commonly used by larvae and age-0 	<ul style="list-style-type: none"> Larvae most commonly found in backwaters and side channels Age-0 and age-1 found in all low-velocity habitats, not riffles
Razorback Sucker		
Adult movement and migration	<ul style="list-style-type: none"> Documented movements mostly for hatchery-stocked juveniles and adults Long-distance movements to spawning sites Longest mean distance moved 454.6 km 	<ul style="list-style-type: none"> Documented movements for hatchery-stocked juveniles and adults Long-distance movements to suspected spawning sites and into and across Lake Powell Individual movements of >600km
Spawning sites	<ul style="list-style-type: none"> Known spawning sites on cobble/gravel bars in high gradients River gradients of 0.0013 and 0.0014 	<ul style="list-style-type: none"> Known spawning area on cobble/gravel bar in low gradient River gradient of 0.0015
Drift corridors	<ul style="list-style-type: none"> Larvae drift from spawning sites to riverside floodplains Distances of 18-97, 1-23, and 1-50km 	<ul style="list-style-type: none"> No defined larval drift corridors Most larvae found in lower reaches
Larval nurseries	<ul style="list-style-type: none"> Riverside floodplains in low to moderate-gradient reaches most commonly used by larvae, age-0, and age-1 	<ul style="list-style-type: none"> Low depressions for riverside floodplains are not present in the San Juan River Young use low-velocity habitats

Mechanical construction of nursery habitats is highly recommended for the San Juan River to enhance present habitat availability and to counterbalance the effects of reduced flows from ongoing drought. A well-designed plan is essential for mechanically constructing habitats that are strategically located and can function under a variety of expected flow conditions and also meet life-history needs. The following sections discuss the need for constructing nursery habitats in the San Juan River and offer considerations for habitat construction, based on experiences from other river basins.

3.1 Requisite nursery habitat characteristics

3.1.1 *Colorado Pikeminnow*

While subadult and adult CPM in the Green and Upper Colorado rivers typically use runs, eddies, and pools (USFWS, 2002a; Table 1) that are among the most common habitats in the San Juan (Bliesner & Lamarra, 2007), the larvae and age-0 stages require a different and more limited habitat type. This is characterized as a backwater that is a small water feature surrounded on three sides by land with a narrow, typically downriver connection to the main channel. The preferred sandy backwaters develop during receding flows as scour channels at the toe and periphery of large main-channel sand bars, or at the lower end of isolated side channels (Muth et al., 2000). They are formed at the end of spring runoff within the active channel and are not floodplain features (Figure 5; USFWS, 2002a, 2020).



Figure 5. Sandy alluvial backwater used as nursery habitat by larvae and age-0 Colorado Pikeminnow in the Green River, Utah (left). Typical floodplain of the Green River, Utah, used as nursery habitat by larvae and age-0 Razorback Sucker (right).

Habitat studies of the San Juan River show that backwaters are among the least numerous habitats present and comprise the least habitat area (Bliesner & Lamarra, 2007). This indicates that there are likely insufficient quantities of this nursery habitat for larvae and age-0 CPM in the San Juan, particularly in the upper predominantly rocky reaches. On a longitudinal scale, the numbers of backwaters are fewer than 5 per mile upriver of the Stateline (RM 120), and fewer than 10 per mile downriver, a pattern that is consistent with the notion that nursery habitat is principally in the lower river (Bliesner & Lamarra, 2007). The numbers of backwaters in the Green and Upper Colorado rivers are two to three times greater than in the San Juan River (Miller, 2014).

3.1.2 *Razorback Sucker*

Subadult and adult RBS in the Green and Upper Colorado rivers typically use deep runs, eddies, large backwaters, and flooded off-channel habitats (USFWS, 2002b; Table 1). These are among the most common habitats in the San Juan River, except for the absence of floodplains (Bliesner & Lamarra, 2007) that are used by the larval and age-0 stages in other rivers. Riverside floodplains (USFWS, 2018) form in bottomlands, low-lying wetlands, and oxbow channels that flood ephemerally and connect to the main channel during spring runoff (Figure 5). These areas provide warm temperatures, low-velocity habitats, and high levels of food in the form of small invertebrates. The density of zooplankton in floodplains of the Green River can be 29 times greater than in backwaters and 157 times greater than in the main channel (Mabey & Shiozawa, 1993). The high productivity of floodplains is important as laboratory studies show that RBS larvae need to feed within 8–19 days of hatching to avoid starvation (Papoulias & Minckley, 1990). The large numbers of RBS found in the Lake Powell inflow (Cathcart et al., 2018) show the species' propensity for lacustrine habitats.

3.2 Efficacy of constructed habitats

3.2.1 Need for large-scale habitat restoration for early life stages

For the nearly 30 years that the SJRIP has been in existence, a great deal has been learned about the geomorphology, hydrology, and biology of the San Juan River, including the life histories of the endangered fishes. The low survival of young and their low recruitment is compelling evidence that the San Juan lacks the full complement of conditions necessary to support self-sustaining populations of CPM and RBS. The time has come to recognize that the river in its present state is not entirely suitable for conservation of the species largely because of a paucity of nursery habitats and the inability of the drought-driven hydrology to shape and maintain those habitats. We recommend a greater focus by the SJRIP toward a habitat restoration program for early life stages of CPM and RBS by utilizing mechanical habitat construction and maintenance as a complement to flow management measures. Increasing the availability of these habitats will provide places for CPM and RBS to grow past the sensitive larval life stage and recruit to the adult populations.

To date, mechanical treatments in the San Juan River have removed non-native vegetation and sediment plugs from secondary channel inlets and old secondary and tertiary channels. Over 27 ha of aquatic habitat were restored between 2008 and 2014 (Bassett, 2015). Preliminary monitoring indicates that mechanical treatments may be producing the intended results on a local level, including similar fish population density and species composition in restored channels and adjacent natural channels (Franssen et al., 2015). Also, preliminary designs and pilot projects (e.g., Keller-Bliesner Engineering, 2018) show that mechanical creation and enhancement of nursery habitats is possible. These types of projects need to be expanded and implemented on a large scale. While the extent of mechanical construction of habitats in the San Juan River to support self-sustaining populations will likely be considerable and costly, a large-scale habitat restoration program offers the most likely path to success as part of an integrated conservation strategy for the species.

As implemented in other basins (see “Constructed habitats in other rivers” subsection), constructed habitats should be carefully designed through use of site-specific hydrologic and geomorphic data and sound design principles (Seavy et al., 2009). These habitats must be strategically located to effectively entrain drifting larvae and provide stable productive environments at a range of available flows (Figure 6). This means constructed habitats will need to be designed and placed so that there are habitats available at both low and high flows. Local mechanical disturbances (e.g., bulldozers) should also be considered to remove non-native vegetation and break up substrate embeddedness.

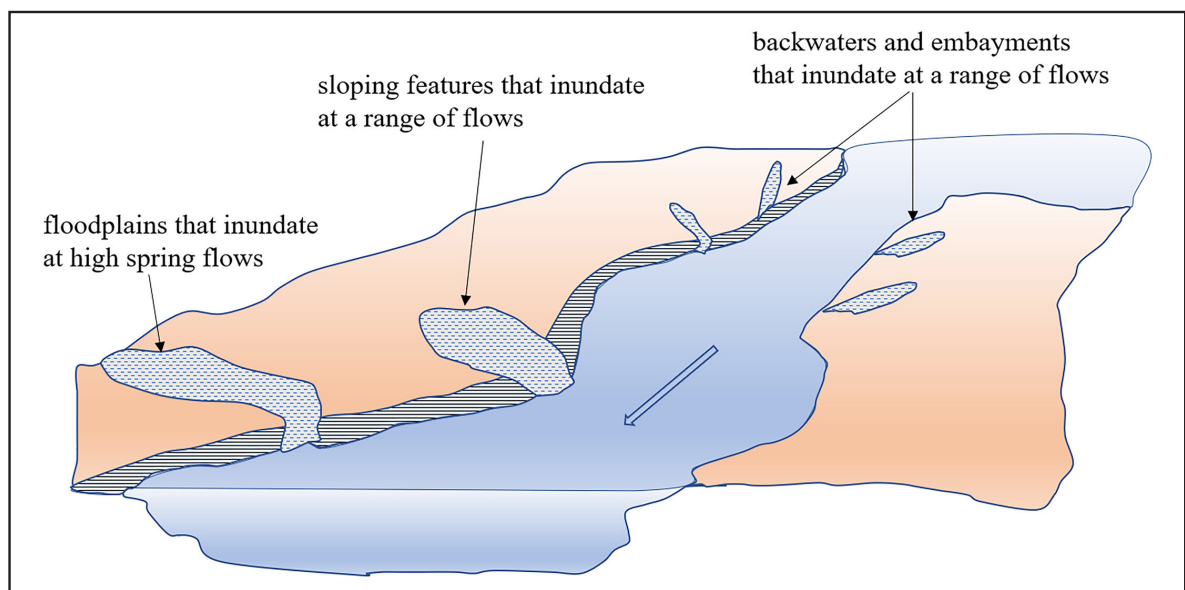


Figure 6. Hypothetical river cross-section illustrating floodplain habitats to be inundated in spring, sloping features that inundate at a range of flows, and separate backwaters and embayments.

3.2.2 Constructed habitats in other rivers

Mechanical construction of early life-stage habitats has effectively offset some effects of reduced flows and has improved survival and recruitment of native species in other river basins. One of the most extensive habitat restoration programs in the southwestern U.S. is in the Middle Rio Grande, New Mexico (<https://webapps.usgs.gov/MRGESCP/>). Since 2003, the Middle Rio Grande Endangered Species Collaborative Program has created or restored about 1600 ha of habitat under a water depletion-neutral framework that mechanically modifies banklines, islands, and old floodplains to create backwaters, embayments, terraces, and depressions that inundate at discharges of 500–3500 ft³/s (14–99 m³/s). Nearly 300 sites ranging from 0.4 to 5 ha in size have been constructed as features designed to seasonally inundate and entrain eggs and larvae of the endangered Rio Grande silvery minnow (*Hybognathus amarus*), a small-bodied cyprinid that relies on spring floodplains as nursery habitats for larvae (Valdez et al., 2020). This habitat restoration program involves floodplain connections and habitats designed with sloping features that become effective under a range of flows. Different habitats are constructed at different locations and various elevations to become inundated at available flows. Managed releases in coordination with the Rio Grande Compact Commission have enhanced inundation of restored floodplains and significantly increased Rio Grande silvery minnow density in the annual population census (Valdez et al., 2019).

In one of the largest habitat restoration programs in the mid-western U.S., the Platte River Recovery Implementation Program (<https://platteriverprogram.org/about/land-plan>) has focused substantial conservation efforts on the creation and maintenance of off-channel nesting habitats adjacent to the river to support habitat use and productivity of the endangered interior least tern (*Sternula antillarum*) and threatened piping plover (*Charadrius melodus*). The Program has also used mechanical methods such as disking and herbicide application to create and maintain unobstructed channel widths that are ≥650 feet and unforested corridor widths that are ≥1100 feet for endangered whooping crane (*Grus americana*) resting and feeding areas, in part due to recognition that short-duration high flow releases, as envisioned, would not alone create and/or maintain the desired in-channel features.

Similar large-scale habitat restoration is taking place in the lower Colorado River, where a consortium of interests has implemented a 50-year program that includes expansive mechanical recontouring of the river channel and adjoining floodplains to create habitat for numerous imperiled aquatic species (BioWest, 2005). Among many conservation activities, the Lower Colorado River Multi-Species Conservation Program (LCRMSCP, 2022) seeks to create more than 8000 acres of riparian, marsh and backwater habitat and introduce more than 1 million combined RBS and bonytail (*Gila elegans*) along 400 miles of the Colorado River from Lake Mead in Nevada to the U.S.–Mexico border (<https://www.lcrmscp.gov/>). Many aspects of this program are similar to the challenges seen in the San Juan River.

A number of habitat restoration projects have also been implemented in the Pacific Northwest to provide habitats for early life stages of various salmon species (*Oncorhynchus* spp.). Mechanically constructed side channels have helped mitigate chronic mortality in parr and smolts (Gibeau et al., 2020), and watershed protections with stream habitat restoration have increased survival and recruitment of young and contributed to recovery of local salmon populations (Battin et al., 2007). Basin-wide restoration of riparian vegetation and channel width has also helped to offset impacts of reduced flows, cooling summer water temperatures by about 1.8–3.5 °C and mitigating climate change impacts to threatened salmon populations (Justice et al., 2017). Restoring lateral floodplain connectivity has also helped to diversify stream habitats and provide salmon smolts with warm protective food-rich environments (Beechie et al., 2012).

Proper planning and engineering are important in scaling habitat features to flow magnitude(s) at which the features are expected to function consistent with species life histories, and to provide protection from exceptionally high flows from floods and storms (Wilby et al., 2010). In summer of 2021, the gate structure, inlet channel, outlet structure, and dirt berm of the Phase III Wetland Project on the San Juan River was damaged and eroded by monsoonal rainstorm floods of up to 7000 ft³/s (198 m³/s) in late July (McKinstry & Matta, 2023). Such floods can damage project structures, result in extra construction costs, and delay benefits to species. This illustrates the challenges in planning, constructing, and maintaining habitat in a river like the San Juan with large periodic flood events.

One negative aspect of creating more low-velocity habitats is that these also provide habitat for non-native species that can prey on and compete with native species. Enhanced inundation of riverside floodplains in the Green River increased densities of non-native fishes, but the expanded habitats and improved production and survival of young RBS have helped to offset the impacts of predation and have increased population numbers (USFWS, 2018).

One of the SJRIP recovery elements is habitat protection, management, and augmentation, and a few habitat projects have already been designed and completed. We do not provide a prescription of mechanical habitat creation for the San Juan River in this paper. Instead, we advocate a more focused and expanded effort on mechanical construction of nursery habitats, including backwaters for CPM and riverside floodplains for RBS, based on a model-driven computation of the amounts of habitat needed to produce the numbers of fish required for species recovery.

4. CONCLUSIONS

4.1 Summary of findings

4.1.1 *Young CPM and RBS have specific habitat needs*

The CPM is a long-distance migrator and its newly hatched larvae drift long distances and have a specific need for small sandy backwaters. The RBS is innately linked to riverine lacustrine habitats and newly hatched larvae also drift long distances with a specific need for productive riverside floodplains. Backwaters are presently limited in the San Juan River and riverside floodplains are absent.

4.1.2 *Flow management alone cannot provide and enhance native fish habitats*

The higher flow targets of the flow recommendations are unlikely to be achieved with reductions in water supply due to ongoing drought and climate change. Flow management alone cannot achieve suitable habitat conditions for CPM and RBS in the San Juan River because of the paucity of nursery habitats and the steep river gradients and non-native vegetation that limit the formation of low-velocity habitats and connecting floodplains.

4.1.3 *Mechanical construction of nursery habitats is highly recommended*

Early life-stage habitats of CPM and RBS are inadequate in the contemporary San Juan River and construction of these habitats is needed. Low-velocity in-channel features such as backwaters and side channels are necessary for larval and age-0 CPM, and large riverside floodplains are necessary for larval and age-0 RBS. These habitats can also be enhanced with local mechanical disturbances that remove non-native vegetation and disrupt substrate embeddedness. These nursery habitats are the most commonly used by the young of these species in other parts of the Colorado River system that support self-sustaining populations.

4.1.4 *Constructed habitats should conform with available flows*

Large-scale mechanical construction of nursery habitats that conform to climate-driven flow changes is recommended to improve survival and recruitment of CPM and RBS in the San Juan River. Properly designed and constructed habitats will facilitate inundation of habitats at critical times for early life stages under a variety of flows. The evolutionary histories of CPM and RBS and the total habitat needed for recovery must be considered when designing and constructing these habitats.

4.2 Areas for further consideration

4.2.1 *Refinement of conceptual designs and pilot studies of constructed habitats*

We recommend further efforts to develop and refine conceptual designs and pilot studies to better assess approaches for constructing nursery habitat features that can withstand extreme flow events and have

increased efficacy under low flow conditions. We also recommend studies looking at utilization of these constructed habitats by non-native species and minimizing predation on CPM and RBS.

4.2.2 Habitat/flow relationships

We recommend assimilation and synthesis of all available habitat information with reconciliation of species and life-stage- specific quantitative relationships between river flow, habitat, and fish abundance. Determining these relationships was a purpose of the 7-year research period, but low numbers of CPM and RBS in the San Juan River precluded quantifying these with certainty. Large numbers of CPM and RBS have been stocked into the San Juan and the habitats used by these fish and their availability should be determinable.

4.2.3 Quantification of habitat needed for recovery

We recommend quantifying the amount of habitat necessary to achieve the species recovery goals for downlisting and delisting the CPM and RBS (USFWS, 2002a, 2002b). Achieving these numbers will require certain amounts of habitat, considering survival and recruitment rates of the hatchery-stocked fish and their progeny. Integrated population models can help determine the amount of habitat necessary to recover the species in the San Juan River and can provide stakeholders with an understanding of the future investment needed for recovery.

4.2.4 Evaluation of flow recommendations

It has not been demonstrated that available flows can effectively create the desired habitat complexity in the San Juan River without complementary mechanical habitat construction. We recommend an evaluation of the flow recommendations using the principles of adaptive management to be informed by the likely availability of future flows. The flow recommendations should be viewed as a large-scale field experiment with the flow targets as hypotheses to be evaluated and possibly revised through ongoing habitat and fish responses. This approach will help inform water management prescriptions and policies for the San Juan River.

AUTHOR CONTRIBUTIONS

Richard A. Valdez: Conceptualization; formal analysis; investigation; methodology; validation; visualization; writing –original draft; writing –review and editing.

Colleen Cunningham: Conceptualization; funding acquisition; investigation; methodology; project administration; supervision; validation; visualization; writing –original draft; writing –review and editing.

Ali Effati: Conceptualization; funding acquisition; project administration; resources; supervision; validation; visualization; writing –review and editing.

Deborah L. Freeman: Conceptualization; investigation; methodology; resources; validation; visualization; writing –original draft; writing –review and editing.

ACKNOWLEDGMENTS

This manuscript was developed with support and funding from the New Mexico Interstate Stream Commission and SWCA. We thank Cody Stropki and Paige Marcus of SWCA for their support and coordination.

CONFLICT OF INTEREST STATEMENT

The authors declare no conflicts of interest.

DATA AVAILABILITY STATEMENT

The only data used in this manuscript are from the U.S. Geological Survey (USGS) Surface-Water Data for the Nation at <https://water.data.usgs.gov/nwis/sw> for the San Juan River near Bluff, Utah (USGS #09379500).

REFERENCES

- Barkalow, A.L., M.P. Zeigler, and J.M. Wick. 2020. "Small-Bodied Fishes Monitoring in the San Juan River: 2019." Annual Final Report Submitted to Bureau of Reclamation. Santa Fe, NM: New Mexico Department of Game and Fish. <https://coloradoriverrecovery.org/sj/science/technical-reports/research-monitoring/>
- Bassett, S. 2015. San Juan River Historical Ecology Assessment, Changes in Channel Characteristics and Riparian Vegetation. Santa Fe, NM: The Nature Conservancy in New Mexico. <https://coloradoriverrecovery.org/sj/science/technical-reports/habitat-restoration/>
- Battin, J., M.W. Wiley, M.H. Ruckelshaus, R.N. Palmer, E. Korb, K.K. Bartz, and H. Imaki. 2007. "Projected Impacts of Climate Change on Salmon Habitat Restoration." *Proceedings of the National Academy of Sciences of the United States of America* 104(16): 6720–25. <https://doi.org/10.1073/pnas.0701685104>
- Beechie, T., H. Imaki, J. Greene, A. Wade, H. Wu, G. Pess, P. Roni, et al. 2012. "Restoring Salmon Habitat for a Changing Climate." *River Research and Applications* 29: 939–60.
- Bennett, K.E., T.J. Bohn, K. Solander, N.G. McDowell, C. Xu, E. Vivoni, and R.S. Middleton. 2018. "Climate-Driven Disturbances in the San Juan River Sub-Basin of the Colorado River." *Hydrology and Earth Systems Sciences* 22: 709–25.
- Bennett, K.E., V.C. Tidwell, D. Llewellyn, S. Behery, L. Barrett, M. Stansbury, and R.S. Middleton. 2019. "Threats to a Colorado River Provisioning Basin under Coupled Future Climate and Societal Scenarios." *Environmental Research Communications* 1(2019): 095001. <https://doi.org/10.1088/2515-7620/ab4028>
- Bestgen, K.R., J.S. Hawkins, G.C. White, K. Christopherson, M. Hudson, M. Fuller, D.C. Kitcheyan, et al. 2007. "Population Status of Colorado Pikeminnow in the Green River Basin, Utah and Colorado." *Transactions of the American Fisheries Society* 136: 1356–80.
- BioWest, Inc. 2005. Colorado River Backwaters Enhancement, Species Profiles Report. Logan, UT: BioWest, Inc. https://lcrms.cp.gov/lcrm-prod/lcrm-prod/pdfs/c03_species_profiles_2005.pdf
- Bliesner, R., and V. Lamarra. 2000. "Hydrology Geomorphology and Habitat." San Juan River Basin Recovery Implementation Program. Logan, UT: Keller-Bliesner Engineering and Ecosystems Research Institute. <https://coloradoriverrecovery.org/sj/science/technical-reports/habitat-restoration/>
- Bliesner, R., and V. Lamarra. 2007. "Hydrology, Geomorphology and Habitat Studies." San Juan River Basin Recovery Implementation Program. Logan, UT: Keller-Bliesner Engineering and Ecosystems Research Institute. <https://coloradoriverrecovery.org/sj/science/technical-reports/habitat-restoration/>
- Cathcart, C.N., K.B. Gido, M.C. McKinstry, and P.D. MacKinnon. 2017. "Patterns of Fish Movement at a Desert River Confluence." *Ecology of Freshwater Fish* 27: 492–505.
- Cathcart, C.N., C.A. Pennock, C.A. Cheek, M.C. McKinstry, P.D. MacKinnon, M.M. Conner, and K.B. Gido. 2018. "Waterfall Formation at a Desert River-Reservoir Delta Isolates Endangered Fishes." *River Research Applications* 2018: 1–9.
- Chen, W., and J.D. Olden. 2017. "Designing Flows to Resolve Human and Environmental Water Needs in a Dam-Regulated River." *Nature Communications* 8: 2158. <https://www.nature.com/articles/s41467-017-02226-4.pdf>
- Diver, T., and W. Wilson. 2018. "Using Molecular Techniques to Determine Effective Number of Breeders (Nb) for Razorback Sucker and Colorado Pikeminnow in the San Juan River." Report to the San Juan River Basin Recovery Implementation Program. Albuquerque, NM: San Juan River Basin Recovery Implementation Program. <https://coloradoriverrecovery.org/sj/science/technical-reports/research-monitoring/>
- Dowling, T.E., W.L. Minckley, P.C. Marsh, and E.S. Goldstein. 1996. "Mitochondrial DNA Variability in the Endangered Razorback Sucker (*Xyrauchenotanus*): Analysis of Hatchery Stocks and Implications for Captive Propagation." *Conservation Biology* 10: 120–27.
- Duffield, W.A. 1997. *Volcanoes of Northern Arizona*. Grand Canyon, AZ: Grand Canyon Association. <https://www.amazon.com/Volcanoes-Northern-Arizona-Canyon-Association/dp/0938216589>
- Farrington, M.A., R.K. Dudley, S.P. Platania, and G.C. White. 2020. "Colorado Pikeminnow and Razorback Sucker Larval Fish Survey in the San Juan River during 2019." Bureau of Reclamation. Albuquerque, NM: American Southwest Ichthyological Researchers. <https://coloradoriverrecovery.org/sj/science/technical-reports/research-monitoring/>
- Franssen, N.R., E.I. Gilbert, and D.L. Propst. 2015. "Effects of Longitudinal and Lateral Stream Channel Complexity on Native and Non-Native Fishes in an Invaded Desert Stream." *Freshwater Biology* 60: 16–30.
- Gibeau, P., M.J. Bradford, and W.J. Palen. 2020. "Can the Creation of New Freshwater Habitat Demographically Offset Losses of Pacific Salmon from Chronic Anthropogenic Mortality?" *PLoS One* 15(12): e0237052.
- Gosnell, H. 2001. "Section 7 of the Endangered Species Act and the Art of Compromise: The Evolution of a Reasonable and Prudent Alternative for the Animas-La Plata Project." *Natural Resources Journal* 561. <http://digitalrepository.unm.edu/nrj/vol41/iss3/4>

- Holden, P.B. (ed.) 1999. "Flow Recommendations for the San Juan River." San Juan River Basin Recovery Implementation Program. Albuquerque, NM: U.S. Fish and Wildlife Service. <https://coloradoriverrecovery.org/sj/science/technical-reports/instream-flow-identification-protection/>
- Holden, P.B. 2000. "Program Evaluation Report for the 7-Year Research Period (1991–1997)." San Juan River Basin Recovery Implementation Program. Albuquerque, NM: U.S. Fish and Wildlife Service. <https://coloradoriverrecovery.org/sj/science/technical-reports/research-monitoring/>
- Hubbs, C.L., and R.R. Miller. 1953. "Hybridization in Nature between the Fish Genera *Catostomus* and *Xyrauchen*." *Papers of the Michigan Academy of Science, Arts, and Letters* 38: 207–33.
- Inskip, E. (ed.). 1995. *The Colorado River through Glen Canyon before Lake Powell, Historic Photo Journal 1872 to 1964*. Moab, UT: Inskip Ink. <https://www.amazon.com/Colorado-River-Through-Glen-Canyon/dp/B01A1N5WJY>
- Irving, D.B., and T. Modde. 2000. "Home-Range Fidelity and Use of Historic Habitat by Adult Colorado Pikeminnow (*Ptychocheilus lucius*) in the White River, Colorado and Utah." *Western North American Naturalist* 60: 16–25.
- Jaeger, K.L., J.D. Olden, and N.A. Pelland. 2014. "Climate Change Poised to Threaten Hydrologic Connectivity and Endemic Fishes in Dryland Streams." *Proceedings of the National Academy of Sciences of the United States of America* 111: 13894–99. <https://doi.org/10.1073/pnas.1320890111>
- Justice, C., S.M. White, D.A. McCullough, D.S. Graves, and M.R. Blanchard. 2017. "Can Stream and Riparian Restoration Offset Climate Change Impacts to Salmon Populations?" *Journal of Environmental Management* 188(2017): 212–27.
- Keller-Bliesner Engineering. 2018. "San Juan River Larval Razorback Sucker Refugia Enhancement Conceptual Design Final Report." San Juan River Basin Recovery Implementation Program. Logan, UT: Keller-Bliesner Engineering. <https://coloradoriverrecovery.org/sj/science/technical-reports/habitat-restoration/>
- Lamarra, V.A., and D. Lamarra. 2016. "San Juan River 2016 Habitat Monitoring." San Juan River Basin Recovery Implementation Program. Logan, UT: Ecosystems Research Institute. <https://coloradoriverrecovery.org/sj/science/technical-reports/habitat-restoration/>
- Large, A.R.G., and G.E. Petts. 1994. "Rehabilitation of River Margins." In *The River's Handbook: Hydrological and Ecological Principles (Volume 2)*, edited by P. Calow and G.E. Petts, 401–18. Oxford, UK: Oxford Blackwell Science. <https://doi.org/10.1002/9781444313871.ch21>
- Lower Colorado River Multi-Species Conservation Program (LCRMSCP). 2022. Final Implementation Report, Fiscal Year 2023 Work Plan and Budget, Fiscal Year 2021 Accomplishment Report. Boulder City, NV: U.S. Bureau of Reclamation. <https://www.lcrmscp.gov/>
- Luchitta, I. 1990. "History of the Grand Canyon and of the Colorado River in Arizona." In *Grand Canyon Geology*, edited by S.S. Beus and M. Morales, 311–32. New York: Oxford University Press. http://geomorphology.sese.asu.edu/Papers/Luchitta_1990_Ch15.pdf
- Mabey, L.W., and D.K. Shiozawa. 1993. Planktonic and Benthic Microcrustaceans from Floodplain and River Habitats of the Ouray Refuge on the Green River, Utah. Provo, UT: Department of Zoology, Brigham Young University. Abstract. <https://www.desertfishes.org/dfc/proceed/1992/24abs27.html>
- McKee, E.D., R.F. Wilson, W.J. Breed, and C.S. Breed. 1967. Evolution of the Colorado River in Arizona: An Hypothesis Developed at the Symposium on Cenozoic Geology of the Colorado Plateau in Arizona, August 1964. Flagstaff, AZ: Museum of Northern Arizona. https://openlibrary.org/books/OL14117519M/Evolution_of_the_Colorado_River_in_Arizona
- McKinstry, M., and M. Matta. 2023. Final Report on the Design, Completion and Evaluation of the Phase III Wetland, San Juan River. Albuquerque, NM: San Juan River Basin Recovery Implementation Program. <https://coloradoriverrecovery.org>
- Miller, P.S. 2014. A Population Viability Analysis for the Colorado Pikeminnow (*Ptychocheilus lucius*) in the San Juan River. Apple Valley, MN: Conservation Breeding Specialist Group (IUCN/SSC). <https://coloradoriverrecovery.org/sj/science/technical-reports/research-monitoring/>
- Miller, R.R. 1961. "Man and the Changing Fish Fauna of the American Southwest." *Papers of the Academy of Sciences, Arts, and Letters* 46: 365–404. <https://docslib.org/doc/1384164/man-and-the-changing-fish-fauna-of-the-american-southwest>
- Minckley, W.L., D.A. Hendrickson, and C.E. Bond. 1986. "Geography of Western North American Freshwater Fishes: Description and Relationships to Intracontinental Tectonism." In *The Zoogeography of North American Freshwater Fishes*, edited by C.H. Hocutt and E.O. Wiley, 519–613. New York: Wiley-Interscience. <https://doi.org/10.1086/415476>
- Morizot, D.C., J.H. Williamson, and G.J. Carmichael. 2002. "Biochemical Genetics of Colorado Pikeminnow." *North American Journal of Fisheries Management* 22: 66–76. Musmann, S.M., M.J. Saltzgeber, T.A. Diver, and B.J. Schleicher. 2022. "Genetic Evaluation of Hybridization among Three Native Sucker Species of the San Juan River." San Juan River Basin Recovery Implementation Program. Albuquerque, NM: U.S. Fish and Wildlife Service. <https://coloradoriverrecovery.org/sj/science/technical-reports/research-monitoring/>
- Muth, R.T., L.W. Crist, K.E. LaGory, J.W. Hayse, K.R. Bestgen, T.P. Ryan, J.K. Lyons, and R.A. Valdez. 2000. Flow and Temperature Recommendations for Endangered Fishes in the Green River Downstream of Flaming Gorge Dam. Denver, CO: Upper Colorado River Endangered Fish Recovery Program. <https://coloradoriverrecovery.org/uc/science/technical-reports/instream-flow-identification-protection/>
- Papoulias, D., and W.L. Minckley. 1990. "Food Limited Survival of Larval Razorback Sucker, *Xyrauchen texanus*, in the Laboratory." *Environmental Biology of Fishes* 29: 73–78.
- Pennock, C.A., L.A. Bruckerhoff, K.B. Gido, A.L. Barkalow, M.J. Breen, P. Budy, W.W. Macfarlane, and D.L. Propst. 2022. "Failure to Achieve Recommended Environmental Flows Coincides with Declining Fish Populations: Long-Term Trends in Regulated and Unregulated Rivers." *Freshwater Biology* 2022: 1–13.
- Petts, G.E. 1998. "Floodplain Rivers and their Restoration: A European Perspective." In *United Kingdom Floodplains*, edited by R.G. Bailey, P.V. José, and B.R. Sherwood, 29–41. Ottery Westbury, UK. <https://westminsterresearch.westminster.ac.uk/item/94722/floodplain-rivers-and-their-restoration-a-european-perspective>

- Precision Water Resources Engineering. 2020. "San Juan Recovery Implementation Program Climate Change Study." San Juan River Basin Recovery Implementation Program. Loveland, CO: Precision Water Resources Engineering. <http://www.precisionwre.com/san-juan-recovery-implementation-program-climate-change-study>
- Rugg, S.H., and S.A. Austin. 1998. "Evidences for Rapid Formation and Failure of Pleistocene "Lava Dams" of the Western Grand Canyon, Arizona." Proceedings of the Fourth International Conference on Creationism. Pittsburg, PA: Creation Science Fellowship, Inc. <http://staticicr.org/i/pdf/technical/Lava-Dams-of-the-Western-Grand-Canyon-Arizona.pdf>
- San Juan River Basin Recovery Implementation Program (SJRIP). 2016. "Long-Range Plan." San Juan River Basin Recovery Implementation Program. Albuquerque, NM: U.S. Fish and Wildlife Service. <https://coloradoriverrecovery.org/sj/documents/program-guidance/>
- San Juan River Basin Recovery Implementation Program (SJRIP). 2018a. "Revised Navajo Dam Operating Procedures for the 1999 San Juan River Flow Recommendations." San Juan River Basin Recovery Implementation Program. Albuquerque, NM: U.S. Fish and Wildlife Service. <https://coloradoriverrecovery.org/sj/science/technical-reports/instream-flow-identification-protection/>
- San Juan River Basin Recovery Implementation Program (SJRIP). 2018b. "2018 Recruitment Bottleneck Workshop." San Juan River Basin Recovery Implementation Program. Albuquerque, NM: U.S. Fish and Wildlife Service. <https://coloradoriverrecovery.org/sj/science/plans-and-protocols/workshops/>
- Seavy, N.E., T. Gardali, G.H. Golet, F.T. Griggs, C.A. Howell, R. Kelsey, S.L. Small, J.H. Viers, and J.F. Weigand. 2009. "Why Climate Change Makes Riparian Restoration more Important than Ever: Recommendations for Practice and Research." *Ecological Restoration* 27: 330–38.
- Thoms, M.C., and F. Sheldon. 2000. "Water Resource Development and Hydrological Change in a Large Dryland River: The Barwon–Darling River, Australia." *Journal of Hydrology* 228: 10–21.
- Tyus, H.M. 1990. "Potamodromy and Reproduction of Colorado Squawfish in the Green River Basin, Colorado and Utah." *Transactions of the American Fisheries Society* 119: 1035–47.
- U.S. Bureau of Reclamation (USBR). 2021. SECURE Water Act Section 9503(c)—Water Reliability in the West, 2021, Report to the U.S. Congress. Denver, CO: Water Resources and Planning Office, Bureau of Reclamation. <https://www.usbr.gov/climate/secure/2021secure.html>
- U.S. Fish and Wildlife Service (USFWS). 1991. Final Biological Opinion for the Animas -La Plata Project, Colorado and New Mexico. Lakewood, CO: U.S. Fish and Wildlife Service. <https://coloradoriverrecovery.org/sj/documents/foundational-documents/formation-documents/>
- U.S. Fish and Wildlife Service (USFWS). 2002a. Colorado Pikeminnow (*Ptychocheilus lucius*) Recovery Goals: Amendment and Supplement to the Colorado Squawfish Recovery Plan. Denver, CO: U.S. Fish and Wildlife Service. <https://coloradoriverrecovery.org/sj/documents/foundational-documents/recovery-goals/>
- U.S. Fish and Wildlife Service (USFWS). 2002b. Razorback Sucker (*Xyrauchen texanus*) Recovery Goals: Amendment and Supplement to the Razorback Sucker Recovery Plan. Denver, CO: U.S. Fish and Wildlife Service. <https://coloradoriverrecovery.org/sj/documents/foundational-documents/recovery-goals/>
- U.S. Fish and Wildlife Service (USFWS). 2018. Species Status Assessment Report for the Razorback Sucker *Xyrauchen texanus*. Denver, CO: U.S. Fish and Wildlife Service. <https://coloradoriverrecovery.org/sj/documents/foundational-documents/recovery-goals/>
- U.S. Fish and Wildlife Service (USFWS). 2020. Species Status Assessment Report for the Colorado Pikeminnow *Ptychocheilus lucius*. Denver, CO: U.S. Fish and Wildlife Service. <https://coloradoriverrecovery.org/sj/documents/foundational-documents/recovery-goals/>
- Valdez, R.A., G.M. Haggerty, K. Richard, and D. Klobucar. 2019. "Managed Spring Runoff to Improve Nursery Floodplain Habitat for Endangered Rio Grande Silvery Minnow." *Ecohydrology* 12: 1–18. <https://doi.org/10.1002/eco.2134>
- Valdez, R.A., S.A. Zipper, S.J. Kline, and G.M. Haggerty. 2020. "Use of Restored Floodplains by Fishes of the Middle Rio Grande, New Mexico, USA." *Ecohydrology* 14(2). <https://doi.org/10.1002/eco.2262>
- Wilby, R.L., H. Orr, G. Watts, R.W. Battarbee, P.M. Berry, R. Chadd, S.J. Dugdale, et al. 2010. "Evidence Needed to Manage Freshwater Ecosystems in a Changing Climate: Turning Adaptation Principles into Practice." *Science of The Total Environment* 408: 4150–64.

Water-quality Change Following Remediation Using Structural Bulkheads in Abandoned Draining Mines, Upper Arkansas River and Upper Animas River, Colorado USA

Katherine Walton-Day, M. Alisa Mast, and Robert L. Runkel

U.S. Geological Survey, Denver, CO

ABSTRACT

Water-quality effects after remediating abandoned draining mine tunnels using structural bulkheads were examined in two study areas in Colorado, USA. A bulkhead was installed in the Dinero mine tunnel in 2009 to improve water quality in Lake Fork Creek, a tributary to the upper Arkansas River. Although bulkhead installation improved pH, and manganese and zinc concentrations and loads at the Dinero mine tunnel, water-quality degradation was observed at the nearby Nelson tunnel. Only manganese concentrations improved in Lake Fork Creek downstream from the tunnel. To improve water quality in Cement Creek, a tributary of the Animas River, multiple bulkheads were installed in mine tunnels during 1996–2003 and a water treatment plant operated from 1989 to 2003 to treat drainage from several draining tunnels. After bulkhead installation and cessation of active water treatment (about 2003), water quality (pH and dissolved copper, manganese, and zinc concentrations) degraded at the mouth of Cement Creek. The patterns and timing were similar to post-bulkhead increased discharge and trace-metal loads at non-bulkheaded tunnels indicating the bulkheads might have been the cause. Pre-1989 water-quality data for Cement Creek are scarce, although limited historical data indicate possible, slight improvement in only manganese concentrations after bulkhead installation. Increased zinc loads in Lake Fork Creek and decreased pH through time in Cement Creek may indicate increased groundwater discharge to the streams after bulkhead installation. In these two study areas, bulkheads did not substantially improve downstream water quality.

1. INTRODUCTION

Abandoned draining mine features including adits and tunnels (horizontal access to mine workings), shafts (vertical access to mine workings), and seeps and runoff from mine waste and tailings are a persistent water-quality problem worldwide (Blowes et al., 2003; 2014; Sheoran and Sheoran, 2006, p. 61 in Wolkersdorfer, 2008). Water interacts with mineralized rock containing pyrite and other sulfides in these features and generates mining-impaired water (mine drainage) that is sometimes acidic and may contain elevated concentrations of various trace metals and metalloids (Nordstrom et al., 2015). In the State of Colorado, over 23,000 abandoned mines impair water quality in about 2,900 stream kilometers (km) (Colorado Department of Public Health and Environment, 2019).

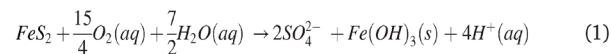
Remediation of mine drainage remains a challenge. Recommended technologies for solid wastes include removal, consolidation, or capping to minimize percolation or generation of mine drainage from the wastes (Colorado Department of Natural Resources Division of Minerals and Geology, 2002; International Network

for Acid Prevention, 2014). Remediation alternatives for draining adits and shafts include operation of water-treatment plants to chemically treat the drainage (Walton-Day, 2003), installation of structural bulkheads to physically limit water discharge from mine workings (Colorado Department of Natural Resources Division of Minerals and Geology, 2002; Johnson and Hallberg, 2005) and combinations of bulkheads and engineering controls to limit infiltration of surface water into underground mine workings (Marks et al., 2008).

Installation of structural bulkheads to reduce discharge from mines is often cited as a preferred alternative because this approach avoids longterm operation and maintenance costs associated with water-treatment plants (Bureau of Land Management, 2006; Younger et al., 2002). A structural bulkhead is an engineered concrete structure extending from floor to ceiling in a mine tunnel with enough thickness to withstand lithostatic pressure of overlying rocks, hydrostatic pressure of the mine pool formed when the bulkhead is sealed, and additional pressure that could occur during a mine blowout (Einarson and Abel, 1990; Sorenson and Brown, 2015). Mine blowout occurs when water impounded behind a collapse or debris in an upgradient part of the mine is abruptly released. Although bulkheads physically limit mine discharge, they are known to leak (p. 24 in Gusek and Figueroa, 2009) and generally do not completely stop discharge from draining mine tunnels.

There are three primary goals associated with installation of a structural bulkhead in a draining mine tunnel: (1) to limit the discharge of poor-quality water from the tunnel (Bureau of Land Management, 2006; Sorenson and Brown, 2015); (2) to protect existing or future infrastructure in front of the mine-tunnel opening and (or) downstream water bodies from the effects of blowouts from the mine workings (Bureau of Land Management, 2006; Stratus Consulting, 2009); and (3) to improve water quality by limiting some of the physical and chemical changes that degrade water quality in underground mine tunnels.

Underground mining and drainage tunnels lower the elevation of the water table thereby increasing contact of pyrite-bearing mineralization to atmospheric oxygen (Figure 1a). Oxygen, infiltrating water from precipitation and snowmelt, and micro-organisms, fuel generation of acid mine drainage (Nordstrom et al., 2015) through the overall reaction (Blowes et al., 2014):



The products of this reaction drive dissolution of metal-sulfide minerals and formation of secondary, variably soluble sulfate minerals, degrading water quality in the mine and its discharge to the surface (Figure 1a) (Alpers et al., 1994; Blowes et al., 2003, 2014; Jambor et al., 2000; Nordstrom, 2011). Seasonal wetting and drying in underground workings exacerbate acid mine drainage and formation of secondary sulfate minerals. During the dry season, secondary sulfate minerals accumulate underground; during the wet season, infiltrating water promotes forward progress of reaction (1), and soluble secondary sulfate minerals that accumulated during the dry season dissolve, causing a wet-season flush of more degraded water compared to other times of year (Alpers et al., 1994; Blowes et al., 2003, 2014; Nordstrom and Alpers, 1999; Nordstrom et al., 2015; U.S. Environmental Protection Agency, 1994). Groundwater backed up behind bulkheads may

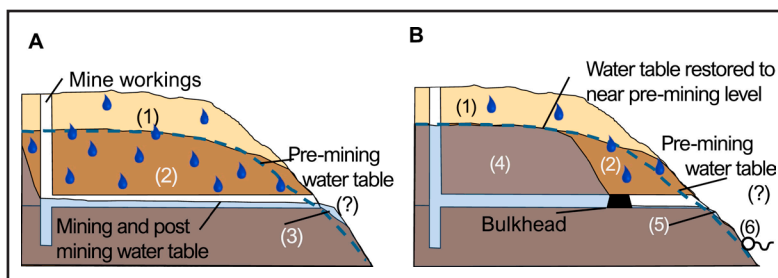


Figure 1. Diagram showing (A) schematic cross section of mineralized rock and mine workings during and after mining. Notable features are (1) leached, mineralized rock above the historical water table; the lower post-mining water table caused by mine workings and tunnels that (2) exposes pyrite in mineralized rock to oxygen and infiltrating water and generates acid mine drainage (3) that flows to and may degrade surface water. (B) After bulkhead

emplacement the water-table elevation increases behind the bulkhead and (4) some of the mineralized rock is re-submerged beneath the water table limiting the extent of acid mine drainage generation potentially causing (5) decreased flow of degraded water from the tunnel and rerouting some flow to other non-bulkheaded mine tunnels and existing or new springs (6). After Schmidt (2007).

re-submerge mineralized bedrock, greatly decreasing dissolved-oxygen influx and limiting the acid mine drainage reaction, thereby potentially improving water quality of the impounded mine pool water and bulkhead leakage (Sorenson and Brown, 2015; Walton-Day and Mills, 2015; Wolkersdorfer, 2008) (Figure 1b). Saturation of mine workings also may decrease or eliminate seasonal wetting and drying (4 in Figure 1b), limiting formation and dissolution of secondary sulfate minerals, further improving water quality. Though where accumulations of soluble sulfate minerals are extreme, their dissolution upon flooding could greatly degrade water quality (Jambor et al., 2000; Nordstrom and Alpers, 1999). Water-quality improvement may also be limited by the relation between the elevation of the final water table and pyrite-bearing rock in the mine workings. The elevated post-bulkhead water table may reroute water from the mine pool through permeable fractures and strata to non-bulkheaded workings, and may increase flow in existing springs or cause emergence of new springs (6 in Figure 1b) potentially offsetting bulkhead-related water-quality improvement (Cowie and Roberts, 2020). Water-quality and discharge monitoring at the tunnel outflow and surrounding area before and after bulkhead installation documents the effects of the bulkhead.

In Colorado, USA, at least 26 structural bulkheads had been installed in mines as of 2015 (Appendix B; Bureau of Reclamation, 2015). Monitoring data documenting water-quality effects of bulkheads are not always readily or publicly available. Lake Fork Creek located in the upper Arkansas River watershed (Figure 2) and Cement Creek, in the upper Animas River watershed (Figure 3), are two areas having available data. In the Lake Fork Creek watershed, the Bureau of Land Management (2006) installed a bulkhead in the Dinero mine tunnel (hereinafter Dinero tunnel) in 2009. In the Cement Creek watershed, four bulkheads were installed in two tunnels from 1996 to 2003. Three were installed in the American tunnel between 1996 and 2002 by Sunnyside Gold Corporation (Sunnyside Gold Corporation, 2003), and one was installed in the Mogul mine tunnel in 2003 by the Gold King Mining Corporation (Bonita Peak Community Advisory Group, 2019a; Bureau of Reclamation, 2015) (Figure 4).

The objective of this paper is to examine water-quality changes in the two mining districts to assess whether bulkhead installation improved downstream water quality. For the Dinero tunnel, which drains into Lake Fork Creek, water-quality and discharge data for four sampling sites are discussed for the period 2006–2017 (Figure 2). To evaluate the American and Mogul tunnel bulkheads, water-quality and discharge data collected near the mouth of Cement Creek from 1971, 1981, and 1995–2015 are presented. Discussion includes discharge and waterquality data compiled from multiple sources (Walton-Day et al., 2020) from 1988 to 2015 for five mine tunnels including the American tunnel and the Mogul, Red and Bonita, Black Hawk, and Gold King mine tunnels. Herein, all are referred to simply as tunnels (e.g. Mogul tunnel).

2. STUDY AREAS AND METHODS

2.1. Upper Arkansas River watershed, Dinero tunnel

The Dinero tunnel is one of five mining tunnels in the Sugar Loaf mining district in the upper Arkansas River watershed (Figure 2). Elevation ranges from about 2,920 meters (m) at the confluence of Colorado Gulch with Lake Fork Creek to over 3,400 m on the ridge comprising the watershed boundary (Figure 2). Mean annual precipitation (1981–2010) is 48 centimeters (cm) of which at least half occurs as snow (Sugarloaf RSVR Colorado at <https://wrcc.dri.edu/cgi-bin/cliMAIN.pl?co8064> accessed 30 Nov 2020). Surface hydrology is dominated by snowmelt with 70% of runoff occurring in May through July (Walton-Day and Mills, 2015). Annual mean streamflow at the U.S. Geological Survey (USGS) streamgage Arkansas River at Leadville, located about 3 km directly east of Dinero tunnel, varied from about 1 to 3 cubic meters per second (m³/s), was punctuated by wet (2011 and 2014) and dry (2012) years, but showed no trend during the study period (Supplemental Figure S1a).

In the Sugar Loaf mining district, silver and some gold, lead, and zinc were mined from Tertiary quartz-sulfide veins in crystalline, Precambrian bedrock (schist, gneiss, and granite) mostly from 1880 until the 1920s (Singewald, 1955). The primary mine tunnels (Figure 2) total approximately 6 km in length. The Dinero tunnel provided drainage and access to higher elevation mine workings at its northwest end, and is a major contributor to degraded water quality, primarily elevated manganese and zinc concentrations in Lake Fork

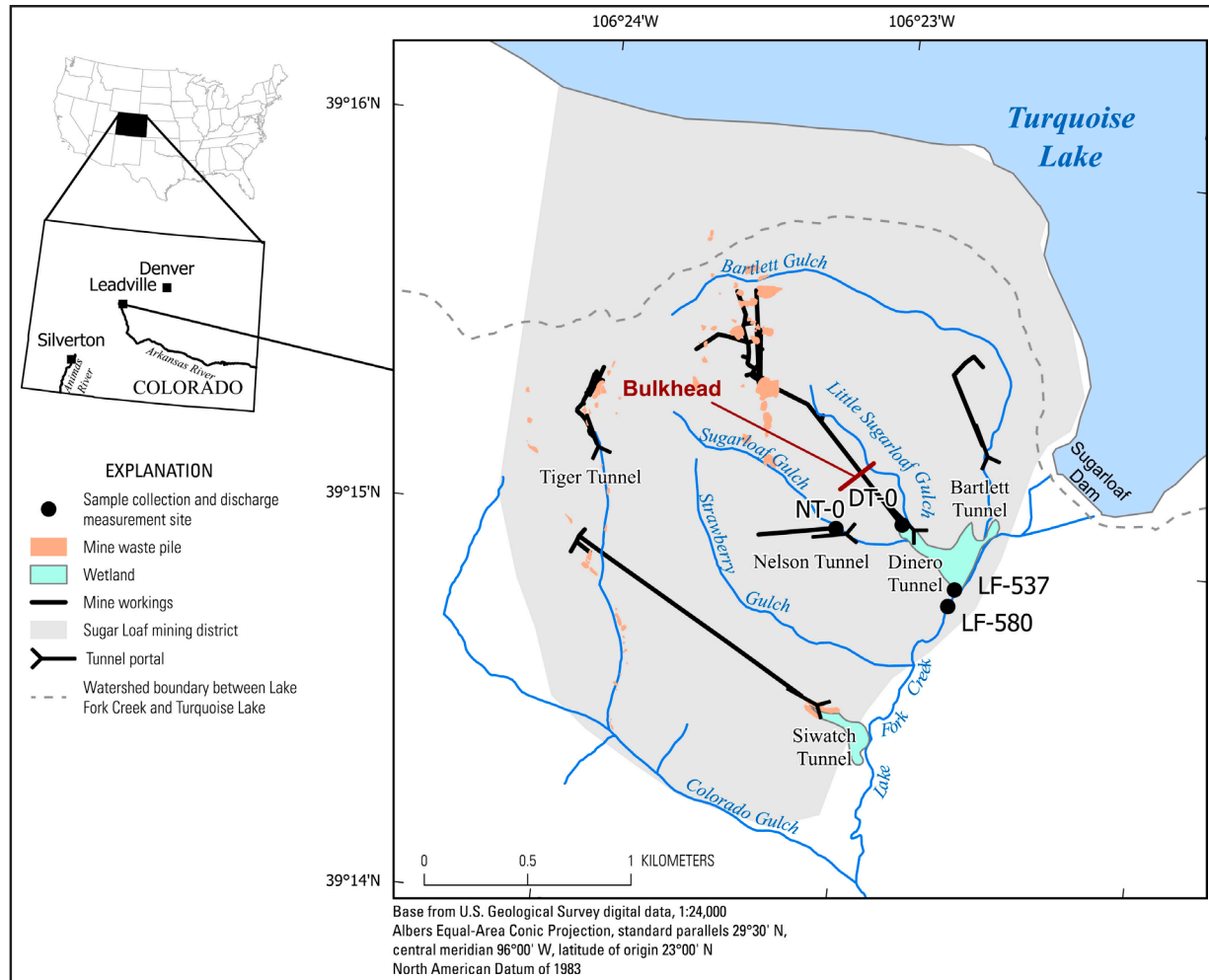


Figure 2. Map showing location of upper Arkansas River watershed study area in Colorado, USA, Sugar Loaf mining district, mine-waste piles, mine tunnels, and sampling sites at the Dinero tunnel (DT-0), Nelson tunnel (NT-0), channel draining wetland downstream from Dinero tunnel (LF-537), and Lake Fork Creek downstream from Dinero tunnel (LF-580). The extent of tunnels was digitized from published maps (Singewald, 1955) and by compilation from mineral surveys (e.g. U.S. Surveyor General's Office, 1912).

Creek (Walton-Day et al., 2005; Bureau of Land Management, 2006), a tributary to the upper Arkansas River. A bulkhead for Dinero tunnel was chosen as the preferred remediation approach and was installed and closed in 2009 (Bureau of Land Management, 2006). The bulkhead is located approximately 390 m into the tunnel at an elevation of 2,984 m. Elevation of ground surface above the bulkhead is 3,049 m.

Controls on groundwater occurrence and flow in the Dinero area are not well understood. Groundwater flow likely is dominantly fracture controlled in the Precambrian rocks. In general, snowmelt likely provides high rates of seasonal recharge to a shallow, active groundwater system that exists over a deeper, inactive groundwater system (Johnson and Yager, 2006; Manning and Caine, 2007; Mayo et al., 2003; Snow, 1968; Walton-Day and Poeter, 2009). There is a groundwater divide near the watershed divide between the area containing most of the mine workings and Turquoise Lake (Figure 2) (Walton-Day and Poeter, 2009). Some groundwater in the Sugar Loaf mining district likely discharges to surface streams (Bartlett, Little Sugarloaf, Sugarloaf, Strawberry, and Colorado Gulches (Figure 2), and also directly to Lake Fork Creek between Sugarloaf Dam and LF-580 where previous work indicated inflow of trace-metal rich groundwater to Lake Fork Creek (p. 45 in Walton-Day et al., 2005). Underground mine workings provide preferential pathways for groundwater flow.

Water-quality data were collected near the Dinero tunnel as part of an extensive monitoring program to understand the water-quality effects of bulkhead installation (Walton-Day et al., 2013; Walton-Day and Mills, 2015). Herein, discussion includes data collected in 2006 (four times between May and October) and from 2010 to 2014 and 2016–2017 (in spring and autumn each year) at sites DT-0 (Dinero tunnel), LF-537, LF-580, and NT-0 (Nelson mine tunnel) (Figure 2). Raw data are stored in the USGS National Water Information System (NWIS) (U.S. Geological Survey, 2019a) and can be retrieved using USGS site IDs (see “Data Availability” section). Water from DT-0 discharges into the wetland located between the Dinero tunnel and Lake Fork Creek (Figure 2). Site NT-0 discharges to Little Sugarloaf Gulch that flows into the same wetland, which is also fed by Sugarloaf Gulch, near Dinero tunnel. The wetland drains to Lake Fork Creek upstream from site LF-580 via surface flow at LF-537 and via seeps and groundwater on the eastern edge of the wetland (Figure 2). Data presented are discharge, pH, and dissolved (<0.45 μm) manganese and zinc concentrations. Sample collection, analytical methods, and quality-assurance information are presented in Walton-Day and Mills (2015). Metal loads were calculated by multiplying instantaneous discharge measured at the time of sample collection by metal concentration and are presented as kilograms per day (kg/day). Discharge, hydrogen ion (from pH), and manganese and zinc concentrations and loads were compared before and after the Dinero bulkhead closure using a two-sample permutation test with the R package ‘perm’ (<https://www.rdocumentation.org/packages/perm/versions/1.0-0.0>). For p-values ≤ 0.05, the difference in the means for the two groups were considered statistically significant.

2.2. Upper Animas River watershed, Cement Creek

Cement Creek is tributary to the upper Animas River, upstream from Silverton, Colorado (Figures 3 and 4). Elevation ranges from about 2,860 m at C48 to more than 4,000 m on the ridge comprising the watershed boundary. Mean annual precipitation (from 1981 to 2010) is 67 cm (Silverton Colorado at <https://wrcc.dri.edu/cgi-bin/cliMAIN.pl?co7656>, accessed 30 Nov 2020). Similar to the Dinero area, most precipitation occurs as snow, and surface hydrology is dominated by melting of the seasonal snowpack. Annual mean streamflow

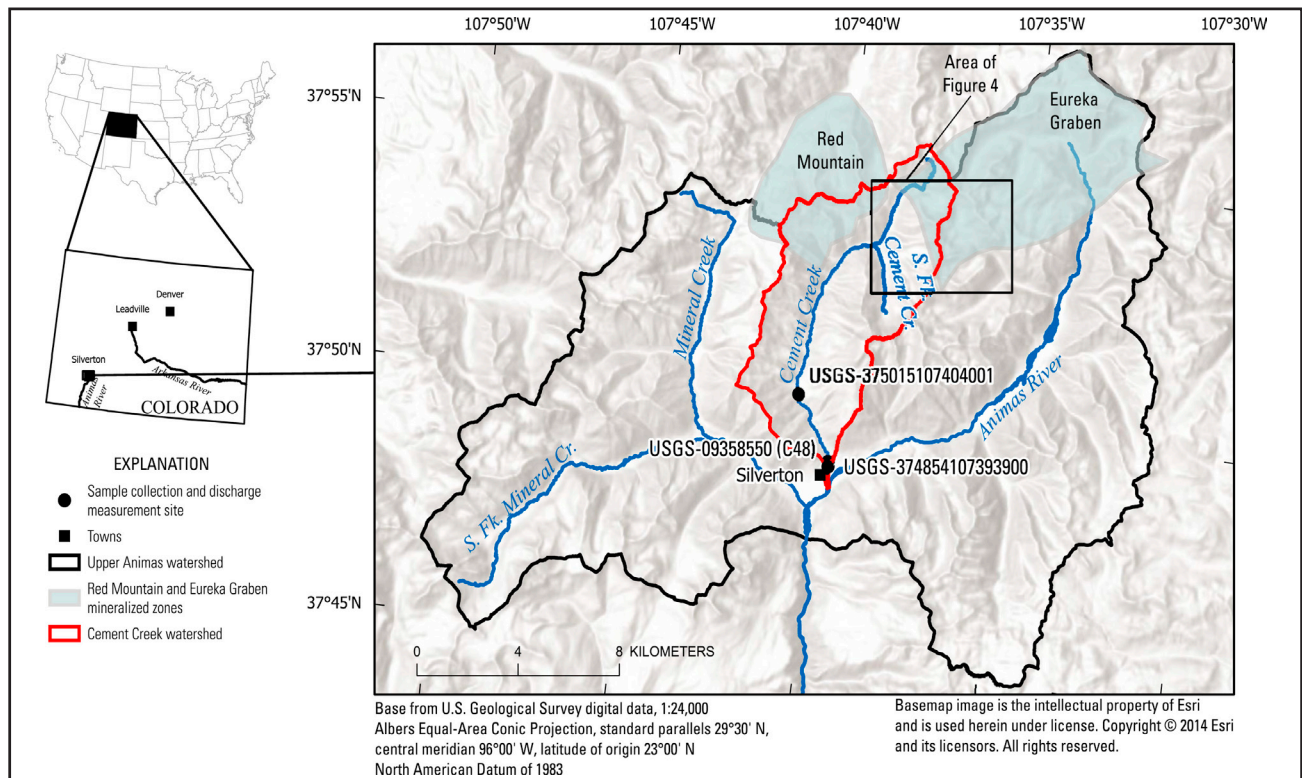


Figure 3. Map showing location of upper Animas River and Cement Creek watersheds in southwestern Colorado, USA, sample monitoring sites, and mineralized areas.

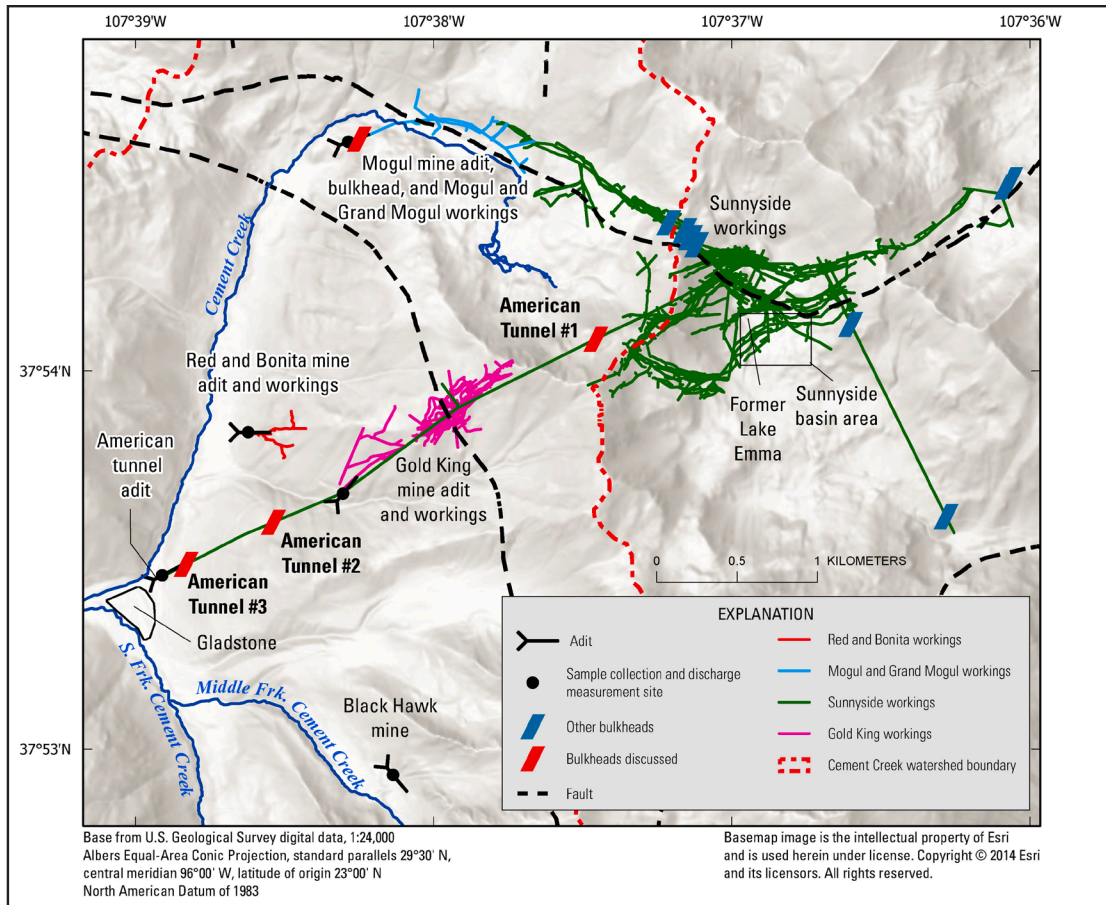


Figure 4. Map showing mine workings for Mogul and Grand Mogul, Red and Bonita, Gold King, and Sunnyside mines, the Black Hawk mine, bulkhead locations, and surface drainage. Water from the American tunnel, Mogul, Red and Bonita, and Gold King tunnels discharges towards Cement Creek upstream from Gladstone. Faults represented as black dashed lines are from Yager and Bove (2007).

at USGS streamgage Cement Creek at Silverton, Colorado (station 09358550, C48) varied from about 0.5 to 1.6 m³/s, was punctuated by wet (1995, 1997, 1999, 2005, 2008, 2011, and 2014–2015) and dry years (2002 and 2012–2013), but showed no trend during the study period (Supplemental Figure S1b).

Cement Creek drains the central part of the collapsed and mineralized Silverton volcanic caldera consisting of Tertiary-age extrusive and intrusive volcanic rocks (von Guerard et al., 2007). Extensive hydrothermal alteration and mineralization associated with the caldera and its collapse form the basis for historical mining in the region. Mining in the upper Animas River watershed occurred from the early 1870s through 1991 and was extensive with over 300 mine, mill, mill tailing, and smelter sites documented (Church, 2007, Figures 2 and 5 in Church et al., 2007a; Jones, 2007). Polymetallic (silver, lead, zinc, copper, ± gold) sulfide veins in fractures and fissures in the Eureka Graben area were the target of the mines in upper Cement Creek (Figures 3–4) (Bove et al., 2007). Mine tunnels (Figure 4) total over 60 km in length (Bonita Peak Community Advisory Group, 2019b). Cement Creek is influenced by both acid mine drainage from mined and mineralized areas (Eureka Graben and Red Mountain areas, Figures 3–4), and acid rock drainage from acid-generating hydrothermally altered areas resulting in low pH stream water (pH = 4–5) having elevated metal concentrations (Bove et al., 2007; Mast et al., 2007).

In the Cement Creek area, groundwater flow is likely fracture controlled (Simon Hydro-Search, 1992, 1993). Similar to the Dinero study area, snowmelt recharge provides most groundwater recharge (Caine and Wilson, 2011). Prior to mining, groundwater is estimated to primarily have moved southwest from the Sunnyside basin to discharge along Cement Creek (Figure 4) (Simon Hydro-Search, 1992).

Remediation and reclamation in the Cement Creek watershed have been ongoing since the early 1980s and include consolidation and capping of mine-waste deposits, passive treatment, and hydrologic controls (Bonita Peak Community Advisory Group, 2019a, table 5 in Church et al., 2007b; Lange, 2019). Water treatment of American tunnel discharge started in the early 1980s and consisted of addition of hydrated lime ($\text{Ca}(\text{OH})_2$) and flocculant, precipitation of solids, and settling in a series of four settling ponds in the Gladstone area (Figure 4) (Colorado Department of Health, 1988; Standard Metals Corporation, 1981). From 1996 to 2003, water treatment expanded to include Cement Creek upstream from Gladstone (upper Cement Creek, including discharge from the Mogul, Red and Bonita, and Gold King tunnels) (Figure 4), up to the capacity of the treatment plant; during 2003–2004 Gold King effluent was sometimes treated (Bonita Peak Community Advisory Group, 2019a). All active treatment of these sources ceased by July 2004 (Bonita Peak Community Advisory Group, 2019a). In summary, *most importantly, nearly continuous, active treatment of the American tunnel occurred from 1989 through 2003 with upper Cement Creek (upstream from Gladstone) being wholly (low discharge) or partially (high discharge) treated from 1996–2003, and the Gold King tunnel discharge discontinuously treated during 2003 and 2004.*

The focus herein is on Cement Creek and the four bulkheads installed into tunnels draining into Cement Creek: (1) American tunnel #1 (AT#1) bulkhead, the most upgradient bulkhead in the tunnel between the overlying Sunnyside and Gold King mine workings, closed in September 1996; (2) American tunnel #2 (AT#2) bulkhead, located downgradient from the overlying Gold King mine workings, closed in August 2001; (3) American tunnel #3 (AT#3), the most downgradient bulkhead, closed in December 2002; and (4) Mogul tunnel bulkhead closed in August 2003 (Bonita Peak Community Advisory Group, 2019a; Sorenson and Brown, 2015). The American tunnel extends northeast from its mouth (elevation about 3,240 m) near Gladstone upgradient to the Sunnyside mine workings (Figure 4) and was completed as a development and exploration tunnel in 1961 (Burbank and Luedke, 1969; Sorenson and Brown, 2015). Additional draining mine tunnels discussed include the Red and Bonita (portal at 3,340 m) and Gold King (portal at 3,487m), that drain into Cement Creek, and the Black Hawk (portal at 3,535 m) that drains into the South Fork Cement Creek via the Middle Fork (Figure 4) (Sorenson and Brown, 2015). The AT#1 bulkhead and multiple bulkheads to the east in the Sunnyside mine workings (Figure 4) were designed to promote groundwater flow towards Cement Creek. The expectation was that groundwater would discharge along Cement Creek in a reach between the Mogul mine and 4–5 km south, rather than to the upper Animas River watershed east of the Cement Creek watershed divide (Lange, 2019; Simon Hydro-Search, 1992, 1993).

Water-quality data were compiled for samples collected at five sites in the vicinity of the USGS streamgage near the mouth of Cement Creek (USGS station 09358550 and site C48 on Figure 3). Data including dissolved ($<0.45 \mu\text{m}$) copper, manganese, and zinc concentrations and pH were retrieved from the Water Quality Portal (WQP) (<https://www.waterqualitydata.us/data> retrieved April 2019; see “Data Availability” section). Mast (2018) describes data aggregation and quality assurance for this data set. Data for two additional samples were retrieved from NWIS including a sample collected on October 4, 1971, at USGS site ID 374854107393900 located 0.5 km downstream from C48, and a sample collected on September 24, 1981, at USGS site ID 375015107404001, 2 km upstream from C48 (Figure 3). Daily mean streamflow values for station 09358550 (C48) also were retrieved from NWIS. This analysis excluded samples collected after the Gold King mine spill occurred in August 2015 (Bureau of Reclamation, 2015).

Annual discharge-weighted-mean (DWM) concentrations of copper, manganese, zinc, and pH for these data in Cement Creek were estimated for 1995–2015. Discharge weighting of concentrations helps to remove the influence of year-to-year streamflow variability on underlying concentration trends. DWMs were computed using a period-weighted approach, which interpolates concentrations between sampling events to estimate solute loads (Aulenbach et al., 2016). In high-elevation streams, the period-weighted approach works well because solute concentrations exhibit a pronounced annual pattern of dilution during snowmelt that minimizes changes in solute concentrations between sampling events. In addition, metal concentrations in Cement Creek changed dramatically over the study period, complicating development of regression equations to predict concentrations based on streamflow. To estimate DWM concentrations, daily concentrations were computed by linear interpolation of concentrations between sampling events, which averaged 18 samples per year and ranged from 10 to 38. The estimated daily concentrations were multiplied by the daily mean discharge (providing loads), which were then summed over the year and divided by the

sum of the daily discharge values to yield an annual DWM concentration in micrograms per liter ($\mu\text{g/L}$). Time-series graphs of the DWM concentrations reproduced the overall trends in the discrete sample data (Supplemental Figure S2). Loads were calculated for samples collected during 2004–2015 to help provide context for the loads at the mine tunnels. Average daily loads were calculated by multiplying the raw data concentration times the mean daily discharge for the day of sample collection, converting to kg/day , and averaging over the total number of samples.

Discharge and dissolved concentrations of copper, manganese, and zinc for the American tunnel (1988–2015), the Mogul tunnel (1992–2015), the Red and Bonita tunnel (1997–2015), the Gold King tunnel (1993–2015), and the Black Hawk tunnel (1991–2005) were compiled from multiple sources (Walton-Day et al., 2020). Metal loads were calculated as described for the Dinero tunnel.

3. RESULTS AND DISCUSSION

3.1. Discharge and water-quality responses to bulkhead closure

3.1.1. Upper Arkansas River watershed, Dinero tunnel

The discharge and water-quality responses to closure of the Dinero tunnel bulkhead were mixed. After bulkhead closure, mean discharge decreased at DT-0 by 85% and increased at LF-537, LF-580, and NT-0 by as much as 200% (Figure 5, Table 1, Supplemental Table S1). Mean pH values increased after bulkhead closure at DT-0 and LF-537 but decreased at LF-580 and NT-0 (Figure 5, Table 1, Supplemental Table S1). Mean

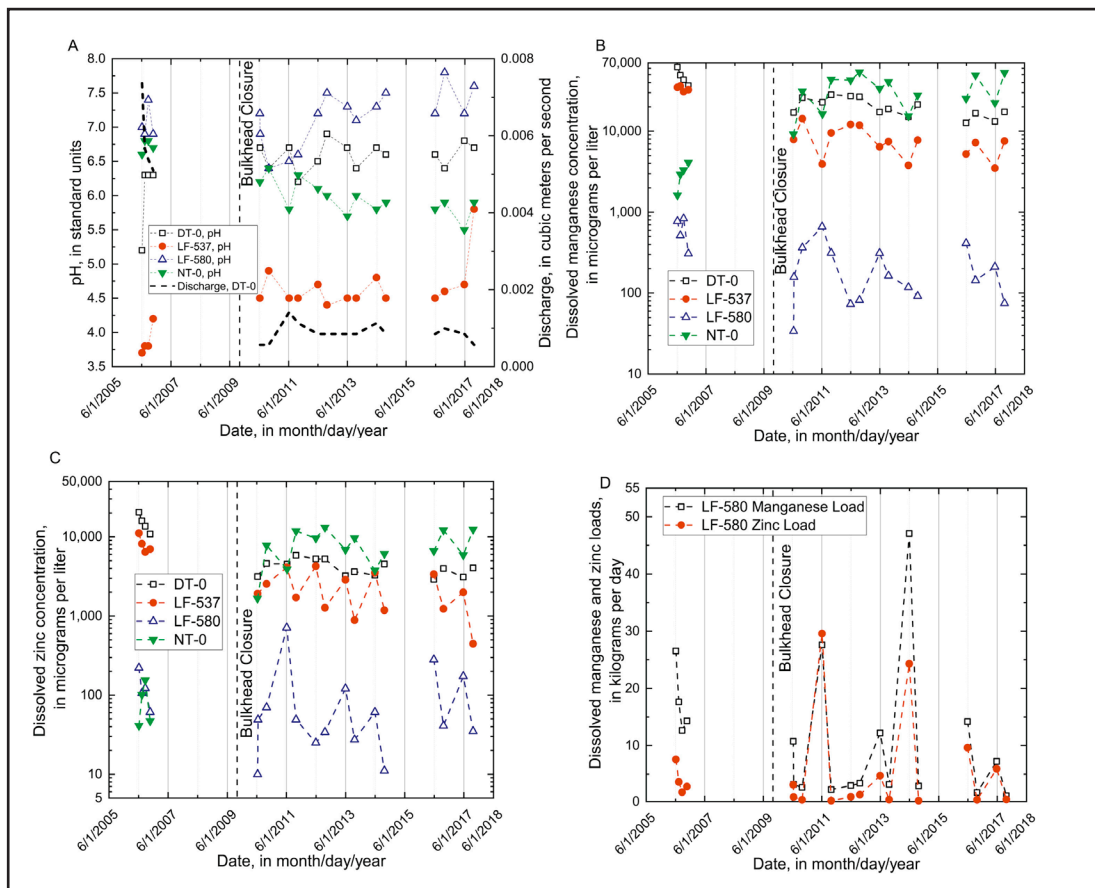


Figure 5. Graphs showing variation in (A) in pH and discharge, (B) dissolved manganese concentrations, (C) dissolved zinc concentrations, and (D) dissolved zinc and manganese loads for sites at the Dinero tunnel (DT-0), LF-537 draining the Dinero wetland, LF-580 on Lake Fork Creek, and Nelson tunnel (NT-0).

dissolved manganese concentrations decreased after bulkhead closure by as much as 77% at DT-0, LF-537, and LF-580 but increased at NT-0 by 1,000% (Figure 5, Table 1, Supplemental Table S1). Similarly, mean dissolved zinc concentrations decreased after bulkhead closure by as much as 73% at DT-0, LF-537, and LF-580, but increased at NT-0 by 9,200% (Figure 5, Table 1, Supplemental Table S1). Mean dissolved manganese loads decreased by as much as 94% at DT-0, LF-537, and LF-580, but increased at NT-0 by 3,100% (Figure 5, Table 1, Supplemental Table S1). Finally, mean dissolved zinc loads decreased by up to 96% at DT-0 and LF-537, but increased at LF-580 and NT-0 by 40% and 23,000% (Figure 5, Table 1, Supplemental Table S1).

Table 1. Statistical comparison of pre- and post-bulkhead discharge and water quality, Dinero study area. Percent change is the difference in mean concentration or load between periods and p-value is from the 2-sample permutation test comparing the 2 periods. Values in bold are significant at 95% confidence. Before closure, n = 4. After closure n = 14 except at LF-580 where n = 15. [DT-0, Dinero tunnel; LF-537, sample site draining wetland downstream from DT-0; LF-580, sample site on Lake Fork Creek downstream from DT-0 and LF-537; NT-0, Nelson tunnel; Dis., dissolved; Conc., concentration; %, percent; <, less than].

Site	Discharge		pH as hydrogen ion concentration		Mean Dis. Manganese Conc.		Mean Dis. Zinc Conc.		Mean Dis. Manganese Load		Mean Dis. Zinc Load	
	% change	p-value	% change	p-value	% change	p-value	% change	p-value	% change	p-value	% change	p-value
DT-0	-85	< 0.05	-85	< 0.05	-58	< 0.05	-73	< 0.05	-94	< 0.05	-96	< 0.05
LF-537	66	0.68	-82	< 0.05	-77	< 0.05	-73	< 0.05	-75	< 0.05	-32	0.64
LF-580	120	0.85	11	0.91	-65	< 0.05	-12	0.88	-47	0.20	40	0.90
NT-0	200	0.05	580	< 0.05	1,000	< 0.05	9,200	< 0.05	3,100	< 0.05	23,000	< 0.05

At the Dinero tunnel portal (DT-0), water quality improved after bulkhead closure evidenced by statistically significant ($p < 0.05$) decreases in discharge, manganese and zinc concentrations and loads, and increases in pH (Table 1; Figure 5a–c). In addition, bulkhead installation seems to have reversed seasonal concentration patterns. Before bulkhead closure (2006 values), the lowest pH and greatest manganese and zinc concentrations occurred during spring runoff coincident with the greatest discharge. The highest pH and lowest metal concentrations occurred during low flow in summer and fall (Figure 5a–c). In contrast, after bulkhead closure (2010–2017), pH values were higher, and metal concentrations were lower during high flow than during base flow (Figure 5a–c). Higher concentrations during snowmelt prior to bulkhead installation may indicate that seasonal wetting and drying in exposed mine workings was likely contributing to a spring flush of low pH, metalrich water (Figure 1a). After bulkhead closure, water levels and chemistry were more stable, limiting pyrite oxidation as mine workings and rocks became submerged (Figure 1b).

Water quality also improved after bulkhead closure at LF-537, the wetland outflow, though not as dramatically as at DT-0. At LF-537, significant ($p < 0.05$, Table 1) water-quality improvement included increased pH and decreased manganese and zinc concentrations and manganese loads (Figure 5a–c). The pH at LF-537 is less than at Dinero tunnel because other acid sources, primarily Sugarloaf Gulch and Little Sugarloaf Gulch, discharge into the wetland. Further, precipitation of iron oxyhydroxides is a reaction that generates acidity (Walton-Day and Mills, 2015) that likely occurs in the wetland. Overall, the bulkhead appeared to improve water quality at LF-537.

Farther downstream, Lake Fork Creek (LF-580) exhibited mixed results with pH decreasing, manganese and zinc concentrations and manganese load decreasing, but mean zinc load increasing (Table 1, Figure 5a–d). Only the decrease in manganese concentration was statistically significant (Table 1).

Despite decreases in zinc concentrations, zinc loads actually increased at LF-580 after the bulkhead due to interannual variability in runoff. For example, the greatest elevated zinc and manganese concentrations and loads occurred during the spring of 2011 (concentrations and loads) and 2014 (loads) (Figure 5c and d), years that were characterized by above average snowfall and spring and annual runoff (Supplemental Figure S1a; Walton-Day et al., 2013; Walton-Day and Mills, 2015; U.S. Geological Survey, 2019b). In addition, post-bulkhead mean zinc loads (5.57 kg/d) were greater than the sum of loads from DT-0, LF-537, and NT-0 (about 1.7 kg/d) indicating other sources are contributing zinc to LF-580 (Supplemental Table S1). Manganese loads show a similar pattern (Supplemental Table S1). The source of this additional loading at LF-580 is not

definitively known but is likely related to additional groundwater and trace-metal input along the west side of Lake Fork Creek upstream from LF-580 where previous studies noted groundwater inflow (p. 45 in Walton-Day et al., 2005), and/or additional runoff of acid-mine drainage from upstream mining features into the wetland after bulkhead closure.

Manganese concentrations from all samples (pre- and post-bulkhead) at site LF-580 met both chronic and acute hardness-based water-quality standards for protection of aquatic life in segment COARUA05a, which includes Lake Fork Creek (p. 174 in Colorado Department of Public Health and Environment Water Quality Control Commission, 2020). Zinc concentrations for almost all samples exceeded both the acute and chronic hardness-based standards, and only two samples in the post bulkhead period (10.0 $\mu\text{g/L}$ on 10 June 2010 and 11.1 $\mu\text{g/L}$ on 30 September 2014) (Figure 5c) met both the acute and chronic zinc standards. Together these data indicate statistically significant ($p < 0.05$) improvement only in manganese concentrations and attainment of zinc water-quality standards for two of 15 samples at Lake Fork Creek monitoring site LF-580 after bulkhead closure.

After bulkhead closure, the Nelson tunnel (NT-0) exhibited statistically significant decreases in pH and increases in discharge and dissolved manganese and zinc concentrations and loads (Table 1; Figure 5a-c) indicating water-quality degradation. The Nelson tunnel is a collapsed draining mine tunnel having more limited workings than Dinero tunnel (Figure 2). Previous work concluded that a fracture and associated vein connect the Nelson tunnel to the mine pool behind the Dinero bulkhead, which caused impounded water from Dinero to reroute to NT-0 after bulkhead closure (Figure 2 in Walton-Day and Mills, 2015). Over the entire study period, seasonal concentration patterns at NT-0 (Figure 5b and c) did not show first-flush effects. The absence of a seasonal first flush may indicate that material generating mine drainage in the Nelson tunnel is submerged within the mine pool, minimizing the annual wetting and drying cycles common in open mine workings.

3.1.2. Cement Creek, upper Animas River watershed

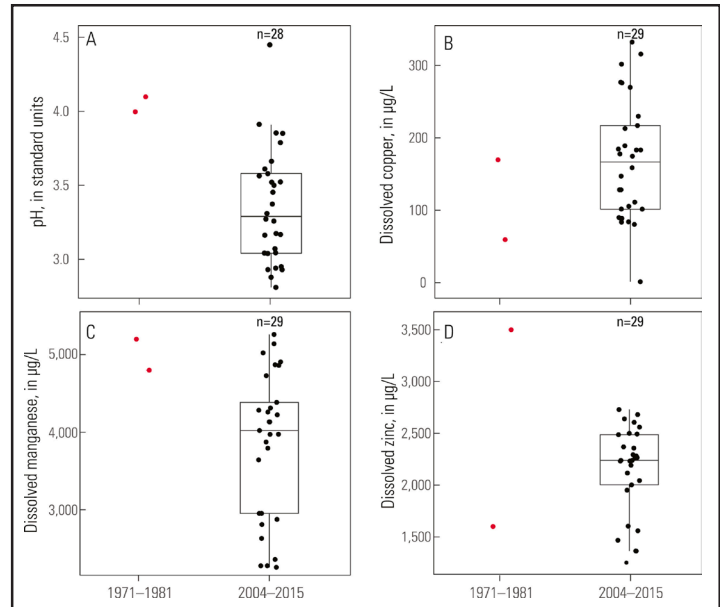
3.1.2.1. Pre- and post-bulkhead water quality at the mouth of Cement Creek

Interpreting effects of bulkhead installation in Cement Creek is complicated by overlap between the timing of bulkhead installation (1996–2003) and active water treatment (1989–2003). Two pretreatment samples collected near or at the mouth of Cement Creek during September and October before treatment and bulkhead closure (1971 and 1981) were compared to samples collected in September and October, 2004–2015, after treatment ceased and bulkheads were closed (Figure 6a–d). After bulkhead closure, these data showed decreased mean pH values (from about 4 to about 3.2), mean manganese concentrations (from about 5,000 to 3,800 $\mu\text{g/L}$), and mean zinc concentrations (from about 2,500 to 2,100 $\mu\text{g/L}$). Mean copper concentrations increased (from about 120 to 170 $\mu\text{g/L}$). The decrease in stream pH indicates no improvement from the bulkheads. The greater pre-bulkhead manganese concentrations (Figure 6c) are clearly separated from lower post-bulkhead values, evidence that the bulkheads improved water quality with respect to manganese. In contrast, pre-bulkhead zinc and copper mean concentrations generally fall within the range of data from 2004 to 2015, indicating no substantial change in concentration after bulkhead installation (Figure 6b). These results indicate the difficulty of drawing any firm conclusions from only two pre-treatment data points, but generally indicate that pH decreased through time and manganese concentrations may have improved slightly after bulkhead installation. Results are inconclusive for copper and zinc.

3.1.2.2. Mine tunnel hydrographs

Mine tunnel hydrographs indicate the range and timing of discharge changes at the tunnels as bulkheads were closed. At the American tunnel, closure of bulkhead AT#1 in 1996 decreased discharge from values greater than 0.1 to about 0.03 m^3/s (Figure 7). Discharge slowly increased to less than 0.06 m^3/s in late 2002 when closure of AT#2 decreased discharge to less than 0.01 m^3/s (Figure 7). Subsequently, discharge increased and seemed to stabilize near 0.02 m^3/s in late 2003 when closure of AT#3 decreased discharge to between 0.005 and about 0.01 m^3/s for the remainder of the study period, representing as much as a 95% decrease from initial conditions (Figure 7). At the Mogul mine portal, discharge increased by almost 100 times (9,100%) from 1992 to 2001 (Table 2, Figure 7), and decreased after closure of the Mogul bulkhead in 2003 to 0.003

Figure 6. Graphs comparing (A) pH, and dissolved (B) copper, (C) manganese, and (D) zinc concentrations (in micrograms per liter [$\mu\text{g/L}$]) at the mouth of Cement Creek in samples collected before active water treatment and bulkhead installation (1971 and 1981) to samples collected after cessation of water treatment and after bulkhead installation (2004–2015). The number of samples (n) indicated for each boxplot. Central line in boxplot is median, lower and upper boundaries of box are 25th and 75th percentiles (inter-quartile range) of the data, and lower and upper whiskers extend to the largest and smallest values no further than 1.5 times the interquartile range. Values beyond this range are shown beyond the whisker. (For interpretation of the references to color in this figure legend, the reader is referred to the Web version of this article.)



m^3/s in 2008 (still more than 1,000% greater than in 1992) (Table 2, Figure 7, Walton-Day et al., 2020). At Red and Bonita, discharge increased from no flow (1997–2001) to a maximum of about $0.03 \text{ m}^3/\text{s}$ in July 2015 (Table 2, Figure 7). Increasing discharge is most notable starting in 2005 after closure of all four bulkheads (Table 2, Figure 7), though increased discharge was noted as early as July 2003 (Bonita Peak Community Advisory Group, 2019a). At Gold King tunnel, discharge increased from no flow in 1994 to about $0.02 \text{ m}^3/\text{s}$ in 2006, generally decreasing after 2006 to values less than $0.005 \text{ m}^3/\text{s}$ in 2015. At Black Hawk tunnel, discharge increased 4,000% from 1991 to 2005 with one greater but unreported measurement during 2002 (Table 2, Figure 7).

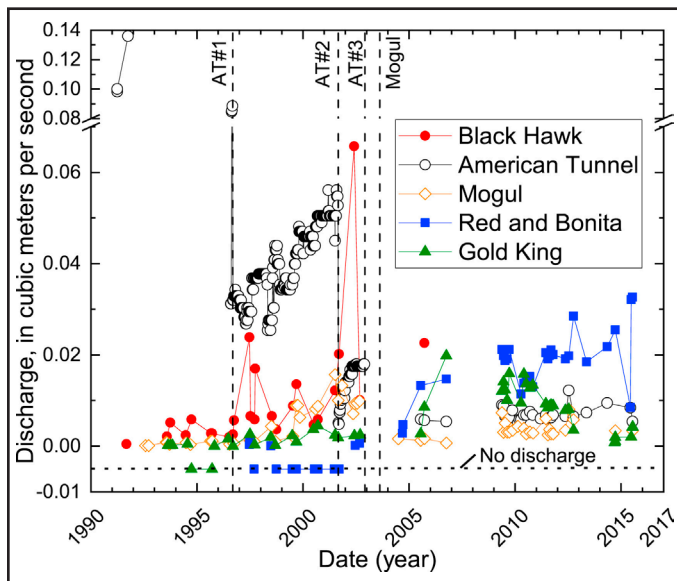


Figure 7. Graph showing variation in discharge from the American tunnel and the Black Hawk, Mogul, Red and Bonita, and Gold King mine tunnels. Vertical lines represent closure of the American tunnel #1 bulkhead (AT#1), American tunnel #2 bulkhead (AT#2), American tunnel #3 bulkhead (AT#3), and the Mogul bulkhead (Mogul). Horizontal line near bottom of graph indicates data points where no discharge was specifically noted in original data records. Data from Walton-Day et al., (2020).

The discharge responses of non-bulkheaded flowing mine tunnels in Cement Creek relate to the timing of bulkhead closure at the American tunnel and Mogul mine and indicate the hydrologic effects of the bulkhead closures. Most of this discussion is derived from Sorenson and Brown (2015) though other data presented herein (Black Hawk) are also interpreted. Three primary sources of water to American tunnel were the basis for locations of the American tunnel bulkheads: (1) the veins and fractures associated with the Sunnyside mine workings and located east of AT#1; (2) water bearing fractures and faults located between AT#1 and AT#2; and (3) diffuse seepage located between AT#2 and the portal (Figure 4) (Sorenson and Brown, 2015). AT#1 was intended to back up and impound fracture-related groundwater within the Sunnyside workings. Bulkheads located in the Sunnyside workings east of the watershed divide (Figure 4) were intended to prevent groundwater impounded in the Sunnyside workings by AT#1 from discharging at the Mogul mine or into the upper Animas River downstream from the Sunnyside basin (Sorenson and Brown, 2015). Final recorded elevation of the

	American Tunnel PE = 3,236 m	Red and Bonita PE = 3,340 m	Mogul PE = 3,475 m	Gold King PE = 3,487 m	Black Hawk PE = 3,536 m
Discharge (m³/s)					
Min. value	0.0048	No flow	0.00017	No Flow	0.000481
Date of min.	14 Sep 2001	Mult. 1997–2001	30 July 1992	29 Sep 1994	7 Sep 1991
Max. value	0.136	0.0326	0.0157	0.0198	0.0657
Date of max.	2 Oct 1991	15 July 2015	9 July 2001	3 Oct 2006	31 May 2002
pH (standard units)					
Min. value	3.8	1.7	1.1	0.9	5.6
Date of min.	29 June 1998	29 June 1998	7 July 1998	29 June 1998	19 Sep 1997
Max. value	9.12	6.5	4.8	5.13	7.64
Date of max.	18 Nov 1988	14 July 2009	19 July 2002	14 Apr 2010	7 Sep 1991
Copper load (kg/d)					
Min. value	0.00248	0.00569	0.0024	0.00739	0.00036
Date of min.	17 Feb 2010	14 July 2009	4 Oct 2006	3 Nov 1993	3 Aug 1993
Max. value	0.732	0.0999	13.2	22.0	0.0388
Date of max.	15 Oct 1997	21 July 2005	3 Sep 1999	2 July 1997	10 Sep 1999
Manganese load (kg/d)					
Min. value	1.5	0.117	0.128	0.0921	0.0749
Date of min.	4 Sep 2001	26 June 1997	30 July 1992	3 Nov 1993	7 Sep 1991
Max. value	228	83.0	28.5	88.9	11.1
Date of max.	2 Aug 2001	2 Oct 2012	9 July 2001	3 Oct 2006	20 Sep 2005
Zinc load (kg/d)					
Min. value	0.87	0.22	0.434	0.0809	0.0237
Date of min.	4 Sep 2001	20 June 2002	23 Sep 1992	3 Nov 1993	7 Sep 1991
Max. value	140	39.5	83.5	57	1.81
Date of max.	2 Aug 2001	2 Oct 2012	1 Oct 1999	1 July 1999	20 Sep 2005

Table 2. Portal elevations, and minimum and maximum values and dates of occurrence for discharge, pH, and copper, manganese, and zinc loads in the American tunnel and Black Hawk, Gold King, Mogul, and Red and Bonita mine tunnels, 1988–2015. Discharge, pH, and load data from Walton-Day et al. (2020), elevation data from Sorenson and Brown (2015) and Google Earth (Black Hawk) [PE, portal elevation; m, meters; m³/s, cubic meters per second; Min, minimum; Mult., multiple; Max., maximum; kg/d, kilograms per day].

water behind the AT#1 bulkhead was 3,557 m measured 14 May 2001 (Sorenson and Brown, 2015). This water level is greater than elevation of all other tunnels (Table 2). Black Hawk tunnel (having the highest portal elevation = 3,536 m) and Mogul tunnel (3,475 m) showed marked increases in discharge after 2001 with minor increases shown for Gold King tunnel (3,487 m) (Figure 7). This increased discharge from the Mogul and Gold King tunnels has been attributed to the mine pool impounded behind AT#1 (Sorenson and Brown, 2015). The elevation and timing of discharge from Black Hawk tunnel indicate that increased discharge at that tunnel is also likely related to water impounded behind AT#1. Even though Red and Bonita portal elevation (3,340 m) is lower than the AT#1 water level, Red and Bonita tunnel remained dry before AT#2 was closed and is likely not hydrologically connected to the Sunnyside mine pool.

Bulkhead AT#2 was designed to limit water draining into American tunnel between AT#1 and AT#2 and closed in August 2001. Groundwater impounded behind the bulkhead equilibrated at an elevation of 3,357m, recorded in August 2002, greater than the elevation of Red and Bonita mine tunnel portal (3,340 m); water impounded behind AT#2 is responsible for the increased Red and Bonita mine-tunnel discharge observed starting in 2003 (Sorenson and Brown, 2015). Because the water elevation behind AT#2 (3,357 m) is less than that at Mogul (3, 475 m) (Sorenson and Brown, 2015), discharge at the Mogul mine was relatively constant after closure of AT#2 (Figure 7, Walton-Day et al., 2020).

Closure of AT#3 (December 2002) was designed to limit diffuse seepage between AT#2 and AT#3 from discharging at the American tunnel portal (Sorenson and Brown, 2015). Closure of the Mogul tunnel bulkhead (2003) was designed to limit discharge at the mouth of the Mogul mine. There were no discharge data for the tunnels in the period between installation of these two bulkheads (most of 2003). After these two bulkheads were installed, discharge decreased at American tunnel and Mogul tunnel, but continued increasing at both the Gold King and Red and Bonita tunnels (Figure 7) (Sorenson and Brown, 2015).

A possible alternate explanation for changing discharge in the tunnels is short-term climate variation of wet years versus dry years. However, climate is likely not the cause of discharge variations because if it were a controlling factor, the hydrographs at different nonbulkheaded tunnels would be showing similar patterns through time, which is generally not the case. In addition, none of the peak discharge years for the tunnels shown on Table 2, for which there is discharge record at USGS station 09358550 (2001, 2002, 2006, 2015; Supplemental Figure S1b), are wet years on the hydrograph; 2002 was notably a dry year.

3.1.2.3. *Water quality at Cement Creek during and after active treatment and bulkhead installation*

Water quality at the mouth of Cement Creek exhibited large changes in the period from 1996 through 2015 (Figure 8). Metal loads at some of the tunnels also exhibited large changes during the same time period (Table 2, Figure 8). Raw and DWM values for pH, and dissolved copper, manganese, and zinc generally show similar long-term patterns, although the DWM curves have lower values than the raw data (Supplemental Figure S2, Figure 8). Discharge weighting gives more weight to higher flow, more dilute concentration samples, resulting in lower DWM concentrations compared to the raw-data mean concentrations.

The DWM pH of Cement Creek decreased from about 4.5 to 3.6 during 1996–2015 (Figure 8). Mine tunnel pH varied from as low as 0.9 at the Gold King tunnel in June 1998 (a year when all tunnels except Black Hawk tunnel demonstrated minimum pH) to 9.12 in November 1988 at the American tunnel. The high value may be related to water-treatment adjustments (Walton-Day et al., 2020 and sources therein). The DWM dissolved copper concentrations increased from about 50 to 150 $\mu\text{g/L}$ between 1996 and 2009, decreasing to about 50 $\mu\text{g/L}$ in 2015 (Figure 8b). Maximum dissolved copper loads from mine tunnels ranged from less than 0.1 kg/d to about 22 kg/d (at Gold King in 1997) (Table 2). The DWM dissolved manganese concentrations increased from about 1,000 to 3,000 $\mu\text{g/L}$ from 1996 to 2012–2013 (Figure 8c). Maximum dissolved manganese loads from mine tunnels ranged from about 11 to 89 kg/d with as much as 228 kg/d at American tunnel in 2001 (Table 2). The DWM dissolved zinc concentrations increased from about 900 to 1,600 $\mu\text{g/L}$ from 1996 to 2013 (Figure 8d). Maximum dissolved zinc loads from mine tunnels ranged from about 2 to 84 kg/d with as much as 140 kg/d at American tunnel in 2001 (Table 2). DWM manganese and zinc concentrations show similar concentration patterns through time with slight decreases from 1996 to 2000, followed by increases in DWM concentrations (and raw data) from about 2000 through 2012–2013 (Figure 8, Supplemental Figure S2). Average daily metal loads at the mouth of Cement Creek for the period 2004–2015 were about 10 kg/d for copper, 200 kg/d for manganese, and 120 kg/d for zinc.

The timing of pH decreases in Cement Creek is not obviously related to patterns and timing of changes in discharge or pH values at the various mine tunnels (Figure 7, Table 2). In addition to the mine tunnels, there are numerous sources of low pH water in Cement Creek related to mining. As well, naturally occurring low pH water also derives from unmined mineralization and hydrothermal alteration in the watershed (Mast et al., 2007; Yager and Bove, 2007; Wirt et al., 2007). The decreased pH through time might indicate increased unsampled groundwater discharge occurred in South Fork after bulkhead installation, as also evidenced by increased discharge at the Black Hawk tunnel during this time. This idea warrants additional investigation.

Increased mine-tunnel discharge in non-bulkheaded tunnels caused increased metal loads from the mine tunnels that coincide with, and likely contributed to, some of the changes in water quality at the mouth of Cement Creek (Figure 8b–d). Loads from the mine tunnels, rather than their concentrations are presented because loads quantify the most important sources of metals to the receiving stream (Kimball et al., 2002; Walton-Day et al., 2005). As previously described, active water treatment removed most of the metal load from the American tunnel during 1989–2003, and some of the load from the Mogul, Red and Bonita, and Gold King tunnels when Cement Creek (1996–2003) and Gold King were being treated (2003–2004). The increased discharge at the Black Hawk tunnel (1996–2002) that drains to the South Fork of Cement Creek (Figures 4 and 7) was not treated. The increased loads of manganese and less strongly zinc that occurred with increased Black Hawk tunnel discharge (Figures 7 and 8c–d) coincide with the onset of gradual increases in DWM manganese and zinc at the mouth of Cement Creek that started around 2000 and are a possible cause for some of these increases (Figure 8c–d). Elevated copper loads at Gold King tunnel during this period were not consistently captured at the treatment plant, and likely contributed to increasing DWM copper concentrations at the mouth of Cement Creek as did minor (untreated) copper loads at the Black Hawk tunnel (Table 2).

After water treatment ended in 2004, untreated discharge and metal loads from the American, Mogul, Red and Bonita, and Gold King tunnels moved downstream and appear to influence water quality at the mouth of Cement Creek. After 2003, the pattern of copper load from the Gold King tunnel closely mimicked the pattern of DWM copper concentrations at the mouth of Cement Creek, which increased until 2009 but then decreased to values similar to those in 1995 (Figure 8b). The other four tunnels (American, Black Hawk, Mogul, and Red and Bonita) had copper loads that were less than 5 percent of the Gold King tunnel during this time (2003–2015) and are not shown (Table 2, and data in Walton-Day et al., 2020). The post-2003 patterns of manganese and zinc DWM concentrations at the mouth of Cement Creek are coincident with increasing loads at the Red and Bonita and Gold King tunnels (Figure 8c–d). The American and Mogul tunnels have zinc and manganese loads that are generally less than 50% of the loads at the Red and Bonita and Gold King tunnels at this time and are not shown (data in Walton-Day et al., 2020). Slight decreases in DWM manganese and zinc concentrations from 2013 to 2015 may have been caused by decreased loading from the Gold King tunnel during this time (Figure 8c–d). During this time, the DWM manganese and zinc concentration decreases are not as steep as the decrease in the DWM copper because the Red and Bonita tunnel provides manganese and zinc load, but minimal copper load (Figure 8b–d). The coincidence in the timing of load increases starting in 2003 from the Gold King and Red and Bonita tunnels with increases in DWM metal concentrations at the mouth of Cement Creek provides evidence that the changes in discharge and loads from these tunnels contributed to the observed increases in copper, manganese, and zinc DWM concentrations at the mouth of Cement Creek. Additional evidence is provided

The coincidence in the timing of load increases starting in 2003 from the Gold King and Red and Bonita tunnels with increases in DWM metal concentrations at the mouth of Cement Creek provides evidence that the changes in discharge and loads from these tunnels contributed to the observed increases in copper, manganese, and zinc DWM concentrations at the mouth of Cement Creek. Additional evidence is provided

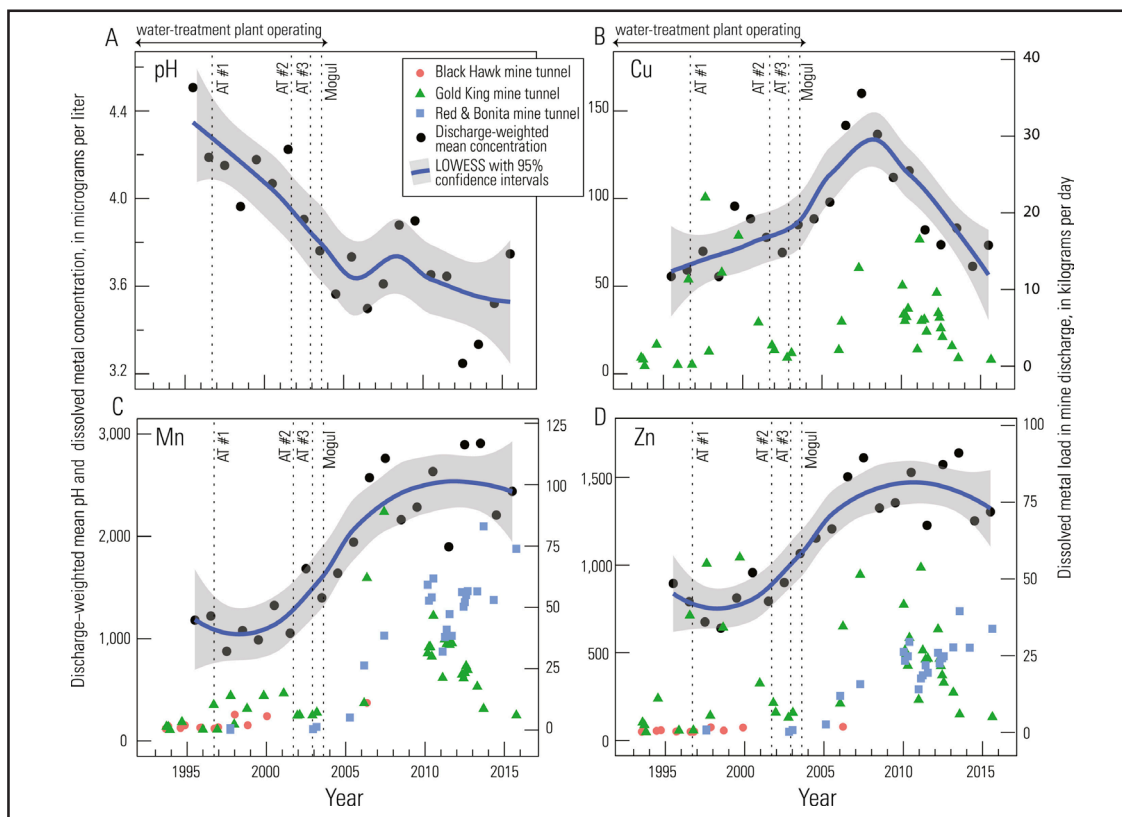


Figure 8. Graphs showing variation in (A) discharge-weighted-mean (DWM) pH at the mouth of Cement Creek, (B) DWM concentrations of copper (Cu) at the mouth of Cement Creek and copper loads from the Gold King mine, (C) DWM concentrations of manganese (Mn) at the mouth of Cement Creek and manganese loads from the Black Hawk, Red and Bonita, and Gold King mine tunnels, (D) DWM concentrations of zinc (Zn) at the mouth of Cement Creek and zinc loads from the Black Hawk, Red and Bonita, and Gold King mine tunnels. All annual average DWM values are represented individually as black dots and as a LOWESS (locally weighted scatter plot smoothing) line with 95% confidence intervals. Vertical lines represent closure of the American tunnel #1 bulkhead (AT#1), American tunnel #2 bulkhead (AT#2), American tunnel #3 bulkhead (AT#3), and the Mogul bulkhead (Mogul).

by the large copper and zinc loads at the Gold King tunnel during 1996–2000, that are of similar magnitude to those that occurred during 2004–2015 (Figure 8b and d). Because of partial treatment of upper Cement Creek in the 1990s, these loads did not fully contribute to water quality at the mouth of Cement Creek. When treatment ceased by 2004, the loads from this tunnel were transported downstream and were partly responsible for increasing copper and zinc DWM concentrations observed at the mouth of Cement Creek (Figure 8b and d). Finally, the mean daily metal loads calculated for 2004–2015 at the mouth of Cement Creek (copper, 10 kg/d; manganese, 200 kg/d; zinc, 120 kg/d) are in the range of metalload values for the tunnels, particularly Gold King and Red and Bonita (Figure 8b–d) indicating that the loads from the tunnels substantially contributed to the loads and thus the concentration increases observed at the mouth of Cement Creek. The lower copper load at the mouth of Cement Creek compared to some tunnel loads likely indicates copper attenuation between upper Cement Creek and the mouth of Cement Creek (Kimball et al., 2002).

4. SUMMARY AND CONCLUSIONS

The water-quality response in two different study areas in Colorado after bulkhead installation for remediation of abandoned draining mines indicated mixed water-quality responses, with only limited improvement in receiving waters. In Lake Fork Creek (upper Arkansas River watershed), a bulkhead installed in Dinero tunnel in 2009 caused significant water-quality improvement (pH and zinc and manganese concentrations and loads) at the Dinero tunnel mouth (DT-0) but significant water-quality degradation at the nearby Nelson tunnel (NT-0). At the downstream-most site on Lake Fork Creek, LF-580, limited water-quality improvement included statistically significant decreased manganese concentrations and attainment of zinc water-quality standards for two of 15 samples after bulkhead closure. At LF-580, increased post-bulkhead zinc loads may indicate increased post-bulkhead, unsampled groundwater contributions from multiple sources upstream from LF-580.

In Cement Creek (upper Animas River watershed) four bulkheads were installed and closed between 1996 and 2003. Water treatment (1989–2003) overlapped with the period of bulkhead installation and complicated interpretation of bulkhead effects. Comparison of limited pre-treatment data with post-bulkhead data from near the mouth of Cement Creek indicates possible improvement in manganese concentrations, decreasing pH through time, and is inconclusive for copper and zinc concentrations. There is no consistent and robust evidence that bulkheads caused substantial positive or negative long-term changes in water quality. In contrast, the lowest concentrations of copper, manganese, and zinc occurred during active treatment (1989–2003). After bulkheads were installed, and active water treatment ceased (2004), water quality in Cement Creek degraded. The timing of water-quality degradation was similar to timing of increased discharge and metal loads from non-bulkheaded tunnels that occurred in response to bulkhead installation in other tunnels, evidence that increased loading from the tunnels contributed to water-quality degradation at the mouth of Cement Creek. In both study areas, data potentially indicate increased, unsampled groundwater discharge after bulkhead installation that caused increased zinc loads at site LF-580 after Dinero bulkhead installation, and decreased pH over time at Cement Creek. Greater understanding of this result could be a topic for future investigations. Overall, the lack of substantial water-quality improvement in these two areas from bulkhead installation indicates that other treatment techniques might warrant consideration.

DATA AVAILABILITY

Data for the four sites discussed in the Dinero tunnel section are available from the National Water Information System (NWIS) (<https://doi.org/10.5066/F7P55KJN>) using USGS site identification numbers 391504106225200 (DT-0); 391454106224201 (LF-537); 391452106224201 (LF-580); and 391501106230601 (NT-0). Data for the mouth of Cement Creek are available from the Water Quality Portal (WQP) (<https://www.waterqualitydata.us/>) using site identifiers 21COL001_WQX-CEM49, ARSG-CC48, CORIVWCH_WQX-323, USEPA_REGION8-CC48, and USGS-09358550. Data for two additional samples, USGS site ID 374854107393900, October 4, 1971, and USGS site ID 375015107404001, September 24, 1981, are available from NWIS at <https://doi.org/10.5066/F7P55KJN>. Data for the five mine tunnels in Cement Creek are available from Walton-Day et al. (2020) at <https://doi.org/10.5066/P9FE667O>.

DECLARATION OF COMPETING INTEREST

The authors declare that they have no known competing financial interests or personal relationships that could have appeared to influence the work reported in this paper.

ACKNOWLEDGEMENTS

Authors acknowledge funding support from the U.S. Geological Survey Environmental Health Program in the Ecosystems Mission Area, the Bureau of Land Management, the State of Colorado Division of Reclamation, Mining and Safety, and Colorado Mountain College. Helpful comments from seven reviewers improved manuscript clarity and interpretations. Nancy J. Bauch (U.S. Geological Survey) assisted with calculation of water-quality standards. Kirstin Brown, Colorado Division of Reclamation, Mining and Safety, provided geographic information for mine tunnels and bulkheads in the Silverton area. Any use of trade, firm, or product names is for descriptive purposes only and does not imply endorsement by the U.S. Government.

APPENDIX A. SUPPLEMENTARY DATA

Supplementary data to this article can be found online at <https://doi.org/10.1016/j.apgeochem.2021.104872>.

REFERENCES

- Alpers, C.N., Nordstrom, D.K., Thompson, J.M., 1994. Seasonal variations of Zn/Cu ratios in acid mine water from Iron Mountain, California. In: Alpers, C.N., Blowes, D. W. (Eds.), *Environmental Geochemistry of Sulfide Oxidation*, vol. 550. Am Chem Soc Symp Series, pp. 324–344. https://www.researchgate.net/publication/236586211_Seasonal_Variations_of_ZnCu_Ratios_in_Acid_Mine_Water_from_Iron_Mountain_California/link/5b335cb2aca2720785e9ce15/download
- Aulenbach, B.T., Burns, D.A., Shanley, J.B., Yanai, R.D., Bae, K., Wild, A., Yang, Y., Yi, D., 2016. Approaches to stream solute load estimation for solutes with varying dynamics from five diverse small watersheds. *Ecosphere* 7. <https://doi.org/10.1002/ecs2.1298>
- Blowes, D.W., Ptacek, C.J., Jambor, J.L., Weisener, C.G., 2003. The geochemistry of acid mine drainage chapter 9.05. In: Holland, H.D., Turekian, K.K. (Eds.), *Treatise on Geochemistry*. Elsevier. <https://doi.org/10.1016/B0-08-043751-6/09137-4>
- Blowes, D.W., Ptacek, C.J., Jambor, J.L., Weisener, C.G., Paktunk, D., Gould, W.D., Johnson, D.B., 2014. The Geochemistry of Acid Mine Drainage Chapter 11.5 *Treatise on Geochemistry*, second ed. Elsevier. <https://doi.org/10.1016/B978-0-08-095975-7.00905-0>
- Bonita Peak Community Advisory Group, 2019a. Official site – Gladstone chronology from Silverton standard. <https://www.bonitapeakcag.org/wp-content/uploads/2019/10/Gladstone-Chronology-from-Silverton-Standard-reformatted.pdf> (Accessed 25 November 2019).
- Bonita Peak Community Advisory Group, 2019b. Official site – mapping. <https://www.bonitapeakcag.org/documents/> (Accessed 22 November 2019).
- Bove, D.J., Mast, M.A., Dalton, J.B., Wright, W.G., Yager, D.B., 2007. Major styles of mineralization and hydrothermal alteration and related solid- and aqueous- geochemical signatures. In: Church, S.E., von Guerard, P., Finger, S.E. (Eds.), *Integrated Investigations of Environmental Effects of Historical Mining in the Animas River Watershed, San Juan County, Colorado*. U.S. Geological Survey Professional Paper 1651 Chapter E7. https://pubs.usgs.gov/pp/1651/downloads/Vol1_combinedChapters/vol1_chapE3.pdf
- Burbank, W.S., Luedke, R.G., 1969. *Geology and Ore Deposits of the Eureka and Adjoining Districts San Juan Mountains, Colorado*. U.S. Geological Survey Professional Paper 535. <https://doi.org/10.3133/pp535>
- Bureau of Land Management, 2006. *Removal Site Inspection and Engineering Evaluation and Cost Analysis (EE/CA) Dinero Tunnel, Acid Mine Drainage, Lake County, Colorado*. Royal Gorge Field Office, Canon City, Colorado.
- Bureau of Reclamation, 2015. *Technical Evaluation of the Gold King Mine Incident, San Juan County, Colorado*. US Department of Interior, Bureau of Reclamation, Technical Service Centre, Denver, Colorado. <https://www.usbr.gov/docs/goldkingminereport.pdf>
- Caine, J.S., Wilson, A.B., 2011. The hydrogeology of the san Juan mountains. In: Blair, R., Bracksieck, G. (Eds.), *The Eastern San Juan Mountains: Their Geology, Ecology and Human History*. University Press of Colorado, pp. 79–98. <https://upcolorado.com/university-press-of-colorado/item/1923-the-eastern-san-juan-mountains>
- Church, S.E., 2007. *Environmental Effects of Historical Mining in the Animas River Watershed, Southwestern Colorado*. U.S. Geological Survey Fact Sheet 2007-3051. <https://doi.org/10.3133/fs20073051>

- Church, S.E., Mast, M.A., Martin, E.P., Rich, C.L., 2007a. Mine inventory and compilation of mine-adit chemistry data. In: Church, S.E., von Guerard, P., Finger, S.E. (Eds.), *Integrated Investigations of Environmental Effects of Historical Mining in the Animas River Watershed*, San Juan County, Colorado. U.S. Geological Survey Professional Paper 1651 Chapter E5. https://pubs.usgs.gov/pp/1651/downloads/Vol1_combinedChapters/vol1_chapE5.pdf
- Church, S.E., Owen, J.R., von Guerard, P., Verplanck, P.L., Kimball, B.A., Yager, D.B., 2007b. The effects of acidic mine drainage from historical mines in the Animas River watershed, San Juan County, Colorado – what is being done and what can be done to improve water quality? In: DeGraff, J.V. (Ed.), *Understanding and Responding to Hazardous Substances at Mine Sites in the Western United States: Geological Society of America Reviews in Engineering Geology XVII*. [https://doi.org/10.1130/2007.4017\(04\)](https://doi.org/10.1130/2007.4017(04))
- Colorado Department of Health, 1988. Annual Inspection of Wastewater Treatment Facilities for Terry Tunnel, Mayflower Mill and American Tunnel, Respectively, CPDES Permit No. CO-0036056, CO-0000426, and CO-0027529, San Juan County: Record Number CO-0027529-742. <https://oitco.hylandcloud.com/CDPHERMPublicAccess/api/Document/AWfQVqh0Ywc3RHI%3%89APyK5Q66B%3%89042Ljd5CT%3%89Va6%3%81VwvK5VxF6NSdv1zla6fecb0Rg996dYoVXqUfIMotCWXi9A%3D/> Accessed 11 Nov 2019.
- Colorado Department of Natural Resources Division of Minerals and Geology, 2002. Best Practices in Abandoned Mine Land Reclamation: the Remediation of Past Mining Activities. <https://drive.google.com/file/d/1y5tpZODtXSTrcBNsLZ50SiE4Lu3SinU/view> (Accessed 26 September 2019).
- Colorado Department of Public Health and Environment, 2019. Mining and Water Quality. <https://www.colorado.gov/pacific/cdphe/wq-mining> (Accessed 26 September 2019).
- Colorado Department of Public Health and Environment Water Quality Control Commission, 2020. Regulation No. 32 - Classifications and Numeric Standards for Arkansas River Basin 5 CCR 1002-1032. <https://www.sos.state.co.us/CCR/GenerateRulePdf.do?ruleVersionId=8114&fileName=5%20CCR%201002-32> (Accessed 3 October 2019).
- Cowie, R., Roberts, S., 2020. Bonita Pear Mining District 2016-2018 Seeps, Springs, and Draining Mines Characterization Report. Mountain Studies Institute, Durango, Colorado. <https://semsub.epa.gov/work/08/100007694.pdf> (Accessed 16 December 2020).
- Einarson, D.S., Abel Jr., J.F., 1990. Tunnel bulkheads for acid mine drainage chap 71. In: Sihna, R.S. (Ed.), *Proceedings International Symposium on Unique Underground Structures Denver, Colorado USA June 12-15, 1990*, 71-1-71-19.
- Gusek, J.J., Figueroa, L.A., 2009. Mitigation of Metal Mining Influenced Water, vol. 2. Society for Mining, Metallurgy, and Exploration, Inc., Littleton, Colorado. -13:978-0-87335-306-9.
- International Network for Acid Prevention, 2014. Global Acid Rock Drainage Guide, Prediction, Prevention, Management. <http://www.gardguide.com/images/5/5f/TheGlobalAcidRockDrainageGuide.pdf> (Accessed 7 November 2019).
- Jambor, J.L., Nordstrom, D.K., Alpers, C.N., 2000. Metal-sulfate salts from sulfide mineral oxidation. In: Alpers, C.N., Jambor, J.L., Nordstrom, D.K. (Eds.), *Sulfate Minerals-Crystallography, Geochemistry, and Environmental Significance*. Rev. Mineral. Geochem, vol. 40, pp. 303–350. <https://pubs.geoscienceworld.org/msa/rimg/article-abstract/40/1/303/140666/Metal-sulfate-Salts-from-Sulfide-Mineral-Oxidation>
- Johnson, D.B., Hallberg, K.B., 2005. Acid mine drainage remediation options: a review. *Sci. Total Environ.* 338, 3–14. <https://doi.org/10.1016/j.scitotenv.2004.09.002>
- Johnson, R.H., Yager, D.B., 2006. Completion Reports, Core Logs, and Hydrogeologic Data from Wells and Piezometers in Prospect Gulch, San Juan County, Colorado. U.S. Geological Survey Open-File Report. 2006-1030. <https://pubs.usgs.gov/of/2006/1030/>
- Jones, W.R., 2007. History of mining and milling practices and production in San Juan County, Colorado 1871—1991. In: Church, S.E., von Guerard, P., Finger, S.E. (Eds.), *Integrated Investigations of Environmental Effects of Historical Mining in the Animas River Watershed*, San Juan County, Colorado. U.S. Geological Survey Professional Paper 1651 Chapter C. https://pubs.usgs.gov/pp/1651/downloads/Vol1_combinedChapters/vol1_chapC.pdf
- Kimball, B.A., Runkel, R.L., Walton-Day, K., Bencala, K.E., 2002. Assessment of metal loads in watersheds affected by acid mine drainage by using tracer injection and synoptic sampling. *Appl. Geochem.* 17, 1183–1207. [https://doi.org/10.1016/S0883-2927\(02\)00017-3](https://doi.org/10.1016/S0883-2927(02)00017-3)
- Lange, S., 2019. Evaluating the effectiveness of Sunnyside gold corporation’s reclamation, san Juan county, Colorado, USA. In: Fourie, A.B., Tibbett, M. (Eds.), *Australian Center for Geomechanics*, Perth. https://papers.acg.uwa.edu.au/p/1915_99_Lange/
- Manning, A.H., Caine, J.S., 2007. Groundwater noble gas, age, and temperature signatures in an Alpine watershed: valuable tools in conceptual model development. *Water Resour. Res.* 43, W04404. <https://doi.org/10.1029/2006WR005349>
- Marks, M.B., Kirk, A.R., Cormier, M., 2008. Assessment and closure of the glengarry adit, new world mining district, cooke city, Montana. In: *Proceedings of the 25th Annual Meeting of American Society of Mining and Reclamation*, Richmond VA June 14-18, 2008, pp. 628–661. In: <https://www.asrs.us/Portals/0/Documents/Conference-Proceedings/2008/0628-Marks.pdf>
- Mast, M.A., 2018. Estimating Metal Concentrations with Regression Analysis and Water-Quality Surrogates at Nine Sites on the Animas and San Juan Rivers, Colorado, New Mexico, and Utah. U.S. Geological Survey Scientific Investigations Report 2018–5116. <https://doi.org/10.3133/sir20185116>
- Mast, M.A., Verplanck, P.L., Wright, W.G., Bove, D.J., 2007. Characterization of background water quality. In: Church, S.E., von Guerard, P., Finger, S.E. (Eds.), *Integrated Investigations of Environmental Effects of Historical Mining in the Animas River Watershed*, San Juan County, Colorado. U.S. Geological Survey Professional Paper 1651 Chapter E7. https://pubs.usgs.gov/pp/1651/downloads/Vol1_combinedChapters/vol1_chapE7.pdf
- Mayo, A.L., Morris, T.H., Peltier, S., Petersen, E.C., Payne, K., Holman, L.S., Tingey, D., Black, B.J., Gibbs, T.D., 2003. Active and inactive groundwater flow systems: evidence from a stratified, mountainous terrain. *Geol. Soc. Am. Bull.* 115, 1456–1472. <https://pubs.geoscienceworld.org/gsa/gsabulletin/article/115/12/1456/1956/Active-and-inactive-groundwater-flow-systems>

- Nordstrom, D.K., 2011. Hydrogeochemical processes governing the origin, transport and fate of major and trace elements from mine wastes and mineralized rock to surface waters. *Appl. Geochem.* 26, 1777–1791. <https://www.sciencedirect.com/science/article/abs/pii/S0883292711003131>
- Nordstrom, D.K., Alpers, C.N., 1999. Negative pH, efflorescent mineralogy, and consequences for environmental restoration at the Iron Mountain Superfund site, California. *Proc. Natl. Acad. Sci. Unit. States Am.* 96, 3455–3562. <https://doi.org/10.1073/pnas.96.7.3455>
- Nordstrom, D.K., Blowes, D.W., Ptacek, C.J., 2015. Hydrogeochemistry and microbiology of mine drainage: an update. *App. Geochem.* (Tokyo. 1967) 57, 3–16. <https://doi.org/10.1016/j.apgeochem.2015.02.008>
- Schmidt, S.E.A., 2007. Hydrologic Evaluation of Plugging Dinero Tunnel to Improve Water Quality in Lake Fork Creek. MS Thesis. Colorado School of Mines Golden, CO, p. 95. <https://mountainscholar.org/handle/11124/79087>
- Sheoran, A.S., Sheoran, V., 2006. Heavy Metal Removal Mechanism of Acid Mine Drainage in Wetlands: A Critical Review. *Minerals Engineering* 19 105-116. <https://doi.org/10.1016/j.mineng.2005.08.006> (Accessed 11 November 2019).
- Simon Hydro-Search, 1992. Preliminary Characterization of the Hydrology and Water Chemistry of the Sunnyside Mine and Vicinity. Prepared for: San Juan County Mining Venture. <https://dnrweblink.state.co.us/drms/0/doc/957462/Page1.aspx?searchid=1252a171-b1d6-4efc-b247-cafa261d1000> (Accessed 11 February 1992).
- Simon Hydro-Search, 1993. Evaluation of Hydraulic and Hydrochemical Aspects of Proposed Bulkheads Sunnyside Mine. Prepared for: Sunnyside Gold Corporation, March 12, 1993. <https://oitco.hylandcloud.com/CDPHERMPublicAccess/api/Document/AZ%C3%89EmnLjhhz9zUOyLZ9XraixYhNH%C3%89YevLXtN1s2K4MBR8nzEVW3sPua5IsPKcg5%C3%81i4K3Xp1guQKMhfCqfkwQZw%3D/>
- Singewald, Q.D., 1955. Sugar Loaf and St. Kevin Mining Districts, Lake County, Colorado. U.S. Geological Survey Bulletin 1027-E. <https://pubs.usgs.gov/bul/1027e/report.pdf>
- Snow, D., 1968. Hydraulic character of fractured metamorphic rocks on the front range and implications to the Rocky Mountain Arsenal well. *Colorado Sch. Mine. Q.* 63, 167–199.
- Sorenson, A., Brown, K., 2015. Design Basis for Water Impounding Concrete Bulkhead, Red and Bonita Mine, San Juan County, Colorado: Colorado Division of Reclamation, Mining, and Safety, May 18, 2015 with Portions Updated Sept 17 and Nov 4, 2015. <https://semspub.epa.gov/work/08/1765387.pdf>
- Standard Metals Corporation, 1981. Mine Drainage Treatment and Sludge Disposal Plan: Record Number CO-0027529-778. <https://oitco.hylandcloud.com/CDPHERMPublicAccess/api/Document/AVR3GFh5odrpFXNOKd1dA%C3%89AN9KG0152K66NgdyiekIRS9mXI5ud7C8fvialvomb%C3%813IikN0FMeEevvE3KAAUwsts%3D/> (Accessed 11 November 2019).
- Stratus Consulting, 2009. Final Restoration Plan and Environmental Assessment for the Tiger and Dinero Tunnels Restoration. Stratus Consulting, Boulder, CO. <https://www.fws.gov/mountain-prairie/nrda/leadvillecolo/FinalRestorationPlanForTigerDineroTunnels08252009.pdf>
- Sunnyside Gold Corporation, 2003. MLR Annual Report File No. M-1977-378, April 2000 to March 2001: 2003-06-06_REP33799_annualreport. <https://dnrweblink.state.co.us/DRMS/0/doc/806626/Page1.aspx?searchid=222aefea-c564-45e8-9cba-50a0f982cc82> (Accessed 15 November 2019).
- U.S. Environmental Protection Agency, 1994. Acid Mine Drainage Prediction. Office of Solid Waste. EPA 530-R-94-036 NTIS PB94-201829. <https://www.epa.gov/sites/production/files/2015-09/documents/amd.pdf>
- U.S. Geological Survey, 2019a. USGS Water Data for the Nation, U.S. Geological Survey National Water Information System Database. <https://doi.org/10.5066/F7P55KJN>
- U.S. Geological Survey, 2019b. USGS Surface-Water Statistics for Colorado. USGS 07081200 Arkansas River Near Leadville, CO, Annual Statistics for Discharge. https://nwis.waterdata.usgs.gov/co/nwis/annual?site_no=07081200&por_07081200_17776=344903,00060,17776,1968,2021&year_type=W&format=html_table&date_format=YYYY-MM-DD&rdb_compression=file&submitted_form=parameter_selection_list (Accessed 3 October 2019).
- U.S. Surveyor General's Office, 1912. Olga No. 2, Silver King, and H.R. Lodes Mineral Survey 19289: Denver, Colorado January 31, p. 1912.
- von Guerard, P., Church, S.E., Yager, D.B., Besser, J.M., 2007. The Animas River watershed, san Juan county, Colorado. In: Church, S.E., von Guerard, P., Finger, S.E.(Eds.), *Integrated Investigations of Environmental Effects of Historical Mining in the Animas River Watershed*, San Juan County, Colorado. U.S. Geological Survey Professional Paper 1651 Chapter B. https://pubs.usgs.gov/pp/1651/downloads/Vol1_combinedChapters/vol1_chapB.pdf
- Walton-Day, K., 2003. Passive and Active Treatment of Mine Drainage Chapter 16: in Jambor JL, Blowes DW and Ritchie AIM, *Environmental Aspects of Mine Waste Mineralogical Association of Canada Short Course Series Volume 31*. <https://www.mineralogicalassociation.ca/publications/topics-in-mineral-sciences/sc31/>
- Walton-Day, K., Flynn, J.L., Kimball, B.A., Runkel, R.L., 2005. Mass Loading of Selected Major and Trace Elements in Lake Fork Creek Near Leadville, Colorado September–October 2001. U.S. Geological Survey Scientific Investigations Report 2005-5151. <https://pubs.usgs.gov/sir/2005/5151/>
- Walton-Day, K., Mills, T.J., 2015. Hydrogeochemical effects of a bulkhead in the Dinero mine tunnel, Sugar Loaf mining district, near Leadville, Colorado. *Appl. Geochem.* 62, 61–74. <https://doi.org/10.1016/j.apgeochem.2015.03.002>
- Walton-Day, K., Mills, T.J., Amundson, A., Dee, K.T., Relego, M.R., Borbely, C., 2013. The water-quality effects of a bulkhead installed in the Dinero mine tunnel, near Leadville, Colorado. In: Wolkersdorfer, C., Brown, A., Figueroa, L. (Eds.), *Reliable Mine Water Technology: Proceedings of the International Mine Water Association Meeting*, Golden, Colorado, August 6–9, 2013, pp. 1157–1163. https://www.imwa.info/docs/imwa_2013/IMWA2013_Walton-Day_396.pdf

- Walton-Day, K., Poeter, E., 2009. Investigating hydraulic connections and the origin of water in a mine tunnel using stable isotopes and hydrographs. *Appl. Geochem.* 24, 2266–2282. <https://doi.org/10.1016/j.apgeochem.2009.09.015>
- Walton-Day, K., Runkel, R.L., Mast, M.A., 2020. Water Quality and Discharge Data from Abandoned Draining Mine Tunnels Near Silverton, Colorado 1988-2015. U.S. Geological Survey data release. <https://doi.org/10.5066/P9FE6670>
- Wirt, L., Vincent, K.R., Verplanck, P.L., Yager, D.B., Church, S.E., Fey, D.L., 2007. Geochemical and hydrologic processes controlling formation of ferricrete. In: Church, S.E., von Guerard, P., Finger, S.E. (Eds.), *Integrated Investigations of Environmental Effects of Historical Mining in the Animas River Watershed, San Juan County, Colorado*. U.S. Geological Survey Professional Paper 1651 Chapter E17. https://pubs.usgs.gov/pp/1651/downloads/Vol2_combinedChapters/vol2_chapE17.pdf
- Wolkersdorfer, C., 2008. *Water Management at Abandoned Flooded Underground Mines, Fundamentals, Tracer Tests, Modelling, Water Treatment*. Springer-Verlag, Berlin.
- Yager, D.B., Bove, D.J., 2007. Geologic framework. In: Church, S.E., von Guerard, P., Finger, S.E. (Eds.), *Integrated Investigations of Environmental Effects of Historical Mining in the Animas River Watershed, San Juan County, Colorado*. U.S. Geological Survey Professional Paper 1651 Chapter E1. https://pubs.usgs.gov/pp/1651/downloads/Vol1_combinedChapters/vol1_chapE1.pdf
- Younger, P.L., Banwart, S.A., Hedin, R.S., 2002. *Mine Water, Hydrology, Pollution, Remediation*. Kluwer Academic Publishers, Dordrecht.

Additional Resources

While these additional publications are not included in this volume due to copyright restrictions, the New Mexico Water Resources Research Institute wishes to acknowledge these additional publications from prior conference presenters.

Sediment Cores in a Municipal Drinking-Water Reservoir as a Record of Geochemical Transport Within a Watershed, Farmington Lake, New Mexico, USA

by Johanna M. Blake, Jeb E. Brown, Christina L. Ferguson, and Rebecca J Bixby

This work appears in the journal *Environmental Earth Sciences* (Volume 81, article 96)
© 2022 Springer Nature <https://doi.org/10.1007/s12665-022-10227-w>

Chapter 4: From Deep Time to Deep Valleys Hydrology and Ecology of the Animas River Drainage

by Cynthia E. Dott, Gary L. Gianniny, and David A. Gonzales

From the book *Gold Metal Waters: The Animas River and the Gold King Mine Spill*
Edited by Brad T. Clark and Peter McCormick

© 2021 University Press of Colorado <https://doi.org/10.5876/9781646421756>

Agricultural Soils of the Animas River Watershed After the Gold King Mine spill: An Elemental Spatiotemporal Analysis Via Portable X-ray Fluorescence Spectroscopy

by Gaurav Jha, Swagata Mukhopadhyay, April L. Ulery, Kevin Lombard,
Somsubhra Chakraborty, David C. Weindorf, Dawn VanLeeuwen, and Colby Brungard

This work appears in the *Journal of Environmental Quality* (Volume 50, Issue 3)
© 2021 John Wiley and Sons <https://doi.org/10.1002/jeq2.20209>

4th Annual Animas and San Juan Watersheds Conference

Successes and Challenges from Headwaters to Lake Powell

June 19–22, 2019

Henderson Fine Arts Center, San Juan College, Farmington, NM



Conference Planning Partners:







Wednesday, June 19, 2019

Morning Session

- 9:00 Welcoming Remarks and Introduction
Dennis McQuillan, New Mexico Environment Department
Victor Snover, City of Aztec Mayor
- 9:15 Congressional Statements via Video
Representative Deb Haaland
Senator Martin Heinrich
Representative Ben Ray Luján
Senator Tom Udall
- 9:30 *Gold King Mine Spill: Analysis of Response by Federal, State, Local, and Tribal Entities*
(Abstract 2)
Randy Velarde, Farmington Police Department
- 9:50 *Water Quality Monitoring in the San Juan River Watershed – Multijurisdictional Efforts Using WIIN Act Appropriations* (Abstract 7)
Robert Cook, U.S. Environmental Protection Agency
Alexandra Ratcliff, Southern Ute Indian Tribe
Kristine Yurdin, New Mexico Environment Department
Steve Austin, Navajo Nation Environmental Protection Agency
Lucy Parham, Utah Department of Environmental Quality
- 10:30 BREAK
- 11:00 *Sampling of Stream and Irrigation Ditch Sediment and Agricultural Crops to Characterize the Nature and Extent of Impact from the August 2015 Gold King Mine Spill* (Abstract 11)
Gaurav Jha, **April Ulery**, New Mexico State University, **Kevin Lombard**, Farmington Agricultural Science Center
- 11:20 *Mining Legacy of the Animas River Watershed Recorded in Aztec Reservoir Sediment Deposition* (Abstract 9)
Christina Ferguson, **Johanna Blake**, and **Jeb Brown**, U.S. Geological Survey
- 11:40 *Stable Isotopic Compositions of Dissolved Sulfate and Inorganic Carbon in Groundwater in the Animas River Valley, New Mexico – Assessing Sulfate Sources and Redox Conditions*
(Abstract 13)
B. Talon Newton, New Mexico Bureau of Geology and Mineral Resources, New Mexico Tech
- 12:00 LUNCHEON
- State of the Trout Fishery – Animas River*
Andrew Todd, U.S. Environmental Protection Agency
Ty Churchwell, Trout Unlimited

Afternoon Session

- 1:30 *Lower San Juan River Sedimentation and Riparian Vegetation Feedback* (Abstract 17)
Gary Gianniny, Cynthia Dott, and **Logan Hartle**, Fort Lewis College
- 1:50 *Watershed Monitoring Across the Persistent to Intermittent Snow Transition Zone in Colorado* (Abstract 22)
Gigi Richard, Fort Lewis College
- 2:10 *Studies of Animas River Watershed Bacterial Communities as Water Quality Indicators and Their Relationship to the Aquatic Food Web* (Abstract 15)
Jennifer Lowell, Fort Lewis College
- 2:30 *Impacts and Recovery: Animas River Water Quality and Aquatic Life Following the 416-Fire* (Abstract 21)
Scott Roberts, Mountain Studies Institute
- 2:50 Poster Session and Reception
Poster Session sponsored by **Fort Lewis College**
- 4:30 ADJOURN

Thursday, June 20, 2019**Morning Session**

- 9:00 *An Ephemeral Landscape: Traversing the Fractured Regulatory Dynamics Surrounding Abandoned Mines and Mining Districts* (Abstract 12)
Anthony Edwards, Bonita Peak Mining District/Sholler Edwards LLC
Paul Nazaryk, Ramboll US Corporation
- 10:00 BREAK
- 10:40 *Water Quality Changes Following Remediation of Abandoned Draining Mines Using Structural Bulkheads, Upper Animas River, and Upper Arkansas River Watersheds, Colorado, USA* (Abstract 5)
Katherine Walton-Day, M.A. Mast, and **R.L. Runkel**, U.S. Geological Survey, Colorado Water Science Center
- 11:00 *New Magnetotelluric Survey in the San Juan-Silverton Caldera Complex, Silverton, Colorado, Reveals Subsurface Rock Properties Important for Interpreting Modern Groundwater and Ancient Hydrothermal Flow Paths in a Mineralized System* (Abstract 4)
Douglas Yager, Brian D. Rodriguez, Maria Deszcz-Pan, Bruce D. Smith, Eric D. Anderson, and **Benjamin R. Bloss**, U.S. Geological Survey
- 11:20 *Assessing Risk to Water Resources from Oil and Gas Activities in the San Juan Basin* (Abstract 18)
Thomas S. Lowry, Sandia National Laboratories
Whitney Thomas, Bureau of Land Management, Farmington
Dave Herrell, Bureau of Land Management, Santa Fe

11:40 *Impact and Recovery of Navajo Agricultural Activity Following the Gold King Mine Spill*
(Abstract 20)
Karletta Chief, University of Arizona

12:00 LUNCHEON

Afternoon Session

1:00 *Risk Communication Workshop – Hands-On Preparation for Any Event*
Christine Osborne, Utah Department of Environmental Quality

1:45 BREAK

2:00 *Risk Communication Workshop* continues

3:00 Closing Remarks
Johanna Blake, U.S. Geological Survey

3:15 ADJOURN

Friday, June 21, 2019 Post-conference Field Trip

9:00 am – 1:00 pm Community Teach-In, Navajo Shiprock Chapter House

Saturday, June 22, 2019 Optional Post-conference Field Trip

10:00 am – 2:30 pm Mild to Wild Rafting Company, Durango, CO

Conference Planning Committee

Steve Austin, Navajo Nation Environmental
Protection Agency

Johanna Blake, U.S. Geological Survey

Robert Cook, U.S. Environmental Protection Agency

Anthony Edwards, Bonita Peak Mining District CAG,

Sam Fernald, NM Water Resources Research Institute

Carolyn Gillette, Eastern Research Group, Inc.

Forrest John, U.S. Environmental Protection Agency

James C. Kenney, NM Environment Department

Michaelene Kyrala, NM Environment Department

Kevin Lombard, New Mexico State University,
ASC Farmington

Melissa May, San Juan Soil & Water
Conservation District

Virginia McLemore, NM Bureau of Geology

Dennis McQuillan, NM Environment Department

Paul Montoia, City of Farmington

Catherine Ortega Klett, NM Water Resources
Research Institute

Alexandra Ratcliff, Southern Ute Indian Tribe

Shera Reems, U.S. Environmental Protection Agency

Andy Shuler, University of New Mexico

Stacy Timmons, NM Bureau of Geology

Thomas Turner, University of New Mexico

Kristine Yurdin, NM Environment Department

2019 Abstracts

(#3, #5, & #9, # 14 withdrawn)

Watershed Technology Innovation Strategies Via Intellectual Property Protection Rights

Ananya Narurkar
Ananya.iploft@gmail.com
Fernandez and Associates, LLP

Abstract 1 – Oral and Poster

Intellectual Property Rights (IPR) protection strategy and ecosystem policy facilitate proprietary innovation and commercialization of early-stage watershed systems, devices, and related applications as well as automated methodologies to promote standardization of best practices and early-stage investment of risk capital. US and international patent, copyright and trade secret IPR laws secure exclusive barriers to competition against unauthorized piracy domestically and globally. For example, novel watershed innovations may deploy smart sensing devices and distributed wireless networks, as well as artificial intelligence software that learn real-time adaptively to solve proprietary next-generation watershed system applications.

Gold King Mine Spill: Analysis of Response by Federal, State, Local, and Tribal Entities

Randy Velarde
rvelarde@fmrn.org
Farmington Police Department

Abstract 2 – Oral

Response to the Gold King Mine spill proved to be less effective because of a lack of adherence to applicable policies and procedures. Improper consequence management and calculation of risk to the environment, contract workers and stakeholders contributed to the U.S. Environmental Protection Agency triggering the spill. The bulk of research pertaining to the Gold King Mine spill focuses on the science of the spill in terms of water chemistry and quality. This study looks at the disaster from the perspective of analyzing actions of government agencies and private stakeholders and their responses to the spill as they made efforts to protect their interests. A qualitative approach was taken using the National Response Framework and the National Incident Management System as relevant frameworks. The concepts of Multi-Agency Coordination System and the concept of Multi-Team Coordination were applied. The Gold King Mine spill demonstrated the result of less than effective planning, communications, and not embracing the utility of effective unified command during a large-scale disaster.

The Gold King Mine Spill mining related accident was triggered by workers from the Environmental Protection Agency on 5 August, 2015. The resulting spill of approximately three million gallons of contaminated water into the Cement Creek eventually flowed into the Animas River near Silverton Colorado (May, 2015). The unprecedented event became the focus of many different federal, state, local and tribal governments each thrust into the task of how to respond and recover from the event (Chief, Artiola, Beamer, Wilkinson, & Maier, 2015).

Since August 2015, a great deal of time and resources have focused specifically on studying the effects of the contamination on the aquatic life of the river and the chemical effects on the environment. A chief concern was the effect the contaminated water would have on all of the users along the watershed and the immediate and potential long-term economic impacts of the spill (Lovingwood et al., 2017).

With scientific focus on studying the measurable ecological effects of the spill, a gap in knowledge exists regarding how governments and stakeholders interacted, cooperated, prepared for, responded to and recovered from the spill. A complete study of the emergency response aspect of the Gold King Mine spill has yet to be conducted and an analysis of the actions of involved government agencies and thousands of Animas River water users before, during and after the spill has yet to be conducted. Responsibility for the event has not been squarely accepted or attributed to any single entity or governmental agency and has generated a large number of lawsuits (Chief et al., 2015; "The State of New Mexico v. United States Environmental Protection Agency," 2016).

The Gold King Mine spill represents a singular focusing event which was not foreseen or prepared for. The many responding entities, both government and private, may not have been able to effectively respond to the spill because individual responsibilities may not have been clearly understood. This research will attempt to find out how each of the disparate entities responded and reacted to the spill and will offer recommendations to facilitate planning, preparation, and collaboration between the different entities before a similar emergency arises in the future (Gobla,

Gemperline, & Stone, 2015). A qualitative analysis of the actions taken by each entity impacted by the spill will be conducted. Specifically, each entity will be analyzed to determine what policy and procedures were in place at the time and whether or not they were followed. How and when responding entities interacted with each other before, during and after the spill will be considered. Finally, an analysis of the relationship between entities and how they communicate needs and concerns will be analyzed with emphasis on the relationship between entities and their specific roles and responsibilities (“Animas River-Gold King Mine Wastewater Spill Response,” 2015).

Data will be collected from the individual entities regarding resources available, activity on the day of the spill, outputs, and results of their individual efforts. The same questions will be asked of each entity and the same types of data sets will be collected in order to enable consistent comparison and analysis of the data.

The Gold King Mine spill caught stakeholders and authorities off guard and the after effects of the spill continue to present challenges to the community. With this understanding of what happened before, during and after the spill, decision-makers can utilize the results of the study and apply it towards the planning process to assist in mitigation, preparation, response and recovery decisions for any future similar emergency. The Gold King Mine continues to emit contaminated water into the Cement Creek and any of the remaining abandoned mines has the potential to experience another uncontrolled release of contaminants into the watershed (Finley, 2015). The study serves as a way to improve understanding of the capabilities and limitations of stakeholders in the event of a future similar emergency.

REFERENCES

- Animas River-Gold King Mine Wastewater Spill Response. (2015). Retrieved from <https://www.env.nm.gov/river-water-safety/animas-river-citizens-advisory-committee-public-participation-page/>
- Chief, K., Artiola, J. F., Beamer, P., Wilkinson, S. T., & Maier, R. M. (2015). Understanding the Gold King Mine Spill. *Superfund Research Program*, (August), 1–7. Retrieved from https://superfund.arizona.edu/sites/superfund.arizona.edu/files/u70/understanding_the_gold_king_mine_spill_v13_preamble_final.pdf
- Finley, B. (2015, August 11). Animas River spill: Gold King Mine one of many in area releasing heavy metals-laced waste. *The Denver Post*. Retrieved from www.denverpost.com/2015/08/11/animas-river-spill-gold-king-mine-one-of-many-in-area-releasing-heavy-metals-laced-waste/
- Gobla, M., Gemperline, C., & Stone, L. (2015). Technical Evaluation of the Gold King Mine Incident, (October), 1–132. Retrieved from <http://www.usbr.gov/docs/goldkingminereport.pdf>
- Lovingwood, T., Kincheloe, C., Rowden, N., Hess, K., Parker, B., Trefry, J., ... Trynosky, J. (2017). *Gold King Mine Release: Inspector General Response*.
- May, M. (2015). Gold King Mine Spill Background and Timeline. San Juan Soil and Water Conservation District.
- The State of New Mexico v. United States Environmental Protection Agency. (2016).

New Magnetotelluric Survey in the San Juan-Silverton Caldera Complex, Silverton, Colorado, Reveals Subsurface Rock Properties Important For Interpreting Modern Groundwater and Ancient Hydrothermal Flow Paths in a Mineralized System

Douglas B. Yager^{1*}, Brian D. Rodriguez²⁺, Maria Deszcz-Pan³, Bruce D. Smith⁴,
Eric D. Anderson⁵, Benjamin R. Bloss⁶

dyager@usgs.gov¹

brod@usgs.gov²

maryla@usgs.gov³

bsmith@usgs.gov⁴

ericanderson@usgs.gov⁵

bbloss@usgs.gov⁶

U.S. Geological Survey, Denver, Colorado, USA

Abstract 4 – Oral*and Poster+

The San Juan-Silverton caldera complex is located near Silverton, Colorado in the Southern Rocky Mountain Volcanic Field. The purpose of our study is to help characterize subsurface rock properties important for understanding surface water and groundwater quality issues, and to improve knowledge of shallow to deep faults and vein-structures that were conduits for hydrothermal fluids that formed mineral deposits. The study has general applications to mineral resource assessments in other areas of the world, and to identifying possible groundwater flow paths and associated geochemistry important in abandoned mine lands cleanup.

The legacy of hard rock mining in headwater catchment areas has caused environmental challenges for local communities and downstream users of water resources. Mining-related sources of metals and acidity overprint and add to geologic sources of metals in surface water and groundwater. Weathering of altered and mineralized rock, often containing pyrite and other sulfides has resulted in acid rock drainage that has been ongoing for millennia.

Newly acquired audiomagnetotelluric (AMT) and magnetotelluric (MT) data are being used to investigate structures of the San Juan-Silverton caldera complex. The San Juan caldera formed at 28.4 Ma, followed by the younger, nested Silverton caldera at 27.6 Ma. In general, calderas are collapsed volcanoes that form when magma is erupted along a ring fault zone at a volcanic margin. Caldera ring fault zones, also called structural margins, can be circular to elliptical and > 15 km in diameter and extend several kilometers into the crust. Rocks overlying the magma chamber (caldera roof) that were at the surface of the volcano prior to eruption, collapse into the void created by eruption of the magma chamber. The volcano-tectonic upheaval during caldera formation cause rocks adjacent to the volcano to be highly-fractured and faulted. Upwelling or resurgence of new magma beneath the intra-caldera volcanic fill, as is likely the case for the San Juan-Silverton caldera complex, can push up and dome the center of the caldera area, causing additional fractures and faults to form. These caldera-related structures can become flow paths for hot fluids that deposit base- and precious-metals.

Along with previously acquired geologic mapping, airborne magnetic, and airborne electromagnetic data, the USGS collected AMT and MT data in July, 2018 at 24 sites along four profiles ranging from 3 to 6 kilometers in length across the northwestern structural margin of

the Silverton caldera in Mineral Creek Basin, across the southeastern margin of the caldera along Cunningham Creek, within the caldera in Eureka Graben, and within the caldera along upper Cement Creek near the Gold King mine. The MT method is a passive ground-based electromagnetic technique that investigates subsurface electrical resistivity at depths of 10s of meters to 10s of kilometers. It does so by measuring time variations in Earth's electric and magnetic fields. Worldwide lightning activity and geomagnetic micropulsations from solar wind-charged particles interacting with Earth's magnetosphere provide the main source of signal used by the AMT and MT methods, respectively. The AMT and MT methods measure electromagnetic properties of rocks and sediments. These properties can vary depending on minerals present, moisture content, and percentage of clay minerals. Rocks and sediments that have sulfide minerals can have low electrical resistivity. Dry bedrock that lacks sulfide minerals tends to have relatively high resistivity. Wet bedrock and clay typically exhibits intermediate resistivity because of conduction through pore fluids and along clay mineral surfaces.

Electrical resistivity modeling helps to characterize the electrical resistivity of mineralized caldera structures and adjacent rocks to great depths. Electrical resistivity models can also reveal low resistivity zones where groundwater flow through volcanic rocks might have higher concentrations of total dissolved solids attributed to bedrock weathering processes.

We present the results of two-dimensional resistivity inversions of the AMT data for each of the four profiles. Along the Mineral Creek Basin profile, the AMT resistivity inversion images what appears to be a megabreccia block of resistive rocks that we interpret to be intermediate lavas down-dropped about 300 meters along the east side of the inferred caldera ring fault. Lower resistivity rocks east of the ring fault in the upper 100 meters are near a dacite intrusion and associated breccia pipe. Along the Cunningham Creek profile, the AMT resistivity inversion images resistive rocks along the entire length of the profile and very resistive rocks in the northern half of the profile that we interpret to be intermediate lavas along the caldera ring fault. Along the Eureka Graben profile, the AMT resistivity inversion images a deep (below 800-meters depth) low resistivity zone south of Lake Emma, hosted in resistive rock, near the trend of the Sunnyside mine vein systems. Along the upper Cement Creek profile, the AMT resistivity inversion images a shallow 20-meter thick low resistivity layer we interpret to be basin fill and a deeper, 500- to 1,000-meters depth, low resistivity zone about 800 meters west of the Gold King mine vein systems. Resistive rock at the north and south end of the profile may be less fractured and less altered than the subsurface rock in the central part of the profile.

Final integration of geologic and other geophysical data for our study will enable construction of 3-D geological and geophysical models of the caldera complex, permitting new interpretations about economic mineralization that are applicable in similar geologic environments in other parts of the world. The models will also allow identification of electrically conductive (low resistivity) structures and deposits that may represent permissive groundwater flow paths and conduits for acidic and metal-rich water important for mine reclamation decisions and abandoned mine cleanup.

Iron Bioaccumulation in *Lemna minor* (Duckweed) and *Pleurotus ostreatus* (Oyster Mushrooms)

Jason Fechner¹, April Ulery², Soum Sanogo³

jfechner@nmsu.edu¹

aulery@nmsu.edu²

ssanogo@nmsu.edu³

New Mexico State University

Abstract 6 – Poster

Over 3,000,000 gallons of contaminated acid mine tailings were released into the Animas and San Juan watersheds on August 15, 2015 leaving behind high concentrations of iron hydroxides. The orange water raised concerns for local farmers who utilized these watersheds for agricultural irrigation. Iron has the ability to complex with similarly structured metals and form hard precipitates out of solution (“ferricrete”). These processes can affect both aquatic life and terrestrial life. Iron can also act as an analogue for characteristics of other transition metals in solution, therefore understanding the behavior of high iron concentrations in watersheds will allow us to better understand how other transition metals are act. Phytoremediation refers to a plant’s ability to remove unwanted elements from the source in which they are present. Some plants, such as *Lemna minor* (duckweed), can absorb certain elements at 1%-5% dry weight biomass and are known as hyperaccumulators. A five-day greenhouse trial was conducted with *L. minor* to demonstrate its effectiveness in removing iron from solution. 0.10 kg *L. minor* was added to 2.9 kg H₂O and 1g fertilizer (20-20-20) contained in plastic vats (boxes) with four treatment levels of an iron supplement (0, 0.5g, 5g, 50g). The 0g iron additive or, control, consisted of water, *L. minor*, and fertilizer only. Experimental blanks were set-up for quality control to determine if the added iron supplement was binding to the fertilizer or precipitating out of solution. Water loss due to evaporation was measured and replenished during the duration of the trial. Water samples were analyzed for total iron content using Inductively Coupled Plasma-Optical Emission Spectroscopy (ICP-OES). *L. minor* was collected and oven-dried at 65°C to a dry weight of 0.5g, microwave digested using EPA Method 3052, and analyzed for total iron content via ICP-OES. Results show the highest iron sorption by *L. minor* to be around 20,000 ppm. Additionally, the assessment of contaminated duckweed management in compost development will be conducted. Once fully composted, the compost will be analyzed for total iron content and oyster mushrooms (*Pleurotus ostreatus*) will be attempted to be grown using the enriched iron compost. The oyster mushrooms will then be analyzed for total iron content to demonstrate their uptake ability. This research will provide an understanding of duckweed in phytoremediation of high iron concentrations while assessing the potential in the utilization of contaminated duckweed within the agricultural sector. I would like to thank NMWRRRI for the funding of this project via account number NMWRRRI-SG-2018.

Water Quality Monitoring in the San Juan River Watershed – Multijurisdictional Efforts Using WIIN Act Appropriations

Robert Cook¹, Alexandra Ratcliff², Dennis McQuillan³, Kristine Yurdin⁴,
Steve Austin⁵, Lucy Parham⁶

cook.robert@epa.gov¹

U.S. Environmental Protection Agency

aratcliff@southernute-nsn.gov²

Southern Ute Indian Tribe

dennis.mcquillan@state.nm.us³

kristine.yurdin@state.nm.us⁴

New Mexico Environment Department

nnepawq@frontiernet.net⁵

Navajo Nation

lparham@utah.gov⁶

Utah Department of Environmental Quality

Abstract 7 – Oral

Water resources in the San Juan watershed, which encompasses the San Juan and Animas Rivers and Lake Powell, are essential for agricultural, cultural, residential, and recreational, uses. Potential contamination sources within the watershed include historic mining activities that disturbed the land and exacerbated naturally occurring mineralization. In 2016, under the Water Infrastructure Improvements for the Nation (WIIN) Act, the U.S. Congress authorized appropriations of \$4 million per year in 2017–2021 for a long-term water quality monitoring program for the San Juan watershed. EPA and the states and tribes in the watershed have worked together to identify watershed-wide and state and tribe-specific priorities that will supplement previous and ongoing monitoring and assessment activities, enhance understanding of the condition of the San Juan watershed, and identify future opportunities for improving watershed protection. Presented will be an overview of current multijurisdictional water quality monitoring of metals, nutrients and sediment within the San Juan Basin as well as planned macroinvertebrate and habitat assessments. Additionally, descriptions of ongoing state and tribe-specific water quality studies funded under the WIIN Act will be presented. These studies include: Southern Ute Indian Tribe studies to identify toxicological risks from use of culturally-significant plants and use of mobile sonde telemetry to inform agricultural inputs and provide real-time water quality data; NMED studies include monitoring metals in irrigation ditches, agricultural fields, and crops, as well as groundwater and sediment in Farmington Lake, and communication about the safety of locally-grown produce irrigated with river water; Navajo Nation studies on the development of local water quality standards for metals, accumulation of metals and other contaminants in fish tissue, and identification of metals sources and contribution rates to loads found in the Navajo Nation portion of the San Juan River; and, UDEQ studies to assess the long term impact of mining on Lake Powell water quality through sediment coring and to evaluate the use of hydroacoustics as a surrogate for suspended sediment concentration in the San Juan River.

Aztec Reservoir #1 Sediment Descriptions and Chemistry

Johanna M. Blake¹, Jeb E. Brown, Christina Ferguson, Tyson Hatch, Tristan Austring

jmtblake@usgs.gov¹
U.S. Geological Survey

Abstract 8 – Poster

The City of Aztec, New Mexico Drinking Water Reservoir #1 has been a surface water containment for drinking water since 1951. From its completion in 1947 to fall 2017, the reservoir accumulated 8 to 10 feet of sediment. The sediment accumulation reduced the holding capacity of the reservoir and therefore the reservoir was drained in November 2017 in preparation for sediment dredging. The water inputs to the reservoir are from the Aztec Ditch, fed by the Animas River, and directly from the Animas River. Following the Gold King Mine Release in 2015, there was interest in evaluating the chemical deposition in the reservoir sediments. The U.S. Geological Survey, in cooperation with the New Mexico Environment Department (NMED), excavated four trenches in the reservoir in May 2018. These trenches were described and sampled along the depth of vertical face which ranged from 120 to 150 cm deep. Sediment samples were analyzed for bulk chemistry by handheld X-ray fluorescence in the field and by digestion and analyses by Inductively coupled plasma-optical emission spectroscopy and mass spectrometry in the laboratory. Results show variable concentrations of metals designated as metals of concern in the Resource Conservation and Recovery Act (RCRA), including arsenic (As), barium (Ba), cadmium (Cd), chromium (Cr), lead (Pb), mercury (Hg), selenium (Se) and silver (Ag). The majority of sediment samples from the reservoir had concentrations (in mg/kg) of the eight RCRA metals less than the toxicity characteristic leaching procedure rule of 20 (TCLP20) concentrations (As <100, Ba < 2000, Cd <20, Cr <100, Pb <100, Hg <4, Se <20, and Ag <100). These results are important for drinking water managers to understand the chemistry of sediments entering the reservoir, to help managers determine water treatment processes and help managers know the content of the sediment so it can be properly disposed.

Water Quality History Derived From Diatom Communities in a Water Treatment Sediment-Settling Reservoir, Aztec, NM

Jeb Brown^{1*}, Becky Bixby², Johanna Blake¹, Christina Ferguson¹

jebbrown@usgs.gov*

¹U.S. Geological Survey, New Mexico Water Science Center

²University of New Mexico

Abstract 10 – Poster

The Animas River and San Juan River watersheds in southern Colorado and northern New Mexico have a long history of anthropogenic land use activities. Some of these activities, including gold, silver, and uranium mining; lead, uranium, and vanadium milling; and oil and gas development, have resulted in adverse environmental impacts. Exposed geology of these watersheds can also contribute to naturally elevated constituents of concern (for example, lead and aluminum) in these rivers. Understanding historic effects of anthropogenic land use can inform future management decisions.

Diatoms are important single-celled photosynthetic protists in aquatic ecosystems that are useful for biomonitoring because they often live in a specific range of environmental conditions. Analysis of depositional layers of sediments in lakes and reservoirs for biological indicators such as diatoms can be used to reconstruct historic water-quality conditions of a watershed.

The U.S. Geological Survey collected bed sediments from four trenches within a drained settling reservoir maintained by the City of Aztec drinking water treatment plant. Analyses of bed sediments include sediment descriptions, chemistry, age dating, and diatom species identification, and provide a history of water quality (1947-2018) in the Animas River watershed upstream of Aztec, NM. This work explores the response of diatom taxa through the reservoir's history to changes in water-quality conditions (e.g. pH, nutrient concentrations, salinity, metals, etc.) that may have occurred in the watershed over the past 71 years.

Diatoms were identified and species composition delineated every 10 centimeters along the length of one sediment core. Diatom communities are characterized on the basis of the life history (e.g., cosmopolitan versus endemic, planktonic versus benthic, etc.) of community species. Chemical, physical, and particle size analysis of sediments are used to interpret drivers of the diatom community structure. These data inform the assessment of conditions of the settling reservoir in Aztec and may predict how upstream changes in water chemistry affect the local reservoir.

Sampling of Stream and Irrigation Ditch Sediment and Agricultural Crops to Characterize the Nature and Extent of Impact from the August 2015 Gold King Mine Spill

Gaurav Jha¹, April Ulery², Kevin Lombard³

GJha@nmsu.edu¹

Graduate Research Assistant
Plant & Environmental Sciences, New Mexico State University

AUlery@nmsu.edu²

Professor
Plant & Environmental Sciences, New Mexico State University

KLombard@nmsu.edu³

Associate Professor and Superintendent
Farmington Agricultural Science Center

Abstract 11 – Oral

The Gold King Mine Spill impacted the cultivation of agricultural crops all across the watershed when irrigation ditches were closed for several weeks while the contamination moved downstream. While contamination from this one event may not have reached the closed irrigation ditches and fields, legacy mining that may have released metals into the watershed over the last 150 years may be affecting the soils. Large areas of the Animas and San Juan River watershed lies in the Navajo Nation and the tribe uses soil and water not only for cultivation but for ceremonial purposes. Thus, it is important to know whether these metals are toxic to plants and environment. The total concentrations of nine elements including arsenic, lead, manganese, iron, copper, calcium, zinc, aluminum, and chromium have been measured in these irrigation ditches, fields, plant tissues and produce for two growing season. Arsenic exceeded the NM Environmental Department or US Environmental Protection Agency recommended soil concentrations at some locations in the alfalfa and vegetable fields above the residential screening level of 7.07 ppm as per the recommendations of NMED. This metalloid may be present in the soil in different forms or species that have varying toxicity or bioavailability. Thus the study determines the concentration of the water soluble and exchangeable fractions of arsenic field soils irrigated by Animas River water and evaluate how the three elements are related to each other and to soil components.

Eight of the nine metals of interest measured in the irrigation ditch sediments were below the EPA Residential Soil Screening Levels (SSL) in the 15 sites evaluated in this study. Only As exceeded the EPA and NMED SSL. Total metal concentrations in the surface sediment collected from the sides of the irrigation ditches were higher than the center sediment concentrations of Al, As, Cr, Fe, and Cu for both pre- and post-growing seasons in the Animas and San Juan watershed. The concentrations of Zn and Ca on the ditch sides were both significantly higher only in the pre-growing season and there were no significant differences in Mn or Pb concentrations between the side and center sampling points. This suggests that center ditch sampling alone may underestimate sediment contamination. The data collected from 8 agricultural fields indicates that with the exception of As, all of the elements evaluated in this study were below the EPA or NMED soil screening limits for residential soils. Almost all of the fields in the study area scanned using pXRF had at least

one point (hotspot) where the As concentration exceeded the NMED soil screening limit of 7.07 ppm. This study also collected and analyzed plant samples from eight agricultural fields. Metal concentrations in alfalfa and pasture grass rinsates were very low and in several cases below the detection limits of the instruments. In vegetable fields, the rinsate collected from corn leaves were the lowest and that from chile leaves were highest, probably because the corn leaves were well above ground level having sampled a fully developed leaf. On analyzing the metal concentrations in leaf tissues collected from alfalfa, pasture and vegetable fields the higher concentrations of As in the hotspots of fields did not correlate with higher concentrations in leaf tissues. The concentrations of metals in corn leaves were much lower than those in pasture grass and alfalfa leaves. The highest concentrations of leaf metals were measured in the cucurbits (pumpkin, squash and melon). A few samples exceeded the MTL for Al, Fe and Ca in animal feed but these metals are not considered high risk for animal health concern.

The representative soil samples from an alfalfa field in Upper Animas and a vegetable field from Lower Animas were analyzed for arsenic for the partial sequential extraction fractions. Water soluble and exchangeable fractions of As also contributes to the plant available pool. These fractions were much below 0.3 mg kg⁻¹ in vegetable field and 0.5 mg kg⁻¹ in alfalfa field, thus, contributing non significantly towards the total concentrations. This research is trying to answer the questions about the safety of the soils, sediments and produce and help the farmers across Animas and San Juan watershed to resume to regular cultivation methods.

An Ephemeral Landscape: Traversing the Fractured Regulatory Dynamics Surrounding Abandoned Mines and Mining Districts

Paul Nazaryk
PNAZARYK@ramboll.com

Anthony Edwards
Solkepler@gmail.com

Abstract 12 – Oral

The authors will give an oral PowerPoint presentation on the subject matter presented for 1-2 hours, which would qualify for CLE credit in both New Mexico and Colorado. The Bonita Peak Mining District Superfund site is located within the Upper Animas Watershed with approximately 400 abandoned mines in San Juan County near Silverton, Colorado. Through the lens of the Gold King Mine spill, this presentation will explore the intersection of the 10th Circuit *Chevron Mining Inc. v. U.S.* decision and other contemporary regulatory developments including the Superfund Reform Plan and the White House Reform Plan with the nuances private and federal land ownership. The presentation will discuss their implications for public and private entities and suggest proposed solutions for addressing legacy mineral waste in the West.

THE OUTLINE

Before the Gold King Spill: Where We Were ...

- The Bonita Peak Superfund Site is in the Upper Animas watershed in San Juan County, Colorado. It's the site of the now infamous Gold King spill or "blow-out" on August 5th, 2015.
- The Upper Animas watershed located in the San Juan Mountains within a collapsed volcano known as the Silverton Caldera which was last active about 27 million years ago. It is a highly mineralized area with high natural background levels of metals which find their way into the Upper Animas River.
- The Federal government is the largest landowner in the county. 88.6% of the land in San Juan County is USFS or BLM land. It is the smallest county in terms of population in Colorado. San Juan County also has the highest mean elevation of any county in U.S at 11,240 feet. The Town of Silverton's elevation is 9,317 feet. It's a land of long winters, deep snowpack, and avalanches.
- This mineralization attracted miners to the area in the 1870s. The last active mine, the Sunnyside Mine, closed in 1991. The Gold King Mine closed in 1922.
- Today there are thousands of abandoned former mining sites in the area. However, a study by the Animas River Stakeholders Group in the 1990s estimated that 33 draining adits and 32 waste piles create 90% of mine-related stream metals loading in the Animas. In fact, it has been suggested 60% of the manmade metal loading in the watershed is from the following four discharging adits: (1) the Red and Bonita, (2) the Gold King; (3) the American Tunnel, and (4) the Mogul Mines.
- The Gold King "blow-out" is one of many mine pool releases that have occurred in the area and is certainly not the largest.

- The State of Colorado and EPA became concerned about water quality in the mid-1990s and EPA began looking at the possibility of listing the area as a Superfund NPL site.
- The Animas River Stakeholders Group (ARSG) consisting of stakeholders from landowners, mining companies, environmental groups, and local, state and federal government agencies was formed in 1994 with the mission of collaborating in the cleanup of abandoned mines and improving water quality.
- The Sunnyside Gold Corporation and the State of Colorado in 1996 reached an agreement in a consent decree allowing the company to shut down its wastewater treatment plant and install bulkheads in exchange for performing some other mine tailings cleanup.
- Over the next decade, ARSG, Trout Unlimited, the State of Colorado, and others participated in approximately 60 mine-related cleanup activities focusing on mine tailings. None of these cleanups involved draining mining adits because of concern over assuming responsibility and financial burden for the discharge in perpetuity under the Clean Water Act.
- Water quality improved in the watershed and EPA agreed to postpone an NPL listing so long as progress was being made to improve water quality in the Upper Animas watershed. But in 2008, water quality began to decline. EPA again turned to CERCLA and conducted a series of investigations under its CERCLA § 104 authority and publicly discussed an NPL listing.
- One of these investigations triggered the Gold King “blow-out” making national news and triggering a public outcry from downstream users and resulting in numerous lawsuits and claims. This publicity resulted in the listing of the Bonita Peaks Mining District as an NPL site on September 6, 2016.

Recent Developments: Where We Are Now...

- Summary of Gold King Litigation
- The lack of viable potentially responsible parties (PRPs)
- The Superfund Process (Current Status)
- Superfund and natural background contamination.
- Questions concerning the boundaries within the NPL listing
- Complex groundwater hydrology
- Superfund is *no* longer a *fund*!

An Uncertain Future: Where Are We Going?

- *Chevron Mining v. U.S.* and federal government liability?
- How much information do we really need to begin cleanup?
- An old quandary with a new twist: How clean is “clean” in a land of high natural background?
- How can we encourage voluntary and private party cleanups? “Good Samaritan” legislation?
- What about liability transfer mechanisms?
- What’s the best way to actually *fund* Superfund?
- Other approaches? Montana, Manitoba, Western Australia?

Stable Isotopic Compositions of Dissolved Sulfate and Inorganic Carbon in Groundwater in the Animas River Valley, New Mexico – Assessing Sulfate Sources and Redox Conditions

B. Talon Newton

talon.newton@nmt.edu

New Mexico Bureau of Geology and Mineral Resources, New Mexico Tech

Abstract 13 – Oral and Poster

Understanding processes that control the water chemistry in the shallow alluvial aquifer along the Animas River in northwestern New Mexico is necessary to assess the potential impacts to water quality by natural and anthropogenic pollutants. Potential contaminants include legacy acid rock and mine drainage from the Animas headwaters in Colorado, naturally occurring contaminants (e.g. iron, manganese, and sulfate), and possible leakage of fluids associated with existing oil and gas wells, and septic fields in the area. Between January 2016 and June 2017, researchers at the New Mexico Bureau of Geology and Mineral Resources conducted a study along the Animas River valley between the New Mexico/Colorado border and Farmington, New Mexico to characterize the local hydrogeology and to assess potential impacts to water quality by the Gold King Mine Spill. Water level and geochemical analyses at different seasonal hydrologic regimes showed:

1. The Animas River mostly gains water from the alluvial aquifer along this reach.
2. The primary recharge source to the shallow aquifer is irrigation water that infiltrates through the bottoms of irrigation canals and agricultural fields.
3. Down-gradient increases in dissolved sulfate concentrations (especially south of Aztec) are likely due to geologic controlled upwelling of regional groundwater into the shallow system.
4. All metals associated with the Gold King Mine Spill were either not detected or well below the primary EPA maximum contaminant levels (MCL) in sampled groundwater.
5. Dissolved iron and manganese concentrations that exceed EPA secondary MCLs cannot necessarily be linked to legacy acid mine drainage or the Gold King Mine Spill.
6. There was no evidence of impacts to groundwater quality from the Gold King Mine Spill.

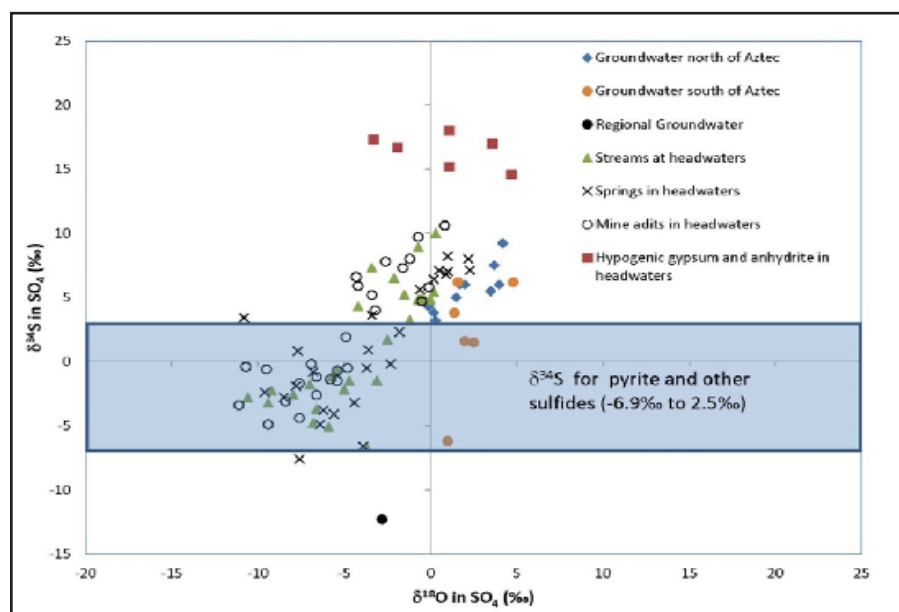
A follow-up study by the NMBGMR was initiated in 2018 to specifically investigate sources of sulfate and controls on redox conditions in the shallow alluvial aquifer. Eighty and sixty groundwater samples were collected in October 2018 and April 2019 respectively. All water samples were analyzed for general chemistry, trace metals, and the stable isotopes of water (hydrogen and oxygen). A subset of samples was analyzed for carbon isotopes in dissolved inorganic carbon (DIC), and sulfur and oxygen isotopes in dissolved sulfate.

Preliminary isotope results show potential to increase our understanding of important processes that control groundwater chemistry in the Animas River valley. Sulfur and oxygen isotope data for dissolved sulfate were compared to values measured by Nordstrom et al. (2007) for streams, springs, mines, and minerals in the upper Animas River Valley above Silverton, Colorado (see figure below). In the headwaters of the San Juan Mountains, most isotope values in groundwater ($\delta^{34}\text{S}(\text{SO}_4) > 4\text{‰}$, $\delta^{18}\text{O}(\text{SO}_4) > 0\text{‰}$) suggest that the primary source of sulfate was hypogenic

gypsum and anhydrite. A slight isotopic shift toward heavier values may be due to fractionation caused by sulfate reduction. Some groundwater samples collected south of Aztec exhibit lighter sulfur and oxygen isotopic compositions.

The lightest composition was observed in a groundwater sample that likely represents regional groundwater ($\delta^{34}\text{S}(\text{SO}_4) = -12.4\text{‰}$, $\delta^{18}\text{O}(\text{SO}_4) = -2.8\text{‰}$). These lighter isotope values for dissolved sulfate probably represent a component of terrestrial gypsum or anhydrite contributed from deeper geologic formations, such as the Nacimiento Formation. These data support previous conclusions about the upwelling of regional groundwater in the southwestern part of the study area.

Carbon isotopes in DIC show a linear inverse correlation with dissolved bicarbonate concentrations, which range from 186 to 429 mg/L. Bicarbonate concentrations do not show a spatial trend, such as the downgradient increase that is seen for sulfate. The range in $\delta^{13}\text{C}$ values (-14.7‰ to -9.8‰) is representative of a mixture of dissolved carbonates and soil CO_2 . The observed trend suggests that the observed variability in bicarbonate concentrations (186 to 429 mg/L) depends somewhat on the decomposition of organic carbon. Organic matter in the area probably exhibits $\delta^{13}\text{C}$ values representative of C3 plants (-33 to -24‰). Therefore, the decomposition of organic carbon would cause the carbon isotopic composition of DIC to decrease. While work is underway with these results, the isotopic data for sulfate and DIC are proving to be useful tools for identifying sulfate sources and assessing redox processes such as sulfate reduction and decomposition.



Sulfur and oxygen isotope data for dissolved sulfate in groundwater along the Animas River in New Mexico plotted with isotope data for streams, springs, mine adits, and minerals in the upper Animas River Basin, north of Silverton, as reported by Nordstrom et al. (2007).

REFERENCES

- Nordstrom, D.K., Wright, W.G., Mast, M.A., Bove, D.J., and Rye, R.O., 2007, Aqueous – Sulfate Stable Isotopes – A Study of Mining-Affected and Undisturbed Acidic Drainage, in Church, S.E., von Guerard, P., and Finger, S.E., ed., Integrated Investigations of Environmental Effects of Historical Mining in the Animas River Watershed, San Juan County, Colorado: USGS Profession Paper 1651, Chapter E8, p. 391 – 413.

Studies of Animas River Watershed Bacterial Communities as Water Quality Indicators and Their Relationship to the Aquatic Food Web

Jennifer Lowell
jlowell@fortlewis.edu
Fort Lewis College

Abstract 15 – Oral and Poster

Microorganisms are the foundation of the aquatic food web. The role of sediment biofilms is central to healthy river ecosystem functioning, water quality, and public health. Sediment biofilm microorganisms decompose organic matter, provide nutrients to the food web via biogeochemical cycling of organic and inorganic compounds, degrade environmental contaminants, and are good indicators of overall water quality and ecosystem health. Microbial biofilm function and diversity are essential to these processes and are severely altered in metal impacted environments. Biomass and ecosystem functions like microbial respiration, which aids in organic matter degradation are also altered with even minimal metal bioavailability. Sediment bacterial communities are highly sensitive to metal deposition because they live in close association with sediment surfaces and respond to metal concentrations an order of magnitude lower than benthic macroinvertebrates (BMIs). Nevertheless, studies of inter-taxa communities examining BMIs as consumers and microbes as decomposers or prey, demonstrated several correlations with bacterial species and macroinvertebrate species that reflected the connectivity between the two communities via the food web. Despite this, microbial communities are generally overlooked as mechanisms for evaluating stream health and bacterial relationships to the aquatic food web. Measurable, sensitive, and rapid sediment microbial community responses to both the introduction and removal of metals, and links to BMI diversity, could contribute to timely water quality assessments following contamination events and stream remediation efforts and may act as powerful precursors to BMI and overall lotic ecosystem recovery. The aims of this study were to 1) use microbial community responses to metals for the development of early-detection water quality indicators and 2) correlate microbial species diversity and richness to BMI species diversity and richness at different metal concentrations to assess food web relationships.

Sediment bacterial communities from five sites in the Animas River Watershed in southwestern Colorado were analyzed. Samples were collected along a gradient of metal concentrations, temperature, and pH. Bacterial diversity and richness were also compared to BMI diversity and richness at one low pH, high metal concentration location (Cement Creek), and one neutral pH and relatively low metal concentration location (Baker's Bridge). Illumina sequencing of 16S rRNA bacterial genes revealed significant bacterial community composition differences between sites ($p = .001$), with the most significant drivers being pH, arsenic and copper. Communities from sites with pH ~ 4.0 and As concentrations below detectable limits (BDL) up to 37 ppm demonstrated similar diversity patterns. However, when As and Cu reached concentrations > 200 ppm and 138 ppm respectively, with pH ~ 4.0, microbial diversity dropped relative to other sites with acidic pH but lower metal concentrations ($p < .01$). Communities from neutral pH sites were significantly more diverse than those from acidic pH sites ($p < .01$) regardless of metal concentrations when As was < 200 ppm, and Cu was between 40 – 60 ppm. Sites high in metals and low in pH were dominated by bacteria from the orders Gallionellales, Rhodospirillales, and Cyanobacteria, which are often associated with iron and copper oxidation and dissolution. This community shift showed an inverse relationship with BMI EPT and Shannon Diversity values. Both bacterial community and BMIs diversity values dropped significantly among sites with low pH. Sites with neutral pH

and fewer metals were characterized by bacteria from Burkholderiales, Rhizobiales, Saprospirales, and Sphingomonadales, which are comprised of more plant and soil associated microbes found in healthy functioning lotic ecosystems. BMI EMT and Shannon Diversity indices showed positive correlations with bacterial diversity indices. Sediment bacterial community analyses show promise as bioindicators that can be applied rapidly in remediation and water quality monitoring, connectivity to the BMI community, and the overall aquatic food web.

Effects of Wildfire on Water Quality and Fish Habitat in a Colorado Mountain River System, Animas River, Durango, CO

Emily Johnson¹, Dr. Heidi Steltzer PhD², Dr. Cynthia Dott PhD³

ebjohnson1@fortlewis.edu¹

steltzer_h@fortlewis.edu²

dott_c@fortlewis.edu³

Fort Lewis College

Abstract 16 – Poster

Extreme climatic events such as higher temperatures, drought and wildfire, along with extreme precipitation, will be more common in the Southwest region due to climate change. One of these related disturbances to the Animas River Valley was the 416 Fire that burned over 50,000 acres in the summer of 2018. Fish were soon killed after the first post-fire rains due to debris and a changing aquatic environment. This observational study looked at pH, total dissolved solids, oxidation-reduction potential, conductivity, turbidity and dissolved oxygen, to infer as to how the fire has effected the Animas River and Hermosa Creek by comparing these measurements to the Animas River above the burn scar and Cascade Creek. These variables were tested using a YSI ProDSS water quality meter. The observations concluded that there were differences between water samples below the wildfire compared to those above the water. These differences, including pH, turbidity, total dissolved solids, oxidation-reduction potential and dissolved oxygen, all influence fish health and habitat. Overall, water throughout the western United States will continue to grow as a crucial resource as changes in our climate continue. This perpetuates our necessity for better understanding of our local river systems and the aquatic life within them.

Lower San Juan River Sedimentation and Riparian Vegetation Feedback

Gary Gianniny¹, Cynthia Dott², Logan Hartle³

gianniny_g@fortlewis.edu¹

loganhartle@gmail.com³

Department of Biology, Fort Lewis College

dott_c@fortlewis.edu²

Department of Geosciences, Fort Lewis College

Abstract 17 – Oral

Sedimentation and vegetation on the Lower San Juan River in southeastern Utah are influenced not only by flows and events on the Animas River, but also by this stretch of river being between Navajo Dam upstream, and Glen Canyon Dam downstream on the Colorado River. Thirty years of observations on this stretch of river indicate that increased sediment storage, and decreased high flows in the canyons of the lower San Juan is causing a shift in riparian vegetation composition and dominance. This has implications for potential of unique geochemical events such as the Gold King Mine Spill, and understanding the dynamics of this river system.

Data to estimate the thickness of sediments that have accumulated in the lower San Juan since Glen Canyon Dam was gathered using a combination of repeat photography, surveying, geologic mapping, and historical survey. Our results are notable: sediment accumulation in the river channel/river banks ranges from 0 meters between Government Rapid and Slickhorn Canyon, to a maximum of 21.5 meters at Clay Hills. Much of this sediment was deposited during the highest levels of Lake Powell in the early 1980s, but sediment continued to accumulate in the stream channel even after lake levels dropped, due to aggradation on lower gradient river segments. Lake Powell has raised base-level and driven a self-reinforcing feedback between river gradient, flow velocity and sediment storage. This formed a sediment wedge filling the lower canyon, with lake sediments on the bottom that thicken downstream, and river sediments superimposed on top that thicken upstream. It is not clear how much Gold King Mine Spill sediments have had long term storage in this reach given that the braid bars are continually reworked by the river. The differences in vegetation patterns we have observed coincide with locations that do and do not exhibit sediment accumulation. Upstream of the sediment wedge (above Slickhorn), the reduction in frequency of high magnitude flows below Navajo Dam has allowed for an increase in density of riparian vegetation via vegetative reproduction. In the region of sediment accumulation (below Slickhorn Canyon), a strikingly different riparian community dominated by *Baccharis salicina* has arisen, but here the main impact is due to the influence of Glen Canyon dam downstream. No studies to date have tested the *Baccharis* stems for heavy metal signatures possibly associated with the Gold King Mine Spill.

Assessing Risk to Water Resources from Oil and Gas Activities in the San Juan Basin

Thomas S. Lowry¹, Whitney Thomas², Dave Herrell³

tslowry@sandia.gov¹

Sandia National Laboratories

l1thomas@blm.gov²

Bureau of Land Management, Farmington

dherrell@blm.gov³

Bureau of Land Management, Santa Fe

Abstract 18 – Oral

Rules governing the regulation and management of hydraulic fracturing on Federal and Indian lands for oil and gas extraction were established in 1982 and later updated in 1988 [BLM, 1997]. Since that time, advancements in drilling and well completion technologies have resulted in an exponential growth in the use of directional drilling (horizontal wells) and hydraulic fracturing. A study of the 'Reasonable Foreseeable Development' (RFD) for Northern New Mexico [Engler et al., 2014] identifies a 200,500-acre high potential region for future oil drilling that could be home to an estimated 1600 additional completions. For gas drilling, Engler et al. [2014] states a conservative estimate of 2000 additional gas wells as the 'economics become favorable' (i.e., the price for gas \geq \$4.25/mmbtu). Common to all these additional wells is the use of horizontal well technologies and a demand for water to complete hydraulic fracturing, which is estimated to be \sim 3.13 af/well [Engler et al., 2014] (Figure 1). Methods for reducing water use for hydraulic fracturing, such as the use of produced water or using hydraulic fracturing foam, are being implemented. Even with this however, there is concern as to the regions ability to meet the increasing water demand in a manner that protects human health and the environment while sustainably meeting the needs of the variety of water users in the region.

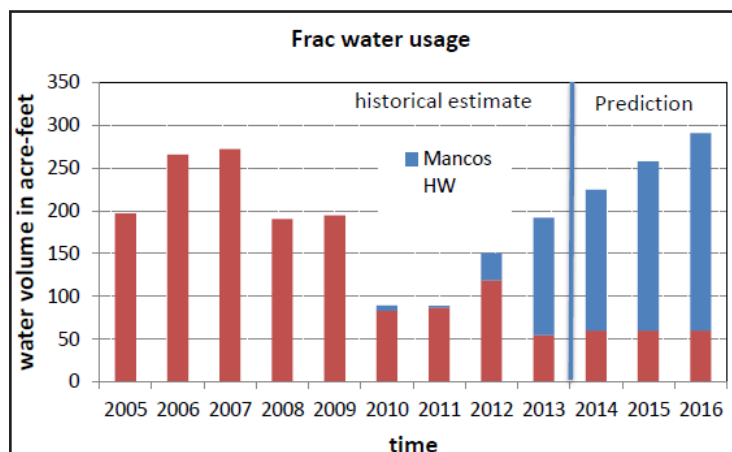


Figure 1. Frac water use by year for conventional (red bars) and horizontal well completions (blue bars) in the San Juan Basin. From Engler et al., 2014.

This presentation describes an ongoing project that uses a multi-disciplinary approach to identify, assess, and evaluate future oil and gas development as predicted in the RFD for the San Juan Basin. Of key importance is identifying the risk to water quantity and quality and establishing a baseline to better detect changing water conditions over time. The project combines activities in data collection, field data verification, field testing, and GIS analysis with the goal of producing insight and understanding that is beyond what can be produced if the activities were executed individually. The objective of the field work is to identify and catalogue the location, water production capacity, source formation, depth to groundwater, etc. of a representative subset of the numerous water wells in the region (Figure 2). Field work is scheduled to begin in the summer of 2019. Once collected, this new information will be combined with existing data and information to map the risks to water quantity and quality across the basin.

To place the San Juan Basin work into context, the presentation will start with the results of a similar project conducted in the Permian Basin, where over 150 wells were cataloged and/or sampled.

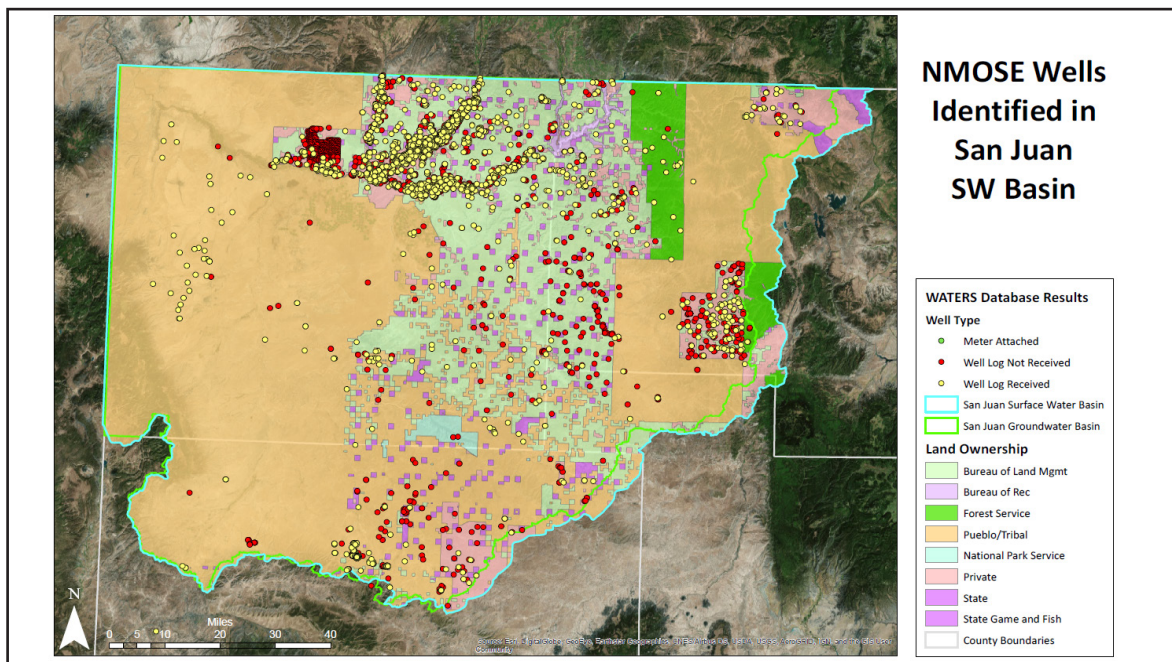


Figure 2. Water wells in the San Juan Basin area underlaid by land ownership. Focus of the field work activities will be on areas predicted to have high potential for future oil and gas exploration.

REFERENCES

Engler T.W., S. Kelley, and M. Cather, 2014, *Reasonable Foreseeable Development (RFD) for Northern New Mexico*, Final Report submitted to Bureau of Land Management Farmington Field Office, October, 38p.

New Magnetotelluric Survey in the San Juan-Silverton Caldera Complex, Silverton, Colorado, Reveals Subsurface Rock Properties Important For Interpreting Modern Groundwater and Ancient Hydrothermal Flow Paths in a Mineralized System

Douglas B. Yager¹, Brian D. Rodriguez², Maria Deszcz-Pan³, Bruce D. Smith^{4**}, Eric D. Anderson⁵, and Benjamin R. Bloss⁶

dyager@usgs.gov¹

brod@usgs.gov²

maryla@usgs.gov³

bsmith@usgs.gov⁴

ericanderson@usgs.gov⁵

bbloss@usgs.gov⁶

U.S. Geological Survey, Denver, Colorado, USA

** (emeritus)

Abstract 19 – Poster

The San Juan-Silverton caldera complex is located near Silverton, Colorado in the Southern Rocky Mountain Volcanic Field. The purpose of our study is to help characterize subsurface rock properties important for understanding surface water and groundwater quality issues, and to improve knowledge of shallow to deep faults and vein-structures that were conduits for hydrothermal fluids that formed mineral deposits. The study has general applications to mineral resource assessments in other areas of the world, and to identifying possible groundwater flow paths and associated geochemistry important in abandoned mine lands cleanup.

The legacy of hard rock mining in headwater catchment areas has caused environmental challenges for local communities and downstream users of water resources. Mining-related sources of metals and acidity overprint and add to geologic sources of metals in surface water and groundwater. Weathering of altered and mineralized rock, often containing pyrite and other sulfides has resulted in acid rock drainage that has been ongoing for millennia.

Newly acquired audiomagnetotelluric (AMT) and magnetotelluric (MT) data are being used to investigate structures of the San Juan-Silverton caldera complex. The San Juan caldera formed at 28.4 Ma, followed by the younger, nested Silverton caldera at 27.6 Ma. In general, calderas are collapsed volcanoes that form when magma is erupted along a ring fault zone at a volcanic margin. Caldera ring fault zones, also called structural margins, can be circular to elliptical and > 15 km in diameter and extend several kilometers into the crust. Rocks overlying the magma chamber (caldera roof) that were at the surface of the volcano prior to eruption, collapse into the void created by eruption of the magma chamber. The volcano-tectonic upheaval during caldera formation cause rocks adjacent to the volcano to be highly-fractured and faulted. Upwelling or resurgence of new magma beneath the intra-caldera volcanic fill, as is likely the case for the San Juan-Silverton caldera complex, can push up and dome the center of the caldera area, causing additional fractures and faults to form. These caldera-related structures can become flow paths for hot fluids that deposit base- and precious-metals.

Along with previously acquired geologic mapping, airborne magnetic, and airborne electromagnetic data, the USGS collected AMT and MT data in July, 2018 at 24 sites along four profiles ranging from 3 to 6 kilometers in length across the northwestern structural margin of the Silverton caldera in Mineral Creek Basin, across the southeastern margin of the caldera along Cunningham Creek, within the caldera in Eureka Graben, and within the caldera along upper Cement Creek near the Gold King mine. The MT method is a passive ground-based electromagnetic technique that investigates subsurface electrical resistivity at depths of 10s of meters to 10s of kilometers. It does so by measuring time variations in Earth's electric and magnetic fields. Worldwide lightning activity and geomagnetic micropulsations from solar wind-charged particles interacting with Earth's magnetosphere provide the main source of signal used by the AMT and MT methods, respectively. The AMT and MT methods measure electromagnetic properties of rocks and sediments. These properties can vary depending on minerals present, moisture content, and percentage of clay minerals. Rocks and sediments that have sulfide minerals can have low electrical resistivity. Dry bedrock that lacks sulfide minerals tends to have relatively high resistivity. Wet bedrock and clay typically exhibits intermediate resistivity because of conduction through pore fluids and along clay mineral surfaces.

Electrical resistivity modeling helps to characterize the electrical resistivity of mineralized caldera structures and adjacent rocks to great depths. Electrical resistivity models can also reveal low resistivity zones where groundwater flow through volcanic rocks might have higher concentrations of total dissolved solids attributed to bedrock weathering processes.

We present the results of two-dimensional resistivity inversions of the AMT data for each of the four profiles. Along the Mineral Creek Basin profile, the AMT resistivity inversion images what appears to be a megabreccia block of resistive rocks that we interpret to be intermediate lavas down-dropped about 300 meters along the east side of the inferred caldera ring fault. Lower resistivity rocks east of the ring fault in the upper 100 meters are near a dacite intrusion and associated breccia pipe. Along the Cunningham Creek profile, the AMT resistivity inversion images resistive rocks along the entire length of the profile and very resistive rocks in the northern half of the profile that we interpret to be intermediate lavas along the caldera ring fault. Along the Eureka Graben profile, the AMT resistivity inversion images a deep (below 800-meters depth) low resistivity zone south of Lake Emma, hosted in resistive rock, near the trend of the Sunnyside mine vein systems. Along the upper Cement Creek profile, the AMT resistivity inversion images a shallow 20-meter thick low resistivity layer we interpret to be basin fill and a deeper, 500- to 1,000-meters depth, low resistivity zone about 800 meters west of the Gold King mine vein systems. Resistive rock at the north and south end of the profile may be less fractured and less altered than the subsurface rock in the central part of the profile.

Final integration of geologic and other geophysical data for our study will enable construction of 3-D geological and geophysical models of the caldera complex, permitting new interpretations about economic mineralization that are applicable in similar geologic environments in other parts of the world. The models will also allow identification of electrically conductive (low resistivity) structures and deposits that may represent permissive groundwater flow paths and conduits for acidic and metal-rich water important for mine reclamation decisions and abandoned mine cleanup.

Impact and Recovery of Navajo Agricultural Activity Following the Gold King Mine Spill

Karletta Chief
kchief23@gmail.com
University of Arizona

Abstract 20 – Oral

On August 5, 2015, the Gold King Mine released 3 million gallons of acid mine drainage into the Animas River, endangering the primary source of irrigation for three Navajo farming communities- Aneth, UT, Upper Fruitland, NM and Shiprock, NM. The objectives are 1) to understand the impact of the Spill on Navajo farming and production and 2) to understand the recovery of farmers to begin farming again, and 3) to understand what informed the decisions of Navajo farmers. A survey was administrated on October 5, 2018 at the 107th Annual Northern Navajo Nation Fair (a community celebration of the year's harvest) by Navajo Community Health Representatives. Participants were asked about their agricultural farming activities and the impact the spill had on their livelihood before and after the spill, and how they received information regarding the impacts. We hypothesized that more than 50% of farmers are not farming three years after the Spill and that they have more information about the Spill and environmental results due to the university-interagency dissemination efforts. Results show that 23 out of 38 participants reported they halted growing crops because of the mine spill and 13 out of those 23 participants reported they have not started agricultural activities since the initial spill, despite the river being declared safe for irrigation by the Environmental Protection Agency. The number of farmers reluctant to use the river has raised concerns why a once prolific farming community choose not to return to their traditional livelihood practices.

Impacts and Recovery: Animas River Water Quality and Aquatic Life Following the 416-Fire

Scott Roberts
scott@mountainstudies.org
Mountain Studies Institute

Abstract 21 – Oral

During the summer of 2018, the 416 Fire burned 54,000 acres in the San Juan National Forest of southwest Colorado. The fire and smoke negatively impacted livelihoods, homeowners, tourism and the fire restricted access to rural towns and communities. Subsequent runoff events and debris flows have occurred within the 416-burn area, creating concern in southwest Colorado communities about the resulting impacts to water quality and aquatic life. Ash and sediment delivered from the 416-burn area have been evident in changes in color, discharge, turbidity, and reports of fish kills in Hermosa Creek and the Animas River.

To investigate these impacts, we formed a research team made up of scientists from the MSI, Colorado School of Mines, and USFS Rocky Mountain Research Station. Preliminary results from our research conducted thus far demonstrate that runoff events from the 416-burn scar can result in elevated levels of sediment, nutrients, and metal concentrations. We will discuss our efforts to document the recovery of water quality and aquatic life following the 416-Fire to share with concerned public members and more broadly to further our understanding of the recovery of river health after wildfire.

Watershed Monitoring Across the Persistent to Intermittent Snow Transition Zone in Colorado

Gigi Richard
garichard@fortlewis.edu
Fort Lewis College

Abstract 22 – Oral

Colorado's winter snowpack is an important component of the state's water supply. Understanding how the snowpack at different elevations in Colorado's mountains accumulates and becomes streamflow in the spring is critical to efficient management of our water resources. Faculty and students from Fort Lewis College, in collaboration with Colorado State University and Colorado Mesa University, are participating in a statewide monitoring effort to enhance our understanding of water yield from snowpack at varying elevations across the state of Colorado. Preliminary results suggest that small elevation differences can result in varying snow persistence and snowmelt timing where temperature plays a key role. In addition, underlying geology appears to play a critical role in streamflow patterns from snowmelt on the Grand Mesa compared to the Colorado front range sites.

2019 Participant List

LeOra Allen
Youth Conservation Corp

Steve Austin
Water Quality/NPDES Program

Michelle Barnard
Youth Conservation Corp

Berrett Bentley
Youth Conservation Corp

Elizabeth Bentley
Youth Conservation Corp

Palmer Bentley
Youth Conservation Corp

Andrew Black
New Mexico Water Resources
Research Institute

Johanna Blake
U.S. Geological Survey

Juliana Bouren
Youth Conservation Corp

Jeb Brown
U.S. Geological Survey

Edward Bullock
San Juan Watershed Group

Heather Cabos
New Mexico Water Resources
Research Institute

Dominous Charley
Youth Conservation Corp

Karletta Chief
University of Arizona

Ty Churchwell
Trout Unlimited

Sandra Connors
Environmental
Protection Agency

Robert Cook
U.S. Environmental Protection
Agency Region 6

Martha Cooper
The Nature Conservancy

Cal Curley
U.S. Senator Tom Udall
(New Mexico)

Karyn Denny
Navajo Nation

Cynthia Dott
Fort Lewis College

Farrah Duncan
Youth Conservation Corp

Leticia Edison
Youth Conservation Corp

Anthony D. Edwards
Bonita Peak Mining District

Jason Fechner
New Mexico State University

Christina Ferguson
U.S. Geological Survey

William Fetner
New Mexico Office of Natural
Resources Trustee

Brandon Francis
New Mexico State University

Gary Gianniny
Fort Lewis College

McKayla Gilbert
Youth Conservation Corp

Carolyn Gillette
Eastern Research Group

Vincent Gomez
Youth Conservation Corp

Cassandra Gould
Bureau of Indian Affairs

Sterling Grogan
Carpe Diem West

Hannah Grover
Farmington Daily Times

Scott Hacking
Department of Environmental
Quality

Justin Holmes
Youth Conservation Corp

Cindy Hurtado
San Juan Generating Station

Kurt Imhoff
San Juan Watershed Group

Viviann Jackson
Youth Conservation Corp

Rachel Jankowitz
New Mexico Environment
Department / Surface
Water Bureau

Kimberly Jaquez
Youth Conservation Corp

Gaurav Jha
New Mexico State University

Forrest John
Environmental
Protection Agency

Ron Kellermueller
New Mexico Department
of Game and Fish

Adriana King
Youth Conservation Corp

Kort Kirkeby
PG Environmental

Gloria Lane
Navajo Ethno-Agriculture

Nonabah Lane
Navajo Ethno-Agriculture

Kevin Lombard
New Mexico State University-
Agricultural Science Center
at Farmington

Jennifer Lowell
Fort Lewis College

Thomas Lowry
Sandia National Laboratories

Ethan Mamer
New Mexico Bureau
of Geology

Shrewd Martinez
Youth Conservation Corp

Melissa May
San Juan Soil & Water
Conservation District

Patrick McCarthy
The Nature Conservancy

Dennis McQuillan
New Mexico
Environment Department

Shannon McQuillan
Fort Lewis College

Paul Montoia
City of Farmington

Teresa Montoya
University of Chicago

Larry D. Moore
Diné College

Chid Murphy
Bureau of Indian Affairs

Ananya Narurkar
Fernandez and Associates, LLP

Brad Talon Newton
New Mexico Tech

Norman Norvelle
Retired Citizen

Cathy Ortega Klett
New Mexico Water Resources
Research Institute

Christine Osborne
Utah Department
of Environmental Quality

Lucy Parham
Utah Division of Water Quality

Isaac Payne
Youth Conservation Corp

Daniel Posegate Youth
Conservation Corp

Alexandra Ratcliff
Southern Ute Indian Tribe

Shera Reems
Environmental
Protection Agency

Bryan Rezin
U.S. Geological Survey

Gigi Richard
Fort Lewis College

Peggy Risner
New Mexico Water Resources
Research Institute

Scott Roberts
Mountain Studies Institute

Brian Rodriguez
U.S. Geological Survey

Lana Rowenko
Kelley Drye & Warren LLP

Robert Sabie
New Mexico Water Resources
Research Institute

Tom Schillaci
Environmental Video

Mark Sheely
New Mexico Water Resources
Research Institute

Victor Snover
Mayor of Aztec, New Mexico

Kate Sullivan
U.S. Environmental Protection
Agency

Leigh Whitney Thomas
Bureau of Land Management

Andrew Todd
Environmental Protection
Agency

Ashley Torres
New Mexico Institute
of Mining & Technology

James Treacy
ESS Group

Forrest Vaughan
Southern Ute Indian Tribe

Randy Velarde
City of Farmington

Katie Walton-Day
U.S. Geological Survey

Madison White
Fort Lewis College

Michael Whiting
New Mexico State University

Jaiden Rose Willetto
Diné College

Samantha Wright
Mountain Independent

Douglas Yager
U.S. Geological Survey

Al Yazzie
Interpreter

Kristine Yurdin
New Mexico
Environment Department

5th Annual Animas and San Juan Watersheds Conference

Managing and Improving Water Quality
in a Multijurisdictional Watershed

June 15-19, 2020
Zoom Webinar Exclusive



Conference Planning Partners:







5th Annual Conference**Animas and San Juan Watersheds Week:***Managing and Improving Water Quality in a Multijurisdictional Watershed*

June 15–19, 2020

Zoom Webinar Exclusive

CONFERENCE PROGRAM**Monday, June 15: Pre-Conference Virtual Field Trip**

11:00 am – 12:00 pm Virtual tour presentation of the NMSU Agricultural Science Center at Farmington

12:00 pm – 1:00 pm Virtual tour of Navajo Agricultural Products Industry Headquarters

Tuesday, June 1610:55 am **Webinar Participation Guidelines**[Mark Sheely](#), NM WRRRI11:00 **Welcoming Remarks**[Sam Fernald](#), NM WRRRI Director[Melissa May](#), San Juan Soil & Water Conservation District11:15 **Congressional Video Statements**

U.S. Senator Tom Udall

U.S. Congresswoman Deb Haaland, NM-1

U.S. Senator Martin Heinrich

11:20 **Multijurisdictional Watershed Coalition Panel**Moderated by [Anthony Edwards](#), Town of Silverton Municipal Court Judge[Suzanne Copping](#), U.S. Bureau of Land Management[Patrick Pfaltzgraff](#), Colorado Department of Public Health and Environment[Melissa May](#), San Juan Soil & Water Conservation District12:00 pm **Break**12:10 *The San Juan Watershed Group: Adapting a Watershed Approach in a Multijurisdictional Watershed* (Abstract 6)[Alyssa Richmond](#), San Juan Watershed Group[Melissa May](#), San Juan Soil & Water Conservation District12:30 *Program Development and Resource Allocation Across Five Counties and Three River Basins in Central Virginia* (Abstract 13)[Greg Wichelns](#), Culpeper Soil and Water Conservation District12:50 **Giveaway Prize Drawing**1:00 **Adjourn Day 1**

Wednesday, June 17

- 11:00 *Investigation into Lead Concentrations in the Animas River in New Mexico* (Abstract 12)
[Kristopher Barrios](#), [Dennis McQuillan](#), [Patrick Longmire](#), [Brad Reid](#), and [Kristine Yurdin](#)
 New Mexico Environment Department
- 11:20 *Overview of Multi-year Groundwater Monitoring along the Animas River, New Mexico*
[Stacy Timmons](#), New Mexico Tech
- 11:40 **Break**
- 11:50 *Sediment Geochemistry in Aztec Drinking Water Reservoir #1 and Farmington Lake, Northwestern New Mexico* (Abstract 3)
[Johanna Blake](#), [Jeb Brown](#), and [Christina Ferguson](#), U.S. Geological Survey
- 12:10 pm *Investigating the Source and Mobility of Manganese in Groundwater and Sediments on the Lee Acres Landfill near Farmington, NM* (Abstract 1)
[Erin Gray](#) and [Christina Ferguson](#), U.S. Geological Survey
- 12:30 Poster Presentation: *Monitoring toxic metal uptake by corn grown in agricultural fields across Animas and San Juan Rivers*
[Michael Whiting](#), [Gaurav Jha](#), [April Ulery](#), and [Kevin Lombard](#), New Mexico State University
- 12:50 **Giveaway Prize Drawing**
- 1:00 **Adjourn Day 2**

Thursday, June 18

- 11:00 am *San Juan River Valley Farmer and Growers' Perspectives Five Years Since the Gold King Mine Spill* (Abstract 11)
[Brandon Francis](#), New Mexico State University Agricultural Science Center at Farmington
- 11:20 *Tell Your Story: Turning Watershed Data into a Compelling Narrative* (Abstract 7)
[Christine Osborne](#), Utah Department of Environmental Quality
- 11:40 *Monitoring of Metal(loid) Contamination in Animas Watershed Agriculture* (Abstract 8)
[Gaurav Jha](#) and [April Ulery](#), New Mexico State University, Dept. of Plant and Environmental Sciences
[Kevin A. Lombard](#), New Mexico State University Agricultural Science Center at Farmington
- 12:00 pm **Break**
- 12:10 *Revisiting Composted Biosolids as a Fertilizer Source: The Case of Iron Deficiency in Hybrid Poplar-Based Agroforestry in Northwest New Mexico* (Abstract 9)
[Kevin A. Lombard](#) and [Sam Allen](#), New Mexico State University Agricultural Science Center at Farmington
[April Ulery](#), New Mexico State University, Dept. of Plant and Environmental Sciences

- 12:30 *Assessing Risk to Water Resources from Oil and Gas Activities in the San Juan Basin* (Abstract 2)
[Thomas S. Lowry](#), Sandia National Laboratories
[Owen Lofton](#), [Whitney Thomas](#), and [Dave Herrell](#), U.S. Bureau of Land Management
[Patricia Johnson](#), INTERA
- 12:50 *Produced Water Reuse Opportunities and Challenges in the San Juan Basin* (Abstract 5)
[Mike Hightower](#), New Mexico Produced Water Research Consortium
- 1:10 **Announcement of Final Giveaway Prize Winners**
- 1:15 **Adjourn Conference**

3–4:30 pm **Animas River Community Forum Meeting**
Hosted by SGM and Animas Watershed Partnership
This separate meeting will feature:

- Post-416 Fire recovery efforts in the Animas River watershed, including water quality monitoring results
- A tour of the Our Animas online story map
- Animas Watershed Partnership's new direction and projects on the Florida River
- Updates from various stakeholders working in the Animas River watershed

Friday, June 19: Post-Conference Virtual Community Teach-In

1:00–3:00 pm

Impact and recovery of Navajo Agricultural Activity following the Gold King Mine Spill
[Karletta Chief](#), The University of Arizona

Social and cultural impacts of the Gold King Mine Spill on Diné communities near the San Juan River
[Carmenlita Chief](#), Northern Arizona University
[Duane "Chili" Yazzie](#), President of Shiprock Chapter, Navajo Nation

Flash Talks from Conference Presenters | Open Discussion and Q&A

2020 Abstracts

Investigating the Source and Mobility of Manganese in Groundwater and Sediments on the Lee Acres Landfill near Farmington, NM

Erin L. Gray¹, Christina L. Ferguson²

egray@usgs.gov¹

cferguson@usgs.gov²

U.S. Geological Survey, New Mexico Water Science Center

Abstract 1 – Oral

The Lee Acres Landfill is a closed 60-acre landfill that was operated on leased Bureau of Land Management (BLM) land from 1962 to 1985. The landfill was closed in 1985 after the berm of a liquid waste lagoon was breached and waste, including chlorinated organic solvents, spent acid, and produced water from oil and gas fields, spilled into the adjacent arroyo upgradient of the San Juan River. In August 1990, the site was placed on the Environmental Protection Agency (EPA) National Priorities List (NPL). Following NPL listing, the U.S. Geological Survey (USGS) has worked with the BLM to perform regular water level and water quality monitoring of the shallow groundwater at the site. Currently (2020), the only remaining constituent of concern is manganese (Mn), which has been measured in the groundwater above maximum contaminant levels outlined in the EPA's Record of Decision (ROD) for the site (346 ppb). To meet requirements outlined in the ROD, an interpretive study is planned to assess the spatial and temporal trends of Mn in groundwater and sediment at the site. Groundwater is contained in one of two aquifers at the site: the alluvial aquifer that is between 30 and 60 feet thick, and the Nacimiento Sandstone aquifer that lies directly beneath the alluvial aquifer. All wells under investigation are completed within the alluvial aquifer. Preliminary analysis of existing data suggests that increased Mn concentrations could be related to redox conditions in the shallow alluvial aquifer. Proposed work includes a geochemical analysis of existing monitoring data, the installation of up to five new wells, and expansion of the water quality monitoring plan to include total and dissolved analyses for major elements and trace metals, ferrous and ferric iron content, total dissolved solids (TDS), dissolved organic carbon (DOC) content, volatile organic carbon content, and sulfides. Sediment samples collected from boreholes will be analyzed for bulk chemistry and used to perform sequential extraction mobility experiments. A sequential extraction experiment will allow investigators to understand how Mn is bound to the sediments at the site and under what environmental conditions bound Mn may be mobilized into groundwater. The results of this study will assist the BLM with satisfying requirements outlined in the ROD.

Assessing Risk to Water Resources from Oil and Gas Activities in the San Juan Basin

Thomas Lowry¹, Owen Lofton², Whitney Thomas³, Dave Herrell⁴, Patricia Johnson⁵

tslowry@sandia.gov¹
Sandia National Laboratories

olofton@blm.gov²
l1thomas@blm.gov³
dherrell@blm.gov⁴
Bureau of Land Management

pjohnson@intera.com⁵
Intera

Abstract 2 – Oral

Rules governing the regulation and management of hydraulic fracturing on Federal and Indian lands for oil and gas extraction were established in 1982 and later updated in 1988 [BLM, 1997]. Since that time, advancements in drilling and well completion technologies have resulted in an exponential growth in the use of directional drilling (horizontal wells) and hydraulic fracturing. A study of the ‘Reasonable Foreseeable Development’ (RFD) for Northern New Mexico [Engler et al., 2014] identifies a 200,500-acre high potential region for future oil drilling that could be home to an estimated 1600 additional completions. For gas drilling, Engler et al. [2014] states a conservative estimate of 2000 additional gas wells as the ‘economics become favorable’ (i.e., the price for gas \geq \$4.25/mmbtu). Common to all these additional wells is the use of horizontal well technologies and a demand for water to complete hydraulic fracturing, which is estimated to be ~3.13 af/well [Engler et al., 2014] (Figure 1). Methods for reducing water use for hydraulic fracturing, such as the use of produced water or using hydraulic fracturing foam, are being implemented. However, there is also a trend to switch to slick water fracking, which will require 10x the water per well. Thus, there is concern as to the regions ability to meet the increasing water demand in a manner that protects human health and the environment while sustainably meeting the needs of the variety of water users in the region.

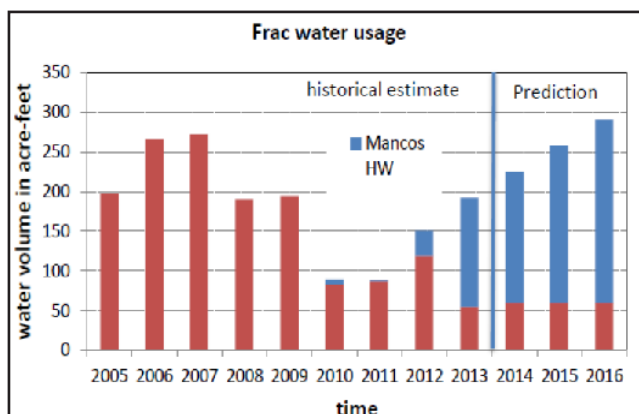


Figure 1. Frac water use by year for conventional (red bars) and horizontal well completions (blue bars) in the San Juan Basin. From Engler et al., 2014.

The project described in this presentation is a multi-disciplinary approach to identify, assess, and evaluate future oil and gas development as predicted in the RFD for the San Juan Basin. Of key importance for the project is identifying the risk to water quantity and quality and establishing a baseline to better detect changing water conditions over time. The project combines activities in data collection, field data verification, field testing, and GIS analysis with the goal of producing insight and understanding that is beyond what can be produced if the activities were executed individually. The objective of the field work is to identify and catalogue the location, water production capacity, source formation, depth to groundwater, etc. of a representative subset of the numerous water wells in the region (Figure 2).

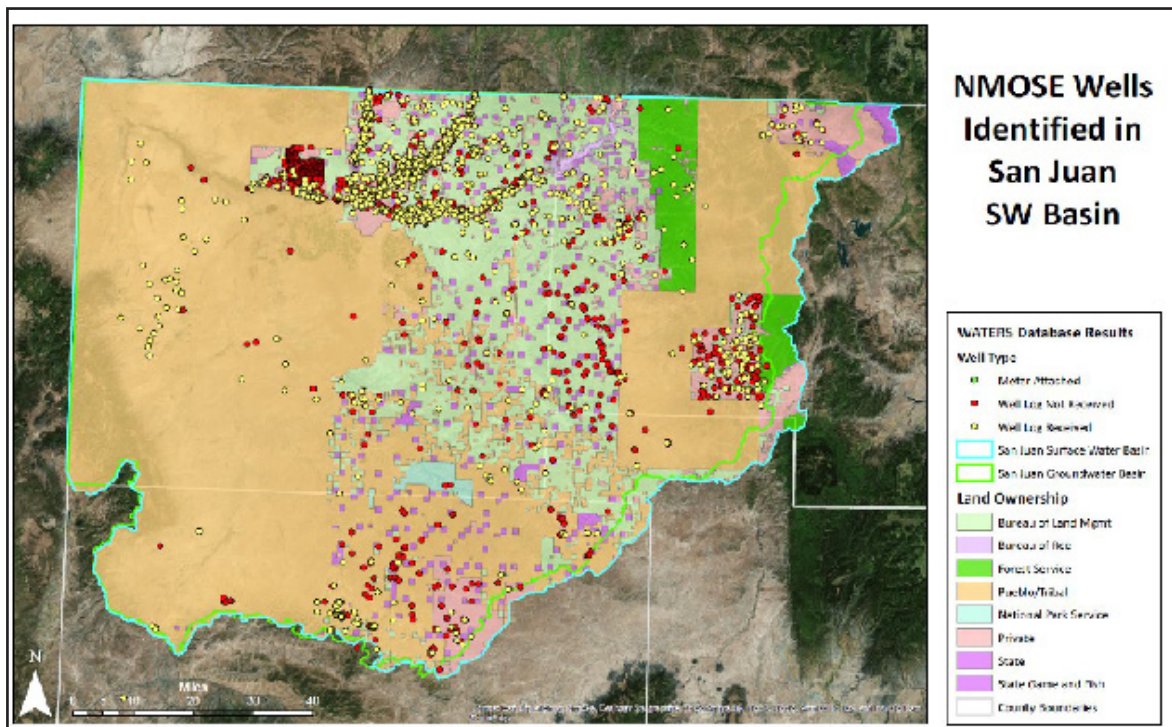


Figure 2. Water wells in the San Juan Basin area overlaid by land ownership. Focus of the field work activities will be on areas predicted to have high potential for future oil and gas exploration.

Field work began in the summer of 2019 and involved 5 weekly efforts over the last year to visit a set of priority wells on BLM land to determine their condition and their suitability and availability for sampling, testing, and long-term monitoring. If conditions allowed, depth to water measurements were made as well as other pertinent data, such as casing size and elevation, and latitude and longitude. In addition, a set of wells on state and Navajo lands were identified for reconnaissance and permission to visit those wells was obtained in early 2020. Unfortunately, efforts to visit those wells were truncated by the COVID-19 crisis.

This presentation will provide an update to the work to date, describing the field efforts, data collected, and balance of work remaining. In addition, we will discuss some of the lessons learned to date.

REFERENCES

Engler T.W., S. Kelley, and M. Cather, 2014, *Reasonable Foreseeable Development (RFD) for Northern New Mexico*, Final Report submitted to Bureau of Land Management Farmington Field Office, October, 38p.

Sediment Geochemistry in Aztec Drinking Water Reservoir #1 and Farmington Lake, Northwestern New Mexico

Johanna M. Blake^{1*}, Jeb Brown¹, Christina L. Ferguson¹

jmtblake@usgs.gov*

¹U.S. Geological Survey, New Mexico Water Science Center
6700 Edith Blvd NE Albuquerque, NM 87113

Abstract 3 – Oral

A legacy signature of historical mining and water quality was investigated in sediments from four trenches in the Aztec drinking water reservoir #1 (AR1; 2018) and four cores in Farmington Lake (2019). Both drinking water reservoirs, located in north western New Mexico, receive water from the Animas River through irrigation ditches and direct pumping from the river. The headwaters of the Animas River lie in the highly mineralized zones near Silverton, CO, an area that was actively mined from the late 1800's until 1991, when all mining operations ceased. Sediment from both reservoirs were collected and analysed for metals through bulk chemistry, mobility experiments, and scanning electron microscopy to determine if the sediments provide a record of upstream mining activity. Cesium-137 age dating was performed on sediments from AR1. This method, which identified the location of the 1963 fallout maximum, combined with the known age of the bottom and top of the sediment trenches, create a polynomial sedimentation rate (average rate = 1.7 cm/yr) for AR1. Results from the Aztec Reservoir sediments indicate elevated concentrations of uranium (U), vanadium (V), arsenic (As), and copper (Cu) in the deepest (oldest) samples, which correspond to a period when mining and milling practices included release of waste directly into surface water. Diatom relative abundance suggests that the water quality in the reservoir was not affected by high metal concentrations. Observed concentrations from leach tests are below regulatory thresholds for delivery of solids to a landfill and are below drinking water standards.

Preliminary results from Farmington Lake reveal concentrations of U, V, As, and Cu similar to AR1, but the patterns of concentrations with depth between the two reservoirs are different. Sediment analysis indicates that the dominant grain size in Farmington Lake is clay and silt. Diatoms show decreasing relative abundance with depth, with the samples closer to the surface containing highest relative abundance. Preliminary handheld X-ray fluorescence results from Farmington Lake sediments show elevated concentrations of strontium, titanium, and zirconium. Results from the chemical analyses of sediments at both sites aid in understanding metal deposition and mobility in these reservoirs. This information will ultimately inform land managers and water system operators about sediment geochemistry in drinking water reservoirs with contributions from upstream legacy mining.

Monitoring Toxic Metal Uptake by Corn Grown in Agricultural Fields across Animas and San Juan Rivers

Michael Whiting¹, Gaurav Jha², April Ulery³, Kevin Lombard⁴

Mikeaid@nmsu.edu¹

gjha@nmsu.edu²

aulery@nmsu.edu³

Plant and Environmental Sciences, New Mexico State University, Las Cruces

klombard@nmsu.edu⁴

Plant and Environmental Sciences, New Mexico State University, Farmington

Abstract 4 – Poster

On August 5th, 2015, more than 3 million gallons of metal contaminated water from the Gold King Mine was released into Cement Creek unintentionally, leading to the contamination of the Animas and San Juan Rivers. Analysis of edible produce collected from fields irrigated with Animas River water was done in 2018 and found three corn samples with lead concentrations above the World Health Organization (WHO) guideline value of 0.05 ppm. Since then, the original samples were reanalyzed, resulting in two corn samples out of 30 still being above the WHO guidelines. The purpose of this study is to investigate these findings and to monitor the metals lead, arsenic, and aluminum in the agricultural fields.

Five fields along the Animas and San Juan Rivers were selected for the study. Samples of soil, leaf tissue, corn husk, and corn kernels were collected through the pre-growing, growing, and post-growing seasons. These samples were analyzed using ICP-MS/OES (Inductively Coupled Plasma-Mass Spectrometry/Optical Emission Spectrometry) and PXRF instrumentation, focusing on the elements Pb (lead), As (arsenic) and Al (aluminum).

Produced Water Reuse Opportunities and Challenges in the San Juan Basin

Mike Hightower
mmhightower@q.com
Program Director
New Mexico Produced Water Research Consortium
New Mexico State University

Abstract 5 – Oral

Over the past decade, New Mexico has been recognized as one of the leaders in the U.S. in pursuing the reuse of produced water to supplement fresh water supplies and reduce or eliminate the use of fresh water in oil and gas development. Past research studies have looked at treatment for flow augmentation of the Pecos River, rangeland rehabilitation, agricultural irrigation, algal biofuels production, and even beer making. These efforts were focused on supporting a more sustainable fresh water management approach in New Mexico, a state with limited fresh water resources that has seen significant reductions in average annual precipitation over the past century.

In passing the 2019 Produced Water Act, the New Mexico Legislature established a regulatory and policy framework for the ownership, management, and reuse of produced water inside and outside of the oil and gas sector. Through this act, statutory control and regulatory authority for the reuse of produced water outside the oil and gas industry was designated to the NM Environment Department (NMED), while reuse of produced water within the oil and gas sector remained under the jurisdiction of the Oil Conservation Division (OCD) of the NM Energy Minerals and Natural Resources Department.

To establish science-based regulations and policies for the treatment and reuse of produced water outside the oil and gas sector, the NMED entered into a Memorandum of Understanding with New Mexico State University (NMSU) in September 2019 to create the **New Mexico Produced Water Research Consortium** (Consortium). The goal of the Consortium is to establish and coordinate a focused research and development program in collaboration with state and federal environmental and natural resource agencies, academia, industry, and non-governmental organizations (NGO's) and associations to: 1) fill scientific and technical knowledge gaps necessary to establish regulations and policies for fit-for-purpose treatment and reuse of produced water, and 2) accelerate technology and process research, development, and implementation for environmentally sound, safe, and cost-effective reuse of produced water for industrial, construction, agricultural, rangeland, livestock, municipal, aquifer storage, surface water, and/or other applications.

While the Consortium was organized to focus on New Mexico regulatory and permitting issues and challenges, it is obvious that the Delaware and Permian Basins in Southeast New Mexico, the San Juan Basin in Northwest New Mexico, and the Raton Basin in Northeast New Mexico are transboundary oil and gas basins with Texas and Colorado respectively. The transboundary nature of the oil and gas fields in New Mexico, the new Produced Water Act, and the establishment of the Consortium, were factors that led the EPA to identify New Mexico and the Consortium to lead their national efforts for the reuse of produced water. The Consortium is one of only four water research organizations selected by EPA to lead a water reuse initiative.

While these initiatives have given New Mexico the opportunity to lead the nation in evaluating opportunities for the fit-for-purpose use and reuse of treated produced water as a way to reduce or

eliminate fresh water use in oil and gas operations, provide water resources to supplement fresh water supplies, and utilize the treated water and associated minerals to spur additional economic development opportunities in New Mexico. But with any development there will be challenges. Of primary importance is for the Consortium's research to ensure that the use of treated produced water is protective of the environment and public health and safety. But more importantly for the San Juan, that the fit-for-purpose applications and uses selected for the treated produced water enhance or improve overall basin water quality and basin watershed health.

For those reasons, the Consortium is organized to encourage broad stakeholder participation in the overall science and technology evaluation, assessment, and demonstration process. General membership is open to all stakeholders including industry, associations, academia, municipalities, and NGO's at a very nominal annual cost. This gives all interested groups and stakeholders the opportunity to provide continual input on the process, follow progress on the research and development projects and analyses, and help in evaluating local and regional water quality and watershed benefits and impacts.

This presentation will provide an overview of the Consortium goals and objectives, local and regional cooperation and collaboration, research priorities and directions, and information on how to get involved and actively participate in the Consortium efforts.

The San Juan Watershed Group: Adapting a Watershed Approach in a Multijurisdictional Watershed

Alyssa Richmond¹, Melissa May²

alyssa.richmond@sanjuanswcd.com¹

melissa.may@sanjuanswcd.com²

¹San Juan Watershed Group

²San Juan Soil & Water Conservation District

Abstract 6 – Oral

While pollution from legacy mining and the mineralized San Juan Mountains has always been of concern on the Upper Animas River, local watershed groups downstream in New Mexico have been focused on other water pollution issues for almost 20 years. Nutrients were first identified as a problem in the San Juan Watershed by the New Mexico Environment Department (NMED) in 2002, when severe algae blooms choked the river and sparked widespread concern about eutrophication. Since then, the San Juan Watershed Group (SJWG) has collaborated with a variety of stakeholders, agencies, and municipalities to conduct nutrient and bacterial water quality monitoring throughout the Lower Animas River. Combined with the Microbial Source Tracking Study spearheaded by the SJWG and San Juan Soil & Water Conservation District (SJSWCD) in 2013-14 to discern sources of fecal bacterial pollution within the Animas River, the Lower Animas Watershed Based Plan was developed to bridge the connection from water quality impairments to routes towards solutions in a multijurisdictional watershed.

Since 2016 the San Juan Watershed Group has implemented a variety of projects within the Lower Animas Watershed Based Plan in an effective partnership with NMED, SJSWCD, Natural Resources Conservation Service (NRCS), Basin Hydrology Inc. (BHI), local landowners, and others. Projects from upland drainage erosion control, to agriculture runoff management and riparian fencing, to a manure management plan for an equine rescue have been accomplished in recent years with the ultimate goal of adapting a watershed approach to nurture the water quality of our Animas. Each of the projects came with unique challenges and rewards that provide valuable insight to continuously update the Lower Animas Watershed Plan, complete future projects, and develop effective partnerships for the wise and sustainable use of shared natural resources.

Tell Your Story: Turning Watershed Data into a Compelling Narrative

Christine Osborne
cosborne@utah.gov
Watershed Protection

Abstract 7 – Oral

Storytelling is an essential part of being human. We use stories to create connections, forge social bonds, share values and beliefs, and make sense of the world. Stories tap into feelings and emotions that pure data often don't. Yet we often overlook storytelling as a powerful tool for linking numbers, research, and studies with the needs and interests of our audiences. When scientists infuse their narratives with the excitement they experience when conducting research and doing field work, audiences are drawn into the scientific process and become more vested in the outcomes. Just as Scheherazade was able to captivate King Shahryar with her stories (and spare her own life in the process), researchers can use storytelling to spark and sustain stakeholder interest in the dynamic nature of their watershed.¹

The Animas-San Juan Watershed has been the subject of numerous water-quality studies, including watershed-wide monitoring and planning, analyses of watershed hydrology, the Superfund cleanup in the Bonita Peaks Mining District, and examination of the impacts of water quality on agricultural users. This extensive research has yielded rich data and valuable insights into water quality issues in the watershed. The question then becomes how to communicate these data and findings so audiences recognize how they, their actions, and their ongoing engagement are important for maintaining a healthy watershed.

This presentation will examine the research on the effectiveness of scientific narratives to convey information², show how scientists can adapt the key elements of storytelling (characters, plot, setting, outcome, and resolution) to create a "narrative arc" to connect with lay audiences, and demonstrate how scientists and community members can share their respective knowledge about local ecosystems to break down barriers and foster collaboration and cooperation.³

1 Green, S. J., Grorud-Colvert, K., & Mannix, H. (2018). Uniting science and stories: Perspectives on the value of storytelling for communicating science. *Facets*, 3(1), 164-173. doi:[10.1139/facets-2016-0079](https://doi.org/10.1139/facets-2016-0079)

2 Dahlstrom, M. F. (2014). Using narratives and storytelling to communicate science with nonexpert audiences. *Proceedings of the National Academy of Sciences*, 111(Supplement_4), 13614-13620. doi:[10.1073/pnas.1320645111](https://doi.org/10.1073/pnas.1320645111)

3 Bayer, S., & Hettinger, A. (2019). Storytelling: A Natural Tool to Weave the Threads of Science and Community Together. *The Bulletin of the Ecological Society of America*, 100(2). doi:[10.1002/bes2.1542](https://doi.org/10.1002/bes2.1542)

Monitoring of Metal(loid) Contamination in Animas Watershed Agriculture

Gaurav Jha¹, Kevin Lombard², April Ulery³

GJha@nmsu.edu¹

Plant & Environmental Sciences, New Mexico State University, Las Cruces, NM

KLombard@nmsu.edu²

New Mexico State University Agricultural Science Center at Farmington

AUlery@nmsu.edu³

Plant & Environmental Sciences, New Mexico State University, Las Cruces, NM

Abstract 8 – Oral

After the catastrophic Gold King Mine spill, the local growers and consumers became concerned that heavy metals from the mining region might be contaminating soils, water and plants across the Animas Watershed. The research team from New Mexico State University began long term monitoring of exposure pathways to humans and livestock as crops are irrigated by water drawn from the Animas and San Juan Rivers. We collected soil and sediments from 15 irrigation ditches and 8 agricultural fields and analyzed them for 9 metal (loid)s using Inductively Coupled Plasma (ICP) and Portable X-Ray Fluorescence spectrometry. All soil concentrations were below environmental screening levels except arsenic. Further research on sequential extraction showed that the arsenic is not bioavailable. We also sampled leaf tissues from pasture grass, alfalfa and vegetable fields and acid digested the oven-dried samples to determine the total metal concentrations in the matrix of the tissue using ICP spectroscopy. Plant tissues did not exceed the maximum tolerable limit (MTL) for any of the metals tested, thus is considered safe for livestock consumption. Extension, outreach and collaborations of this project have successfully helped the farmers and growers in New Mexico and the Navajo Nation make science-based decisions for their agricultural practices. Further investigations on uptake of metals (like arsenic and lead) by corn kernels and husks are underway. This research has also led to further investigations on metal uptake by corn kernels and husks.

Revisiting Composted Biosolids as a Fertilizer Source: The Case of Iron Deficiency in Hybrid Poplar-based Agroforestry in Northwest New Mexico

Kevin A. Lombard¹, Sam Allen², April Ulery³

KLombard@nmsu.edu¹

samallen@nmsu.edu²

New Mexico State University Agricultural Science Center at Farmington

AUlery@nmsu.edu³

Plant & Environmental Sciences, New Mexico State University, Las Cruces, NM


Abstract 9 – Oral

Iron (Fe) salts are used to remove excess phosphorus (P) from wastewater at municipal treatment facilities. Dewatered sewage sludge (biosolids) are then removed and often landfilled. New Mexico soils typically are alkaline, which challenges some tree crops and their ability to extract soil Fe, an essential element needed for plant growth. Deficiency symptoms manifest as yellowing of new leaves (chlorosis) yield loss and decline if left untreated. Composted biosolids, however, supply plant available Fe and may represent a sustainable alternative to more costly chelated Fe fertilizers used to supplement nutrition in hybrid poplar test plots of elevated soil pH. To test the growth response of poplar, field plots were amended in 2005 with a one-time application of composted biosolids (originating from the Albuquerque Bernalillo County Water Utility Authority Soil Amendment Facility) applied at two agricultural rates: 22.75 and 44.5 Mg ha⁻¹ (10 and 20 tons acre⁻¹). Iron EDDHA served as a fertilizer check and control plots received no amendment. The hybrid poplar OP-367 (*Populus deltoides* x *P. nigra*) was planted on a 3.6 m (12 ft) grid spacing. Significant amounts of phosphorous and iron originating from the sewage treatment process were detected in soils 13 months after amending. Chlorosis evaluated with a SPAD-502 meter, showed that poplars amended with composted biosolids remained the least chlorotic and had greater tree growth when compared to Fe EDDHA and control plots during two growing seasons. After a one-time application of composted biosolids in 2005, in 2020, tree plots were not significantly different in terms of growth/yield compared to control plots. After 15 years, some lingering questions remain: Would repeated applications of composted biosolids make a difference? Are there any risks of emerging contaminants (e.g. personal care products)? Is it sustainable to landfill biosolids? Still, for establishing trees, composted biosolids showed promise as a cost effective alternative for the remediation of Fe chlorosis in hybrid poplar agroforestry plantations and may present new opportunities in northwestern New Mexico for municipalities seeking alternatives to landfilling sewage sludge.

Revisiting composted biosolids as a fertilizer source: The case of iron deficiency in a hybrid poplar-based agroforestry system in northwest New Mexico

Kevin A. Lombard, April Uleary and Sam Allen


Agriculture, Consumer and Environmental Sciences | NMSU-ASC Farmington



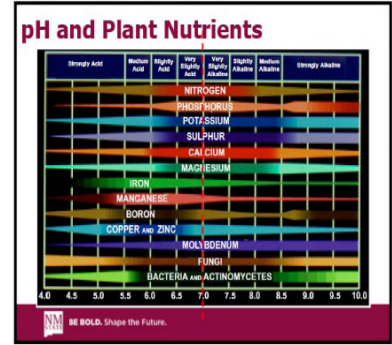
BE BOLD. Shape the Future.

NMSU Agricultural Science Center at Farmington

The mission of the NMSU-ASC Farmington is to conduct research, demonstration, and educational programs that will best fill the needs of the Agricultural community of San Juan County and the Navajo Nation in particular, and the State of New Mexico, Four Corners Region, and Nation in general




BE BOLD. Shape the Future.



Composted Biosolids

- Plant available Fe
- City of Albuquerque: 1:3 ratio of biosolids to garden waste/clippings
- Mixed and composted to heat and kill pathogens
- Benefits must not exceed cost to Environment



BE BOLD. Shape the Future. www.biosolids.org

Materials and Methods

Treatments:


- Two application rates:
 - 10 T/acre (22.75 mT/ha)
 - 20 T/acre (45.5 mT/ha)
- Sprint 138
- Control: no amendment



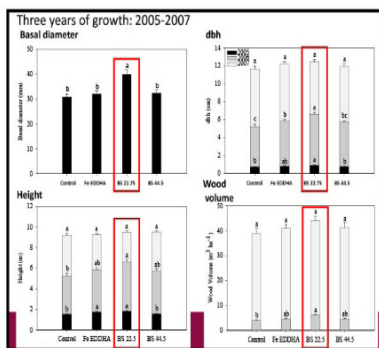
BE BOLD. Shape the Future.

Materials and Methods (continued)

- Double row of drip tape
- Clone OP-367
- 3.6 x 3.6 m



BE BOLD. Shape the Future.



Results – Composted Biosolids

- Highest SPAD values
- Residual Soil Fe, Mn, and P
- Greater biomass
- Salinity - no
- Minimal environmental risk from heavy metals
- Organic pollutants?
- Future in Farmington?

BE BOLD. Shape the Future.

Geochemistry of the Animas River Alluvial Aquifer, San Juan County, New Mexico: Assessing Groundwater Recharge, Flowpaths, and Solute Sources

B. Talon Newton
talon.newton@nmt.edu
New Mexico Bureau of Geology and Mineral Resources
New Mexico Tech

Abstract 10 – Oral

Understanding processes that control the water chemistry in the shallow alluvial aquifer along the Animas River in northwestern New Mexico is necessary to assess the potential impacts to water quality by natural and anthropogenic pollutants. Potential contaminants include acid rock and mine drainage from the Animas headwaters in Colorado, natural upwelling of deep brines or hydrocarbons, possible leakage of fluids associated with existing oil and gas wells, septic fields in the area, and natural local occurrences of metals such as manganese and iron. Newton et al. (2017) conducted a groundwater study along the New Mexico reach of the Animas River to characterize the local hydrogeology and to assess potential impacts to water quality by the Gold King Mine Spill. Water level and geochemical analyses at different seasonal hydrologic regimes showed:

1. The Animas River mostly gains water from the alluvial aquifer along this reach.
2. The primary recharge source to the shallow aquifer is irrigation water that infiltrates through the bottoms of irrigation canals and agricultural fields.
3. Down-gradient increases in dissolved sulfate concentrations (especially south of Aztec) are likely due to geologic controlled upwelling of regional groundwater into the shallow system.
4. All metals associated with the Gold King Mine Spill were either not detected or well below the primary EPA maximum contaminant level (MCL) in sampled groundwater.
5. Dissolved iron and manganese concentrations that exceed EPA secondary MCLs cannot necessarily be linked to legacy acid mine drainage or the Gold King Mine Spill.
6. There was no evidence of impacts to groundwater quality from the Gold King Mine Spill.

A follow-up study by the NMBGMR was initiated in 2018 with the following objectives:

1. To assess the source of dissolved constituents in shallow groundwater along the Animas River in New Mexico.
2. To evaluate controls on redox conditions in the shallow alluvial aquifer in the Animas Valley in New Mexico, specifically related to the occurrence and source of dissolved manganese and iron.
3. To identify specific locations where surface water, including the river and irrigation canals, actively recharges the shallow groundwater system under certain conditions.

Groundwater samples were collected in October 2018 (78 samples) and April 2019 (57 samples) and were analyzed for general chemistry, trace metals and stable isotopes of water (hydrogen and oxygen). A subset of samples were analyzed for carbon isotopes in dissolved inorganic carbon (DIC), and sulfur and oxygen isotopes in dissolved sulfate.

Results for this study were very similar to those of Newton et al. (2017). Sulfate and TDS concentrations increase down-gradient (to the southwest), reflecting the apparent mixing of fresh river water (irrigation recharge) and a high-sulfate, high-TDS regional groundwater. Stable isotope data for dissolved sulfate was compared to data presented by Nordstrom et al. (2007), which included stable isotopic compositions of sulfate for springs, streams, and rocks in the Upper Animas watershed in Colorado. For groundwater that is chemically similar to river water (fresh water endmember), it appears that sulfate and likely most other dissolved constituents originate from volcanic rocks and alterations minerals in the Animas headwaters in the San Juan Mountains.

The conceptual model that describes geologic controlled upwelling of high-sulfate regional groundwater was largely confirmed. However, this study highlighted some complexities. The stable isotopic compositions of sulfate and DIC suggest that the source of the sulfate being added to the system is likely terrestrial gypsum or anhydrite from underlying Cretaceous strata. However, water chemistry data and the stable isotopic composition of water indicate that although the additional sulfate originates from the same geologic formation(s), the water sources and flowpaths of this high sulfate water may vary significantly.

Many dissolved metals of concern (both natural and anthropogenic) are present in surface water in the Upper Animas River watershed, which ultimately defines groundwater chemistry in the northern part of the study area. Fortunately, geochemical conditions (pH and redox) result in the precipitation of most of these metals before entering the groundwater system in New Mexico. We saw no evidence of groundwater contamination related to the Gold King Mine spill or legacy acid mine/rock drainage in the San Juan Mountains. Dissolved manganese and iron that is observed to exceed secondary MCLs in some areas is likely due to manganese oxides and iron (hydr)oxides that were deposited as sediments that make up the shallow aquifer.

The infiltration of contaminated irrigation water to recharge the shallow aquifer does present potential risk for contamination of groundwater. We found that wells that produced water with high dissolved oxygen concentrations ($DO > 3$ mg/L) and relatively low specific conductance values ($SC < 1,200$ mS/cm) likely indicate areas where irrigation water infiltrates through agricultural fields and canal beds to recharge the shallow aquifer.

REFERENCES

- Newton, B.T., Mamer, E., and Timmons, S., 2017, Hydrogeology and Geochemistry of the Animas River Alluvial Aquifer after the Gold King Mine Spill, San Juan County, New Mexico: New Mexico Bureau of Geology and Mineral Resources Open-file Report 592, 64 p.
- Nordstrom, D.K., Wright, W.G., Mast, M.A., Bove, D.J., and Rye, R.O., 2007, Aqueous – Sulfate Stable Isotopes – A Study of Mining-Affected and Undisturbed Acidic Drainage, in Church, S.E., von Guerard, P., and Finger, S.E., ed., Integrated Investigations of Environmental Effects of Historical Mining in the Animas River Watershed, San Juan County, Colorado: USGS Profession Paper 1651, Chapter E8, p. 391 – 413.

San Juan River Valley Farmer and Growers Perspectives 5 years since the Gold King Mine spill

Brandon Francis

bfrancis@nmsu.edu

New Mexico State University, Agricultural Science Center at Farmington

Abstract 11 – Oral

August 5th will mark 5 years since the Gold King Mine event of 2015. The NMSU Agricultural Science Center located in Farmington was a part of the emergency response in the months of August and September. This initial period of data collection along the irrigation ditches led to a long-term monitoring project along Animas River and San Juan River from Cedar Hill to Shiprock.

One of the NMSU Ag Science Center's missions from its inception has been to help the growers in San Juan County with their agriculture needs. The region has a long history of agriculture dating back millennia. The conditions Four Corners provide unique challenges to agriculturists and farmers must adapt to them to survive. Farming has always been a community effort and kinship necessary for success.

There is diverse range of farmers, as well as the variety crops grown and scale of their operations. The long-term monitoring project led to many partnerships between the many organizations conducting research and helping restore consumer confidence in the produce grown in the region lost as a result of the spill. This partnership includes many farmers whose livelihood and way of life depends on the waters of the Animas and San Juan for their farms.

In the years since 2015, many discussions have been had with them and these questions always came up. Has the farmers' perception of the river changed five years since the spill? The work and research being done has it improved or impaired their perspective? Have their agricultural practices changed or remained the same? The perspective of the San Juan River grower will be shared.

Investigation into Lead Concentrations in the Animas River in New Mexico

Kristopher Barrios¹, Dennis McQuillan², Patrick Longmire³, Brad Reid⁴, Kristine Yurdin⁵

kristopher.barrios@state.nm.us¹

dennis.mcquillan@state.nm.us²

patrick.longmire@state.nm.us³

brad.reid@state.nm.us⁴

kristine.yurdin@state.nm.us⁵

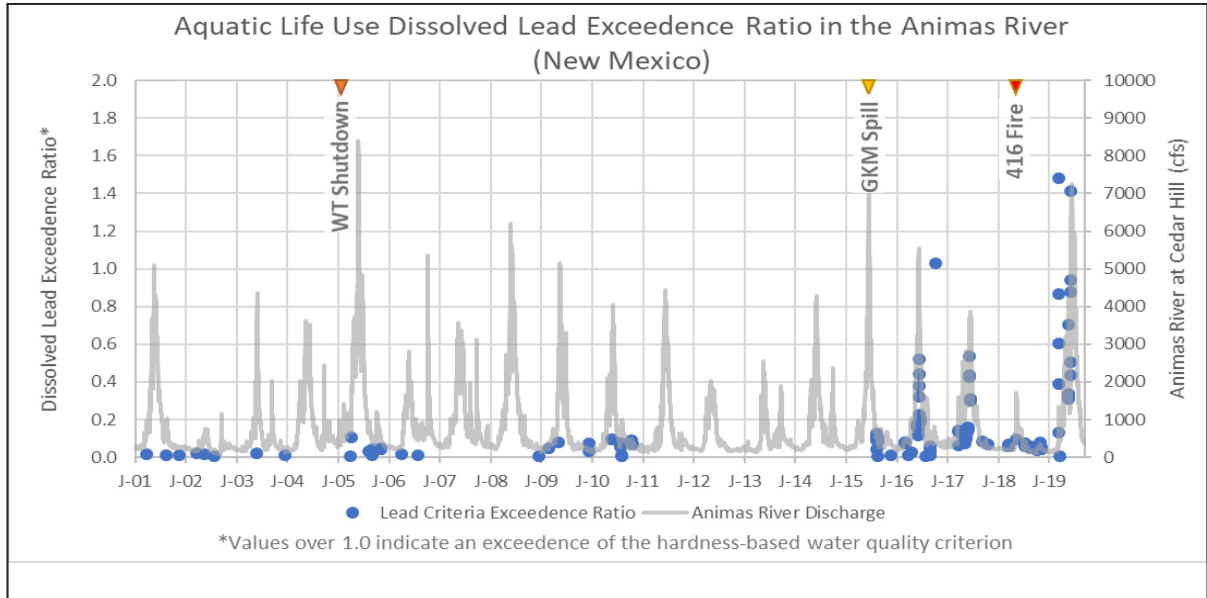
New Mexico Environment Department

Abstract 12 – Oral

The New Mexico Environment Department (NMED) recently completed an evaluation of available surface water flow and chemical data for the Animas River in New Mexico for the purpose of reporting the state's surface water quality for the Federal Clean Water Act 303(d)/305(b) biennial Integrated Report (or IR). The data sources include post-Gold King Mine (GKM) monitoring by NMED and EPA, NMED sampling of the San Juan River watershed in 2017-2018, and continued monitoring by EPA Region 8 through WIIN-Act funding. Out of the compiled dataset, three samples from the past three years exceed the dissolved lead criteria for aquatic life use and may lead to listing of the Animas River in New Mexico as impaired for lead.

Suspended and dissolved lead has been monitored in the Animas River in New Mexico since 1971. The post-GKM dissolved lead exceedences are a concern for the health of aquatic life. Dissolved lead concentrations post-GKM, unlike results measured historically, are more closely related to discharge of the Animas River. In addition, increases in turbidity resulting from stormflow events have been correlated to measurable total lead concentrations in the Animas River requiring the City of Farmington to shut down drinking water system intakes when turbidity exceeds 400 NTU. Periods of high flow mobilize sediment in the Animas River floodplain and reintroduce dissolved and suspended metals into the water column.

An analysis of historical and current data show that both suspended and dissolved lead concentrations increased following the GKM incident. Lead concentrations have continued to increase in the New Mexico reaches of the Animas River with spikes occurring in the springs of 2016 through 2019. The pattern of sample results indicates continued transport of contaminated sediment downstream from Colorado to New Mexico. The predominant source of lead is sediment deposition resulting from legacy mine and mill workings in the Bonita Peak Mining District, which includes the GKM spill. Other contributions include inflow of contaminated groundwater from the former Durango Smelter and sediment loading resulting from the 416 Fire of 2018.



Program Development and Resource Allocation Across 5 Counties and Three River Basins in Central Virginia

Greg Wichelns
gregw@culpeperswcd.org
District Manager
Culpeper Soil and Water Conservation District, Culpeper VA

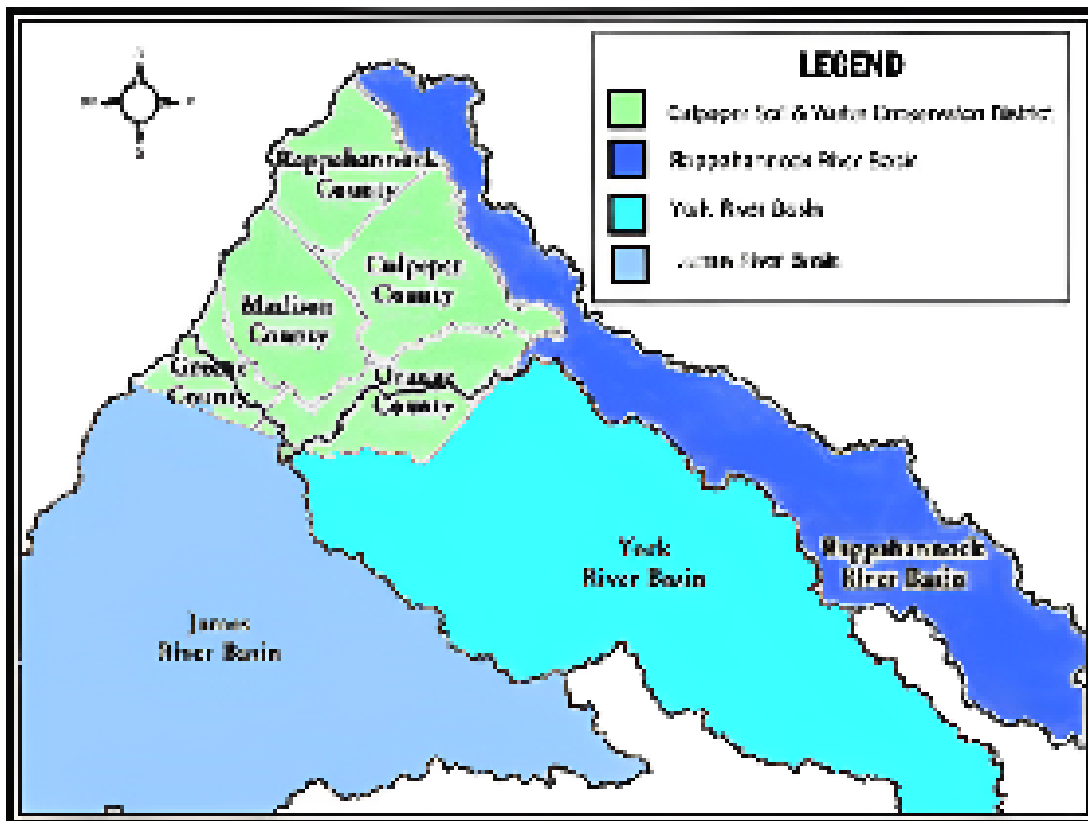
Abstract 13 – Oral

The Culpeper Soil and Water Conservation District (CSWCD), a 5 county SWCD located in the Piedmont Region of Central Virginia, is the largest of Virginia's forty-seven conservation districts. It serves an area of 1,445 square miles with nearly 120,000 constituents and numerous small towns; three of significant size. There are 263,180 acres of agriculture land dedicated primarily to beef / hay production, corn grain and soybeans, with many other agriculture commodities of significance although not on a total acreage basis. Hardwood timber production also continues to be a significant resource here in the CSWCD.

The District's five counties are nestled on the eastern flank of the Blue Ridge Mountains and as such, drain exclusively to the Chesapeake Bay through three major river basins. The Chesapeake Bay is an estuary that has received for many years, and will continue to for many more, significant state and federal pressure and attention for restoration. Nitrogen, Phosphorus and Sediment are the three pollutants targeted by restoration efforts, regardless of land use. Agriculture is considered the primary contributor to non-regulated, nonpoint source pollution loading and as such the CSWCD has a robust agricultural cost share program of several million dollars per year; from funding provided to all Virginia SWCDs by the Virginia General Assembly through the Water Quality Improvement Fund (WQIF). Within the afore mentioned river basins there exists many smaller watersheds that do not currently meet Virginia's Surface Water Quality Standards; primarily E. Coli exceedances in CSWCD but more frequently as of late are identified benthic impairments. The first benthic TMDL in the CSWCD was just recently completed and Implementation Planning is scheduled. The two primary E Coli sources modeled for reduction by TMDL development efforts are livestock fecal matter "direct deposit" into streams and adjacent pasture runoff management, and secondly, ailing and failing residential septic systems. Many of these small impaired watersheds have completed TMDL Implementation Plans for E Coli and the CSWCD has active implementation grants from both state and federal sources to address all of the aforementioned pollutant sources.

The CSWCD has over the most recent ten years developed a five-county-wide, residential on-site septic system cost share program. Supported by state efforts towards program and manual development, the CSWCD has successfully assembled a collection of program specific funding opportunities that has sustained itself district wide over the most recent for four years. Strongly supported by a multitude of partners both public and private, the program has become very well-known and utilized. The CSWCD will highlight how the septic cost share program was developed, how the partnerships were formed, what have been some of the key lessons learned and what vulnerabilities still exist for program longevity. In addition, CSWCD will highlight how the five-county, multi river basin district is funded, how other major programs at the SWCD are funded and what strengths and vulnerabilities are known to exist.

About Us



Impact and Recovery of Navajo Agricultural Activity following the Gold King Mine Spill

Karletta Chief, Malik Hastiin-Tso Scott, Dean Billheimer (PhD),
Yoshira Ornelas Van Horne (MS), Paloma Beamer (PhD)

Community Teach-In Abstract

On August 5, 2015, the Gold King Mine released 3 million gallons of acid mine drainage into the Animas River, endangering the primary source of irrigation for Navajo farming communities in Northern New Mexico. The objectives of this study are to: 1) understand impacts of the Spill on Navajo farming practices and 2) understand what informed the decisions of Navajo farmers. A survey was administered on October 5, 2018 at the 107th Annual Northern Navajo Nation Fair (an annual harvest celebration) by the University of Arizona (UA) and Navajo Community Health Representatives. Participants were asked about agricultural activities and the impact the Spill on their livelihood, and how they received information related to the Spill. Among 38 respondents, majority were Native American (95%), were from Shiprock Agency (94%), were 41 years or older (65%), and learned farming through traditional practices (73%). A majority of the participants, 23 of 38, reported that they halted growing crops because of the Spill. In 2015, the river was declared to meet agricultural water standards by the U.S Environmental Protection Agency (EPA). Despite this declaration, 13 out of 23 participants did not resume farming. The negative impacts were loss of crops and discontinuation of farming. The top reasons for why farmers resumed farming included Navajo EPA declaring the river safe and attending UA People's Teach-Ins. Solutions mentioned were improving community support, communication, and education. Support is needed to develop interventions that will help a once prolific farming community return to their traditional livelihood practices.

2020 Participant List

Abiodun Adeloye
Bureau of Land Management

Diane Agnew
Albuquerque Bernalillo County
Water Utility Authority

Luis Aguirre
New Mexico Office
of the State Engineer

Samuel Allen
New Mexico State University
Agricultural Science Center
at Farmington

Stan Allison
Bureau of Land Management

Garrett Altmann
Santa Clara Pueblo Forestry

Gilbert Anaya
U.S. International Boundary
& Water Commission

Danielle Angeles
U.S. Environmental Protection
Agency Region 9

Thelma Antonio
High Water Mark LLC

Diana Aranda
New Mexico
Environment Department

Cherylin Atcity
Taos Pueblo

Steve Austin
Navajo Nation Environmental
Protection Agency

Terri Austin
Navajo farmer

Yining Bai
New Mexico Water Resources
Research Institute

Jason Banegas
New Mexico State University
College of Business

Daniel Barrio Gonzalez
New Mexico Water Resources
Research Institute

Kristopher Barrios
New Mexico
Environment Department

Ryan Barton
Navajo Nation

Maria Bautista
U.S. Department of Agriculture
/ National Agricultural Statis-
tics Service / NM FO

Kathryn Becker
New Mexico
Environment Department

Aaron Beckworth
New Mexico
Environment Department

Megan Begay
New Mexico
Highlands University

Leiloni Begaye
First Nations
Development Institute

Kimberly Beisner
U.S. Geological Survey

Rebecca Best
Northern Arizona University

Trevor Birt
New Mexico Interstate
Stream Commission

Becky Bixby
The University of New Mexico

Andrew Black
New Mexico Water Resources
Research Institute

Johanna Blake
U.S. Geological Survey

Andy Bleckinger
San Juan Soil & Water
Conservation District

Ryan Blickem
New Mexico Department
of Agriculture

Daniel Bloedel
Natural Resources
Conservation Service

Christi Bode
Media

Brittany Bolinger
Davis & Elkins College

Talia Boyd
Grand Canyon Trust

Kenneth Boykin
New Mexico State University

Kevin Boyko
New Mexico Water Resources
Research Institute

Klemens Branner
Venture Snowboards

Holly Brause
New Mexico Water Resources
Research Institute

Jeb Brown
U.S. Geological Survey

Henry Bulloch
San Juan Watershed Group

Longino Bustillos
U.S. Department of Agriculture

Brigette Buynak
Brigette C Buynak

Victor Cassela
OTT hydroMet

Sean Chambers
Chambers Econ & Analytics

Patrick Chavez
New Mexico State University

Elaine Chick
Water Information Program

Carmenlita Chief
Northern Arizona University

Karletta Chief
Univeristy of Arizona

Pauletta Chief-Lee
Homemaker

Becky Clausen
Fort Lewis College

Sandra Connors

Lily Conrad
New Mexico Water Resources
Research Institute

Robert Cook
U.S. Environmental Protection
Agency Region 6

Colleen Cooley

Barbara Cooney
New Mexico
Environment Department

Suzanne Copping
Bureau of Land Management

Linda Corwin

Charlotte Craig
Alternative Resources, Inc.

Bryan Crawford-Garrett
Thornburg Foundation

Livia Crowley
U.S. Forest Service

Cal Curley
U.S. Senator Tom Udall

Theresa Davis
Albuquerque Journal

Kato Dee
University of Oklahoma
School of Geosciences

Raeleen DeGroat
Navajo Agricultural
Products Industry

Dave DeWalt
National Agricultural
Statistics Service

Patricia Dominguez
U.S. Senator Martin Heinrich

Mereda Doss
City National Bank

Henry Drake
Native Plant Society
of New Mexico

John Draper
Draper & Draper LLC

Jim Dumont
U.S. Senator Martin Heinrich

Diana Duran
Ysleta Middle School & TMN

Anthony Edwards
San Juan County Colorado

James Evangelisti
Southern Ute Tribe

MaryBeth Ewing
New Mexico Water Resources
Research Institute

Tamara Faust
Bureau of Land Management

Christina Ferguson
U.S. Geological Survey

Sam Fernald
New Mexico Water Resources
Research Institute

Elena Fernandez
Amigos Bravos

Joanne Ferrary
State Legislature

William Fetner
New Mexico Office of Natural
Resources Trustee

Jennifer Foote
New Mexico
Environment Department

Brandon Francis
New Mexico State University
Agricultural Science Center
at Farmington

Jennifer Fullam
State of New Mexico

Michelle Furi
Mountain Studies Institute

Ana Cristina Garcia Vasquez
New Mexico Water Resources
Research Institute

Joy Garratt
New Mexico State Legislature

Marcus Gay
New Mexico Water Resources
Research Institute

Marcel Gaztambide
San Juan Citizens Alliance

Emily Geery
Independent Contractor

Tiana Gibson
New Mexico Water Resources
Research Institute

Raul Gil
New Mexico Water Resources
Research Institute

Carolyn Gillette
Eastern Research Group, Inc.

Molly Givens
New Mexico Water Resources
Research Institute

Steve Glass
Ciudad Soil and Water
Conservation District

Katie Goetz
New Mexico Department
of Agriculture

Natalie Goldberg
New Mexico State University

Robert Gomez
New Mexico
Highlands University

Judy Graham
Chamber

Erin Gray
U.S. Geological Survey

Tylee Griego
The University of New Mexico

Austin Griggs
New Mexico
Highlands University

Hannah Grover
The Daily Times

Ralph Gruebel
New Mexico Office of Natural
Resources Trustee

Daniel Guevara
New Mexico
Environment Department

Lynette Guevara
Surface Water Quality Bureau

Jessica Gutierrez
New Mexico
Environment Department

Lisa Hale-BlueEyes
City of Farmington

Jennifer Hart
Industrial Economics, Inc.

Maggie Hart Stebbins
New Mexico Office of Natural
Resources Trustee

Hannah Hartley
U.S. Geological Survey Utah
Water Science Center

Terra Harvey
Diné College

Lionel Haskie
Navajo Agricultural
Products Industry

Maddy Hayden
New Mexico
Environment Department

Heidi Henderson
New Mexico
Environment Department

Max Henkels
New Mexico Department
of Agriculture

Dave Herrell

Mike Hightower
New Mexico Produced Water
Research Consortium

Stephanie Hinds
Souder, Miller & Associates

Dalene Hodnett
New Mexico Farm
and Livestock Bureau

Wade Holdeman
Fort Sumner Irrigation District

Susan Holdsworth
U.S. Environmental
Protection Agency

Andrew Homer
Kelley Drye & Warren LLP

Xiaobo Hou
University of Arizona

Donna House
Consultant

Natalie Houston
U.S. Geological Survey

Scott Hynek
U.S. Geological Survey Utah
Water Science Center

Tanya Ishikawa
Uncompahgre Watershed
Partnership

Hazel James-Tohe
San Juan Collaborative
for Health Equity

Rachel Jankowitz
New Mexico
Environment Department

Gaurav Jha
New Mexico State University

Forrest John
U.S. Environmental
Protection Agency

Jason John
Navajo Nation

Teri John
Teacher

Tricia Johnson
INTERA Inc

Jessica Johnston

Michaela Jones
The University of New Mexico

Robert Kasuboski
Center of Excellence

Will Keener

Ronald Kellermueller
New Mexico Department
of Game and Fish

Amanda Kuenzi
Mountain Studies Institute

Nonabah Lane
Navajo Ethno-Agriculture

Gloria Lane

Saeed Langarudi
New Mexico State University

Chambliss Lantana
U.S Department of Agriculture

Colin Larrick
Ute Mountain Ute Tribe

Joslynn Lee
Fort Lewis College

John Leeper
Wood Environment
and Infrastructure

Gloria Lehmer
River Reach Foundation

Teal Lehto
Cottonwood Consulting

Shelly Lemon
New Mexico
Environment Department

Christopher Lewis
Industrial Economics, Inc.

Robert Lewis
New Mexico
Highlands University

William Linderfelt
INTERA, Inc.

Jennifer Lindline
New Mexico
Highlands University

Leslee Lohrenz
National Agricultural
Statistics Service

Kevin Lombard
New Mexico State University
Agricultural Science Center
at Farmington

Thomas Lowry
Sandia National Laboratories

Carol Lydic
U.S. Geological Survey

Theresa Macias

Ethan Mamer
New Mexico Bureau
of Geology

Quantina Martine
Audubon New Mexico

Marcella Martinez
Bureau of Land Management

Ahmed Mashaly
New Mexico Water Resources
Research Institute

Art Mason
Retired

Annie Maxfield
New Mexico
Environment Department

Connie Maxwell
New Mexico Water Resources
Research Institute

Sabrina Maxwell
Department of Defense
Education Activity

Melissa May
San Juan Soil & Water
Conservation District

Rebecca McCarthy
Voice of Witness

Carlee McClellan
Navajo Nation Water
Management Branch

Teresa McDill
New Mexico
Environment Department

Dylan McDonald
New Mexico State
University Library

Peter McKay
San Juan County

Virginia McLemore
New Mexico Tech

Elizabeth McNally
Animas Environmental
Services LLC

Dennis McQuillan
New Mexico
Environment Department

Karen Menetrey
New Mexico
Environment Department

Wayne Mietty
Riverside Nature Center

Carolina Mijares
New Mexico Water Resources
Research Institute

Emma Millar
Cottonwood Consulting LLC

Amy Miller

Stephen Monroe

Paul Montoia
City of Farmington

Tammy Montoya
Pueblo of Santa Ana

Miguel Montoya
New Mexico
Environment Department

Teresa Montoya
University of Chicago

Laurel Morales
KJZZ

Terry Morris
Bonita Peak Mining District
Community Advisory Group

Lalitha Muthu Subramanian
New Mexico Water Resources
Research Institute

Emily Newberry

Talon Newton
New Mexico Tech

Christina Noftsker
New Mexico Interstate
Stream Commission

Norman Norvelle
Retired Citizen

Liam O'Fallon
National Institute of
Environmental Health Sciences

James Ohlman
Peabody Western
Coal Company

Christine Osborne
Utah Department of
Environmental Quality

Elva Osterreich
Las Cruces Bulletin

Ashley Page
New Mexico Water Resources
Research Institute

Carole Palmer
Community Outreach
Patient Empowerment

Lucy Parham
Utah Department
of Environmental Quality

Laura Paskus
New Mexico PBS

Kevin Perez
New Mexico Water Resources
Research Institute

Patrick Pfaltzgraff
Colorado Water Quality
Control Division

Samantha Phillips
Sage & Lila Company

Emily Pieroni

John Pijawka
New Mexico
Environment Department

Sabrina Poessl
England Water Conservation

Jerri Pohl
New Mexico Office
of the State Engineer

Stanley Pollack
Navajo Nation

Cheyenne Poyer
New Mexico Water Resources
Research Institute

Jorge Preciado
New Mexico Water Resources
Research Institute

Arielle Quintana
Quivira Coalition

Greta Quintana

Kristen Rakes
Kyrene School District

Matt Ramey
Center of Excellence

Jalal Rastegary
New Mexico State University

Alex Ratcliff
Southern Ute Indian Tribe

Leslie Rauscher
U.S. Environmental Protection
Agency Region 6

Shera Reems
U.S. Environmental
Protection Agency

David Reese
Animas Environmental
Services

April Reese
Freelance journalist

Brad Reid
New Mexico
Environment Department

Nadji Remer
Samaritan's Purse

Suzanne Rice
New Mexico
Highlands University

Gigi Richard
Fort Lewis College

Alyssa Richmond
San Juan Soil & Water
Conservation District

Angela Roberson
Dona Ana County

Scott Roberts
Mountain Studies Institute

Rusty Rodke
Santa Fe Community College

Carmen Rodriguez
Carmen Cares Consulting

Edicia Rodriguez

Shannon Romeling

Amigos Bravos

Casey Root

Utah Water Science Center

Bob SabieNew Mexico Water Resources
Research Institute**Rossana Sallenave**

New Mexico State University

Kaitlin Sandoval

High Water Mark, LLC

Joe SavageNew Mexico
Environment Department**Emile Sawyer**New Mexico
Environment Department**Ryan Schmidt**

Center of Excellence

Andrew Schuler

The University of New Mexico

Leigh Sellari

U.S. Department of Agriculture

Kenneth Sexton

University of North Carolina

Erin SheaNew Mexico
Environment Department**Mark Sheely**New Mexico Water Resources
Research Institute**Tami Sheldon**

Department of the Interior

Zach Shephard

U.S. Geological Survey

Kyle Siesser

Cottonwood Consulting LLC

Duncan Sill**Benjamin Simon**

George Washington University

Neilroy Singer

Dine College

Toni Sitta

City of Farmington

Buck Skillen

Animas Watershed Partnership

Sue SmallValencia Soil & Water
Conservation District**Adam Stack**

Industrial Economics, Inc

Laila SturgisNew Mexico Bureau
of Geology**Whitney Thomas**

Bureau of Land Management

Catherine Thomas-Kemp

Studio Jeweler

Monica Tilden

Bureau of Land Management

Stacy TimmonsNew Mexico Bureau
of Geology**John Tole**

Evergreen Systems

Judy ToleRappahannock Historical
Society**Jeanette Torres**New Mexico Water Resources
Research Institute**Sara Torres**New Mexico Water Resources
Research Institute**Rebecca Travis**U.S. Geological Survey
New Mexico Water
Science Center**Crystal Tulley-Cordova**

Navajo Nation

William Turner

WaterBank

Thomas Turner

The University of New Mexico

April Ulery

New Mexico State University

Joseph ValdezRural Community
Assistance Corporation**Daniel Valenta**New Mexico
Environment Department**Forrest Vaughan**

Southern Ute Indian Tribe

Rachel Vaughn

Southern Ute Indian Tribe

Miguel Vigil

Taos Pueblo

Katie Walton-Day

U.S. Geological Survey

Jingjing Wang

The University of New Mexico

Youzhi Wang

New Mexico State University

William Weaver

New Mexico State University

Greg WeilerU.S. Environmental
Protection Agency**Michael Whiting**

New Mexico State University

Greg Wichelns
Culpeper Soil & Water
Conservation District, Virginia

MeLissa Wientjes
Bureau of Land Management

Shawn Williams
New Mexico Office
of the State Engineer

Elzbieta Wisniewski
The University of Arizona

Barbara Witmore
Bureau of Land Management

Charles Wohlenberg
Retired State Engineer Office

Emily Wolf
National Parks
Conservation Association

E. Nikki Woodward
Pueblo of Laguna

Samantha Wright
Independent Journalist

Juchao Yan
Eastern New Mexico Uni-
versity

Letisha Yazzie
New Mexico State Engineers
Office

Duane Yazzie

Al Yazzie

Seraphine Yazzie
Navajo Nation

Kristine Yurdin
New Mexico
Environment Department

2022

Animas and San Juan Watersheds Conference

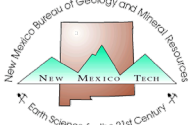
Collaborations, Perspectives, and Science Across the Watersheds

June 8–9, 2022

San Juan College Henderson Fine Arts Center & Online



Conference Planning Partners:







AGENDA

June 8, Morning Session

- 9:00 **WELCOMING REMARKS AND INTRODUCTION**
Paul Montoia, City of Farmington
Michele Truby-Tillen, San Juan County Community Development Director
- 9:20 **UPDATE ON BONITA PEAK MINING DISTRICT ACTIVITIES (ABSTRACT 10)**
Peter Butler, Bonita Peak Mining District Community Advisory Group
- 9:50 **S. 3571 – THE GOOD SAMARITAN REMEDIATION OF HARDROCK MINES ACT (ABSTRACT 18)**
Ty Churchwell, Trout Unlimited
- 10:20 **NEW MEXICO ENVIRONMENT DEPARTMENT RIVER STEWARDSHIP PROGRAM OVERVIEW**
Shelly Lemon, New Mexico Environment Department
- 10:40 **BREAK**
- 11:00 **THE SAN JUAN WATERSHED GROUP: A LEGACY OF MICROBIAL SOURCE TRACKING AND WATERSHED PLANNING IN THE SAN JUAN WATERSHED OF NEW MEXICO (ABSTRACT 3)**
Alyssa Richmond, San Juan Watershed Group
- 11:30 **THE ORIGIN AND DEVELOPMENT OF THE LEE HAMMOND DOMESTIC WATER SYSTEM (ABSTRACT 17)**
Carol Cloer, Secretary/Treasurer, Lee Hammond MDWCA
Aaron Lee, Director, Lee Hammond MDWCA
- 12:00 **LUNCHEON WITH KEYNOTE PRESENTATION: “JUST ADD WATER!!!”**
Aaron Chavez
 Executive Director, San Juan Water Commission
 President, Colorado River Water Users Association

June 8, Afternoon Session

- 1:30 **50-YEAR WATER PLAN + NEXT STEPS**
Sara Goldstein, New Mexico Interstate Stream Commission
- 2:00 **STREAM MANAGEMENT PLANNING IN THE ANIMAS BASIN – SCOPING (ABSTRACT 5)**
Warren Rider, Animas Watershed Partnership

- 2:30 **MAPPING THE GLOBAL-TO-LOCAL FOOD-ENERGY-WATER SUPPLY CHAINS OF THE FOUR CORNERS AREA (ABSTRACT 8)**
Richard Rushforth, Northern Arizona University
- 3:00 **MAIZE GROWTH, YIELD, YIELD COMPONENTS, AND WATER PRODUCTIVITY AS AFFECTED BY PLANTING DATE AND PLANT DENSITY (ABSTRACT 2)**
Koffi Djaman, NMSU Agricultural Science Center at Farmington
- 3:30 **SOIL MOISTURE SENSORS FOR IMPROVING IRRIGATION MANAGEMENT IN THE COMMERCIAL POTATO FIELDS: SOIL WATER DYNAMICS, EFFECTIVE ROOT ZONE, AND CROP EVAPOTRANSPIRATION (ABSTRACT 1)**
Koffi Djaman, NMSU Agricultural Science Center at Farmington
- 4:00 **POSTER SESSION AND RECEPTION**
- POSTER PRESENTATIONS:**
- NMSU GROWING FORWARD FARM PROJECT (ABSTRACT 4)**
Bonnie Hopkins, NMSU San Juan County Cooperative Extension
- DEVELOPMENT OF AN HSPF MODEL TO ASSESS EFFECT OF LAND USE SCENARIOS ON NUTRIENT LOADING IN THE ANIMAS RIVER WATERSHED (ABSTRACT 6)**
Zach Shephard, U.S. Geological Survey
- MAPPING THE GLOBAL-TO-LOCAL FOOD-ENERGY-WATER SUPPLY CHAINS OF THE FOUR CORNERS AREA (ABSTRACT 8)**
Richard Rushforth, Northern Arizona University
- ASSESSING RISK TO WATER RESOURCES FROM OIL AND GAS ACTIVITIES IN THE SAN JUAN BASIN (ABSTRACT 9)**
Thomas Lowry, Sandia National Laboratories
- SEM ANALYSIS OF EPHEMERAL TRIBUTARY SEDIMENTS IN THE FOUR CORNERS REGION, USA (ABSTRACT 11)**
Rachel L. Mixon, U.S. Geological Survey
- 5:00 **ADJOURN DAY 1**

June 9, Morning Session

- 9:00 **COMPARISON OF SEDIMENT CHEMISTRY DATA COLLECTED FROM THREE RESERVOIRS IN THE ANIMAS AND SAN JUAN WATERSHEDS (ABSTRACT 14)**
Christina Ferguson, U.S. Geological Survey
- 9:30 **COMPILATION OF THE LEE ACRES-GIANT BLOOMFIELD REFINERY DATABASE: PRELIMINARY RESULTS (ABSTRACT 13)**
Christina Ferguson, U.S. Geological Survey

- 10:00 HYDROACOUSTIC–TURBIDITY SURROGATE MEASUREMENTS FOR METALS AND SUSPENDED–SEDIMENT CONCENTRATION IN THE ANIMAS RIVER NEAR CEDAR HILL, NEW MEXICO (ABSTRACT 15)
Jeb Brown, U.S. Geological Survey
- 10:30 BREAK
- 11:00 INVESTIGATIONS OF THE SOURCES OF METALS TO THE SAN JUAN RIVER (ABSTRACT 12)
Johanna Blake, U.S. Geological Survey
Steve Austin, Navajo Nation Environmental Protection Agency
- 11:30 IMAGERY DERIVED FROM SMALL UNCREWED–AERIAL SYSTEMS USED FOR STAGE–DISCHARGE MODELING OF EPHEMERAL CHANNELS ALONG THE SAN JUAN RIVER NEAR THE FOUR CORNERS REGION OF THE SOUTHWESTERN UNITED STATES (ABSTRACT 16)
Jeb Brown, U.S. Geological Survey
- 12:00 LUNCHEON

June 9, Afternoon session

- 1:15 CLIMATE OUTLOOK OF THE SAN JUAN BASIN
Dave DuBois, New Mexico State Climatologist
- 1:45 U.S. BUREAU OF RECLAMATION, NAVAJO UNIT OPERATIONS
Susan Behery, U.S. Bureau of Reclamation
- 2:15 BREAK
- 2:30 MULTIJURISDICTIONAL EFFORTS USING WIIN ACT APPROPRIATIONS IN THE SAN JUAN WATERSHED
Shelly Lemon, New Mexico Environment Department
Lucy Parham, Utah Department of Environmental Quality
- 3:00 NM OFFICE OF THE NATURAL RESOURCES TRUSTEE DEVELOPMENT OF A NATURAL RESOURCE RESTORATION PLAN FOR INJURIES FOLLOWING THE 2015 GOLD KING MINE RELEASE INTO THE ANIMAS AND SAN JUAN RIVERS
Maggie Hart Stebbins, New Mexico Office of the Natural Resources Trustee
- 3:30 CLOSING REMARKS
- 3:40 ADJOURN CONFERENCE

2022 CONFERENCE PLANNING COMMITTEE MEMBERS

Steve Austin Navajo Nation EPA

Melissa Benfer US EPA, Region 6

Johanna Blake US Geological Survey

Carol Cloer Lee Hammond Water Users Cooperative
Association

Robert Cook US EPA, Region 6

Anthony Edwards Bonita Peak Mining District CAG

Sam Fernald NM WRRRI Director

Shelly Lemon New Mexico Environment Department

Kevin Lombard New Mexico State University

Yessenia Lugo-Homs US EPA, Region 6

Melissa May San Juan Soil and Water Conservation District

Carolina Mijares NM WRRRI Program Manager

Paul Montoia City of Farmington

Talon Newton NM Bureau of Geology & Mineral Resources

Shera Reems US EPA, Region 6

Alyssa Richmond San Juan Watershed Group

Mark Sheely NM WRRRI Program Specialist

Jeanette Torres NM WRRRI Program Coordinator

ADDITIONAL 2022 CONFERENCE PARTNERS

PRE-CONFERENCE SHIPROCK SUSTAINABILITY FAIR



POST-CONFERENCE FIELD TRIPS



2022 Abstracts

(#7 *withdrawn*)

Soil Moisture Sensors for Improving Irrigation Management in the Commercial Potato fields: Soil Water Dynamics, Effective Root Zone, and Crop Evapotranspiration

Koffi Djaman

kdjaman@nmsu.edu

Department of Plant and Environmental Sciences, New Mexico State University,
Agricultural Science Center at Farmington, P.O. Box 1018, Farmington, NM 87499, USA

Abstract 1 – Oral

Potato (*Solanum tuberosum*) is a very sensitive crop to water stress and timely irrigation water management improves tuber yield and quality. The objectives of this study were to (1) investigate soil water dynamics under potato crops across their root zone and (2) estimate potato crop evapotranspiration (ETa) under sprinkler irrigation on the sandy loam soil. The field experiment was conducted during the 2018 and 2019 growing seasons at the Navajo Farms within the Navajo Agricultural Products Industry, Farmington, NM. Two irrigation scheduling methods were evaluated as FAO-56 approach evapotranspiration-based scheduling and soil moisture sensing irrigation scheduling. Sentek capacitance soil moisture probe was used across four commercial potato fields in each year after calibration to the soil texture just after installation. Crop Evapotranspiration values estimated by the water balance method and the two-step approach were compared to the satellite-based models used in OpenET. The results showed that the potato's effective rooting zone is the upper 40 cm soil layer. Potato plants extracted more than 50% of total water from the upper 15 cm of the soil profile. Non-significant water was extracted from the 40-60 cm soil water. Potato crop seasonal evapotranspiration averaged 580 to 645 mm in 2018 and 2019, respectively. The Two-step approach ETa 795.5 and 832.7 mm in 2018 and 2019, respectively, and were higher than the soil water balance estimated ETa. The satellite modeled ETa varied with field and years and ranged from 437 to 7625.28 mm in 2018 and from 484.07 and 617.09 mm in 2019 and averaged 572.96 and 590.01 mm in 2018 and 2019, respectively. Soil moisture probe-based irrigation scheduling improved irrigation water management and the irrigation water use of potatoes in the semiarid climate.

Maize Growth, Yield, Yield Components, and Water Productivity as Affected by Planting Date and Plant Density

Koffi Djaman

kdjaman@nmsu.edu

Department of Plant and Environmental Sciences, New Mexico State University,
Agricultural Science Center at Farmington, P.O. Box 1018, Farmington, NM 87499, USA

Abstract 2 – Oral

Weather conditions in the southwestern United States are variable and influence crop growing periods with late spring and early fall frosts which significantly impact cropping seasons. With the development of new maize hybrids, grain yield, evapotranspiration, and water use efficiency can be substantially impacted by planting density and planting date. Thus, the optimum plant density and planting date for maximum grain yield must be determined for local conditions. Field experiments were conducted at NMSU Agricultural Science Center in Farmington to evaluate six plant densities (54,700; 64,600; 74,600, 88,000; 101,700; and 120,100 pph) under seven planting dates (from April 23 to June 5 in 2019 and from April 21 to June 10 in 2020) to determine the planting window and the optimum density. Plots were sprinkler irrigated and crop management was similar across all planting dates during the two growing seasons. The results showed that crop height and leaf area index varied with plant density and planting date. Grain yield also varied with plant density and planting date. The highest grain yield (16.8 Mg ha⁻¹) was observed under the density 101,700 pph which showed statistically similar yield as the density 88,000 pph and the first planting trended to provide the best grain yield in 2019. In 2020, the highest grain yield (17.77 Mg ha⁻¹) was obtained under the density 88,000 pph on May 18 planting date. Plant density 88,000 pph was revealed as the optimum density that maximized grain yield and WUE and maize planting after May 25 is not recommended.

The San Juan Watershed Group: A Legacy of Microbial Source Tracking and Watershed Planning in the San Juan Watershed of New Mexico

Alyssa Richmond
alyssa.richmond@sanjuanswcd.com
San Juan Watershed Group Coordinator

Abstract 3 – Oral

Bacteria pollution has been an ongoing concern within the San Juan Watershed and poses human health risks for communities along the San Juan River and its tributaries. The stretch of the San Juan River from the Navajo Nation Boundary at the Hogback to the Animas River Confluence has been on the New Mexico Environment Department (NMED) Surface Water Quality Bureau (SWQB) 303(d) Impairment list for E.coli since 2005, with the stretch of the San Juan River from the confluence of the Animas River to the confluence of Canon Largo listed as impaired for E.coli since 2006.

Building from water quality sampling, initial watershed planning efforts, and pilot best management project implementation in the year 2000's, the San Juan Watershed Group (SJWG) worked with NMED SWQB through Clean Water Act funding to conduct a microbial source tracking (MST) study in 2013-2014 with the goal of identifying fecal bacteria hosts at 5 sites in the Animas and San Juan Rivers. The study found that 46% of San Juan River E.coli samples exceeded the single sample standard for primary contact (ie: swimming). This study also tested for presence/absence of various source categories of bacteria and found that 94% of samples tested positive for human source bacteria and 90% positive for ruminant source bacteria. The majority (79%) of all samples were quantifiable for human source bacteria and were analyzed for magnitude of concentrations, revealing a seven-fold increase in human source bacteria between Farmington and the Hogback. While ruminant source bacteria was expected due to livestock production in the river corridor (cattle, sheep) and the presence of wildlife (deer, elk), the near-constant presence of human sewage in the river was unexpected and alarming. Potential sources of human fecal bacteria, including failing or improperly installed septic systems, illegal dumping of septage waste, leaking sewer infrastructure, legal (permitted) discharges from wastewater treatment facilities, and/or outdoor defecation were summarized in the Lower Animas Watershed Based Plan.

While the 2013-2014 MST study provided a baseline for determining the presence of human fecal bacteria, the specific nonpoint sources of human bacteria and the impact on point contributions from wastewater treatment plants to the San Juan River system remained mostly unknown. To work towards filling this data gap, the SJWG partnered with NMED SWQB to conduct another MST study specifically for human source bacteria in 2021 with the alternative sampling design: a higher sampling location density and less sampling frequency. Preliminary data indicates an overall improvement in human source bacteria quantities since 2014, but considerable work is still needed to reduce human bacteria in our rivers. This data is essential to further characterize sources of human bacteria pollution, identify opportunities to reduce bacteria pollution from human sources, inform collaborative efforts to mitigate these contributions, and guide future microbial source tracking efforts in the Middle San Juan restoration planning process.

NMSU Growing Forward Farm Project

Bonnie Hopkins¹, Andrew Foster²

bhopkins@nmsu.edu¹

foster@nmsu.edu²

NMSU San Juan County Cooperative Extension

Abstract 4 – Poster

Growing Forward Farm is a collaborative project between the San Juan County Government and the New Mexico State University Cooperative Extension Service to develop vacant land within the Government complex into an agricultural training center. The Extension office and its partners seek to put the principles of the Extension into practice and provide hands-on opportunities for the community.

Growing Forward Farm aims to become the central location for all things agriculture and become a source hub for all ages of our community. The property will be used to serve the diversity of populations of our community, and will actively seek out new ways to incorporate new programs that address current and emerging issues facing our agricultural community. Having hands-on opportunities for our fellow youth, gardeners, and farmers and ranchers will be an invaluable opportunity that will directly contribute to the vitality of our local economy by strengthening our local food system and education.

Growing Forward Farm began as a fallow field, overwhelmed with noxious weeds, prairie dogs and bare soil. The program staff, community partners and agencies have worked diligently to bring the land back to life to create an outdoor educational facility for the community of San Juan County.

Stream Management Planning in the Animas Basin - Scoping

Warren Rider
warren@riderwater.com
Animas Watershed Partnership

Abstract 5 – Oral

The Animas Watershed Partnership is in the very beginning phases of the development of a Stream Management Plan for the Animas Basin. Stream Management Plans are being promoted by the State of Colorado to better understand what rivers and streams need from both a recreational and environmental standpoint. Plans have varied across the State from small, reach specific plans to large plans covering entire basins.

The Animas Watershed Partnership has secured funding to begin a SMP process for the Animas River. The eventual Scale of the plan has not been established at this time. The Animas Watershed Partnership has chosen to begin their SMP process with a scoping phase to gather feedback from stakeholders within the basin to determine the appropriate scope for the SMP. This Phase I of the planning process seeks to gather feedback from basin stakeholders, develop a SMP steering committee, and generate enthusiasm for the planning process to be carried out in subsequent phases.

The Animas Watershed Partnership will benefit from the experience of prior planning processes across Colorado and past water resource investigations in the Animas Basin. This community led scoping process will help AWP and the stakeholders settle on a scope that is appropriate for our basin at this time.

Development of an HSPF Model To Assess Effect of Land Use Scenarios on Nutrient Loading in the Animas River Watershed

Zach Shephard¹, Benjamin Linhoffm², Erin Gray³

zshephard@usgs.gov¹

blinhoff@usgs.gov²

egray@usgs.gov³

U.S. Geological Survey

Abstract 6 – Poster

Nutrient loading and eutrophication are of current (2022) concern to stakeholders in the Animas River Watershed following large algal blooms in the Animas River in 2002. The New Mexico Environment Department's Surface Water Quality Bureau has identified the Animas River as an impaired waterbody pursuant to the Clean Water Act because of exceedances in water quality standards of total phosphorus, nutrients, turbidity, temperature, and *Escherichia coli*. Many factors influence the relation between land use and nutrient loading in surface water, including soil type, crop type, weather, crop yields, groundwater inputs, and land management practices. This poster presents the early stages and development of a Hydrologic Simulation Program Fortran (HSPF) model to characterize nutrient loading and assess land use scenarios in the Animas River Watershed. Model development is part of a larger study to geochemically characterize and estimate nutrient sources that contribute to eutrophication on the Animas and Florida Rivers. The modeling approach includes tabulating and collecting physical watershed data and water quality calibration data, initial model setup, calibrating and validating the model performance, and potential development and execution of land use, climate, and other potential scenarios. The addition of a watershed nutrient model, together with the collection of geochemical data will further understanding of the relation between local land use and observed nutrient loading throughout the Animas River Watershed. Simulation of potential land use changes will support assessment of the overall effectiveness of a change before it is implemented.

Mapping the Global-to-Local Food-Energy-Water Supply Chains of the Four Corners Area

Richard Rushforth¹, Jessica Archibald², Stephanie Deyo³, Anona Miller⁴,
Darren Bingham⁵, Sean M. Ryan⁶

Richard.Rushforth@nau.edu¹

la396@nau.edu²

Stephanie.Deyo@nau.edu³

anonamiller@gmail.com⁴

drb386@nau.edu⁵

Sean.Ryan@nau.edu⁶

Northern Arizona University

Abstract 8 – Oral and Poster

Local business leaders, policymakers, elected officials, city planners, emergency managers, and private citizens are responsible for, and deeply affected by, the performance of lifeline supply chains and related infrastructures. The food-energy-water system (FEW) is at the center of lifeline supply chains, which are vital to a community's well-being, resilience, and sustainability. In the 21st century, managing local FEW systems requires accurate data describing the function and structure of a community's supply chains. However, data is not enough; we need data-informed conversation and technical and political capacity building among local stakeholders to utilize the data effectively. While some regional FEW system data are available for most communities, many communities lack detailed data about their global-to-local FEW system connections, which connect their local community to the global economy. For this study, we developed a first-of-its-kind global-to-local FEW system dataset for the Four Corners region to enable participatory community planning and to study FEW system supply chains in rural and remote locations. Our study utilized multiple data sources and collection methods to build the global-to-local dataset. First, we gathered data from the NSF-funded FEWSION Project (<http://www.fewsion.us>) to characterize regional FEW supply chains. Next, we gathered local FEW system supply chain data using the FEWSION for Community Resilience (F4R) process (<http://fewsion.us/f4r>). Finally, we merged these two datasets using a multilayer network approach to build the comprehensive global-to-local dataset. This study aims to develop a comprehensive global-to-local dataset for the Four Corners region to enable data-driven insights about the social network that manages FEW system resources and systems-level resilience and vulnerability.

Assessing Risk to Water Resources from Oil and Gas Activities in the San Juan Basin

Thomas Lowry¹, Whitney Thomas², Owen Lofton³, Patricia Johnson⁴, Lynn Acosta⁵,
Orlando Reyna⁶, Mike Farinacci⁷, Keith Sauter

tslowry@sandia.gov¹

owlofto@sandia.gov³

orreyna@sandia.gov⁶

Sandia National laboratories

l1thomas@blm.gov²

Keith Sauter

Bureau of Land Management

Lynn.Acosta@respec.com⁵

Respec

pjohnson@intera.com⁴

MFarinacci@intera.com⁷

Intera

Abstract 9 – Poster

Rules governing the regulation and management of hydraulic fracturing on Federal and Indian lands for oil and gas extraction were established in 1982 and later updated in 1988 [BLM, 1997]. Since that time, advancements in drilling and well completion technologies have resulted in an exponential growth in the use of directional drilling (horizontal wells) and hydraulic fracturing. A study of the 'Reasonable Foreseeable Development' (RFD) for Northern New Mexico [Engler et al., 2014] identifies a 200,500-acre high potential region for future oil drilling that could be home to an estimated 1600 additional completions. For gas drilling, Engler et al. [2014] states a conservative estimate of 2000 additional gas wells as the 'economics become favorable' (i.e., the price for gas \geq \$4.25/mmbtu). Common to all these additional wells is the use of horizontal well technologies and a demand for water to complete hydraulic fracturing, which is estimated to be ~3.13 af/well [Engler et al., 2014] (Figure 1). Methods for reducing water use for hydraulic fracturing, such as the use of produced water or using hydraulic fracturing foam, are being implemented. However, there is also a trend to switch to slick water fracking, which will require 10x the water per well. Thus, there is concern as to the regions ability to meet the increasing water demand in a manner that protects human health and the environment while sustainably meeting the needs of the variety of water users in the region.

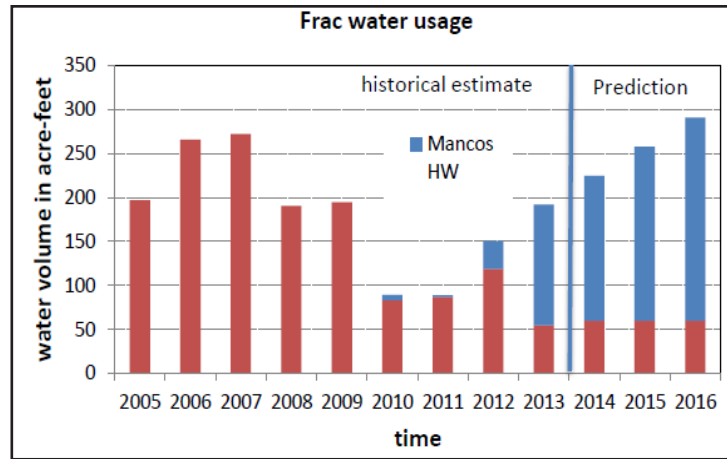


Figure 1. Frac water use by year for conventional (red bars) and horizontal well completions (blue bars) in the San Juan Basin. From Engler et al., 2014.

This poster is a progress update of a multi-disciplinary project to measure and catalogue the groundwater resources in the San Juan Basin to identify the risk to water quantity and quality and to establish a baseline to better detect changing water conditions over time. The project combines activities in data collection, field data verification, field testing, and GIS analysis with the goal of producing insight and understanding that is beyond what can be produced if the activities were executed individually. The objective of the field work is to identify and catalogue the location, water production capacity, source formation, depth to groundwater, etc. of a representative subset of the numerous water wells in the region (Figure 2).

Field work began in the summer of 2019 but were put on hold in 2020 due to COVID. They resumed again in 2021 and have involved 5 efforts over the last year. To date we have been able to sample 32 wells, get depth to water measurements in 30 wells, and have instrumented 4 wells for long-term monitoring.

This poster provides provide an update to the work to date, describing the field efforts, data collected, and balance of work remaining.

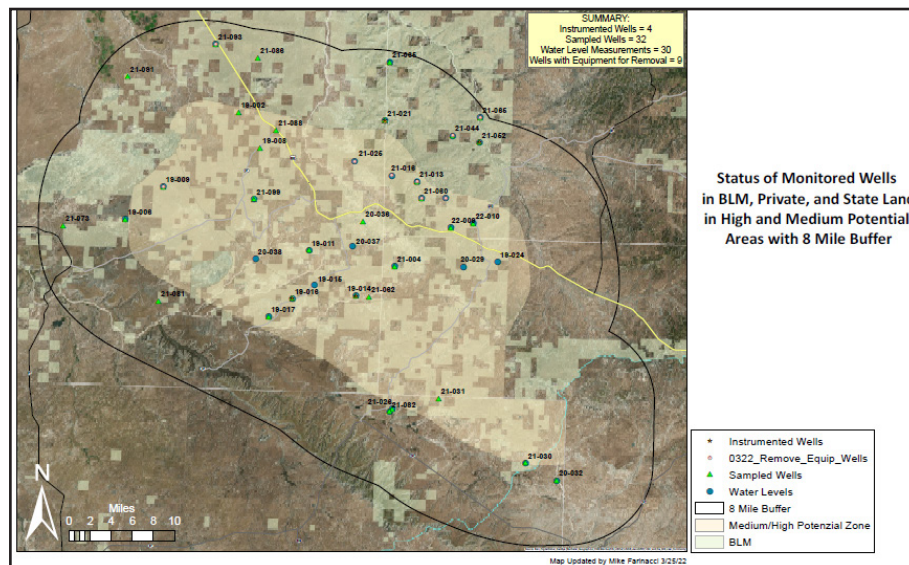


Figure 2. Surveyed water wells in the San Juan Basin area underlaid by land ownership. Well status is indicated by the shape and color of the well symbol.

Update on Bonita Peak Mining District Activities

Peter Butler
butlerpeter2@gmail.com
Bonita Peak Community Advisory Group

Abstract 10 – Oral

Mine remediation to improve water quality has been ongoing for thirty years in the Silverton Caldera. Over the last six years, that work has occurred under the Superfund designation of the Bonita Peak Mining District. The presentation will provide an overview of recent activities in the Caldera including data collection, remediation efforts, proposed water quality standards, and liability settlements.

REFERENCES

Engler T.W., S. Kelley, and M. Cather, 2014, Reasonable Foreseeable Development (RFD) for Northern New Mexico, Final Report submitted to Bureau of Land Management Farmington Field Office, October, 38p

SEM Analysis of Ephemeral Tributary Sediments in the Four Corners Region, USA

Rachel L. Mixon¹, Johanna M. Blake², Jeb E. Brown³, Shaleene B. Chavarria⁴,
Christina L. Ferguson⁵, Douglas B. Yager⁶

rlmixon@usgs.gov¹

jmtblake@usgs.gov²

jebbrown@usgs.gov³

schavar@usgs.gov⁴

cferguson@usgs.gov⁵

dyager@usgs.gov⁶

U.S. Geological Survey

Abstract 11 – Poster

The San Juan River is a vital source of water for drinking, irrigation, and recreation for the semi-arid Four Corners Region, much of which is within the Navajo Nation. Within the study area, from Navajo Dam, NM, to Mexican Hat, UT, there are numerous tributaries, most of which are ephemeral. Sediment contribution from tributaries reflect the watershed geochemistry and land use within the watershed. Some potential anthropogenic sources of metals in the watershed include oil drilling operations, abandoned uranium mines and mills, agricultural land, natural gas power plants, and illegal dumping of waste. In cooperation with the Navajo Nation Environmental Protection Agency (NNEPA), the U.S. Geological Survey (USGS) is working to determine which tributaries are contributing metals to the San Juan River, and in conjunction, the relative contributions from anthropogenic and natural sources. Twenty-one sediment samples from different tributaries, collected during an August 2021 precipitation event, were examined using a scanning electron microscope (SEM). Analysis of these tributary sediments was conducted primarily using backscatter electrons and energy dispersive X-ray spectroscopy. Preliminary mineralogy results show substantial amounts of iron oxide, ilmenite, monazite, pyrite, montmorillonite, and barite often with strontium substitution; these particles are small and often seen attached to, or lodged within, quartz, clays, or feldspar grains. Occurring less frequently, but worthy of note, are the metals copper, chromium, radium, and gold. Analysis and interpretation are ongoing.

Investigations of the Sources of Metals to the San Juan River

Johanna Blake¹, Steve Austin², Jeb Brown³, Fred Johnson⁴

jmtblake@usgs.gov¹
jebbrown@usgs.gov³
U.S. Geological Survey

nnepawq@frontier.net²
navajoh20@hotmail.com⁴
Navajo Nation Environmental Protection Agency

Abstract 12 – Oral

Metals attached to suspended sediments or dissolved in river water pose a potential health risk to communities that depend on that water for agricultural and domestic uses. Navajo Nation communities along the San Juan River are exposed to metals—especially lead and arsenic—that exceed Navajo Nation Environmental Protection Agency (NNEPA) surface water quality standards. The Animas River is known to contribute high metal loads to the San Juan River from natural and mining sources surrounding its headwaters. In addition to the Animas River, there are other potential sources of metals to the San Juan River, including but not limited to, local geology, oil and gas development, and abandoned uranium mines, that may enter the San Juan River from predominantly ephemeral tributaries during storm events. The U.S. Geological Survey (USGS) is working with NNEPA to identify sources of these metals entering the San Juan River from tributaries in the study reach, which flows from Navajo Dam to Mexican Hat, Utah. The objective of this work is to identify the sources of metals and trace elements including arsenic, lead, uranium, and other inorganic contaminants released to the San Juan River, and to quantify the contributions from natural and anthropogenic sources. Understanding the contribution from each source can help the Navajo Nation take action, where possible, to improve San Juan River water quality and reduce the potential risk to human health and the environment. To investigate these sources, the USGS and NNEPA are collecting surface water and sediment samples from the San Juan River and its tributaries and quantifying maximum surface water discharge from selected tributaries. Preliminary geochemistry results from water and sediment will be presented.

Compilation of the Lee Acres-Giant Bloomfield Refinery Database: Preliminary results

Christina Ferguson¹, Erin Gray²

cferguson@usgs.gov¹

egrays@usgs.gov²

U.S. Geological Survey

Abstract 13 – Oral

The Lee Acres-Giant Bloomfield Refinery Database (LAGBRD) is a compilation of monitoring data that have been collected for over 30 years by several different agencies at the Lee Acres Landfill and the Giant Bloomfield Refinery near Farmington, New Mexico. This database was compiled in cooperation with the Bureau of Land Management, which operates the Lee Acres Landfill, in order to facilitate future studies into the characteristics of potential groundwater contamination and background geochemistry at the landfill and refinery sites. The database includes monitoring data beginning in 1985, when awareness was increasing regarding releases from liquid waste lagoons at the landfill and fuel releases at the refinery. Water quality and groundwater elevation data from 134 sampling locations at the landfill and the refinery are included in LAGBRD. Preliminary investigations using these data have shown changes in concentrations of manganese and chloride that seem to coincide with water balance calculations for the area. Driller's logs and well construction information gathered for the database have changed the aquifer classification for some of the wells, including the upgradient shallow alluvial well used to establish background concentrations of manganese, nickel, and volatile organic compounds. Groundwater elevation gradients will be used to elucidate the pattern of flow in the shallow alluvial, deep alluvial, and bedrock aquifers in which wells are completed. Information from this study will aid the Bureau of Land Management in any future remediation efforts needed at the Lee Acres Landfill.

Comparison of Sediment Chemistry Data Collected from Three Reservoirs in the Animas and San Juan Watersheds

Christina L. Ferguson¹, Johanna M. Blake, Jeb E. Brown

cferguson@usgs.gov¹

USGS-New Mexico Water Science Center
6700 Edith Blvd NE, Albuquerque, NM 87113

Abstract 14 – Oral

Drinking water reservoir sediments record the geochemical history of a watershed. Suspended sediments carried by the rivers that provide water to the reservoirs can affect water quality in the region, and part of the treatment of this water is allowing for settling of the suspended sediments. These reservoirs can also be susceptible to metals contamination from processes such as geochemical weathering, mining, milling, wildfires, or coal fired power plants. Before it enters the San Juan River, the Animas River drains a highly mineralized area. The geologic and anthropogenic history of the area result in dissolved metals in the water column and metals adsorbed to the sediment in the Animas River, which are then transported to and deposited in the reservoirs. To understand what constituents might exist within these deposits, cores of reservoir bed sediments were collected at three reservoirs: (1) Aztec Reservoir #1 (built in 1947) filled by the Animas River; (2) Farmington Lake (built in the early 1960s) also filled by the Animas River; and (3) the PNM-San Juan Generating Station raw-water reservoir (built in 1971) filled by the San Juan River. The sediment major ion chemistry (calcium, potassium, magnesium, sodium, aluminum, iron, and titanium) is similar in all three reservoirs, but trace element data vary. Aztec Reservoir #1 sediments have elevated concentrations of arsenic, uranium, vanadium, and copper at the bottom of the reservoir, which is likely from historic milling operations upstream in Durango, CO. Farmington Lake sediments do not show the same high concentration in metals, in part because this reservoir is younger than the Aztec Reservoir #1 and milling operations had ceased prior to the reservoir being built. In addition, Farmington Lake is larger than Aztec Reservoir #1 and does not have an impermeable layer at the base allowing for direct interaction with groundwater. Farmington Lake sediments do have notable patterns in manganese and sulfur. The PNM-San Juan Generating Station raw water reservoir also does not show the increase in arsenic, uranium, vanadium, and copper seen in Aztec Reservoir #1, but sediments do show elevated lead concentrations at some depths, which could be associated with the coal-fired power plant at this site. Because reservoirs can act as a repository whose sediments record the changing geochemical history of a region, results of this study provide valuable information to drinking water resource managers as well as an understanding of how actions like mining and development have altered the geochemical makeup of the Animas and San Juan Rivers.

Hydroacoustic-turbidity Surrogate Measurements for Metals and Suspended-sediment Concentration in the Animas River near Cedar Hill, New Mexico

Jeb Brown,¹ Johanna Blake, Grady Ball, Justin Nichols, Bryan Rezin

jebbrown@usgs.gov¹
U.S. Geological Survey

Abstract 15 – Oral

Metals attached to suspended sediments pose a potential health risk to communities that depend on water for domestic and agricultural uses. Metals and other constituents have been documented as preferentially sorbing to clay sized suspended sediments. Surrogate methods for estimating suspended-sediment concentration (such as turbidity, hydroacoustic, laser diffraction, and densimetric) have been widely published in the literature. Surrogate measurements provide near-real-time data which may inform daily operational changes by water managers. Temporally dense surrogate data (values collected every 15 minutes) can also increase the understanding of transport mechanisms of metals and suspended-sediment concentration. The objective of this work is to determine if a regression model can be developed through correlation of hydroacoustic-turbidity measurements with suspended-sediment concentration and concentrations of suspended metals such as aluminum, arsenic, and lead. If a reasonable regression model can be developed for suspended metals, near-real-time data will be displayed on USGS webpages. Preliminary hydroacoustic-turbidity, metals, and suspended sediment data will be presented.

Imagery Derived from Small Uncrewed-Aerial Systems Used for Stage-Discharge Modeling of Ephemeral Channels along the San Juan River near the Four Corners Region of the Southwestern United States

Jeb Brown¹, Johanna Blake², Grady Ball³, Zach Shephard⁴, Keely Miltenberger⁵

jebbrown@usgs.gov¹

jmtblake@usgs.gov²

gball@usgs.gov³

zshephard@usgs.gov⁴

kmiltenberger@usgs.gov⁵

U.S. Geological Survey

Abstract 16 – Oral

Streamflow data are required to calculate loads of constituents, such as metals. In locations, such as ephemeral channels, where direct measurements of streamflow are inconvenient or impossible to obtain, streamflow can be computed from stage information when paired with a stage-discharge rating. Digital terrain models can be used to model streamflow at various water depths, resulting in a model derived stage-discharge rating for specific stream locations. However, obtaining the terrain data necessary to develop a stage-discharge rating can be time intensive and cost prohibitive. Recent developments in photogrammetry, combined with low cost uncrewed-aerial systems (UAS), have created new approaches to generating high-fidelity terrain models using low-cost digital cameras deployed on small UAS. This approach is being used to quantify streamflow in approximately 35 ephemeral channels near the San Juan River from Navajo Dam to Mexican Hat. Preliminary results of these streamflow modelling efforts will be presented.

The Origin and Development of the Lee/Hammond Domestic Water System

Carol Cloer¹, Aaron Lee

ccloer@comcast.net¹

Secretary/Treasurer

Lee/Hammond Domestic Water System

Aaron Lee

Director

Lee/Hammond Domestic Water System

Abstract 17 – Oral

Starting a domestic water system can be challenging. Listen to a presentation on the origin and 52-year development of a system that started with 12 members and has grown to 3000-plus users. Political intrigue and sabotage created pitfalls that had to be overcome with dogged determination to succeed, and succeed they did. Dr. Cloer and Aaron Lee will offer how the original water system grew, built a water treatment plant, and merged with another system and look forward to the future where new obstacles will be overcome. In the process of the water system's creation, the value of land of its members greatly increased from \$474 an acre to more than \$20,000 an acre through the offering of clean, clear, water to drink.

S. 3571 – The Good Samaritan Remediation of Hardrock Mines Act of 2022

Ty Churchwell
ty.churchwell@tu.org
Mining Coordinator
Trout Unlimited - Durango, CO - 970-903-3010

Abstract 18 – Oral

The EPA estimates there are approximately a half a million abandoned mines in the U.S., and that 40% of headwater streams in the west are impacted by acid mine drainage from abandoned mines. This places over 110,000 miles of streams on the 303d list for impairments from acidity and metals. At present, it is only under a Superfund action can anyone – including the EPA – treat mine water from abandoned mines. Unfortunately, however, only the worst of the worst sites would ever qualify as a Superfund site. Case in point – there are approximately 160 draining mines in the upper Animas River basin, but only a relative few of those qualified for a Superfund cleanup at Bonita Peak Mining District (San Juan County, CO). This leaves roughly 120 abandoned, draining mines in the Animas basin, alone, with no means for anyone to clean them up.

Good Samaritan legislation endeavors to fix this legal conundrum and provide a mechanism by which well-qualified, non-responsible parties can take-on cleanup projects without running afoul of the Clean Water Act. These so-called ‘Good Sams’ include the state mine remediation agencies, watershed groups, NGOs and others.

In February of this year, Senators Martin Heinrich (D-NM) and Jim Risch (R-ID) introduced bipartisan S. 3571 to create a pilot program under EPA supervision to authorize voluntary cleanups at 15 low-risk abandoned sites anywhere in the country. Joining in co-sponsorship are twelve other western Senators, evenly split between Republicans and Democrats. These co-sponsors include both Colorado’s, Arizona’s and New Mexico’s Senators.

The Animas River has been the poster child for Good Sam for two decades. In the wake of the Gold King spill, a renewed and enthusiastic effort is underway in D.C. to finally resolve the issue of pollution from abandoned mines. Simply, Superfund is underfunded, undermanned, and not the right tool for most of America’s draining mines. Good Sam is that fix.

Trout Unlimited is working directly with the bill’s sponsors to advance and pass S. 3571. We would welcome the opportunity to update the conference’s attendees on the issue, the fix and the path forward with Good Sam.

2022 Participant List

Anik Alvi
New Mexico Water Resources
Research Institute

Jordan Anderson
New Mexico
Environment Department

Diana Aranda
New Mexico
Environment Department

Jessica Archibald
Northern Arizona University
& FEWSION for Community
Resilience Program

Floyd Ashley

David Atencio
New Mexico
Environment Department

Steve Austin
Navajo Nation Environmental
Protection Agency

Yining Bai
New Mexico State University

Matthew Baker

Jason Banegas
New Mexico State University

Megan Begay
New Mexico
Highlands University

Susan Behery
U.S. Bureau of Reclamation

Mike Beitner

Ronald Benally
Aneth Community School

Mark Bibeault
Los Alamos
National Laboratory

Johanna Blake
U.S. Geological Survey

Larriet Blake
Dine College

Paul Bossert
New Mexico Office
of the State Engineer

Siona Briley
New Mexico Environmental
Dept. Hazardous Waste Bureau

Jeb Brown
United States
Geological Survey

Wallace Buck Jr.
Toohnii Binaneest'a'
Altaas'ei Alliance

Henry Bulloch
San Juan Watershed Group, Inc.

Peter Butler
Bonita Peak Mining District
Community Advisory Group

Monica Carey

Julian Cata
High Water Mark, LLC.

Michael Chacon
New Mexico
Environment Department

Kyla Chandler
Environmental Protection
Agency

Taryn Chaya
Southern Ute Indian Tribe

Karletta Chief
Department of Environmental
Science, University of Arizona

Ty Churchwell
Trout Unlimited

Becky Clausen
Fort Lewis College

Arnold Clifford

Carol Cloer
Cloer Hay Farm

Robert Cook
EPA Region 6

Charlotte Craig

John Critchfield
William J. Miller Engineers, Inc.

Rachelle Crosby
City of Farmington PRCA

Amber Kanazbah Crotty
Navajo Nation

Colleen Cunningham
New Mexico Interstate
Stream Commission

Caitlin Dee

Geizi Dejka
San Juan College High School

Jonathan Delgado
Eastern New Mexico University

Elvira Dennison
Navajo Family Voices

Gloria Dennison
Navajo Family Voices

Stephanie Deyo
Northern Arizona University

Nikki Dictson

Koffi Djaman
New Mexico State University

Stacy Dodd

Dale Doremus
Sierra Club,
Rio Grande Chapter

Dave DuBois
New Mexico State
Climate Office

Cara Dukepoo
Shush Povi Farms

Steve Earsom

Zelraine Edgewater
Dine College

Anthony Edwards
San Juan County, Colorado

MaryBeth Ewing
New Mexico Water Resources
Research Institute

Christine Ferguson
U.S. Geological Survey-
New Mexico Water
Science Center

Robert Finch

Brian Fontenot
EPA Region 6

Davis Fosdeck
North Farmington Ditch

Andrew Foster
San Juan New Mexico
State University
Cooperative Extension

Joseph Fox
New Mexico
Environment Department

Lauren Fox
Halff

Brandon Francis
New Mexico State University-
Agricultural Science Center
at Farmington

Bonnie Frey
New Mexico Institute
of Mining & Technology

Marcus Gay
New Mexico Water Resources
Research Institute

Sara Gerlitz
New Mexico Office of the
Natural Resources Trustee

Max Gersh
New Mexico Office
of the State Engineer

Gill Giese
New Mexico State University

Katie Goetz
New Mexico Department
of Agriculture

Sara Goldstein
NMDSE-Interstate Stream
Commission

Robert Gomez
New Mexico Energy,
Minerals and Natural
Resources Department

Lucas Graunke
New Mexico
Environment Department

Beth Greyeyes

Tulley Greyeyes

Sarah Griffin
SWCA

Tito Gruen

Clara Harig
University of New Mexico

Julie Hasty
Santa Fe Watershed Association

Heidi Henderson
New Mexico
Environment Department

Max Henkels
New Mexico Department
of Agriculture

Kathy Hilimire
Fort Lewis College

Andrew Homer
Southern Ute Environmental
Programs Division

Andrew Homer
Kelley Drye & Warren LLP

Bonnie Hopkins
New Mexico State University
CES San Juan County

Clifton Horace
Nexstar 1 LLC

Faith Ingwersen-Crosby
New Mexico State Land Office

Jerry James
Kayenta Boarding School

Rachel Jankowitz
New Mexico
Environment Department

Art Jaques

Neil Johns
Navajo Nation
Gaming Enterprise

David Johnson
New Mexico State Land Office

Fred Johnson
Navajo Nation Environmental
Protection Agency Water Qual-
ity / National Pollutant Dis-
charge Elimination System

Phillip Johnson
Jacobs

Athena Jones
U.S. EPA, Region 8

Erin Jordan Arizona Department of Environmental Quality	Yessenia Lugo Homs U.S. Environmental Protection Agency, Region 6	Korbin Nakai New Mexico Farmington Agriculture Science Center
John Kadlecek Rio en Medio Mutual Domestic Water Consumers Association	Ethan Mamer New Mexico Bureau of Geology	Christina Noftsker New Mexico Interstate Stream Commission
Will Keener Words and Pictures	Laris Manuelito U.S. Rep. Leger-Fernandez	Norman Norvelle San Juan Watershed Group, Inc.
Ron Kellermueller New Mexico Department of Game and Fish	Marcella Martinez Bureau of Land Management	Mickey O'Hara The Nature Conservancy
Alan Klatt New Mexico Environment Department	Kaitlin Mattos Fort Lewis College	Every oldham
Barbara Klein Dine College	Beverly Maxwell Toohnii Binaneest'a' Altaas'ei Alliance	Tosin Olofinsao The University of New Mexico
Maggie Knapp New Mexico Coalition to Enhance Working Lands Fellowship	Melissa May San Juan Soil & Water Conservation District	Christine Osborner Utah Department of Environmental Quality
Gloria Lane Navajo Ethno-Agriculture	Jorge Mayo The University of Texas at El Paso	Jessica Oshier
Aaron Lee Lee Hammond Water Users Cooperative Association, Inc.	Sarah McCarthy Northern Arizona University	Marie Owens AE2S
Derrick Lee Ute Mountain Ute Tribe	Emiliano McLane Navajo Ethno-Agriculture / New Mexico State University	Lucy Parham UDEQ
Teresa Leger Fernandez	Dennis McQuillan High Desert Science	Sherri Paul New Mexico Department of Homeland Security & Emergency Management
Gloria Lehmer	Rui Mendes Lisboa E-Nova - Energy and Environment Agency of Lisbon	Charlie Paynter Trout Springs Ranch, LLC.
Shelly Lemon New Mexico Environment Department	Bill Miller William J. Miller Engineers, Inc.	Maggie Pierce U.S. Environmental Protection Agency
Kevin Lombard New Mexico State University- Agricultural Science Center at Farmington	Rachel Mixon U.S. Geological Survey	Jorge Preciado New Mexico Water Resources Research Institute
Thomas Lowry Sandia National Laboratories	Tammy Montoya Pueblo of Santa Ana, Department of Natural Resources	Wilzave Quiles Guzman University of Arizona
		Kaustuv Raj Neupane New Mexico Water Resources Research Institute

Shera Reems
U.S. Environmental
Protection Agency

Brad Reid
New Mexico
Environment Department

Rachel Renz
Environmental
Protection Agency

Bryan Rezin
U.S. Geological Survey

John Roderick
New Mexico
Environment Department

Alyssa Richmond
San Juan Soil & Water
Conservation District

Carlos Rincon
U.S. Environmental
Protection Agency

Jaimie Ritchie
The University of New Mexico

James Ritchie

Scott Roberts
Mountain Studies Institute

Russell Rodke
Santa Fe Community College

Liz Rogers
U.S. Environmental
Protection Agency

Lana Rowenko
Kelley Drye & Warren LLP

Richard Rushforth
Northern Arizona University
School of Informatics

Katie Russell
Colorado State University

Monique Russell
New Mexico State University
Agricultural Science Center
at Farmington

Marsha Rutledge

Lula Sandoval

Keith Sauter
Bureau of Land Management

Tom Schillaci
Environmental Documentary
Video

Jack Scott

Antoinette Sedillo Lopez
New Mexico Senate

Elizabeth Serrano

Tasnim Kamal Shamma
New Mexico Water Resources
Research Institute

Donica Sharpe

Mark Sheely
New Mexico Water Resources
Research Institute

Karlie Shelby
San Juan County

Tami Sheldon
U.S. Bureau of Reclamation

Zach Shepard
United States
Geological Survey

Larry Shore

Bhimsen Shrestha
New Mexico State University

Oscar Simpson
Rio Grande Indivisible

Toni Sitta
City of Farmington

Linnea Spears-Lebrun
SWCA

Erik Stanley
Eastern New Mexico University

Maggie Stebbins
New Mexico Office of Natural
Resources Trustee

Elizabeth Stuffings
New Mexico Environmental
Department-Surface Water
Quality Bureau

Laila Sturgis
New Mexico Bureau
of Geology

Daisy Swadesh

Matthew Symonds

Whitney Thomas
Bureau of Land Management

Anne Tillery
United States
Geological Survey

Emily Toczek
New Mexico Environmental
Department-Surface Water
Quality Bureau

John Tole
Evergreen Systems

Judy Tole
Rappahannock
Historical Society

Jeanette Torres
New Mexico Water Resources
Research Institute

Michele Truby Tillen
San Juan County

Cora Tso
Navajo Nation

Vince Tsosie
BIA-BNR

Crystal Tulley-Cordova
Navajo Nation-Department
of Water Resources-Water
Management

Nikki Tulley
University of Arizona

Diane Van Hoy
New Mexico
Environmental Department

Caleb Van Zante
United States Geological
Survey New Mexico Water
Science Center

Edmund Vandever
High Water Mark, LLC.

Rachel Vaughn
Southern Ute Indian Tribe

Lauren Vigil
High Water Mark
University of New Mexico

Laurie Weahkee
Laurie Weahkee & Associates

Brunlissa Williams
Aneth Community School

Barbara Whitmore
Bureau of Land Management

Rob Wood
Las Cruces Coalition of Conser-
vatives in Action

Douglas Yager
United States
Geological Survey

Letisha Yazzie
New Mexico
Office of the State Engineer

Meredith Zeigler
New Mexico
Environmental Department

2023

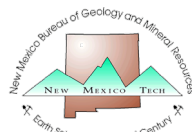
Animas and San Juan Watersheds Conference

Less Water: Planning, Adapting, and Resiliency

June 21–22, 2023
San Juan College Henderson Fine Arts Center & Online



Conference Planning Partners:







Agenda

June 21, Morning Session

- 9:00 WELCOME AND OPENING REMARKS
Mark Sheely, NM Water Resources Research Institute
- 9:10 NM OFFICE OF NATURAL RESOURCES TRUSTEE:
NATURAL RESOURCE RESTORATION PLANS AND PROJECTS
FROM THE GOLD KING MINE SETTLEMENTS
Sara Gerlitz Peck, NM Office of the Natural Resources Trustee
- 9:30 UPDATE ON ACTIVITIES AT THE BONITA PEAK SUPERFUND SITE
(ABSTRACT 10)
Peter Butler, Bonita Peak Mining District Community Advisory Group
- 9:50 SAN JUAN WETLAND JEWELS (ABSTRACT 1)
Steven Fry, Amigos Bravos
- 10:10 EXAMINING SPATIAL HETEROGENEITY AND TOURISM POTENTIAL OF
WATER RESOURCES IN NEW MEXICO (ABSTRACT 5)
Jason Banegas, New Mexico State University
- 10:30 BREAK
- 11:00 LONG-TERM TRENDS IN SPRING SEASON LAND SURFACE ROUGHNESS
AND APPLICATION OF THE WRF-CHEM MODEL IN SIMULATING
DUST-ON-SNOW EVENTS ACROSS THE SOUTHWESTERN UNITED STATES
(ABSTRACT 13)
Saroj Dhital, NEW MEXICO STATE UNIVERSITY
- 11:20 PRELIMINARY RESULTS OF HYDROACOUSTIC-TURBIDITY SURROGATE
MEASUREMENTS USING THE LISST-AOBS FOR METALS AND
SUSPENDED-SEDIMENT CONCENTRATION IN THE ANIMAS RIVER
NEAR CEDAR HILL, NEW MEXICO (ABSTRACT 16)
Jeb Brown, U.S. Geological Survey
- 11:40 ALUMINUM, ARSENIC, AND LEAD CONCENTRATIONS IN THE
NAVAJO NATION IN THE SAN JUAN RIVER WATERSHED, FOUR CORNERS
REGION, USA (ABSTRACT 12)
Christina Ferguson, U.S. Geological Survey
- 12:00 LUNCHEON

June 21, Afternoon Session

- 1:30 IMPLEMENTATION OF A WATER LEASE AGREEMENT FOR FISH HABITAT IMPROVEMENT IN THE SAN JUAN BASIN (ABSTRACT 6)
Colleen Cunningham, New Mexico Interstate Stream Commission
Jacob Mazzone, Jicarilla Apache Nation Department of Game and Fish
Joseph Trungale, The Nature Conservancy
- 2:10 THE NEED FOR CONSTRUCTING ENDANGERED FISH HABITATS THAT CONFORM TO CLIMATE-DRIVEN FLOW CHANGES IN A WESTERN U.S. RIVER (ABSTRACT 11)
Colleen Cunningham, New Mexico Interstate Stream Commission
- 2:30 BREAK AND REMARKS FROM REMARKS FROM U.S. REPRESENTATIVE TERESA LEGER FERNÁNDEZ (NM-3)
- 2:50 WATER QUALITY AT CHACO CULTURE NATIONAL HISTORICAL PARK AND THE POTENTIAL EFFECTS OF HYDROCARBON EXTRACTION (ABSTRACT 7)
Benjamin Linhoff, U.S. Geological Survey
- 3:10 GROUNDWATER FLOW MODEL INVESTIGATION OF THE VULNERABILITY OF WATER RESOURCES AT CHACO CULTURE NATIONAL HISTORICAL PARK RELATED TO UNCONVENTIONAL OIL AND GAS DEVELOPMENT (ABSTRACT 8)
Zach Shephard, U.S. Geological Survey
- 3:30–5:00 POSTER SESSION RECEPTION AND ADJOURN DAY 1
- POSTER PRESENTATIONS:
- PARTNERING WITH NATURE: ESTABLISHING THE ROLE OF CONSERVATION AGRICULTURE FOR ECOLOGICAL RESILIENCE AND ADAPTABLE FOOD SYSTEMS IN THE U.S. SOUTHWEST (ABSTRACT 2)
Sarah McCarthy, Northern Arizona University
- HIGH-RESOLUTION ASSESSMENT OF CRITICAL RUNOFF GENERATION AREAS IN THE SAN JUAN RIVER BASIN: IMPLICATIONS FOR WATER SECURITY IN THE FOUR CORNERS REGION (ABSTRACT 3)
Eric Sjöstedt, Northern Arizona University
- FIFTY-FOUR YEARS OF CLIMATOLOGICAL DATA (1969–2022): NMSU AGRICULTURAL SCIENCE CENTER AT FARMINGTON (ABSTRACT 4)
Margaret West, NMSU Agricultural Science Center at Farmington
- EXAMINING SPATIAL HETEROGENEITY AND TOURISM POTENTIAL OF WATER RESOURCES IN NEW MEXICO) (ABSTRACT 5)
Jason Banegas, New Mexico State University

APPROACH, METHODS, AND CHALLENGES TO COLLECTING
SUSPENDED SEDIMENT AND SURFACE WATER SAMPLES FROM
REMOTE EPHEMERAL CHANNELS IN THE SAN JUAN RIVER WATERSHED
(ABSTRACT 9)

Caleb Van Zante, U.S. Geological Survey

June 22, Morning Session

- 9:00 WELCOME AND OPENING REMARKS
Mark Sheely, NM Water Resources Research Institute
- 9:10 WATERSHED SCALE PATTERNS OF WATER QUALITY RELATED TO METALS
AND NUTRIENTS IN THE ANIMAS AND SAN JUAN RIVERS OBSERVED
DURING WIIN ACT MONITORING SINCE 2018 (ABSTRACT 15)
Kate Sullivan, U.S. Environmental Protection Agency
- 9:30 MULTIJURISDICTIONAL EFFORTS USING WIIN ACT APPROPRIATIONS IN THE
SAN JUAN WATERSHED (ABSTRACT 17)
Shelly Lemon, New Mexico Environment Department
- 9:50 APPLYING INNOVATIVE TECHNOLOGIES TO FACILITATE WATER JUSTICE
FOR TRIBAL COMMUNITIES
Ranalda Tsosie, New Mexico Tech
- 10:10 BREAK
- 10:30 ACEQUIA DROUGHT CHALLENGES AND COLLABORATIVE STRATEGIES
FOR RESILIENCE IN THE SAN JUAN BASIN
Serafina Lombardi, New Mexico Acequia Association
Connie Maxwell, New Mexico Water Resources Research Institute
Kevin Lombard, NMSU Agricultural Science Center at Farmington
- ACEQUIA LEADERS PANEL
Mark Lukow, Eledge Ditch
Allan Walvaren, Farmer's Mutual Ditch
Doug Dykeman, North Farmington Ditch
Martin Nee, Lower Animas Community Ditch
- 12:00 LUNCHEON AND ADJOURN CONFERENCE

June 22, Post-Conference Afternoon Activities

- 1:00–5:00 pm POST-CONFERENCE FIELD TRIP:
Visit to Lower Animas Watershed-Based Plan Implementation Project Sites
San Juan Soil and Water Conservation District and New Mexico Environment Department (Attendees must register online)
- 1:00–3:30 pm Gathering of Acequia Leaders and Collaborators: Planning for the Future:
- All San Juan County acequia irrigators and leaders, along with anyone who works with regional ditches and the watersheds that feed them are encouraged to join us for this dialogue-based planning session, facilitated by the NM Water Resources Research Institute and the NM Acequia Association.
- Building on the previous session, this planning session will dig deeper into the challenges and needs of regional acequias and collectively problem-solve and dream big about how they can be addressed. These two sessions are launching a longer multi-year conversation in the San Juan Basin that aims to identify regional water and agriculture plans and assess the potential impacts of alternative approaches.

Special Thanks to our Presenters!

Jason Banegas New Mexico State University

Jeb Brown U.S. Geological Survey

Peter Butler Bonita Peak Mining District CAG

Colleen Cunningham New Mexico Interstate Stream Commission

Saroj Dhital New Mexico State University

Doug Dykeman North Farmington Ditch

Christina Ferguson U.S. Geological Survey

Steven Fry Amigos Bravos

Sara Gerlitz Peck NM Office of the Natural Resources Trustee

Shelly Lemon New Mexico Environment Department

Benjamin Linhoff U.S. Geological Survey

Kevin Lombard NMSU Agricultural Science Center at Farmington

Serafina Lombardi New Mexico Acequia Association

Mark Lukow Eledge Ditch

Jacob Mazzone Jicarilla Apache Nation Department of Game and Fish

Connie Maxwell New Mexico Water Resources Research Institute

Sarah McCarthy Northern Arizona University

Martin Nee Lower Animas Community Ditch

Zach Shephard U.S. Geological Survey

Eric Sjöstedt Northern Arizona University

Kate Sullivan U.S. Environmental Protection Agency

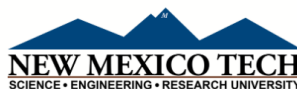
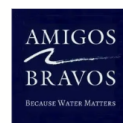
Joseph Trungale The Nature Conservancy

Ranalda Tsosie New Mexico Tech

Caleb Van Zante U.S. Geological Survey

Allan Walvaren Farmer's Mutual Ditch

Margaret West NMSU Agricultural Science Center at Farmington



2023 Conference Planning Committee Members

Steve Austin Navajo Nation EPA
Johanna Blake US Geological Survey
Oralia Bridge San Juan Soil and Water Conservation District
Carol Cloer Lee Hammond Water Users Association
Anthony Edwards Bonita Peak Mining District CAG
Sam Fernald NM WRRRI Director
Sara Gerlitz Peck NM Office of the Natural Resources Trustee
Shelly Lemon New Mexico Environment Department

Kevin Lombard New Mexico State University
Yessenia Lugo Homs US EPA, Region 6
Carolina Mijares NM WRRRI Program Manager
Talon Newton NM Bureau of Geology & Mineral Resources
Alyssa Richmond Animas Environmental Services
Mark Sheely NM WRRRI Program Specialist
Jeanette Torres NM WRRRI Program Specialist

2023 Conference Field Trip Hosts



2023 Abstracts

San Juan Wetland Jewels

Steven Fry
Sfry@amigosbravos.org
Policy and Project Specialist
Amigos Bravos
Taos, NM

Abstract 1 – Oral

The San Juan Wetland Jewels project combines high-detailed mapping analysis with local watershed user's input on desired watershed functions to identify and prioritize critical wetlands for restoration in order to promote resiliency within the watershed.

The presentation will detail how the project got started, the process for collecting stakeholder input and the final results, the wetlands identified through the mapping analysis, and how Amigos plans to implement restoration at the identified sites with partners in the watershed. It will also provide an opportunity for Conference attendees to interact with the publicly available storymap, which can be used by anyone to pursue funding, as well as engage with other project partners.

A key aspect of the Wetland Jewels is collaboration with individual land managers/owners as well as State/Federal agencies to improve ecological function to terrestrial and aquatic landscapes as well as support downstream communities with a cool, clean, and consistent supply of water throughout the year.

Partnering With Nature: Establishing the Role of Conservation Agriculture for Ecological Resilience and Adaptable Food Systems in the U.S. Southwest

Sarah McCarthy¹, Richard Rushforth²

Sgm254@nau.edu¹

Graduate Research Assistant
School of Forestry

Richard.Rushforth@nau.edu²

Assistant Research Professor
School of Informatics, Computing, and Cyber-Systems

Northern Arizona University

Abstract 2 – Poster

As data show rising temperatures and water insecurity across the Intermountain West, adaptations can ensure increased resilience of food production systems. While trying to operate during fluctuating drought years, agricultural producers may be understandably hesitant to try new techniques. However, lack of acclimatization or overly intensive production can have severe consequences, including soil degradation leading to the desertification of arable land. By implementing ecological solutions to agricultural production, watersheds and ecosystems can benefit from reduced fertilizer and pesticide runoff, mitigated soil erosion, and water resource stewardship.

Conservation agriculture, as used in this study, refers to implementation of Nature-based Solutions (NbS) by agricultural producers for production. Examples of NbS include agroforestry, cover cropping, and development of healthier soil. This project seeks to understand attitudes and perceptions of NbS in Southwest Colorado's Montezuma County based on a survey of agricultural producers. This project is designed to help inform conservation districts and researchers about best modalities for NbS implementation based on input from current producers and consideration of greatest benefit to ecosystem wellbeing and food system resistance to disruption. The survey is a collaboration with Montezuma County's High Desert and Mancos Conservation Districts, Northern Arizona University, and the NSF-funded Transformation Network. It is scheduled for distribution in late Spring 2023 through Fall 2023. The poster will outline the process of collaborative survey creation, explain climatic changes and food growing trends in the region, and outline how conservation farming and ranching could benefit the watershed. Our goal is to illustrate constructive collaboration between agricultural producers, communities, and researchers toward stewardship and food system adaptation in the Four Corners. Such collaboration could help foster pathways of communication and encourage more applicable, symbiotic, and accessible conservation agriculture research based on the needs of producers, the land, and changing climate.

High-Resolution Assessment of Critical Runoff Generation Areas in the San Juan River Basin: Implications for Water Security in the Four Corners Region

Eric Sjöstedt¹, Richard Rushforth²

ecs389@nau.edu¹

PhD student

Richard.Rushforth@nau.edu²

Assistant Research Professor

School of Informatics, Computing, and Cyber-Systems

Northern Arizona University

Abstract 3 – Poster

The San Juan River Basin (SJR) is an essential water source for the arid southwestern United States, functioning as a vital tributary for the Colorado River. The river basin holds vital importance for the entire Colorado River Basin, particularly for the downstream city of Farmington, NM. Prior studies have found that watershed basin headwaters are disproportionately generating runoff flows compared to their downstream counterparts. Given the mounting pressure on western water resources from climate change, population growth, water use demands, land use change, and pollution, there is a critical need to understand the dependency of downstream communities on upstream areas generating freshwater resources. This study aims to identify and characterize the critical runoff generation areas in the SJRB using a high-resolution version of the relative water yield (RWY) equation developed by Viviroli et al. (2007). By pinpointing critical runoff generation areas in the basin, we can target vital land areas for conservation and preservation efforts, ensuring the long-term sustainability of Farmington's freshwater supply. This study expands beyond the RWY by incorporating groundwater and snowmelt versions of the RWY equation, allowing for a comprehensive analysis of three major aspects of water resources and providing a holistic assessment of inter-basin water security for the Four Corners region. While mountainous runoff and lowland dependency have been studied on coarser spatial scales, detailed basin-scale analyses of this system dynamic remain limited. Addressing this need for basin-scale water resource management and decision-making, we present a high-resolution analysis for the Four Corners region. Our findings will aid in guiding decision-makers in developing effective strategies for water resource management, including water allocation, infrastructure planning, and ecosystem restoration efforts.

Keywords: San Juan River Basin, Four Corners Region, Water Security, Relative Water Yield, Water Resource Management

Fifty-four Years of Climatological Data (1969-2022): NMSU Agricultural Science Center at Farmington

Margaret West
mwest@nmsu.edu
Research Scientist, Assoc.
NMSU ASC Farmington

Abstract 4 – Poster

Surface water in the semi-arid climate of the Four Corners Region of New Mexico is a crucial life resource. Vigilant monitoring of weather conditions and efficient water-use is necessary for productive life in this water-deficit region, which averages 7.90 inches (200 mm) of precipitation per year (54 year average). Meteorological data are collected at two weather stations located at the New Mexico State University Agricultural Science Center near Farmington (ASCF).

The National Weather Service (NWS) Station (Latitude 36.68972, Longitude -108.30861, (Elevation 5625.0 ft. (1715 m)) is a manual data collection station in service since 1969. The data are collected and reported daily to the NWS in Albuquerque, NM: <https://www.weather.gov/abq/>. Weather data components include air, soil, and water temperatures, precipitation, pan evaporation, and wind movement.

The New Mexico Climate Center (NMCC) weather station (Latitude 36.69, Longitude -108.31, Elevation 5643.0 ft., (1720 m)) is an automated station with daily and five minute frequency computer online accessible weather data: <https://weather.nmsu.edu/>. Weather components include air temperature and dewpoint, windchill and heat index, relative humidity, maximum and mean wind speed, mean wind direction, rainfall, and solar radiation.

Summaries of these weather data components are presented in the ASCF Annual Progress report: <https://farmingtonsc.nmsu.edu/>. Summaries include precipitation, air temperatures, extreme air temperatures, freeze-free days, average and total evaporation, wind movement, soil temperatures, solar radiation, and growing degree days.

Historical weather data collected over 54 years at ASCF has been used in many applications, such as identifying plant hardiness zones, crop-management plans, ET calculations for irrigation of crops and landscapes, and weather forecast modeling. Growers, foresters, natural resource managers, municipal planners, weather forecasters and other community members utilize ASCF weather data, demonstrating the importance of long-term weather monitoring to the region.

Examining Spatial Heterogeneity and Tourism Potential of Water Resources in New Mexico

Jason Banegas

zumbabwe@nmsu.edu

Doctoral Student/Research Assistant

Department of Agricultural, Consumer, and Environmental Sciences
New Mexico State University

Abstract 5 – Oral & Poster

Increasing outdoor tourism in New Mexico and growing demand for water-based tourism amenities requires developing innovative strategies for resource allocation and service integration among many existing and potential recreation locations. Identifying tourism potential and optimizing resource allocation has been addressed in studies using a multitude of models, methods and algorithms; however, variations between the influential factors of tourism locations are best analyzed with a Geographical Information System (GIS) based research model that can examine diverse spatial relationships in these environments. This study uses a Geographically Weighted Regression (GWR) method to illustrate that variables related to drivers of tourism are locally distinct. This tool is used to examine the spatial non-stationarity of relevant water-based tourism variables. Spatial discrepancies are shown to exist in the explanatory variables useful for developing tourism resources in rural and urban locations in the New Mexico study area. This GWR analysis can strengthen the decision process and allow policy makers to identify distinct influential factors and areas where resources for expanding water based tourism should be focused.

Keywords: Outdoor Tourism, Water-based Tourism, Geographic Information Systems (GIS), Geographically Weighted Regression (GWR), Rural Development

Implementation of a Water Lease Agreement for Fish Habitat Improvement in the San Juan Basin

Colleen Cunningham¹, Jacob Mazzone², Joe Trungale³

colleen.cunningham@ose.nm.gov¹
Environmental Coordinator

jacob.a.mazzone@gmail.com²
Fisheries Biologist

joseph.trungale@tnc.org³
Hydrologist

¹New Mexico Interstate Stream Commission

²Jicarilla Apache Nation Department of Game and Fish

³The Nature Conservancy

Abstract 6 – Oral

The Strategic Water Reserve statute authorizes the New Mexico Interstate Stream Commission (NMISC) to acquire water or water rights to assist the State in complying with interstate river agreements, or compacts, and benefitting threatened or endangered species. The January 2022 lease agreement between the NMISC, the Jicarilla Apache Nation (Nation), and The Nature Conservancy (TNC) allows the NMISC to lease up to 20,000 acre-feet per year of the Nation's water stored in Navajo Reservoir, and release it in the San Juan River, a major tributary of the Colorado River in New Mexico.

Additionally, the implementation of this lease agreement supports recovery of native aquatic species, including the endangered Colorado pikeminnow and the threatened razorback sucker, and helps improve instream habitat for approximately 106 miles of the San Juan River in New Mexico from Navajo Reservoir to the New Mexico-Utah state line, while also allowing for additional downstream benefits in Utah.

The first release of water under this lease will take place in calendar year 2023. The three lease parties elicited input from fourteen experts in hydrology, geomorphology, and fisheries with direct knowledge of the San Juan River to explore different options for the 2023 release that maximize benefits for the native fish species. The lease parties are currently working with the San Juan River Recovery Implementation Program to develop a plan to monitor the effects of lease releases on fish habitat. The data collected during this monitoring will be used to gain knowledge about the efficacy of the instream flow augmentation to benefit backwater habitats.

The implementation of this lease agreement is a first-of-its-kind agreement between a Tribal Nation, a state agency, and a nonprofit organization. It demonstrates how Tribal Nations and state governments can work together on a sovereign-to-sovereign basis, with support from conservation organizations, to find collaborative solutions that benefit multiple interests and users. It also advances Tribal self-determination in the management of Tribal water resources and attainment of economic security.

Water Quality at Chaco Culture National Historical Park and the Potential Effects of Hydrocarbon Extraction

Benjamin S. Linhoff¹, Kimberly R. Beisner², Andrew G. Hunt³, Zachary M. Shephard⁴

blinhoff@usgs.gov¹

Research Hydrologist

kbeisner@usgs.gov²

ahunt@usgs.gov³

Noble Gas Laboratory

zshephard@usgs.gov⁴

Hydrologist

New Mexico Water Science Center, U.S. Geological Survey

Abstract 7 – Oral

Study Region:

Chaco Culture National Historical Park (CCNHP) is located in the San Juan Basin of northwestern New Mexico, U.S.A. Its only water supply is in Gallup Sandstone aquifer, stratigraphically surrounded by layers long targeted for oil and natural gas extraction.

Study Focus:

To assess groundwater flow direction, age, mixing between aquifers, and whether hydrocarbons extraction may affect water quality, we completed a geochemical groundwater sampling campaign. Groundwater at 11 sites was analyzed for major ions, volatile organic carbon (VOC) compounds associated with hydrocarbons, noble gases, and the isotope systems $\delta^2\text{H}$, $\delta^{18}\text{O}$, $^{87}\text{Sr}/^{86}\text{Sr}$, $\delta^{13}\text{C}$, and ^{14}C .

New Hydrological Insights for the Region:

Results demonstrate that all waters sampled are exceedingly old and geochemically evolved, with a median ^{14}C age of ~41,000 years before present and a north-south flow path. Three lines of evidence suggest mixing between aquifers with hydrocarbon influenced groundwater: 1) noble gases are fractionated through mixing with connate water expelled during hydrocarbon genesis; 2) several wells, including the park's main supply well, contained trace amounts of VOC compounds suggesting interaction with hydrocarbons; and 3) major ion analysis shows mixing trends between aquifers separated by relatively impermeable shale. Cross-aquifer mixing may be facilitated through the region's numerous hydrocarbon related boreholes. Whether our findings are the result of oil and gas extraction infrastructure or represent the natural state of the aquifers will require more research.

Groundwater Flow Model Investigation of the Vulnerability of Water Resources at Chaco Culture National Historical Park Related to Unconventional Oil and Gas Development

Zachary M. Shephard¹, Benjamin S. Linhoff², Andre Ritchie³, John Lunzer⁴

zshephard@usgs.gov¹
Hydrologist
New Mexico Water Science Center
U.S. Geological Survey

blinhoff@usgs.gov²
Research Hydrologist
U.S. Geological Survey

abritchie@usgs.gov³
Hydrologist
U.S. Geological Survey

John.Lunzer@mt.gov⁴
Surface Hydrologist
Montana Department of Natural Resources & Conservation

Abstract 8 – Oral

Chaco Culture National Historical Park (CCNHP), located in northwestern New Mexico, United States, protects the greatest concentration of Chacoan historical sites in the American Southwest. Geologically, CCNHP is located within the San Juan structural basin, which consists, in part, of complex Cretaceous stratigraphy and hosts a variety of energy resources. CCNHP visitors and staff generally rely on a single drinking water source, namely groundwater from the Gallup Sandstone aquifer. As part of a larger study to investigate the vulnerability of water resources at CCNHP related to oil and natural gas drilling, a MODFLOW groundwater model of the Mancos Shale and Gallup Sandstone units was created by the USGS, in cooperation with the National Park Service to assess advective groundwater flow paths and travel times through these units. Inactive oil and gas related wells could be sources of contamination for the CCNHP main supply well via vertical mixing of hydrocarbon bearing waters and Gallup Sandstone aquifer waters. This study aims to answer the question of whether the water source at CCNHP may be susceptible to contamination from nearby oil and gas extraction activity through groundwater advective transport. Results indicate that groundwater flow directions currently trend from south-southeast to north-northwest within the vicinity of CCNHP, groundwater travel time through the Gallup Sandstone ranges from thousands to tens of thousands of years, and travel time through the Mancos Shale may range from millions to tens of millions of years. The capture zone width spans approximately 12 miles to the south-southeast of the CCNHP well and varies depending on main CCNHP well pumping rate. Differencing of historical and modern-day potentiometric surfaces of the Gallup Sandstone indicate a drop in groundwater levels between 34 and 96 feet within the CCNHP boundaries. Simulated increased hydraulic conductivity zones decreased groundwater travel times (from millions to thousands of years) and acted as permeable pathways from the Mancos Shale to the Gallup Sandstone. Evidence of vertical mixing between aquifers and potential sources of drinking water contamination will also be discussed.

Approach, Methods, and Challenges to Collecting Suspended Sediment and Surface Water Samples from Remote Ephemeral Channels in the San Juan River Watershed

Caleb A. Van Zante¹, Rachel L. Mixon²

cvanzante@usgs.gov¹
Hydrologist

rlmixon@usgs.gov²
Hydrologist

New Mexico Water Science Center, U.S. Geological Survey

Abstract 9 – Poster

Residents of Navajo Nation, and many surrounding communities in the Four Corners region, rely on the San Juan River for drinking water, irrigation, and watering stock. During routine water quality monitoring of the San Juan River, the Navajo Nation Environmental Protection Agency detected elevated concentrations of the metals aluminum, arsenic, and lead. The U.S. Geological Survey (USGS), in collaboration with the Navajo Nation Environmental Protection Agency, initiated a study to determine the sources of these and other dissolved metals in the San Juan River. Twenty-eight ephemeral channels and 5 perennial streams were sampled from Navajo Lake, in northwest NM, to Mexican Hat, UT. Due to the remote location of sampling sites, a limited budget, and the short duration of flow in the ephemeral channels, that usually occur sporadically during the summer monsoon season, this project required a new approach to collecting suspended sediment and water samples.

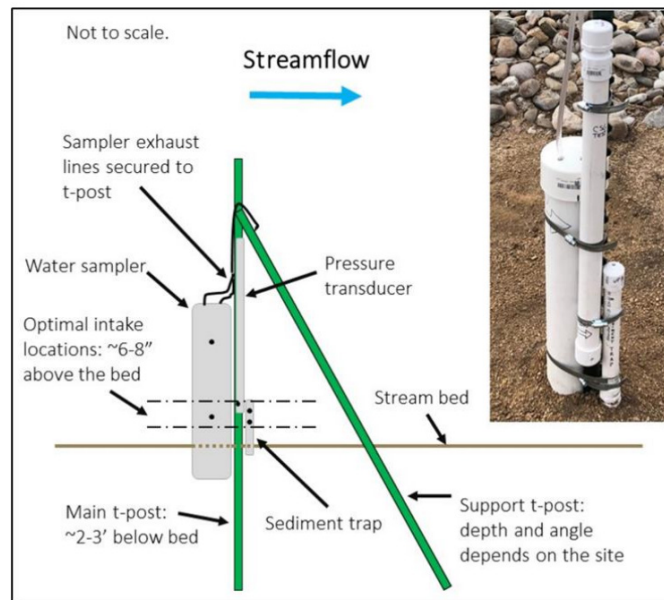


Figure 1. Concept and photograph of novel "sed-chem" monitoring gage and deployment method.

Scientists at the USGS designed and deployed 33 novel monitoring gages, referred to by the gage designers and technicians as sed-chem gages for their capacity to collect both sediment and water quality samples. The sed-chem gages were equipped with a suspended sediment settling trap, a water quality sampler that holds two 1-liter Nalgene bottles, and a pressure transducer. A conceptual model and image of the setup are shown in Figure 1. The sed-chem gages were deployed close to the channel thalweg, where possible, by mounting the individual components to a vertical t-post, anchored 2-3 feet below the channel bed and supported by an angled t-post, anchored similarly. The goal of the sed-chem gages was to collect suspended sediment, water quality samples, and stage during short duration flow events using low-cost, readily available materials. This poster presents the approach, methods, and challenges to meeting that goal.

Update on Activities at the Bonita Peak Superfund Site

Peter Butler
butlerpeter2@gmail.com
Chair
Bonita Peak CAG

Abstract 10 – Oral

The Bonita Peak Mining District Superfund site was designated in 2016, approximately one year after the Gold King Mine release. Since the site's inception, U.S. EPA has spent around \$85 million and other entities have spent close to \$30 million in the site area, yet other than continued treatment of the Gold King Mine drainage, significant improvements in water quality have not been realized. The presentation will discuss what has been done over the past seven years and what activities are planned for this summer and beyond.

The Need for Constructing Endangered Fish Habitats That Conform to Climate-Driven Flow Changes in a Western U.S. River

Colleen Cunningham¹, Richard Valdez², Ali Effati³, Deborah Freeman⁴

colleen.cunningham@ose.nm.gov¹

Environmental Coordinator
New Mexico Interstate Stream Commission

valdezra@aol.com²

Consultant
SWCA Environmental Consultants

ali.effati@ose.nm.us³

Colorado River Basin Bureau Chief
New Mexico Interstate Stream Commission

dfreeman@troutlaw.com⁴

Attorney
Trout Raley Montañó Freeman Sinor Thompson P.C.

Abstract 11 – Oral

Warmwater fish habitat in the San Juan River of the southwestern U.S. has been reduced by over 30% as a result of water depletion, reservoir inundation, and cold-water dam releases combined with drought-related changes in hydrology. This reduction and a suite of other factors has contributed to declines in native fish populations including the federally listed Colorado Pikeminnow (*Ptychocheilus lucius*) and Razorback Sucker (*Xyrauchen texanus*). Conservation efforts for these species include determining flow needs; protecting, managing, and augmenting habitats; and stocking hatchery fish. But the young of stocked fish have low survival due largely to a paucity of nursery habitat not being reformed and maintained under current conditions. Flow recommendations for Navajo Dam releases designed to mimic the river's natural hydrograph have not been met due to water shortages, and the desired outcomes of increased channel complexity and enhanced fish habitat have not been observed. Forecasted hydrology that includes ongoing drought, shows that achieving the flow targets through further dam reoperations is unlikely. Mechanical construction of early life-stage habitats is a highly recommended complement to flow management for offsetting the effects of flow reduction and habitat loss. Habitats with features that are effective and resilient under a range of flows are important in counterbalancing the effects of climate change.

Link to the published paper: <https://doi.org/10.1111/1752-1688.13114>

Aluminum, Arsenic, and Lead Concentrations in the Navajo Nation in the San Juan River Watershed, Four Corners Region, USA

Christina Ferguson¹, Johanna Blake², Jeb Brown³

cferguson@usgs.gov¹
Hydrologist

jmtblake@usgs.gov²
Research Hydrologist

jebbrown@usgs.gov³
Hydrologist

U.S. Geological Survey - New Mexico Water Science Center

Abstract 12 – Oral

The San Juan River watershed covers an area of approximately 64,000 km² in the states of New Mexico, Colorado, Utah, and Arizona. Approximately half of the watershed is occupied by the Navajo Nation. The San Juan River is fed by many tributaries, both perennial and ephemeral, and is used by the people in the area as the main source of water for livestock, agriculture, and domestic use. During regular sampling events, the Navajo Nation Environmental Protection Agency (NNEPA) found exceedances of aluminum, arsenic, and lead in the San Juan River. To further investigate possible sources of these metals, the NNEPA collaborated with the U.S. Geological Survey New Mexico Water Science Center (USGS) to conduct a study on the surface water in the region that included the San Juan River and many of its tributaries. Because of the ephemeral nature of most of the tributaries and the remoteness of the sites, USGS developed a novel passive sampling method to capture precipitation-driven flows at approximately 40 tributaries to the San Juan River. Water samples collected during these events were analyzed for a full suite of major and trace elements. A baseflow synoptic sampling event was conducted in February 2022 to assess low flow concentrations of aluminum, arsenic, and lead in the San Juan River as a baseline for comparison to concentrations during high flow events in the river and in inflows from tributaries. The results of these sampling campaigns show that high flow events within the river increase the concentration of the constituents of concern. Initial data review has suggested that much of the aluminum, arsenic, and lead in the San Juan River has come from the tributaries. The source(s) of these elements is under investigation, but they could be attributed to the geology, agriculture, oil and gas activities, mining activities, or other human activity in the area.

Long-Term Trends in Spring Season Land Surface Roughness and Application of the Wrf-Chem Model in Simulating Dust-On-Snow Events across the Southwestern United States

Saroj Dhital¹, Nicholas Webb², Adrian Chappell³, Sarah McCord⁴, Michael Kaplan⁵, Gayle Tyree⁶,
Travis Nauman⁷, Michael Duniway⁸, Sandra LeGrand⁹, Theodore Letcher¹⁰, McKenzie Skiles¹¹,
Patrick Naple¹², Nathaniel Chaney¹³, Jizxuan Cai¹⁴

sdhital@nmsu.edu¹

New Mexico State University

nick.webb@usda.gov²

sarah.mccord@usda.gov⁴

USDA-ARS Jornada Experimental Range

chappella2@cardiff.ac.uk³

School of Earth and Ocean Sciences, Cardiff
University

michael.kaplan@dri.edu⁵

Division of Atmospheric Sciences, Desert
Research Institute

gtyree@nmsu.edu⁶

mduniway@usgs.gov⁸

U.S. Geological Survey, Southwest Biological
Science Center

travis.nauman@usda.gov⁷

USDA-NRCS National Soil Survey Center

sandra.l.legrand@erdc.dren.mil⁹

U.S. Army Engineer Research and
Development Center,
Geospatial Research Laboratory

theodore.w.letcher@erdc.dren.mil¹⁰

U.S. Army Engineer Research and
Development Center,
Cold Regions Research and Engineering
Laboratory

m.skiles@geog.utah.edu¹¹

pat.naple@utah.edu¹²

Department of Geography, University of Utah

nathaniel.chaney@duke.edu¹³

jiaxuan.cai@duke.edu¹⁴

Department of Civil and Environmental
Engineering, Duke University

Abstract 13 – Oral

Increasing springtime (March–May) dust activity across the southwest United States is a growing problem as it impacts the following environmentally sensitive disciplines: 1) human health through the degradation of air quality, 2) natural ecosystems and agricultural production through loss of soil nutrients, and 3) water resources through dust deposition on snow. In the Southwest, dust transported from regionally active source areas affects mountain snowpack. Deposited dust changes snow properties, accelerates snowmelt, and alters the hydrologic cycle in the Colorado River Basin (CRB) and Rio Grande Basin (RGB), which are the main sources of the Southwest's water resources sustaining more than 40 million people. Predicting future dust activity and possible dust source regions across the Southwest requires a complete understanding of the current state of the land surface roughness – a first order control on aeolian processes – and how vegetation community changes influence land surface roughness. Moreover, an accurate prediction of dust-on-snow events that impact snowmelt rates is essential to support water resource management in the Southwest where communities and agriculture face critical water shortages, presently compounded by a regional multi-year megadrought.

In this study, we analyzed spatiotemporal patterns of land surface roughness and vegetation cover and their relationships within the Southwest dust source areas. We used an albedo-based roughness model to calculate the normalized surface wind shear velocity, u_{s^*}/U_H , applying 20 years (2001-2020) of MODIS daily albedo and vegetation functional group cover datasets from the Rangeland Analysis Platform (both rescaled to 4 km). These data were subsequently employed to calculate decadal and long-term roughness trends using the Mann-Kendall trend test. We then examined correlations between land surface roughness and vegetation cover to elucidate the contributions of annual and perennial herbaceous and woody vegetation change to roughness trends. Additionally, we test the capability of the Weather Research and Forecasting model coupled with Chemistry (WRF-Chem) with the same MODIS albedo-based drag partition model in simulating dust storms that result in dust-on-snow episodes. For this purpose, we simulated two springtime Southwest dust episodes. Our results show where springtime surface roughness is changing and where those trends are linked to vegetation change. The trends in surface roughness and vegetation cover provide insights needed to predict future vegetation dynamics and active dust sources. This trend analysis highlights how the albedo-based roughness model can be used to monitor land surface roughness change and identify how ecosystem changes contribute to changes in surface roughness, which provides a direct link to dust mitigation and land management practices. Additionally, our simulation results suggest that the WRF-Chem model with the albedo-based drag partition in the Air Force Weather Agency dust emission module may be a viable tool for resolving dynamic aeolian processes and simulating dust-on-snow episodes in the Southwest United States.

Keywords: Vegetation, Land-cover change, Surface roughness, Dust

Barriers Beget Barriers: The Political-Ecological Drivers and Consequences of Managing Aquatic Invasive Species (AIS)

Christian Fauser
chf32@nau.edu
Graduate Researcher
Free-Flowing Rivers Lab
Northern Arizona University

Abstract 14 – Oral

The establishment and spread of Aquatic Invasive Species (AIS) is considered a threat to the ecological health and Aquatic Native Species (ANS) populations of the Southwestern United States' freshwater ecosystems. Current management efforts to address AIS with fish barriers accompany significant policy and ecological challenges. While effective at preventing the upstream spread of AIS, fish barriers often mimic the aesthetic and functional qualities of a dam in disrupting the hydrological connectivity of a river. Additionally, by "disrupting a river's free-flowing nature," barrier use potentially disqualifies a river from Wild and Scenic Rivers Act (WSRA) eligibility and accompanying Federal protections for designated rivers and surrounding ecosystems. Conflict between the WSRA and fish barrier use has not been aligned or negotiated, and mitigating the impact of AIS with barriers threatens the conservation potential of the Act as well as the ecosystems and ANS they state to protect. A current proposal for two barriers on the WSRA-eligible, free-flowing portion of the Upper Verde River (UVR) in support of expanding AZ Game and Fish's recreational sport fishing program highlights the political-ecological influences driving AIS management actions at the expense of the river's free-flowing nature and concomitant Federal environmental protection potential. Using the proposed UVR barriers and New Mexico House Bill(s) 183/184 as representative case studies and completing a literature review, analysis of relevant policy drivers, and several spatial analyses, this research seeks to 1.) investigate the federal policy mismatch of AIS management on free-flowing river systems and 2.) the shortcomings of charging economically incentivized state fish and game agencies with conserving riverine ecosystem and recovering ESA-listed ANS. Findings can be used by Arizona and New Mexico's river conservation advocates, local stakeholders, and AIS management entities to identify where conflicts between WSRA designations, ANS recovery, fish barrier use, and recreational sport fisheries could manifest and be addressed currently and in the future.

Watershed Scale Patterns of Water Quality Related to Metals and Nutrients in the Animas and San Juan Rivers Observed During WIIN Act Monitoring Since 2018

Kate Sullivan
sullivan.kate@epa.gov
Office of Research and Development
U.S. Environmental Protection Agency

Abstract 15 – Oral & Poster

The Animas and San Juan Rivers were extensively monitored for metals in the water and sediments by EPA, state and tribal agencies during and through the year following the Gold King Mine release that occurred in August 2015. Congress funded additional water quality monitoring along the length of the impacted river and expanded scientific study within the San Juan River watershed for 5 years through the Water Infrastructure Improvements for the Nation Act (WIIN) beginning in 2018. Numerous scientific studies and monitoring projects were initiated with the goal to improve understanding of watershed processes, pollutant sources and sinks within the river, tributaries, and receiving water bodies. The program also expanded water quality monitoring to nutrients and other chemical constituents and funded installation of sondes at USGS gages. This talk will summarize some of the key observations of water quality related to metals and nutrients during the past five years with emphasis on basin scale patterns and river processes.

Preliminary Results of Hydroacoustic-Turbidity Surrogate Measurements Using the Lisst-Aobs for Metals and Suspended-Sediment Concentration in the Animas River near Cedar Hill, New Mexico

Jeb E. Brown¹, Justin R. Nichols², Grady P. Ball³, Johanna M. Blake⁴, Bryan J. Rezin⁵

jebbrown@usgs.gov¹

jrnichols@usgs.gov²

gball@usgs.gov³

jmtblake@usgs.gov⁴

brezin@usgs.gov⁵

U.S. Geological Survey

Abstract 16 – Oral

Metals attached to suspended sediments pose a potential health risk to communities that depend on water for domestic and agricultural uses. The Animas River in southern Colorado and northern New Mexico has been shown to transport elevated amounts of metals. These constituents have been documented as preferentially sorbing to clay-sized suspended sediments. Surrogate methods for estimating suspended-sediment concentration (such as turbidity, hydroacoustic, laser diffraction, and densimetric) have been widely published in the literature. Surrogate measurements, such as the LISST-AOBS instrument explored in this project, provide near-real-time data which may inform daily operational changes by water managers. Temporally dense surrogate data (values collected every 15 minutes) can also increase the understanding of transport mechanisms of metals and suspended-sediment concentration. However, rivers with widely varying suspended particle sizes reduce reliability of surrogate measurements. The objective of this work is to determine if a regression model can be developed through correlation of hydroacoustic-turbidity measurements (LISST-AOBS instrument) with suspended-sediment concentration and concentrations of suspended metals such as aluminum, arsenic, and lead. If a reasonable regression model can be developed for suspended metals, near-real-time data will be displayed on USGS webpages. Preliminary hydroacoustic-turbidity, metals, and suspended sediment data will be presented.

Multijurisdictional Efforts Using WIIN Act Appropriations in the San Juan Watershed

Shelly Lemon
Shelly.Lemon@env.nm.gov
New Mexico Environment Department

Abstract 17 – Oral

Water resources in the San Juan watershed, which encompasses the San Juan and Animas Rivers and Lake Powell, are essential for recreational, agricultural, cultural, and residential uses. As a result of the Gold King Mine spill, in 2016 Congress authorized appropriations under the Water Infrastructure Improvements for the Nation (WIIN) Act, and EPA has funded state and tribal projects across the San Juan Watershed.

In addition, EPA and the states and tribes adjoining the watershed - Colorado, New Mexico, Utah, the Navajo Nation, the Ute Mountain Ute Tribe, and the Southern Ute Indian Tribe - are working together to develop and implement a water quality monitoring program that will:

- Collect annual water quality (and sediment) data and determine the need for additional monitoring,
- Communicate information about the condition of the watershed to the public, and
- Carry out targeted monitoring and research activities to inform state and tribe-specific decision-making for the watershed.

This presentation will provide an update on the Multijurisdictional efforts in the San Juan Watershed funded by WIIN Act appropriations, including Tribal and State projects and the multijurisdictional water quality monitoring program.

2023 Participant List

Afeez Ayoade Adegbite
Ogun State Polytechnic
of Health and Allied Sciences
Ilese-Ijebu, Nigeria

Abba Ahmed
Aurora Water

Minhajuddin Ahmed
New Mexico Water Resources
Research Institute

Usama Mohamed Ahmed
Independent Arbitrator

James Allen

Beth Anderson
U.S. Forest Service

Colleen Anderson

Diana Aranda
New Mexico
Environment Department

Diego Araujo
U.S. Fish and Wildlife Service

Kylie Arrieta
New Mexico Water Resources
Research Institute

Victoria Atencio
Nambe Pueblo

Steve Austin
Navajo Nation Environmental
Protection Agency

Adrian Avila
Senate Majority Office
New Mexico Legislature

Elizabeth Bainbridge
U.S. Fish and Wildlife Service

Jason Banegas
New Mexico State University

Zoe Barker
Conservation Voters
New Mexico

Shayln Baushlicher
U.S. Environmental
Protection Agency

Scott Baxstrom
Eledge Ditch

Lucina Bernalley

Johanna Blake
U.S. Geological Survey

Paul Bossert
Office of the State Engineer

Oralia Bridge
San Juan Soil & Water
Conservation District

Jeb Brown
U.S. Geological Survey

Madison Buechter

Henry Bulloch
San Juan Watershed Group, Inc.

Sara Burch
San Juan Citizens Alliance

Peter Butler
Bonita Peak Mining District
Community Advisory Group

Brigette Buynak

Nina Carranco
Water Foundation

Carol Cloer
Cloer Hay Farm

Catherine Conran
Water Protection Division,
New Mexico Environment
Department

Melvin Cooley
New Mexico State University-
Farmington

Amber Kanazbah Crotty
New Mexico State University-
Farmington

Collen Cunningham
New Mexico Interstate
Stream Commission

Arden Day
Northern Arizona University

Shannon Demuth
Eastern New Mexico University

Katy DeYoe
SWCA

Saroj Dhital
New Mexico State University

Stacy Dodd
Bloomfield Irrigation District

Sage Dunn
Bureau of Land Management,
Taos Field Office

Doug Dykeman
North Farmington Ditch

James Evangelisti
Southern Ute Indian Tribe

Sarah Faber
Conservation Corps
New Mexico

Christian Fauser
Northern Arizona University

Christina Ferguson
U.S. Geological Survey
New Mexico Water
Science Center

Irene Fernald
Middlebury Institute
of International Studies

Sam Fernald
New Mexico Water Resources
Research Institute

Lauren Fox
Halff

Brandon Francis
New Mexico State University
Agricultural Science Center
at Farmington

Bonnie Frey
New Mexico Institute
of Mining & Technology

Steven Fry
Amigos Bravos

David Gallegos
New Mexico State Land Office

Emily Geery
Water + Planning

Sara Gerlitz Peck
New Mexico Office of Natural
Resources Trustee

Max Gersh
New Mexico Office
of the State Engineer

Megan Gleason
Source New Mexico

Jake Golden
City of Phoenix

Sara Goldstein
Interstate Stream Commission

Alice Gomez
University of New Mexico

Eric Gopsill
Tallgrass Water

Sarah Griffin
SWCA

Steve Grey
Grey, LLC.

Olivia Groeber
Farmington Metropolitan
Planning Organization

Bekki Harjo
National Weather Service
Arkansas-Red Basin River
Forecast Center

Maggie Hart Stebbins
New Mexico Office of Natural
Resources Trustee

Julie Hasty
Santa Fe Watershed Association

Gabrielle Henderson
New Mexico State University

Donna House
Independent Consultant

Lei Hu
New Mexico
Environment Department

Joe Hubbard

Jessica Hubbling
New Mexico Environment
Department-Ground Water
Quality Bureau

Faith Ingwersen Crosby
New Mexico State Land Office

Rachel Jankowitz
New Mexico
Environment Department

Fred Johnson
Navajo Nation Environmental
Protection Agency Water Qual-
ity / National Pollutant Dis-
charge Elimination System

Tricia Keffer
City of Albuquerque
Open Space Division

Ron Kellermueller
New Mexico Department
of Game and Fish

Steve Kem
Southern Ute
Indian Tribe

Kenric Kesler
Northern Arizona University

Alan Klatt
New Mexico
Environment Department

Symone Kumar
Aquatic Informatics

Jake Kurzweil
Mountain Studies Institute

Gloria Lane

Joslynn Lee
Fort Lewis College

Shelly Lemon
New Mexico Environment
Department-Surface Water
Quality Bureau

Runwei Li
New Mexico State University

Sydney Lienemann
New Mexico
Environment Department

Benjamin Linhoff
United States
Geological Survey

John Lofgren
Farmers Irrigation District

Kevin Lombard
New Mexico State University
Agricultural Science Center
at Farmington

Serafina Lombardi
New Mexico
Acequia Association

Yessenia Lugo Homs

U.S. Environmental Protection
Agency, Region 6

Mark Lukow

Eledge Ditch

Gasper Martinez

New Mexico State University
Agricultural Science Center
at Farmington

Melissa May

Mountain Studies Institute

Jacob Mazzone

Jicarilla Apache Nation

Kelly McAllister

Tallgrass Energy LP

Sarah McCarthy

Northern Arizona University

Rachel Mixon

United States
Geological Survey

Paul Montoia

RESIC

Miguel Montoya

Surface Water Quality Bureau

Cris Morton

New Mexico Bureau of Geol-
ogy and Mineral Resources

Jennifer Muus

New Mexico Environment
Department, River Stewardship
Program

Lanier Nabahe

The Nature Conservancy

Martin Nee

Lower Animas
Community Ditch

Brad Newton

New Mexico Institute
of Mining and Technology

Christina Noftsker

New Mexico Interstate
Stream Commission

Norvelle Norman

San Juan Watershed Group, Inc.

Odunayo Oduguwa

Student

Tosin Olofinsao

The University of New Mexico

Jaimie Park

New Mexico
Acequia Association

John Phillips

Parametrix

Sharllyn Pimentel

Dudek

Brookelynn Pitsch

Mountain Studies Institute

Kaustuv Raj Neupane

New Mexico Water Resources
Research Institute

Zev Ratigan

United States
Geological Survey

Stacie Reece

Climate Assessment
for the Southwest-University
of Arizona

Md Mhahabubur Rhaman

Eastern New Mexico University

John Rhoderick

New Mexico
Environment Department

Alyssa Richmond

Animas Environmental
Services

James Rogers

Jewett Valley Water Users

Sean Ryan

Northern Arizona University

Lorenzo Salgrado

NV5

Keith Sauter

Bureau of Land Management

Tom Schillaci

Environmental Documentary
Video

Sarbagya Shakya

Eastern New Mexico University

Mark Sheely

New Mexico Water Resources
Research Institute

Zach Shephard

United States
Geological Survey

Anani Shomour

United States
Geological Survey

Bhismsen Shrestha

New Mexico State University

Toni Sitta

City of Farmington

Eric Sjostedt

Northern Arizona University

Linnea Spears-Lebrun

SWCA

Elizabeth Stuffings

New Mexico
Environment Department

Kate Sullivan

U.S. Environmental
Protection Agency

Edward Sustaita**Vincent Tafoya**

Jicarilla Apache Nation

Christine Tang
New Mexico State University /
New Mexico Water Resources
Research Institute /
Worcester Polytechnic Institute

Dennis Taylor
Farmers Irrigation District

Whitney Thomas
Bureau of Land Management

Jeanette Torres
New Mexico Water Resources
Research Institute

Vittoria Totaro
The University of New Mexico

Emily Trejo Sypolt
NV5

Joseph Trungale
The Nature Conservancy

Adriano Tsinigine
U.S. Fish & Wildlife Service

Ranalda Tsosie
New Mexico Institute
of Mining and Technology

William Turner
WaterBank

Erica Valdez
New Mexico Farm
& Livestock Bureau

Richard Valdez
SWCA Environmental
Consultants

Diane Van Hoy
New Mexico
Environment Department

Caleb Van Zante
United States Geological
Survey, New Mexico Water
Science Center

Edmund Vandever
High Water Mark, LLC.

Codie Vileno
New Mexico
Environment Department

Allan Walraven
Farmers Mutual
Community Ditch

Maeven Weber
Conservation Corps
New Mexico

Shannon Weld
New Mexico Interstate Stream
Commission

Margaret West
New Mexico State University
Agricultural Science Center
at Farmington

Kate Wilkins
United States
Geological Survey

Shawn Williams
New Mexico Office
of the State Engineer

Barbara Witmore
Bureau of Land Management

2024

Animas and San Juan Watersheds Conference

Water Without Borders - Four Corners, Three Rivers

June 12–13, 2024

Henderson Fine Arts Center, San Juan College, Farmington, NM, & Online



Conference Planning Partners:







AGENDA

Wednesday, June 12, Morning Session

- 7:45 AM BREAKFAST, CHECK-IN, AND WALK-IN REGISTRATION
- 8:50 WELCOMING REMARKS
Mark Sheely, NM WRRRI Program Specialist
- 9:00 BUILDING CAPACITY TO IMPLEMENT WATERSHED RESTORATION IN THE SAN JUAN BASIN (**ABSTRACT 9**)
Stacy Beough, Strategic By Nature, Inc.
- 9:30 MULTIJURISDICTIONAL EFFORTS USING WIIN ACT APPROPRIATIONS IN THE SAN JUAN WATERSHED
Elizabeth Stuffings, New Mexico Environment Department
- 10:00 RECREATIONAL DEVELOPMENT OF THE SAN JUAN RIVER
Ryan Dudgeon, Desert River Guides
- 10:30 BREAK
- 11:00 SURFACE WATER QUALITY BUREAU HARMFUL ALGAL BLOOMS PROGRAM (**ABSTRACT 12**)
Nathaniel Kamm, New Mexico Environment Department
- 11:30 LEVERAGING CONSERVATIVE TRACERS, STABLE ISOTOPES, AND MICROBIAL SOURCE TRACKING TO IDENTIFY THE SOURCES AND FATE OF NUTRIENTS WITHIN THE ANIMAS RIVER (**ABSTRACT 3**)
Justin Nichols, U.S. Geological Survey
- 12:00 PM UNDERSTANDING E.COLI IN THE SAN JUAN WATERSHED: PRELIMINARY DATA GAP ANALYSIS AND RECOMMENDATIONS FOR A MULTIJURISDICTIONAL E.COLI WATERSHED MONITORING PROGRAM (**ABSTRACT 11**)
Alyssa Richmond, Animas Environmental Services
- 12:30 CONFERENCE LUNCH

Wednesday, June 12, Afternoon Session

- 1:30 ALUMINUM, ARSENIC, AND LEAD IN THE SAN JUAN RIVER WATERSHED (**ABSTRACT 10**)
Johanna Blake, U.S. Geological Survey

- 2:00 GEOLOGIC UNIT DISTRIBUTION AND CHEMICAL WEATHERING INDICES AS A METHOD TO EVALUATE LITHOLOGICAL SOURCES OF ALUMINUM, ARSENIC, AND LEAD TO THE SAN JUAN RIVER, FOUR CORNERS REGION, USA (**ABSTRACT 6**)
Christina Ferguson, U.S. Geological Survey
- 2:30 URANIUM AND POTENTIAL SOURCES OF URANIUM TO THE SAN JUAN RIVER, FOUR CORNERS REGION, USA (**ABSTRACT 8**)
Rachel Mixon, U.S. Geological Survey
- 3:00 NEAR REAL-TIME SUSPENDED SEDIMENT AND METALS CONCENTRATIONS DERIVED FROM HYDROACOUSTIC TURBIDITY SURROGATE MEASUREMENTS USING THE LISST-AOBS IN THE ANIMAS RIVER NEAR CEDAR HILL, NEW MEXICO (**ABSTRACT 5**)
Jeb Brown, U.S. Geological Survey
- 3:30 POSTER SESSION AND RECEPTION
- POSTER PRESENTATIONS:
- CONSERVATION PERSPECTIVES OF AGRICULTURAL PRODUCERS IN A SOUTHWEST COLORADO HEADWATER COMMUNITY (**ABSTRACT 1**)
Sarah McCarthy, Northern Arizona University
- AGRIVOLTAICS: IMPACT OF PHOTOVOLTAIC ARRAY AND INTERCROPPING DESIGN ON CULTURALLY VALUED CROPS OF THE FOUR CORNERS REGION (**ABSTRACT 2**)
Emiliano McLane, New Mexico State University
- USING INFLUENCE FUNCTIONS IN CONTAMINATED DATA TO IDENTIFY THE OUTLIERS (**ABSTRACT 4**)
Prabha Shrestha, Eastern New Mexico University
- AERIAL INSIGHTS: MODELING STREAMFLOW IN EPHEMERAL CHANNELS ALONG THE SAN JUAN RIVER, FOUR CORNERS REGION, USA (**ABSTRACT 7**)
Caleb Van Zante, U.S. Geological Survey
- 5:00 ADJOURN DAY 1

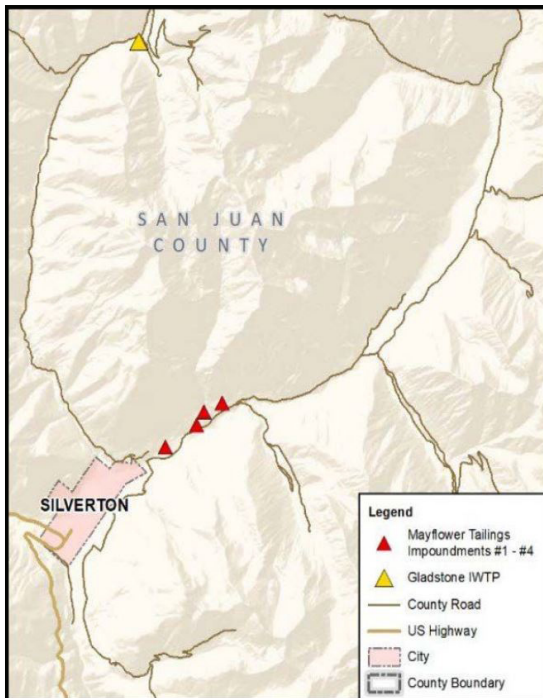
Thursday, June 13, Morning Session

- 7:45 AM BREAKFAST, CHECK-IN, AND WALK-IN REGISTRATION
- 8:50 WELCOMING REMARKS
Mark Sheely, NM WRRRI Program Specialist
- 9:00 DAY 2 KEYNOTE PRESENTATION
Justin Pioche, Executive Chef and Owner – Pioche Food Group

9:30	NAVAJO ETHNO-AGRICULTURE HYDROPONICS Breanna Lameman , The University of Arizona
10:00	NAVAJO-GALLUP WATER SUPPLY PROJECT Bart Deming , U.S. Bureau of Reclamation
10:30	BREAK
11:00	UPDATE ON BONITA PEAK MINING DISTRICT ACTIVITIES Chara Ragland , Bonita Peak Mining District Community Advisory Group
11:30	THE REMEDIATION OF ABANDONED MINE LANDS IN THE ANIMAS AND SAN JUAN WATERSHEDS Robert Runkel , U.S. Geological Survey Claudia Trueblood , New Mexico Environment Department
12:30 PM	ADJOURN DAY 2

Friday, June 14, Post-Conference Field Trip

8:00 AM – 5:00 PM



BONITA PEAK MINING DISTRICT

In collaboration with the **Bonita Peak Mining District (BPMD) Community Advisory Group**, NM WRRRI invites registrants to a field visit of the Gladstone Interim Water Treatment Plant and Bonita Peak Repository.

Registration for this field trip is free of charge, and attendees must sign up through the conference registration process, as capacity is limited.

Pickup and drop off will take place outside the Henderson Fine Arts Center at San Juan College in Farmington, New Mexico. Lunch and rest stops will be provided to attendees.

What to bring: Weather-appropriate clothes and outerwear, along with good walking shoes. Water and boxed lunches will be provided, but you are free to bring your own food and beverage.

SPECIAL THANKS TO OUR PRESENTERS!

Stacy Beagh Strategic By Nature, Inc.

Johanna Blake U.S. Geological Survey

Jeb Brown U.S. Geological Survey

Bart Deming U.S. Bureau of Reclamation

Ryan Dudgeon Desert River Guides

Christina Ferguson U.S. Geological Survey

Nathaniel Kamm NM Environment
Department

Breanna Lameman The University of
Arizona

Rachel Mixon U.S. Geological Survey

Justin Nichols U.S. Geological Survey

Justin Pioche Pioche Food Group

Chara Ragland Bonita Peak Mining District
Community Advisory Group

Alyssa Richmond Animas Environmental
Services

Robert Runkel U.S. Geological Survey

Elizabeth Stuffings NM Environment
Department

Claudia Trueblood NM Environment
Department



2024 CONFERENCE PLANNING COMMITTEE MEMBERS

Steve Austin Navajo Nation EPA

Johanna Blake US Geological Survey

Anthony Edwards Bonita Peak Mining
District Community Advisory Group

Sam Fernald NM WRRRI Director

Shelly Lemon New Mexico Environment
Department

Kevin Lombard New Mexico State
University

Yessenia Lugo Homs US EPA, Region 6

Anissa Mahkee NM WRRRI Student
Assistant

Carolina Mijares NM WRRRI Program
Manager

Paul Montoia Farmington Community
Member

Alyssa Richmond Animas Environmental
Services

Mark Sheely NM WRRRI Program Specialist

Elizabeth Stuffings New Mexico
Environment Department

Jeanette Torres NM WRRRI Program
Specialist

2024 CONFERENCE FIELD TRIP HOSTS



**Bonita Peak Mining District
Community Advisory Group (CAG)**

2024 Abstracts

Conservation Perspectives of Agricultural Producers in a Southwest Colorado Headwater Community

Sarah McCarthy¹, Richard Rushforth²

sarah.mccarthy@nau.edu¹
Graduate Research Assistant

Richard.Rushforth@nau.edu²
Assistant Research Professor

¹School of Forestry, Transformation Network (NSF #2115169)

²School of Informatics, Computing, and Cyber-Systems, Transformation Network (NSF #2115169)
Northern Arizona University

Abstract 1 – Poster

Data show trends of reduced snowfall and water availability as aridification intensifies in the Intermountain West. The Southwest region of the U.S. is integrated into local and widespread food systems, so establishing modes of adaptability is critical. For this work, producers in a San Juan headwaters county in Southwest Colorado participated in a survey that was developed collaboratively with community partners. The objective of data collection was to inform conservation districts, local policy, and future research. The survey addressed perceptions about soil degradation, water laws, effects of climate, and ways to reduce barriers to Nature-based Solutions (NbS). Respondents identified water availability and climate changes as most negatively affecting operations and had interest in agroforestry methods like windbreak trees and drought-resistant crops. Organic soil building was identified as already being used. Cost was selected as the leading perceived barrier to implementing nature-based agricultural solutions. Programs most chosen to ease difficulty included opportunities for training, cost subsidy, and access to equipment. Focusing on soil building could serve as an introduction to NbS, and producers already utilizing this NbS could help establish regional protocols. The health of a community's watershed determines its wellbeing, especially in rural communities reliant on functioning ecosystem services. We intend to contribute this model for wider applications in other regions to uncover place-based solutions to resource challenges.

Agrivoltaics: Impact of Photovoltaic Array and Intercropping Design on Culturally Valued Crops of the Four Corners Region

Emiliano McLane
emilmcla@nmsu.edu
Graduate Student
New Mexico State University

Abstract 2 – Poster

To address the issues of increasing food demands, energy consumption, and water use while mitigating the negative effects of climate change, scientists are investigating innovative agricultural systems in Agrivoltaics (AgV). AgV combines food and energy production by placing agricultural systems within the same space as photovoltaic panels and vice versa. The shade on the soil created from the panels and the reduction of light intensity on the plants allow for increased water retention in the system. AgV creates a food, energy, and water nexus to moderate resources and reduce external inputs. Implementation of AgV began in Japan and Germany in the early 2000s with a rise of interest in innovative agricultural techniques as the negative effects of climate change and human population became more apparent. This project will study the optimal growth of select culturally valued crops of the Four Corners Region intercropped in an AgV system. The project seeks to achieve adequate yields while reducing inputs and supporting the energy needs of an adjacent controlled environment system. The results will aid in understanding how regional crops will perform in an AgV system in different regions using specific crop designs.

Leveraging Conservative Tracers, Stable Isotopes, and Microbial Source Tracking to Identify the Sources and Fate of Nutrients Within the Animas River

Justin R. Nichols^{1*}, Rachel L. Mixon^{2*}, Zachary M. Shephard^{3*}, and Benjamin S. Linhoff⁴

jrnichols@usgs.gov¹

Hydrologist

rlmixon@usgs.gov²

Hydrologist

zshephard@usgs.gov³

Hydrologist

*U.S. Geological Survey, New Mexico Water Science Center

blinhoff@usgs.gov⁴

Research Hydrologist

U.S. Geological Survey Water Mission Area

Abstract 3 – Oral

Nutrients play a critical role in a functioning ecosystem; however, anthropogenic sources can lead to unbalanced nutrient cycles, causing nutrient excess, eutrophication, harmful algal blooms (HABs), and water quality degradation. The Animas River is a major tributary within the San Juan River watershed that provides water to multiple municipalities and irrigated agriculture, but nutrient concentrations within the river have occasionally exceeded the Clean Water Act total maximum daily loads, resulting in localized HABs and water quality impairment. A better understanding of the source of these nutrients is critical to effectively implement best management practices to mitigate the negative effects of excess nutrients. During a one-year study, we leveraged a multi-tracer approach coupled with a Bayesian mixing model (MixSIAR) and novel microbial source tracking techniques to quantify nutrient sources at nine sampling sites through 125 miles of river continuum of varying land-use (Figure 1).

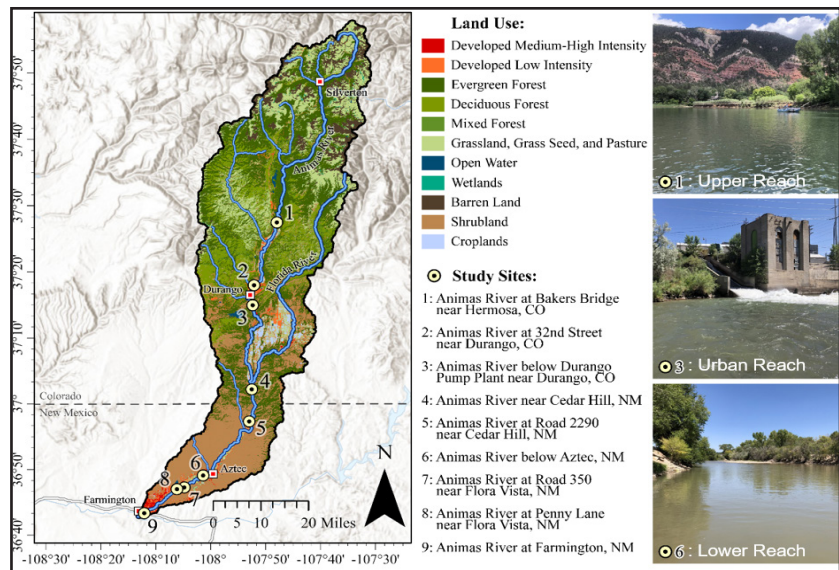


Figure 1. Animas River watershed color coded by land-use type with sampling sites annotated in numerical order from upstream to downstream.

Our results indicate that dissolved organic carbon, nitrate plus nitrite, and total phosphorus loads in the Animas River were substantially higher during the high streamflow monsoon season and generally increased in downstream reaches. Regardless of seasonal weather fluctuation the dominant source of nutrients transitions from ammonium in precipitation and fertilizer in the upstream reach to soil nitrogen, domestic sewage, and manure further downstream. Microbial source tracking results support the change in nutrient sources by indicating an increase in human fecal markers within the middle stream reach between Durango CO and Aztec NM, while there was an increase in waterfowl fecal markers in the lower stream reach between Aztec NM, and Farmington, NM. Our multi-tracer approach concludes that domestic sewage and animal waste are the primary sources of nutrient exceedances within the middle and lower reaches of the Animas River.

Using Influence Functions in Contaminated Data to Identify the Outliers

Prabha Shrestha
prabha.shrestha@enmu.edu
Eastern New Mexico University, Portales, NM

Abstract 4 – Oral & Poster

Sufficient dimension reduction (SDR) models are very popular in the past two decades in regression analysis. However, most current methods do not have robustness in mind when they were built. Therefore, these methods may under-perform when the distribution of the predictors is heavy-tailed or when outliers exist in the data. We introduce robust dimension reduction methods using the concept of influence function. An influence function (IF) measures the sensitivity of a functional to small perturbations from the data. We investigated the IF of several functionals and settled on the one for canonical correlation in our research. During our research, we also observed that using this tool, we can identify the outliers that affect the estimation process. So in this presentation I will show an overview of how IF can play an important role in identifying the outliers in a contaminated data. A simulation study will be discussed and presented.

Near Real-Time Suspended Sediment and Metals Concentrations Derived from Hydroacoustic-Turbidity Surrogate Measurements Using the Lisst-Aobs in the Animas River near Cedar Hill, New Mexico

Jeb E. Brown¹, Justin R. Nichols², Grady P. Ball³, Johanna M. Blake⁴, Bryan J. Rezin⁵, Caleb Van Zante⁶

jebbrown@usgs.gov¹
Hydrologist

jrnichols@usgs.gov²
Hydrologist

gball@usgs.gov³
Hydrologist

jmtblake@usgs.gov⁴
Research Hydrologist

brezin@usgs.gov⁵
Hydrologic Technician

cvanzante@usgs.gov⁶
Hydrologist

U.S. Geological Survey, New Mexico Water Science Center, Albuquerque, NM
6700 Edith Blvd NE Albuquerque, NM 87113

Abstract 5 – Oral

Metals adsorbed to suspended sediments pose a potential health risk to communities that depend on surface water for domestic and agricultural uses. The Animas River in southern Colorado and northern New Mexico has been shown to transport elevated concentrations of metals due in part to the rocks through which the river flows. These constituents have been documented as preferentially sorbing to clay-sized suspended sediments. Surrogate methods for estimating suspended-sediment concentration (such as turbidity, hydroacoustic, laser diffraction, and densimetric) have been widely published in the literature. Surrogate measurements, such as measured by the LISST-AOBS (a paired turbidity and acoustic sensor) instrument explored in this project, can provide near-real-time suspended sediment and metal concentrations. Near real-time measurements could inform daily operational changes by downstream water managers. Temporally dense surrogate data (values collected every 15 minutes) can also increase our understanding of transport mechanisms of metals and suspended-sediment concentration. However, rivers with widely varying suspended particle sizes reduce the reliability of surrogate measurements. The objective of this work is to determine if a regression model can be developed by correlating hydroacoustic-turbidity measurements (LISST-AOBS instrument) with suspended-sediment concentration and concentrations of metals such as aluminum, arsenic, and lead in unfiltered surface water samples. Regression model results estimating suspended sediment, aluminum, arsenic, and lead concentrations will be presented. Comparison of model approaches, including machine learning models using Support Vector Machine and XGBoosted Random Forest, will also be presented.

Geologic Unit Distribution and Chemical Weathering Indices as a Method to Evaluate Lithological Sources of Aluminum, Arsenic, and Lead to the San Juan River, Four Corners Region, USA

Christina L. Ferguson¹, Johanna M. Blake², Caleb A. Van Zante³, Rachel Mixon⁴

cferguson@usgs.gov¹
Hydrologist

jmtblake@usgs.gov²
Research Hydrologist

cvanzante@usgs.gov³
Hydrologist

rlmixon@usgs.gov⁴
Hydrologist

U.S. Geological Survey, New Mexico Water Science Center, Albuquerque, NM
6700 Edith Blvd NE Albuquerque, NM 87113

Abstract 6 – Oral

In arid to semi-arid landscapes, sporadic monsoonal events, varying widely in scale and distribution, can generate streamflow in ephemeral channels that often contain sediments that are the result of the weathering and erosion of local geologic units. These sediments will become suspended in water during storm events and can then be carried to perennial streams. The sediments may contain elevated levels of metals depending on their geologic provenance and thus they can be a major source of trace metals detected in local waterways. To evaluate the potential contribution of aluminum, arsenic, and lead to the San Juan River by the geology, the distributions of geologic units were calculated for twelve hydrologic basins within the greater San Juan River watershed and data for the aluminum, arsenic, and lead concentrations in these units were compiled from the National Geochemical Database. In addition, the chemical weathering indices were calculated for the major (greater than 5 percent coverage) geologic units in each of the twelve hydrologic basins. Results indicate that there are about 41 distinct geologic units within the San Juan River watershed, and the majority of those are sedimentary. The sedimentary geologic units with dominant coverage in the entire San Juan River watershed are: the Mesaverde Group (33.2 percent), the San Jose Formation (10.7 percent), the Glen Canyon Group (7.86 percent), the Chinle Formation (7.11 percent), the Morrison Formation (6.94 percent), the Mancos Shale (6.61 percent), and the Cutler Group (6.38 percent). The remaining units (about 34) each represent less than 5 percent of the total San Juan River watershed geology. Dominant geology in each of the twelve hydrologic basins varies by location, but each contains one or more of the units listed as dominant for the entire watershed. Of the watershed-dominant geological units, the one most susceptible to weathering is the Chinle Formation (chemical weathering index of 93.3). However, the Dakota Sandstone and the Mancos Shale both have chemical weathering indices greater than 82, indicating that, in the hydrologic basins where these units are dominant, they could be large contributors of sediment to the San Juan River. The greatest median concentrations of aluminum (81,900 parts per million), arsenic (12.0 parts per million), and lead (19.0 parts per million) are seen in the Mancos Shale. Based on its high chemical weathering index (82.6), it is possible that the Mancos Shale is a

large contributor of sediment and, therefore, aluminum, arsenic, and lead, to the San Juan River in areas where it is one of the dominant geologic units. In contrast, the Chinle Formation has the highest chemical weathering index but has relatively low median concentration values for aluminum (19,000 parts per million), arsenic (below reporting limits), and lead (below reporting limits). This indicates that, while it may contribute a large volume of sediment to the San Juan River, the Chinle Formation likely does not contribute much to the overall aluminum, arsenic, and lead concentrations in the San Juan River.

Aerial Insights: Modeling Streamflow in Ephemeral Channels along the San Juan River, Four Corners Region, USA

Caleb Van Zante¹, Jeb Brown², Zach Shephard³, Keely Miltenberger⁴

cvanzante@usgs.gov¹
Hydrologist

jebbrown@usgs.gov²
Hydrologist

zshephard@usgs.gov³
Hydrologist

kmiltenberger@usgs.gov⁴
Hydrologist

U.S. Geological Survey, New Mexico Water Science Center, Albuquerque, NM
6700 Edith Blvd NE Albuquerque, NM 87113

Abstract 7 – Poster

Streamflow plays a critical role in calculating the loads of various water quality constituents, including metals. Streamflow can be determined based on stage values (the height of water above a known reference point) when combined with a stage-discharge rating. However, in locations like ephemeral channels, where directly measuring streamflow is difficult, costly, or nearly impossible due to remote and short-duration flow events, establishing meaningful stage-discharge ratings becomes challenging. To address this, digital terrain models are used to simulate streamflow at different water depths, resulting in a model-derived stage-discharge rating for specific stream locations. Nevertheless, acquiring the necessary terrain data for developing such a rating can be time-consuming and expensive. Novel advancements in photogrammetry, coupled with low-cost uncrewed aerial systems (UAS), offer new methods for creating high-resolution terrain models using affordable digital cameras mounted on a small UAS. Due to changes in terrain and channel geomorphology, photogrammetry measurements should be repeated over time to obtain more accurate measurements, which is afforded by the low-cost UAS approach. Once meaningful terrain models are developed, scientists can use modeling tools to compute streamflow, thus allowing for an accurate estimate of loads for constituents of concern. Models developed using these tools can then be exported to a three-dimensional (3D) printer to produce a physical representation of the real-world channel morphologies. The result of streamflow estimates, loads, and an example of 3D printing capabilities of ephemeral channels in the San Juan River watershed will be presented.

Uranium and Potential Sources of Uranium to the San Juan River, Four Corners Region, USA

Rachel Mixon¹, Johanna M. Blake²

rlmixon@usgs.gov¹
Hydrologist

jmtblake@usgs.gov²
Research Hydrologist

U.S. Geological Survey, New Mexico Water Science Center, Albuquerque, NM
6700 Edith Blvd NE Albuquerque, NM 87113

Abstract 8 – Oral

Uranium (U) is found naturally in the geologic formations of the southwestern United States including in the San Juan River watershed. Historically, U has been viewed as a resource to locate and extract; the San Juan River watershed played an important role in that history. In the San Juan River watershed, U acquisition has taken many forms including exploratory borehole drilling, open pit mining, underground tunnel mining, in situ leaching, heap leaching, and U recovery through milling. Mining and other activities that seek to extract U from rock disrupts the natural geology and can increase U exposure to the environment. In the Colorado Plateau, U is hosted in geologic formations often containing aquifers or residing just below aquifers, creating an environment for increased solid-groundwater interaction that can allow for U dissolution or desorption from solids. Surface water chemistry can be influenced by many factors including groundwater chemistry and overland flow which can mobilize U-rich sediments. While many people in the San Juan River watershed have access to filtered and treated water, there are many people whose primary access to water is not reliable; those people may take advantage of ephemeral channel surface water flow, typically occurring during snowmelt or storm events, for their water needs. Therefore, to maintain local water supplies and access, it is imperative to quantify the spatial distribution, sources, and transport of U in the San Juan River watershed.

Data collected during a broader project investigating the source of metals to the San Juan River will be presented to summarize U concentrations in surface water samples collected from ephemeral and perennial tributaries to the San Juan River. The environmental protection agency (EPA) defines the maximum contamination limit (MCL) for U in drinking water as 30 µg/L. The average U concentrations from 8 sites exceeded the EPA MCL, and from 27 sites had a maximum U concentration exceeding the EPA MCL. Figure 1 depicts the study area from which data for this presentation were collected, and the maximum U concentration in unfiltered water samples associated with each tributary sampling site.

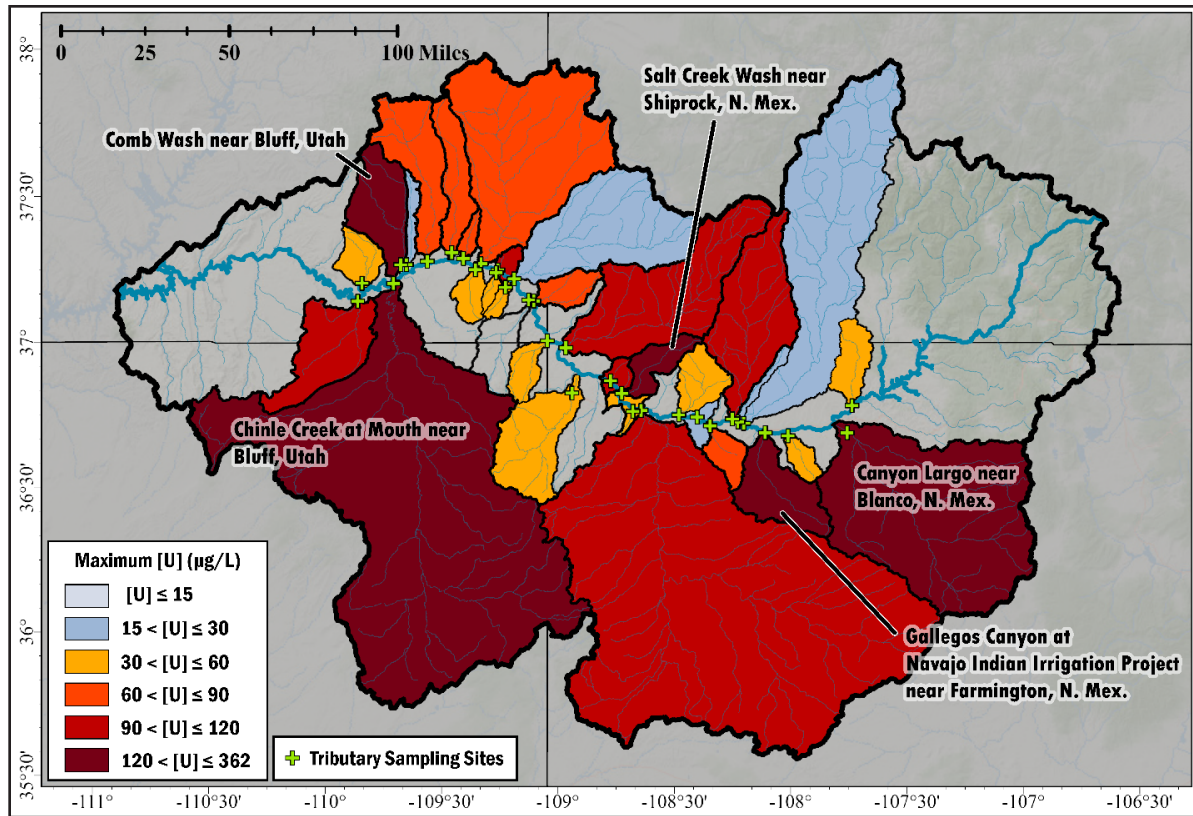


Figure 1. Study area of the broader project investigating the source of metals to the San Juan River. Tributary sub-watersheds are shaded according to the maximum concentration of U found at the corresponding tributary sampling site. Sites with maximum U concentrations below the EPA MCL are shaded with cool colors, sites with maximum U concentrations above the EPA MCL are shaded with warm colors.

The highest maximum U concentrations in unfiltered water within the study area were seen in the following tributaries: Chinle Creek at Mouth near Bluff, Utah (362 ug/L), Gallegos Canyon at Navajo Indian Irrigation Project near Farmington, N. Mex. (206 ug/L), Comb Wash near Bluff, Utah (163 ug/L), Salt Creek Wash near Shiprock, N. Mex. (155 ug/L), Canyon Largo near Blanco, N. Mex. (139 ug/L). Each watershed has a unique historic record and geologic makeup that contribute to the potential for high U concentrations in the surface water within it. The data presented here, and the inferences made from it will be used to investigate what potential sources exist upstream of sampling points that could be contributing U to the San Juan River.

Building Capacity to Implement Watershed Restoration in the San Juan Basin

Stacy Beaugh¹, Elle Benson², Steve Wolff³, Monika Rock⁴, Carrie Padgett⁵,
Mary Cornforth⁶, Alex Funk⁷

stacy@beststrategicbynature.com¹

President/Co-Owner
Strategic By Nature, Inc., Durango, CO

ebenson@trcp.org²

Theodore Roosevelt Conservation Partnership,
Albuquerque, NM

steve@swwwcd.org³

morock@swwwcd.org⁴

Southwestern Water Conservation District,
Durango, CO

carrie@durangowater.com⁵

Harris Water Engineering, Durango, CO

marycornforth970@gmail.com⁶

Strategic By Nature, Inc, Grand Junction, CO

afunk@trcp.org⁷

Theodore Roosevelt Conservation Partnership,
Denver, CO

Abstract 9 – Oral

Southwestern Water Conservation District (SWCD) and a coalition of partners are creating a community navigator program to help local proponents in the San Juan Basin to aggregate projects and access federal funding opportunities available in the Colorado River Basin through the Bipartisan Infrastructure Law (BIL) and Inflation Reduction Act (IRA).

The program is comprised of the following components:

- **Implement a programmatic approach to funding water conservation and drought resilience:** Position SWCD to apply for federal dollars to expand their local water grant program to distribute funds to local partners and provide coordination support to secure matching dollars.
- **Support project development:** Connect project proponents to resources to help them further develop their projects (e.g., grant writing, project design and engineering, collaborative support, etc.).
- **Build a regional projects database.** Gain an understanding of the types of projects that exist in the region, and then be able to bundle projects according to project type, landownership, geography, or other likenesses to present a collection of projects that achieve a larger scale and, thus, higher funding request amount, both of which are of interest to federal and state funders.
- **Advocate for funding to support local needs.** TRCP supports policy efforts that connect local funding needs with national, regional, and state funding programs.

Theodore Roosevelt Conservation Partnership (TRCP), www.trcp.org, a policy-oriented nonprofit with the mission to guarantee all Americans quality places to hunt and fish, is providing support for this program. This work leverages recommendations from the July 2022 TRCP report, *Challenges in Accessing and Utilizing Federal Funding to Support Cross-Boundary Watershed Scale Restoration*.

Aluminum, Arsenic, and Lead in the San Juan River Watershed

J.M. Blake¹, Steve.A. Austin², Fred Johnson³, Jeb Brown⁴, Shaleene Chavarria⁵, Rachel Mixon⁶
Caleb Van Zante⁷, Kate Wilkins⁸, Mike Whiting⁹, Christina L. Ferguson¹⁰, Zach Shephard¹¹
Keely Miltenberger¹², Tristan Austring¹³, Zev Ratigan¹⁴, Anani Shomour¹⁵, Doug Yager¹⁶

jmtblake@usgs.gov^{1,a}
Research Hydrologist

mwhiting@usgs.gov^{9,a}
Physical Scientist

nnepawq@frontiernet.net^{2,b}
Sr. Hydrologist

cferguson@usgs.gov^{10,a}
Hydrologist

navajoh2o@hotmail.com^{3,b}
Environmental Specialist

zshephard@usgs.gov^{11,a}
Hydrologist

jebbrown@usgs.gov^{4,a}
Hydrologist

kmiltenberger@usgs.gov^{12,a}
Hydrologist

schavar@usgs.gov^{5,a}
Hydrologist

taustring@usgs.gov^{13,a}
Physical Scientist

rlmixon@usgs.gov^{6,a}
Hydrologist

zratigan@usgs.gov^{14,a}
Student Hydrologist

cvanzante@usgs.gov^{7,a}
Hydrologist

ashomour@usgs.gov^{15,a}
Hydrology Student

katewilkins17@gmail.com^{8,a}
Hydrologist

douglasyager@gmail.com^{16,c}
Geologist

^aU.S. Geological Survey, New Mexico Water Science Center, Albuquerque, NM 87113

^bNavajo Nation Environmental Protection Agency, Window Rock, AZ and Shiprock, NM

^cU.S. Geological Survey, Geology, Geophysics, Geochemistry Science Center, Lakewood, CO

Abstract 10 – Oral

The San Juan River is an important water source in the Four Corners region. During routine monitoring, staff from the Navajo Nation EPA identified elevated concentrations of aluminum (Al), arsenic (As), and lead (Pb) in the San Juan River. To further evaluate the inputs of these elements to the San Juan River, unfiltered surface water samples were collected from tributaries to and the main stem of the San Juan River during a range of hydrologic regimes, including baseflow and storm events in 2021 and 2022. Overall, concentrations of Al, As, and Pb were lower in 2021 than in 2022, which may be related to more rain events in the region in 2022 which could mobilize more metals from sediments into the water. The maximum unfiltered Al concentration (441 mg/L) in 2021 was measured in the San Juan River at Bloomfield while the maximum concentration (1,300 mg/L) in 2022 was measured in the San Juan River at the Four Corners. Maximum As concentration in 2021 was 70 µg/L at the San Juan River near Bluff (Mexican Hat) and in 2022 was 170 µg/L from San Juan River at Nenahnezad and Shiprock. The maximum Pb concentration in 2021 was 580 µg/L from San Juan River at Nenahnezad and in 2022 was 1,500 µg/L from the San Juan River at Four Corners. The variation in metals inputs among locations of metals inputs suggests that there could be multiple sources of Al, As, and Pb to the San Juan River. Results from the 2-year study will be presented.

Understanding *E.coli* in the San Juan Watershed: Preliminary Data Gap Analysis and Recommendations for a Multijurisdictional *E.coli* Watershed Monitoring Program

Alyssa Richmond
alyssa.richmond94@gmail.com
Environmental Project Manager
Animas Environmental Services, Farmington, NM

Abstract 11 – Oral

Surface water contamination of *Escherichia coli* (*E.coli*) and its positive correlation to human health risk from other more harmful pathogenic bacteria has been an ongoing concern within the San Juan Watershed (Watershed) since *E.coli* was adapted as a water quality standard in the Four Corners in 2004. As a species of fecal bacteria that lives in the intestines of all mammals, *E.coli* alone cannot provide a definitive link to sources of fecal pollution. Microbial Source Tracking (MST) is a suite of analytical methods that quantifies DNA markers correlating to specific hosts. On behalf of the Water Infrastructure Improvements for the Nation (WIIN) Act Group, Animas Environmental Services conducted an analysis on the availability and spatial and temporal trends of *E.coli* and microbial source tracking data within the Watershed between 2004 and 2021 to potentially identify sources of fecal pollution.

A total of 2,875 *E.coli* and 1,011 microbial source tracking samples collected from 410 discrete sample locations over 117 waterways comprised the dataset included in this analysis. Data was acquired through a download of publicly available data from the U.S. Environmental Protection Agency (USEPA) Water Quality Portal and provided by collaborating entities. Data included in the analysis underwent a thorough quality assurance process via data mapping, Microsoft Access Append Queries, and data scrubbing using Microsoft Excel to ensure that results originated from comparable methods and had the integrity of their metadata preserved during the database consolidation process.

Sample locations generally had the highest density in the middle and upper portions of the Watershed in the Upper San Juan, Animas, Middle San Juan, Mancos, and McElmo sub-watersheds of Colorado and New Mexico. In comparison, sample location density was less in the western portions of the Watershed in the Navajo Nation and Utah. Approximately 17% (487 results) of the 2,875 *E.coli* samples were over the USEPA Recreational Water Quality Criteria (RWQC) for primary recreation. Of note, the percentage of exceedances over the USEPA RWQC for each sub-watershed within the dataset were calculated for the Upper San Juan (17%), Middle San Juan (27%), Animas (11%), Lower San Juan – Four Corners (20%), McElmo (16%), and Lower San Juan (17%) sub-watersheds. A limited and preliminary temporal analysis indicated that exceedances over the USEPA RWQC were more prevalent between May and October. A total of 38 out of 117 waterways met the minimum sample size required for a preliminary statistical analysis and had varied standard deviations, indicating that *E.coli* results are highly variable over time. Out of these 38 waterways, seven had no exceedances and/or detections of *E.coli*, 13 had one or more exceedances over the USEPA RWQC but below the *E.coli* quantification limit, and 18 waterways had one or more *E.coli* results that were at the quantification limit. While limited in comparison to the *E.coli* data included in the analysis, MST has been done by the San Juan Watershed Group in the Animas, Upper San Juan, and Middle San Juan sub-watersheds between 2013 and 2021. MST sampling was

conducted for human, ruminant, bird, cow, general bacteroides. Based on 2013 and 2014 dataset, human source bacteria was detected 77% of the time and ruminant source bacteria was detected 94% of the time in the Animas and San Juan Rivers in New Mexico.

Urban development, wastewater treatment infrastructure, irrigated pasture, and grazing were preliminarily analyzed for potential impacts to fecal contamination in waterways within the Watershed. Urban development is limited to the upper portions of the Watershed in New Mexico and Colorado, generally correlating to the higher sampling density in these regions. Approximately 85% (79) of the 93 communities within the Watershed are unincorporated rural communities that have not had their adjacent waterways sampled frequently, if at all. Wastewater infrastructure mirrors this pattern with wastewater treatment plants concentrated in the upper portions of the Watershed near incorporated communities, indicating that much of the Watershed downstream of Shiprock, New Mexico, are on on-site liquid waste systems. Irrigated pasture is also highly concentrated in the upper portions of the Watershed within the waterways. Each of these land use and land cover conditions may indicate potential correlations to *E.coli* concentrations exhibited and require further research.

Limited conclusions could be made based on the currently extensive, but relatively unrobust dataset, to definitively define potential vectors of fecal contamination to surface waters. Further development and implementation of a watershed scale *E.coli* and MST monitoring program, protocols for assembling and sharing datasets, and a regional quality assurance project plan is recommended to build a dataset that can support efforts to prioritize waterways for watershed planning on a multijurisdictional scale.

Surface Water Quality Bureau Harmful Algal Blooms Program

Nathaniel Kamm
Nathaniel.Kamm@env.nm.gov
Water Quality Standards Scientist
Surface Water Quality Bureau
New Mexico Environment Department, Santa Fe, NM

Abstract 12 – Oral

Harmful algal blooms (HABs) are overgrowths of algae that pose a health risk to people and animals. HABs in New Mexico are caused by cyanobacteria, also known as blue-green algae. Some cyanobacteria blooms can produce cyanotoxins with a potential to severely affect human and animal health. HABs have become a more common occurrence in New Mexico's lakes. As a growing environmental and public health concern, New Mexico Environment Department's Surface Water Quality Bureau (SWQB) is ramping up efforts to address HABs in New Mexico. Working with federal, state, and local agencies, the SWQB is increasing the state's capacity to monitor, assess, and communicate HABs risks to the public.

2024 Participant List

Art Allison

Arthur Allison Jr.
Desert River Guides

Anik Alvi
New Mexico Water Resources
Research Institute

Beth Anderson
United States Forest Service

Rachael Apodaca
Bureau of Land Management

Kylie Arrieta
New Mexico Water Resources
Research Institute

Steve Austin
Navajo Nation Environmental
Protection Agency

Kristin Barnett
WaterVation

Stacy Beaugh
Strategic By Nature, Inc.

Eddie Begay

Johanna Blake
United States
Geological Survey

Scott Brake
Public Service Company
of New Mexico

Janice Brown
Pioche Food Group

Jeb Brown
United States Geological
Survey

Michael Brown
San Juan Soil and Water
Conservation District

Henry Bulloch
San Juan Watershed
Group, Inc.

Oni Butterfly
Past: Groundwater Section
Chief EPA Region II

Sarah Cerra
Alamogordo Public Schools

Linda Corwin

Bart Deming
United States Bureau
of Reclamation

Heather Dostaler
San Juan Soil & Water
Conservation District

Delilah Dougi
New Mexico Environment
Department / Ground Water
Quality Bureau

Ryan Dudgeon
Desert River Guides

Katie Dunnahoo
New Mexico Water Resources
Research Institute

Shandi Edgar
Edgars Farm

Anthony Edwards
Bonita Peak Mining District
Community Advisory Group

James Evangelisti
Southern Ute Indian Tribe

Christina Ferguson
U.S. Geological Survey-
New Mexico Water
Science Center

Sam Fernald
New Mexico Water Resources
Research Institute

Joseph Fox
New Mexico
Environment Department

Brandon Francis
New Mexico State University
Agricultural Science
Center Farmington

Isaac Garza
New Mexico Water Resources
Research Institute

Alice Gomez
The University of New Mexico

Lynette Guevara
New Mexico Environment
Department / Surface Water
Quality Bureau

Lisa Hale-BlueEyes
San Juan County

Jocelyn Harimon
New Mexico Environment
Department / Surface Water
Quality Bureau

Gary Hathorn
San Juan Soil & Water Conser-
vation District

Nicole Heckathorn
New Mexico State University /
Student

Jessica Hubbling
New Mexico Environment
Department-Ground Water
Quality Bureau

Kyle Jim
Dine Introspective

Fred Johnson
Navajo Nation EPA Water
Quality / National Pollutant
Discharge Elimination System

Nathaniel Kamm
New Mexico
Environment Department

Ron Kellermueller
New Mexico Department
of Game and Fish

Jillian Kugle
Southern Ute Indian Tribe

Breanna Lameman
The University of Arizona

Gloria Lane
Navajo Ethno Agriculture

Derrick Lee
Navajo Abandoned
Mine Lands Reclamation
Department

Shelly Lemon
New Mexico
Environment Department

Kevin Lombard
New Mexico State University
Agricultural Science
Center at Farmington

Jaden Love
New Mexico State University

Yessenia Lugo Homs
United States Environmental
Protection Agency, Region 6

Cayden Manuelito
New Mexico State University

Eluid Martinez

Lee Anna Martinez
Navajo Nation Environmental
Protection Agency

Marcella Martinez

Art Mason

Sarah McCarthy
Northern Arizona University
School of Forestry

Emiliano McLane
New Mexico State University

Rachel Mixon
United States
Geological Survey

Paul Montoia
Farmington Community
Member

Korbin Nakai
New Mexico Farmington
Agriculture Science Center

M Nee
LACD

Justin Nichols
United States
Geological Survey

Norman Norvelle
San Juan Watershed Group, Inc.

Itofa-Oghena Osigbemhe
Chukwuemeka Odumegwu
Ojukwu University

Ruth Pannill
Indigenous Resilience Center -
University of Arizona

Justin Pioche
Pioche Food Group

Tia Pioche
Pioche Food Group

Chara Ragland
Bonita Peak Mining
District Community
Advisory Committee

Bryan Rezin
United States
Geological Survey

Alyssa Richmond
Animas Environmental
Services

Rob Runkel
United States
Geological Survey

Tom Schillaci
Environmental
Documentary Video

Mark Sheely
New Mexico Water Resources
Research Institute

Prabha Shrestha
Eastern New Mexico
University, Portales

Noah Silber-Coats
United States Department
of Agriculture Southwest
Climate Hub

Courtney Spencer
San Juan Soil & Water
Conservation District

Elizabeth Stuffings
New Mexico
Environment Department

Rin Tara
The University of New Mexico
Utton Center

William Thomas
AES

Shirley Tolth
National Security Agency

Jeanette Torres
New Mexico Water Resources
Research Institute

Michele Truby Tillen
San Juan County

Claudia Trueblood
New Mexico
Environment Department

Adriano Tsinigine
United States Fish
& Wildlife Service

William Turner

WaterBank

Diane Van Hoy

New Mexico
Environment Department

Caleb Van Zante

United States Geological
Survey, New Mexico Water
Science Center

Pilja Vitale

New Mexico State University

Margie Whitcotton

United States Department
of Agriculture National
Agriculture Statistics Service,
New Mexico Field Office

Michael Whiting

United States
Geological Survey

Jared Wood

New Mexico
Environment Department

Owen Yazzie

Bowling Green
State University

Rueisha Yazzie

San Juan College

Meredith Zeigler

Surface Water Quality Bureau



New Mexico Water Resources Research Institute
3170 S. Espina Street
New Mexico State University
Las Cruces, NM 88003-8001

(575) 646-4337 • nmwrrri@nmsu.edu